A New Population of Galactic Bulge Planetary Nebulas

By

Travis Stenborg

A thesis submitted to Macquarie University
for the degree of
Doctor of Philosophy
Department of Physics and Astronomy
January 2016

Typeset in LaTeX 2_ε.

Except where acknowledged in the customary manner, the material presented in this thesis is, to the best of my knowledge, original and has not been submitted in whole or part for a degree in any university.

Travis Stenborg

Contents

Abstract

A new population of Galactic bulge planetary nebulas is presented. Nebula candidates were discovered by systematically reviewing archival [O III] on/off band survey imaging of the central $-5^\circ \leqslant l \leqslant 5^\circ$, $-5^\circ \leqslant b \leqslant 5^\circ$ region around the Galactic centre. An image segmentation and interleaving scheme was developed to facilitate this review. The resultant candidates (> 200) were then double checked against complementary archival Hα sky survey data to screen for obvious planetary nebula (PN) mimics or spurious image artefacts.

Confirmatory spectroscopy of the PN candidates was pursued with thin slit, fibre multi-object and wide field spectrographs. Custom software was built to streamline interfacing with third-party spectroscopic management tools and a parallel greedy set cover algorithm implemented for efficient field selection in constrained multi-object observations.

The combined imaging and spectroscopic evidence yielded true (4), probable (31) and possible (83) PNs toward the bulge. Secondary discoveries such as new PN mimics and late-type stars were by-products of the confirmatory spectroscopy. Instances of literature PN duplication encountered during the investigation were noticed and documented.

Spectral analysis of new PNs, including those obtained with a new optimised sky subtraction technique devised and demonstrated here, provided diagnostic data allowing radial velocity and Balmer decrement determination. Using a combined diameter and radial velocity criterion, bona fide bulge PNs were distinguished from new foreground PNs. Where Balmer decrements were available for new bulge PNs, differential aperture photometry was used to provide a modest data increment to Galactic bulge planetary nebula luminosity function (PNLF).

The PNLF was revised with data from some new bulge PNs, but more significantly, by a series of corrections to the data derived from previously known bulge PNs ($\sim$225), such as improved filter transmission effects, statistically justified binning and application of a uniform bulge-relevant extinction law. The result was the most rigorous bulge PNLF to date. An improvement on the legacy PNLF, the revised PNLF exhibited a form inconsistent with typical extragalactic examples, an expected result of the unusual extinction correction method used to address bulge-specific observational limitations. Issues restricting the accuracy of the bulge PNLF were identified. Until those restrictions are ameliorated, the utility of the PNLF in aiding physical understanding of its constituent members or their progenitors cannot be realised.

Acknowledgements

The efforts of all members of Macquarie University's Department of Physics and Astronomy who contributed to the completion of this thesis are appreciated. Internal and external contributors to this project via supervisory, proposal preparation or other efforts include, but are not limited to, Ivan Bojičić, Russell Cannon, Judith Dawes, Orsola De Marco, Dimitri Douchin, Danica Drašković, David Frew, George Jacoby, Matthias Kronberger, Carol McNaught, Quentin Parker, Lizette Ramirez-Guzman, Raghvendra Sahai, Richard Shaw, Lee Spitler, Frédéric Vogt and Albert Zijlstra. Special thanks go to Orsola De Marco, Macquarie University, for guidance in improving the scientific rigour of this work. Special thanks go also to Lee Spitler, Macquarie University, for proactive service observing with the AAOmega spectrograph on the 3.9 m Anglo-Australian Telescope (AAT).

Thanks go to Donna Burton, University of Southern Queensland, for providing guidance in the use of the Wide Field Spectrograph (WiFeS), Telescope Automation and Remote Observing System (TAROS) and Telescope Control System on the Australian National University (ANU) 2.3 m telescope. Thanks go to Aaron Rizzuto, the University of Texas at Austin, for a modest donation of unused observing time on that same telescope.

Primary financial support for this research was provided by a Macquarie University Research Excellence Scholarship. Supplemental funding was provided by contributions from a Gutenberg Chair award, the Macquarie University Postgraduate Research Fund, a Macquarie University Research Development Grant and miscellaneous departmental level funding.

This research is partly based on observations made with the *Spitzer Space Telescope*, which is operated by the Jet Propulsion Laboratory (JPL), California Institute of Technology (Caltech), under contract with NASA. Observations made with the NASA/European Space Agency (ESA) *Hubble Space Telescope* (*HST*), obtained from the data archive at the Space Telescope Science Institute (STScI), were also used. STScI is operated by the Association of Universities for Research in Astronomy (AURA), Inc. under NASA contract NAS 5-26555.

Additionally, this research used online resources:

- selected imaging data sourced online and presented here, were obtained with the Andalucia Faint Object Spectrograph and Camera (ALFOSC), which is provided by the Instituto de Astrofisica de Andalucia under a joint agreement with the University of Copenhagen and the Nordic Optical Telescope Scientific Association (NOTSA),
- services and data provided by the National Optical Astronomy Observatory (NOAO)

Science Archive. NOAO is operated by the AURA, Inc. under a cooperative agreement with the National Science Foundation,

- the Atomic Spectra Database (Kramida et al., 2014), hosted by the National Institute of Standards and Technology,
- the European Southern Observatory (ESO) Science Archive Facility, including imaging obtained with ESO telescopes at the La Silla Paranal Observatory under program 179.B-2002(B),
- the NASA Astrophysics Data System (ADS), hosted by the Harvard-Smithsonian Center for Astrophysics,
- the NASA/Infrared (IR) Processing and Analysis Center (IPAC) Infrared Science Archive, operated by the JPL, Caltech, under contract with NASA,
- the NASA/IPAC Extragalactic Database (NED), operated by the JPL, Caltech, under contract with NASA,
- the SIMBAD (Set of Identifications, Measurements and Bibliography for Astronomical Data, Wenger et al., 2000) and VizieR (Ochsenbein et al., 2000) databases and Aladin sky atlas (Bonnarel et al., 2000), all hosted by the Centre de Données astronomiques de Strasbourg (Strasbourg Astronomical Data Centre),
- and the Spanish Virtual Observatory (SVO) supported by the Spanish Ministerio de Ciencia e Innovación (Ministry of Science and Innovation) / Ministerio de Economiá y Competitividad (Ministry of Economy and Competitiveness) through grants AyA2008-02156 and AyA2011-24052.

Where the thesis discusses material also presented in the author's publications released over the course of the project (appendix D), selected elements are closely based on that published material but referenced, and verbatim reproduction generally avoided. Where material has been included for which reproduction is logical, such as algorithms, equations or figures, references are generally provided. In case of inadvertent reference omission, material is included from Stenborg & Parker (2014) and Stenborg (2014, 2015, 2016)[1].

Thesis preparation was done with the MacTEX typesetting environment (Schulz, 2005) and incorporated the ADS bibliographic identifier standard (Schmitz et al., 1995).

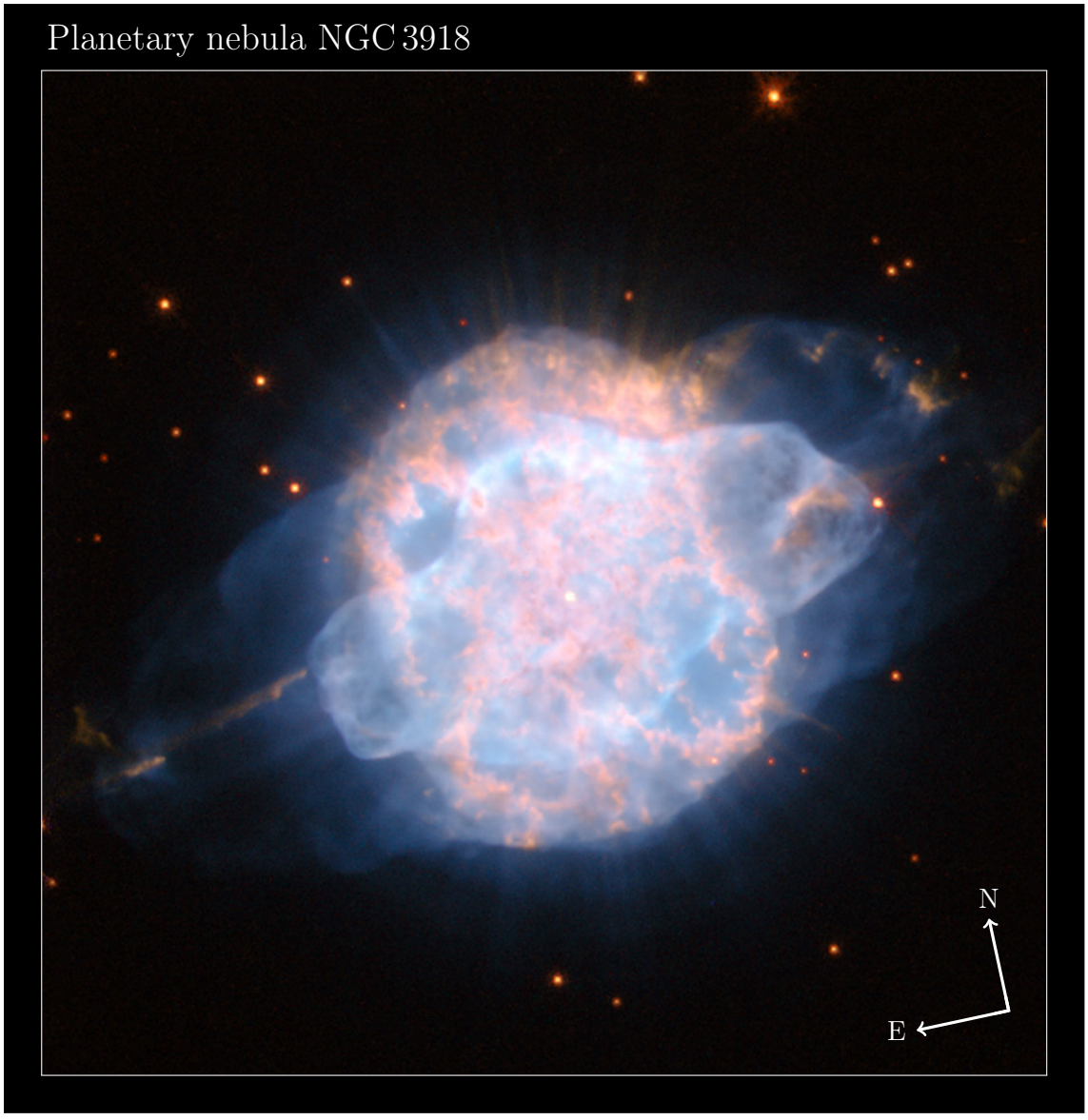

FIGURE 1: Southern sky planetary nebula NGC 3918 (Evans & Thackeray, 1950), taken with the Wide Field Planetary Camera 2 (WFPC2) on the *HST*. The image is a synthetic colour image, built using data from the camera's F502N (mean wavelength $\bar{\lambda} = 501.2\,\text{nm}$), F555W ($\bar{\lambda} = 520.2\,\text{nm}$), F658N ($\bar{\lambda} = 659.1\,\text{nm}$) and F814W ($\bar{\lambda} = 820.3\,\text{nm}$) filters (McMaster & et al., 2008), displayed in blue, green, red and orange respectively, over a a $33'' \times 33''$ field of view (FOV). Image courtesy NASA/ESA *HST* and STScI/AURA.

Nomenclature and Style

Abbreviations and Acronyms

Abbreviations and acronyms are introduced once, in either singular or plural form, appropriate to context. A subsequent, separate definition for the opposite form will not be given. Plural forms are easy to identify however, being suffixed with a lower case letter. For example, planetary nebula (PN) or white dwarfs (WDs), may be introduced as abbreviations but PNs and WD for the opposing forms subsequently used without explicit definition. Only the singular form will be defined in the list of abbreviations and acronyms.

Anglicised Latin Plurals

Anglicised latin plurals for certain astronomical phenomena are adopted here, e.g. "planetary nebulas" and "supernovas", instead of "planetary nebulae" and "supernovae". The adopted plural forms are valid (Stevenson, 2010), but an acknowledged departure from the general practice in the discipline. This is intended as a demonstration of alternate practice and driver of language change.

This approach to astronomical Latin plurals is not without precedent (Ball, 1928). Indeed the form "planetary nebulae" itself evolved from a previous accepted form using a ligature, "planetary nebulæ" (Herschel, 1785), coined by a scientist himself a proponent of anglicisation (Herschel anglicised his own name, Harland, 2007). Moreover, the approach was not arbitrary, it was adopted in response to repeatedly witnessing confusion over their pronunciation and written usage by academics. Mispronunciation of Latin scientific terms in academic settings is not new and efforts have been made to address the issue (Craver, 1947). Using anglicised Latin plurals however, has the pragmatic value of minimising such confusion. Pronunciation of a suffixed "s" is less ambiguous than the diphthong "ae", and errors in written communication are deemed less likely due to conformance with an established norm for English plurals. This is a manifestation of Zipf's Principle of Least Effort leading to more efficient communication, with articulation made easier for the communicator, without making comprehension harder for the recipient (Carston, 2005).

Astronomical Coordinates

Astronomical coordinates are given truncated, not rounded, as per Dickel et al. (1987).

Dark, Grey and Bright Time

The following definitions of dark, grey and bright time, in terms of lunar illumination fraction, are assumed here:

Dark time:	$< 15\%$ or Moon below the horizon.
Grey time:	15%–85%.
Bright time:	$> 85\%$.

I. S. Shklovsky

Scientist I. S. Shklovsky developed a statistical distance determination method for PNs (e.g. Osterbrock & Ferland, 2006). The native form of his surname is in Russian Cyrillic, Шкловский (e.g. Shklovsky, 1951). This surname, and associated scientific terminology, has historically been transliterated into Latin script inconsistently, e.g.:

Shklovski	(Benedict et al., 2009),
Shklovskii	(Jacoby et al., 1998),
Shklovskiĭ	(Minkowski, 1964),
Shklovskij	(Weinberger & Ziener, 1988),
Shklovskiy	(Oster, 1961),
Shklovsky	(Buckley et al., 1993),
Shklowskii	(De Marco et al., 2001),
Shlowskii	(Preite-Martinez, 1988).

Here, when referring to a literature reference, any transliteration used in the reference's bibliographic details will be maintained. When discussing the PN distance determination method and related scientific concepts however, the form "Shklovsky" will be used. This form is used because it is succinct and consistent with anglicised language forms adopted here.

Mathematical Symbols

Mathematical symbols are presented here in their standards forms. It is noted however that the symbol $\sim$ is used to denote either a relationship between quantities having the same order of magnitude or being very approximately equal. The two meanings are distinct, but the symbol's intended meaning is generally identifiable from context. The symbol $\approx$ is intended to denote the related, but different, relationship of approximately equal, e.g.:

$6.60 \times 10^2 \sim 8.40 \times 10^2$	same order of magnitude.
$6.60 \times 10^2 \sim 7.00 \times 10^2$	very approximately equal to.
$6.60 \times 10^2 \approx 6.59 \times 10^2$	approximately equal to.

PN Common Names

Common names for PNs are avoided in this work. Whilst some common names are well recognised within the PN research community, or even referenced in SIMBAD as identifiers, they can be informal and non-authoritative. IC 418 for example, is known not only as the Spirograph Nebula, but also as the Chameleon Nebula, Raspberry Nebula (Bakich, 2010), etc. A formal scientific designation reduces ambiguity.

Spacecraft

The names of spacecraft, including space telescopes, are denoted here in italics, e.g. the *Hubble Space Telescope*.

Spectral Lines

The stellar spectral classification convention of denoting spectral line wavelength in angstroms with a prefixed Greek λ, rather than appended with the angstrom symbol Å, is adopted here. For example, Hα λ6563, not Hα 6536 Å. Two or more lines in a series, or a spectral range, are prefixed $\lambda\lambda$, e.g. [O III] $\lambda\lambda$4959, 5007.

A summary of atomic spectral features referenced in this work is provided in appendix A. In general, features discussed outside of the appendix will be referenced rounded to the nearest angstrom.

Symbiotic Star Classes

Symbiotic stars (SySs) can be grouped into two classes. Examination of their 1–4 μm continuum shows one class dominated by dust emission, type D, and another class with only a cool companion star, type S (Allen, 1982). These are referred to in this work hyphenated and in lower case, i.e. d-type and s-type, to avoid confusion with the S-type late-type giant stars (e.g. R Gem, Keenan, 1954), as is done by Gray & Corbally (2009).

Transition Lines

Spectral lines resulting from atomic transitions are denoted using a square bracket system, depending on the transition type, as per, for example, Kitchin (1995):

Allowed:	no brackets, e.g. Hα λ6563.
Semi-forbidden:	one bracket, e.g. C III] λ1909.
Forbidden:	two brackets, e.g. [O III] λ5007.

List of Abbreviations, Acronyms and Symbols

2dF	Two-degree Field
2dFdr	2dF data reduction package
2MASS	Two Micron All Sky Survey
6dF	Six-degree Field
a	Generic real number variable
AAO	Anglo-Australian Observatory (to June 30, 2010)
AAO	Australian Astronomical Observatory (from July 1, 2010)
AAT	Anglo-Australia Telescope
ADS	Astrophysics Data System
ADU	Analog to digital units
AGB	Asymptotic giant branch
ALFOSC	Andalucia Faint Object Spectrograph and Camera
ANU	Australian National University
APT	Aperture Photometry Tool
ATT	Advanced Technology Telescope
AURA	Association of Universities for Research in Astronomy
$A(V)$	Absolute visual extinction
$A(\lambda)$	Absolute extinction at wavelength λ
b	Galactic latitude
B-W	Baade-Wesselink distance determination method
c	Speed of light

Caltech	California Institute of Technology
CCD	Charge-coupled device
CCDSpec	CCD spectrograph
CE	Common envelope
CGPN	Catalogue of Galactic Planetary Nebulae
$c(\mathrm{H}\beta)$	Logarithmic Balmer decrement
CSPN	Central star of a planetary nebula
CTIO	Cerro Tololo Inter-American Observatory
D_{xy}	Pixel data value at CCD physical coordinate (x, y)
d	Distance
DEB	Detached eclipsing binary
Dec	Declination
DSH	Deep Sky Hunters
$\mathrm{D_n}$-σ	Photometric diameter-velocity dispersion distance determination method
$E(B-V)$	Selective extinction
ESA	European Space Agency
ESO	European Southern Observatory
F	Flux
f	Focal length
$f(\lambda)$	Extinction factor
FITS	Flexible Image Transport System
FLAIR	Fibre-Linked Array-Image Reformatter
FOV	Field of view
FWHM	Full width at half maximum
GALEX	*Galaxy Evolution Explorer*
GCLF	Globular cluster luminosity function

GLIMPSE Galactic Legacy Infrared Mid-Plane Survey Extraordinaire

GUI Graphical user interface

h Planck constant

$\hbar$ Reduced Planck constant

$\hat{h}$ Bin size

HERMES High Efficiency and Resolution Multi-Element Spectrograph

HST *Hubble Space Telescope*

I Intensity

i Generic integer variable

IAU International Astronomical Union

IC Index Catalogue

IPAC Infrared Processing and Analysis Center

IPHAS Isaac Newton Telescope Photometric Hα Survey

IQR Interquartile range

IR Infrared

IRAF Image Reduction and Analysis Facility

IRAS *Infrared Astronomical Satellite*

ISM Interstellar medium

J Total angular momentum

j Emission coefficient

j Generic integer variable

JNLP Java Network Launching Protocol

JPL Jet Propulsion Laboratory

k Generic integer variable

L Luminosity

L Total orbital angular momentum

L_i Orbital angular momentum of electron i

$L_\odot$ Solar luminosity

l Galactic longitude

l Orbital quantum number

LIER Low ionisation emitting region

LMC Large Magellanic Cloud

M Absolute magnitude

M^* Planetary nebula luminosity function absolute magnitude cutoff

$M_\odot$ Solar mass

m Apparent magnitude

m Generic integer variable

m_* Central star of planetary nebula apparent magnitude

mag Magnitudes

MASH Macquarie/AAO/Strasbourg Hα

MGPS2 Molonglo Galactic Plane Survey

[M/H] Metal abundance ratio

MIPSGAL Multiband Infrared Photometer for Spitzer Galactic Plane Survey

MOS Multi-object spectrograph

MPI Message passing interface

MSX *Midcourse Space Experiment*

N Planetary nebula population

n Generic integer variable

n Polynomial degree

n Refractive index

$N_{\rm bin}$ Planetary nebula population of a data bin

$n_{\rm e}$ Electron density

n_{fit}	IRAF dispersion solution fitting order
n_{sky}	Number of sky fibres
NED	NASA/Infrared Processing and Analysis Center Extragalactic Database
NGC	New General Catalogue of Nebulae and Stars
NOAO	National Optical Astronomy Observatory
NOTSA	Nordic Optical Telescope Scientific Association
nsum	Number of pixels summed along CCD spatial axis
NVSS	National Radio Astronomy Observatory Very Large Array Sky Survey
$\mathcal{O}$	Landau's symbol
P	Pressure
p	Parallax
pc	Parsec
PFADC	Prime Focus Atmospheric Dispersion Compensator
PN	Planetary nebula
PNLF	Planetary nebula luminosity function
$P_n(x)$	Legendre polynomial of the first kind
R	Resolving power
r	Radius
RA	Right ascension
RGB	Red giant branch
RGB	RGB colour model
RMSE	Root mean square error
R_V	Ratio of total to selective extinction
S	Target population set
S	Total spin angular momentum
S_i	Spin angular momentum of electron i

S_x Summed pixel flux at physical coordinate x along CCD dispersion axis

s Spin quantum number

SAAO South African Astronomical Observatory

SBF Surface brightness fluctuation

SB-r Surface brightness-radius

SDSS Sloan Digital Sky Survey

SECGPN Strasbourg-European Southern Observatory Catalogue of Galactic Planetary Nebulae

SHS SuperCOSMOS Hα Survey

SIMBAD Set of Identifications, Measurements and Bibliography for Astronomical Data

SITe Scientific Imaging Technologies, Inc.

SMC Small Magellanic Cloud

SN Supernova

S/N Signal-to-noise ratio

SNR Supernova remnant

SNs Ia Type Ia supernovas

SPIE Society of Photo-Optical Instrumentation Engineers

SR Short red

SSO Siding Spring Observatory

SSS SuperCOSMOS Sky Survey

STScI Space Telescope Science Institute

SVO Spanish Virtual Observatory

SyS Symbiotic star

T Temperature

$T_{\rm e}$ Electron temperature

$T_{\rm eff}$ Effective temperature

$T_{\rm exp}$ Exposure time

T_n Target proximity comparisons

TAROS Telescope Automation and Remote Observing System

Ti*k*Z Ti*k*Z ist kein Zeichenprogramm
(German, recursive: Ti*k*Z is not a drawing program)

TRGB Tip of the red giant branch

$T_n(x)$ Chebyshev polynomial of the first kind

UKIDSS UK Infrared Telescope Deep Sky Survey

UKST UK Schmidt Telescope

USNO US Naval Observatory

UT Universal Time

UV Ultraviolet

v Velocity

$v_{\rm r}$ Radial velocity

VBA Visual Basic for Applications

VVV Visible and Infrared Survey Telescope for Astronomy Variables in the Via Lactea

WD White dwarf

WELS Weak emission line stars

WFPC2 Wide Field Planetary Camera 2

WiFeS Wide Field Spectrograph

WISE *Wide-field Infrared Survey Explorer*

WR Wolf-Rayet star

[WR] Wolf-Rayet planetary nebula central star

X Airmass

X Hydrogen mass fraction

x Generic numeric variable

x Physical coordinate along CCD dispersion axis

y Physical coordinate along CCD spatial axis

$y_{\rm f}$ Upper pixel summation bound along CCD spatial axis

$y_{\rm i}$ Lower pixel summation bound along CCD spatial axis

$y_{\rm mid}$ Geometric centre of *nsum* along CCD spatial axis

YSO Young stellar object

Z Metallicity

$\mathbb{Z}$ The set of all integers

$\mathbb{Z}^+$ The set of positive integers $\{1, 2, 3, \dots\}$

z Zenith distance

$|z|$ Absolute Galactic height

ZAHB Zero-age horizontal branch

Δ Difference

Δ Uncertainty

$\Delta\lambda$ Doppler shift

$\Delta\lambda$ Spectral resolution

λ Wavelength

$\bar{\lambda}$ Mean wavelength

λ_0 Rest wavelength

$\lambda_{\rm c}$ Central wavelength

$\lambda_{\rm eff}$ Effective wavelength

$\lambda_{\rm iso}$ Isophotal wavelength

$\lambda_{\rm peak}$ Peak wavelength

μ Distance modulus

σ Standard deviation

List of Figures

List of Tables

1

Planetary Nebulas – History and Overview

1.1 Introduction

PNs are clouds of gas ejected and then ionised during the late stage evolution of low to intermediate mass stars ($\sim$1–8 $M_\odot$, Osterbrock & Ferland, 2006). By this stage in their evolution, such stars have become hot enough, typically 5×10^4 K (Osterbrock & Ferland, 2006), to emit mainly in the ultraviolet (UV), consistent with Wien's displacement law[1]. UV-ionised PNs emit strongly at visible wavelengths, due to their constituent gaseous atoms and ions transitioning from one bound electronic state to another of lower energy (Kwok, 2000). This strong visible emission generally makes them much more luminous than their central stars (CSPNs). Comparative data for 25 prominent PNs and CSPNs, with known apparent magnitudes m and m_* are given in table 1.1, below, for example, and yield an average $m_* - m \approx 2.6$ mag (Moore & Rees, 2011).

PN gaseous envelopes expand at a typical expansion rate of 25 km s^{-1}, until too diffuse to be observed (Osterbrock & Ferland, 2006). The nebula phase is thus brief, of order of 10^5 yr vs. the $\sim 10^{10}$ yr solar main sequence phase (Carroll & Ostlie, 2007), making PNs relatively rare. Due to their strong emission line spectra however, they are visible at large Galactic and extragalactic distances, and several thousand have been catalogued. To date $\sim$3400 Galactic PNs (Boumis et al., 2003) are known amongst the $\sim 2 \times 10^{11}$ Galactic stars. Estimates of the total Galactic PN population are typically $\sim$25 000 (Jacoby et al., 2010), with extremes ranging from $\sim$6600 (De Marco & Moe, 2005) to $\sim$140 000 (Ishida & Weinberger, 1987).

[1] Wien's displacement law: $\lambda_{\text{peak}} T = 2.898 \times 10^{-3}$ mK, where λ_{peak} is the peak wavelength of a source's Planck spectrum and T its temperature (Jewett & Serway, 2006).

TABLE 1.1: Apparent magnitudes of prominent PNs, m, and their central stars, m_* (Moore & Rees, 2011). PNs are generally, but not always, much more luminous than their central stars. The PNs listed have an average $m_* - m \approx 2.6$ mag. Panels a–c show table extrema and average; a) NGC 1514 ($m_* - m = -0.6$ mag, northeast is to the top left) from the ALFOSC on the Nordic Optical Telescope, using B (central wavelength $\lambda_c = 440$ nm, full width at half maximum FWHM = 100 nm), V ($\lambda_c = 530$ nm, FWHM = 80 nm) and R ($\lambda_c = 650$ nm, FWHM = 130 nm) filters (López-Sánchez, 2006), b) NGC 1535 ($m_* - m = 2.6$ mag, northeast is top left) from a Santa Barbara Instruments Group STX-16803 CCD camera on an 81 cm (32 inch) Schulman telescope (Hubbell, 2013) using B ($\lambda_c \approx 448$ nm, FWHM ≈ 110 nm), G ($\lambda_c \approx 542$ nm, FWHM ≈ 70 nm) and R ($\lambda_c \approx 668$ nm, FWHM ≈ 60 nm) Astrodon Generation 2 E-series filters, and c) M 27 ($m_* - m = 6.3$ mag, northeast is 2.2° clockwise of top left) from the Focal Reducer and Low Dispersion Spectrograph 1 (Appenzeller et al., 1998) on the Very Large Telescope, using B ($\lambda_c = 429$ nm, FWHM = 88.0 nm), [O III] ($\lambda_c = 500.1$ nm, FWHM = 5.7 nm) and Hα ($\lambda_c = 656.3$ nm, FWHM = 6.1 nm) filters (O'Brien, 2008) displayed in blue, green and red respectively. Image scales are inconsistent. Images courtesy Jyri Näränen/NOTSA (a), Adam Block/Mount Lemmon SkyCenter/University of Arizona (b) and ESO (c).

Name	Reference	m	m_*
IC 418	[1]	10.7	10.7
IC 4406	[1]	10.6	14.7
IC 4593	[1]	10.9	11.3
M 27	[2]	7.6	13.9
M 57	[2]	9.7	14.8
M 76	[2]	12.2	17.0
NGC 40	[3]	10.7	11.6
NGC 246	[3]	8.0	11.9
NGC 1514	[3]	10.0	9.4
NGC 1535	[3]	9.6	12.2
NGC 2818	[3]	13.0	13.0
NGC 3918	[3]	8.4	10.9
NGC 4361	[3]	10.3	13.2
NGC 5189	[3]	10.0	14.0
NGC 5882	[3]	10.5	12.0
NGC 6058	[3]	13.3	13.8
NGC 6210	[3]	9.3	12.9
NGC 6309	[3]	10.8	14.4
NGC 6572	[3]	9.0	13.6
NGC 6741	[3]	10.8	14.7
NGC 6751	[3]	12.5	13.9
NGC 6790	[3]	10.2	13.5
NGC 6891	[3]	11.7	12.4
NGC 7662	[3]	9.2	13.2
PN Sp 1	[4]	13.6	13.8

[1] Dreyer (1895, 1908)
[2] Messier (1781)
[3] Dreyer (1888)
[4] Shapley (1936)

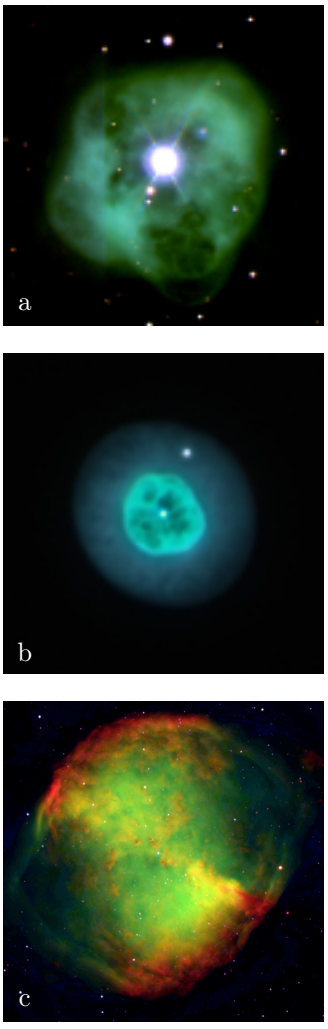

PN spectra consist of a series of discrete emission lines superimposed over the very weak continuous background of their CSPNs (vs. the Sun's many dark absorption lines superimposed over a continuum emission). This emission line spectral signature is very different to that of stars and most other celestial objects, usually enabling PNs to be identified even when they are otherwise ambiguous observational targets. Some of these emission lines caused confusion for early astronomers, even prompting discovery claims for a new element nebulium (Huggins & Miller, 1864), until the phenomena of atomic de-excitation via forbidden transitions, favoured over collisional de-excitation in extremely low density PN plasmas, was deduced (Bowen, 1928).

The chemical composition of nebulas deduced from spectra helps us understand the composition and evolution of their progenitor stars (e.g. via He and N), chemical abundances in the interstellar medium (ISM) at the time of progenitor formation, through presence of elements probably unaffected by stellar evolution (e.g. Ne, S, Cl and Ar), and finally how the ISM is in turn being enriched by PN ejecta (Peimbert, 1978, Maciel & Costa, 2003). The origin, evolution and physics of PNs are covered more comprehensively in dedicated works elsewhere (Gurzadyan, 1997, Kwok, 2000, Osterbrock & Ferland, 2006).

1.2 PN Formation

Following stellar formation, low to intermediate mass stars ($\sim$1–8 $M_{\odot}$) will spend $\sim10^{7}$–10^{10} yr, on the order of $\sim$90% of their lifetimes, in the main sequence phase of stellar evolution (Schaller et al., 1992, Gurzadyan, 1997, Carroll & Ostlie, 2007). Main sequence stars fuse core hydrogen (H) into helium (He), primarily via the proton-proton chain reactions for low mass stars ($\leqslant 1.5\,M_{\odot}$) or carbon-nitrogen-oxygen cycles for intermediate mass stars ($> 1.5\,M_{\odot}$) (Hester et al., 2002). Stars are in hydrostatic equilibrium during this period, with outward pressure (gas pressure and radiation pressure) balancing against inward gravitational collapse. Eventually core H is exhausted, reducing outward pressure and allowing core gravitational contraction and heating. H fusion begins in a shell around the core. The stellar envelope then expands and cools, forming a stellar red giant.

Red giant branch (RGB) stars with lower mass main sequence progenitors ($\lesssim 1.8\,M_{\odot}$, Herwig, 2005) develop electron-degenerate He cores, experience a He flash on attaining a core temperature of $\sim1 \times 10^{8}$ K (Osterbrock & Ferland, 2006) and begin core He fusion in a zero-age horizontal branch (ZAHB) stellar phase. RGB stars with higher mass progenitors also move into a core He fusion, ZAHB phase, but make a less violent, flashless, transition. After core He too is exhausted, core contraction, heating and subsequent expansion and cooling of the outer stellar layers again occurs, forming an asymptotic giant branch (AGB) star.

During the AGB phase, lasting $\sim10^{6}$ yr (Kwok, 2000), stars suffer significant mass loss via stellar winds ($\sim10^{-8}$–$10^{-4}\,M_{\odot}\,\mathrm{yr}^{-1}$, Golriz et al., 2014) and post-thermal pulse mass ejection. Thermally-pulsing AGB mass loss is dust driven, with radiation pressure ejecting dust particles, in turn transferring momentum to molecular gas and ejecting it too (Habing,

1996). Mass lost during the AGB phase can later form halos around PNs. AGB halos are difficult to detect, with surface brightness 10^{-2}–10^{-4} times less than peak nebula shell brightness (Corradi et al., 2003).

AGB mass loss eventual yields a hot, exposed central stellar core. This stellar core emits a fast stellar wind which interacts with the slower moving AGB phase wind ($\sim 10^3\,\mathrm{km\,s^{-1}}$ vs. $\sim 10\,\mathrm{km\,s^{-1}}$, Balick, 1987, Delfosse et al., 1997), producing an expanding nebula shell around a central cavity. This interaction is described elsewhere in more detail by Generalised Interacting Stellar Winds models (e.g., Frank, 1999, Balick & Frank, 2002). Stellar ejecta comprising the nebula are ionised by the star's UV emission, forming a PN and concluding the AGB phase.

By this stage, the combined residual mass of CSPNs and their nebula shells is typically $< 1\,M_\odot$, much less than the mass of their progenitor main sequence stars (Kwok, 2000). CSPN masses are observed within a narrow mass range around $\sim 0.6\,M_\odot$ (Kwok, 2000). More massive CSPNs would evolve quickly, ionising their nebula shells too briefly to be observable. Less massive central stars, the "lazy PNe" (Pollacco & Bell, 1994) would evolve too slowly to ionise the PN before nebula dissipation.

Specific mass estimates of PN shells continue to be refined. Photoionisation modelling of PN shells which considers carbon monoxide (CO) molecules existing associated only in nebula CO regions and mostly dissociated in nebula H_2 regions, instead of the uniform nebula CO association assumed by earlier models, suggests molecular masses within PNs have been underestimated by up to three orders of magnitude in the past (Kimura et al., 2012). These improved molecular chemistry considerations still have deficiencies however, and scope remains for their improvement.

PNs expand over about 5×10^5 yr until completely diffused into the ISM (Carroll & Ostlie, 2007), acting as mass return and chemical enrichment agents of their host environments. The remaining exposed central star is left to dim and cool, eventually becoming a white dwarf (WD). Stellar evolution through to the WD phase is summarised pictorially in figure 1.1. Additionally, the relationship between luminosity (L) and effective temperature (T_{eff}) during evolution of an example $2\,M_\odot$, solar metallicity star, is shown on a Hertzsprung-Russell diagram in figure 1.2 (adapted from Herwig, 2005).

1.3 PN Discovery History

1.3.1 Galactic PNs

As PNs are stellar, not planetary phenomena, the term "planetary nebula" is a misnomer, a historical artefact of their similarity to planets when viewed through 18th century telescopes (Herschel, 1785). These emission nebulas appear in the early Messier catalogue, where again, a note was made of a planet-like appearance (Messier, 1781). Explicit reference continued to be made to a planetary appearance of these emission nebulas in the 19th century (e.g. Herschel,

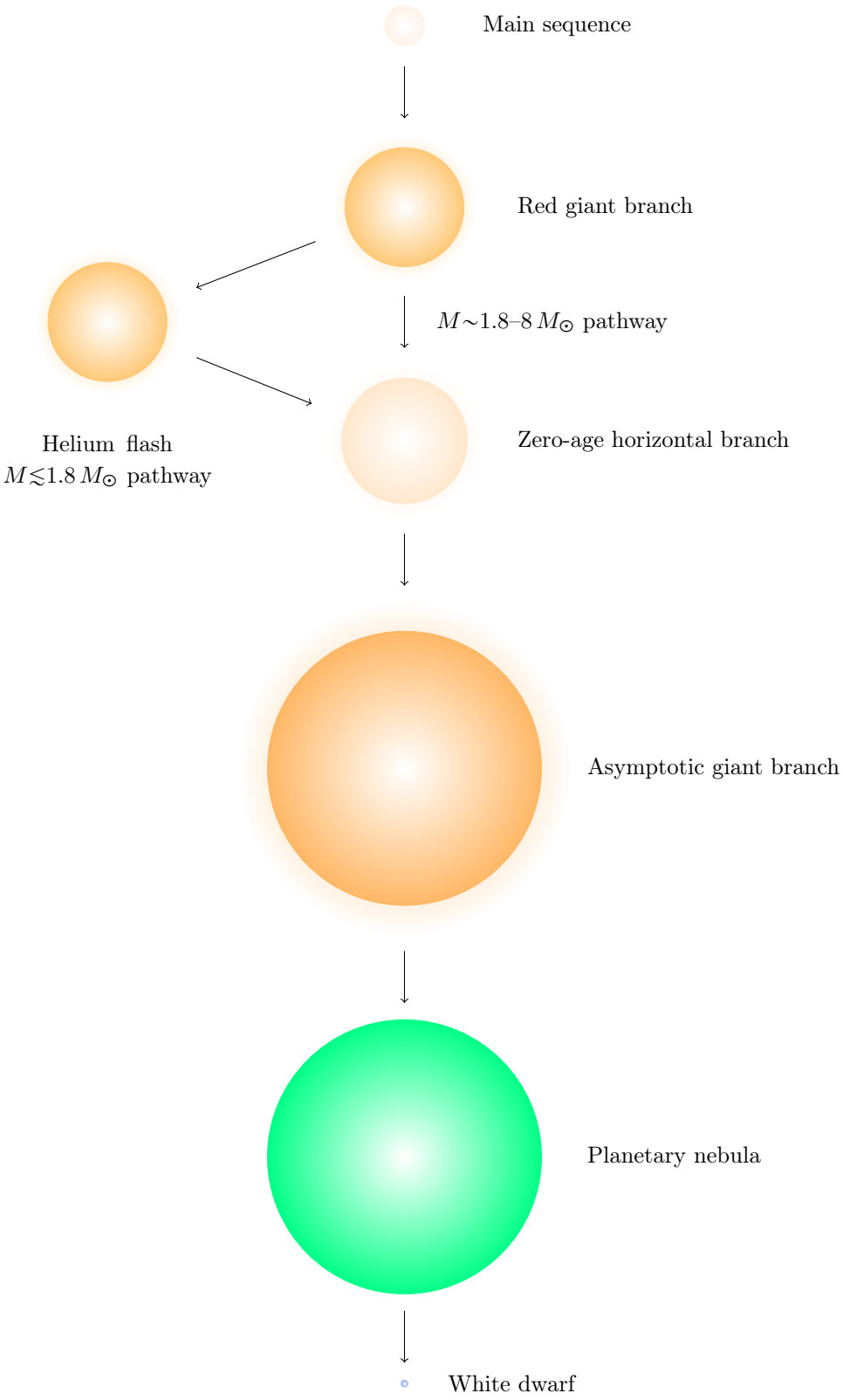

Figure 1.1: Low to intermediate mass ($\sim$1–8 $M_\odot$) stellar evolution from the main sequence to white dwarf phase. RGB stars with lower mass progenitors ($M \lesssim 1.8\,M_\odot$) experience a He flash prior to the ZAHB. Radii are stylised, stellar colours Charity approximations (Charity, 2002) and the PN an xcolor rendering (appendix A) of [O III] emission in a flux ratio $F_{5007}/F_{4959} = 2.94$ (as per §1.5).

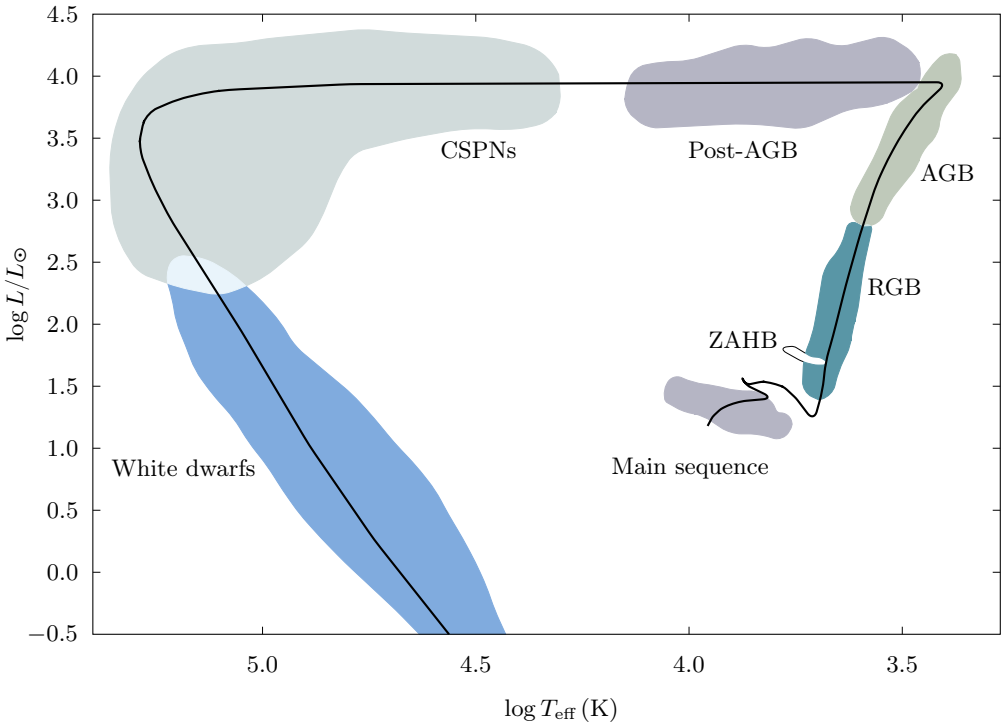

FIGURE 1.2: Hertzsprung-Russell diagram of the evolution of a $2\,M_\odot$, solar metallicity star from the main sequence through to white dwarf phase. Image adapted from Herwig (2005) using custom splines (e.g. Hearn & Baker, 2004) for raster-vector graphic conversion.

1834) and they featured in the landmark New General Catalogue of Nebulae and Stars (NGC, Dreyer, 1888) and supplementary Index Catalogue (IC, Dreyer, 1895, 1908) works.

PN discoveries, along with their inappropriate naming, have continued since the days of Messier, Dreyer and the Herschels. These discoveries have been made with techniques progressing from direct vision prisms (e.g. Pickering, 1880, 1882a,b), to inspection of objective prism plate spectra or broadband photographic plates (Abell, 1966, Henize, 1967), through to charge-coupled device (CCD) imaging (e.g. Cappellaro et al., 2001). Notably this century, the Anglo-Australian Observatory (AAO)/UK Schmidt Telescope (UKST)[2] Hα southern Galactic plane survey was digitised into the SuperCOSMOS Hα Survey (SHS) online atlas (Parker et al., 2005), in turn leading to the Macquarie/AAO/Strasbourg Hα (MASH) PN catalogue (Parker et al., 2006). MASH detailed ∼900 new PNs, the largest ever incremental increase in catalogued Galactic PNs. Subsequent careful SHS evaluation yielded the supplementary catalogue MASH-II (Miszalski et al., 2008), detailing another ∼350, harder to distinguish, new PNs.

PN data catalogued continues to grow not only in terms of absolute numbers discovered, but in terms of multiwavelength attributes. PN discovery and data collection is to be expected

[2]The UKST was operated in Australia from 1973 by the Royal Observatory, Edinburgh, but incorporated into the AAO in 1988 (Leverington, 2013).

in general multiwavelength sky surveys and indeed these are discussed in more detail in §1.7. Non-optical observations specifically targeting PNs are however undertaken. Radio (cm wavelength) observations of ∼250 MASH PNs have been conducted and a 5 GHz radio density catalogue for 682 non-MASH PNs developed, for example (Bojičić, 2009, Bojičić et al., 2011).

A summary of significant Galactic PN surveys and catalogues, including the Strasbourg-European Southern Observatory Catalogue of Galactic PNe (SECGPN, Acker & Ochsenbein, 1993), southern Galactic bulge (Beaulieu et al., 1999), Catalogue of Galactic PNe (CGPN, Kohoutek, 2001), MASH, MASH-II, Galactic bulge (Boumis et al., 2003, 2006), Deep Sky Hunters (DSH, Jacoby et al., 2010) and the northern Galactic plane Isaac Newton Telescope Photometric Hα survey (IPHAS, Viironen et al., 2009a,b, Sabin et al., 2010, 2014), is provided in table 1.2, below. Note that there is significant SECGPN/CGPN overlap such that they cover essentially the same PNs, but that they represent the historical PN discovery record from Herschel to the end of the pre-MASH era.

PNs are now known across the Galactic environment, from the Galactic bulge, the disc and out to the halo, having formed in isolation and in both globular (e.g. Pease, 1928, Jacoby et al., 1997) and open clusters (e.g. Parker et al., 2011a,b).

Table 1.2: Significant Galactic PN surveys and catalogues.

Survey / Catalogue	Number of PNs	Reference
Pre-MASH		
SECGPN	1490*	(Acker & Ochsenbein, 1993)
Galactic bulge	56	(Beaulieu et al., 1999)
Galactic bulge	64	(Van de Steene & Jacoby, 2001a)
CGPN	1510*	(Kohoutek, 2001)
Post-MASH		
MASH	905	(Parker et al., 2006)
MASH-II	∼350	(Miszalski et al., 2008)
Galactic bulge	44	(Boumis et al., 2003, 2006)
DSH	81	(Jacoby et al., 2010)
IPHAS	159	(Sabin et al., 2014)

* Significant overlap, essentially the same PNs.

1.3.2 Extragalactic PNs

The PN populations of the Magellanic Clouds, the highest apparent brightness Local Group galaxies (applying the distance modulus relation to Local Group data by van den Bergh, 2000), have been studied in some detail. Early Hα objective prism photographs of the Magellanic Clouds (Henize, 1956) captured PNs, although they weren't catalogued distinctly from other types of emission nebulas. Hα surveys of the Magellanic Clouds continued, with PNs

catalogued explicitly, refining the known extragalactic PN population (Lindsay, 1961, Henize & Westerlund, 1963).

Jacoby (2006) summarises significant modern (from 1978) Large Magellanic Cloud (LMC) and Small Magellanic Cloud (SMC) PN surveys and gives a total estimated SMC PN population of ∼132. A subsequent record incremental increase in catalogued LMC PNs raised its observed total to 760 and estimated total to 956 ± 141 (Reid & Parker, 2006a,b, Reid, 2007).

Aside from the Magellanic Clouds, PNs have been observed throughout the Local Group, from large spiral galaxies such as M 31[3,4] and M 33[3,5] (Ciardullo, 2010), to satellite systems such as M 32[3] (Richer et al., 1999) and the Sagittarius dwarf spheroidal galaxy (Walsh et al., 1997, Zijlstra et al., 2006), and to irregulars (e.g. NGC 6822, Hernández-Martínez et al., 2006). Once PN extragalactic candidates are identified in sky survey data, spectroscopic follow-up is practical with even 2 m-class telescopes in some cases (e.g. for M 31, Kniazev et al., 2014).

PN discovery history extends beyond the Local Group to the Local Supercluster level. [O III] on/off band imaging surveys on 4 m-class telescopes for example, have identified significant populations in galaxies of the Leo I group (e.g. 249 PNs, Ciardullo et al., 1989a). Kinematical studies of PNs in the NGC 4697 galaxy of the Virgo II cloud (Sambhus et al., 2006) is another example of accessible populations at this level. Indeed, PN discovery is not even restricted to the Local Supercluster level, but extends to the Coma Supercluster, with relevant photometric and spectroscopic survey techniques reviewed by Gerhard (2006).

1.4 PN Morphologies

1.4.1 Taxonomy

PNs exhibit varied morphologies, with round, elliptical, bipolar, bipolar-core, multipolar, point symmetric and other more exotic, unclassified configurations (Kwok et al., 2010, Maciel & Costa, 2011). Many PNs then have microstructures such as knots, jets and filaments nested within the large scale features of their nebula shells (Kwok, 2000, O'Dell et al., 2002). Some PNs also sport dim halos around their shells, as discussed in §1.2. For the rare case of a supernova (SN) igniting within an existing PN, their interaction is thought to produce structures such as the axi-symmetric protrusions of Kepler's supernova remnant (SNR) and G299.2-2.9 SNR (Tsebrenko & Soker, 2013). Examples of varied PN morphologies captured in *HST* imaging are given in figure 1.3.

Correctly determining such morphologies takes some care. Elliptical or bipolar PNs inclined at certain viewing angles will appear round to an observer, for example. This morpho-inclination degeneracy can be addressed by spatio-kinematic modelling using combined PN imaging, spatially resolved spectroscopy with integral field units and software tools such as

[3]Messier object (Messier, 1781)
[4]M 31: the Andromeda Galaxy (e.g., Humason & Zwicky, 1947).
[5]M 33: the Triangulum Galaxy (e.g., Takase, 1957).

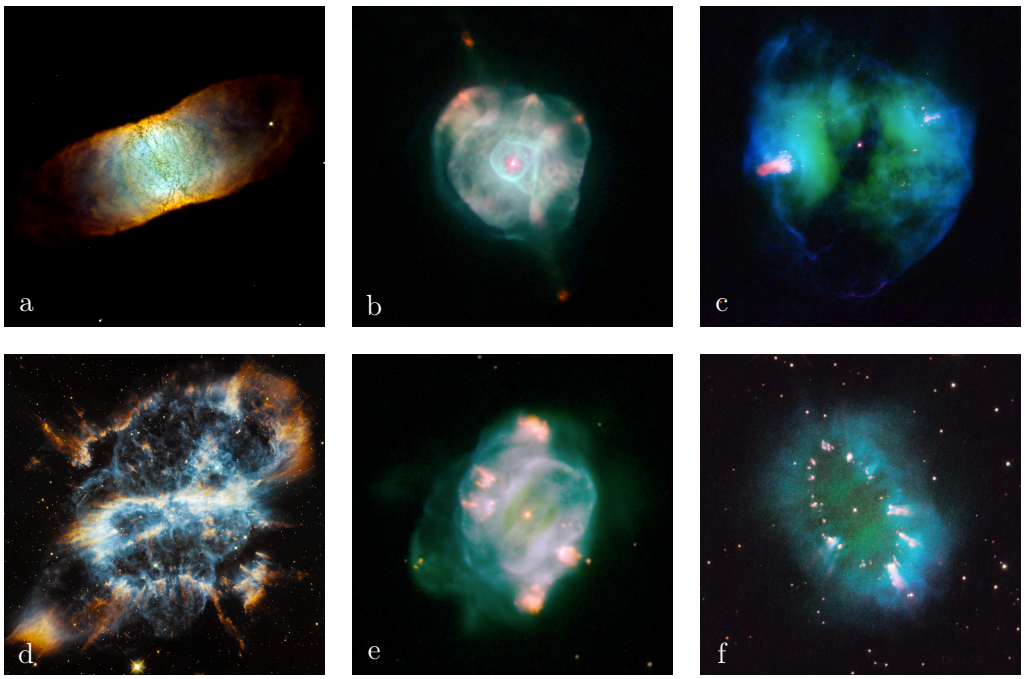

Figure 1.3: *HST* synthetic colour imaging of the varied PN morphologies of a) IC 4406, b) IC 4593, c) NGC 2371, d) NGC 5189, e) NGC 5307 and f) PN G054.2-03.4. Image filters, orientations and scales are inconsistent. Images a–c and e were taken with the WFPC2 and images d and f with the Wide Field Camera 3. Images courtesy ESA (except a), NASA and the Hubble Heritage Team (STScI/AURA).

SHAPE (Steffen & López, 2006). Figure 1.4 gives an example of morpho-inclination degeneracy for PN Sp 1. Cursory analysis of the Sp 1 image would lead to its designation as round, when in fact spatio-kinematic modelling reveals an hourglass morphology viewed end-on.

Many PN morphological classifications schemes have been employed in the literature, generally increasing in sophistication with time. No doubt this is a function of the increase in PN morphological detail discernible with telescope capability advances over time. Examples include the simple schemes of Jewitt et al. (1986) (four classes), Chu et al. (1987) (three classes, four subclasses), Schwarz et al. (1993) (five classes, two subclasses), Corradi & Schwarz (1995) (six classes), (Manchado et al., 2000) (three classes), the moderate complexity schemes of Gurzadyan (1997) (ten classes) and Parker et al. (2006) (six classes, five subclasses), through to the comprehensive scheme of Sahai et al. (2011) (seven classes, 31 subclasses).

1.4.2 Origins

The origins of the range of PN morphologies are unclear (Balick & Frank, 2002). Magnetic fields are known in CSPNs (Jordan et al., 2005) and in their precursory protoplanetary nebulas (Bains et al., 2003, 2004), and have been nominated as a PN shaping mechanism (e.g. Blackman et al., 2001). Angular momentum, energy and ambipolar diffusion considerations show single stars can't generate magnetic fields capable of large scale PN shaping (Soker,

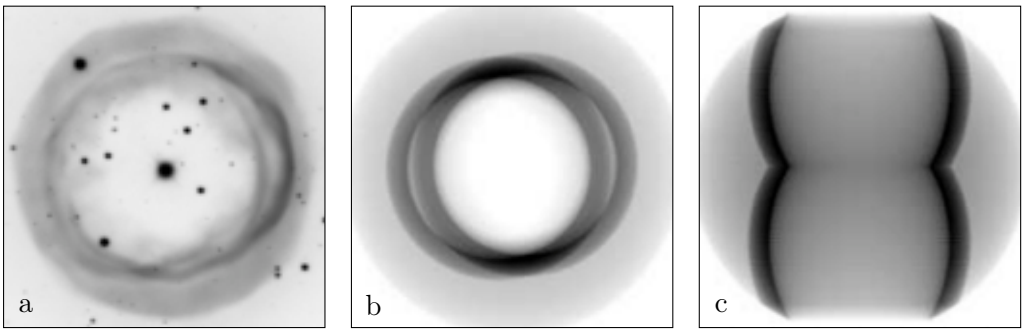

FIGURE 1.4: PN morpho-inclination degeneracy. From left: (a) apparently round PN Sp 1, north-east is top left, (b) corresponding spatio-kinematic model and (c) the model inclined at 90°, revealing its true hourglass morphology. Image scale is $\approx(75.7 \times 75.7)''$. Panel (a) is a colour-inverted, greyscale rendering of a synthetic colour (built using data from B ($\lambda_c = 440.0\,\mathrm{nm}$) and [O III] ($\lambda_c = 500.4\,\mathrm{nm}$) filters displayed in blue, V ($\lambda_c = 547.6\,\mathrm{nm}$) filter in green, R ($\lambda_c = 643.1\,\mathrm{nm}$) filter in orange and H$\alpha$ ($\lambda_c = 657.7\,\mathrm{nm}$) filter in red) Sp 1 image taken with the ESO Faint Object Spectrograph and Camera on the New Technology Telescope, courtesy ESO. Panels (b) and (c) were derived from Jones et al. (2012), which inspired the comparison layout.

2006b). Magnetic fields may contribute however, as a secondary PN shaping mechanism.

Binary CSPN interactions are a more plausible primary mechanism for generating aspherical PNs (see De Marco, 2009, for a review). The shaping effect is thought to be strongest for post-common envelope (CE) binary CSPNs (Jones et al., 2011), with theoretical models predicting equatorial CE ejection and subsequent nebular symmetry perpendicular to the binary orbital plane (Nordhaus & Blackman, 2006). Imaging studies and spatio-kinematic analysis of PNs hosting known post-CE binary central stars support these models. Of a sample of 30 PNs with post-CE binary central stars, a bipolar morphology of 30% was deduced via imaging (Miszalski et al., 2009b). Subsequent spatio-kinematic analysis of six of the sample revealed the expected nebular symmetry anti-alignment with binary orbital plane in every case (Jones et al., 2010, 2011) and raised the sample's confirmed aspherical fraction to ∼43%. The total sample aspherical fraction may be higher and is pending further spatio-kinematic analysis. It should be noted that although a strong theoretical-observational correlation was observed for this sample, 30 PNs is a small statistical sample and further investigation is needed.

In the past, it had been proposed, and hotly debated, that most PNs evolve from binary systems (the Binary Hypothesis, Moe & De Marco, 2006, De Marco, 2009), though this is no longer strongly supported (Frew, 2008, Miszalski et al., 2009a). There are ∼70 binary CSPNs confirmed of ∼3400 known Galactic PNs so far (∼2.3%, Weidmann & Gamen, 2011), with the total estimated close binary fraction 10–20% (Miszalski et al., 2009a). Given some observed spatio-kinematic support for binary CSPNs shaping nebulas, but a low close binary fraction compared to the aspherical Galactic PN fraction observed (∼81%, Parker et al., 2006), it seems binary CSPNs play an important, but not critical role in shaping aspherical nebulas.

Substellar CSPN companions, such as brown dwarfs and gas-giant planets, may shape

up to 20% of PNs, accounting for more of the observed aspherical PNs (De Marco & Soker, 2011). Although substellar CSPN companions haven't yet been detected (De Marco, 2009), some substellar objects are thought to survive being engulfed by a RGB envelope of the type preceding PN formation (Geier et al., 2009), remaining as close potential future nebula shapers.

1.4.3 Preferential Alignment of PNs

Determining any preferential alignment of individual Galactic stars (Guthrie, 1985), binaries (Brazhnikova et al., 1976, Rudy, 1979), SNRs (Gaensler, 1998) and other celestial objects is important in understanding the origin and evolution of the Galactic stellar population. Historically, there has been some debate over whether such a preferential alignment in the major axes of elongated PNs relative to the Galactic equatorial plane or Galactic magnetic field does (Grinin & Zvereva, 1968, Melnick & Harwit, 1975, Phillips, 1997) or doesn't (Akhundova & Seidov, 1970, Corradi et al., 1998) exist. Magnetic effects (Grinin & Zvereva, 1968) and compression effects due to PN motion relative to the ISM (Melnick & Harwit, 1975) have been posited as possible causes, but concerns with them being the principal agents of such alignment have been raised (Phillips, 1997).

A more recent statistical study of 440 elongated PNs reveals no preferential alignment however, with the exception of a possible weak preference near the Galactic centre for PNs with Galactic position angle $\sim 100^{\circ}$ (Weidmann & Díaz, 2008). More recently still, a study of 130 putative bulge PNs, with only 19 in common with the 440 Weidmann & Díaz (2008) PN sample, supports a preferred alignment for bulge PNs (Rees & Zijlstra, 2013). Repeating these studies with a larger sample of PNs, potentially assessing assumed semi-major axes with spatio-kinematic mapping, would provide a more rigorous result.

1.5 PN Spectra

In the visible domain, PNs exhibit emission line spectra primarily of recombination lines of H and He and collisionally excited lines of metals. Secondary emission line contributions result from Bowen fluorescence (Bowen, 1934, 1935). As mentioned in §1.1, these emission line spectra are unique enough to allow their discrimination from stars and most other celestial objects. Some spectroscopic mimics exist, especially other emission line objects, and are discussed further in §1.7. Mimics can in many cases be identified on morphological grounds, or through spectral examination over a sufficiently large wavelength range. True PN spectra share common features, but can exhibit significant object to object differences.

In general, the most intense PN emission lines are the doubly ionised oxygen [O III] $\lambda\lambda$4959, 5007 lines (Jaschek & Jaschek, 1995). Exceptions arise from asymmetrical extinction (Mathis, 1990), or as a consequence of intrinsic nebula properties (e.g. low excitation, Gurzadyan, 1997). Red Hα λ6563 emission is typically prominent (Kwok, 2007). Bracketing [N II] $\lambda\lambda$6548,

6583 emission can be prominent, but the observed flux, F, ratio $(F_{6548} + F_{6583})/F_{\mathrm{H}\alpha}$ varies considerably amongst PNs, e.g. >12:1 (PN G321.6+02.2, Corradi et al., 1997), <0.04:1 (PN K 1-3, Kaler et al., 1990), etc.

Estimated ratios for prominent PN lines in a spectral series can be calculated theoretically. The estimated collisionally excited [O III] ratio F_{5007}/F_{4959} is 2.94:1 (Osterbrock & Ferland, 2006). The PN emission line ratio $F_{\mathrm{H}\alpha}/F_{\mathrm{H}\beta}$, the Balmer decrement used for interstellar extinction calculations, is also expected theoretically to have a typical ratio of ∼3:1 (Brocklehurst, 1971). Observed line ratios are used in a variety of schemes (e.g. Dopita & Meatheringham, 1990, Gurzadyan, 1997, Stanghellini et al., 2002) to classify PNs into excitation classes. Low excitation PNs host the coolest CSPNs and high excitation PNs host the hottest. The Ex_ρ scheme of Reid & Parker (2010), resulting from a critical evaluation of past schemes, will be used here to determine excitation classes. The Ex_ρ scheme, incorporating Hβ λ4861, He II λ4686 and [O III] $\lambda\lambda$4959, 5007 fluxes, determines low excitation class according to

$$\mathrm{Ex}_\rho = 0.45 \left(\frac{F_{5007}}{F_{\mathrm{H}\beta}} \right) \tag{1.1}$$

and medium to high excitation class using

$$\mathrm{Ex}_\rho = 5.54 \left(\frac{F_{4686}}{F_{\mathrm{H}\beta}} + \log \frac{F_{4959} + F_{5007}}{F_{\mathrm{H}\beta}} \right). \tag{1.2}$$

Low excitation PNs are then defined as those with $\mathrm{Ex}_\rho < 5$, medium excitation $5 \leqslant \mathrm{Ex}_\rho < 10$ and high excitation $\mathrm{Ex}_\rho \geqslant 10$.

PN emission lines are considered primarily in the context of the visible domain here, but are manifest at both shorter, e.g. UV: C IV $\lambda\lambda$1548, 1551 (Feibelman, 1983), and longer wavelength domains. PN spectral phenomena present in the visible that continue into the IR include H emission lines (e.g. members of the Paschen, Brackett and Pfund series), faint lines of neutral or ionised He (e.g. He I λ10 830, Scrimger (1984)), faint H_2 lines (Gurzadyan, 1997) and other miscellaneous metallic lines (e.g. [Mg IV] λ44 868, Beckwith et al. (1984) and [S IV] λ105 076, Phillips et al. (2010)), etc. Beyond the visible, spectral contributions from the hot CSPN, two-photon emission, dust, other molecular ro-vibrational transitions, thermal bremsstrahlung, etc. also become important (Kwok, 2000).

1.6 CSPN Spectra

Spectroscopic data has been collected for ∼13% of Galactic CSPNs (Weidmann & Gamen, 2011). Amongst this modest population sample, a dichotomy exists between a majority with H-rich atmospheres and a minority with H-deficient atmospheres. The ∼4:1 population ratio between these groups of CSPNs is consistent with that observed for WDs generally (Kwok, 2000).

The first class of PNs with H-deficient CSPNs are the Wolf-Rayet PNs ([WR] PNs). [WR]

CSPNs exhibit spectral similarities to the classical hot, massive Wolf-Rayet (WR) stars (Wolf & Rayet, 1867), known for their strong, broad emission lines due to a vigorous stellar wind (Gray & Corbally, 2009). Similar to WR stars, [WR] PNs are characterised by fast nebula expansion velocities, typically 40–45% greater than ordinary PNs (Medina et al., 2006), and high mass loss rates ($>10^{-6}\,M_{\odot}\,\mathrm{yr}^{-1}$). In the same way that WR stars are divided into WC, WN and WO classes, [WR] PNs too can be divided into [WC], [WN] and [WO] classes based on prominent carbon, nitrogen and oxygen CSPN spectral features, respectively (e.g. the classification schemes of Crowther et al., 1998, Acker & Neiner, 2003). There is evidence for an evolutionary sequence along some of these subclasses (DePew, 2011).

Of the [WR] subclasses, [WN] is the rarest. It is only recently in fact, that a member of the [WN] subclass was confirmed, IC4663 (Miszalski et al., 2012a). Only two prior [WN] candidates, PM5 (Morgan et al., 2003) and N66 (Peña et al., 1995), were known in the entire universe and even then they were contentious nominations (Hamann et al., 2003, Werner & Herwig, 2006, Frew & Parker, 2010).

The other classes of PNs with H-deficient CSPNs are the weak emission line stars (WELS) featuring [WR]-like spectra, albeit with weaker, narrower emission lines, and the PG 1159 stars sharing features of both [WR] and WD stars.

Population statistics are complicated by the issue of misclassification of CSPNs between classes of the H-deficient group. Bearing in mind the statistics may thus have some degree of inaccuracy, the Galactic [WR] PNs number ∼103, with the total estimated Galactic [WR] PN fraction 5–7% (DePew, 2011, DePew et al., 2011). There are also five in the LMC, two in the SMC (Peña et al., 1997) and, notably, three in the Sagittarius dwarf spheroidal galaxy which has a total PN population of four (Walsh et al., 1997, Zijlstra, 2001, Zijlstra et al., 2006). The high [WR] PN fraction (75%) for the Sagittarius dwarf galaxy compared with the Galactic fraction, especially for such a small sample size, was noted as suspicious by De Marco (2009).

The mean absolute Galactic height $|z|$ is 270 parsecs (pc) for [WR] PNs, 391 pc for WELS and 398 pc for PG 1159 stars (DePew, 2011). The significant separation between $|z|$ for [WR] PNs and the other H-deficient classes suggest WELS and PG 1159 stars can evolve independently of [WR] PNs. This and other data suggest that despite some spectral similarities, these classes of CSPN are distinct, not all simply different stages of a common evolutionary pathway (DePew, 2011). Why some CSPNs develop [WR] features in the first place and others don't, remains unknown. As low Galactic height generally correlates to higher mass and metallicity stellar populations however, it appears [WR] PNs evolve from higher mass and metallicity progenitors than WELS and PG 1159 stars.

1.7 PN Mimics

The spectral signatures of PNs vary somewhat in emission lines featured and their relative intensity ratios, but are distinct enough as a group to usually enable PN discrimination from galactic, stellar and other celestial objects (Gurzadyan, 1997). Unfortunately PN mimics

exist, some spectroscopic, some morphological. When only one criteria is used for PN identification, the chance of misidentification increases. Mimics include H II regions and Strömgren zones, reflection nebulas, Population I circumstellar nebulas, SNRs, young stellar objects (YSOs) and their associated Herbig-Haro objects, B[e] stars, SySs and outflows, late-type stars, cataclysmic variable stars, galaxies, other miscellaneous emission nebulas and even plate or imaging defects. A comprehensive mimic review, associated diagnostic tools and mitigation strategies are available (Frew & Parker, 2010).

PN mimics are becoming easier to discriminate thanks to the ever increasing availability of multiwavelength sky survey data. Examples of significant multiwavelength sky surveys providing coverage over the UV, optical, IR and radio are given in table 1.3. Here the term "survey" refers to both studies formally designated as surveys and more loosely as the collated data products of spacecraft and instruments. Wavelength λ coverage bounds for each of these surveys is listed, as are the relevant number of passbands, though the wavelength coverage they provide should not be assumed to be continuous over the coverage bounds.

Whilst some mimic removal has been conducted for the MASH PN catalogue (Cohen et al., 2007, Boissay et al., 2012), the level of mimic contamination in older PN catalogues remains unknown.

1.8 PN Distance Determination

Inability to carry out accurate distance determination to Galactic PNs has been a serious issue in PN research (Cahn et al., 1992). Historically, distances to extragalactic PNs, such as those in the Magellanic clouds, were more reliably known than to Galactic PNs, especially for disc PNs. Distance to the planetary nebula NGC 7027 was published twice, in the same year, differing by almost a factor of 10 (178 pc vs. 1500 pc, Daub, 1982, Pottasch et al., 1982, Kwok, 2000). Derivation of key PN physical properties, such as CSPN luminosity, ionised mass and PN size hinge on accurate distance determination however, so this issue requires careful treatment. A range of primary and statistical distance determination methods exist, each with their own strengths, weaknesses and regimes of applicability. Detailed reviews of these methods are given by Gurzadyan (1997), and more recently, Frew (2008), but some notes will be made here.

As a primary distance determination method, direct trigonometric parallaxes of CSPNs yield distances with well-defined uncertainties, but can only be used in the Solar neighbourhood, $\leqslant 1$ kpc (e.g. Benedict et al., 2009). Stellar parallaxes are generally too small to measure accurately beyond that. Even precise parallax p measurements, such as from the Hipparcos satellite, had an average standard error of $\sim 9 \times 10^{-4}\,''$ (Mignard, 1997), allowing accurate ($\pm 10\%$) distance d determination to only $\sim$101 pc, assuming $d \sim 1/p$. This situation will be improved by the *Gaia* satellite mission, expected to deliver parallax measurements to accuracies of $\sim(8\text{–}25) \times 10^{-6}\,''$ (Lindegren et al., 2012).

Table 1.3: Significant multiwavelength sky surveys. Examples include the *Galaxy Evolution Explorer* survey (*GALEX*), Sloan Digital Sky Survey (SDSS), Deep Near Infrared Survey of the Southern Sky (DENIS), UK IR Telescope IR Deep Sky Survey (UKIDSS), Visible and IR Survey Telescope for Astronomy Variables in the Via Lactea (VVV) survey, Two Micron All Sky Survey (2MASS), *AKARI*, *Wide-Field IR Survey Explorer* (*WISE*), Galactic Legacy IR Mid-Plane Survey Extraordinaire (GLIMPSE), *Midcourse Space Experiment* (*MSX*) Galactic plane survey, *IR Astronomical Satellite* (*IRAS*) survey, Multiband IR Photometer for Spitzer Galactic Plane Survey (MIPSGAL), National Radio Astronomy Observatory Very Large Array Sky Survey (NVSS) and Molonglo Galactic Plane Survey (MGPS2).

Sky Survey	Wavelength	Passbands	Reference
Ultraviolet			
GALEX	(134.4–283.1) nm	2	(Morrissey et al., 2007)
Optical			
SDSS	(355.0–913.0) nm	5	(York et al., 2000)
IR			
DENIS	(0.82–2.15) μm	3	(Epchtein et al., 1994)
UKIDSS	(0.83–2.37) μm	5	(Lawrence et al., 2007)
VVV	(0.9–2.5) μm	5	(Minniti et al., 2006, 2010)
2MASS	(1.25–2.16) μm	3	(Skrutskie et al., 2006)
AKARI	(2–180) μm	13	(Murakami et al., 2007)
WISE	(3.4–22) μm	4	(Wright et al., 2010)
GLIMPSE	(3.6–8.0) μm	4	(Churchwell et al., 2009)
MSX	(6–25) μm	4	(Price et al., 2001)
IRAS	(12–100) μm	4	(Neugebauer et al., 1984)
MIPSGAL	(24–70) μm	2	(Carey et al., 2009)
Radio			
NVSS	$\approx$21 cm	0	(Condon et al., 1998)
MGPS2	$\approx$35.6 cm	0	(Green, 2002)

Other primary distance determination methods such as spectroscopic or photometric parallax of resolved binaries (e.g. Bond & Ciardullo, 1999) can't be used for single CSPNs. Shell expansion parallax methods (e.g. Reed et al., 1999), applicable to both single and binary CSPN systems, can be insufficiently rigorous in modelling PN shell kinematics (Mellema, 2004, Schönberner et al., 2005).

For statistical distance determination, the Shklovsky method (e.g. Shklovskii, 1957, Osterbrock & Ferland, 2006) models PNs as having a constant ionised mass, not allowing for the range of ionised masses of real PNs (yet enjoys better than expected success, Buckley et al., 1993), etc. Using a sample of bulge PNs, Bensby & Lundström (2001) critically examine the use of historical statistical distance determination methods, such as those that are derivations of the Shklovsky method, and provides a refined mass-radius relationship method.

The recently developed Hα surface brightness-radius (SB-r) relation has a robust applicability range and allows accurate distance determination for PNs based only on a knowledge

of target angular size, integrated Hα flux and reddening to the target (Frew, 2008).

1.9 Discussion

In addition to providing a history and overview of PN research, specific concepts relevant to this project have been presented, as will become evident in later chapters. Many of the significant PN catalogues and surveys identified are used as resources to double check observational work against, for example. Rare PNs, such as those with H-deficient central stars, have been reviewed, assisting quick identification if encountered. A range of PN mimics were introduced and care is taken later to use multiwavelength data and other mitigation measures to ensure only bona fide PNs are presented as such.

2

The Planetary Nebula Luminosity Function

2.1 Introduction

The PNLF describes the distribution of PN population N, as a function of [O III] λ5007 luminosity, in a system at a known distance. The [O III] λ5007 emission line is used as it is typically the brightest PN emission line (Gurzadyan, 1997). The empirical form of the function, featuring an exponential cutoff at the bright end, is equation 2.1 (Ciardullo et al., 1989b, Ciardullo, 2010),

$$N(M_{5007}) \propto e^{0.307 M_{5007}} \left[1 - e^{3(M^*_{5007} - M_{5007})}\right], \tag{2.1}$$

where M_{5007} is [O III] λ5007 absolute magnitude and $M^*_{5007} = -4.48$ is the M_{5007} of the most luminous PNs observed, in a magnitude system defined by equation 2.2 (Ciardullo et al., 2004),

$$m_{5007} = -2.5 \log F_{5007} - 13.74. \tag{2.2}$$

The PNLF has a consistent maximum luminosity ($\sim$600 $L_\odot$ at λ5007) with a sharp, bright end cutoff invariant to galactic age and type and insensitive to metallicity (Ciardullo et al., 2005). The PNLF hence acts as a powerful standard candle across Hubble types, comparable in accuracy to other extragalactic distance indicators such as Cepheids (e.g. figure 2.1) or Type Ia supernovas (SNs Ia, Jacoby, 1997, Ciardullo, 2010, 2012). Uniquely however, the PNLF can be used to cross-check rungs of the extragalactic distance ladder that are based on standard candles drawn from only a specific stellar population type, or on geometrical methods (cf. figure 2.2). Conveniently too, the [O III] line is at least twice as bright as Hϵ for

PNLF bright end PNs (top ∼1 mag), allowing their discrimination from H II region mimics, which have instead Hϵ as their brightest line (Ciardullo, 2003).

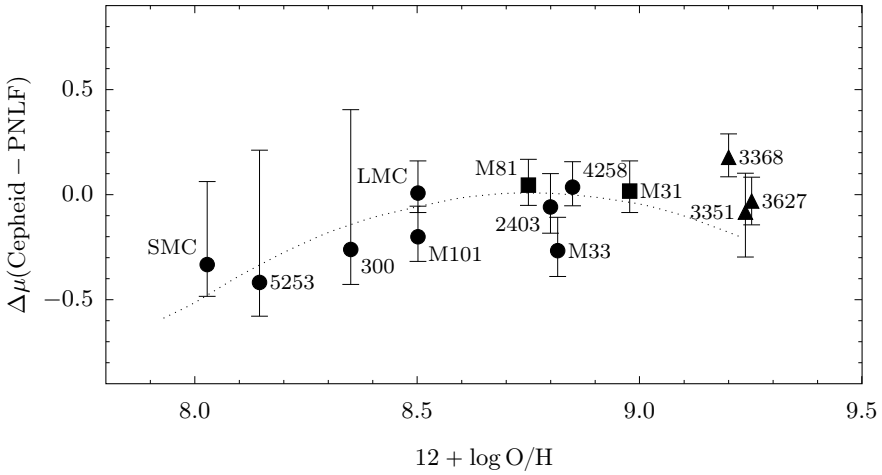

FIGURE 2.1: Comparison of Cepheid and PNLF distance moduli μ, versus galaxy oxygen abundance, adapted from (Ciardullo et al., 2002). Circles denote PNLF measurements in galactic discs, squares in galactic bulges and triangles in outer discs or halos. Error bars give uncertainties added in quadrature where small galaxies have few detected PNs and yield larger errors. The dotted curve is the expected PNLF reaction to metallicity from (Dopita et al., 1992). The validity of the PNLF cosmological standard candle is clear.

An example of PNLF invariance is shown in figure 2.3 (image adapted from Ciardullo, 2010), where the PNLFs for four disparate example galaxies, M 31, NGC 5128, the SMC and M 33 are given. A feature of figure 2.3 is the presence of statistically significant mid-magnitude PNLF dips away from the plotted exponential for the SMC and M 33. These "Jacoby dips" were noted in a PNLF by Jacoby & De Marco (2002), who suggest they arise from PNs with young stellar progenitors in which central star evolution proceeds quickly. Alternatively, the dips may correspond to bimodal PNLFs resulting from episodic star formation (Rodríguez-González et al., 2015).

A weak variance of the PNLF across stellar populations heterogeneous in metallicity is expected (Dopita et al., 1992). Oxygen acts as coolant in PNs, so a decrease in oxygen abundance would lower [O III] flux, but cause a rise in nebula electron temperature. Increased electron temperature causes more collisional excitation of nebula ions however, again increasing [O III] flux, offsetting the lower luminosity caused by lower oxygen abundance. Together, this leads to a [O III] flux that can be modelled as having a square root dependence on oxygen abundance. Conversely in CSPNs, UV flux, and hence [O III] emission, has an inverse cube root dependence on metallicity. These competing effects result in a weak dependence of [O III] flux on metallicity (Ciardullo, 2003).

The invariant PNLF maximum luminosity observed across stellar populations of different ages is, by contrast, more difficult to explain. The initial-final mass relation dictates PNs

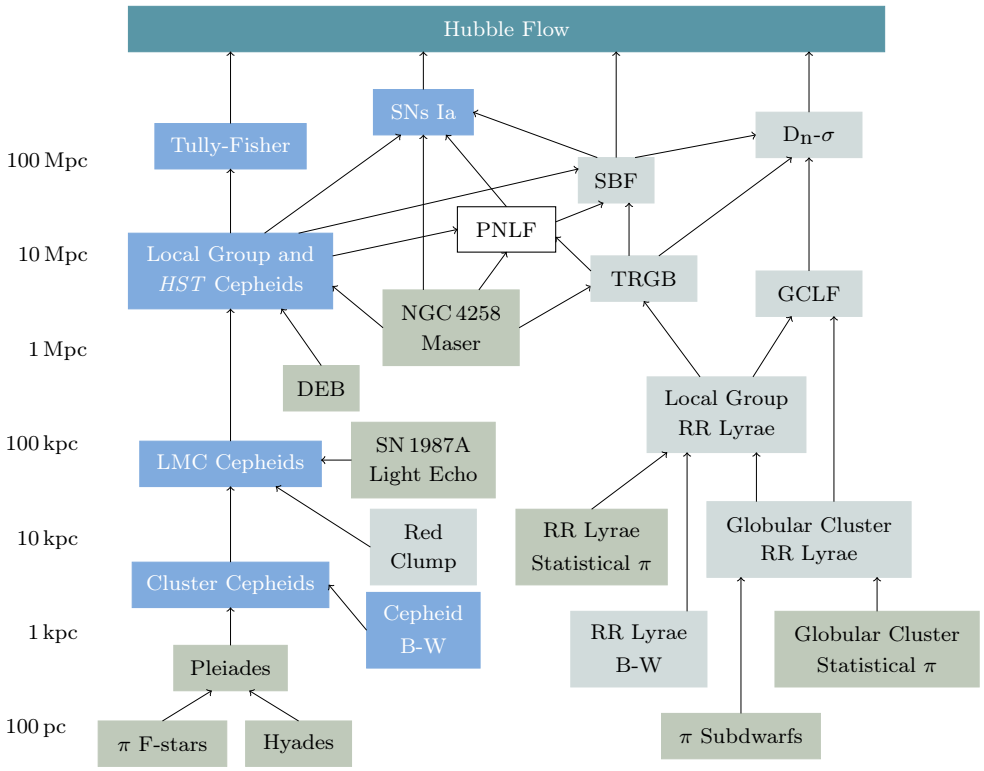

Figure 2.2: The extragalactic distance ladder (adapted from Ciardullo, 2012). Indicators shaded blue apply to star-forming galaxies (e.g. SNs Ia), gray to Population II systems (e.g. globular cluster luminosity function; GCLF, surface brightness fluctuation; SBF, tip of the red giant branch; TRGB, photometric diameter-velocity dispersion relation; D_n-σ) and olive indicators derive from geometrical measurements (e.g. detached eclipsing binaries; DEB). Application of the Baade-Wesselink (B-W) method (e.g. Carney et al., 1992, Gieren et al., 2013) is not limited by population, only the availability of a pulsating star. Arrows denote calibrated ladder steps. The invariance of the PNLF to environment makes it important for cross-checking other cosmological distance indicators.

at the PNLF bright end evolve from massive ($\gtrsim 2\,M_\odot$, Kalirai et al., 2008, Ciardullo, 2012), short-lived ($\sim$1–2 Gyr, Iben & Laughlin, 1989) main sequence stars. Theoretically derived PNLFs for old, elliptical galaxy, stellar populations are dimmer (5 mag) than those for young, spiral galaxy stellar populations (Marigo et al., 2004). Highly [O III]-luminous PNs are observed however, amongst old ($\sim$10 Gyr) stellar populations devoid of young, massive stellar progenitors. The contradiction of highly [O III]-luminous PNs in old stellar environments remains a significant mystery which has defied explanation for over 20 years (Jacoby, 1989, Ciardullo et al., 1989b, Jacoby et al., 1992, Ciardullo, 2010, 2012).

Evolutionary time scales for $\geqslant 0.6\,M_\odot$ CSPNs thought to govern the PNLF bright end (Schönberner et al., 2007) appear correct. If they weren't, the observed PNLF wouldn't exhibit the shape it does, a faster evolutionary time scale would produce a steeper, lower luminosity truncation and a slower evolutionary time scale would lead to a shallower, higher luminosity cutoff (Jacoby, 1997). PN modelling with 1D radiation-hydrodynamical code also precludes [WR] CSPNs of $\sim$0.6 $M_\odot$ from populating the PNLF bright end (Schönberner et al., 2007).

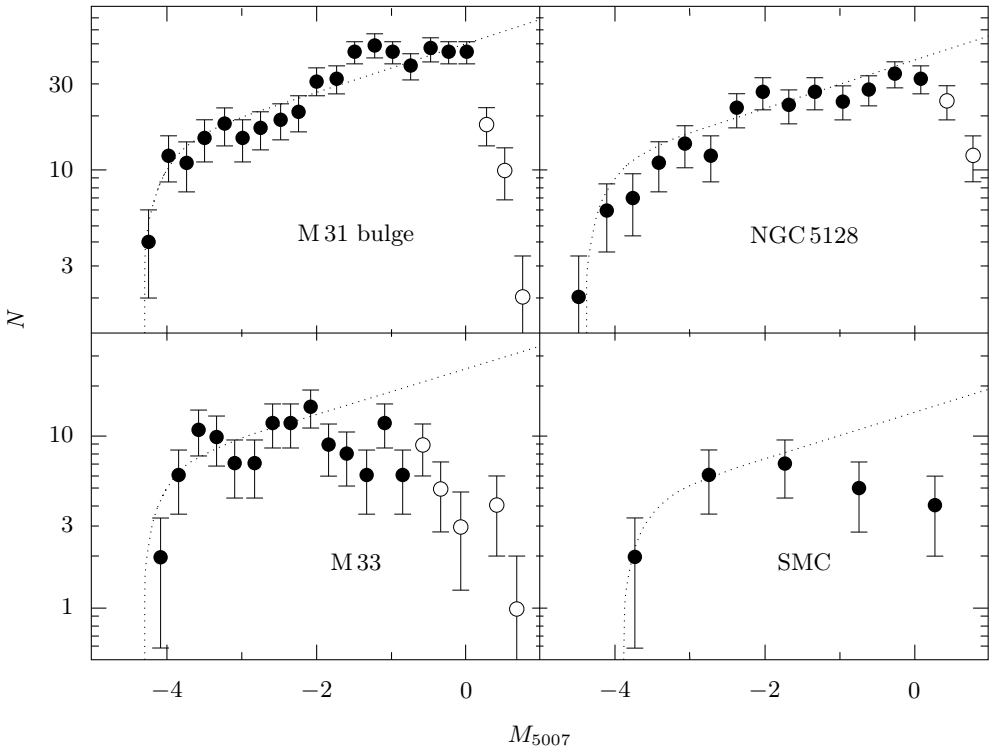

FIGURE 2.3: PN population distribution across M_{5007} for disparate example galaxies: M 31 (the barred spiral Andromeda), NGC 5128 (the lenticular or elliptical Centaurus A), the SMC (dwarf irregular) and M 33 (the spiral Triangulum). Data for M 31 are restricted to bulge PNs. Open circles denote incomplete data bins. The dotted curves are overlays of the empirical PNLF defined by equation 2.1. Image adapted from Ciardullo (2010).

Several hypotheses to explain the contradiction of highly [O III]-luminous PNs in old stellar environments have been posited. Highly [O III]-luminous old population PNs may evolve from blue stragglers, massive ($\sim$2 $M_\odot$) stars formed from smaller mass ($\sim$1 $M_\odot$) binary star mergers or mass transfers (Ciardullo et al., 2005). The initial-final mass relation used to extrapolate PN progenitor mass from the WD central star has been revised in the past (Weidemann, 2000, Ferrario et al., 2005) and may still be wrong. Symbiotic nebulas mimicking [O III]-luminous PNs have been considered (Soker, 2006a), but no evidence for them was found in characterisation of the PNs contributing to the Galactic bulge [O III] PNLF (Kovacevic, 2011). Is some other underlying physics being missed?

2.2 Exploring the Galactic Bulge PNLF

A logical first step towards reconciling the contradictory [O III]-luminous PN ubiquity would be to examine PN physical properties at the PNLF bright end cutoff in an old stellar population. Noting the Galactic bulge is an observationally accessible, predominantly old ($\geqslant$10 Gyr) stellar population with some rough similarities to that of an old, elliptical galaxy, Kovacevic

(2011) carried out an [O III] on/off band PN imaging survey in much of the central $10^\circ \times 10^\circ$ bulge region, using the Mosaic II CCD imager (Muller et al., 1998) on the 4 m (158 inch) Blanco telescope (Leverington, 2013) at the Cerro Tololo Inter-American Observatory (CTIO)[1], providing in part such additional bright end PN data. This survey imaged some ∼80% of known PNs in the region at the time and was supplemented by complementary spectroscopy. PN [O III] flux data obtained allowed construction of the Galactic bulge PNLF (Kovacevic, 2011, Kovacevic et al., 2011b), shown in figure 2.4. Note, care was taken to describe the bulge as a rough and not close elliptical galaxy proxy. Its complex environment, hosting a mixed PN population with a range of observed O/H abundances, varying from those of Galactic disc PNs through to underabundant examples, suggests some star formation spanning an extended time period (Maciel & Costa, 2003).

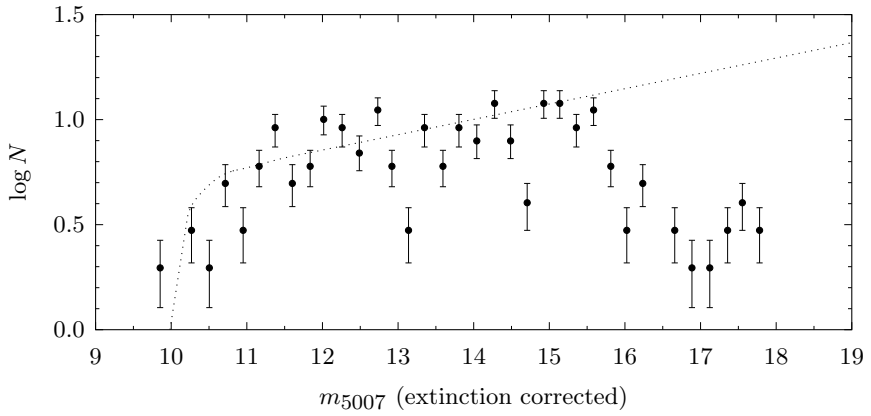

Figure 2.4: The Galactic bulge [O III] λ5007 PNLF (adapted from Kovacevic, 2011). The dotted curve is a modified version of the empirical PNLF defined by equation 2.1. Assuming a bulge bright end PNLF absolute magnitude cutoff at $M^*_{5007} = -4.47^{+0.02}_{-0.03}$ (Ciardullo et al., 2002) yields a bulge distance of 7.8 ± 0.2 kpc, in agreement with the putative distance of $\approx 7.9 \pm 0.3$ kpc (e.g. McNamara et al., 2000).

Attempts have been made in the past to use the PNLF as a standard candle to estimate the distance to the Galactic centre (Pottasch, 1990). Use of the Kovacevic (2011) PNLF however recovers a bulge distance of 7.8 ± 0.2 kpc, in agreement with the putative distance of $\approx 8.0 \pm 0.5$ kpc (e.g. Reid, 1993).

Kovacevic (2011) found that the most [O III]-luminous bulge PNs were unbiased in radial velocity and had compact, low angular diameter morphologies usually associated with young PNs. Higher resolution *HST* imaging of some of the Kovacevic (2011) PNs (Sahai et al., 2011) has however shown the Mosaic II imaging to have insufficiently resolved their true morphological properties, e.g. the distinct ring of PN H 2-13 (Haro, 1952). Additional examples are shown in figure 2.5.

Scope clearly remains to recover more accurate morphological data for bulge PNs. High resolution imaging of PNLF bright end PNs may help unravel its unexplained success as a

[1]CTIO: east longitude $-70^\circ 48.9'$, latitude $-30^\circ 09.9'$, 2215 m above sea level (Bell & Urban, 2012).

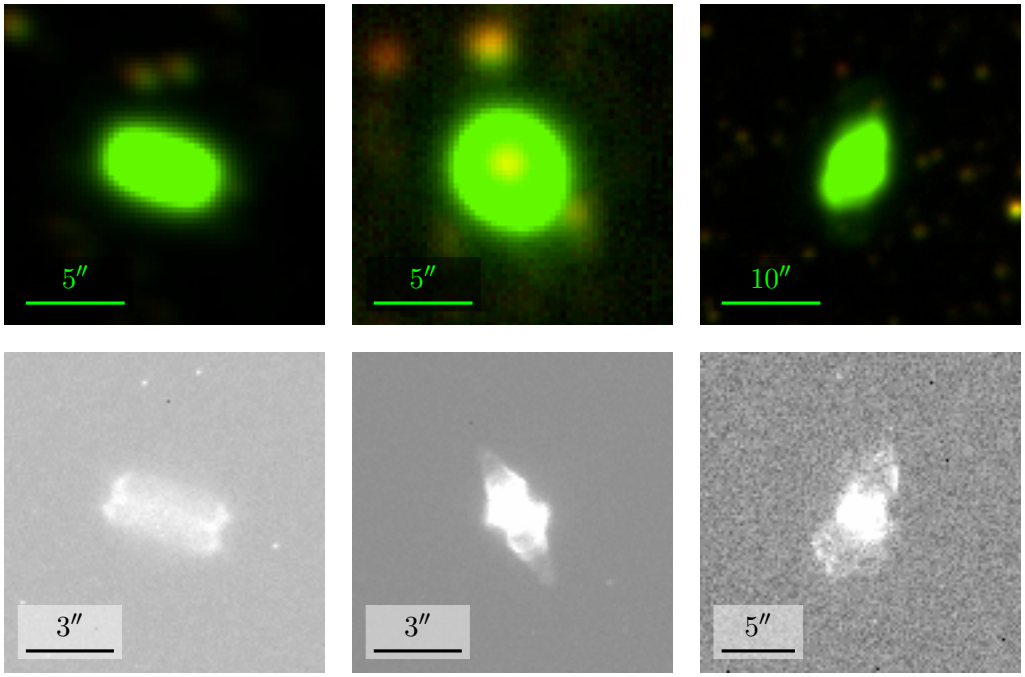

FIGURE 2.5: Low vs. high resolution Galactic bulge PN imaging. Left to right: PN H 2-37 (Haro, 1952), PN M 2-14 (Minkowski, 1947) and PN M 3-14 (Minkowski, 1948). Top row: Blanco Mosaic II [O III] on/off band images (filter specifications are listed in §3.2, table 3.3). Image intensity scale is linear 99.5%. Bottom row: counterpart *HST* WFPC2, F656N (Hα; $\bar{\lambda} = 656.4$ nm, McMaster & et al., 2008) filter images, courtesy NASA/ESA *HST* and STScI/AURA. Image intensity scales are linear 99%, 99.5% and zscale respectively. Northeast is top left. The Blanco imaging is clearly missing fine morphological details present in the *HST* imaging. PN morphological classifications, especially for compact PNs, thus represent resolution-limited assignments subject to change. This comparison was inspired by figure 6.11, Kovacevic (2011).

distance indicator. Such imaging could be used to explore the relationship between the PNLF bright end, PN morphology and central star binarity. There are particular morphological trends expected to be consistent with a blue straggler origin of [O III]-luminous PNs (Ciardullo et al., 2005) for example.

Spectroscopy of [O III]-luminous PNs is another means of gleaning clues to the PNLF invariance. Deep spectroscopy would expose other properties and allow mass determinations (e.g. Pottasch, 1996), testing the initial-final mass relation at the PNLF bright end. Multiple avenues of investigation to address the origins of the PNLF invariance thus remain as future work.

3

New Bulge PNs

Chapter 1 gave a history and overview of PN research and chapter 2 introduced the PNLF, especially in the context of the Galactic bulge. The related new work performed here is now introduced; careful, systematic review of the [O III] on/off band survey fields of Kovacevic (2011) has yielded a significant new population of PN candidates toward the Galactic bulge (> 200, Stenborg & Parker, 2014). As discussed in §2.2, this bulge survey was carried out by Kovacevic (2011) with the Mosaic II CCD imager on the CTIO's 4 m Blanco telescope. Confirmatory spectroscopy has been taken here of selected candidates, limited by available observing time, and is presented where reduced. Bona fide PN members of this new population will refine the bulge [O III] PNLF and known Galactic PN population more generally.

3.1 Candidate Discovery

Identification of new PN candidates resulted from a methodical review of the Mosaic II bulge survey Flexible Image Transport System (FITS) files prepared by Kovacevic (2011). Each FITS file contains data from a single pointing, a (8192×8192) pixel image mosaicked from eight smaller (2048×4096) pixel images, each taken by one of the eight CCDs comprising the Mosaic II system. The mosaicking geometry is shown in figure 3.1 and reflected in the Mosaic II data structure, a multi-extension format FITS file per exposure (Valdes & Tody, 1998) comprised of a header and eight data extensions. The system covers a $36' \times 36'$ FOV at the Blanco's prime focus, to an image resolution of $\approx 2.7 \times 10^{-1}\,''\,\mathrm{pixel}^{-1}$ (Schmidt, 2006).

Kovacevic (2011) observed each field separately with two filters, a narrow band filter to capture [O III] emission and an off band filter. Detailed filter specifications are supplied in

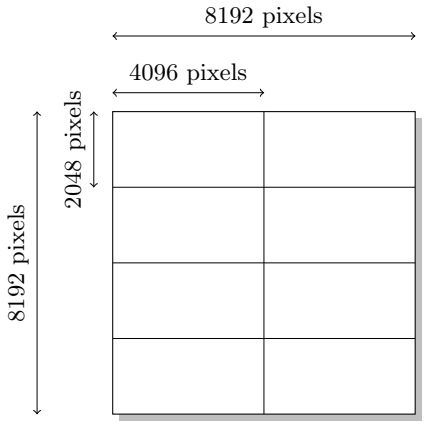

FIGURE 3.1: Mosaic II CCD geometry. Eight (2048×4096) pixel CCDs were mosaicked to form a (8192×8192) pixel image covering an $36' \times 36'$ field of view on the CTIO 4 m Blanco telescope.

§3.2, table 3.3. In total, 125 survey fields were available for review, comprised of 119 unique pointings. All field centres were located within a $10^\circ \times 10^\circ$ region around the Galactic Centre, i.e. $-5^\circ \leqslant l \leqslant 5^\circ$, $-5^\circ \leqslant b \leqslant 5^\circ$, where l is Galactic longitude and b Galactic latitude. It is suspected some fields were observed twice to ameliorate poor seeing, unexpected image saturation from bright objects, or other data acquisition issues. A listing of the fields is given on p. 246 of Kovacevic (2011), where field names were derived from a truncation of the right ascension (RA) and declination (dec), respectively, in J2000 coordinates, of each field's centre. This list suffers several errors however, including omission of two fields observed and reviewed here, an incomplete listing of fields observed twice and some field names not correctly derived from actual field centres. Some fields were missing either reduced on or off band data, but difference images had been produced by Kovacevic (2011) before their loss. A corrected list of all the fields observed, reflecting the actual reduced data used, is supplied here in appendix B with supplementary notes. Two more fields with unique pointings, missing both reduced on band data and corresponding difference images, were observed by Kovacevic (2011) but cannot be used for PN detection and weren't included in appendix B.

The SAOImage DS9 astronomical imaging and visualisation tool (Joye & Mandel, 2003) was used to open FITS files and search the survey fields. Synthetic RGB colour model (hereafter RGB) images of fields were created in DS9 by loading [O III] on band data into the green frame and off band data into the red. Some manual corrections were made to minor inconsistencies (e.g. $\Delta\text{dec} \sim 27''$) in the world coordinate system (e.g. Greisen & Calabretta, 2002) solution between selected on/off band FITS files applied by Kovacevic (2011), so that RGB image alignment was correct. Once aligned, PNs would then stand out in green against a background of yellow stars. Assigning on band data to the green frame, instead of the red, for example, was done deliberately to reflect the actual correspondence of [O III] λ5007 emission with green in the visible spectrum (see e.g. appendix A). Indeed, the green appearance of many PNs in nature due to prominent [O III] emission is noted in Seaton (1960). In addition, FITS files generated by subtracting the off band from the on band data were produced by Kovacevic (2011), to isolate PN flux from stellar and continuum flux. Both the RGB images synthesised here and the difference images produced by Kovacevic (2011), for each survey field,

were examined for PNs. In general, RGB images were best for identifying bright, compact PNs and difference images best for fainter PNs. Being bulge fields of typically high object density, visual evaluation of each field was non-trivial. RGB images of each nebula candidate are provided in figure 3.6, sorted by RA then dec, with north east to the top left of each image. The default image intensity range is linear zscale. For very faint nebulas in RGB candidate images, the corresponding difference image typically reveals morphologies well. For cases where alternate intensity ranges are used, a note is usually made.

Once PNs were identified in a survey field, they were cross-checked against known objects in SIMBAD. The spatial distribution of new PN candidates remaining after this cross-check are shown in figure 3.2, with further details given in table 3.2. For reference, SIMBAD database coordinates of the Galactic Centre are also listed in table 3.2. The naming convention used for new emission line objects adopts the Dickel et al. (1987) standard, which is compliant with International Astronomical Union (IAU) resolutions C3 and C12 on astronomical designations and radio source nomenclature. A designation prefix "CTIO" is used, reflecting the name of the observatory the discovery imaging was obtained at. Data supplied includes epoch J2000 equatorial coordinates in RA and dec, nebula major and minor axis diameters, candidate potential expressed as either a probable or possible PN, morphology and supplementary notes. The typical point source astrometric error of (1–2) $\times 10^{-1}\,''$ in the FITS files quoted by Kovacevic (2011) is used to assume a PN coordinate uncertainty here of $\Delta\mathrm{RA} = 1 \times 10^{-2}\,\mathrm{s}$, $\Delta\mathrm{dec} = 2 \times 10^{-1}\,''$.

PN major and minor axis diameters in table 3.2 are listed with an uncertainty of $\pm\,0.8''$, rounded from the $\pm\,0.75''$ diameter-independent value statistically determined for this data set by Kovacevic (2011). Nebula axes were determined with the contour tool in DS9, using default settings of 10% intervals of the difference image zscale intensity range[1] and a four pixel smoothness level, modified on a case-by-case basis for difficult to analyse nebulas.

A range of morphological classification schemes were mentioned in §1.4.1. The moderate complexity scheme of Parker et al. (2006) was adopted after being assessed as appropriate to the level of detail visible in the Mosaic II imaging data. This classification scheme is described in table 3.1 and examples of it applied to MASH catalogue PNs are given in figure 3.3. In this scheme, PNs were generally assigned a single class, with multiple subclasses, listed alphabetically, as appropriate. Uncertain classes were allowed a dual designation such as R/B. Care should be taken in use of morphological data presented however. Nebula morphology can vary with emission wavelength, e.g. low excitation emission line morphology is typically different from high excitation emission line morphology (Chu et al., 1987).

3.1.1 Workflow Automation

Generation of table 3.2 required analysis of a significant amount of data. Kovacevic (2011) produced some ∼57.73 GB of imaging data and then additional RGB image synthesis done

[1]The Blanco on band image zscale intensity range was used for fields lacking difference images.

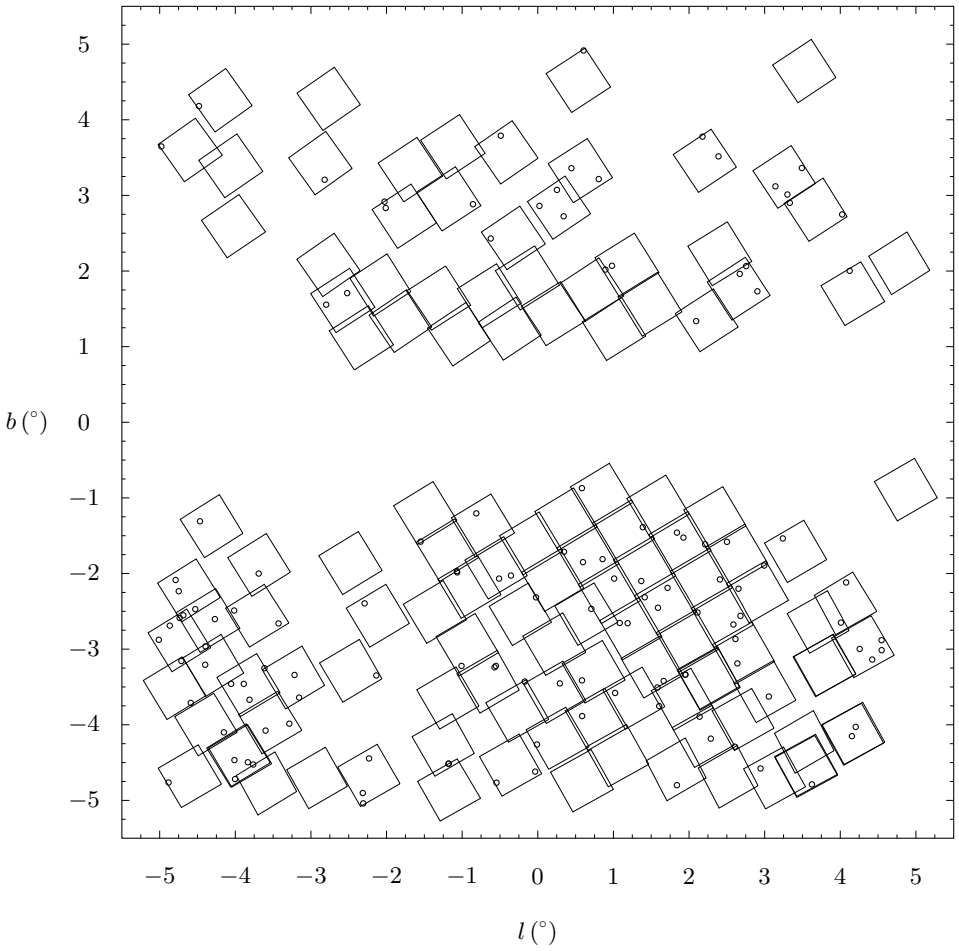

FIGURE 3.2: Spatial distribution of new PN candidates around the Galactic Centre. Here circles represent PNs and squares Mosaic II field pointings. The circles are of uniform size and not to scale. Note the deliberate paucity of pointings around $b = 0^\circ$ aimed at avoiding the apparent transverse bisection of the Milky Way at visible wavelengths by dust clouds. Dust extinction of the Galactic Centre, at optical wavelengths, is at least 30 magnitudes (Simons et al., 2006).

here was added to that. A combination of AppleScript, DS9 command line scripting, Unix shell scripting and Visual Basic for Applications (VBA) programming was carried out to help automate data management and validation, RGB image synthesis and SIMBAD queries. Reverse engineering the SIMBAD Web query mechanism and integrating it into data management systems here eliminated manual query data entry through Web forms. This efficiency backfired, temporarily. Google Search settings on the relevant computer detected the unusual speed and context of the outgoing automated queries, incorrectly assessing them as the work of an unattended Web bot. Google sent a notice to this effect to the originating computer and blocked the queries. The restrictions were soon lifted however, presumably after query evaluation as benign or sufficiently intermittent by Google, and work continued apace.

Automated data decomposition incorporating metaprogramming—writing software to itself generate software, was run over RGB and difference FITS files to produce subfield images

Table 3.1: PN morphological classification. Capital letters denote classes and lowercase letters subclasses. Round nebulas are those with major and minor axes differing by $< 5\%$.

Class	Description
E	Elliptical
R	Round
B	Bipolar
I	Irregular
A	Asymmetric
S	Star-like
a	Asymmetry
m	Multiple shells or external structure
p	Point symmetry
r	Ring
s	Resolved internal structure

(Stenborg, 2014). More specifically, for Mac OS X platform operations, Unix shell script metaprogramming was used for file and loop handling whilst AWK and DS9 command line scripting were used as object languages for floating point calculations and FITS segmentation respectively. A less sophisticated equivalent was developed for the Microsoft Windows platform, for the purposes of software portability, using VBA to generate DS9 command line scripting embedded within a batch file. The algorithmic logic used for this FITS segmentation is given in figure 3.4, where instances of floor[2] and ceiling[3] operators should not be confused with ordinary square brackets, and a visualisation is given in figure 3.5. These subfields were programmatically assigned file names such that RGB and difference images were interleaved, in order, on the file system, enabling use of a image viewer as a continuous-feed blink comparator. The load time for these subfields into an image viewer was much less than that for the FITS files into DS9, significantly reducing time taken for PN discovery. The DS9 interface also doesn't facilitate accurate linear traversal of large images. Every survey field was thus decomposed into a subfield small enough (1280×421 pixels) to be viewed on a single screen, eliminating the possibility of missing part of a field through manual error using DS9's traversal tool. Blinking on/off band images with associated difference images is not new, e.g. Boumis et al. (2003), but the image segmentation and interleaving scheme devised, allowing single-click screen-sized continuous-feed blinking hasn't been encountered elsewhere in the literature.

[2] $\lfloor a \rfloor \equiv \max \{n \in \mathbb{Z} \,|\, n \leqslant a\}$, where a is a real number and n is an integer.
[3] $\lceil a \rceil \equiv \min \{n \in \mathbb{Z} \,|\, n \geqslant a\}$.

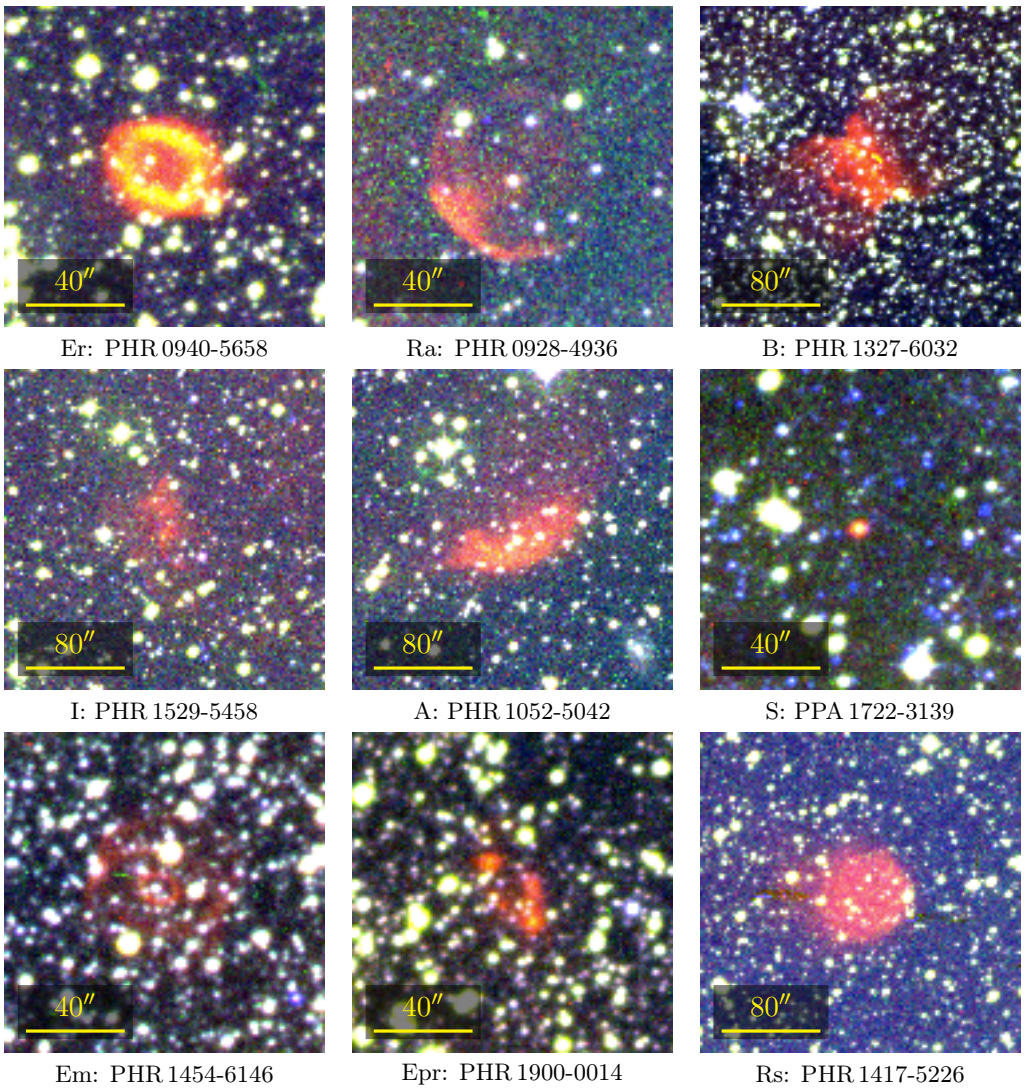

FIGURE 3.3: PN morphological classification examples. Selected MASH PNs are given with their morphological classifications and names. Northeast is top left. These synthetic RGB images use SHS Hα filter data as red, SHS short red (SR) filter data as green and SuperCOSMOS Sky Survey (SSS, Hambly et al., 2001) near-IR filter data as blue. Filter specifications are given in table 3.3.

3.1.2 Scientific Computing Practices

Computing done in the course of this research, such as the scripting and programming mentioned above, and more discussed later, used practices designed to produce accurate results efficiently. To reduce round-off errors in numerical operations, double-precision floating point variables rather than single-precision variables were used and same signed values were summed in order of smallest to largest magnitude (as per, e.g. Mak, 2003). To improve execution speed, division operations were replaced with multiplication where possible (e.g. using $x \times 0.5$ instead of $x/2$), typically a faster operation on modern computing architectures (Dahlquist & Björck, 2008). Other practices were implemented, but those listed above are representative.

procedure FITSSegmentation

input *sourceList*, *sourceWidth*, *sourceHeight*, *displayWidth*, *displayHeight*

1: $i := 1$
2: $x_{\max} := \lceil sourceWidth/displayWidth \rceil - 1$
3: $y_{\max} := \lceil sourceHeight/displayHeight \rceil - 1$
4: **forall** *source* **in** *sourceList*
5: **for** $x = 0$ **to** $x_{\max}$ **do**
6: **for** $y = 0$ **to** $y_{\max}$ **do**
7: $horzPan = \lfloor sourceWidth \times (x/(x_{\max} + 1) - x_{\max}/(2 \times (x_{\max} + 1))) \rceil$
8: $vertPan = \lfloor sourceHeight \times (y/(y_{\max} + 1) - y_{\max}/(2 \times (y_{\max} + 1))) \rceil$
9: DS9.SAVEIMAGE($source, horzPan, vertPan, i$)
10: $i := i + 1$
11: **end for**
12: **end for**
13: **end for**
14: **exit**

Figure 3.4: Algorithm for mosaicked FITS file segmentation (adapted from Stenborg, 2014). The algorithm evenly partitions an input FITS file into segments for viewing at a smaller display size. The algorithm handles arbitrary input dimensions for both the input source file and target segment display size. Metaprogramming was used to generate DS9 scripting that in turn saved the segments.

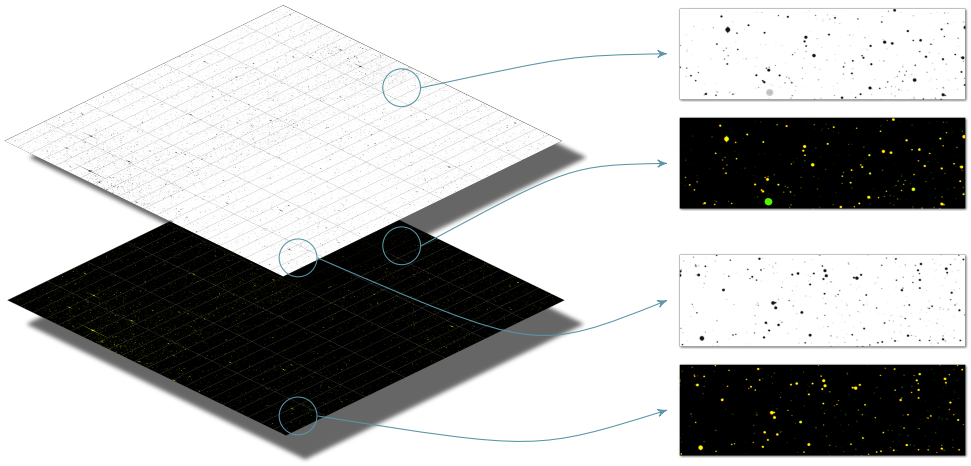

Figure 3.5: Mosaicked FITS segmentation with Blanco Mosaic II RGB and difference image frame interleaving. The segmentation displayed corresponds to an early, slightly less efficient scheme than is described in figure 3.4, but illustrates the principles. Bidirectional single-click frame navigation allowed image blinking for PN detection. Image adapted from Stenborg (2014).

For software development environments where explicit variable data types were available, explicit rather than implicit variable declarations were made. This reduces exposure to computationally expensive data type conversions during program execution. Implicitly assigned variables can also occupy more space in memory than needed, e.g. implicit assignment of an 16-byte Variant to a counter variable in VBA when a 4-byte Integer would have sufficed, and so explicit type declaration was used to reduce overall memory footprint. Minimising a program's memory footprint allows a computer, where possible, to maximise use of cache instead of main memory (or virtual memory beyond that), speeding data access (Warford, 2009). In addition, variables were declared in descending size order, including within composite data types such as structures. This was done in an effort to optimise data alignment in memory, minimising memory padding and hence reducing the number of memory input-output cycles needed to run the software (Riley, 2006). It is acknowledged compilers may not maintain high level variable declaration order, but this approach was adopted as default best practice as it required little effort. Finally, where doing so didn't compromise program clarity, instructions referencing the same variables were grouped to maximise the cache reuse ratio, and hence performance, due to data access temporal locality (Hager & Wellein, 2010).

Table 3.2: PN candidates, in J2000 coordinates. For reference, coordinates of the Galactic Centre are also supplied.

Object Name	RA (h m s) ± 0.01 s	Dec (° ′ ″) $\pm 0.2''$	Diameter (″) $\pm 0.8''$	Morph	Notes
Galactic Centre	17 45 40.04	−29 00 28.1	–	–	–
CTIO J171813.83−302357.0	17 18 13.83	−30 23 57.0	21.1 ×9.0	A	Possible PN or image artefact.
CTIO J171856.81−310641.5	17 18 56.81	−31 06 41.5	10.3 ×8.1	R	Possible PN or image artefact.
CTIO J172616.29−293451.2	17 26 16.29	−29 34 51.2	22.7 ×11.4	A	Possible PN.
CTIO J172822.84−254727.9	17 28 22.84	−25 47 27.9	22.8 ×18.4	Bam	Probable PN.
CTIO J172923.07−290500.9	17 29 23.07	−29 05 00.9	5.9 ×5.4	E	Probable PN.
CTIO J172944.81−290657.7	17 29 44.81	−29 06 57.7	27.6 ×22.8	Eas	Probable PN.
CTIO J172954.51−271918.7	17 29 54.51	−27 19 18.7	2.5 ×2.0	S	Possible PN or mimic.
IRAS 17292−2805	17 32 25.90	−28 07 29.6	2.4 ×2.0	S	Mimic. IR object.
CTIO J173241.47−302829.4	17 32 41.47	−30 28 29.4	12.1 ×12.1	Rs	Possible PN.
CTIO J173247.88−300932.4	17 32 47.88	−30 09 32.4	4.7 ×4.4	S	Possible PN.
CTIO J173348.40−264623.4	17 33 48.40	−26 46 23.4	6.0 ×6.0	R	Probable PN.
CTIO J173425.71−270524.7	17 34 25.71	−27 05 24.7	2.1 ×1.6	E	Possible PN. Faint.
CTIO J173440.23−272356.8	17 34 40.23	−27 23 56.8	10.5 ×7.7	I	Possible PN. Faint.
CTIO J173444.22−281023.7	17 34 44.22	−28 10 23.7	139.9 ×96.6	Em	Probable PN. Extended nebula.
CTIO J173513.37−263254.0	17 35 13.37	−26 32 54.0	24.0 ×16.0	Es	Possible PN. Faint.
CTIO J173557.97−271214.2	17 35 57.97	−27 12 14.2	7.6 ×7.5	R	Probable PN.
CTIO J173623.26−250528.7	17 36 23.26	−25 05 28.7	5.4 ×3.2	E	Probable PN.
CTIO J173751.75−250309.2	17 37 51.75	−25 03 09.2	13.5 ×13.5	A	Possible PN. Possible brightened rim arc visible.
CTIO J173949.95−332524.4	17 39 49.95	−33 25 24.4	10.4 ×8.6	E	Possible PN.
CTIO J173958.08−270647.1	17 39 58.08	−27 06 47.1	2.6 ×2.6	E	Possible PN or mimic.
CTIO J173959.11−270047.9	17 39 59.11	−27 00 47.9	54.1 ×53.3	Ea	Possible PN. Very faint, arc only.
CTIO J174100.05−241204.0	17 41 00.05	−24 12 04.0	3.2 ×2.5	S	Possible PN or mimic.
CTIO J174105.94−243732.0	17 41 05.94	−24 37 32.0	1.9 ×1.9	R	Possible PN or mimic. 2MASS J band bright.
CTIO J174152.05−243252.1	17 41 52.05	−24 32 52.1	6.6 ×5.3	E	Possible PN.

Table 3.2: PN candidates, in J2000 coordinates (continued).

Object Name	RA (h m s) ± 0.01 s	Dec (° ′ ″) $\pm 0.2''$	Diameter (″) $\pm 0.8''$	Morph	Notes
CTIO J174211.00−340626.1	17 42 11.00	−34 06 26.1	1.8 ×1.4	S	Possible PN or mimic.
IRAS 17393−2435	17 42 21.26	−24 34 43.5	9.3 ×7.0	E	Mimic. IR object.
CTIO J174253.89−340902.1	17 42 53.89	−34 09 02.1	9.7 ×9.1	Ras	Probable PN.
CTIO J174409.95−253030.3	17 44 09.95	−25 30 30.3	3.3 ×3.0	S	Possible PN or mimic.
CTIO J174421.47−253803.3	17 44 21.47	−25 38 03.3	1.7 ×1.1	S	Possible PN or mimic.
CTIO J174421.73−341558.2	17 44 21.73	−34 15 58.2	2.0 ×1.9	S	Possible PN.
CTIO J174423.18−341931.7	17 44 23.18	−34 19 31.7	2.6 ×1.6	S	Possible PN or mimic.
CTIO J174425.66−340519.0	17 44 25.66	−34 05 19.0	19.2 ×8.6	A	Possible PN. Very faint.
CTIO J174428.83−342922.4	17 44 28.83	−34 29 22.4	1.3 ×1.3	S	Possible PN or mimic.
CTIO J174431.07−240412.5	17 44 31.07	−24 04 12.5	2.7 ×2.6	S	Possible PN or mimic.
CTIO J174435.93−330742.0	17 44 35.93	−33 07 42.0	19.2 ×19.2	Ra	Possible PN.
CTIO J174453.14−344239.9	17 44 53.14	−34 42 39.9	5.0 ×4.5	E	Possible PN. Outside central bulge region.
CTIO J174523.43−262706.2	17 45 23.43	−26 27 06.2	4.0 ×3.7	S	Possible PN or mimic.
CTIO J174537.17−335608.1	17 45 37.17	−33 56 08.1	20.5 ×19.3	Es	Possible PN. Faint.
CTIO J174546.15−253319.8	17 45 46.15	−25 33 19.8	2.1 ×1.8	R	Possible PN or mimic.
CTIO J174547.44−333932.4	17 45 47.44	−33 39 32.4	79.2 ×24.7	I	Probable PN. Sinuous.
CTIO J174648.06−341342.3	17 46 48.06	−34 13 42.3	5.6 ×5.4	R	True PN.
CTIO J174648.23−343603.0	17 46 48.23	−34 36 03.0	2.8 ×2.6	S	Possible PN or mimic.
CTIO J174732.26−242218.9	17 47 32.26	−24 22 18.9	3.4 ×2.8	S	Possible PN or image artefact.
CTIO J174748.01−342126.4	17 47 48.01	−34 21 26.4	6.3 ×1.8	A	Possible PN.
CTIO J174756.67−331444.4	17 47 56.67	−33 14 44.4	12.3 ×9.9	I	Probable PN.
CTIO J174808.57−310445.3	17 48 08.57	−31 04 45.3	114.4 ×49.6	Rp	Possible PN. Extremely large ionised structure in CTIO and SHS data.
CTIO J174825.12−301520.7	17 48 25.12	−30 15 20.7	3.1 ×1.2	S	Possible PN.
CTIO J174925.72−344647.2	17 49 25.72	−34 46 47.2	29.7 ×23.2	Ra	Probable PN.

Table 3.2: PN candidates, in J2000 coordinates (continued).

Object Name	RA (h m s) ± 0.01 s	Dec (° ′ ″) $\pm 0.2''$	Diameter (″) $\pm 0.8''$	Morph	Notes
CTIO J174938.55−320801.5	17 49 38.55	−32 08 01.5	2.3 ×1.7	S	Possible PN.
CTIO J174941.81−341135.0	17 49 41.81	−34 11 35.0	1.6 ×1.3	R	Mimic. Possible nova.
CTIO J174955.44−334234.7	17 49 55.44	−33 42 34.7	34.7 ×34.7	Ra	Possible PN at CCD edge.
CTIO J175006.71−340258.6	17 50 06.71	−34 02 58.6	7.2 ×6.9	R	Possible PN.
CTIO J175024.35−285312.2	17 50 24.35	−28 53 12.2	9.9 ×5.6	I	Mimic.
CTIO J175051.08−305206.5	17 50 51.08	−30 52 06.5	12.5 ×11.6	E	Possible PN.
SHS J175055.57−305224.0	17 50 55.57	−30 52 24.0	6.3 ×4.5	S	Mimic. Possible M-type star.
CTIO J175056.96−350046.3	17 50 56.96	−35 00 46.3	18.1 ×14.9	B	PN G355.3-04.1.
CTIO J175110.13−340529.8	17 51 10.13	−34 05 29.8	1.3 ×1.2	S	Mimic. Emission line star.
CTIO J175115.83−332447.3	17 51 15.83	−33 24 47.3	1.8 ×1.4	S	Mimic. Suspected emission line star.
CTIO J175208.32−343607.0	17 52 08.32	−34 36 07.0	2.0 ×2.0	S	Mimic.
CTIO J175234.11−302619.6	17 52 34.11	−30 26 19.6	7.1 ×7.1	E	Probable PN.
CTIO J175238.99−333047.2	17 52 38.99	−33 30 47.2	52.6 ×34.0	Ea	Probable PN.
CTIO J175246.55−301700.4	17 52 46.55	−30 17 00.4	11.5 ×6.5	E	Possible PN.
CTIO J175308.41−353356.7	17 53 08.41	−35 33 56.7	22.1 ×11.0	E	Possible PN or image artefact.
CTIO J175310.09−293108.6	17 53 10.09	−29 31 08.6	2.7 ×2.3	S	Probable [WR] PN.
CTIO J175323.14−340653.7	17 53 23.14	−34 06 53.7	33.2 ×24.2	Eas	Probable PN.
CTIO J175346.02−334753.3	17 53 46.02	−33 47 53.3	2.4 ×1.8	S	Mimic. Emission line star.
CTIO J175353.88−322907.7	17 53 53.88	−32 29 07.7	5.2 ×5.2	R	Possible PN. Abuts PN G357.8-03.3.
CTIO J175401.23−343958.7	17 54 01.23	−34 39 58.7	18.9 ×18.5	Ra	Probable PN.
CTIO J175417.64−292221.0	17 54 17.64	−29 22 21.0	37.5 ×4.9	I	Probable PN. Irregular.
CTIO J175417.98−282724.3	17 54 17.98	−28 27 24.3	20.7 ×14.9	E	Possible PN. Faint.
CTIO J175434.30−343140.4	17 54 34.30	−34 31 40.4	2.1 ×1.9	S	Mimic.
CTIO J175442.23−300836.1	17 54 42.23	−30 08 36.1	21.1 ×21.1	R	Probable PN. Faint.
CTIO J175444.26−290744.2	17 54 44.26	−29 07 44.2	20.1 ×17.4	Ea	Probable PN.

Table 3.2: PN candidates, in J2000 coordinates (continued).

Object Name	RA (h m s) ± 0.01 s	Dec ($^\circ$ ′ ″) $\pm 0.2''$	Diameter ($''$) $\pm 0.8''$	Morph	Notes
CTIO J175452.18−342852.1	17 54 52.18	−34 28 52.1	22.0 ×20.5	Ear	Possible PN.
CTIO J175505.83−344705.9	17 55 05.83	−34 47 05.9	1.6 ×0.9	S	Possible PN or mimic.
CTIO J175536.99−280611.2	17 55 36.99	−28 06 11.2	5.5 ×1.9	B	Possible PN.
CTIO J175603.00−312658.9	17 56 03.00	−31 26 58.9	34.2 ×34.2	Ra	Possible PN.
CTIO J175604.17−280343.0	17 56 04.17	−28 03 43.0	3.3 ×2.3	I	Possible PN.
CTIO J175606.37−290733.7	17 56 06.37	−29 07 33.7	16.0 ×15.9	R	Probable PN.
IRAS 17538−2935	17 57 00.37	−29 35 17.4	1.3 ×1.2	S	Mimic.
CTIO J175703.45−284955.2	17 57 03.45	−28 49 55.2	8.5 ×5.4	B	Possible PN.
CTIO J175703.93−275130.4	17 57 03.93	−27 51 30.4	15.0 ×13.2	E	Possible PN. Round ring nebula.
CTIO J175706.52−310324.5	17 57 06.52	−31 03 24.5	16.5 ×16.2	R	Possible PN.
CTIO J175708.64−310453.4	17 57 08.64	−31 04 53.4	36.3 ×15.7	Ba	Possible PN or mimic.
CTIO J175735.64−273532.5	17 57 35.64	−27 35 32.5	14.8 ×11.4	R	Possible PN.
CTIO J175800.70−285401.9	17 58 00.70	−28 54 01.9	2.4 ×1.9	Ba	Probable PN. Faint, compact.
CTIO J175811.57−330701.0	17 58 11.57	−33 07 01.0	6.7 ×6.0	E	Possible PN.
CTIO J175812.20−283436.9	17 58 12.20	−28 34 36.9	2.9 ×2.7	S	True PN.
CTIO J175836.40−292120.0	17 58 36.40	−29 21 20.0	52.9 ×50.9	R	Possible PN. Faint.
CTIO J175850.06−304943.3	17 58 50.06	−30 49 43.3	13.7 ×9.7	I	Possible PN.
CTIO J175851.48−291559.8	17 58 51.48	−29 15 59.8	22.6 ×21.2	Rps	Probable PN.
CTIO J175857.26−284902.5	17 58 57.26	−28 49 02.5	2.1 ×1.7	S	Probable PN.
CTIO J175904.60−265547.3	17 59 04.60	−26 55 47.3	2.3 ×1.9	S	Possible PN or mimic.
CTIO J175919.98−275515.3	17 59 19.98	−27 55 15.3	17.4 ×14.7	R	Possible PN.
CTIO J175954.11−332453.4	17 59 54.11	−33 24 53.4	2.1 ×2.1	Eam	Possible PN.
CTIO J175955.50−271916.7	17 59 55.50	−27 19 16.7	18.3 ×16.1	Ras	Possible PN. Visible structure?
CTIO J180000.03−302618.5	18 00 00.03	−30 26 18.5	21.7 ×7.6	I	Possible PN, possible misc. ejection nebula.
CTIO J180021.99−274607.7	18 00 21.99	−27 46 07.7	9.4 ×7.1	Eas	Probable PN.

Table 3.2: PN candidates, in J2000 coordinates (continued).

Object Name	RA (h m s) ± 0.01 s	Dec ($^\circ$ ′ ″) $\pm 0.2''$	Diameter ($''$) $\pm 0.8''$	Morph	Notes
CTIO J180023.29−282341.9	18 00 23.29	−28 23 41.9	1.3 ×1.3	R	Mimic.
CTIO J180029.12−332834.8	18 00 29.12	−33 28 34.8	48.4 ×19.6	I	Possible PN or image artefact. Outside central bulge region.
CTIO J180030.42−300952.7	18 00 30.42	−30 09 52.7	18.4 ×16.7	Ear	Possible PN.
CTIO J180056.24−321421.2	18 00 56.24	−32 14 21.2	29.4 ×28.8	Ra	Possible PN.
CTIO J180056.33−321421.5	18 00 56.33	−32 14 21.5	30.4 ×29.5	R	Possible PN. Faint.
CTIO J180150.14−275526.4	18 01 50.14	−27 55 26.4	10.6 ×7.2	B	Probable PN.
CTIO J180204.70−280340.5	18 02 04.70	−28 03 40.5	40.9 ×38.6	E	Probable PN.
CTIO J180210.24−295159.3	18 02 10.24	−29 51 59.3	1.3 ×1.3	S	Possible PN or mimic. Variable star OGLE BW1 V209?
CTIO J180224.88−302343.7	18 02 24.88	−30 23 43.7	1.6 ×1.5	S	Possible PN or mimic.
CTIO J180235.03−310555.9	18 02 35.03	−31 05 55.9	22.0 ×20.1	Ra	Probable PN.
CTIO J180253.79−280755.6	18 02 53.79	−28 07 55.6	36.9 ×35.2	Rr	Probable PN.
CTIO J180258.75−291347.5	18 02 58.75	−29 13 47.5	35.3 ×35.2	Ra	Possible PN.
CTIO J180308.22−292038.0	18 03 08.22	−29 20 38.0	3.6 ×3.3	S	Possible PN.
CTIO J180311.83−262927.0	18 03 11.83	−26 29 27.0	5.5 ×4.9	S	Possible PN.
CTIO J180317.18−285614.6	18 03 17.18	−28 56 14.6	2.2 ×2.1	S	Mimic. Assumed emission line star.
CTIO J180317.18−285627.5	18 03 17.18	−28 56 27.5	2.1 ×1.8	S	Possible PN or mimic.
CTIO J180325.70−314839.4	18 03 25.70	−31 48 39.4	31.3 ×23.5	E	Possible PN. Edge-on bipolar?
CTIO J180359.49−311740.8	18 03 59.49	−31 17 40.8	3.0 ×2.9	S	Possible PN.
CTIO J180410.54−292638.5	18 04 10.54	−29 26 38.5	35.3 ×21.2	I	Possible PN.
CTIO J180413.75−281602.2	18 04 13.75	−28 16 02.2	2.6 ×2.2	S	Probable PN. Abuts PN G002.6-03.1.
CTIO J180507.08−264839.2	18 05 07.08	−26 48 39.2	29.4 ×27.3	A	Possible PN. Faint.
CTIO J180555.61−290246.3	18 05 55.61	−29 02 46.3	29.3 ×28.6	Ea	Possible PN.
CTIO J180652.90−280706.0	18 06 52.90	−28 07 06.0	18.6 ×16.6	E	True PN.
CTIO J180701.33−264550.2	18 07 01.33	−26 45 50.2	60.7 ×58.8	Rms	Probable PN.

Table 3.2: PN candidates, in J2000 coordinates (continued).

Object Name	RA (h m s) ± 0.01 s	Dec ($^\circ$ $'$ $''$) $\pm 0.2''$	Diameter ($''$) $\pm 0.8''$	Morph	Notes
CTIO J180711.70−262719.2	18 07 11.70	−26 27 19.2	21.9 ×15.6	A	Possible PN. Faint.
CTIO J180724.90−290326.0	18 07 24.90	−29 03 26.0	33.8 ×31.5	Ras	Possible PN.
CTIO J180742.79−263104.0	18 07 42.79	−26 31 04.0	40.5 ×37.5	E	Possible PN. Faint.
CTIO J180755.67−264114.1	18 07 55.67	−26 41 14.1	2.8 ×2.0	S	True PN.
CTIO J180832.52−284950.6	18 08 32.52	−28 49 50.6	1.2 ×1.2	S	Possible PN.
CTIO J180854.57−294441.0	18 08 54.57	−29 44 41.0	24.0 ×23.3	Rrs	Possible PN.
CTIO J181026.15−284016.3	18 10 26.15	−28 40 16.3	41.1 ×40.1	Ra	Possible PN. Very faint.
CTIO J181057.79−271822.5	18 10 57.79	−27 18 22.5	17.3 ×16.6	E	Possible PN.
CTIO J181120.34−272432.4	18 11 20.34	−27 24 32.4	2.4 ×1.6	S	Possible PN or mimic.
CTIO J181244.61−281033.3	18 12 44.61	−28 10 33.3	34.5 ×21.7	Ea	Probable PN.

3.2 Candidate Ranking and Artefact Rejection

In addition to PN candidate cross-checks against known SIMBAD objects, the SHS and SSS online atlases were cross-checked for corresponding Hα and near-IR emission. Analogous to synthetic RGB image creation for Blanco Mosaic II data in DS9, equivalents were created for UKST data, using SHS Hα filter data in red frames, SHS SR filter data in green frames and SSS near-IR filter data in blue frames. An example of this was presentation of PN morphological examples, figure 3.3. Using UKST Hα/SR/IR data, PN emission stands out in red, again roughly corresponding to the correct part of the visible spectrum. It is acknowledged the SHS narrow band filter transmits Hα and [N II] λ6583 nebula emission, and even, though less efficiently, [N II] λ6548. It will nonetheless be referred to as a Hα filter for brevity, as per Parker et al. (2005). It is also acknowledged the SHS and SSS imaging was taken at different times, and some synthetic colours may be consequent artefacts of variable objects, rather than true representations of objects' spectra. No quantification of the statistical impact on the images presented here is attempted, it is simply a caveat that may assist interpretation of unusual results.

A candidate visible in both Blanco and UKST imaging suggested a viable PN candidate, not an image artefact. A candidate failing this emission cross-check wasn't discounted immediately but simply ranked as less likely to be a true PN and given less observational priority. Some candidates later confirmed as bona fide PNs indeed failed this cross-check, suggesting their flux ratios $(F_{\mathrm{H}\alpha} + F_{6583})/F_{5007}$ were too low (e.g. high excitation PNs) to offset the aperture gain of the 4 m Blanco telescope over the 1.2 m UKST used for the SHS, even allowing for preferential extinction of [O III] emission compared with Hα emission (effective aperture gain would of course also be affected by other factors such as the relative filter transmission and detector efficiencies on each telescope). Aperture gain issues aside, no real objects were expected to be intrinsically present as mimics in Blanco imaging but not UKST imaging.

Candidates were initially cross-checked against only UKST Hα/SR. Without the added astrophysical information provided by the SSS IR (I band) filter data however, some PN mimics were retained in the candidate pool, e.g. the possible M-type star SHS J175055.57-305224.0 (§3.4.4). I band data, added later, not only helps filter out late-type stars, but other mimics with a reflection component (Frew & Parker, 2010).

A comparison of the Mosaic II [O III] on/off band, SHS SR/Hα and SSS filter specifications is given in table 3.3. Specifications include λ_{c}, FWHM and peak transmission, where such data is available. Significant figure differences in specifications have generally been preserved from their source material. Note, Mosaic II specifications apply to filter use in the Blanco's $f/2.87$ beam at prime focus with the Prime Focus Atmospheric Dispersion Compensator (PFADC), which incorporates a blueshift of $\approx$1.5 nm compared to transmission measured in parallel light. Some Mosaic II filter specifications (Schweiker, 2014) are however inconsistent with the associated transmission curves. Where such discrepancies exist, transmission curve

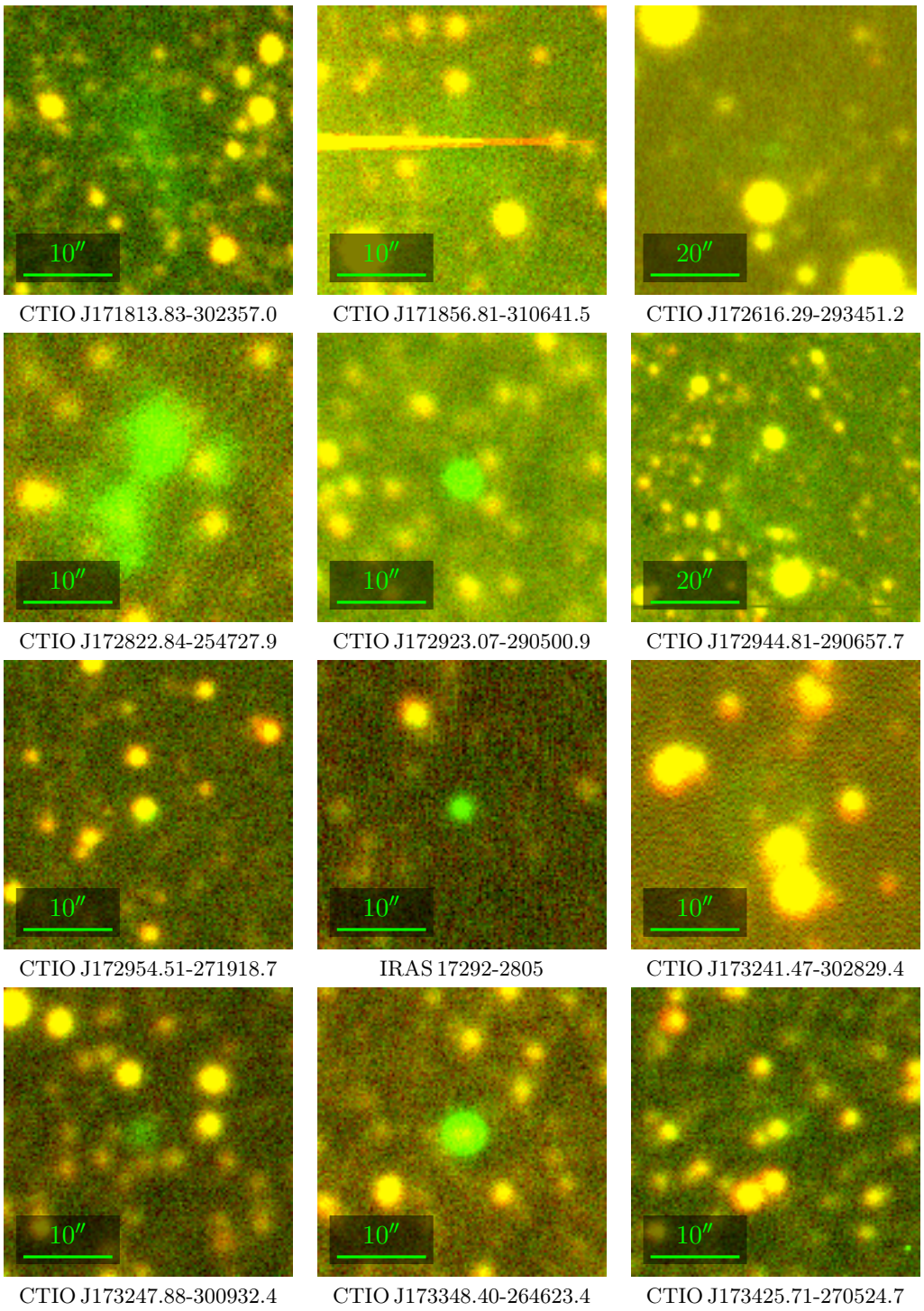

Figure 3.6: PN candidate images. North east is to the top left of each image.

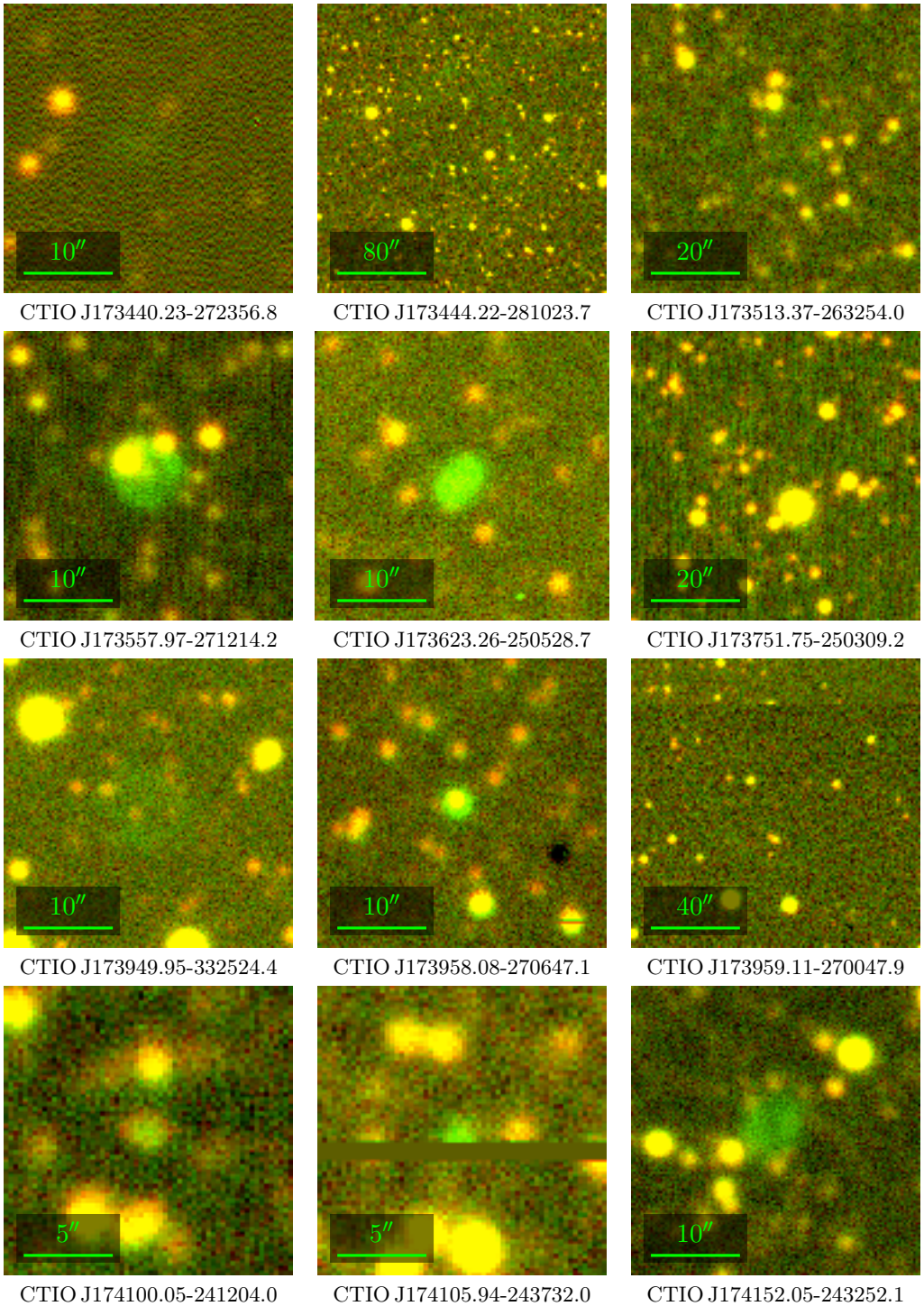

CTIO J173440.23-272356.8 CTIO J173444.22-281023.7 CTIO J173513.37-263254.0

CTIO J173557.97-271214.2 CTIO J173623.26-250528.7 CTIO J173751.75-250309.2

CTIO J173949.95-332524.4 CTIO J173958.08-270647.1 CTIO J173959.11-270047.9

CTIO J174100.05-241204.0 CTIO J174105.94-243732.0 CTIO J174152.05-243252.1

Figure 3.6: PN candidate images (continued). North east is to the top left of each image.

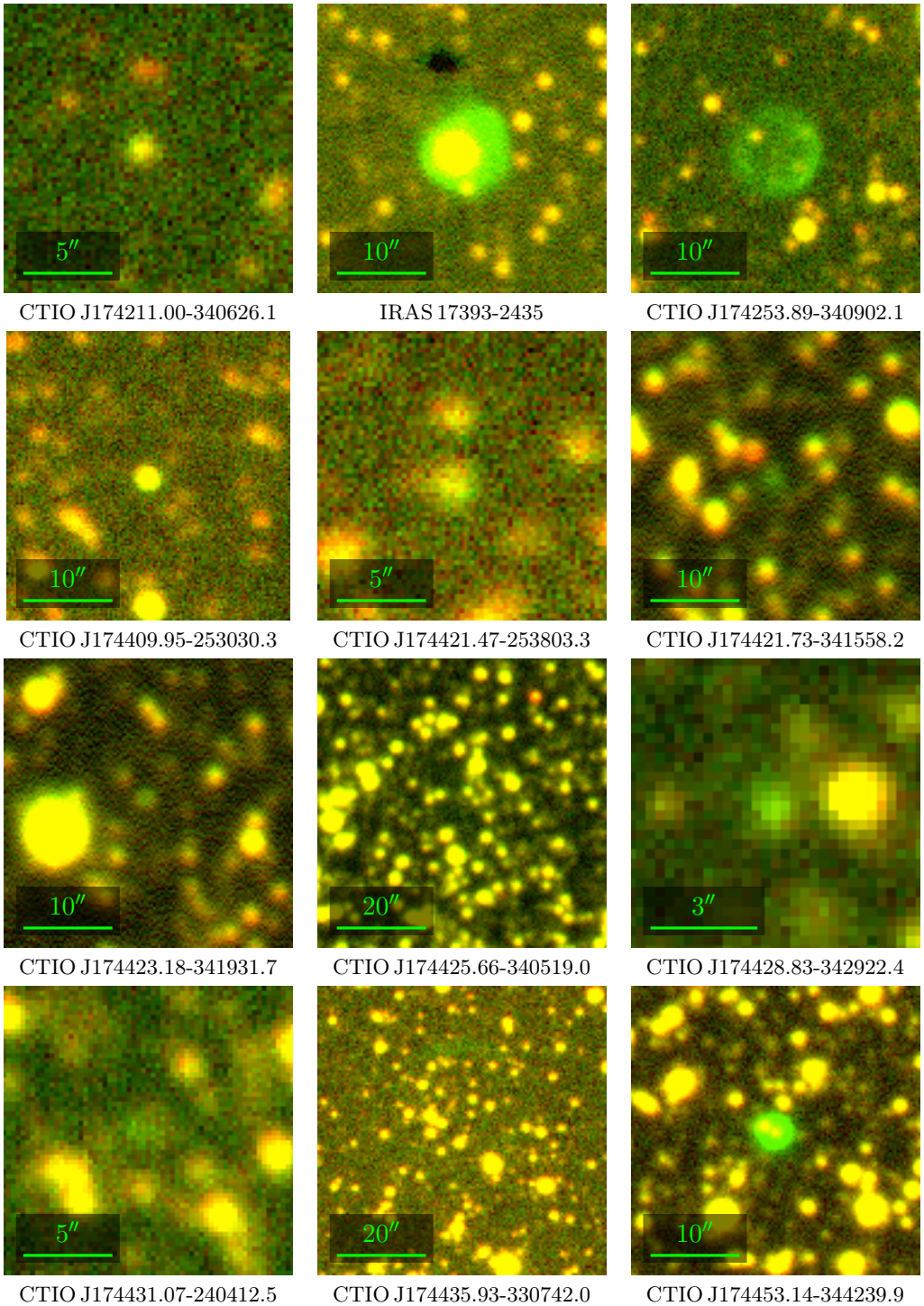

CTIO J174211.00-340626.1 | IRAS 17393-2435 | CTIO J174253.89-340902.1

CTIO J174409.95-253030.3 | CTIO J174421.47-253803.3 | CTIO J174421.73-341558.2

CTIO J174423.18-341931.7 | CTIO J174425.66-340519.0 | CTIO J174428.83-342922.4

CTIO J174431.07-240412.5 | CTIO J174435.93-330742.0 | CTIO J174453.14-344239.9

Figure 3.6: PN candidate images (continued). North east is to the top left of each image.

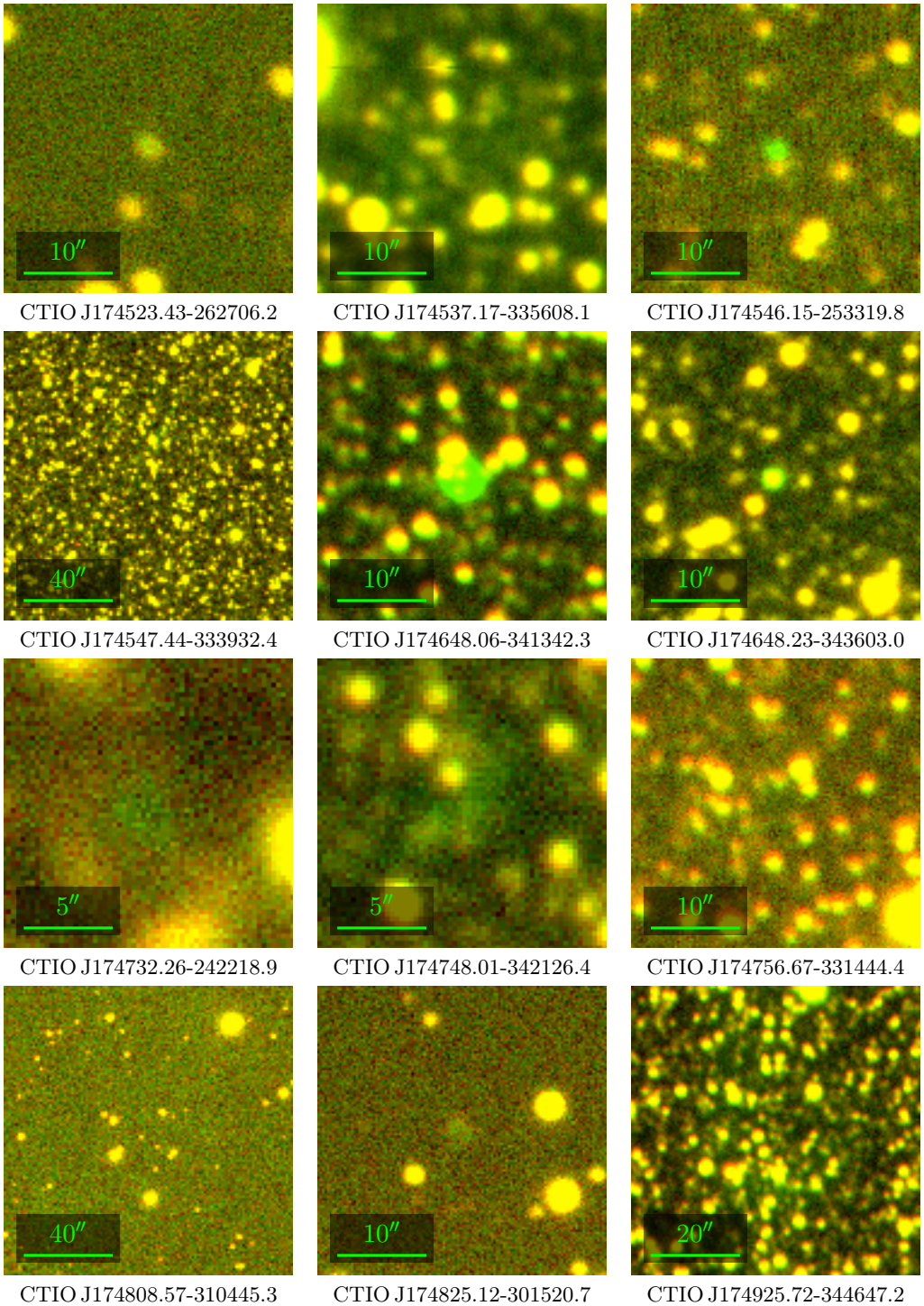

CTIO J174523.43-262706.2 CTIO J174537.17-335608.1 CTIO J174546.15-253319.8

CTIO J174547.44-333932.4 CTIO J174648.06-341342.3 CTIO J174648.23-343603.0

CTIO J174732.26-242218.9 CTIO J174748.01-342126.4 CTIO J174756.67-331444.4

CTIO J174808.57-310445.3 CTIO J174825.12-301520.7 CTIO J174925.72-344647.2

Figure 3.6: PN candidate images (continued). North east is to the top left of each image.

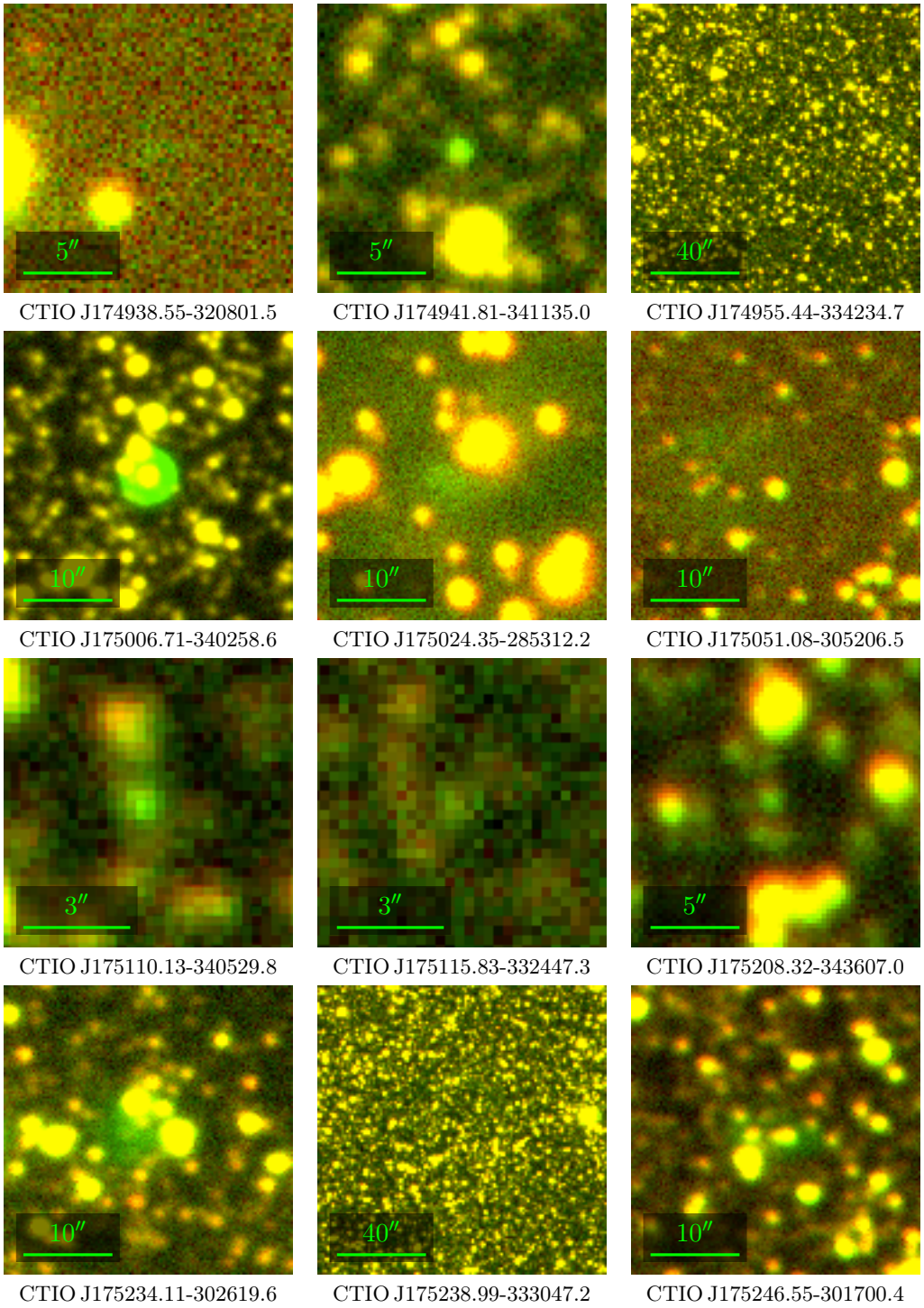

CTIO J174938.55-320801.5 CTIO J174941.81-341135.0 CTIO J174955.44-334234.7

CTIO J175006.71-340258.6 CTIO J175024.35-285312.2 CTIO J175051.08-305206.5

CTIO J175110.13-340529.8 CTIO J175115.83-332447.3 CTIO J175208.32-343607.0

CTIO J175234.11-302619.6 CTIO J175238.99-333047.2 CTIO J175246.55-301700.4

Figure 3.6: PN candidate images (continued). North east is to the top left of each image.

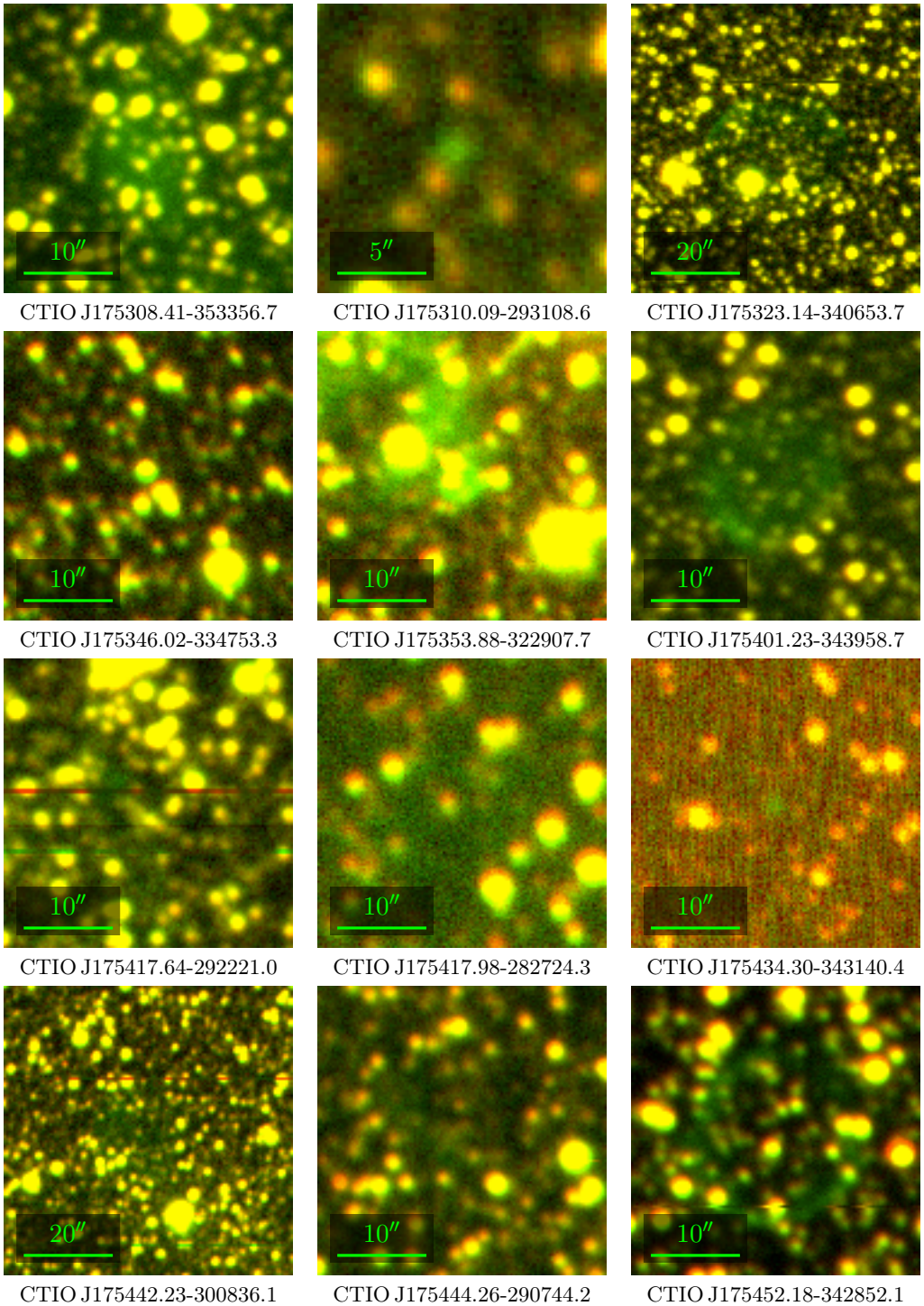

CTIO J175308.41-353356.7 CTIO J175310.09-293108.6 CTIO J175323.14-340653.7

CTIO J175346.02-334753.3 CTIO J175353.88-322907.7 CTIO J175401.23-343958.7

CTIO J175417.64-292221.0 CTIO J175417.98-282724.3 CTIO J175434.30-343140.4

CTIO J175442.23-300836.1 CTIO J175444.26-290744.2 CTIO J175452.18-342852.1

Figure 3.6: PN candidate images (continued). North east is to the top left of each image.

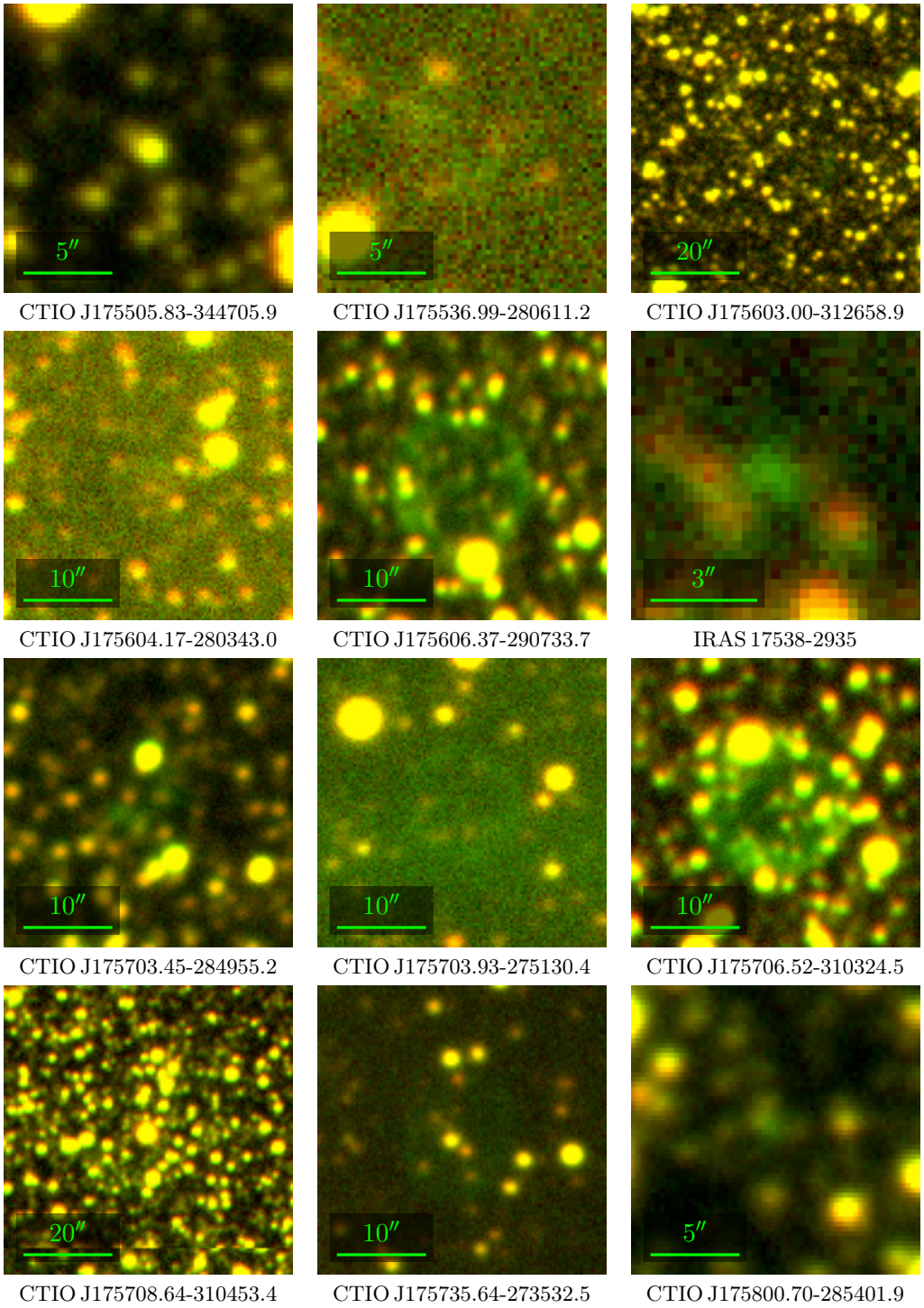

CTIO J175505.83-344705.9 CTIO J175536.99-280611.2 CTIO J175603.00-312658.9

CTIO J175604.17-280343.0 CTIO J175606.37-290733.7 IRAS 17538-2935

CTIO J175703.45-284955.2 CTIO J175703.93-275130.4 CTIO J175706.52-310324.5

CTIO J175708.64-310453.4 CTIO J175735.64-273532.5 CTIO J175800.70-285401.9

Figure 3.6: PN candidate images (continued). North east is to the top left of each image.

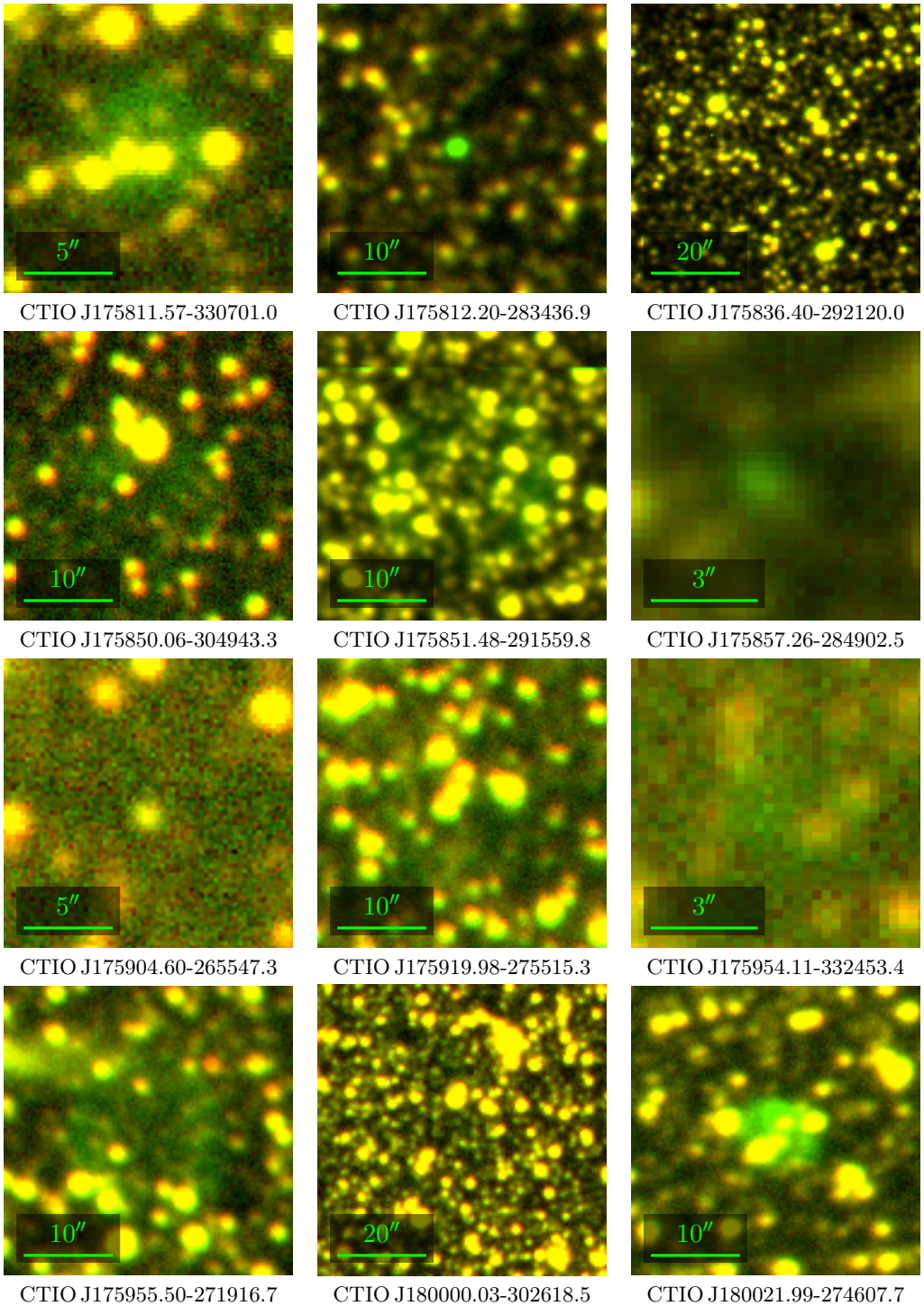

CTIO J175811.57-330701.0 CTIO J175812.20-283436.9 CTIO J175836.40-292120.0

CTIO J175850.06-304943.3 CTIO J175851.48-291559.8 CTIO J175857.26-284902.5

CTIO J175904.60-265547.3 CTIO J175919.98-275515.3 CTIO J175954.11-332453.4

CTIO J175955.50-271916.7 CTIO J180000.03-302618.5 CTIO J180021.99-274607.7

Figure 3.6: PN candidate images (continued). North east is to the top left of each image.

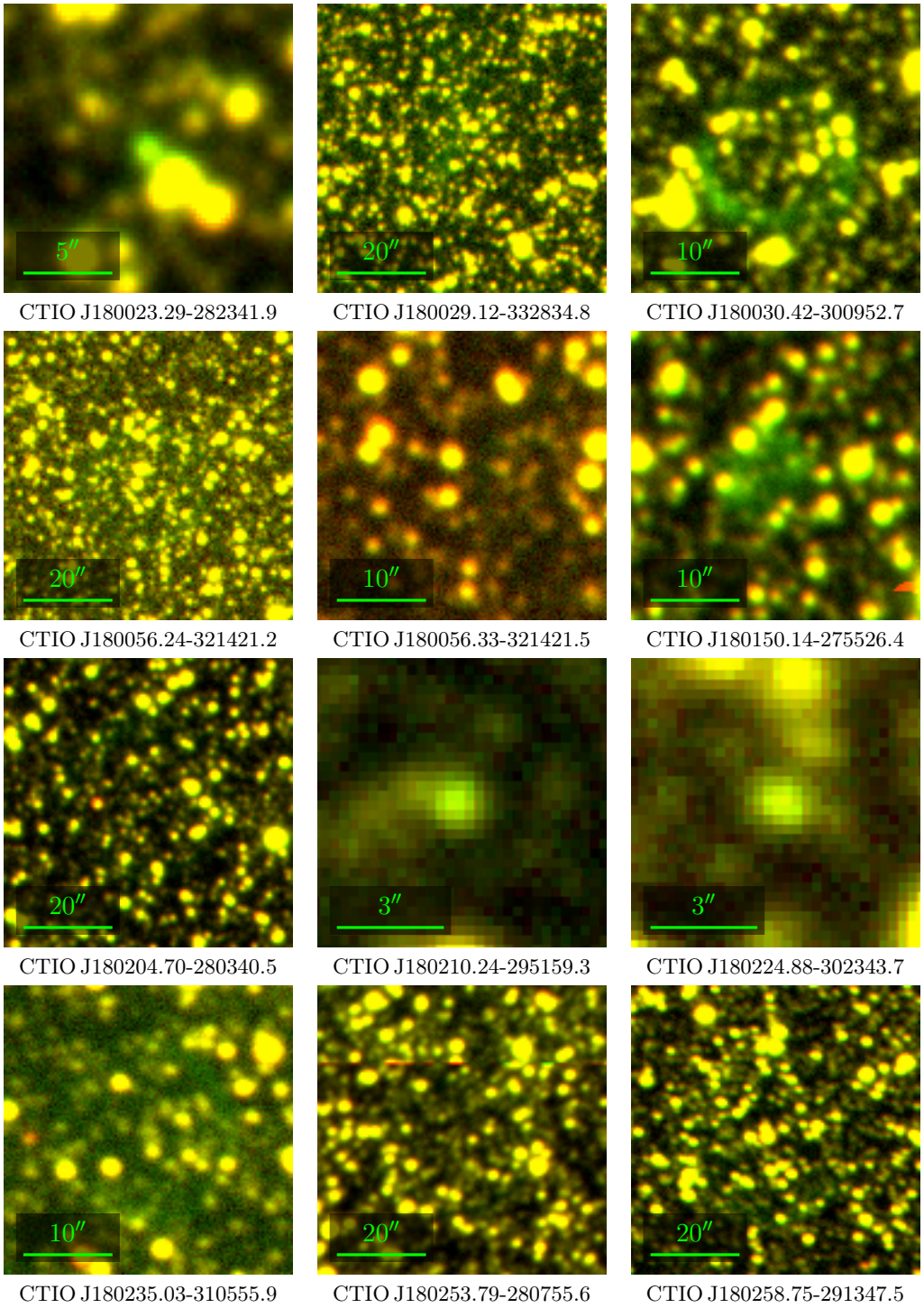

Figure 3.6: PN candidate images (continued). North east is to the top left of each image.

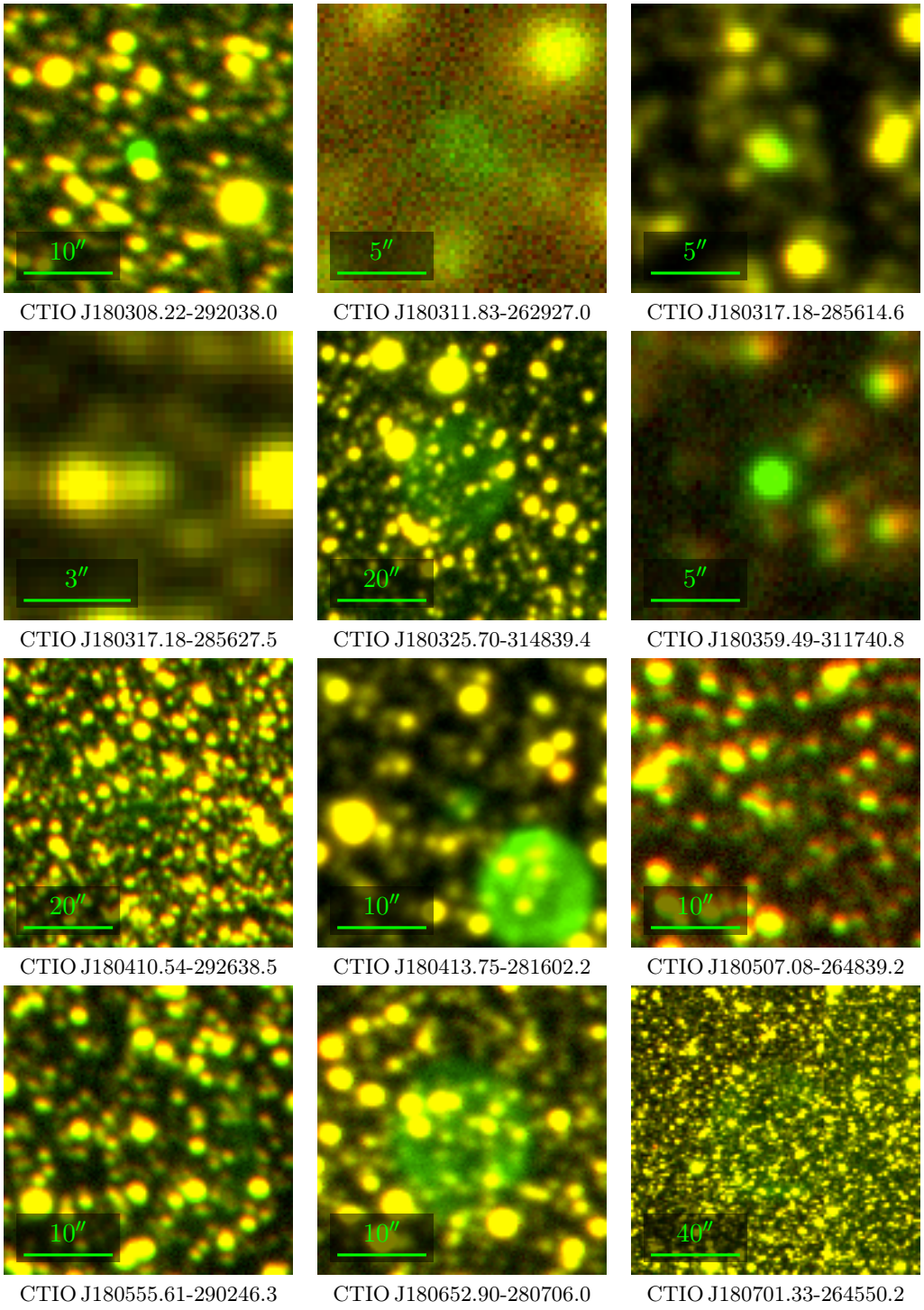

CTIO J180308.22-292038.0 CTIO J180311.83-262927.0 CTIO J180317.18-285614.6

CTIO J180317.18-285627.5 CTIO J180325.70-314839.4 CTIO J180359.49-311740.8

CTIO J180410.54-292638.5 CTIO J180413.75-281602.2 CTIO J180507.08-264839.2

CTIO J180555.61-290246.3 CTIO J180652.90-280706.0 CTIO J180701.33-264550.2

Figure 3.6: PN candidate images (continued). North east is to the top left of each image.

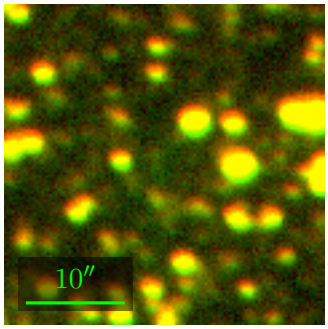

CTIO J180711.70-262719.2

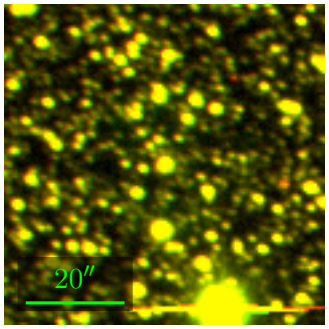

CTIO J180724.90-290326.0

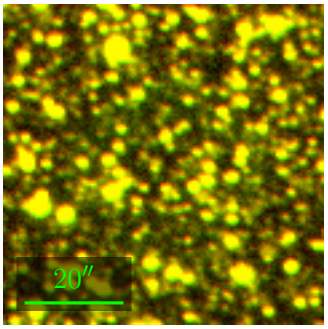

CTIO J180742.79-263104.0

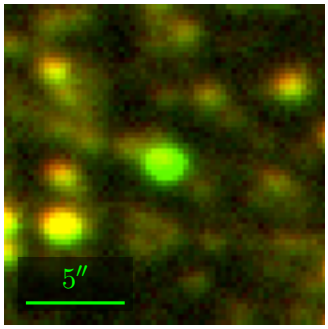

CTIO J180755.67-264114.1

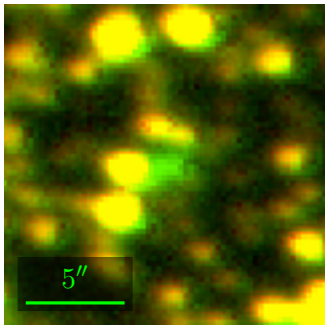

CTIO J180832.52-284950.6

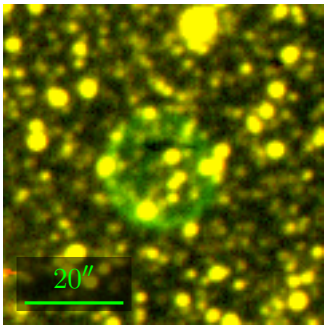

CTIO J180854.57-294441.0

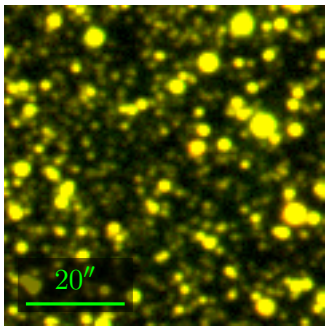

CTIO J181026.15-284016.3

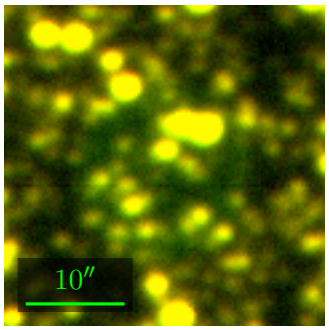

CTIO J181057.79-271822.5

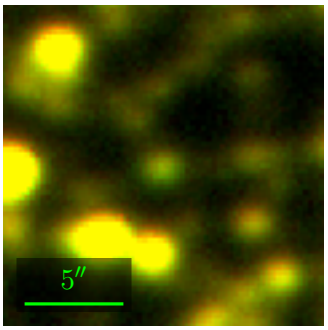

CTIO J181120.34-272432.4

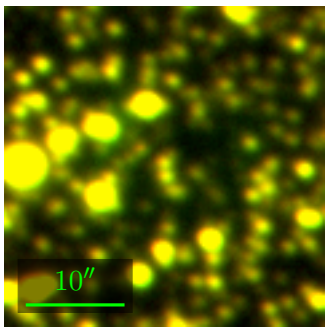

CTIO J181244.61-281033.3

Figure 3.6: PN candidate images (continued). North east is to the top left of each image.

data will be used[4]. This will lead later to aperture photometry refinements consistent with Kovacevic (2011).

Table 3.3: Multi-survey filter specifications. Mosaic II specifications apply to filter use in the Blanco's $f/2.87$ beam at prime focus with the PFADC.

Filter	λ_c (nm)	FWHM (nm)	Peak transmission (%)	Reference
[O III] c6014	500.0*	5.0	74.09	[1]
off band k1015	530.254	24.269	92.79†	[1]
SHS SR	∼640.0	∼100.0	–‡	[2,3]
SHS Hα	659.0 ± 2.5	7.0 ± 0.3	⩾85	[4]
SSS I	790	157 ± 2	–‡	[5]

* Assumed $\lambda_c = \lambda_{peak}$.
† Measured in parallel light, $f/2.87$ data unavailable.
‡ Data unavailable.
[1] Schweiker (2014)
[2] Parker et al. (2005)
[3] Frew et al. (2014)
[4] Parker & Bland-Hawthorn (1998)
[5] Hartley & Dawe (1981)

It is acknowledged some PN mimics exhibit spectra with both [O III] and Hα emission peaks, e.g. emission line galaxy PHR J0950-5223 (Frew & Parker, 2010), and would thus be indistinguishable from compact PNs on the basis of the Mosaic II and SHS imaging examined here. The number of candidates in this category are expected to be low based on candidate analysis done for the MASH and MASH-II catalogues. Amongst PN mimics rejected from those catalogues, only 4% were a galaxy of some kind (Boissay et al., 2012). As the Blanco imaging, unlike MASH, examines the high extinction bulge region[5] exclusively, the percentage of galactic contaminants is expected to be lower still. Nonetheless, many very compact candidates were checked not only against SIMBAD objects, but against the many NED objects in the bulge region (as of 12 March 2015, 09:00:00, Pacific Daylight Time, 15 346 NED objects lay within a 5° radius of the Galactic Centre). It is anticipated any remaining PN candidates that are actually galaxies would be revealed as such during spectroscopic candidate analysis.

To further identify PN mimics, PN candidates discovered here could have been cross-checked further against multiwavelength surveys such as those in listed in table 1.3 (§1.7). Indeed, selective use has been made here of *WISE* imaging, aimed especially at distinguishing compact PNs from late-type stars. For WISE images, the default intensity range, set in DS9, is linear zscale, as for the Blanco and UKST imaging. This default works poorly however in distinguishing bright objects with small apparent separations. In such cases, an alternate intensity scale, such as linear 99%, will be used, but not explicitly documented in each case.

[4] A supplementary [O III] c6014 filter transmission profile is given in figure 6.1, page 205.
[5] The high and variable bulge extinction reaches up to 35 mag V band and 3.5 mag K_S band total extinction (Chen et al., 2013).

As *WISE* imaging is publicly available online, interested parties can experiment with image presentation at their leisure. *WISE* passband specifications are given in table 3.4, analogous to table 3.3 for the Blanco and UKST filters, but with the addition here of isophotal wavelength $\lambda_{\rm iso}$ (Tokunaga & Vacca, 2005a,b).

TABLE 3.4: *WISE* near- and mid-IR passband specifications (Wright et al., 2010, Jarrett et al., 2011).

Passband	$\lambda_{\rm c}$ (μm)*	$\lambda_{\rm iso}$ (μm)	FWHM (μm)*	Relative response photon^{-1} (%)
1	3.4	3.3526 ± 0.0132	0.630	88 ± 3
2	4.6	4.6028 ± 0.0168	1.090	75 ± 3
3	12	11.5608 ± 0.0446	6.270	43 ± 3
4	22	22.0883 ± 0.1184	4.730	30 ± 3

* Approximate value.

Two types of synthetic RGB image will be presented, each using data from different *WISE* passband combinations. Firstly, "near-IR" synthetic RGB images will be constructed using data from passbands 3 (red), 2 (green) and 1 (blue). Secondly, "mid-IR" synthetic RGB images will be constructed using data from passbands 4 (red), 3 (green) and 2 (blue).

3.2.1 Cosmics

The Mosaic II imaging suffered from cosmics, with the term cosmics used hereafter to refer to CCD image artefacts induced by both true cosmic rays and, more broadly, any type of ionising radiation. Cosmics manifest in multiple ways in CCD images, such as straight muon tracks and spots and worms generated by beta particles or recoil electrons from Compton scattered gamma rays (Groom, 2004). Cosmics can be recognised by sudden, significant intensity changes from pixel to pixel and high peak intensity (e.g. change $\geqslant$ (1.5–2)σ above background, 5σ peak, Smith et al., 2002), unlike the more gradual intensity change of a genuine astronomical point spread function over a number of pixels. Example suspected cosmics in Mosaic II imaging are shown in 3.7. Care was taken not to confuse large cosmic spots as compact PN candidates. Judicious spectroscopy of ambiguous cases failed to return emission line data from any member of this class of artefact.

3.2.2 Amplifier Crosstalk Echoes

Amplifier crosstalk signals echoing bright objects, at or approaching saturation ($>$ 21 000–44 000 analog to digital units (ADU), CCD dependent), were another type of image artefact present in the Mosaic II imaging. The eight CCD Mosaic II imager had four Arcon controllers, i.e. each controller read data from a pair of CCDs (Muller et al., 1998, Smith, 1998). Bright object echoes are produced by electrical unidirectional crosstalk in Arcon controlled CCD pairs, such

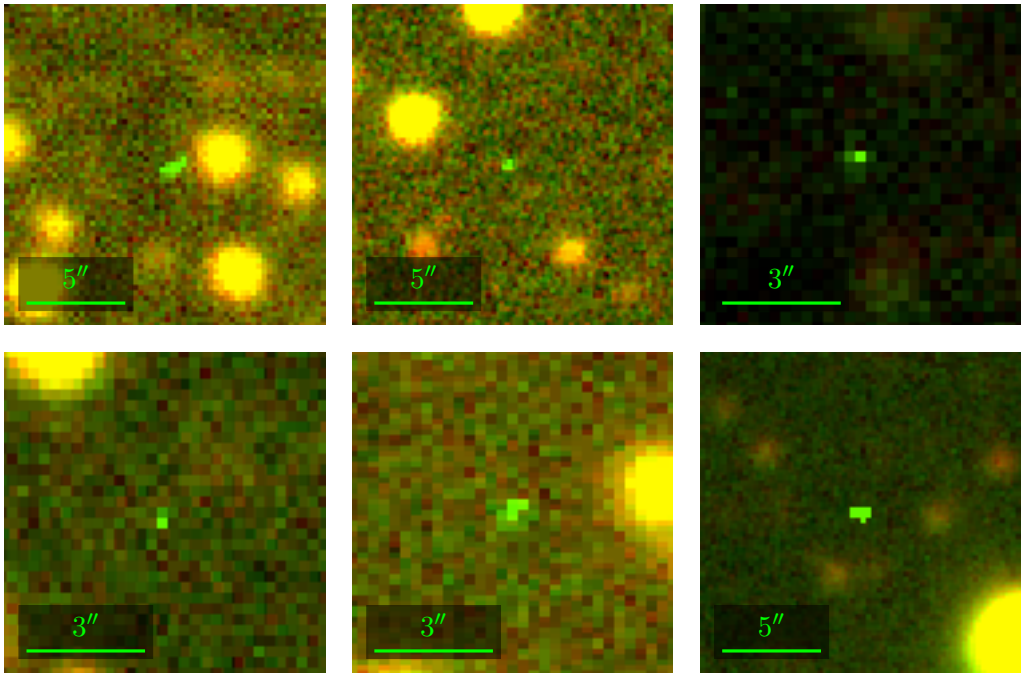

Figure 3.7: Example cosmics in Mosaic II [O III] on/off band images.

that echoes in CCDs 1, 3, 6 and 8 are artefacts of real stars in CCDs 2, 4, 5 and 7 respectively (Armandroff et al., 1999). Furthermore, the Arcon crosstalk is such that three echoes are produced, a primary echo in the neighbouring CCD, an intraCCD echo at a position reflected around the mid-point of the CCD's long axis and a secondary interCCD echo equivalent of the intraCCD echo. An example of image artefacts produced by an Arcon echo cascade is given in figure 3.8, originating from bright object PN Hb 5 (Hubble, 1921, Kohoutek et al., 1965). As they are the result of saturated or nearly saturated objects, the echoes typically featured bleed trails allowing their identification. Some echoes however had indistinct bleed trails, leaving them resembling a nebulosity. Care was taken to check for indistinct bleed trails during PN candidate identification.

3.2.3 Multi-lobed Artefacts

Suspected symmetrical multi-lobed image artefacts somewhat resembling (but not thought to be) the lobes of Fanaroff-Riley class II radio galaxies (Fanaroff & Riley, 1974), were noted in several Mosaic II images. Each approximately ellipsoidal lobe rim would be more intense in either the on or off band data. Two examples of such multi-lobed artefacts are shown in figure 3.9, where consistent with a Mosaic II artefact nature, no Hα emission is noted. It is suspected these artefacts result from passing asteroids imperfectly removed during image stacking (suggestion courtesy Dr. Lee Spitler, personal communication, 19 July 2015).

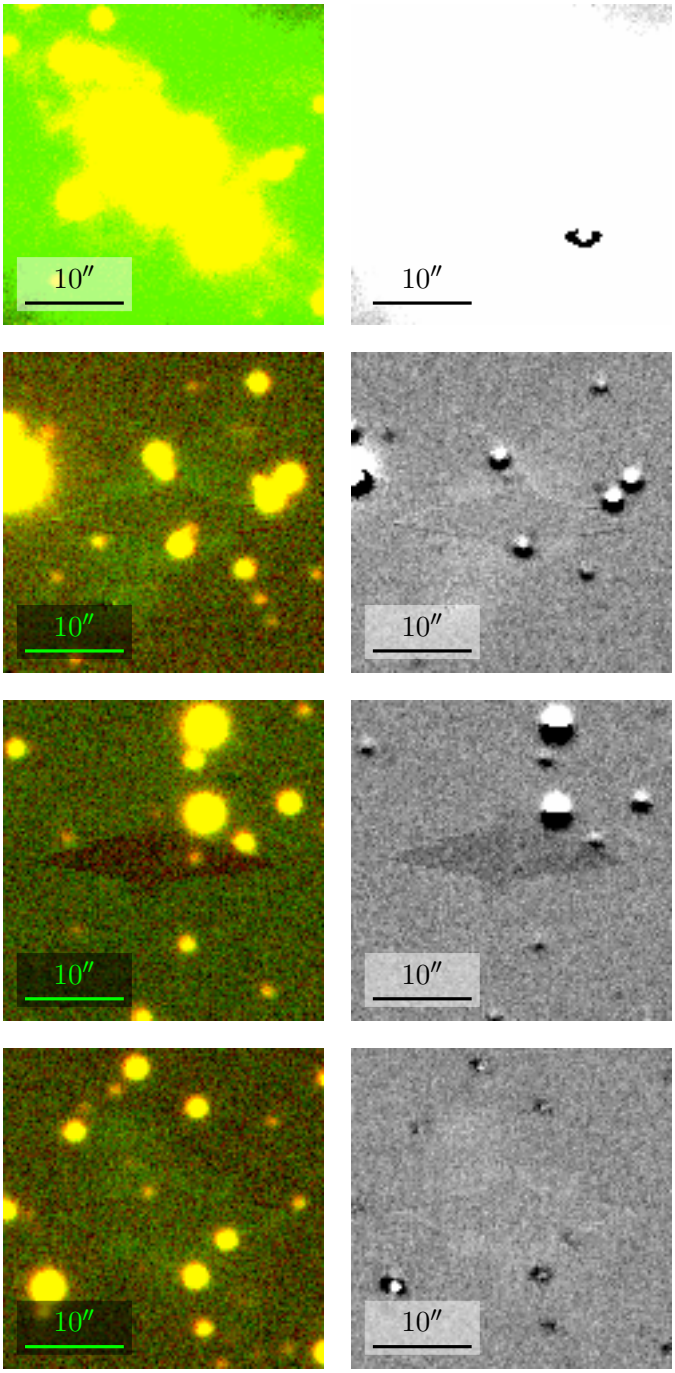

Figure 3.8: Example Mosaic II Arcon echo cascade. Top row, from left: Mosaic II [O III] on/off band (green/red) and difference images of bright object PN Hb 5. Second row: Corresponding primary interCCD echo. Third row: Corresponding intraCCD echo. Bottom row: Corresponding secondary interCCD echo. Potential exists for mistaking echoes with an indistinct bleed trail as PN candidates. Northeast is top left.

3.2.4 Parenthetical Artefacts

During review of PN candidates, several were dismissed as image artefacts. Some however were retained and assigned a correspondingly low observational priority. During review of the

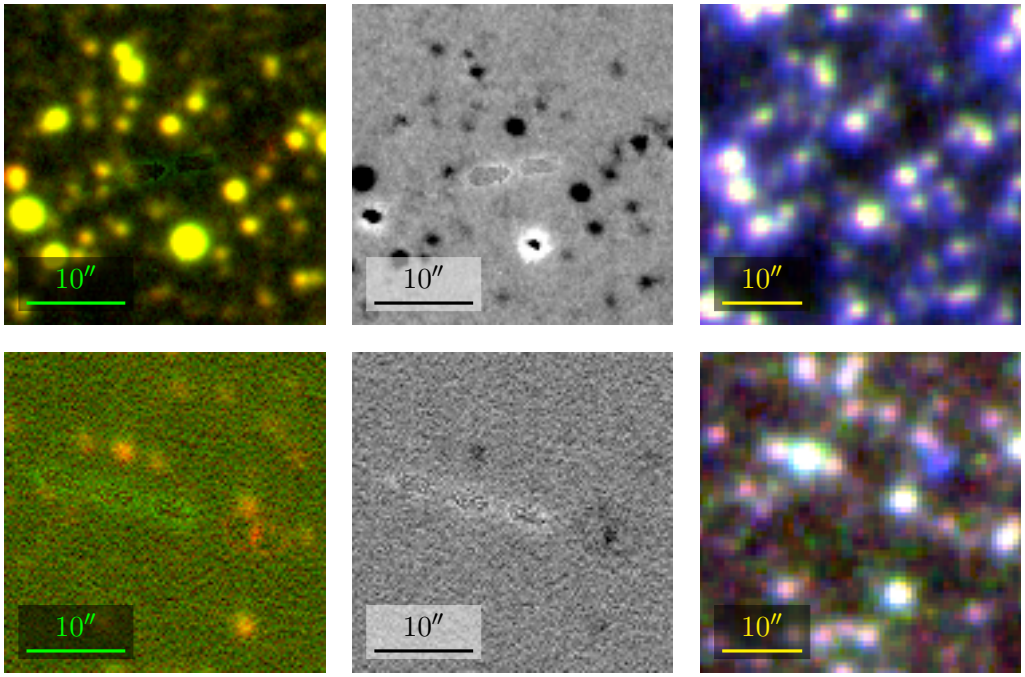

Figure 3.9: Example Mosaic II lobed artefacts. Each row shows the Blanco [O III] on/off band, difference and UKST Hα/SR/IR images of an artefact. Top row: Artefact with two distinct lobes. Careful examination of the [O III] on/off band image reveals at least two more fainter lobes, one green and one red. Bottom row: Another lobed artefact. Both lobed features are absent from the UKST images, consistent with them being artefacts. It is suspected these artefacts result from passing asteroids imperfectly removed during image stacking. Northeast is top left.

Blanco imaging data set, it became obvious that some candidates were members of a family of similar PN candidates. All have approximately the same dimensions and brightness. All appear close ($\leqslant 20''$) to the outer edge of a Mosaic II CCD, i.e. an edge not abutting another CCD, and are aligned parallel to the edge. All share the same morphology, reminiscent of a parenthesis and as such, will be referred to hereafter as parenthetical artefacts. These parenthetical artefacts are suspected of being some type of artificial image artefact. A cursory comparison of their positions on CCDs didn't reveal reoccurrence at the same physical position, aside from the shared edge proximity, which may have been a manifestation of a physical filter or CCD defect. Example locations of these artefacts on the Mosaic II CCD array are shown in figure 3.10. Example artefact images are shown in figure 3.11.

Despite their apparently dubious promise as PN candidates, some parenthetical artefacts were observed with a fibre multi-object spectrograph (MOS), where spare fibres could be assigned to their observation without wasting otherwise important observing time. This spectroscopy revealed no evidence of the suspected artefacts being real emission line objects. Coupled with their lack of corresponding visibility in UKST imaging, these artefacts are assessed here as indeed artificial.

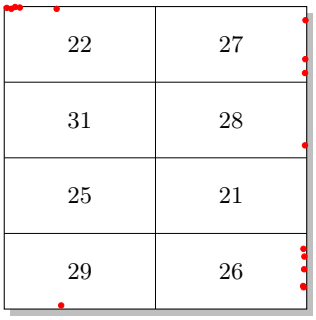

FIGURE 3.10: Example Mosaic II parenthetical artefact locations. The artefacts are represented by red dots overlaying the Mosaic II CCD geometry. CCD numbers are NOAO designations, as listed in the associated FITS header data.

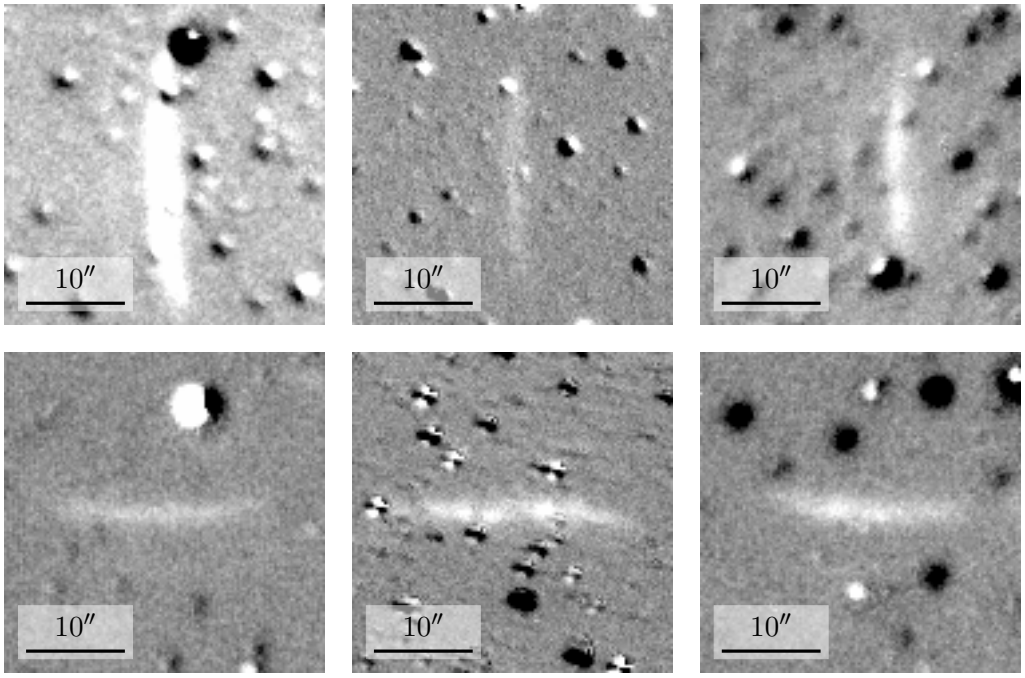

FIGURE 3.11: Example Mosaic II parenthetical artefacts. [O III] difference images are shown. Northeast is top left. Note the consistent north-south or east-west alignment of the artefacts.

3.2.5 Miscellaneous Artefacts

Finally, a motley assortment of other image artefacts defying straightforward classification were present. These were identified by unusual morphologies, diameters or intensity distributions. A conservative approach to artefact rejection was taken, with them considered candidates until discounted by review of associated flat field and multiwavelength data. Figure 3.12 shows an example mottled [O III] artefact of unknown origin. This particular example had no counterpart in the Mosaic II flat field (V, Harris c6026 filter), SHS or SSS imaging.

3.3 Spectroscopic Confirmation

Spectra of selected PN candidates detailed in §3.1 were taken over a series of observing runs on a variety of telescopes, detailed below. Different types of spectrograph were used, including a wide field spectrograph (well suited to observations of extended PNs), a fibre-fed MOS and

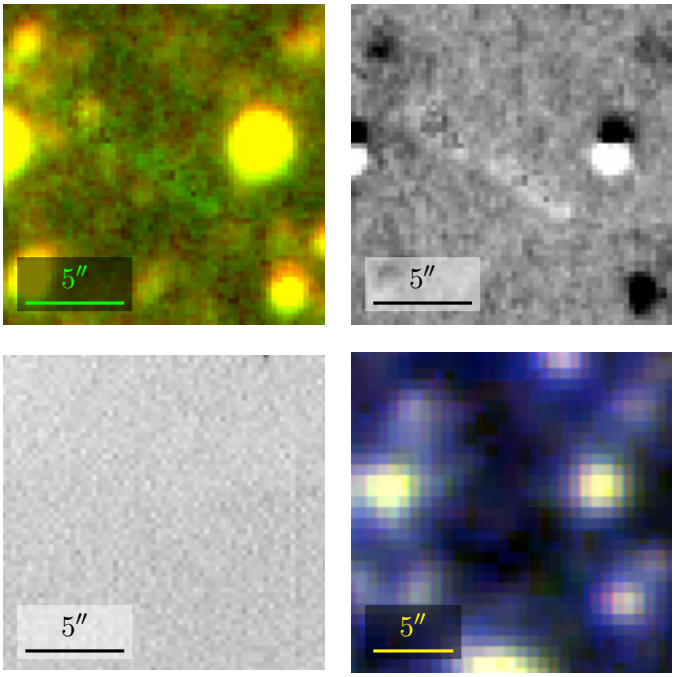

Figure 3.12: Example Mosaic II miscellaneous artefact. Top row, from left: Blanco [O III] on/off band and difference images. Bottom row, from left: flat field (V, Harris c6026 filter) and UKST Hα/SR/IR imaging. Northeast is top left. No artefact counterpart exists in the flat field or UKST images.

a single object grating spectrograph.

The observing strategy adopted was to first rank each PN candidate in order of likelihood of being a true emission line object, rather than being a cosmic, noise or other image artefact in the Mosaic II data reviewed. For spectroscopic confirmation pursued on single object spectrographs, the targets were generally observed in order of this ranking, albeit with each observing night's target groupings reordered to maximise observability over the relevant night. Where observing time allocations were available on multiple telescopes, faint candidates were preferentially assigned to observation on the largest aperture telescopes.

For spectroscopic confirmation pursued on a MOS, a greedy set cover algorithm was implemented in C++ (discussed further in §3.3.2), and target fields were prioritised by running it over all unobserved targets in table 3.2. Fields were then observed in order of target density.

Target observability data (e.g. rise and set times, relative airmass, lunar illumination factor) was obtained from Staralt (Patris, 2010), hosted by the Isaac Newton Group of Telescopes and planned around sunset, sunrise and twilight (civil, nautical and astronomical) timings obtained from the US Naval Observatory's (USNO) Data Services[6], using time zone adjustments relevant to the observing site. These timings are quoted to the nearest minute by the USNO. As a result, calculations presented here involving these quantities have assumed an uncertainty of 30 s. These timings also neglect solar parallax, variations in local atmospheric refraction

[6]http://aa.usno.navy.mil/data/

and observer height above sea level (Bell & Urban, 2012) and so the assumed uncertainty of 30 s is acknowledged as too conservative, but refinement neglected due to its assumed small impact on the science results presented here.

During classical observing runs, observations were carried out mindful of safe and efficient telescope operating practices. On commencement of observing, dome shutters were allowed to open fully and only then were mirror covers opened, and the reverse done on conclusion of observing. This was done to avoid having any wind-borne debris fall onto the telescope and its optics, e.g. dirt, dust, leaves, small branches, etc. When there was no threat of rain, telescope domes were kept open during nights. This minimised the temperature difference between the interior and exterior environment of the dome, minimising data degradation due to thermally induced dome seeing and mirror seeing effects (e.g. Wood & Ryan, 1995, Ryan & Wood, 1995). When there was some threat of rain however, the approach was to err on the side of caution, close the dome and protect the telescope optics from even minor exposure to precipitation.

3.3.1 Advanced Technology Telescope

Seven observing runs were undertaken over 2013–2015 using the TAROS (Wilson et al., 2005) and the WiFeS wide field slitlet spectrograph (Dopita et al., 2007, 2010) on the ≈2.3 m (2 337 mm, 92 inch) Advanced Technology Telescope (ATT, Mathewson et al., 2013) at the Siding Spring Observatory[7] (SSO). TAROS is a Java based graphical user interface (GUI) to the telescope control system, itself written in C++ running on the QNX6 real time operating system (Nielsen & Hovey, 2010). Observing in remote operation mode (as defined by Longair et al., 1986) was attempted twice but proved untenable each time due to damaged or misconfigured observatory infrastructure, resulting in unnecessary loss of observing nights. Remote operation observing was not pursued again. All data-yielding observing conducted in the course of this work, both on this telescope and others, was conducted in traditional observing mode.

Interface Streamlining

The TAROS GUI is traditionally invoked by navigating to the TAROS Web page[8] and then clicking on a relevant hyperlink to launch the TAROS via Java Web Start (Marinilli, 2002). Consistent with the workflow automation approach to tasks adopted here (e.g. §3.1.1), a custom package was built to allow single-click invocation of the TAROS from the Mac OS X Launchpad. This package, shown in figure 3.13, executes a simple shell script to trigger an encapsulated Java Network Launching Protocol (JNLP) call to Java Web Start, launching the TAROS GUI.

[7] SSO: east longitude 149°03.7′, latitude −31°16.4′, 1149 m above sea level (Bell & Urban, 2012).
[8] www.mso.anu.edu.au/local/observing/taros

Figure 3.13: TAROS Mac OS X package, shown in the Launchpad. The package allows efficient, dynamic, single-click retrieval and launch of the latest version of the TAROS via JNLP and Java Web Start. Icon adapted from an image courtesy Wetherell, T., ANU.

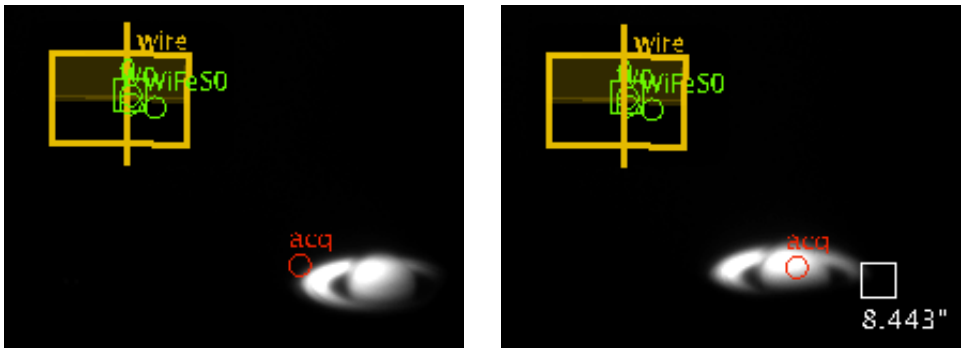

Figure 3.14: ATT pointing calibration. The view shown is from the ATT's acquisition camera in the TAROS acquisition and guiding window, during calibration against a readily identifiable target, Saturn (12 ms grey time, nautical twilight exposure 3 Aug 2014, ≈08:01:30 Universal Time (UT)). TAROS image overlays displaying details of defined apertures, the WiFeS FOV, etc. can be seen. The red circle, labelled "acq", denotes the telescope's current pointing in response to input target coordinates. Pointing is initially offset from Saturn's centre, left, but then corrected, right.

Pointing and Focus Calibration

The TAROS provides a facility for pointing calibration of this telescope. Such calibration is necessary to correct accumulated pointing errors, such as from mechanical hysteresis (e.g. Hovey, 1974). There is no observing assistant employed for the ATT, this calibration is a user responsibility. A Solar System object was typically used for initial gross pointing calibration. Saturn or Jupiter were often chosen as both appear as readily identifiable observational targets in the ATT's acquisition camera (McGregor et al., 2000), Saturn because of its rings and Jupiter because of its atmospheric banding. They are also bright enough to allow pointing calibration during twilight (e.g. $m = 0.87$ in figure 3.14)[9], leaving more night time free for science observations. Although not as bright, the Neptune-Triton system ($m_{\text{Neptune}} = 7.86$ and $m_{\text{Triton}} = 14.23$ in figure 3.15)[9] is another useful initial pointing calibration target. The large Triton to Neptune mean radius ratio (≈5.5%, Thomas, 2000, Seidelmann et al., 2007), Triton's high geometric albedo (V band ≈ 0.802, Hicks & Buratti, 2004) and planetocentric orbital inclination (≈157°, Jacobson, 2009) make the system easily identifiable.

[9]Extincted apparent magnitude calculated with Stellarium version 0.13.1 (http://stellarium.org).

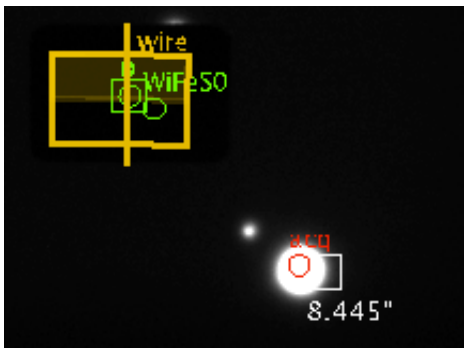

FIGURE 3.15: Neptune and Triton pointing calibration (5 s dark time, night time exposure 29 May 2014, ≈19:24:53 UT), from the ATT's acquisition camera in the TAROS. A large Triton to Neptune mean radius ratio (≈5.5%, Thomas, 2000, Seidelmann et al., 2007), Triton's high geometric albedo (V band ≈ 0.802, Hicks & Buratti, 2004) and planetocentric orbital inclination (≈157°, Jacobson, 2009) make the system easily identifiable.

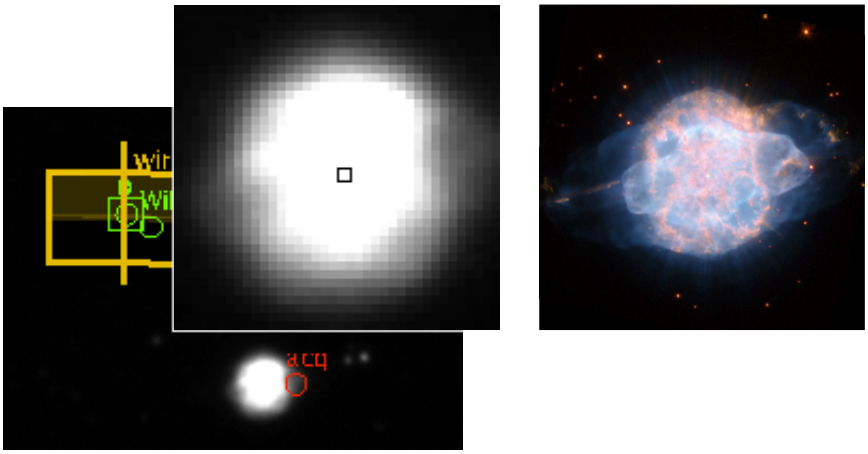

FIGURE 3.16: Left: PN NGC 3918 pointing calibration (2 s dark time, night time exposure 27 May 2014, ≈10:38:13 UT), from the ATT's acquisition camera in the TAROS. Right: *HST* image of NGC 3918, simply a scaled, rotated (12.1° clockwise) version of figure 1 on page xiii. Northeast is top left in both images. Some large scale PN structure in the *HST* image is discernible in the TAROS image, especially when using the acquisition camera zoom tool, as shown.

After initial pointing calibration against a Solar System object, pointing was then fine-tuned against a prominent Galactic object such as Antares (α Sco) or Spica (α Vir). Prominent PNs were sometimes used too, especially where such objects could be distinctly identified due to non-stellar (non-spherical) morphologies, such as NGC 3918, shown in figure 3.16.

The TAROS also provides a utility for telescope focus calibration. Globular clusters worked well as focus calibration targets, providing many closely spaced stars with which to calculate an optimal focus solution (e.g. figure 3.17). As for bright planets, prominent southern sky globular clusters (e.g. NGC 5139; ω Cen) can be use for calibration purposes during twilight, again maximising night time available for science observations. Example calibration exposure times used are given in table 3.5.

Additional Calibration and Data Reduction

Once targets were acquired within the WiFeS FOV ($25'' \times 38''$), spectra were captured with two Fairchild 4096×4096 pixel, 15 μm pixel CCDs, each one placed in a separate camera, with

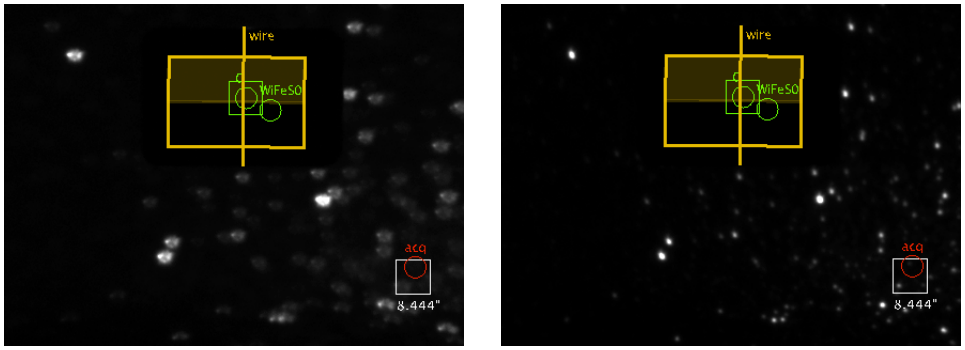

Figure 3.17: ATT focus calibration. Calibration against globular cluster NGC 4590 (3 s dark time, night time exposure 25 May 2014, ≈09:09:30 UT), from the ATT's acquisition camera in the TAROS, is shown. Focus is clearly suboptimal, left, but then corrected, right.

Table 3.5: ATT calibration: example acquisition camera exposure times. Data are ordered by extincted apparent magnitude, as derived from Stellarium version 0.13.1.

Target	Exposure time (s)	m	Type	Calibration
Mars	$10–12 \times 10^{-3}$	− 0.28	planet	pointing
Saturn	$12–13 \times 10^{-3}$	0.53–0.87	planet	pointing
Procyon (α CMi)	4	0.61	binary star	pointing
Spica (α Vir)	11×10^{-3}	1.14	variable star	pointing
NGC 5139	$15–100 \times 10^{-2}$	3.86–3.87	globular cluster	focus
NGC 3201	3	6.94	globular cluster	focus
NGC 3918	1–2	8.15	PN	pointing
M 68	3	8.34	globular cluster	focus
NGC 5694	3	10.35	globular cluster	focus
Neptune-Triton	5	7.86, 14.23	planet, moon	pointing

one optimised for the red end of the spectrum and one for the blue (Dopita et al., 2007). Small targets, those with apparent spatial dimensions smaller than the WiFeS FOV, were generally captured within the WiFeS field. Some however may not have been fully captured within the WiFeS FOV due to target acquisition issues. Larger nebulas were generally targeted such that their entire apparent spatial extent wasn't captured, but a region of local flux maximum was, such as a bright rim arc, along with a region of empty sky to enable proper sky subtraction. It is acknowledged such larger PNs may not be true bulge PNs, but new foreground objects.

Data flat field calibration was done using exposures of both an artificial flat field, generated with a quartz iodide lamp, and, weather permitting, evening and morning twilight flats. As the most evenly illuminated twilight sky occurs on the solar circle, offset from the zenith by (0–40)° in the direction of the solar antihorizon (Chromey & Hasselbacher, 1996), twilight flats were taken at zenith or at a 20° zenith offset. For reduction of data from nights missing associated twilight flats, twilight flats were substituted from another night. If twilight flats from a clearly proximate night were available, those were substituted. Alternatively, for nights

without a clearly proximate substitute available, such as twilight flats being available on both the previous and subsequent nights, flats from the twilight with the least lunar illumination were substituted to maximise the uniformity of sky illumination sampled.

Target observations were usually taken with bracketing NeAr lamp arc exposures, but at minimum with a single leading or trailing arc, to compensate for WiFeS grating dispersion changes with temperature (Dopita et al., 2010). WiFeS spectra were semi-reduced using the PyWiFeS pipeline (Childress et al., 2014), with supporting Python packages managed using pip (Lubanovic, 2014).

3.3.2 Anglo-Australian Telescope

Multi-object spectroscopy of PNs was taken over five pointings with the AAT's Two-degree Field (2dF) facility, four with the AAOmega spectrograph (Saunders et al., 2004, Smith et al., 2004, Sharp et al., 2006) and one with the High Efficiency and Resolution Multi-Element Spectrograph (HERMES, Barden et al., 2010, Heijmans et al., 2012) at the SSO. These spectrographs are supplied by the AAT's 3.89 m primary[10]. Each robotically-positioned 2dF fibre has a projected diameter $\sim 2''$ at the prime focus corrector's focal plane (Sharp & Parkinson, 2010). The prime focus corrector incorporates an atmospheric dispersion corrector.

Automating Optimally Dense Multi-object Field Selection

PN candidate coordinates were checked against 2MASS imaging for accuracy, prudent as candidate coordinates in some Mosaic II FITS files indeed featured a coordinate offset from actual on-sky positions. After checking coordinate accuracy, a greedy set cover algorithmic approach was used to ensure MOS field pointings were efficiently selected. As detailed in Stenborg (2015), circular MOS pointings over target populations were modelled as instances of the set cover problem (e.g. Chvátal, 1979, Slavík, 1997). This model assumes an observational target population set S of n targets. The greedy set cover algorithm determines the cover (MOS pointing) containing the maximum number of targets from S each iteration, then removes those targets from S before the next iteration. This is useful for the case of limited available total pointings, the case here, as it produces a pointing list maximising target density. A single iteration of the greedy set cover algorithm is described in figure 3.18.

Each possible target pair (i, j) in S must be checked for coverage by a MOS FOV of radius r. For an array of all target pairs, the number of inter-pair distance d_{ij} calculations T_n is $\mathcal{O}(n^2)$ with, naively, $T_n = n(n-1)$. As can be done for other astrophysical all-pairs problems however (e.g. the n-body problem, Stenborg, 2009), computational cost can be reduced by leveraging problem symmetries, then ameliorated by parallel computation. Here, realising $d_{ij} = d_{ji}$ leaves $T_n = n(n-1)/2$, scaling as the triangular number sequence, equation 3.1,

[10]The primary, which saw first light in 1974 (Haynes et al., 1996, Leverington, 2013), is constructed of Cer-Vit, an opaque, very low expansion glass-ceramic material (coefficient of thermal expansion of order $0 \pm 1.5 \times 10^{-7}/^{\circ}\text{C}$, Dietz & Barnes, 1968).

procedure GreedySetCoverFieldSelection

input n, r, *TargetArray* // Target: a custom data type storing RA, dec
output *GreedyCover*, *TargetArray* // GreedyCover: stores a pointing RA, dec

```
1:  x := 0
2:  for i = 0 to (n − 2) do
3:      for j = (i + 1) to (n − 1) do
4:          IndexPairArray[x].Target1 := i
5:          IndexPairArray[x].Target2 := j
6:          x := x + 1
7:      end for
8:  end for

9:  forall IndexPair in IndexPairArray
10:     d := CalculateSeparation(TargetArray, IndexPair.Target1, IndexPair.Target2)
11:     if d = 2r then
12:         AddOneCover(CoverArray)
13:     else if d < 2r then
14:         AddTwoCovers(CoverArray)
15: end for

16: MaxTargets := 0
17: forall Cover in CoverArray
18:     x := TargetsCovered(TargetArray, Cover, r)
19:     if x > MaxTargets then
20:         MaxTargets := x
21:         GreedyCover := Cover
22: end for

23: RemoveTargetsCovered(TargetArray, Cover, r)
24: return GreedyCover, TargetArray
```

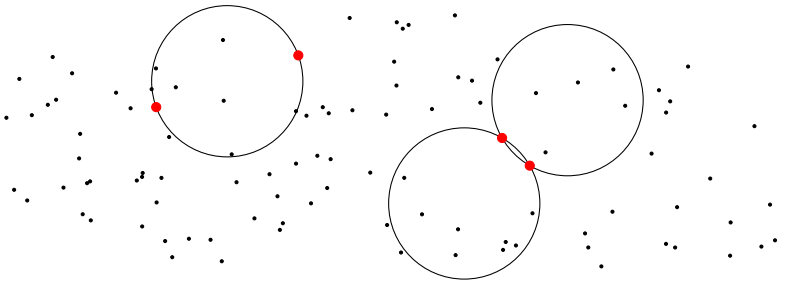

Figure 3.18: Top: Algorithm for greedy set cover field selection in multi-object spectroscopy. Bottom: Example test set covers for multi-object field selection. Covers for the $d = 2r$ case (left, single cover) and the $d < 2r$ case (right, dual covers). Associated target pairs are shown exaggerated in red. Algorithm and image adapted from Stenborg (2015).

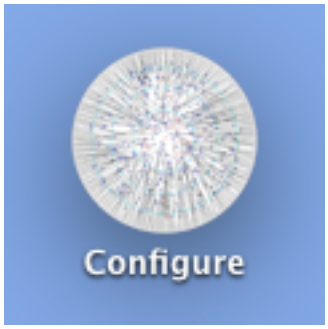

FIGURE 3.19: Configure Mac OS X package, allowing efficient, single-click launch of Configure. The icon was adapted from the 2dF Galaxy Redshift Survey image gallery (Colless, M., viewed 16 April 2015, www.2dfgrs.net).

$$T_n = \sum_{k=1}^{n-1} k = 1 + 2 + 3 + \cdots + n - 1 = \frac{n(n-1)}{2}. \tag{3.1}$$

Each inter-pair distance was calculated and the associated number of covers was determined. For $d > 2r$, no covers result, for $d = 2r$, one cover results and for $d < 2r$, two covers result. This is shown graphically in figure 3.18. After all possible covers were constructed over S, the cover enclosing the maximum targets was determined. This maximum is limited practically by the available MOS fibres, but was never reached for the bulge PN S examined here. Coordinates of the optimal cover were then returned, its enclosed targets deleted from S and the algorithm repeatedly iterated to find the next most efficient pointing. Cover construction and subsequent enclosed target counting were parallelised by distributing the calculations over available processors.

The custom greedy set cover field selection program was written here in C++ with Eclipse Luna's (version 4.4.1) Parallel Tools Platform (release 8.0) and run over the Open MPI (message passing interface) library (version 1.8.3, Gabriel et al., 2004). Architecture-independent `-o3` (level 3) C++ compilation optimisation (von Hagen, 2006) was performed. MPI was chosen for parallel programming due to its widespread usage (Hempel & Walker, 1999) and flexible applicability to both distributed and shared memory systems.

Service Observations and Data Reduction

AAOmega field configuration files were then prepared using the Configure software utility (Lewis et al., 2002). As was done for the TAROS, a custom Mac OS X package, shown in figure 3.19, was built here for efficient invocation of Configure. Each pointing consisted of target PN candidates, sky fibres, guide stars and 1–4 MASH PN(s) used as ad hoc PN standards, all aligned to 2MASS astrometry. Every sky fibre position was checked in 2MASS imaging to ensure it avoided stellar coincidence. Guide stars were preferentially selected from the Guide Star Catalog II[11] (Lasker et al., 2008). Once validated in Configure, the field configuration files were forwarded to service astronomers who performed the observations.

The AAOmega system was upgraded between field observations, with a new blue CCD

[11] http://gsss.stsci.edu/Catalogs/GSC/GSC2/gsc2.htm

installed in February 2014 (Brough et al., 2014). This new CCD increased throughput by ≈5% and has only 0.04% bad pixels, down from 0.8% in the old CCD. The AAO also replaced the red CCD later the same year, on 16 September 2014 (Dr. Andrew Green, personal communication, 17 July 2015). The new red CCD provides increased throughput and extends wavelength coverage to ≈1 micron. Specifications for the AAOmega and HERMES gratings used are given in table 3.6. The HERMES gratings were fixed, but the AAOmega gratings adjustable, with alternate configurations available (e.g. dispersion, range), but simply not used here.

Table 3.6: AAOmega and HERMES grating specifications, sourced from Sharp et al. (2006), Barden et al. (2010) and FITS file header values. Spectrograph resolving power $R \equiv \lambda/\Delta\lambda$, where $\Delta\lambda$ is spectral resolution.

Instrument	Grating	Dispersion (Å pixel^{-1})	Useful range (Å)	Blaze (Å)	R
AAOmega	580V	1	3700–5800	4500	1300
AAOmega	385R	1.6	5600–8800	7000	1300
HERMES	Blue	0.045	4715–4900	4833	28 000
HERMES	Green	0.055	5649–5873	5788	28 000
HERMES	Red	0.063	6478–6737	6642	28 000
HERMES	IR	0.073	7585–7887	7781	28 000

A summary of all 2dF pointings taken is given in table 3.7. Spectroscopic data collected from these pointings were reduced with the AAO's 2dF data reduction package (2dFdr, Croom et al., 2004), version 6.0. 2dFdr provided a facility for automatic combination and application of biases, darks (taken for HERMES only) and flat fielding to target data collected. Reduction of some fields proved problematic due to invalid or missing FITS file header data. Fortunately, the FITS headers had enough supplementary data in other header keywords to enable derivation of the expected values, which were then manually inserted using Fv (Pence et al., 1997, Pence, 1998). After additional inspection of reduced data for obvious gross errors in DS9, data were extracted from the FITS files with IRAF and Fv, and semi-automated data conversion used to render spectra.

The HERMES pointing was taken at very high airmass, $X \approx 2.3$ (assuming $X \approx \sec z$, where z is zenith distance, Sterken & Manfroid, 1992) and only yielded a single field exposure. The HERMES data are thus peppered with cosmics and partial bright columns due to cosmics induced charge bleeding. Automated cosmics removal, to the three standard deviations (3σ) level, based on Laplacian edge detection (van Dokkum, 2001), was run over the HERMES data but only partially ameliorated cosmic artefacts. Spurious bright columns proved especially resistant to automated cosmics removal software. Manual artefact repair is possible, but remains a task for future work. A caveat is thus given that HERMES data presented is of low signal-to-noise ratio (S/N), taken in poor weather at high airmass and retains spurious artefacts. As will be seen, some PN emission data were viable, but unusual apparent emission

lines should be dismissed.

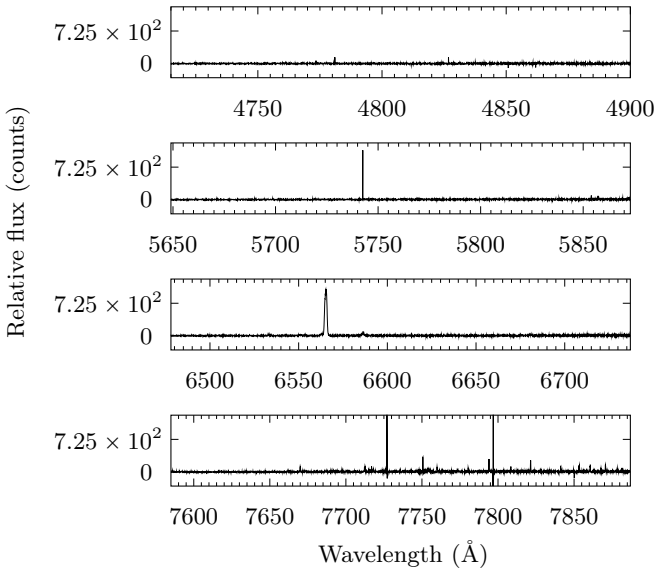

FIGURE 3.20: Example HERMES multi-channel data. A high airmass ($Z \approx 2.3$) spectrum (1200 s dark time exposure) of known PN, PN G001.1-01.2 is shown. Blue, green, red and IR channel data are shown from top to bottom, respectively. Several apparent features of the spectrum are probably artificial. Genuine Hα emission is however prominent.

An example reduced HERMES spectrum, in this case for known nebula PN G001.1-01.2 (Parker et al., 2006), is given in figure 3.20. Blue, green, red and IR channel data are shown from top to bottom, respectively. For the targets pursued, only the red channel returned unambiguous emission line data, as it spans prominent PN Hα and [N II] $\lambda\lambda$6548, 6583 emission. Although the blue HERMES channel had the potential to return Hβ data, the combination of high airmass, target faintness and modest exposure time restricted it in this case. As only the red channel returned unambiguous nebula emission line data, only that single channel will be presented in subsequent HERMES spectra discussions.

TABLE 3.7: 2dF pointings. Field centres are specified in J2000 coordinates. The number of sky fibres used, $n_{\rm sky}$, is indicated for each field.

Field	Instrument	Field centre		Date	Exposures (s)	$n_{\rm sky}$
		RA (h m s)	Dec (° ′ ″)			
A1	AAOmega	18 01 19.0	−28 24 36	26 Jul 2013	3 × 1200	30
A2	AAOmega	18 01 49.0	−28 00 47	5 Sep 2013	4 × 1200	25
A3	AAOmega	17 50 00.0	−34 10 00	5 Jun 2014	3 × 1200	28
A4	AAOmega	17 53 46.0	−29 12 31	18 Jun 2014	3 × 1800	28
H1	HERMES	17 57 28.9	−28 16 22	27 Aug 2014	1 × 1200	28

3.3.3 Radcliffe Telescope

Further spectroscopy of bulge PN candidates with the Cassegrain slit spectrograph on the ≈1.9 m (74 inch) Radcliffe telescope (Glass, 1978, 1989) at the South African Astronomical Observatory[12] (SAAO) near Sutherland, was taken over 2013–2014. Grating seven was deployed. Grating specifications are listed in table 3.8, below (Kilkenny & Worters, 2014). Resultant spectra were captured with a Scientific Imaging Technologies, Inc. (SITe) 266 × 1798 pixel, 15 μm pixel CCD, using 1 × 2 binning. The CCD spectrograph system will be referred to hereafter as the CCDSpec.

Effort was made to adapt to conditions during observing. Slit width was judiciously widened during noticeably poor seeing, especially for compact objects. This was done to admit as much of the point spread function as possible through the slit, whilst still restricting as much sky background as possible (as per, e.g. Howell, 2006).

Table 3.8: Radcliffe telescope CCDSpec grating seven specifications (Kilkenny & Worters, 2014).

Grating:	7
Lines (mm^{-1}):	300
Order:	1
Dispersion (Å mm^{-1}):	210
Useful range (Å):	4200
Blaze (Å):	4600
Resolution (Å):	5

Reduction of Radcliffe telescope FITS data was carried out with IRAF revision 2.16, developed by the National Optical Astronomy Observatory (Tody, 1986, 1993). FITS file validation was first done with DS9 and/or QLFits (Foellmi, 2009) imaging and visualisation tools. These exposed data issues, such as corrupt exposures or instances of incorrectly assigned IMAGETYP values in FITS file headers. Exposures were then reduced (hot pixel corrected, trimmed, bias-subtracted, dome and twilight flat-fielded, cosmics removed, etc.) with the aid of custom IRAF command line and Unix shell scripts developed here to semi-automate this reduction.

An example FITS spectrum segment, selected at random from the 2013–2014 Radcliffe data, before and after reduction is given in figure 3.21. Highlighted in green circles here are discrete emission line spectral peaks characteristic of PNs and other astronomical emission line objects. The number, wavelength and intensities of these spectral peaks are the crucial nebula diagnostic data to be extracted from the image data. Note in the top (pre-reduction) image in figure 3.21 the many small, scattered, irregular dots. These will be familiar to an observational astronomer as the spurious signal generated in the CCD from cosmic rays incident on the CCD during the 1200 s image exposure.

Nebula emission doesn't overlay a perfectly dark sky background in figure 3.21. This of course reflects the situation in nature; the night sky can have background illumination

[12]SAAO: east longitude 20°48.6′, latitude −32°22.8′, 1798 m above sea level (Bell & Urban, 2012).

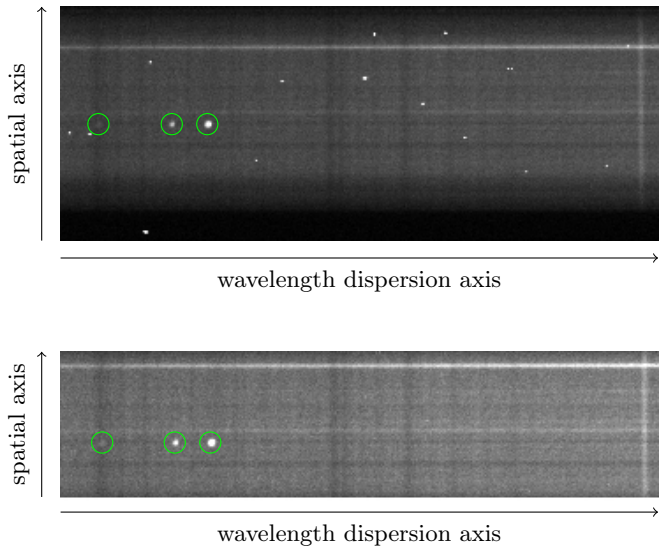

FIGURE 3.21: Example 1.9 m Radcliffe telescope PN slit spectrum segment before (top) and after (bottom) reduction. Nebula emission line peaks are highlighted in green circles and correspond to, from left to right, Hβ and [O III] $\lambda\lambda$4959, 5007 emission.

due to moonlight, airglow, zodiacal light, the gegenschein, scattered starlight, artificial light pollution, etc[13]. Also noticeable in figure 3.21 are a series of light and dark columns and rows. Columnar features arise from unavoidable solar, via moonlight, and atmospheric molecular absorption features (dark columns) or airglow emission features (light columns). Light rows correspond to stars, and their continuous spectra, near the target object which are captured by the slit spectrograph. Finally, dust or other material on the slit compromises light intensity incident across some CCD rows, creating dark rows.

Any nebula emission extraction scheme for the image shouldn't over or undersubtract contributions from the assorted noise sources, but instead isolate the nebula signal as accurately as possible.

Simplified Spectral Extraction Scheme

Spectra were first extracted with a sum extraction and buffer-offset sky subtraction technique, where S_x, the total nebula signal at physical coordinate x along the dispersion axis is given by equation 3.2. Induced CCD signal corresponds here to pixel brightness, represented as a 16-bit intensity value, i.e. a pixel value of 0 for ideal darkness and a pixel value of 65 535 for a saturated, maximally bright signal.

[13]Consider too the poorly studied contribution of episodic large-scale extreme marine bioluminescence to light pollution (e.g. $\geqslant 1.4 \times 10^{11}$ photons cm^{-2} s^{-1} over $\approx 1.5 \times 10^4$ km^2, Miller et al., 2006), visible to the naked eye during dark time and possibly discernible from observatories near coastal waters.

$$S_x = \sum_{y=y_i}^{y_\mathrm{f}} D_{xy} - \frac{\sum_{y=y_i+nsum+1}^{y_\mathrm{f}+nsum+1} D_{xy} + \sum_{y=y_i-nsum-1}^{y_\mathrm{f}-nsum-1} D_{xy}}{2} \tag{3.2}$$

where,

$$\begin{aligned} y_f &= y_\mathrm{mid} + \lceil (nsum-1)/2 \rceil, \\ y_i &= y_\mathrm{mid} - ((nsum-1) \backslash 2)\,. \end{aligned}$$

S_x was generally determined by summing the signal over $nsum$ pixels in the spatial axis direction y centred on $y = y_\mathrm{mid}$, with $(nsum, y_\mathrm{mid} \in \mathbb{Z}^+)$ selected such that the extracted region spanned the nebula emission recorded. The sky background signal over $nsum$ pixels along the spatial axis, averaged from an $nsum$ pixel region below and another above the nebula, was then subtracted from this original extraction. The edge of nebula emission in the spatial direction was determined approximately by eye. To increase the extracted spectra's S/N, the sky subtraction regions didn't directly abut the approximate nebula edge, they were offset by a pixel. This provided a buffer to avoid subtraction of very low, but non-zero nebula emission difficult to make out by eye.

Here D_{xy} is the 16-bit intensity value of the pixel at physical coordinates x, y on the CCD. Note that the integer division[14], denoted $\backslash$ in the lower bound of summation, should not be confused with the ordinary division used in the upper bound of summation in equation 3.2, nor the ceiling operator in the upper bound confused with ordinary square brackets.

The actual region of nebula or sky background signal extracted didn't exactly correspond to the bounds described in equation 3.2 in all cases. As observations were being carried out of crowded stellar fields of the Galactic bulge, adjustments to the extraction regions sometimes had to be made on a case-by-case basis to avoid unwanted contributions to spectra from other stars. Dark rows due to material on the slit would also vary from observing run to observing run, or even mid-run, as the telescope moved and the slit was widened or narrowed for different observations. Extraction regions were thus similarly adjusted to avoid significant dark rows. In all cases however, an averaged sky subtraction region equal to the spatial extent of the nebula extraction was maintained.

Enhanced Spectral Extraction Scheme

Sky subtraction using background signal averaged from buffer offset regions above and below the nebula emission, on the CCD spatial axis, as described above, was trialled and returned acceptable results, but can be enhanced. It has already been mentioned that case-by-case adjustment was made to the sky subtraction regions to avoid very bright rows arising from other stars or very dark rows produced by material on the slit. Subtler sky brightness variations

[14] Integer division returns the quotient and discards the remainder, e.g. $5 \backslash 2 = 2$.

can nonetheless be present from row to row, caused by faint or small apparent diameter stars, or unresolved background objects for slightly brighter rows, or very small pieces of matter on the slit for slightly darker rows.

An enhanced sky subtraction scheme was thus devised to compensate for even minor spurious brightness variations (Stenborg, 2016). First, the median pixel values were calculated along each of a series of 150 pixel wide horizontal calibration lines, centred on $x_{\mathrm{H}\alpha}$, the centre of the nebula's Hα emission. Hα emission is usually prominent and easy to identify in a nebula spectrum. In addition, these calibration lines naturally span the Fraunhofer C Hα λ6563 line, but otherwise avoid significant nearby telluric molecular absorption (e.g. Fraunhofer B O_2 $\lambda\lambda$6867–7000 and water vapour H_2O $\lambda\lambda$7186–7273) bands (Kirkpatrick et al., 2011) and airglow emission (e.g. [O I] $\lambda\lambda$5577, 6300, 6364) features (Hanuschik, 2003). These lines were positioned along the CCD's spatial axis such that they intersected each row of nebula emission and extended $3nsum$ rows beyond each buffer offset.

The median pixel values for lines intersecting the nebula emission were averaged to give a target median. This target median is given by (3.3).

$$\widetilde{D}_{xy_{\mathrm{target}}} = \frac{1}{nsum} \sum_{y=y_i}^{y_{\mathrm{f}}} \widetilde{D}_{xy} \tag{3.3}$$

where,

$$\begin{aligned} y_f &= y_{\mathrm{mid}} + \lceil (nsum - 1)/2 \rceil, \\ y_i &= y_{\mathrm{mid}} - ((nsum - 1) \backslash 2)\,, \\ x &= (x_{\mathrm{H}\alpha} + k)_{k=-74}^{75}\,, \\ \widetilde{D}_{xy} &= \text{median value of } D_{xy}. \end{aligned}$$

Sky subtraction then proceeded using $2nsum$ sky rows as in equation 3.2. Instead of using sky data extending $nsum$ rows immediately above and below the nebula emission and the buffer offsets however, sky rows were drawn from within the $3nsum$ rows above and below each buffer offset. Rows were selected corresponding to the calibration lines whose median values most closely matched the target median. The median pixel values of the $6nsum$ calibration lines beyond the region of nebula emission and its buffer offsets (hereafter, a sky median) are given by the sequence in (3.4),

$$\begin{aligned} &\left(\widetilde{D}_{xy_{\mathrm{sky}}}\right)_{y \in \{y_i - 3nsum - 1, y_i - 3nsum, \ldots, y_f - nsum - 1\}} \\ &\qquad \cup \{y_i + nsum + 1, y_i + nsum + 2, \ldots, y_f + 3nsum + 1\} \end{aligned} \tag{3.4}$$

where y_f, y_i and x are defined as for (3.3).

Sky median selection was semi-automated here in VBA, with the absolute difference of each

sky median from the target median calculated and those differences sorted using a quicksort method, as per the algorithm described in figure 3.22. The rows represented by the first $2nsum$ items in the sorted set were used for sky subtraction, as described by (3.5) As nebula emission typically extended $\ll$150 pixels in both the spatial and dispersion directions, using calibration lines intersecting it produced target medians influenced little by the nebula itself, but maximally consistent with the sky conditions nearest the nebula.

---

procedure SkyMedianSelection

input $2nsum$, $skyMedianArray$, $\widetilde{D}_{xy_{\text{target}}}$
output *skyRowsArray*

1: $i := 0$
2: **forall** $skyMedian$ **in** $skyMedianArray$
3: $\quad skyMatchArray[i].y = skyMedian.y$
4: $\quad skyMatchArray[i].difference = \left|skyMedian.median - \widetilde{D}_{xy_{\text{target}}}\right|$
5: $\quad i := i + 1$
6: **end for**
7: Quicksort($skyMatchArray$) {Order by difference}
8: **for** $i = 0$ **to** $(2nsum - 1)$ **do**
9: $\quad skyRowsArray[i] := skyMatchArray[i].y$
10: **end for**
11: **return** *skyRowsArray*

Figure 3.22: Algorithm for selection and sorting of optimum sky medians

$$S_x = \sum_{y=y_i}^{y_f} D_{xy} - \frac{1}{2}\sum_{y \in skyRowsArray} D_{xy} \tag{3.5}$$

where y_f and y_i are defined as for (3.3).

A quicksort algorithm (Hoare, 1961, 1962) was selected on the basis of its fast execution speed (average performance $\mathcal{O}(n \log n)$, where n items are being sorted, easily sufficient for the small data set being sorted here), wide documentation and ease of implementation as determined from previous personal experience in related programming languages. Sky row selection is subject of course to the physical bounds of the CCD but no restriction was placed such that a minimum number of rows needed to be selected from either top or bottom region, so if the optimum sky medians came entirely from either the top or bottom sky region, those were selected.

The enhanced spectral scheme was applied in general, but not blindly. In some cases, its application would risk artificially modifying the true spectrum, e.g. for the case of a spectrum with a high apparent brightness CSPN within a compact PN, for which the CSPN's signal over the spatial axis was $\leqslant 3nsum$.

Extraction Scheme Comparison

The example spectrum used in figure 3.21 was used to compare the simple and enhanced spectral extraction schemes. The PN spectrum extracted using the simplified spectral extraction scheme, and then the enhanced scheme, appears in figure 3.23. The three nebula emission peaks highlighted in figure 3.21 are clearly visible, as is a strong Hα peak. Figure 3.23 illustrates the enhanced scheme more accurately aligning the nebula's apparent zero signal baseline with a zero relative flux count. The enhanced scheme doesn't produce perfectly zero-baselined spectra, but generally outperforms the simplified scheme. In figure 3.23 for example, both the simplified and enhanced sky subtraction schemes oversubtract background sky signal around $\lambda\sim5000$ Å, but the average offset of nebula apparent zero signal from the zero flux count level, per signal interval across the entire wavelength range, is (desirably) less for the enhanced scheme. Accurately zero-baselined spectra are important if used in absolute flux determinations, or if relative line fluxes are used, for example Balmer decrements for extinction calculations.

The improvement in accurately zero-baselining spectra gained by using the enhanced sky subtraction extraction scheme, rather than the simplified scheme, can be quantified for sample data. Spectra from half a dozen high S/N PNs analysed with the CCDSpec were processed with both schemes. The average offset of the apparent zero signal from a zero relative flux count was measured for these spectra and is given in table 3.9. The enhanced spectral extraction scheme consistently produced a more accurate zero baseline for reduced spectra.

TABLE 3.9: Spectral extraction scheme comparison. Spectra from sample high S/N PNs are analysed. The average offset of apparent nebula zero signal from a zero relative flux count, per unit signal, over the CCDSpec spectral range is tabulated. Data from the simplified scheme are shown on the left (shaded) and data from the enhanced scheme on right. The enhanced scheme consistently produced a more accurate zero-baseline for reduced spectra.

Object Name	Flux offset (counts)	Flux offset (counts)
CTIO J173557.97-271214.2	11.99791	4.86381
CTIO J173623.26-250528.7	− 3.04354	0.52584
CTIO J174253.89-340902.1	− 32.26685	−4.08821
CTIO J174648.06-341342.3	− 43.80466	−3.95229
CTIO J175234.11-302619.6	−268.56040	−14.55346
CTIO J175401.23-343958.7	−103.98282	−5.41085

As was done for AAT 2dF data, Fv was used to extract data from the reduced spectra and that spectral data then rendered with vector graphics generated from a semi-automated data conversion process.

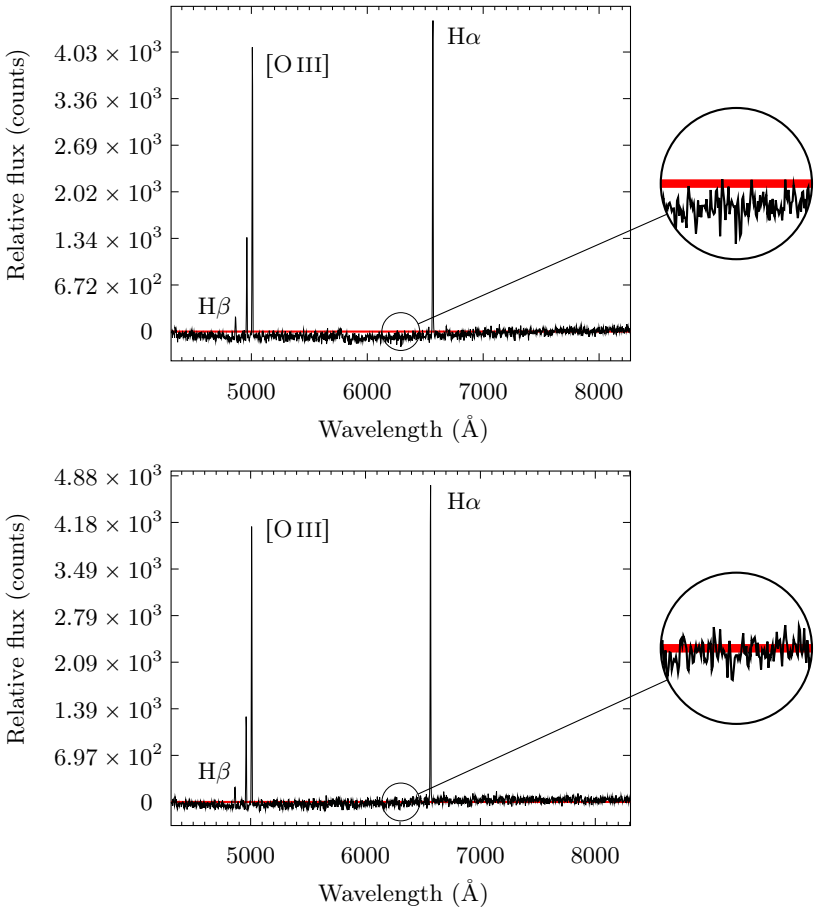

Figure 3.23: Top: Radcliffe 1.9 m telescope spectrum with typical PN emission line features. The spectrum was produced using the simplified spectral extraction scheme. A horizontal red line denoting zero relative flux is overlaid. Deviation of the spectrum's apparent baseline from this line highlights the incorrect determination of the nebula's zero flux level. Bottom: The same Radcliffe 1.9 m telescope data, processed this time using the enhanced spectral extraction scheme devised here. Note the (accurately) higher emission line fluxes returned (flux count axis divisions are scaled to each spectrum's maximum flux, not kept consistent between spectra). Again, a horizontal red line denoting zero relative flux is overlaid. The red line is difficult to distinguish from the nebula's zero flux level, meaning it has been determined more accurately.

Spectral Tilt Correction

Many SITe CCD spectra were tilted with respect to the dispersion axis by a pixel from the red end to the blue end. Although this may seem a minor tilt, nebula spectra recorded sometimes only extended a few pixels in the spatial direction, so the tilt was significant enough to produce incorrect emission line ratios and subsequent misidentification of candidate excitation class if left unaddressed. There was no appreciable tilt of data with respect to the spatial axis (i.e. < 1 pixel), as determined from examination of arc and sky lines.

To compensate for tilt, data was divided along the dispersion axis and each section reduced separately. Division was done about $\lambda = 5785$ Å, the midpoint of two typically strong PN emission lines, [O III] λ5007 and Hα λ6563. This division point is itself not coincident with

significant anticipated PN emission lines, the nearest being the [N II] λ5755 line. Reduction used a common *nsum* in each section but values of y_{mid} offset by one pixel. The reduced spectral sections were then combined and presented as one contiguous spectrum for each PN, with typically negligible discontinuity around $\lambda = 5785$ (see e.g. spectra presented in §3.4).

Dome Flats

Dome flats were generally combined on a per run, not per night, basis for data reduction purposes. Manual alignment of telescope and flat screen each night probably produced small differences in screen-telescope perpendicularity. As the dome flat field lamp is mounted on the end of the telescope, combining dome flats across a run was done to compensate for the resulting non-uniform screen illumination. There was an instance of a spectrograph grating angle change mid-run, and for that case, only dome flats taken with the relevant grating angle were used to reduce the associated observations. Each dome flat was checked to ensure no part of the flat exceeded the CCD's linearity maximum ($\sim$40 000 counts pixel^{-1}, Kilkenny & Worters, 2014).

A response function for the flat field lamp was produced from the combined dome flats with IRAF's RESPONSE task (as per, e.g. Massey, 1997). To obtain a response function derived from only large scale, wavelength dependent characteristics of the flat field lamp, a fitting function was used with a number of stationary points across the CCD data region not exceeding that of the lamp spectrum's large scale structure. Within the bounds of this restriction, an optimum fit, one minimising fit root mean square error (RMSE), was sought. Fitting options offered by IRAF include linear and cubic splines and Chebyshev $T_n(x)$ and Legendre $P_n(x)$ polynomials of the first kind. These are calculated with a user-specified fitting order n_{fit} (or number of pieces for spline fits), related to polynomial degree n by $n_{\text{fit}} = n + 1$. Hence, specifying $n_{\text{fit}} = 3$ produces a 2nd order polynomial fit for example.

An optimum flat field fitting function was determined by interactively testing each combination of linear spline, cubic spline and Chebyshev fit over $1 \leqslant n_{\text{fit}} \leqslant 100$. Stopping fit testing at $n_{\text{fit}} = 100$ was arbitrary, but deemed acceptable as an excellent fit had been obtained (RMSE = 214.3 for 2013 data, RMSE = 189.6 for 2014 data, both using a $n_{\text{fit}} = 79$ cubic spline) and high order fits were in general breaching the stationary points restriction adopted here, fitting smaller and smaller features, rather than the large scale structure desired. Also testing Legendre fits would have been superfluous, with justification demonstrated and discussed later in the context of wavelength calibration.

Twilight Flats

Evening twilight flats for Radcliffe telescope observing runs were taken at zenith. As discussed for ATT twilights, this was deemed a reasonable choice for producing twilight flat fields based on the sky illumination characterisation of Chromey & Hasselbacher (1996). Similarly, target data for nights missing twilight flats were reduced using substitutions implemented

in the same manner as described for the ATT. These twilight flats were combined on a per night basis and illumination calibration carried out with IRAF's ILLUMINATION task. As for producing a response function for the flat field lamp, the goal with illumination calibration is to fit the large scale structure of the flat (Massey et al., 1992). Five dispersion bins were used (as per, e.g. Massey, 1997). To avoid fitting solar or telluric absorption features, IRAF's default cubic spline fit with *low_reject* and *high_reject* parameters set to 2σ was used. Interactive adjustment of n_{fit} was made to produce a smooth low order ($n_{\text{fit}} \leqslant 12$) fit to each dispersion bin's large scale features. Use of a low order linear spline produced suboptimal jagged fits. Use of a Chebyshev fit (and by extension, a Legendre fit) of low order also failed to produce a smooth fit to large scale features, instead either producing erroneous high amplitude oscillatory fits to large scale features, or producing unwanted good fits to small scale features. An optimum cubic spline fit was determined by interactively testing fit order over $1 \leqslant n_{\text{fit}} \leqslant 12$. As n_{fit} was increased from one, RMSE would decrease as large scale features were better fit. An optimum value of n_{fit} would be reached (typically $n_{\text{fit}} = 4$–8), from which RMSE would again increase before falling again as small scale structures began to be fit. An optimum smooth low order fit was therefore defined here as the n_{fit} yielding the first minimum in RMSE as $n_{\text{fit}} \rightarrow 12$.

Cosmic Ray and Hot Pixel Correction

Due to the large number of targets for the available observing time, single-shot target exposures were generally taken. As a result, initial cosmics removal was done with the dcr software utility (Pych, 2004) integrated into the reduction scripts discussed above, rather than via replacement pixel value calculation from complementary exposures (Shaw & Horne, 1992, Windhorst et al., 1994, Zhang, 1995, Freudling, 1995, Fruchter & Hook, 1997).

For the selected cases where multiple equidurational target exposures were taken, a pixel-averaged image was produced with IRAF's IMCOMBINE task. The *crreject* rejection parameter was set to remove cosmics from the combined image before further processing. The spectrograph control software writes CCD readout noise (6.5 electrons, root mean square value) and gain ($1\,\text{electron}\,\text{ADU}^{-1}$) values to FITS headers, which were referenced through the task's *rdnoise* and *gain* parameters and used by the *ccreject* algorithm. Use of IMCOMBINE proved very effective in cosmics removal and allowed diagnosis of CCD hot pixels, e.g. figure 3.24, which could then be corrected.

For the Radcliffe telescope SITe CCD, a cursory examination of hot pixel effects suggested negligible noise contribution at the short exposure times used for biases, arcs and flats, with significant noise becoming apparent only at the longer exposure times used for PN candidate observations. Hot pixel behaviour can be complex however, exhibiting linear and non-linear dark current dependence on exposure time (Widenhorn et al., 2010) and sometimes even random fluctuations of dark current between discrete values over time (Hopkinson et al., 2004). As a result, the cursory examination of hot pixel effects conducted here wasn't considered

definitive and hot pixel correction was carried out with IRAF's FIXPIX task (as per, e.g. Wells & Bell, 1994) over all exposures, both calibration and target, early in the reduction process to minimise hot pixel impact on spectral reduction.

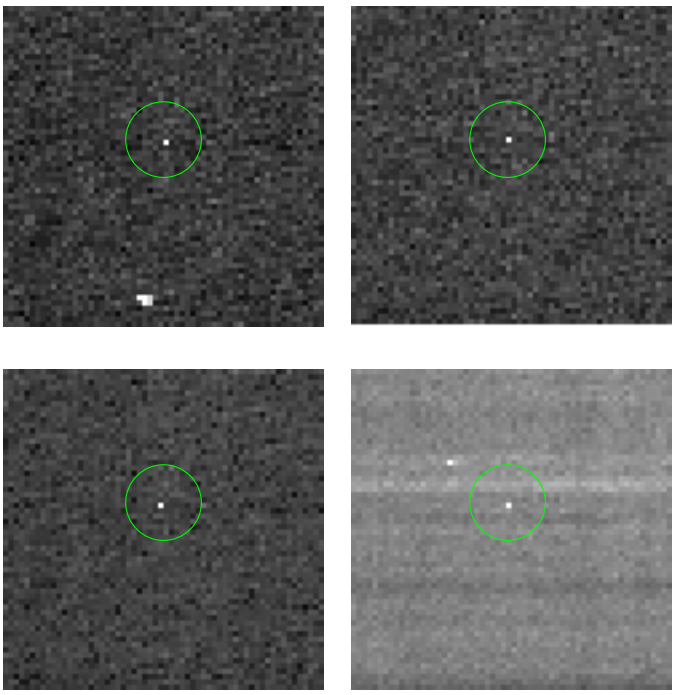

FIGURE 3.24: Example Radcliffe telescope SITe CCD hot pixel at physical coordinates ($x = 677, y = 70$). Top row: IRAS 17292-2805 spectrum segment, first exposure, left, then second exposure, right. Bottom row: Combined IRAS 17292-2805 spectrum segment, left, then exposure of alternate target CTIO J174648.06-341342.3, taken the previous year, right. Exposure-to-exposure artefacts, such as the cosmic in the spectrum segment at top left, are filtered in combined data. Hot pixel artefacts by contrast, such as the one circled here, persist in combined data and across targets.

Running dcr with its default parameters removed obvious cosmics but, erroneously, valid target data. Increasing both the dcr subframe size parameters from ($x = 9, y = 9$) to ($x = 15, y = 15$), following the example of Husemann et al. (2012), and increasing the detection threshold from 3σ to 4σ ameliorated this issue. Some observational target frames still suffered erroneous removal of valid spectral data. The number of such instances was small enough however to allow cosmics removal with alternate, manually set dcr parameters, selective manual use of L.A.Cosmic (van Dokkum, 2001), Fv or IRAF's IMEDIT or EPIX tasks.

Alternatives to script-integrated dcr were considered, such as IRAF's JCRREJ2 (Rhoads, 2000) and XZAP tasks, L.A.Cosmic (as a primary, rather than supplementary option, as discussed above), PyCosmic (Husemann et al., 2012) and SExtractor (Bertin & Arnouts, 1996), with discussion and evaluation data available for guidance (Farage & Pimbblet, 2005, Husemann et al., 2012). Such evaluations however were either focussed on a different observational regime, such as imaging instead of spectroscopy (Farage & Pimbblet, 2005), or only considered some of the alternatives mentioned (Husemann et al., 2012). Nonetheless, several of these alternatives may have offered better cosmic detection efficiency than dcr. As cosmics removal

with dcr suffered here more from spurious removal of valid data rather than from inadequate detection of real cosmics, and dcr is both computationally efficient and less prone to spurious data removal than jcrrej2, L.A.Cosmic and PyCosmic in some comparisons (Farage & Pimbblet, 2005, Husemann et al., 2012), it was deemed adequate for cosmics removal here.

Wavelength Calibration

Spectra were extracted and wavelength calibrated with IRAF's identify and reidentify tasks run over CuAr arc lamp spectra. For most targets, bracketing arcs, not just a single arc, were available. An orthogonal polynomial fit of up to 50 lines was used and the parameter *maxfeatures* = 50 correspondingly set in identify and reidentify. Poorly fitting lines, some potentially due to blended features (e.g. the Ar II $\lambda 4072.0806 \pm 0.0001$ blend of $\lambda\lambda 4072.0043 \pm 0.0001$, 4072.3843 ± 0.0001)[15], were rejected interactively to optimise the fit.

Literature examples of wavelength calibration for the Radcliffe telescope's CuAr lamp were available, e.g. (Honey et al., 1988), but gave no motivation for the parameters used. Without a priori knowledge of an optimum fitting parameter set, a random Radcliffe telescope CuAr arc lamp spectrum was selected and dispersion solution convergence tested across fitting function types and n_{fit}. For the arc tested, initial line identification produced two gross outliers (line identifications with residual ratio magnitude $> 2\%$ mean). Solution convergence was tested both with the outliers included and after their removal. Removal of the outliers didn't change the general form of the solution convergence, only its speed (iterations to optimal convergence). Each fitting function type would converge until the non-linear component of the dispersion solution would fail the vertical line test (Ferland, 2008), i.e. be a relation but no longer a function. Solution convergence data for n_{fit} leaving the non-linear solution component passing the vertical line test are given in table 3.10. Orthonormal polynomial solution convergence was identical in this case, hence a single "Chebyshev, Legendre" heading.

In general, a wavelength dispersion solution minimising fit RMSE is sought. Use of large n_{fit} values in blind pursuit of fit RMSE minimisation should be avoided however, as unphysical dispersion solutions inconsistent with the grating equation can be produced. An optimum dispersion solution was therefore determined here by incrementing n_{fit} from one, minimising fit RMSE, as long as the non-linear dispersion solution component passed the vertical line test and until $|\Delta\text{RMSE}|\,\% < 1$.

Subject to these optimisation constraints, table 3.10 demonstrates the advantage of calculating a fit with an orthonormal polynomial rather than splines, but provides no evidence of superiority of one polynomial fit over the other. The asymptotic rate of convergence of Chebyshev and Legendre series are known to be identical, however as $n \to \infty$, the maximum pointwise error of a Legendre series truncated after n terms will be $\mathcal{O}(\sqrt{n})$ larger than that for a Chebyshev series correspondingly truncated after n terms (Boyd, J.P., 2001). As a result,

[15]This blended Ar II feature is given, without derivation, as $\lambda 4072.11$ by Zuiderwijk & Knapen (1989). An alternate value is given here, calculated as the average wavelength of the contributing lines weighted by their relative intensities, 708:178, given in Saloman (2010). Wavelengths in air, not vacuum, are specified.

TABLE 3.10: IRAF dispersion solution convergence for an example arc taken with the Radcliffe telescope's CuAr lamp. Orthonormal polynomial solution convergence was identical in this case, hence a single "Chebyshev, Legendre" heading.

Linear spline			Cubic spline			Chebyshev, Legendre		
n_{fit}	RMSE	ΔRMSE %	n_{fit}	RMSE	ΔRMSE %	n_{fit}	RMSE	ΔRMSE %
1	7.844	–	1	0.8052	–	1	1064	–
2	2.382	69.63	2	0.7863	2.35	2	7.844	99.26
3	1.321	44.54	3	0.7876	−0.17	3	0.8463	89.21
4	0.9196	30.39	4	0.7824	0.66	4	0.8052	4.86
5	0.8523	7.32	5	0.7840	−0.20	5	0.7864	2.33
–	–	–	–	–	–	6	0.7859	0.06
–	–	–	–	–	–	7	0.7854	0.06
–	–	–	–	–	–	8	0.7845	0.11
–	–	–	–	–	–	9	0.7719	1.61
–	–	–	–	–	–	10	0.7641	1.01
–	–	–	–	–	–	11	0.7566	0.98

Chebyshev fitting was deemed preferable here to Legendre fitting and used as the default setting for all subsequent wavelength calibration.

Accuracy of the calibration was increased further in each instance by interactively removing additional poorly fitting lines (those with residual ratio magnitude $> 0.01\%$ mean). Some calibrations could be further optimised by making final minor adjustments to n_{fit}, likely necessitated by the system flexure and thermal expansion effects (Kitchin, 2014).

Further Data Analysis

Source flux calibration with IRAF is in progress. SAAO atmospheric extinction data (tabulated in Loubser, 2005), was used to build a custom IRAF extinction table, saaoextinct.dat. It is acknowledged this static extinction data neglects potential dynamic conditions on-site, with Sutherland previously affected by pyrogenic aerosols from wildfires (Winkler, 2000), wind-borne dust from the Northern Cape and even volcanic ash (Kilkenny, 1995). On at least two observing runs, municipal waste was observed being burnt at a dump site immediately outside Sutherland, approximately 10 km from the Radcliffe telescope. This custom extinction table provides however, a more accurate calibration than relying on the default southern hemisphere extinction table supplied with IRAF, ctioextinct.dat for the CTIO.

3.3.4 Observing Summary

A summary of observing undertaken to perform spectroscopic confirmation of new bulge PN candidates is given in table 3.11. All observing time awarded is listed, including nights lost to bad weather (e.g. figure 3.25) and equipment failures. A range of standard stars and

known PNs were observed to calibrate candidate PNs against, e.g. spectrophotometric (Stone & Baldwin, 1983, Baldwin & Stone, 1984) and emission line (Dopita & Hua, 1997) standards. During parts of the night when the bulge wasn't accessible, supplementary PN science was conducted, such as spectroscopic observations of candidate Galactic, LMC and SMC PNs.

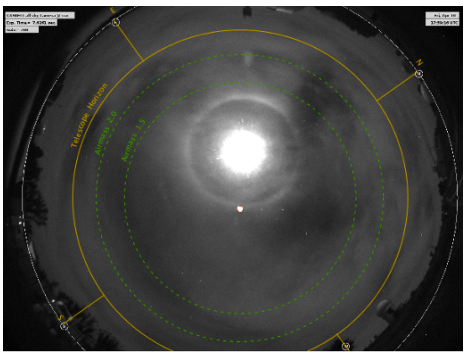

Figure 3.25: A lunar 22° halo caused by refraction of light by atmospheric hexagonal I_h ice crystals (Whalley, 1983, Lynch & Schwartz, 1985, Können et al., 1994). This halo was captured with the TAROS's Hungarian-made Automated Telescope Network-South All Sky fisheye camera (Bakos et al., 2013) feed during grey time, on the night 10 April 2015, ≈18:02:15 UT. This night's observing was compromised by variable cloud cover.

Table 3.11: Confirmatory spectroscopy observing summary. Diameters of telescope primary mirrors have been rounded to one decimal place for clarity. Observers listed include the author (TS), Quentin Parker (QP) and Warren Reid (WR), all associated with Macquarie University's Department of Physics and Astronomy.

Telescope	Instrument	Grating(s)	Wavelength coverage (Å)	Run dates (yyyy-mm-dd)	Observers
ATT 2.3 m	WiFeS	B7000, R7000	4184–4850;* 5294–7060	2013-06-13:15	TS
ATT 2.3 m	WiFeS	B3000, R3000	3200–5900, 5300–9800	2013-06-16:18	TS
AAT 3.9 m	2dF/AAOmega	580V, 385R	3700–5800, 5600–8800	2013-07-26	– †
ATT 2.3 m	WiFeS	B7000, R7000	4184–4850;* 5294–7060	2013-08-01:02	TS
Radcliffe 1.9 m	CCDSpec	7; 300 l mm^{-1}	4307–8302;‡ 3223–7225‡	2013-08-14:20	QP, TS
AAT 3.9 m	2dF/AAOmega	580V, 385R	3700–5800, 5600–8800	2013-09-05	– †
Radcliffe 1.9 m	CCDSpec	7; 300 l mm^{-1}	3304–7293	2014-03-05:11	QP, TS
ATT 2.3 m	WiFeS	U7000, B7000, R7000, I7000	3290–4380, 4184–5580, 5294–7060, 6832–9120	2014-04-24	TS
ATT 2.3 m	WiFeS	B3000, R3000	3200–5900, 5300–9800	2014-04-24:26	TS
ATT 2.3 m	WiFeS	B3000, R3000	3200–5900, 5300–9800	2014-05-24:28	TS
AAT 3.9 m	2dF/AAOmega	580V, 385R	3700–5800, 5600–8800	2014-06-05	– †
AAT 3.9 m	2dF/AAOmega	580V, 385R	3700–5800, 5600–8800	2014-06-18	– †
Radcliffe 1.9 m	CCDSpec	7; 300 l mm^{-1}	3530–7527	2014-06-25:07-01	TS, WR
ATT 2.3 m	WiFeS	B3000, R3000	3200–5900, 5300–9800	2014-08-02:04	TS
AAT 3.9 m	2dF/HERMES	B28 000, G28 000, R28 000, I28 000	4715–4900, 5649–5873, 6478–6737, 7585–7887	2014-08-27	– †
ATT 2.3 m	WiFeS	B3000, R3000	3200–5900, 5300–9800	2015-04-10	TS
ATT 2.3 m	WiFeS	B3000, R3000	3200–5900, 5300–9800	2015-05-08:09	TS

* The normal B7000 wavelength coverage of 4184–5580 Å was truncated due to incorrect dichroic configuration.
† Observations conducted in service mode.
‡ Grating angle was changed mid-run, shifting wavelength coverage to the blue.

3.4 Candidate Evaluation

Each Galactic bulge PN candidate is presented in more detail here. Blanco Mosaic II, and UKST SHS and SSS imaging, and any spectroscopic data are compiled and used to draw conclusions about each candidate. Emission line identification was done though a combination of consulting a dedicated PN emission line catalogue (Kaler et al., 1997) and general literature searches. Spectra accompany each object and summarise gross spectral features. Full enumeration of spectral features appears in the discussion accompanying each object. These features were obtained from analysis of spectra magnified in IRAF to more detail than is presented here. Only features manifest above the level of noise are documented.

A five-set Venn diagram constructed from four congruent ellipses (e.g. Grünbaum, 1975) and one smaller ellipse denoting a subset, given in figure 3.26, represents the logical relations between evaluation criteria sets used to classify candidates as either true, probable or possible PNs (as per the classification schemes of e.g., Hartl & Tritton, 1985, Parker et al., 2006, Miszalski et al., 2008). Here "characteristic PN spectral line species" means those emission lines typically most prominent in PNs and that belong to the same ionic species. Thus, the Balmer series (Hα, Hβ, etc.), [N II] $\lambda\lambda$6548, 6583, [O III] $\lambda\lambda$4959, 5007 and He II λ4686, etc. (Gurzadyan, 1997), would all be considered different from each other, but Hα and Hβ or [O III] λ4959 and [O III] λ5007 would be considered as belonging to the same ionic species. Reference to candidate distinctness in (narrow) on band imaging is assumed to correspond to a candidate being visible only in on band imaging and not also in the corresponding off band imaging. Finally, a "high" S/N spectrum is defined as one that, in §3.4.1 onwards, doesn't require one or more major tick marks in the negative direction, along the relative flux axis, to quantify noise.

In addition to adopting the criteria represented by figure 3.26 for candidate evaluation, relative emission line ratios were examined for correspondence to known mimic trends. Specifically, for suitably deep spectra, relative line ratios were compared to the $\log\left(F_{\mathrm{H}\alpha}/F_{[\mathrm{N\,II}]}\right)$ versus $\log\left(F_{\mathrm{H}\alpha}/F_{[\mathrm{S\,II}]}\right)$ diagnostic diagrams of Frew & Parker (2010).

3.4.1 True PNs

CTIO J174648.06-341342.3

Within apparent proximity of the centre of dark nebula [DB2002b] G355.61-2.96 (ΔRA $\leqslant$ 1 s, Δdec $\leqslant 39''$, Dutra & Bica, 2002), this candidate has likely avoided previous detection due to being compact and partially coincident with a stellar object, as demonstrated in the UKST image in figure 3.27. A Radcliffe 1.9 m telescope spectrum (1200 s grey time exposure) of this candidate, shown in figure 3.27, exhibits a characteristic PN spectrum (e.g. Gurzadyan, 1997). For this exposure, the grating angle was accidentally set 1° lower than intended (16.5° instead of 17.5°), shifting the spectrum's λ_{c} by $\approx$1000 Å. Emission lines detected include Hβ, [O III] $\lambda\lambda$4959, 5007, Hα, He I λ6678 and [Ar III] λ7136. Based on imaging and spectroscopic

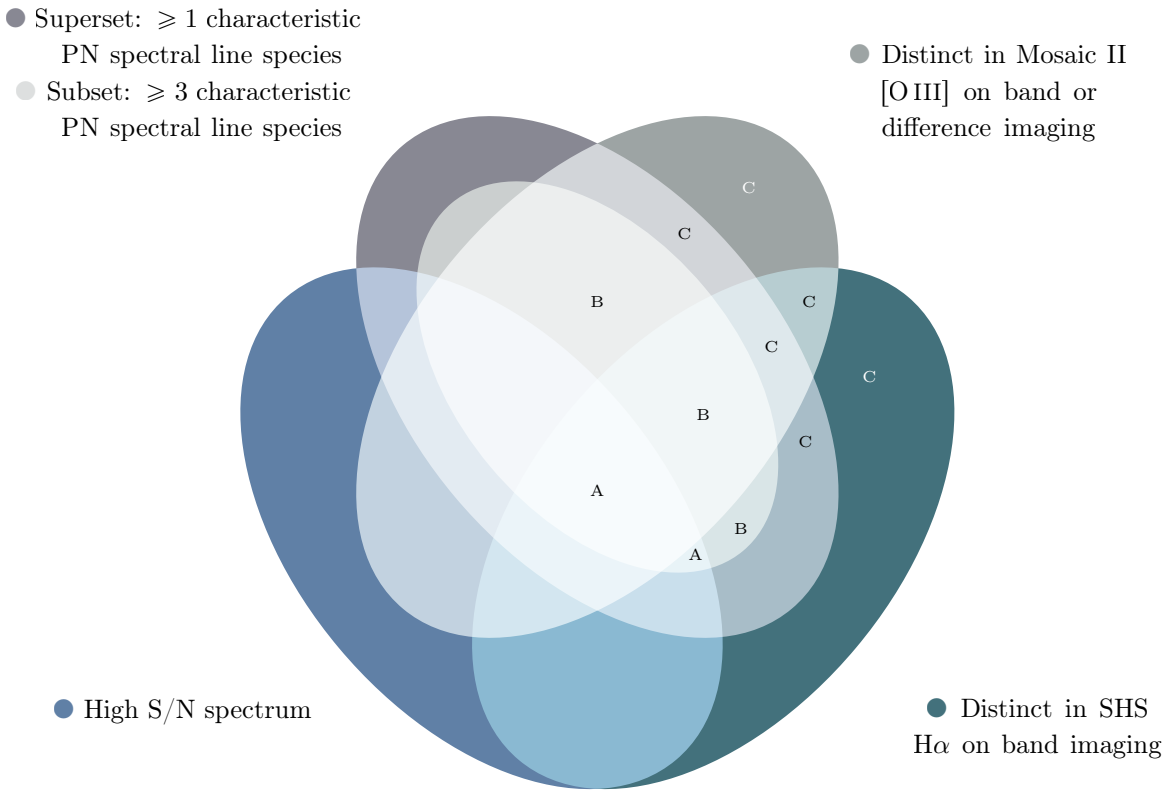

Figure 3.26: Five-set Venn diagram describing the logical relations between evaluation criteria sets used to classify PN candidates as true (A), probable (B) or possible (C).

evidence, CTIO J174648.06-341342.3 is classified here as a true PN.

CTIO J175812.20-283436.9

Compact PN CTIO J175812.20-283436.9 is shown in figure 3.28. An AAOmega spectrum (3×1200 s grey time exposure), given in the same figure, shows a characteristic PN spectrum. Emission lines detected include probable [Ar III] $\lambda\lambda$7136, 7751, [Ar IV] $\lambda\lambda$7171, 7238, [Cl IV] $\lambda\lambda$7531, 8046, Hα, Hβ, He I λ8750, He I $\lambda\lambda$5876, 6678, 7065, [K VI] λ8827, [N II] $\lambda\lambda$6548, 6583, [O I] λ5577 (airglow), [O II] $\lambda\lambda$7319, 7331, [O III] $\lambda\lambda$4959, 5007, [S II] $\lambda\lambda$6716, 6731 and [S III] λ6312. A HERMES spectrum (1200 s dark time exposure) taken at high airmass ($Z \approx 2.3$), also given in figure 3.28, provides reinforcing Hα and faint [N II] λ6583 emission. Based on these spectra and distinct detection in [O III] and Hα imaging, CTIO J175812.20-283436.9 is assessed a true PN.

CTIO J180652.90-280706.0

A spectrum of elliptical nebula CTIO J180652.90-280706.0, taken with the Radcliffe 1.9 m telescope (1800 s dark time exposure), is shown in figure 3.29. This spectrum shows clear [O III] $\lambda\lambda$4959, 5007, Hα and [N II] λ6583 emission and probable Hβ emission. [O I] $\lambda\lambda$5577, 6300

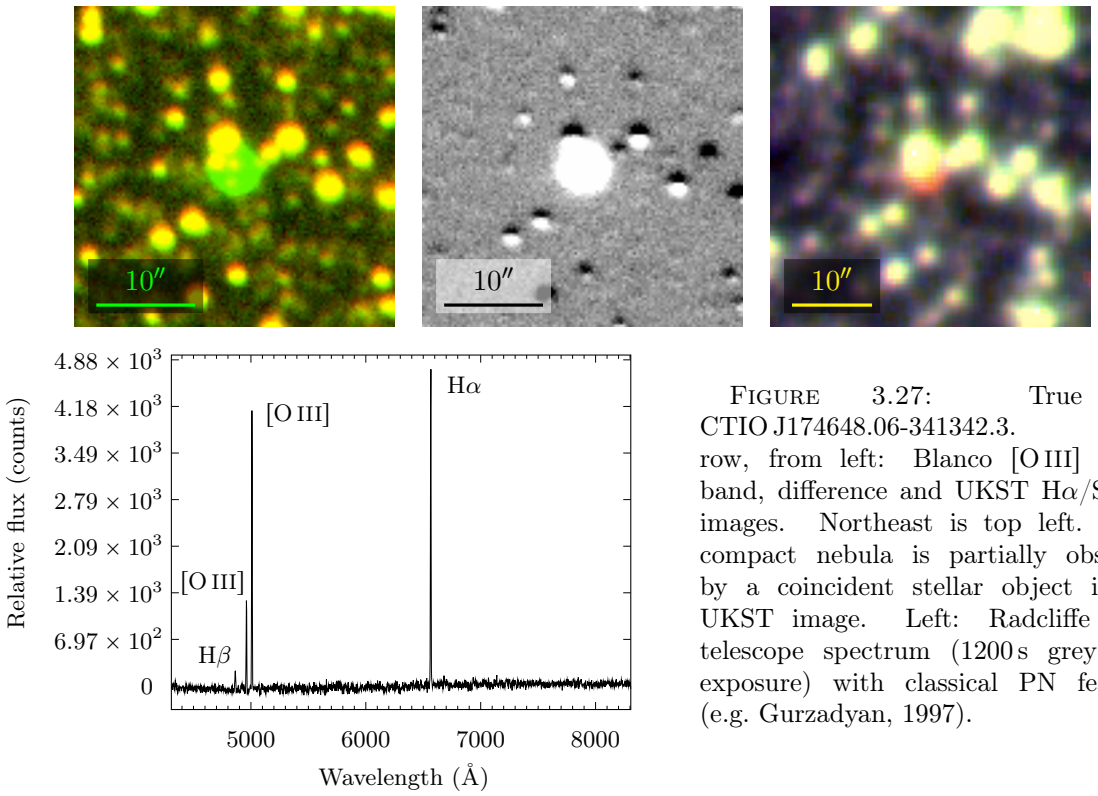

Figure 3.27: True PN CTIO J174648.06-341342.3. Top row, from left: Blanco [O III] on/off band, difference and UKST Hα/SR/IR images. Northeast is top left. This compact nebula is partially obscured by a coincident stellar object in the UKST image. Left: Radcliffe 1.9 m telescope spectrum (1200 s grey time exposure) with classical PN features (e.g. Gurzadyan, 1997).

airglow processing artefacts are present and have been truncated for clarity. CTIO J180652.90-280706.0 is assessed as a true PN on morphological and spectroscopic grounds.

CTIO J180755.67-264114.1

A spectrum of CTIO J180755.67-264114.1 taken with the Radcliffe 1.9 m telescope (900 s bright time exposure), is shown in figure 3.30. The spectrum exhibits the classical PN indicators of [O III] $\lambda\lambda$4959, 5007, Hα and [N II] λ6583. It has been assumed here features not explicitly labelled are noise. This candidate has likely avoided previous detection due to its compact apparent size in the optical. It is noted this object's core appears to be surrounded by a larger near-IR-luminous nebula component. Based on imaging and spectroscopic evidence, CTIO J180755.67-264114.1 is now classified as a true PN.

3.4.2 Probable PNs

CTIO J172822.84-254727.9

Multiwavelength imaging, shown in figure 3.31, suggests this is a probable PN. A spectrum for this candidate was obtained with the Radcliffe 1.9 m telescope (1800 s dark time exposure) and, despite residual [O I] $\lambda\lambda$5577, 6300, 6364 airglow artefacts, shows emission line features consistent with a PN, including [O III] λ5007, Hα and [N II] λ6583.

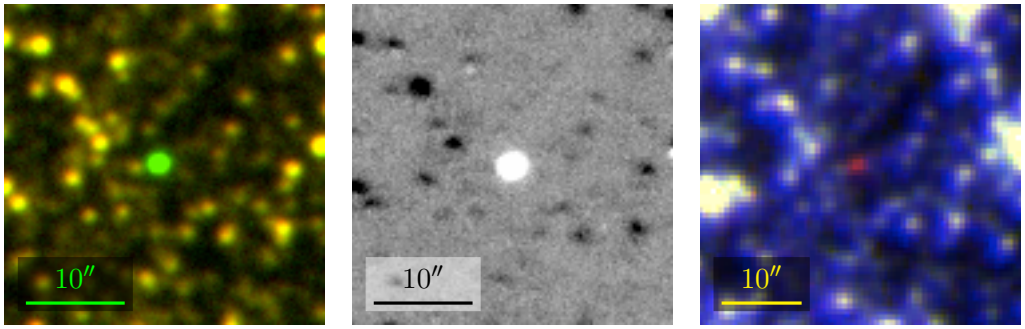

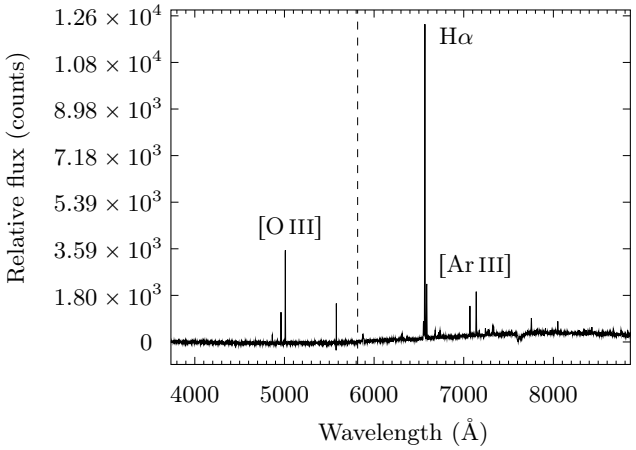

FIGURE 3.28: True PN CTIO J175812.20-283436.9. Top row, from left: Blanco [O III] on/off band, difference and UKST Hα/SR/IR images. Northeast is top left. Left: AAOmega spectrum (3 × 1200 s grey time exposure). AAOmega red and blue arm data are separated by the dashed line.

Right: HERMES red channel spectrum (1200 s dark time exposure) at high airmass ($Z \approx 2.3$). Several spurious artefacts are present, but genuine Hα and faint [N II] emission are displayed.

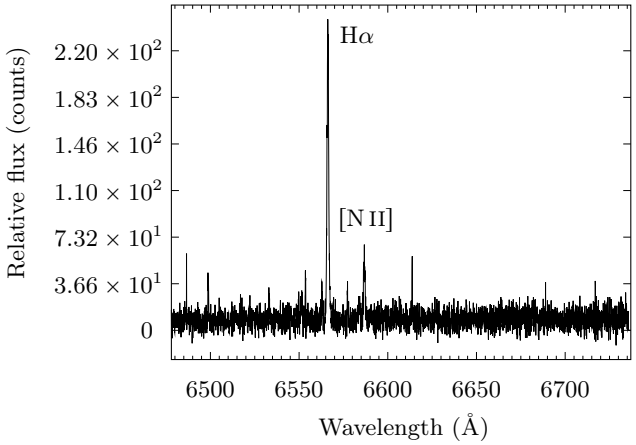

CTIO J172923.07-290500.9

This probable PN candidate has likely avoided detection in the MASH and MASH-II surveys due to its very faint apparent Hα emission in their associated imaging data, shown contrasting with Blanco [O III] emission in figure 3.32. Candidate spectra taken with the Radcliffe 1.9 m telescope (1500 s bright time exposure), shown also in figure 3.32, is of low S/N but shows some characteristic PN features. Emission lines include [O III] λ5007, Hα and strong [N II] λ6583. Deeper spectroscopy is recommended for a definitive evaluation of this candidate.

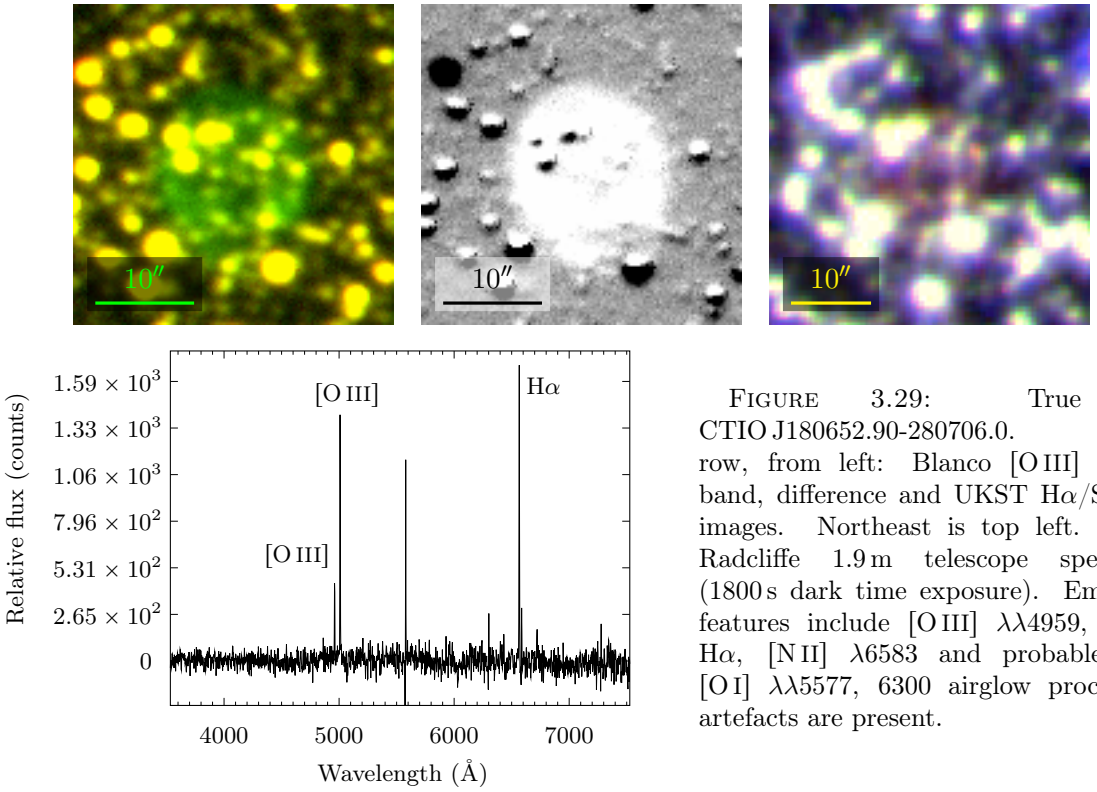

Figure 3.29: True PN CTIO J180652.90-280706.0. Top row, from left: Blanco [O III] on/off band, difference and UKST Hα/SR/IR images. Northeast is top left. Left: Radcliffe 1.9 m telescope spectrum (1800 s dark time exposure). Emission features include [O III] $\lambda\lambda$4959, 5007, Hα, [N II] λ6583 and probable Hβ. [O I] $\lambda\lambda$5577, 6300 airglow processing artefacts are present.

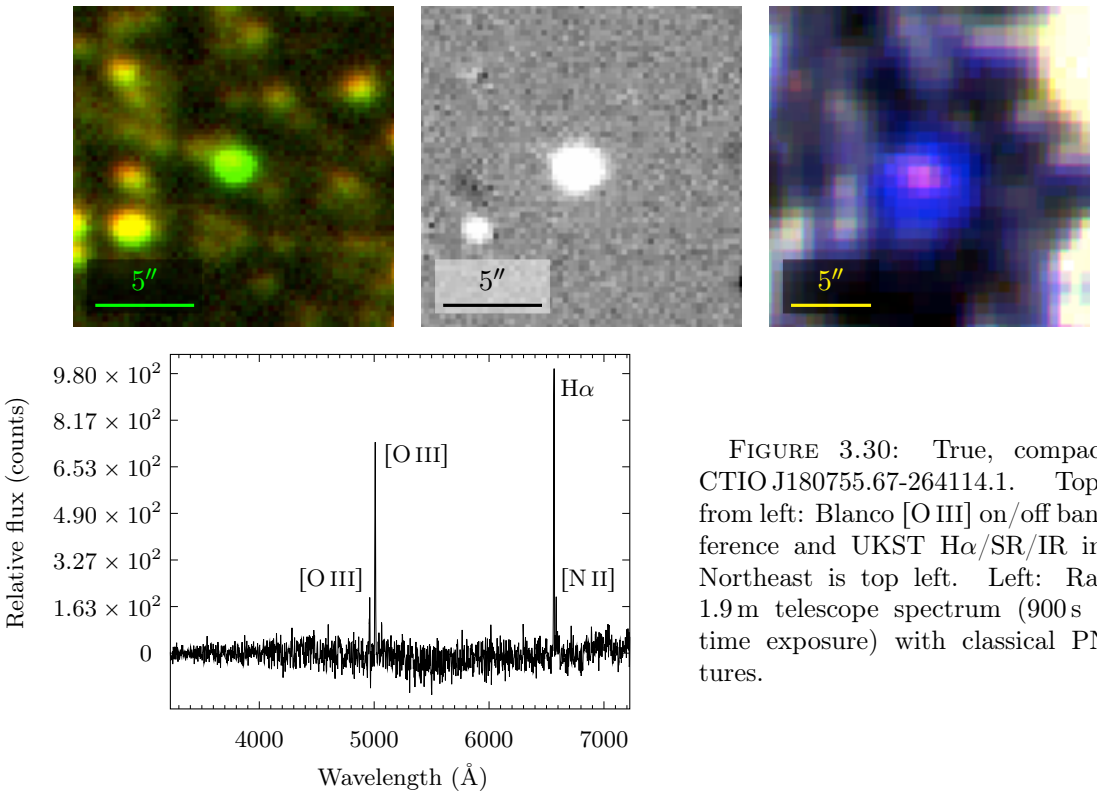

Figure 3.30: True, compact PN CTIO J180755.67-264114.1. Top row, from left: Blanco [O III] on/off band, difference and UKST Hα/SR/IR images. Northeast is top left. Left: Radcliffe 1.9 m telescope spectrum (900 s bright time exposure) with classical PN features.

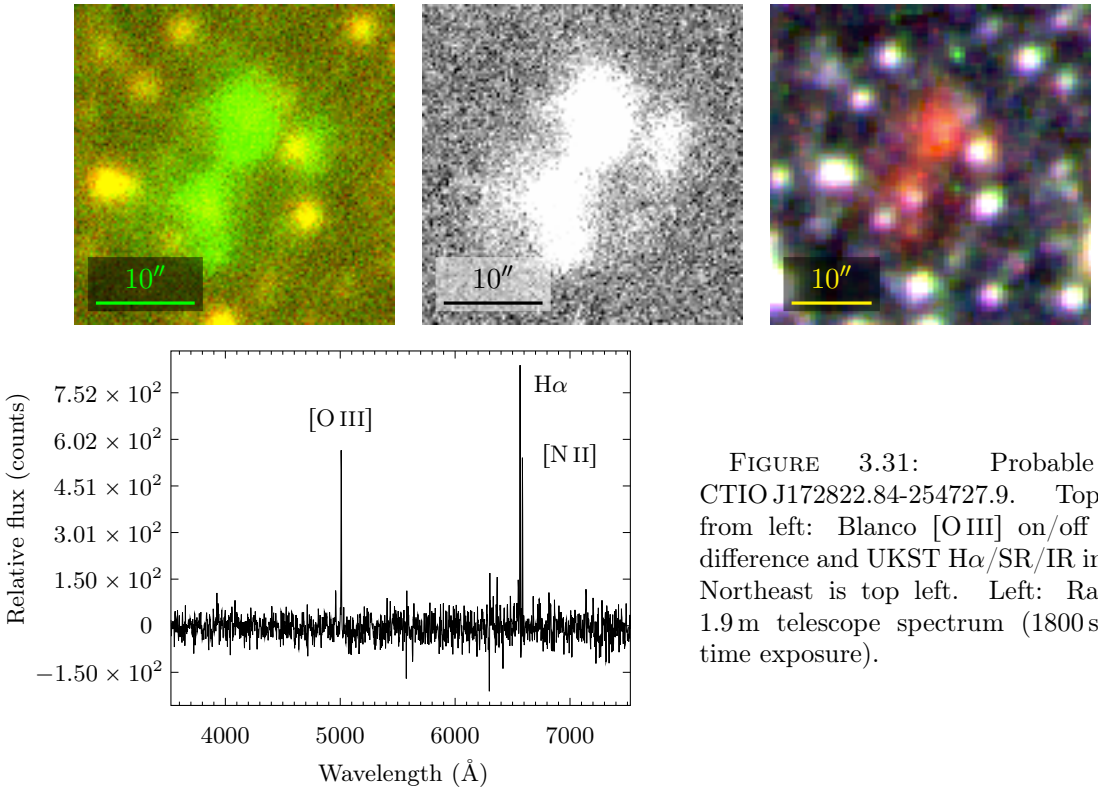

FIGURE 3.31: Probable PN CTIO J172822.84-254727.9. Top row, from left: Blanco [O III] on/off band, difference and UKST Hα/SR/IR images. Northeast is top left. Left: Radcliffe 1.9 m telescope spectrum (1800 s dark time exposure).

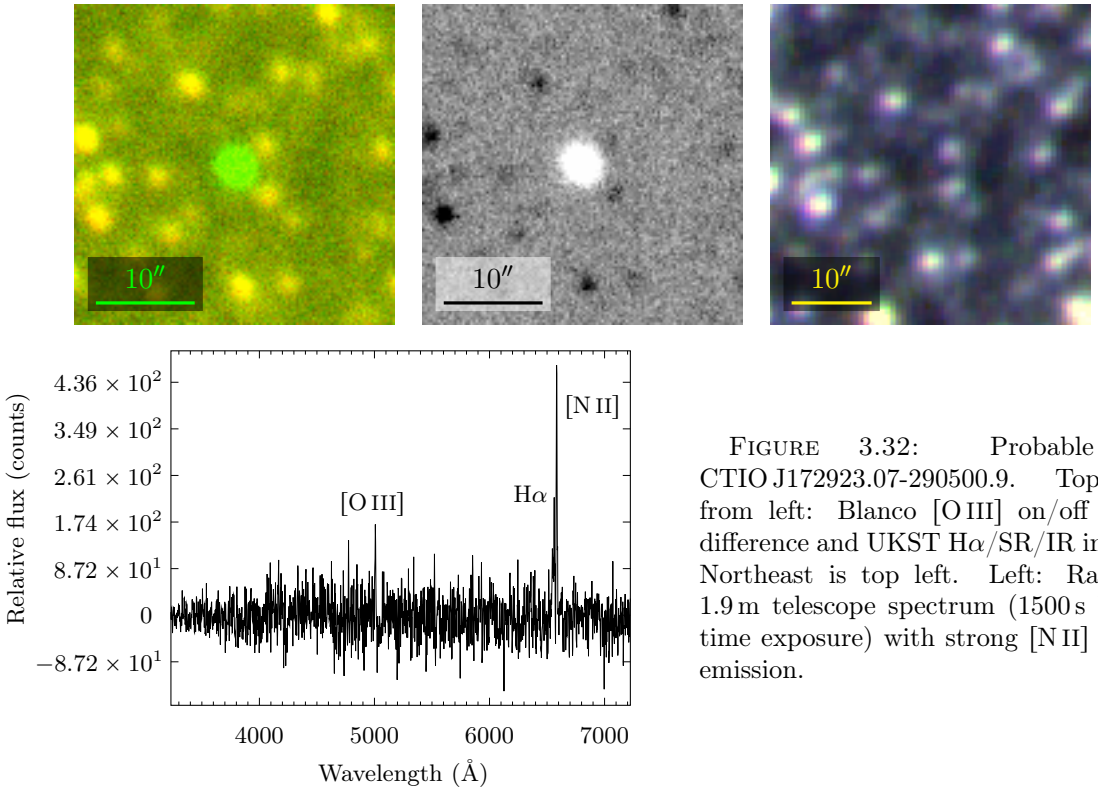

FIGURE 3.32: Probable PN CTIO J172923.07-290500.9. Top row, from left: Blanco [O III] on/off band, difference and UKST Hα/SR/IR images. Northeast is top left. Left: Radcliffe 1.9 m telescope spectrum (1500 s bright time exposure) with strong [N II] λ6583 emission.

CTIO J172944.81-290657.7

Probable round PN CTIO J172944.81-290657.7 exhibits, in a low S/N Radcliffe 1.9 m telescope spectrum (1800 s dark time exposure), shown in figure 3.33, the key PN emission lines [O III] $\lambda\lambda$4959, 5007, Hα and [N II] $\lambda\lambda$6548, 6583. Deeper spectroscopy is recommended for improved evaluation of this PN candidate.

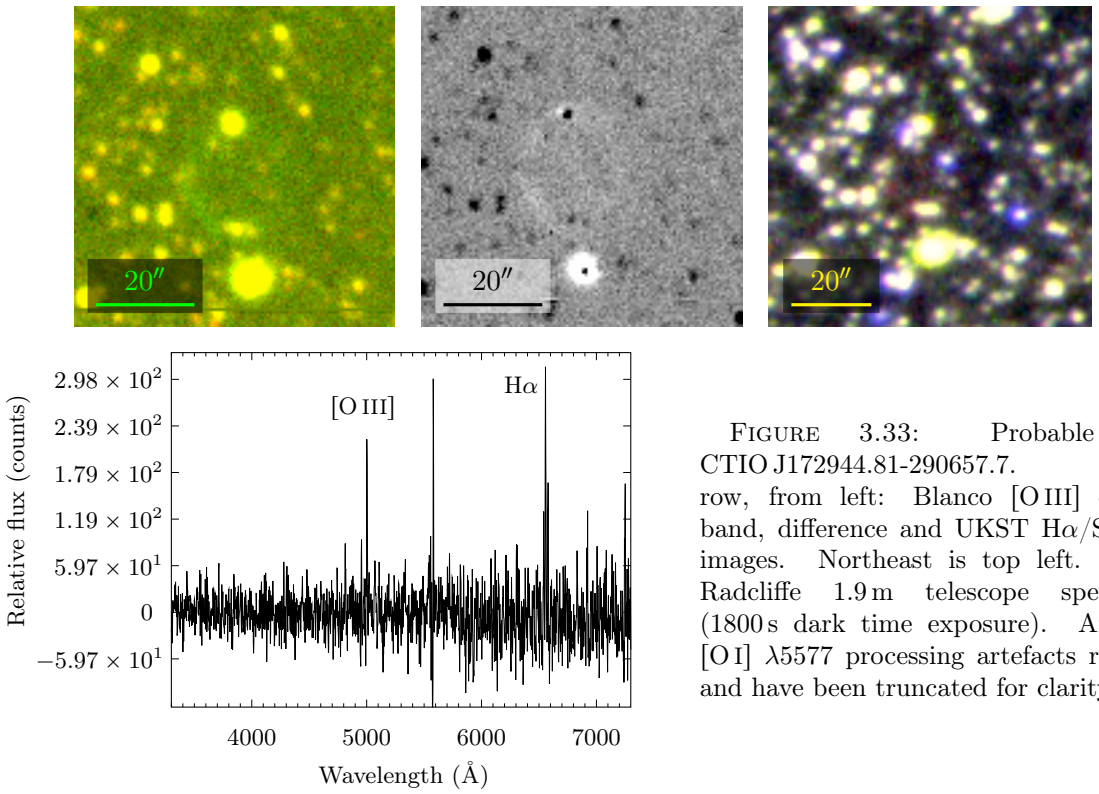

Figure 3.33: Probable PN CTIO J172944.81-290657.7. Top row, from left: Blanco [O III] on/off band, difference and UKST Hα/SR/IR images. Northeast is top left. Left: Radcliffe 1.9 m telescope spectrum (1800 s dark time exposure). Airglow [O I] λ5577 processing artefacts remain and have been truncated for clarity.

CTIO J173348.40-264623.4

A spectrum for this compact PN candidate was obtained with the Radcliffe 1.9 m telescope (average flux of 2×600 s dark time exposures) and is shown in figure 3.34. [O I] $\lambda\lambda$5577, 6300, 6364 airglow artefacts remain. [O III] λ5007, Hα and [N II] $\lambda\lambda$6548, 6583 emission lines are present, but all split, indicative of a high nebula expansion velocity.

CTIO J173444.22-281023.7

This object is the largest apparent diameter PN candidate $\approx(139.9'' \times 96.6'')$ found amongst the Blanco imaging. A Blanco difference image of this faint nebula is shown in figure 3.35. The large apparent diameter of this candidate suggests it is a foreground, rather than bulge, object. A spectrum obtained from the geometrical centre of this extended candidate with the Radcliffe 1.9 m telescope (1800 s bright time exposure) revealed no nebula emission. A subsequent attempt with the same telescope (1800 s dark time exposure, running (450 ± 30) s

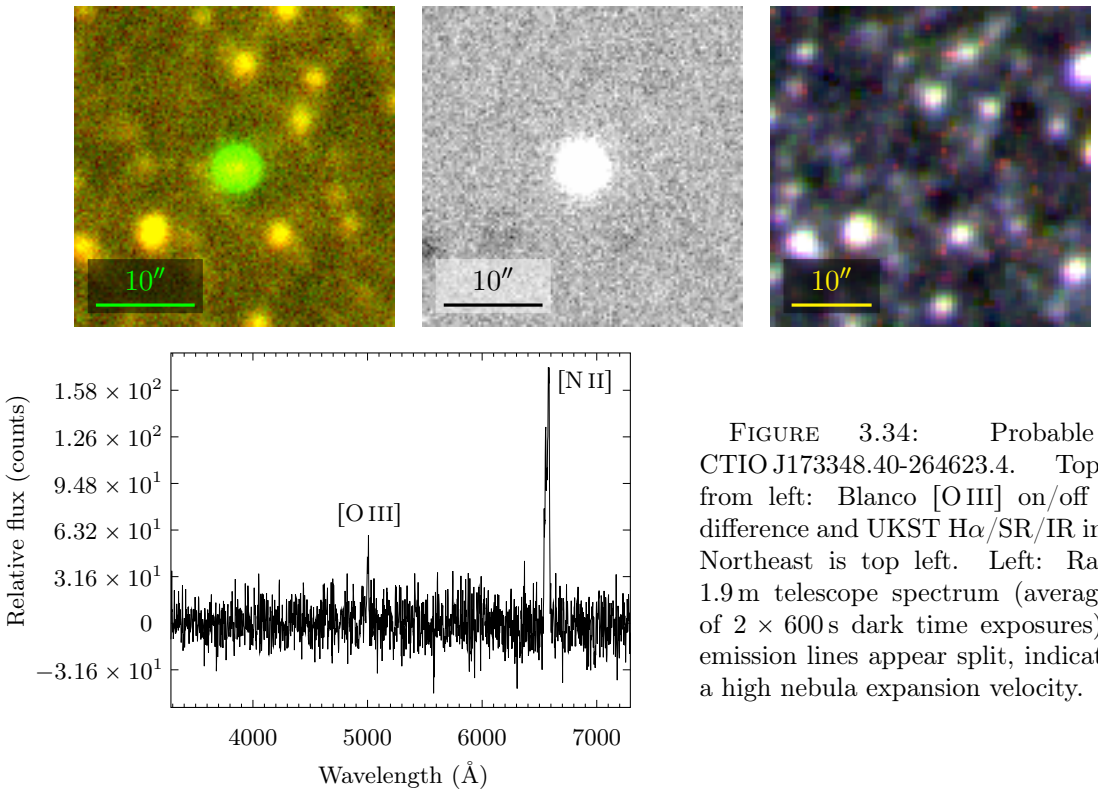

FIGURE 3.34: Probable PN CTIO J173348.40-264623.4. Top row, from left: Blanco [O III] on/off band, difference and UKST Hα/SR/IR images. Northeast is top left. Left: Radcliffe 1.9 m telescope spectrum (average flux of 2 × 600 s dark time exposures). All emission lines appear split, indicative of a high nebula expansion velocity.

into astronomical twilight) was made at a bright nebula segment and is shown in figure 3.35. Significant [O I] λ5577 airglow processing artefacts remain but have been truncated for clarity. Emission lines detected here include [O III] λ5007, Hα and [N II] λ6583. Reobservation during dark night time, with no astronomical twilight component, is recommended for improved spectral diagnosis of this candidate.

CTIO J173557.97-271214.2

A spectrum of this round, partially obscured nebula, taken with Radcliffe 1.9 m telescope (1800 s dark time exposure), as shown in figure 3.36, features key PN emission lines including [O III] $\lambda\lambda$4959, 5007 and Hα. On morphological and spectroscopic grounds, this object is assessed as a probable PN.

CTIO J173623.26-250528.7

A candidate spectrum taken with the Radcliffe 1.9 m telescope (1800 s bright time exposure), shown in figure 3.37, shows a clear PN signature with distinct [O III] $\lambda\lambda$4959, 5007 and Hα emission. Based on imaging and spectroscopic evidence, CTIO J173623.26-250528.7 is classified here as a probable PN.

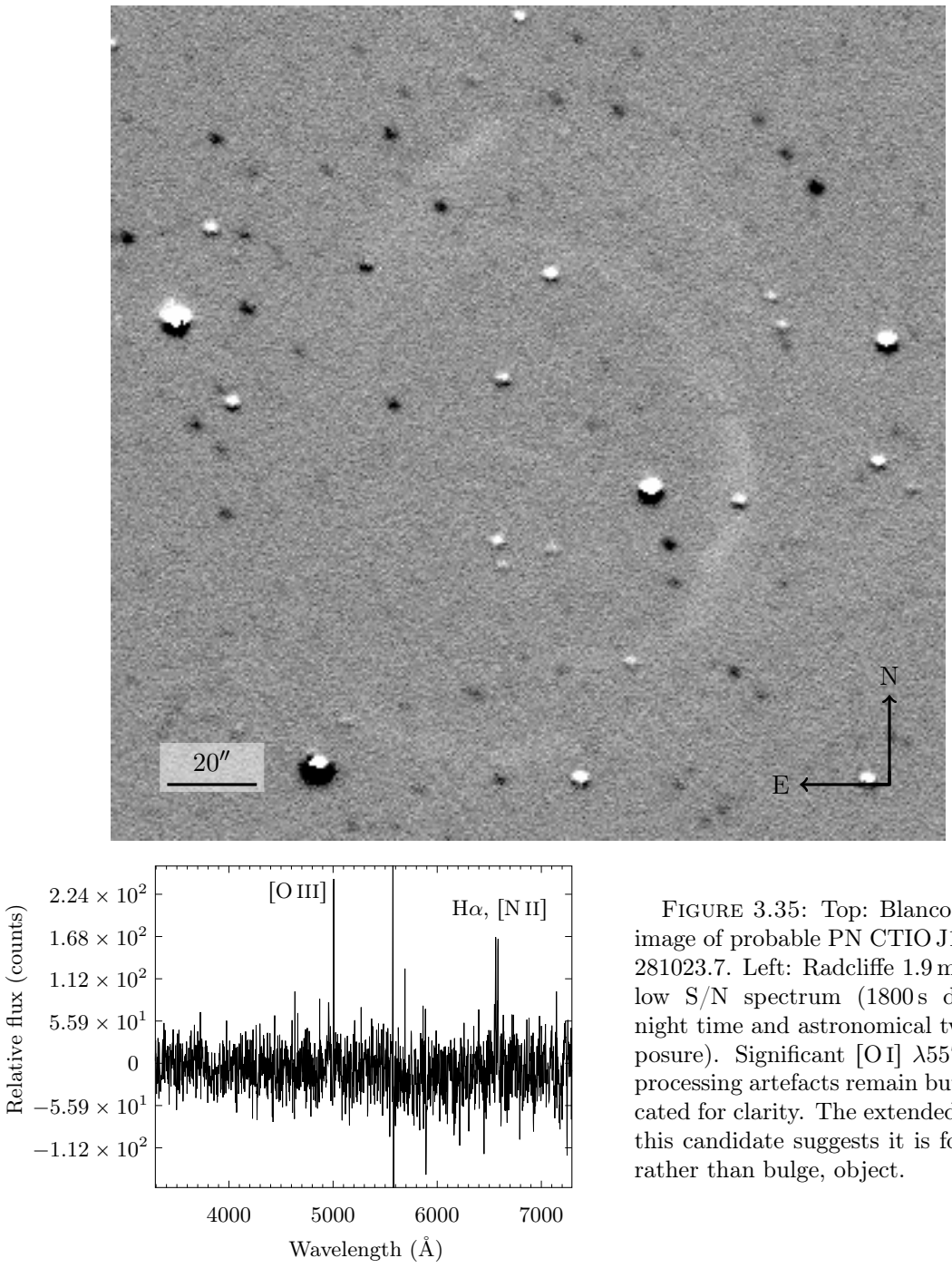

FIGURE 3.35: Top: Blanco difference image of probable PN CTIO J173444.22-281023.7. Left: Radcliffe 1.9 m telescope low S/N spectrum (1800 s dark time, night time and astronomical twilight exposure). Significant [O I] λ5577 airglow processing artefacts remain but are truncated for clarity. The extended nature of this candidate suggests it is foreground, rather than bulge, object.

CTIO J174253.89-340902.1

This object exhibits a classic round PN shape with some rim brightening. A corresponding spectrum, taken with the Radcliffe 1.9 m telescope (1800 s dark time exposure), is given in figure 3.38 and, despite residual [O I] λ5577 airglow processing artefacts, shows typical PN Hβ, [O III] $\lambda\lambda$4959, 5007 and Hα emission lines. On the basis of morphological and spectroscopic grounds, this object is assessed as a new probable PN.

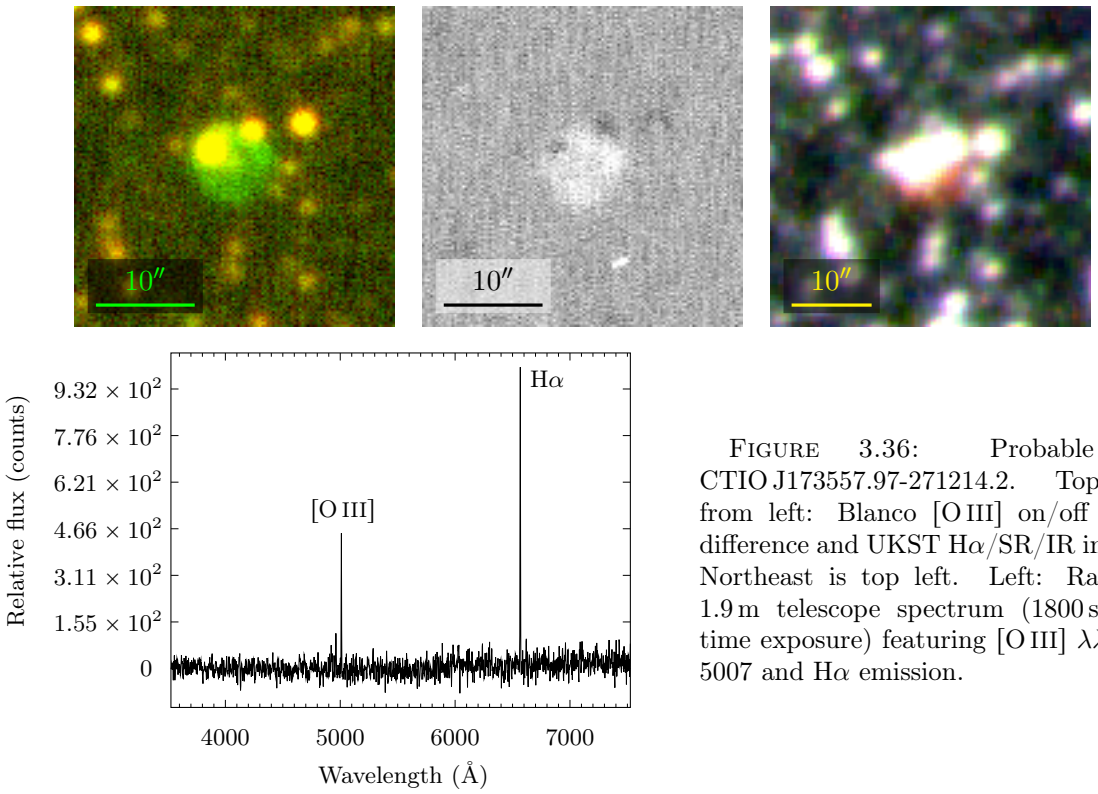

FIGURE 3.36: Probable PN CTIO J173557.97-271214.2. Top row, from left: Blanco [O III] on/off band, difference and UKST Hα/SR/IR images. Northeast is top left. Left: Radcliffe 1.9 m telescope spectrum (1800 s dark time exposure) featuring [O III] $\lambda\lambda$4959, 5007 and Hα emission.

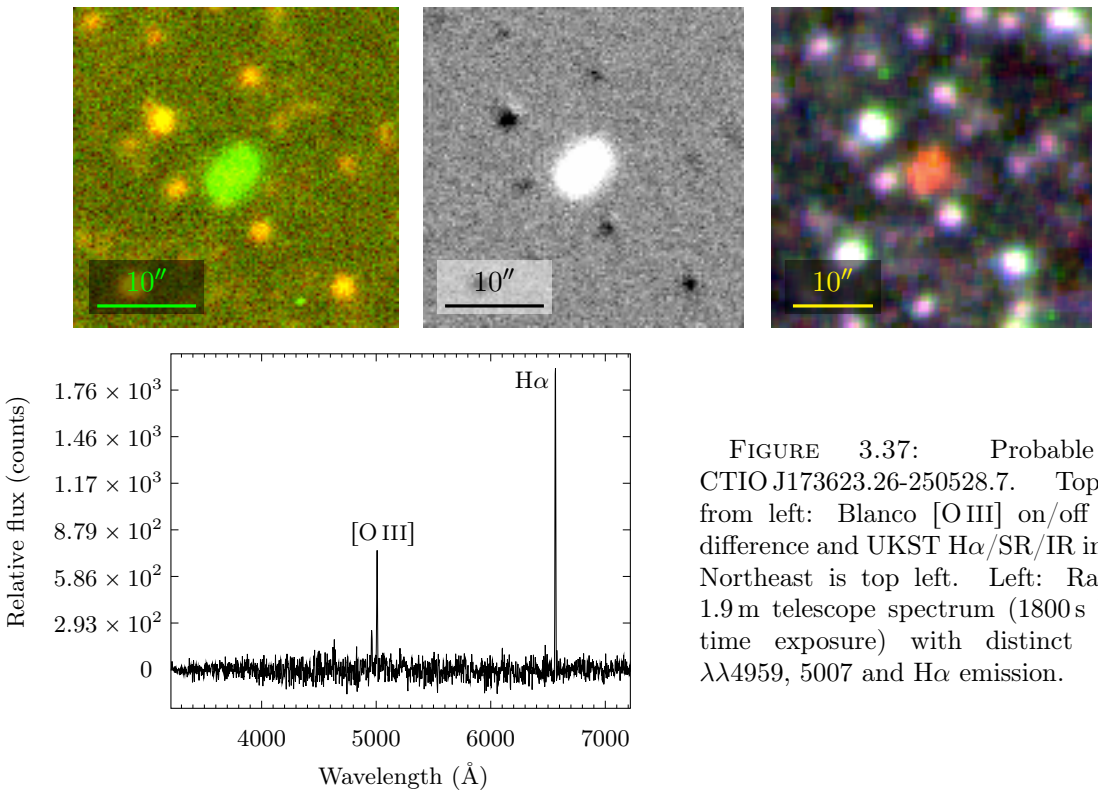

FIGURE 3.37: Probable PN CTIO J173623.26-250528.7. Top row, from left: Blanco [O III] on/off band, difference and UKST Hα/SR/IR images. Northeast is top left. Left: Radcliffe 1.9 m telescope spectrum (1800 s bright time exposure) with distinct [O III] $\lambda\lambda$4959, 5007 and Hα emission.

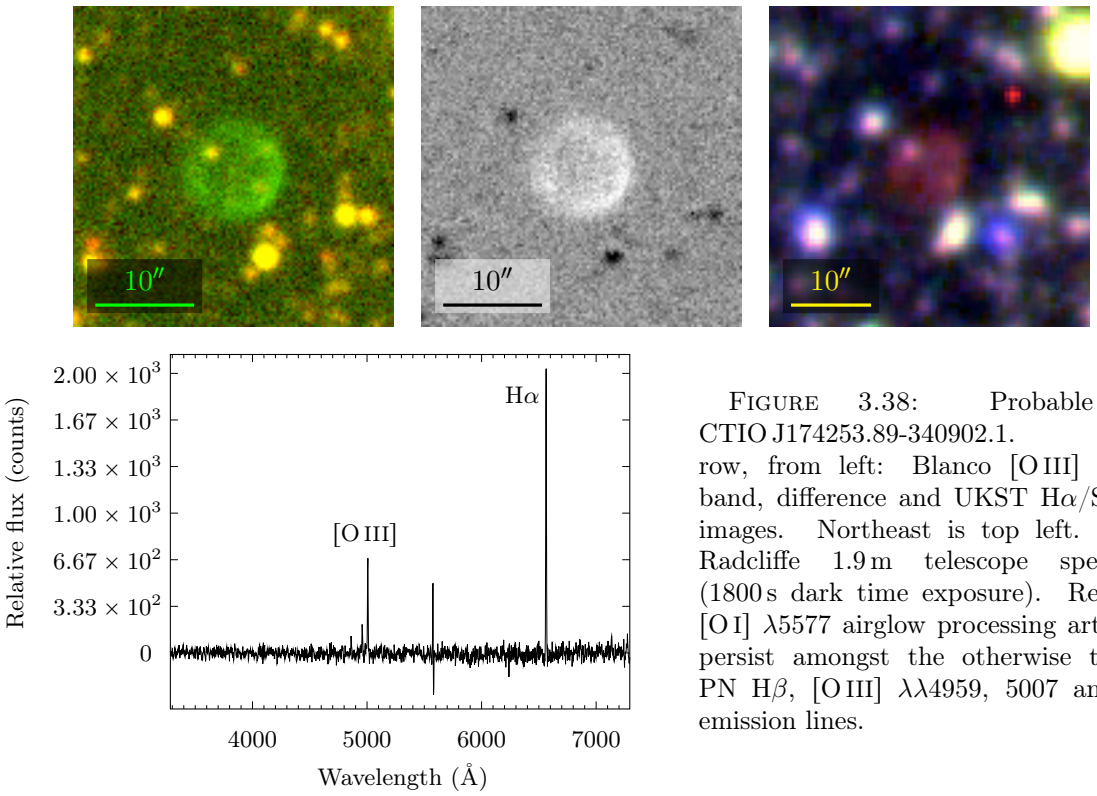

Figure 3.38: Probable PN CTIO J174253.89-340902.1. Top row, from left: Blanco [O III] on/off band, difference and UKST Hα/SR/IR images. Northeast is top left. Left: Radcliffe 1.9 m telescope spectrum (1800 s dark time exposure). Residual [O I] λ5577 airglow processing artefacts persist amongst the otherwise typical PN Hβ, [O III] $\lambda\lambda$4959, 5007 and Hα emission lines.

CTIO J174547.44-333932.4

CTIO J174547.44-333932.4 appears in imaging (figure 3.39) as an asymmetric, sinuous stream. An accompanying AAOmega spectrum (3 × 1200 s dark time exposure) of a bright segment is shown. Despite a stellar contaminant and [O I] $\lambda\lambda$5577, 6300 airglow artefacts, key PN emission lines are present including Hα, [N II] $\lambda\lambda$6548, 6583, [O III] λ5007, [S II] $\lambda\lambda$6716, 6731 and possible He I λ7065. Assumed artificial far blue and red reduction processing artefacts mar this spectrum. This object is assessed as probable PN.

CTIO J174756.67-331444.4

Imaging of faint, irregular, probable PN CTIO J174756.67-331444.4 is shown in figure 3.40. An associated AAOmega spectrum (3 × 1200 s dark time exposure), displaying characteristic PN emission lines of Hα, [N II] λ6583, [O III] $\lambda\lambda$4959, 5007 is supplied. Assumed miscellaneous far red and blue reduction processing artefacts are present, along with oversubtracted [O I] λ5577 airglow (truncated for clarity) and miscellaneous other features atypical for a PN, possibly noise.

CTIO J174925.72-344647.2

Faint probable PN is shown in Blanco on/off band, difference and UKST imaging in figure 3.41. An associated AAOmega spectrum (3 × 1200 s dark time exposure), in the same figure, suffers

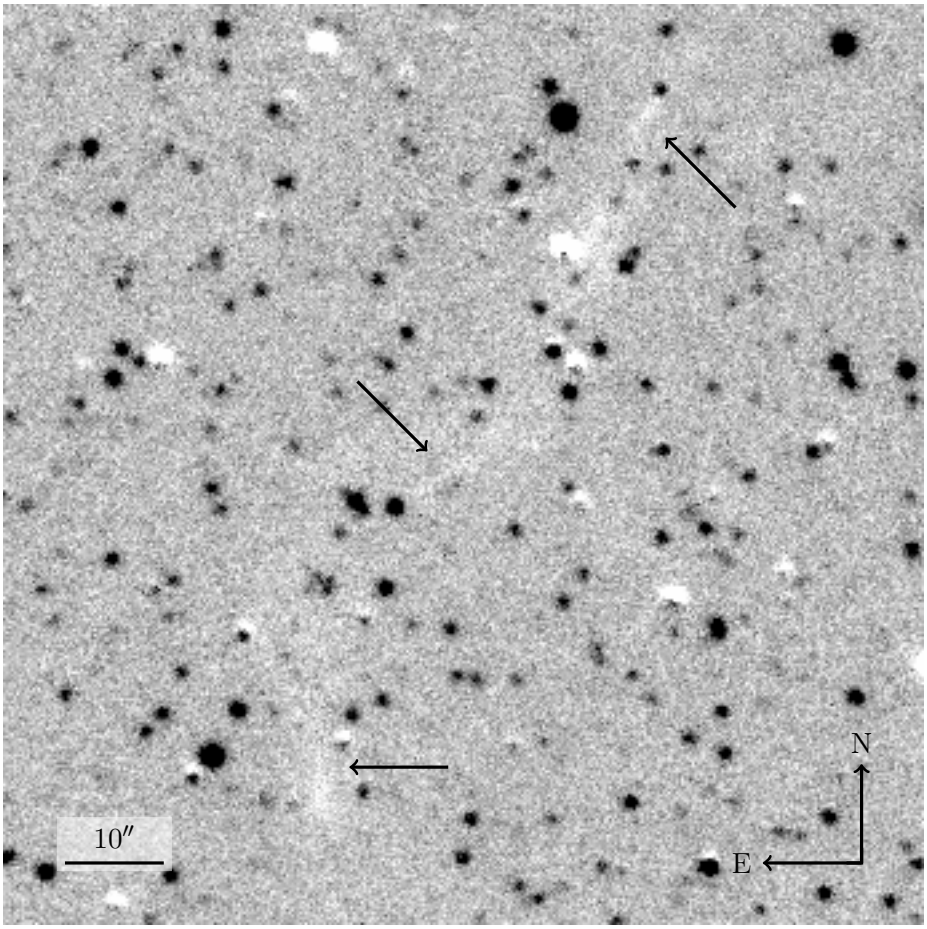

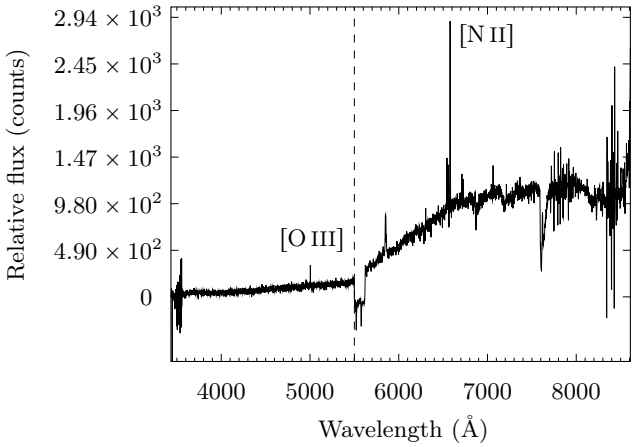

Figure 3.39: Top: Blanco difference image of probable PN CTIO J174547.44-333932.4. Arrows highlight this sinuous object's position. Left: AAOmega spectrum (3 × 1200 s dark time exposure). Despite a stellar contaminant, key PN emission lines are present, including [N II] λ6583 dominating Hα.

a stellar contaminant, minor [O I] $\lambda\lambda$6300, 6364 airglow processing artefacts and miscellaneous spurious reduction processing artefacts in both the far blue and far red. Despite these, several key PN emission lines are present. These include Hα, Hβ, [N II] $\lambda\lambda$6548, 6583, [O III] $\lambda\lambda$4956, 5007, [S II] $\lambda\lambda$6716, 6731 and probable [Ar III] $\lambda\lambda$7136, 7751 emission.

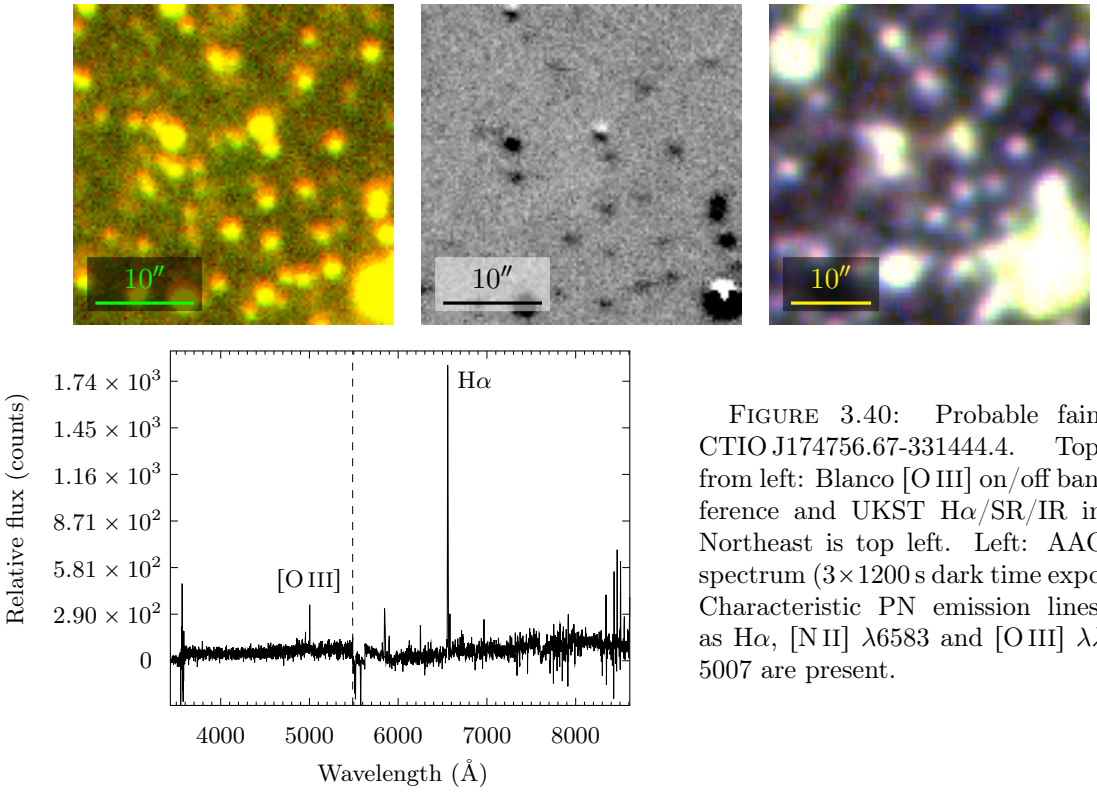

Figure 3.40: Probable faint PN CTIO J174756.67-331444.4. Top row, from left: Blanco [O III] on/off band, difference and UKST Hα/SR/IR images. Northeast is top left. Left: AAOmega spectrum (3×1200 s dark time exposure). Characteristic PN emission lines such as Hα, [N II] λ6583 and [O III] $\lambda\lambda$4959, 5007 are present.

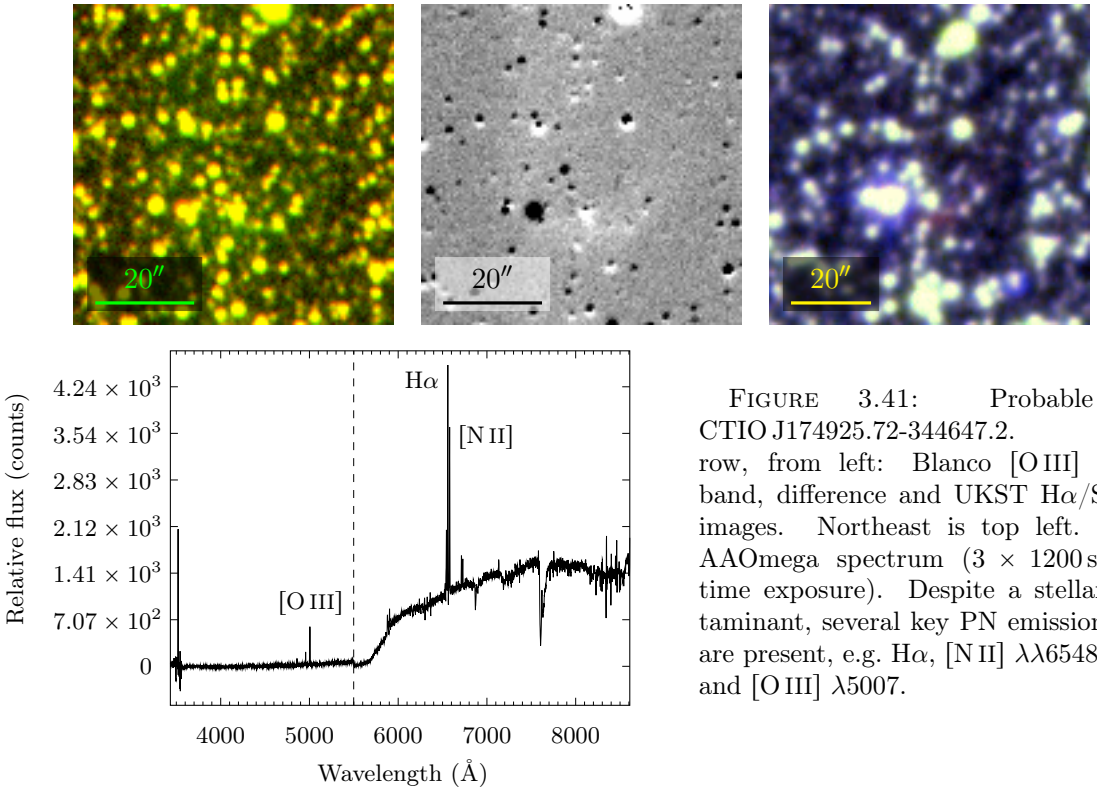

Figure 3.41: Probable PN CTIO J174925.72-344647.2. Top row, from left: Blanco [O III] on/off band, difference and UKST Hα/SR/IR images. Northeast is top left. Left: AAOmega spectrum (3 × 1200 s dark time exposure). Despite a stellar contaminant, several key PN emission lines are present, e.g. Hα, [N II] $\lambda\lambda$6548, 6583 and [O III] λ5007.

CTIO J175234.11-302619.6

A spectrum for putative probable PN CTIO J175234.11-302619.6 was taken with the Radcliffe 1.9 m telescope (900 s dark time, astronomical twilight exposure), as shown in figure 3.42. Despite being an astronomical twilight observation, this object is bright enough to yield [O III] $\lambda\lambda$4959, 5007 and Hα emission lines in its spectrum.

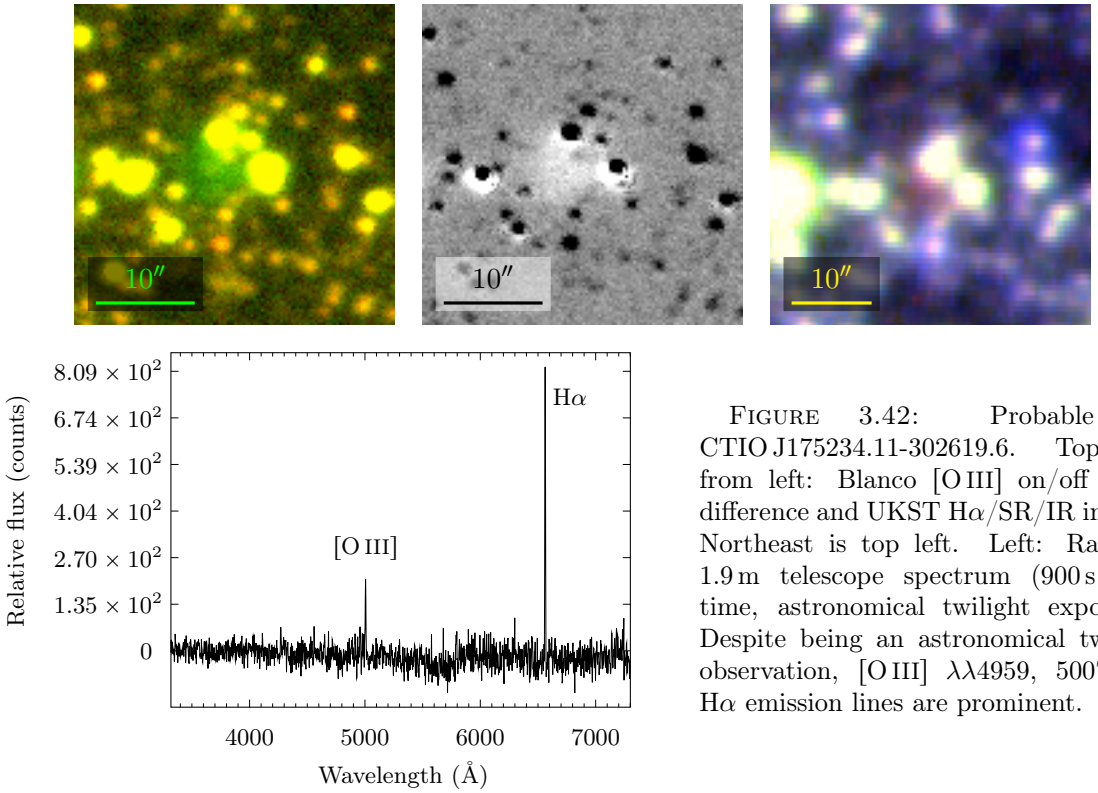

FIGURE 3.42: Probable PN CTIO J175234.11-302619.6. Top row, from left: Blanco [O III] on/off band, difference and UKST Hα/SR/IR images. Northeast is top left. Left: Radcliffe 1.9 m telescope spectrum (900 s dark time, astronomical twilight exposure). Despite being an astronomical twilight observation, [O III] $\lambda\lambda$4959, 5007 and Hα emission lines are prominent.

CTIO J175238.99-333047.2

CTIO J175238.99-333047.2 is a faint PN candidate showing rim-brightened features in Blanco difference imaging, as shown in figure 3.43. A corresponding AAOmega spectrum (3×1200 s dark time exposure), obtained from a fibre placed on the bright rim, is given in figure 3.43. The low S/N spectrum, though suffering miscellaneous processing artefacts (truncated for clarity) and [O I] $\lambda\lambda$5577, 6300 airglow artefacts, exhibits several characteristic PN emission lines. These include Hα, [N II] $\lambda\lambda$6548, 6563, [O III] $\lambda\lambda$4959, 5007 and [S II] λ6716. Possible He I λ5876 is present, though its large intensity in absence of any other helium lines is consistent with it simply being noise. The candidate's large apparent diameter $\approx(52.6'' \times 43.0'')$ suggests it is a foreground PN, not a bulge object. This candidate is assessed a probable, albeit faint PN, based on the imaging and morphological evidence available.

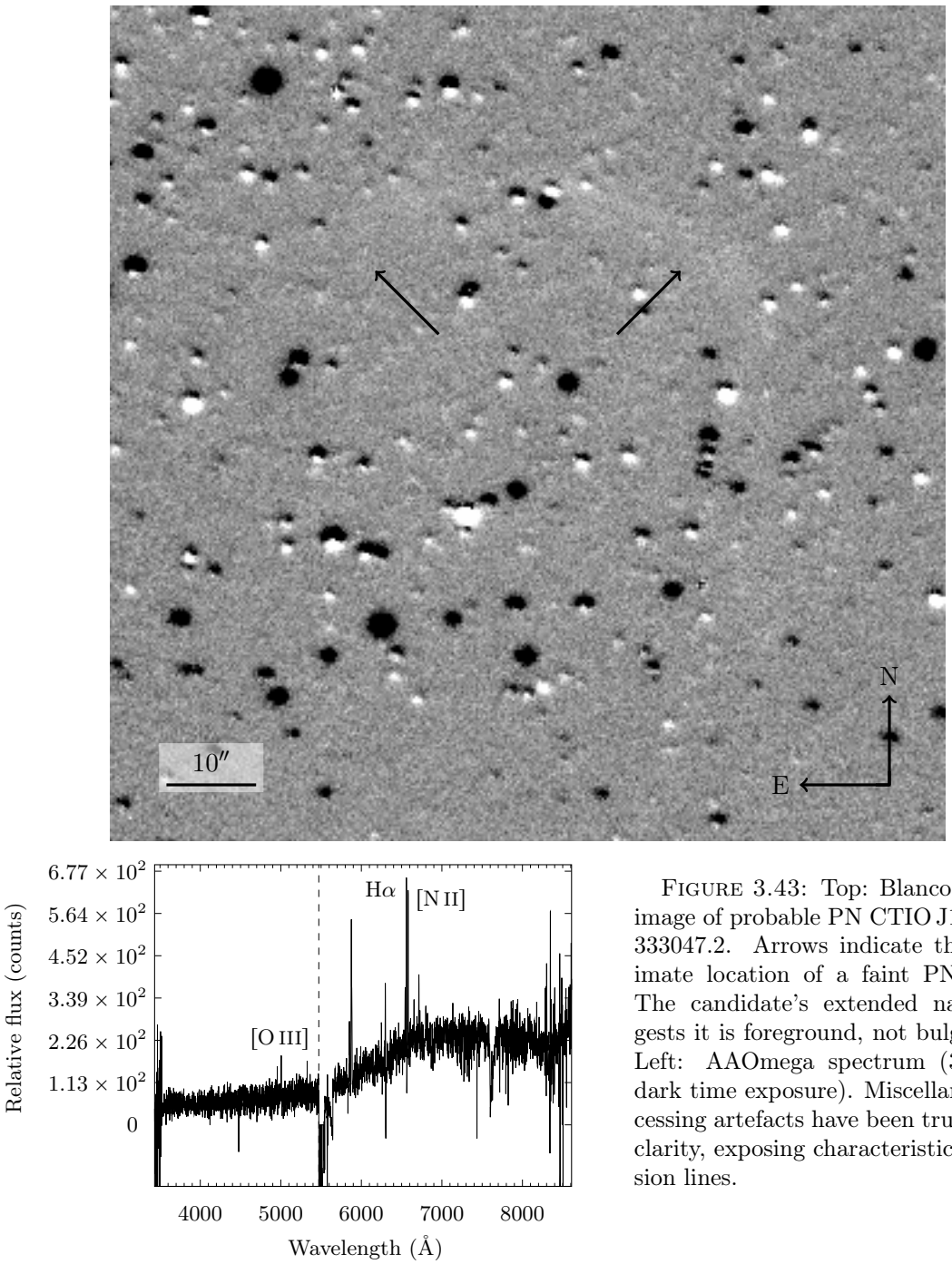

FIGURE 3.43: Top: Blanco difference image of probable PN CTIO J175238.99-333047.2. Arrows indicate the approximate location of a faint PN rim arc. The candidate's extended nature suggests it is foreground, not bulge, object. Left: AAOmega spectrum (3×1200 s dark time exposure). Miscellaneous processing artefacts have been truncated for clarity, exposing characteristic PN emission lines.

CTIO J175310.09-293108.6

CTIO J175310.09-293108.6, uniquely amongst the PN candidates observed here, is a suspected [WR] PN (as per §1.6). Blanco [O III] on/off band, difference and UKST imaging, and an AAOmega spectrum (3×1800 s grey time exposure) are given in figure 3.44. A suspected late-type stellar contaminant complicates the spectrum. Examination of VVV imaging supports the presence of a late-type stellar contaminant, potentially more than one, but deeper, higher

resolution imaging is needed to clarify the local environment.

The spectrum's many apparent emission lines in the far red are suspected reduction processing artefacts. Apart from these artefacts and assumed others due to [O I] $\lambda\lambda$5577, 6300 airglow, [O III] $\lambda\lambda$4959, 5007 emission is prominent. Other estimated emission includes N III λ4641 and broad C III $\lambda\lambda$4647/4650/4651, C IV $\lambda\lambda$5801/5812, C III $\lambda\lambda$6727/6731, C II $\lambda\lambda$7053/7064 and C II $\lambda\lambda$7116/7120 blends. Due to the preponderance of broad C features, and consistent with the formal [WR] PN classification scheme of Acker & Neiner (2003), this object probably belongs to the [WC] subclass. Consistent with CTIO J175310.09-293108.6 being a [WR] PN and thus a H-deficient object, there are no prominent Balmer series emission components.

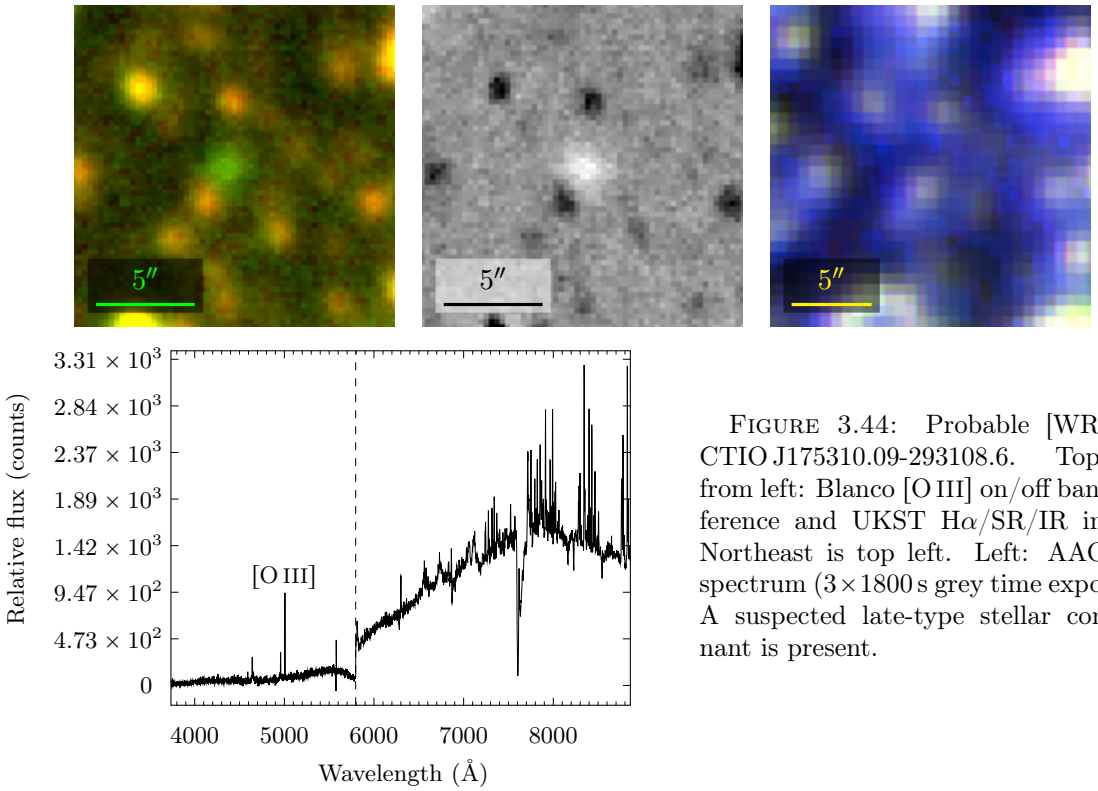

FIGURE 3.44: Probable [WR] PN, CTIO J175310.09-293108.6. Top row, from left: Blanco [O III] on/off band, difference and UKST Hα/SR/IR images. Northeast is top left. Left: AAOmega spectrum (3×1800 s grey time exposure). A suspected late-type stellar contaminant is present.

CTIO J175323.14-340653.7

Elliptical PN candidate CTIO J175323.14-340653.7 is shown in imaging in figure 3.45. An associated AAOmega spectrum (3 × 1200 s dark time exposure), given in the same figure, is marred by a modest stellar contaminant and to a lesser extent, an [O I] λ5577 airglow processing artefact. Despite this several key PN emission lines are present, including Hα, Hβ, [N II] $\lambda\lambda$6548, 6583, [O III] $\lambda\lambda$4959, 5007 and possible [Ar III] λ7136. CTIO J175323.14-340653.7 is assessed here a probable PN.

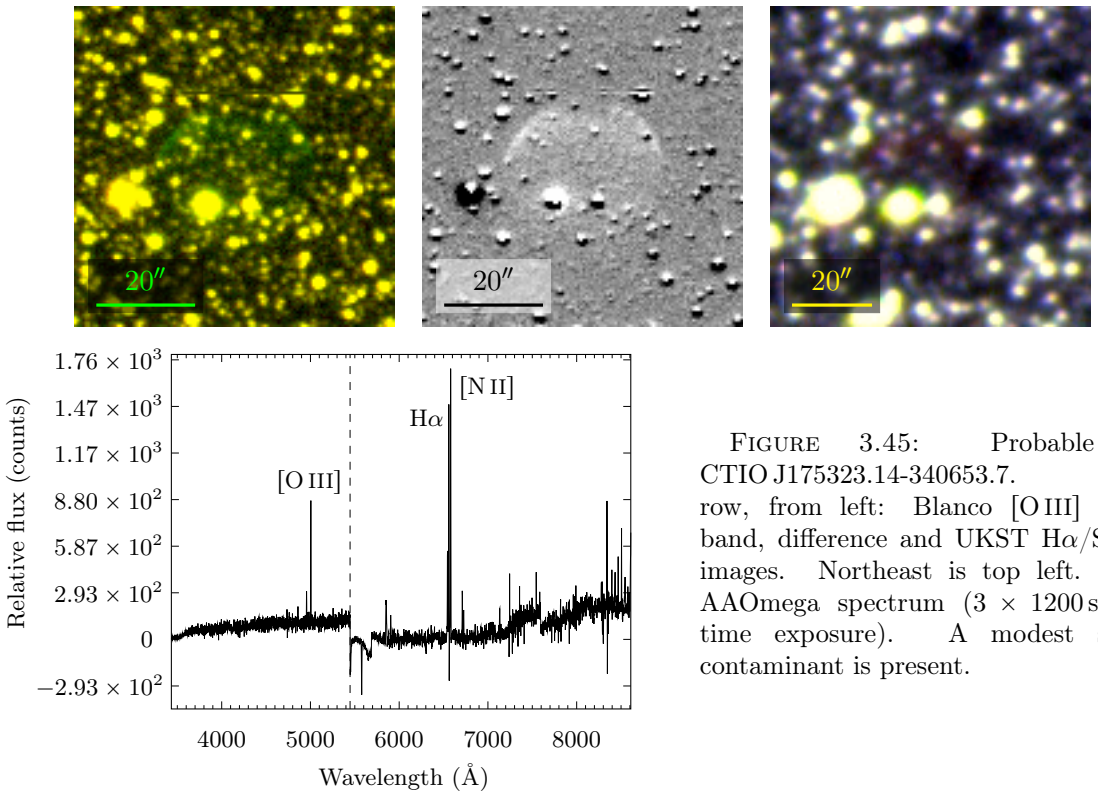

Figure 3.45: Probable PN CTIO J175323.14-340653.7. Top row, from left: Blanco [O III] on/off band, difference and UKST Hα/SR/IR images. Northeast is top left. Left: AAOmega spectrum (3 × 1200 s dark time exposure). A modest stellar contaminant is present.

CTIO J175401.23-343958.7

Morphologically, CTIO J175401.23-343958.7 appears to be a round PN. A Radcliffe 1.9 m telescope spectrum (1800 s dark time exposure), shown in figure 3.46 supports this contention, with signature PN [O III] $\lambda\lambda$4959, 5007 and Hα emission present. An [O I] λ5577 airglow processing artefact in the spectrum has been truncated for clarity.

CTIO J175417.64-292221.0

CTIO J175417.64-292221.0 is a probable irregular PN, probably undiscovered until now due to its faintness. Multiwavelength imaging and an AAOmega (3 × 1800 s grey time exposure) spectrum are shown in figure 3.47. The spectrum of this elongated PN suffers an inadvertent late-type stellar contaminant and an [O I] λ5577 airglow processing artefact. Emission lines present include at least [Ar III] λ7136, Hα, Hβ, [N II] $\lambda\lambda$6548, 6583, [O III] $\lambda\lambda$4959, 5007 and [S II] $\lambda\lambda$6716, 6731.

CTIO J175442.23-300836.1

CTIO J175442.23-300836.1 is a probable PN, probably undiscovered until now due to its faintness. Blanco [O III] on/off band, difference and UKST Hα/SR/IR imaging and a corresponding AAOmega (3 × 1800 s grey time exposure) spectrum are shown in figure 3.48. The spectrum hosts a modest late-type stellar contaminant and an [O I] λ5577 airglow processing

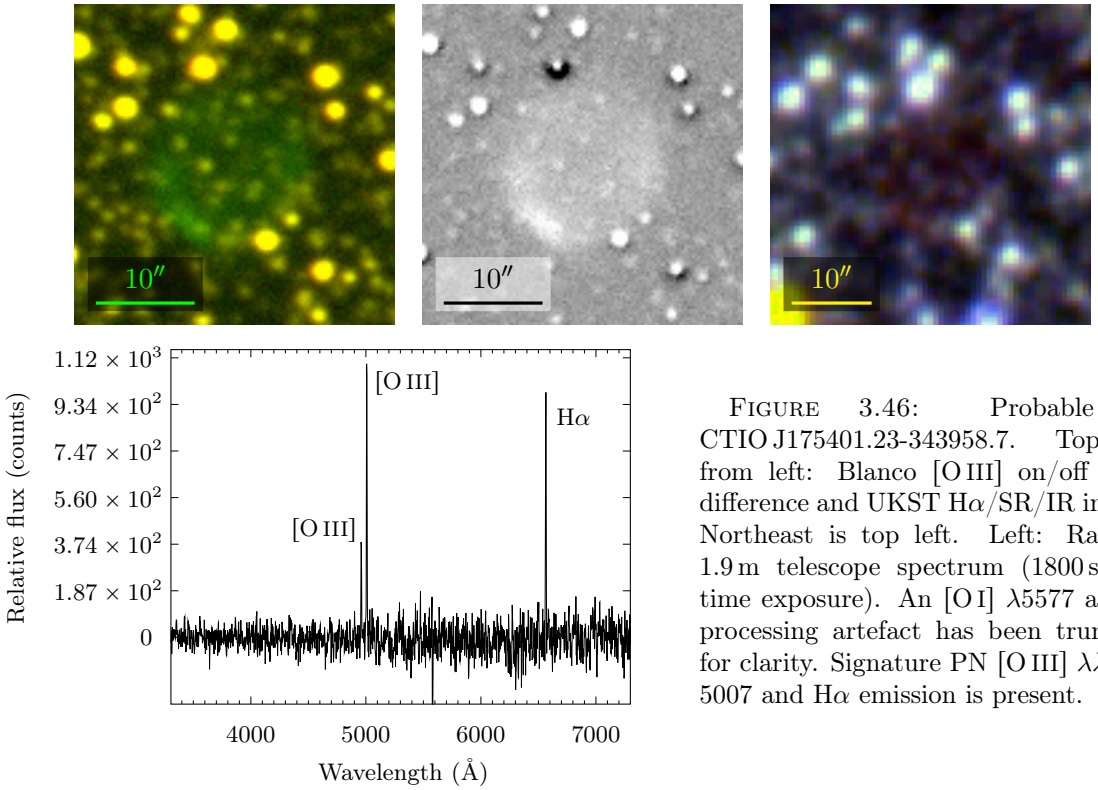

FIGURE 3.46: Probable PN CTIO J175401.23-343958.7. Top row, from left: Blanco [O III] on/off band, difference and UKST Hα/SR/IR images. Northeast is top left. Left: Radcliffe 1.9 m telescope spectrum (1800 s dark time exposure). An [O I] λ5577 airglow processing artefact has been truncated for clarity. Signature PN [O III] $\lambda\lambda$4959, 5007 and Hα emission is present.

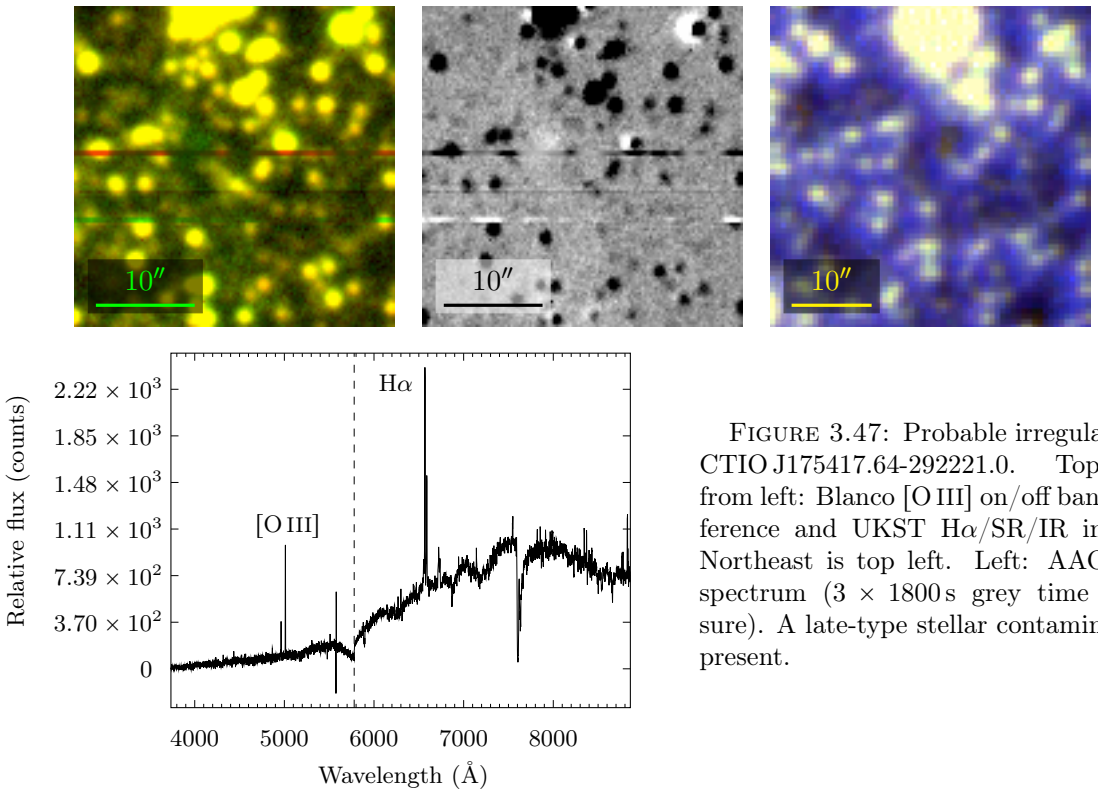

FIGURE 3.47: Probable irregular PN, CTIO J175417.64-292221.0. Top row, from left: Blanco [O III] on/off band, difference and UKST Hα/SR/IR images. Northeast is top left. Left: AAOmega spectrum (3 × 1800 s grey time exposure). A late-type stellar contaminant is present.

artefact which has been truncated for clarity. Putative PN emission lines present include at least Hα, Hβ, [N II] $\lambda\lambda$6548, 6583, [O III] $\lambda\lambda$4959, 5007 and [S II] $\lambda\lambda$6716, 6731.

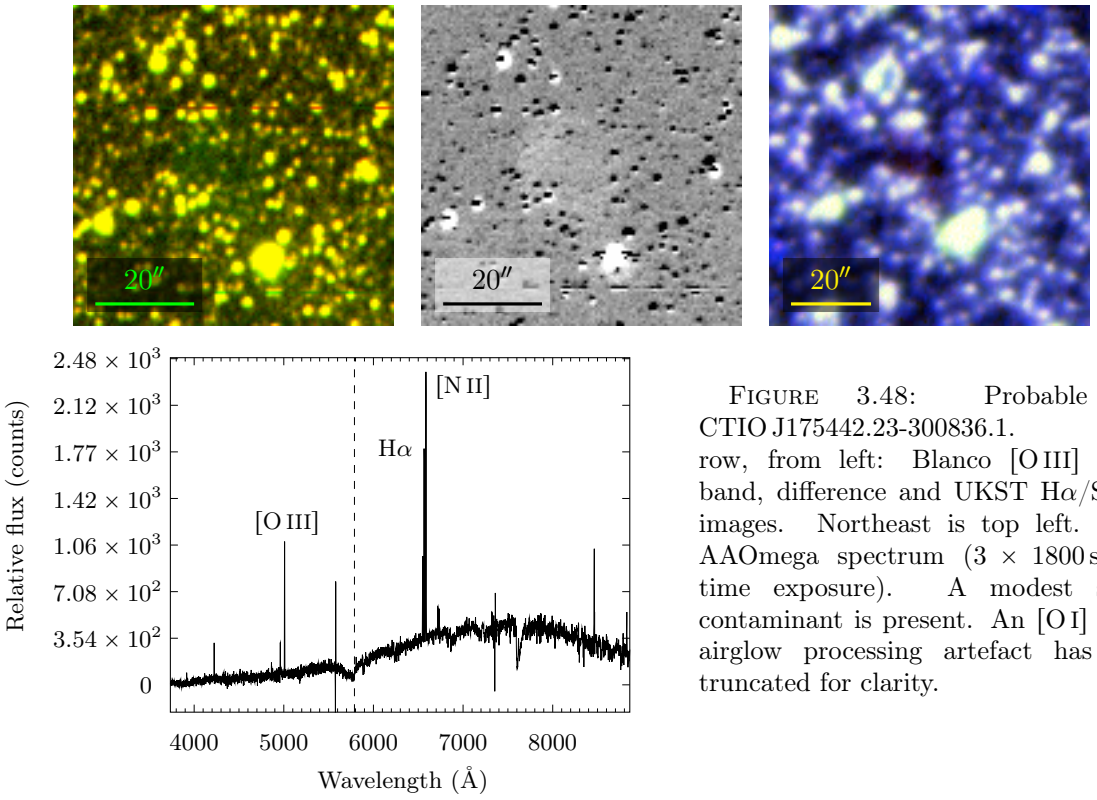

Figure 3.48: Probable PN, CTIO J175442.23-300836.1. Top row, from left: Blanco [O III] on/off band, difference and UKST Hα/SR/IR images. Northeast is top left. Left: AAOmega spectrum (3 × 1800 s grey time exposure). A modest stellar contaminant is present. An [O I] λ5577 airglow processing artefact has been truncated for clarity.

CTIO J175444.26-290744.2

Probable PN CTIO J175444.26-290744.2, faint in Blanco imaging and imperceptible in UKST imaging (figure 3.49), appears manifest as either an asymmetric nebula or a brightened rim arc of a large ($r \sim 24''$), very faint round or elliptical nebula. A corresponding AAOmega spectrum (3 × 1800 s grey time exposure) is given in figure 3.49, but is of low S/N and marred by multiple stellar contaminants. Superimposed on these contaminants are [O I] $\lambda\lambda$5577, 6300 airglow processing artefacts, but also key PN emission lines including Hα, [N II] $\lambda\lambda$6548, 6583, [O III] $\lambda\lambda$4959, 5007 and probable [S II] $\lambda\lambda$6716, 6731. An additional HERMES spectrum (1200 s dark time exposure) taken at high airmass ($Z \approx 2.3$) also shows probable, but faint (S/N < 2), Hα and [N II] λ6583 emission.

CTIO J175606.37-290733.7

Imaging of CTIO J175606.37-290733.7, shown in figure 3.50, is consistent with a classic round, rim-brightened PN. A corresponding Radcliffe 1.9 m telescope spectrum (1800 s dark time, night time exposure, running (1167 ± 30) s into astronomical twilight), suffers an [O I] λ5577 airglow processing artefact, but is also consistent with a PN. [O III] $\lambda\lambda$4959, 5007 and Hα

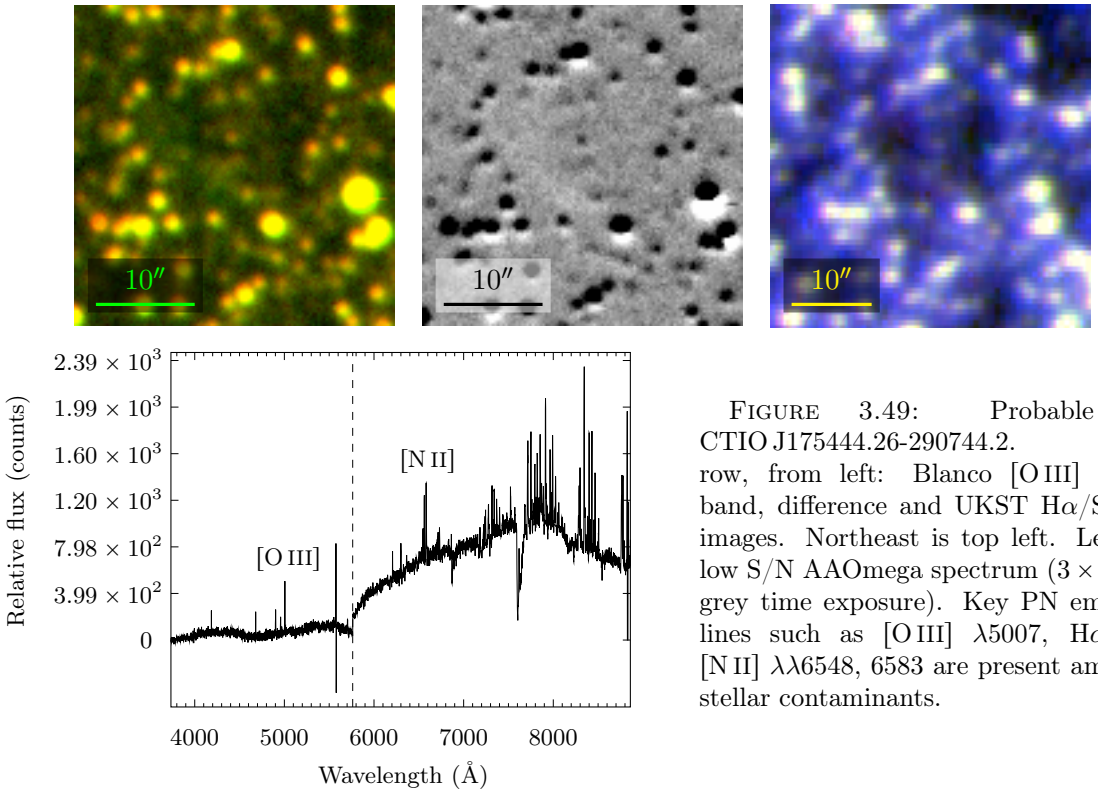

FIGURE 3.49: Probable PN CTIO J175444.26-290744.2. Top row, from left: Blanco [O III] on/off band, difference and UKST Hα/SR/IR images. Northeast is top left. Left: A low S/N AAOmega spectrum (3×1800 s grey time exposure). Key PN emission lines such as [O III] λ5007, Hα and [N II] $\lambda\lambda$6548, 6583 are present amongst stellar contaminants.

emission are all present. An additional HERMES spectrum, taken at high airmass ($Z \approx 2.3$), is also given in figure 3.50. Blueshifted Hα is present in the spectrum.

CTIO J175800.70-285401.9

PN candidate CTIO J175800.70-285401.9 appears as a compact knot in Blanco imaging, shown in figure 3.51. An AAOmega spectrum (3×1200 s grey time exposure) for the object suffers a significant airglow [O I] λ5577 artefact and at least one stellar contaminant. Amongst the contaminants, the PN emission lines manifest include [O III] λ5007, Hα and possible He II λ4686. An unexplained, unusual, intense λ5805 artefact is present, possibly due to a cosmic. A complementary HERMES spectrum (1200 s dark time exposure) exhibits possible very faint (S/N << 2) Hα emission, but no other features, including no recurrence of a λ5805 artefact.

CTIO J175851.48-291559.8

An AAOmega spectrum (3×1200 s grey time exposure), taken at the geometric centre of this object, is given along with imaging in figure 3.52. The spectrum is probably contaminated by at least two separate coincident stars. Despite this stellar spectrum contamination and airglow [O I] $\lambda\lambda$5577, 6300 processing artefacts, PN emission lines can be discerned. These include [Ar III] λ7136, Hα, Hβ, [N II] λ6583 and [O III] $\lambda\lambda$4959, 5007. A HERMES spectrum (1200 s dark time exposure) confirms Hα and [N II] λ6583 emission.

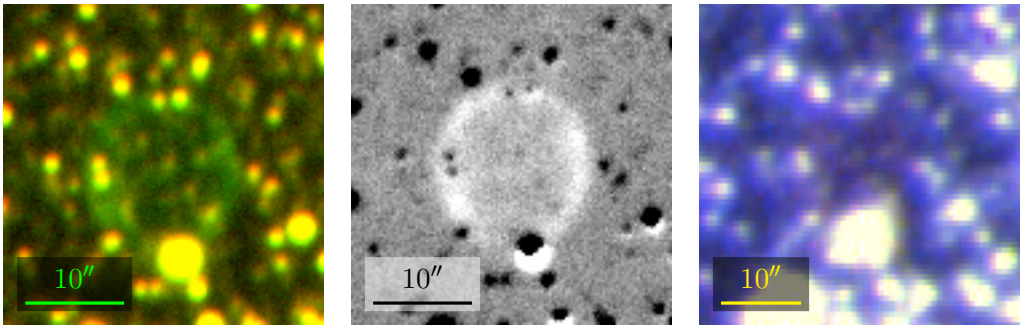

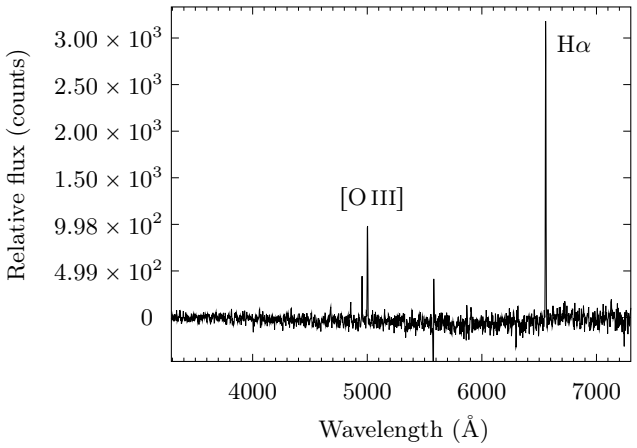

Figure 3.50: Probable, round PN CTIO J175606.37-290733.7. Top row, from left: Blanco [O III] on/off band, difference and UKST Hα/SR/IR images. Northeast is top left. Left: Radcliffe 1.9 m telescope spectrum (1800 s dark time, night time and astronomical twilight exposure). An [O I] λ5577 airglow processing artefact has been truncated for clarity. Right: HERMES red channel spectrum (1200 s dark time exposure) at high airmass ($Z \approx 2.3$). Hα emission is present.

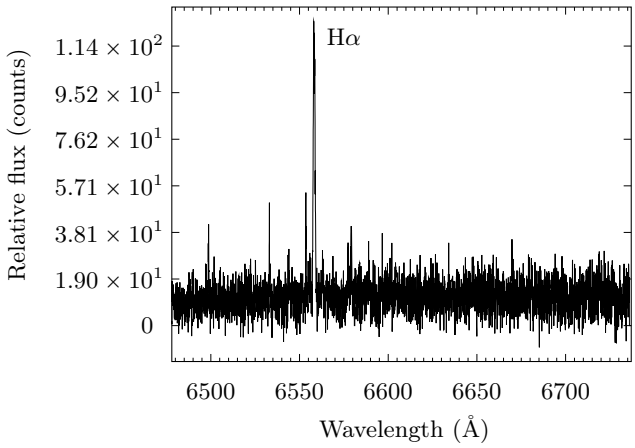

CTIO J175857.26-284902.5

Compact PN candidate CTIO J175857.26-284902.5 is visible in both Blanco and UKST imaging, given in figure 3.53. An AAOmega spectrum (3 × 1200 s grey time exposure), given in the same figure is marred by [O I] λλ5577, 6300 airglow and a suspected faint late-type stellar contaminant. Many emission lines are present in the spectrum however, including at least Hα, Hβ, He I λλ5876, 6678, 7065, [N II] λλ6548, 6583, [O III] λλ4959, 5007 and [S II] λλ6716, 6731. A complementary high airmass ($Z \approx 2.3$) HERMES spectrum (1200 s dark time exposure), shown in the same figure, confirms at least Hα and [N II] λ6583. On the basis of imaging and spectroscopic evidence, CTIO J175857.26-284902.5 is assessed a probable PN.

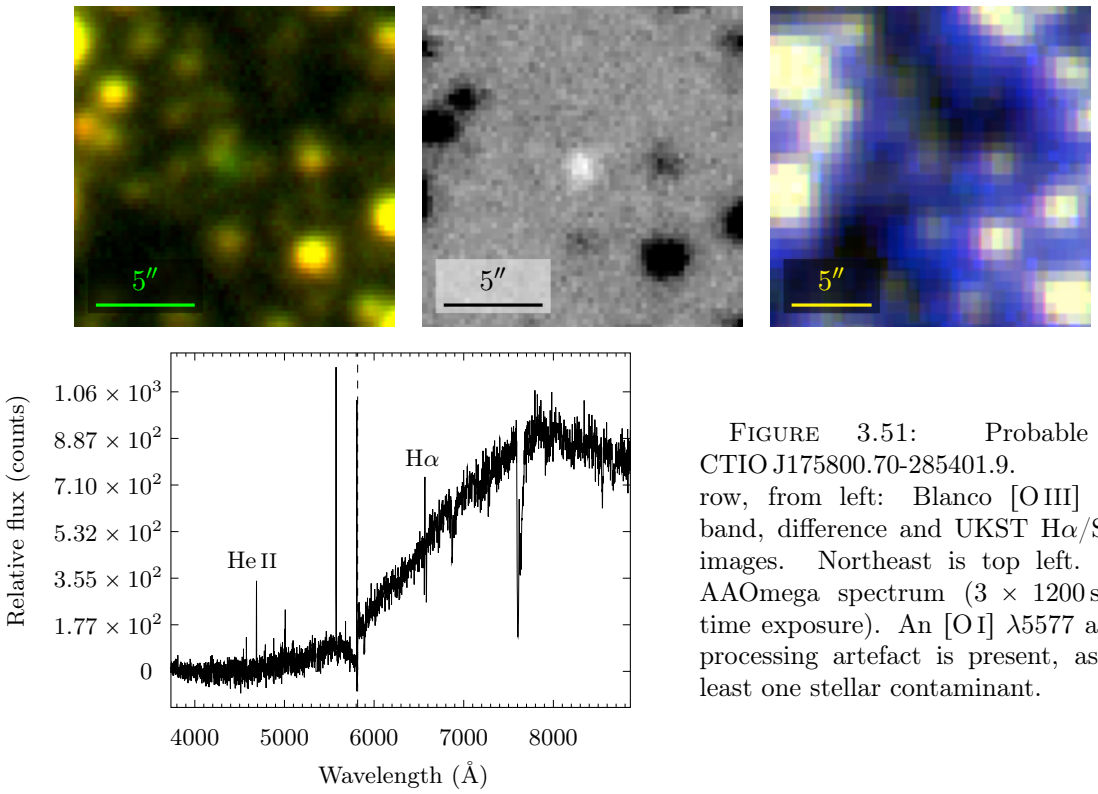

FIGURE 3.51: Probable PN, CTIO J175800.70-285401.9. Top row, from left: Blanco [O III] on/off band, difference and UKST Hα/SR/IR images. Northeast is top left. Left: AAOmega spectrum (3 × 1200 s grey time exposure). An [O I] λ5577 airglow processing artefact is present, as is at least one stellar contaminant.

CTIO J180021.99-274607.7

Imaging and spectra for CTIO J180021.99-274607.7 are given in figure 3.54. An AAOmega spectrum (3 × 1200 s grey time exposure) spectrum is consistent with a PN, but suffers an [O I] λ5577 airglow processing artefact and unwanted stellar contamination due to suboptimal fibre positioning. Nonetheless, many PN emission lines are present in the spectrum, including [Ar III] λ7136, [Ar V] λ7006, Hα, Hβ, He II λ4686 and [O III] $\lambda\lambda$4959, 5007. A low S/N HERMES spectrum (1200 s dark time exposure), contains mostly spurious artefacts (see §3.3.2), but amongst these probable Hα emission.

CTIO J180150.14-275526.4

PN candidate CTIO J180150.14-275526.4 features a rich emission line spectrum, as shown in figure 3.55. An AAOmega spectrum (3 × 1200 s grey time exposure) displays, aside from an [O I] λ5577 airglow processing artefact, [Ar III] λ7136, Hα, Hβ, He II λ4686, [N II] $\lambda\lambda$6548, 6583, [O III] $\lambda\lambda$4959, 5007 and [S II] λ6716. An undesired stellar contribution, from a faint star visible in Blanco imaging, contaminates that spectrum.

A supplementary, albeit low S/N, HERMES spectrum (1200 s dark time exposure) is also given in figure 3.55. Putative bona fide Hα, Hβ and [N II] λ6583 emission are present, supporting CTIO J180150.14-275526.4's PN candidature.

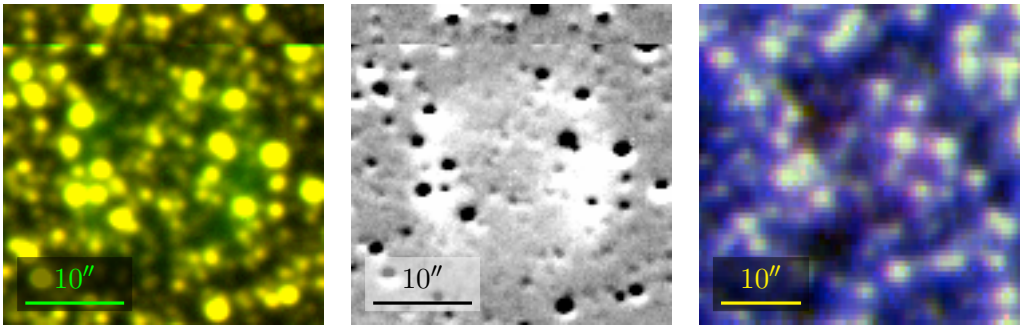

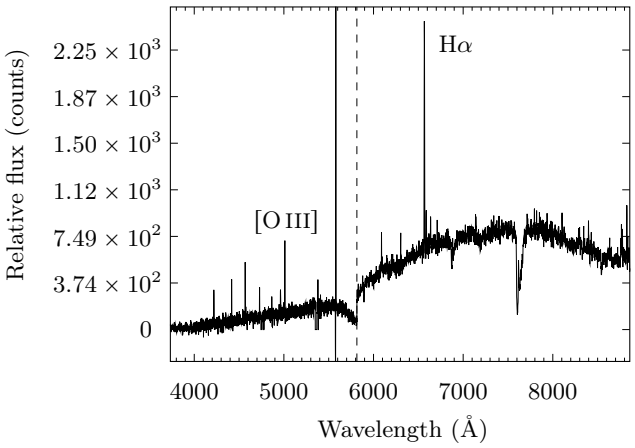

Figure 3.52: Probable PN, CTIO J175851.48-291559.8. Top row, from left: Blanco [O III] on/off band, difference and UKST Hα/SR/IR images. Northeast is top left. Left: AAOmega spectrum (3 × 1200 s grey time exposure). An [O I] λ5577 airglow processing artefact has been truncated for clarity. Multiple stellar contaminants are present but don't mask PN emission such as [O III] λ5007. Right: CTIO J175851.48-291559.8 HERMES red channel spectrum (1200 s dark time exposure) at high airmass ($Z \approx 2.3$). Hα and [N II] λ6583 emission are present.

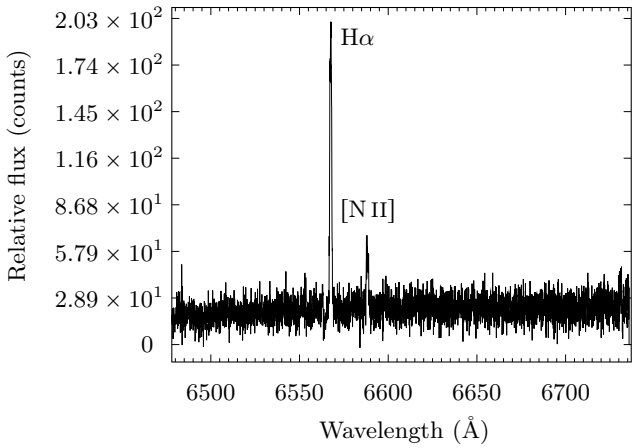

CTIO J180204.70-280340.5

PN candidate CTIO J180204.70-280340.5, shown in figure 3.56, has a morphology consistent with a round, rim-brightened PN. AAOmega spectroscopy (3 × 1200 s grey time exposure), taken at the centre of the candidate, exhibited [N II] λ6583 and possible faint [O III] λ5007. The spectrum was of low S/N however, as might be expected for the faint central region of the PN, and was marred by contributions from coincident stellar sources. An acknowledged low S/N HERMES spectrum (1200 s dark time exposure) of the brighter rim is given in the same figure. Hα and [N II] λ6583 emission are present, supporting this object's PN candidature.

Deeper AAOmega spectroscopy (4 × 1200 s dark time exposure) centred on the brighter rim

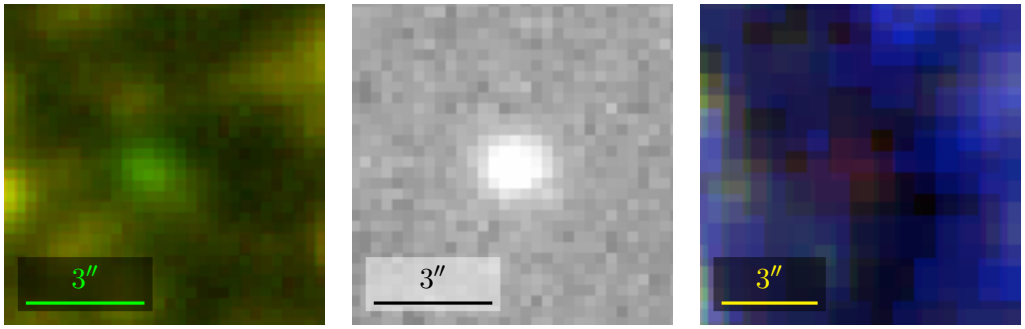

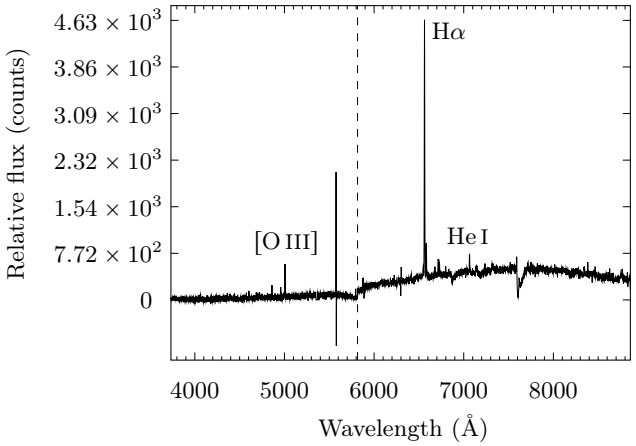

FIGURE 3.53: Probable PN CTIO J175857.26-284902.5. Top row, from left: Blanco [O III] on/off band, difference and UKST Hα/SR/IR images. Northeast is top left. Left: AAOmega spectrum (3 × 1200 s grey time exposure). A suspected late-type stellar contaminant is present. Right: CTIO J175857.26-284902.5 HERMES red channel spectrum (1200 s dark time exposure) at high airmass ($Z \approx 2.3$). Some apparent emission lines are likely spurious (see §3.3.2) but genuine nebula Hα and [N II] λ6583 emission are present.

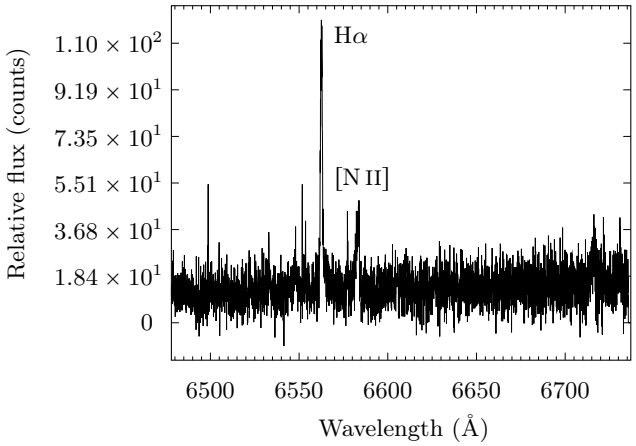

yielded signature PN emission features. These features include Hα, Hβ, [N II] $\lambda\lambda$6548, 6583, [O III] $\lambda\lambda$4959, 5007 and possible [Ar III] λ7136 and [S II] $\lambda\lambda$6716, 6731. Spectrum artefacts include the typical [O I] λ5577 airglow processing artefact and two features at $\lambda\sim$3460 Å thought to be less intense equivalents of those seen, for example, in figure 5.13, data for which was derived from the same 2dF field.

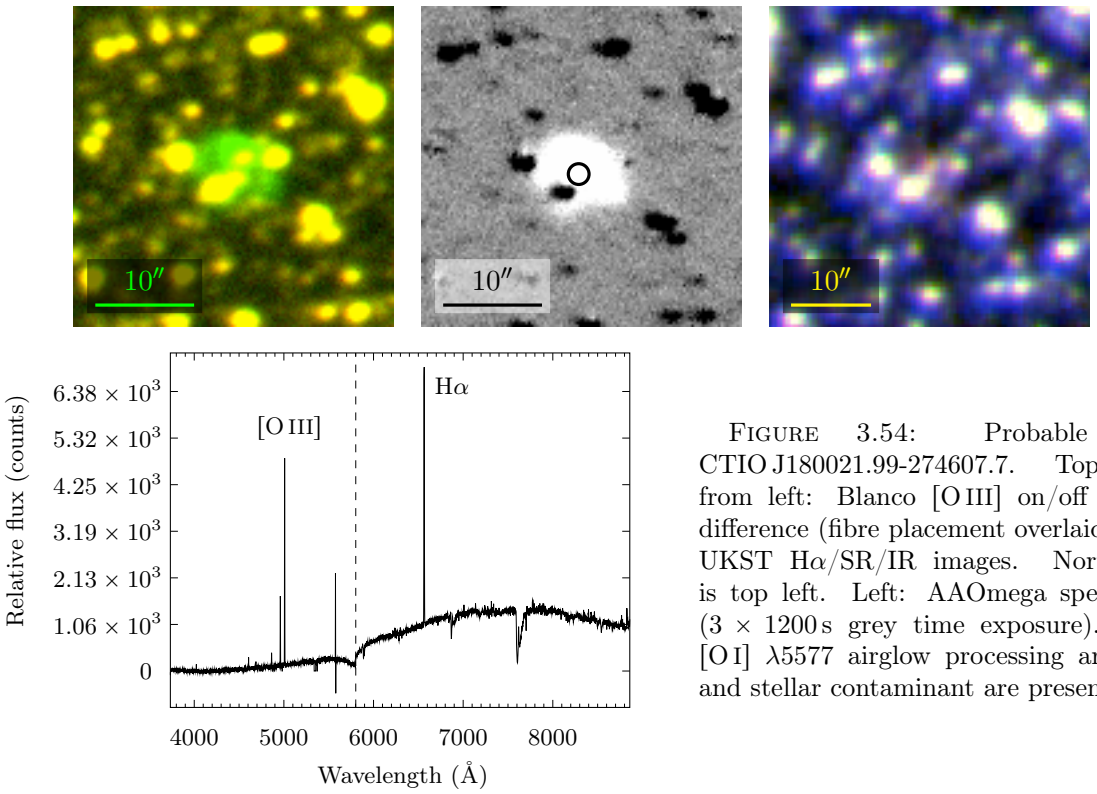

Figure 3.54: Probable PN, CTIO J180021.99-274607.7. Top row, from left: Blanco [O III] on/off band, difference (fibre placement overlaid) and UKST Hα/SR/IR images. Northeast is top left. Left: AAOmega spectrum (3×1200 s grey time exposure). An [O I] λ5577 airglow processing artefact and stellar contaminant are present. Right: CTIO J180021.99-274607.7 HERMES red channel spectrum (1200 s dark time exposure). A spurious apparent feature of this high airmass ($Z \approx 2.3$) observation has been truncated for clarity. Hα emission is present.

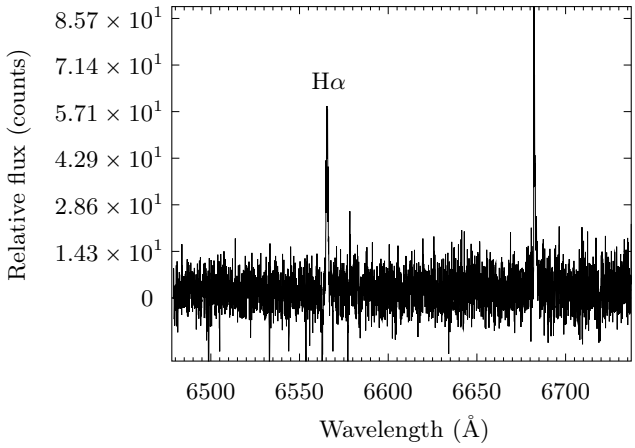

CTIO J180235.03-310555.9

A low S/N spectrum of putative round PN, CTIO J180235.03-310555.9, taken with the Radcliffe 1.9 m telescope (2100 s dark time exposure), is shown in figure 3.57. The object's spectrum exhibits [O III] λ5007, Hα and [N II] λ6583 emission. Deeper spectroscopy is recommended for a definitive evaluation of this candidate.

CTIO J180253.79-280755.6

PN candidate CTIO J180253.79-280755.6 is visible, albeit faintly, in both Blanco and UKST imaging, given in figure 3.58. The candidate exhibits a classic round, rim-brightened PN

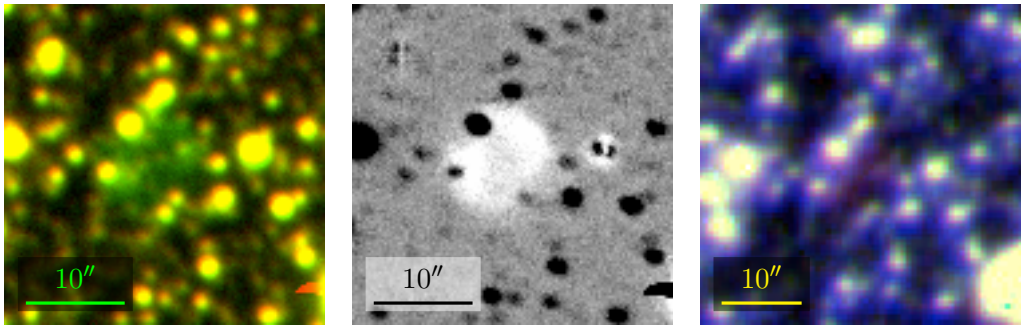

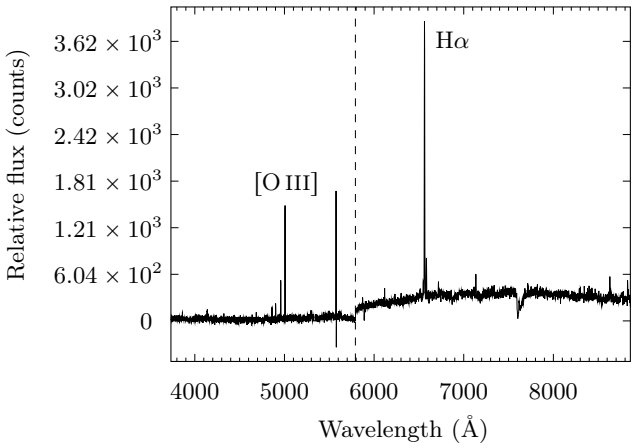

FIGURE 3.55: Probable PN, CTIO J180150.14-275526.4. Top row, from left: Blanco [O III] on/off band, difference and UKST Hα/SR/IR images. Northeast is top left. Left: AAOmega spectrum (3 × 1200 s grey time exposure). An [O I] λ5577 airglow processing artefact and modest stellar contaminant are present.

Right: Low S/N CTIO J180150.14-275526.4 HERMES red channel spectrum (1200 s dark time exposure). Despite being a high airmass ($Z \approx 2.3$) observation, genuine Hα and [N II] λ6583 emission are manifest.

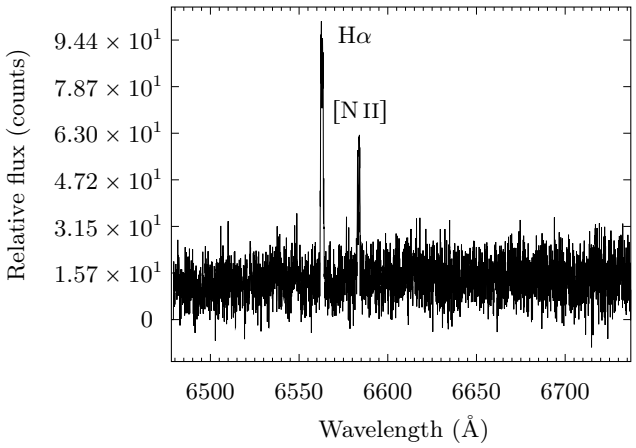

morphology. An AAOmega spectrum (3 × 1200 s grey time exposure) taken at the centre of the candidate is shown in 3.58. Undesired stellar continuum, thought to be from up to three closely coincident stars, complicates the spectrum. A significant [O I] λ5577 airglow processing artefact has been captured too. Despite the contaminated spectrum, key PN diagnostic lines including faint [O III] λ5007 and more prominent Hα and [N II] λ6583 are present. Based on spectroscopic and especially morphological grounds, CTIO J180253.79-280755.6 is assessed a probable PN. Reobservation of this probable PN is recommended however, better avoiding coincident stars and targeting a bright rim segment to maximise S/N.

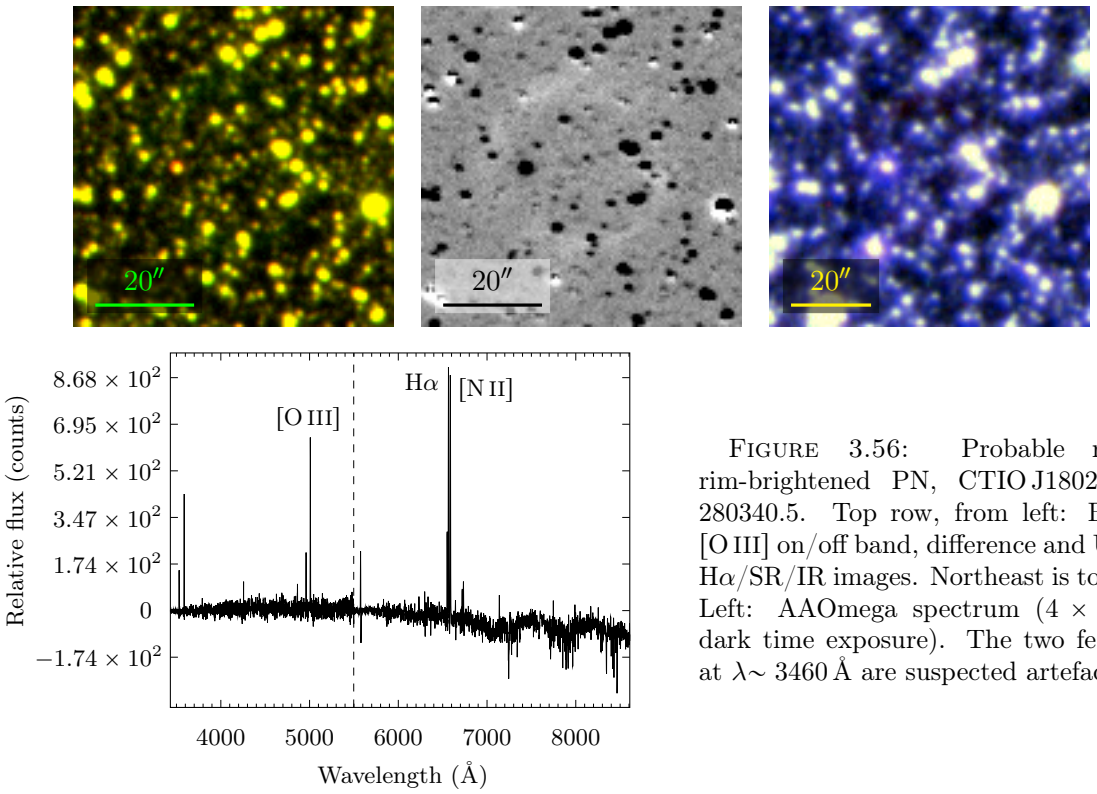

Figure 3.56: Probable round, rim-brightened PN, CTIO J180204.70-280340.5. Top row, from left: Blanco [O III] on/off band, difference and UKST Hα/SR/IR images. Northeast is top left. Left: AAOmega spectrum (4 × 1200 s dark time exposure). The two features at $\lambda\sim$ 3460 Å are suspected artefacts. Right: Low S/N CTIO J180204.70-280340.5 HERMES red channel spectrum (1200 s dark time exposure). Some apparent features of this high airmass ($Z \approx 2.3$) observation are likely spurious (see §3.3.2) and some have been truncated for clarity. Bona fide Hα and [N II] λ6583 emission are however present.

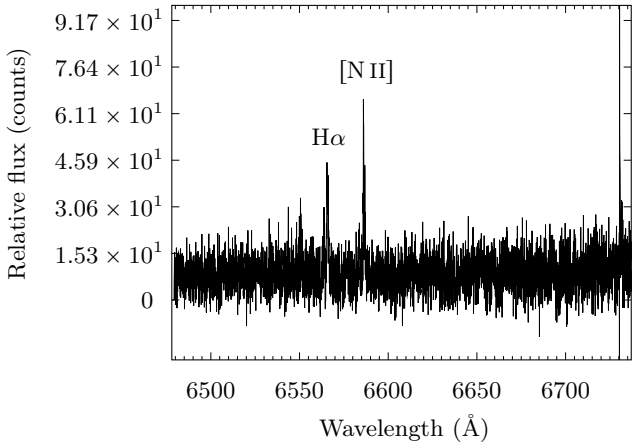

CTIO J180413.75-281602.2

The PN candidate CTIO J180413.75-281602.2 is in close apparent proximity to known PN, PN G002.6-03.1 (Parker et al., 2006). Imaging and an AAOmega spectrum (3 × 1200 s grey time exposure) for CTIO J180413.75-281602.2 is given in figure 3.59. Careful examination of the figure shows the candidate is coincident with at least two stars and that undesired stellar spectral contribution has been captured. Undesired [O I] λλ5577, 6300 airglow emission has been captured too. PN emission lines are however present, including [Ar III] λ7136, Hα, Hβ, He II λ4686, [N II] λλ6548, 6583, [O III] λλ4959, 5007 and [S II] λλ6716, 6731.

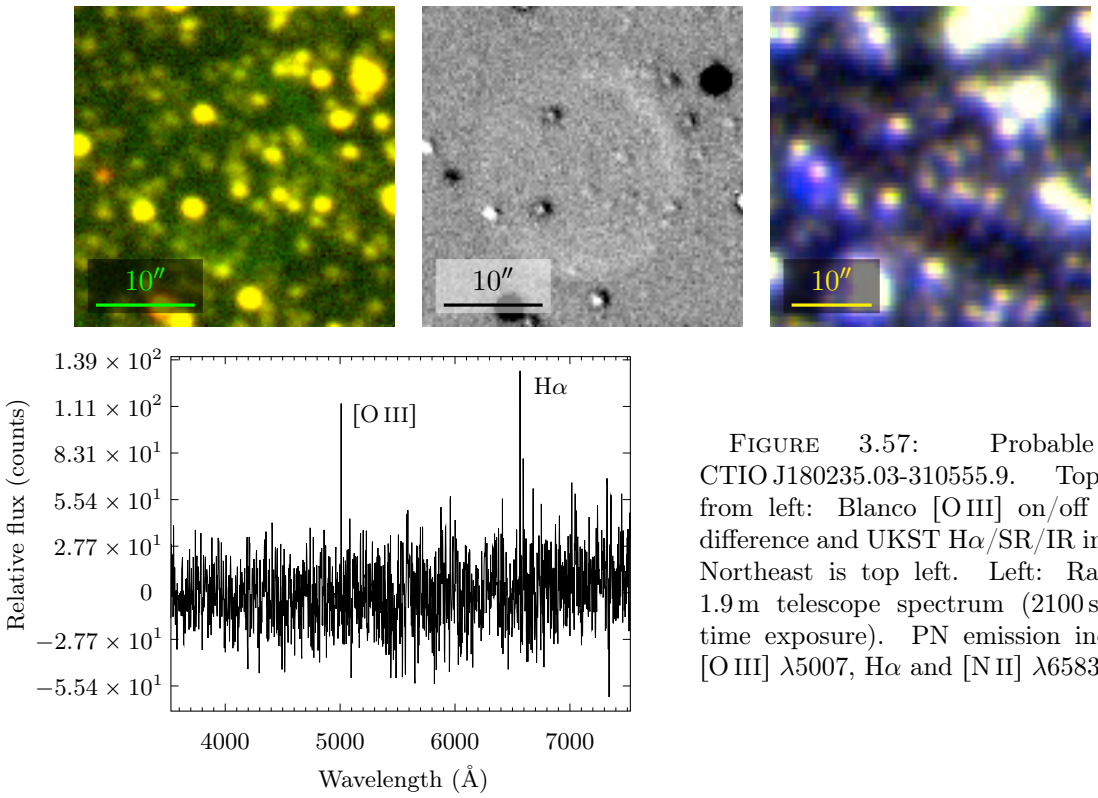

FIGURE 3.57: Probable PN CTIO J180235.03-310555.9. Top row, from left: Blanco [O III] on/off band, difference and UKST Hα/SR/IR images. Northeast is top left. Left: Radcliffe 1.9 m telescope spectrum (2100 s dark time exposure). PN emission includes [O III] λ5007, Hα and [N II] λ6583 lines.

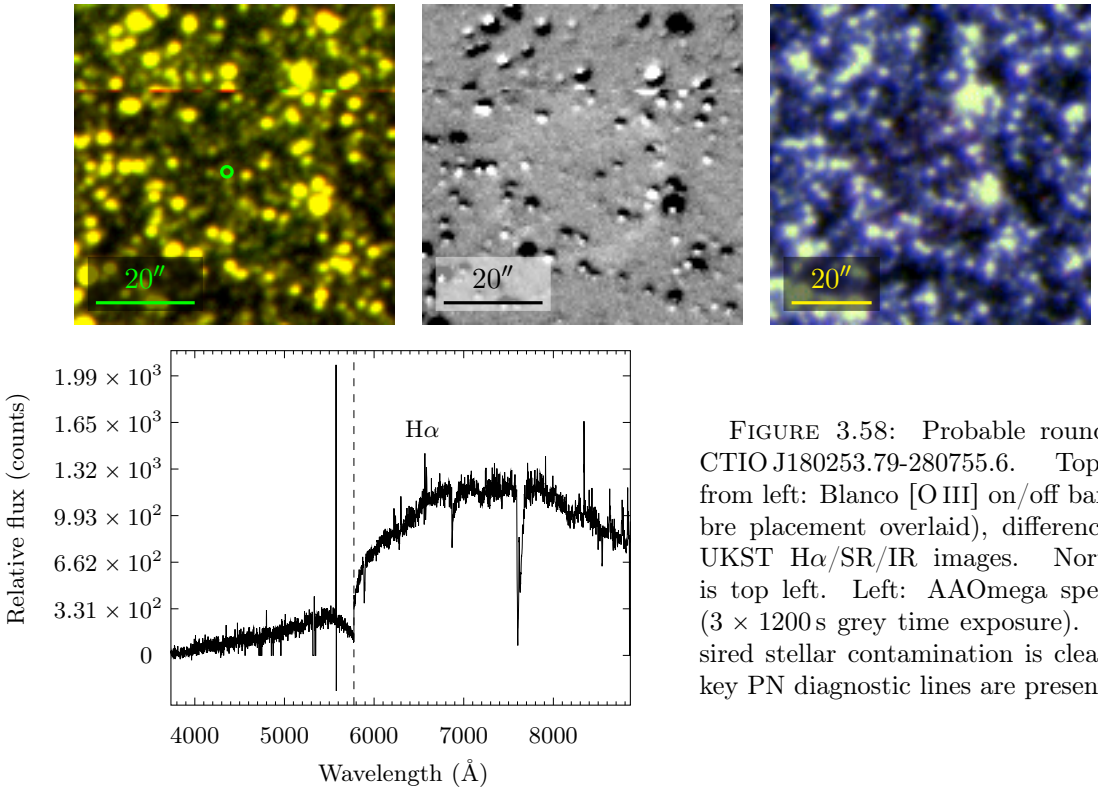

FIGURE 3.58: Probable round PN, CTIO J180253.79-280755.6. Top row, from left: Blanco [O III] on/off band (fibre placement overlaid), difference and UKST Hα/SR/IR images. Northeast is top left. Left: AAOmega spectrum (3 × 1200 s grey time exposure). Undesired stellar contamination is clear, but key PN diagnostic lines are present.

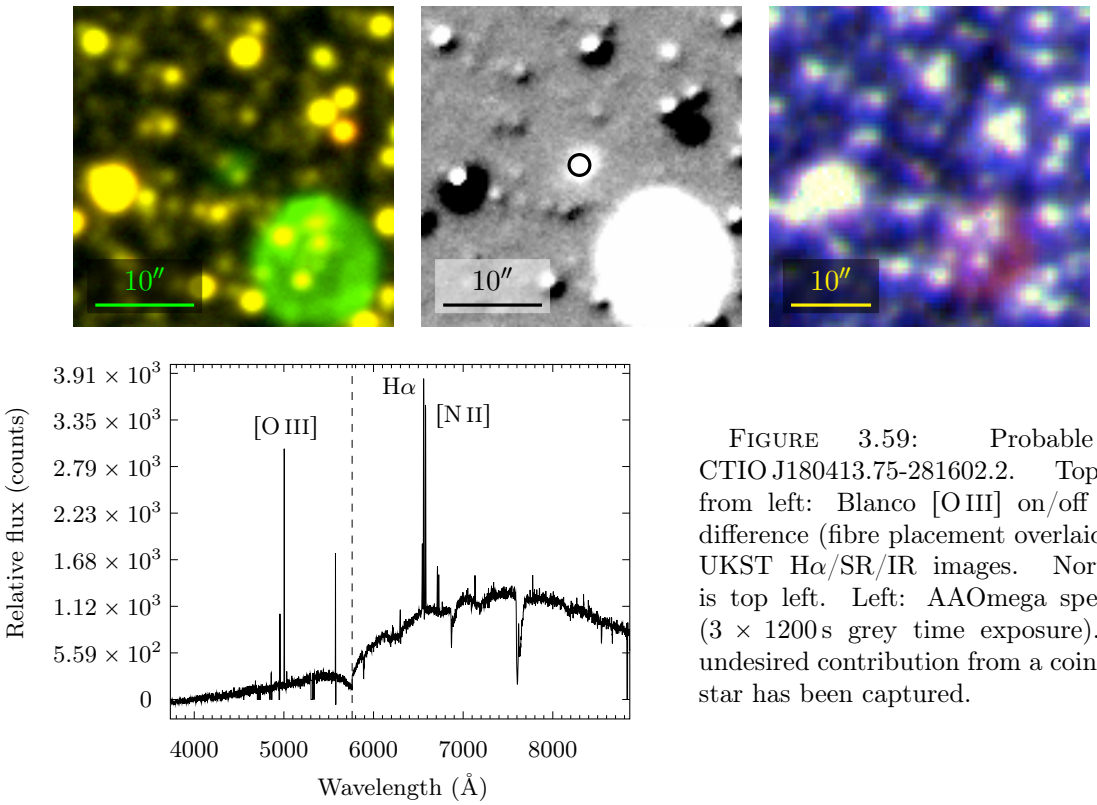

FIGURE 3.59: Probable PN CTIO J180413.75-281602.2. Top row, from left: Blanco [O III] on/off band, difference (fibre placement overlaid) and UKST Hα/SR/IR images. Northeast is top left. Left: AAOmega spectrum (3 × 1200 s grey time exposure). An undesired contribution from a coincident star has been captured.

The apparent proximity of CTIO J180413.75-281602.2 to PN G002.6-03.1 raises the possibility that it is not an independent PN, but some type of small extension of PN G002.6-03.1. In support of this idea, both objects exhibit, very approximately, the same intensity whether viewed in Blanco or UKST imaging. Contravening this idea however, is that no symmetrical second small nebula or extension appears on the opposite side of PN G002.6-03.1.

Three MASH spectra of PN G002.6-03.1 span the wavelength domain (6260–6820) Å. Of these, a FLAIR II (Fibre-Linked Array-Image Reformatter, Watson et al., 1993, Morgan & Parker, 1998) and Six-degree Field (6dF, Watson et al., 1998) spectrum have $(F_{6548} + F_{6583})/F_{\mathrm{H}\alpha} < 0.1$, conflicting with the spectrum obtained here, but one (FLAIR II) spectrum has $(F_{6548}+F_{6583})/F_{\mathrm{H}\alpha}\sim1.2$, consistent with it. Furthermore, an additional MASH (FLAIR II, low dispersion mode) spectrum capturing [O III] $\lambda\lambda$4959, 5007 emission of PN G002.6-03.1 suffers such significant stellar contamination as to render a comparison with the spectrum obtained here unreliable, but a correlation is nonetheless not obvious. For the purposes of determining whether CTIO J180413.75-281602.2 is an independent PN, this comparison of AAOmega spectroscopy with legacy MASH spectra is deemed inconclusive.

CTIO J180413.75-281602.2 is assessed as a probable compact PN, with a confirmatory radial velocity comparison with PN G002.6-03.1 recommended.

CTIO J180701.33-264550.2

Probable PN CTIO J180701.33-264550.2, the second largest apparent diameter ≈(60.7″ × 58.8″) object discovered in this investigation, is shown in figure 3.60. A 2.3 m ATT WiFeS blue arm spectrum for this candidate (1800 s dark time exposure) exhibits probable [O III] $\lambda\lambda$5007, 4959, Hβ, Hγ and He II λ4686 emission.

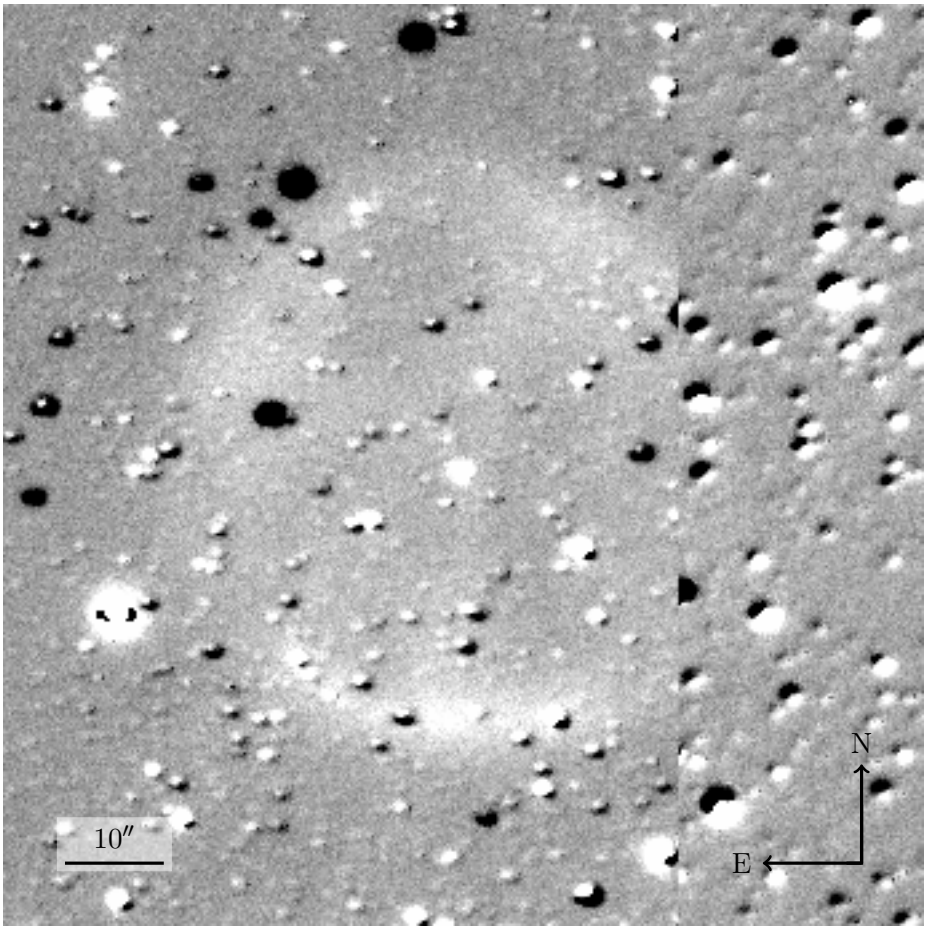

Figure 3.60: Blanco difference image of probable PN CTIO J180701.33-264550.2. The imperfect joining of imaging from adjacent CCDs within the Mosaic II system somewhat truncates one edge of the nebula. The candidate's extended nature is consistent with it being a foreground, rather than bulge, object.

CTIO J181244.61-281033.3

The faintness and crowded field of probable PN, CTIO J181244.61-281033.3, makes its true spatial extent and apparent centre difficult to determine accurately. An associated spectrum, taken with the Radcliffe 1.9 m telescope (2160 s dark time exposure), is shown in figure 3.61. Aside from a [O I] λ5577 artefact, this spectrum shows clear [O III] λ5007, Hα, [N II] λ6583 and [S II] λ6717 emission. The broad red feature is assumed to be a poorly subtracted

contribution from a late-type star in the crowded field.

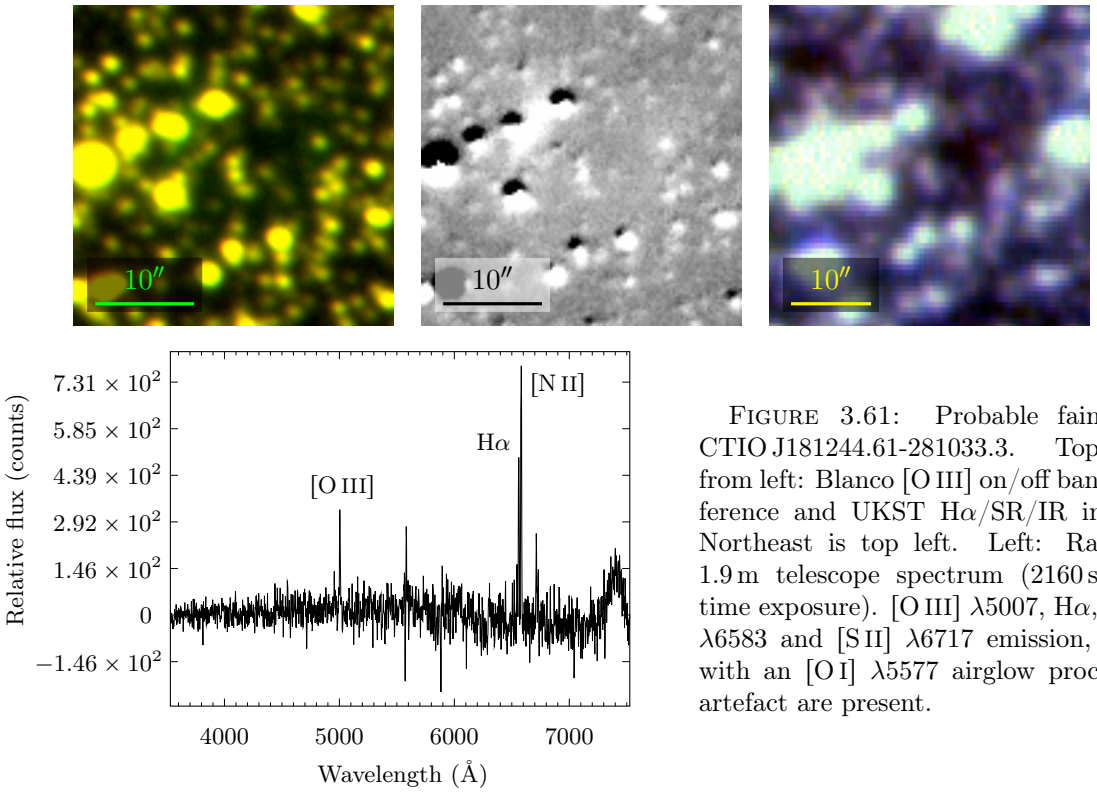

Figure 3.61: Probable faint PN CTIO J181244.61-281033.3. Top row, from left: Blanco [O III] on/off band, difference and UKST Hα/SR/IR images. Northeast is top left. Left: Radcliffe 1.9 m telescope spectrum (2160 s dark time exposure). [O III] λ5007, Hα, [N II] λ6583 and [S II] λ6717 emission, along with an [O I] λ5577 airglow processing artefact are present.

3.4.3 Possible PNs

Candidates rated as possible PNs are presented here. The quality of these candidates varies considerably. Some objects are visible in multiwavelength imaging, or exhibit morphologies very consistent with known nebula forms, for which follow up spectroscopy is recommended. Conversely, a disparate array of apparent objects likely to be mimics or miscellaneous image artefacts, but which are nonetheless possible PNs, also appear.

CTIO J171813.83-302357.0

Possible PN or image artefact CTIO J171813.83-302357.0 is shown in figure 3.62.

CTIO J171856.81-310641.5

Possible round PN or image artefact CTIO J171856.81-310641.5 is shown in figure 3.63.

CTIO J172616.29-293451.2

Possible PN CTIO J172616.29-293451.2, shown in figure 3.64, displays putative [O III] λ5007 and, more obviously, Hα emission.

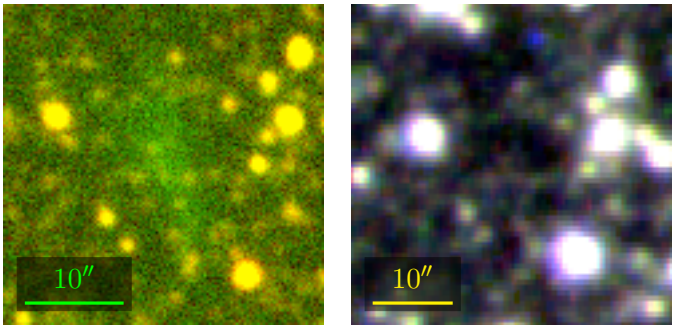

Figure 3.62: Possible PN or image artefact, CTIO J171813.83-302357.0. From left: Blanco [O III] on/off band and UKST Hα/SR/IR images. Northeast is top left.

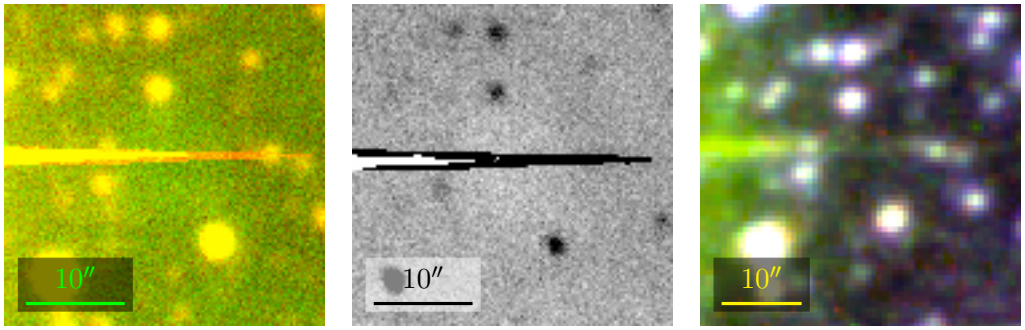

Figure 3.63: Possible round PN or image artefact, CTIO J171856.81-310641.5. From left: Blanco [O III] on/off band, difference and UKST Hα/SR/IR images. Northeast is top left.

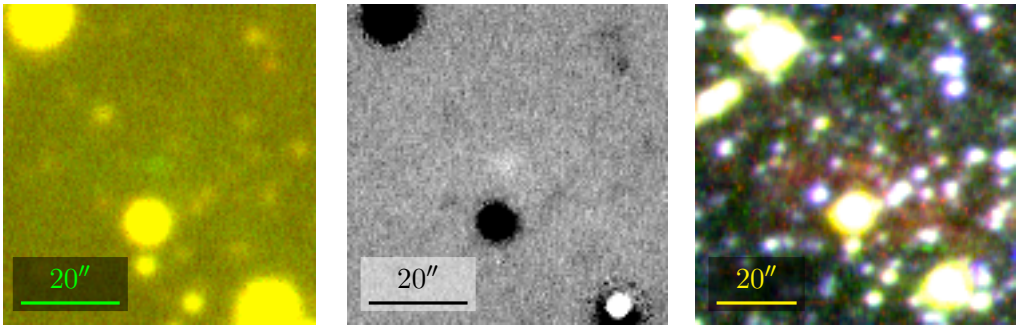

Figure 3.64: Possible PN, CTIO J172616.29-293451.2. From left: Blanco [O III] on/off band, difference and UKST Hα/SR/IR images. A nebula is discernible in each image. Northeast is top left.

CTIO J172954.51-271918.7

Possible PN or mimic, CTIO J172954.51-271918.7, is shown in figure 3.65. This candidate is slightly green in the Blanco [O III] on/off band image, but could have been missed were it not for its prominence in associated difference imaging. Combined with its absence from UKST Hα/SR/IR imaging, this candidate is probably a compact PN, early-type emission line star, or other mimic.

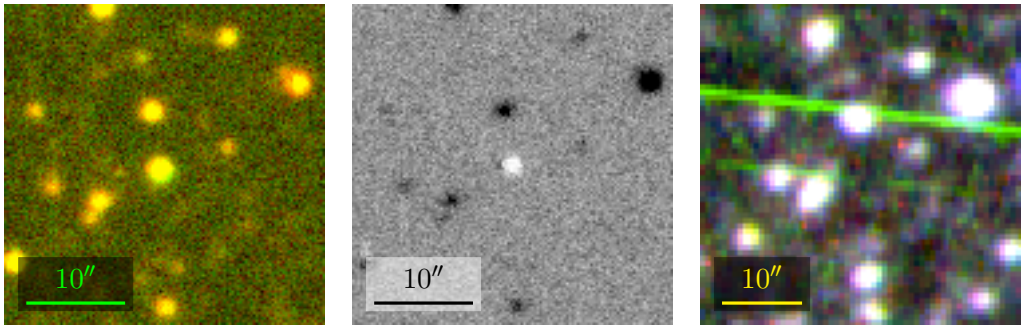

Figure 3.65: Possible PN or mimic, CTIO J172954.51-271918.7. From left: Blanco [O III] on/off band, difference and UKST Hα/SR/IR images. Northeast is top left. Despite having an almost stellar appearance in Blanco [O III] on/off band imaging, the candidate is distinct in difference imaging and absent from the UKST Hα/SR/IR. An aircraft trail or similar artefact mars the rightmost image.

CTIO J173241.47-302829.4

Possible round PN CTIO J173241.47-302829.4 is shown in figure 3.66. The classic round nebula morphology and multiwavelength emission characteristics exhibited make this a strong PN candidate.

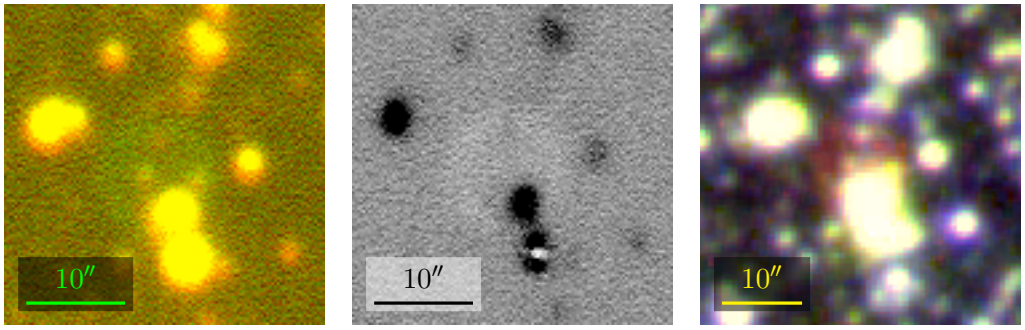

Figure 3.66: Possible round PN, CTIO J173241.47-302829.4. From left: Blanco [O III] on/off band, difference and UKST Hα/SR/IR images. Northeast is top left.

CTIO J173247.88-300932.4

Possible PN CTIO J173247.88-300932.4 is shown in figure 3.67.

CTIO J173425.71-270524.7

Possible faint PN CTIO J173425.71-270524.7 is shown in figure 3.68.

CTIO J173440.23-272356.8

A spectrum for this faint PN candidate was obtained with the Radcliffe 1.9 m telescope (1800 s dark time exposure) and is shown in figure 3.69. A low S/N spectrum confirmed Hα emission. Deeper spectroscopy is recommended for a definitive evaluation of this candidate.

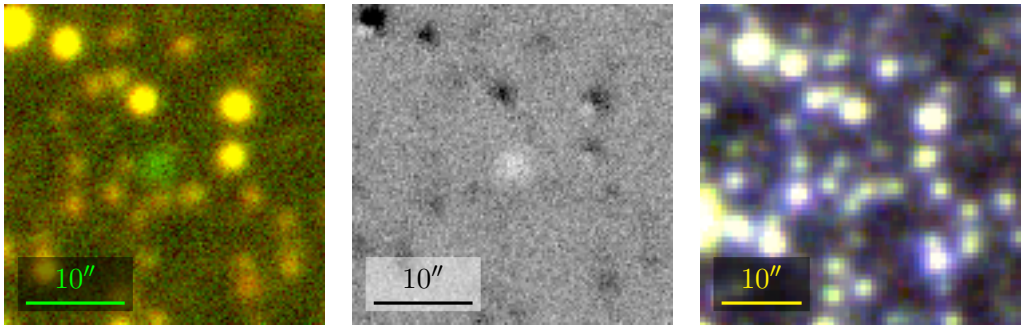

FIGURE 3.67: Possible PN, CTIO J173247.88-300932.4. From left: Blanco [O III] on/off band, difference and UKST Hα/SR/IR images. Northeast is top left.

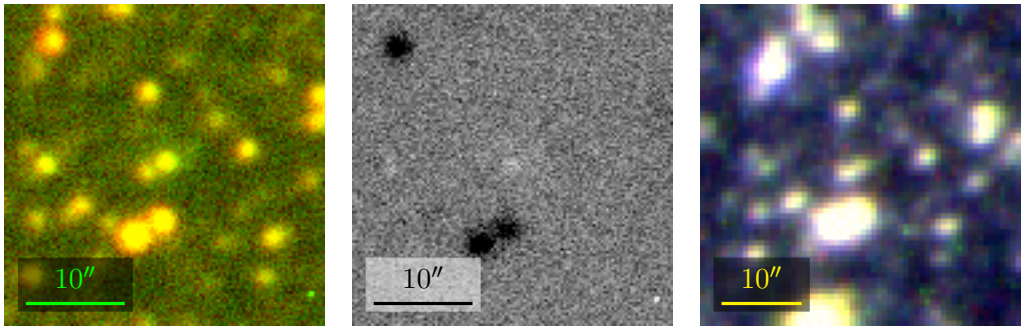

FIGURE 3.68: Possible faint PN, CTIO J173425.71-270524.7. From left: Blanco [O III] on/off band, difference and UKST Hα/SR/IR images. Northeast is top left.

CTIO J173513.37-263254.0

Possible faint PN CTIO J173513.37-263254.0 is shown in figure 3.70.

CTIO J173751.75-250309.2

Possible PN CTIO J173751.75-250309.2 is shown in figure 3.71.

CTIO J173949.95-332524.4

A spectrum of CTIO J173949.95-332524.4 taken with the Radcliffe 1.9 m telescope (1800 s dark time exposure), is shown in figure 3.72. This spectrum shows clear Hα emission. Deeper spectroscopy is recommended however to recover the [O III] λ5007 emission visible in Blanco imaging.

CTIO J173958.08-270647.1

Possible bright, compact PN or mimic CTIO J173958.08-270647.1 is shown in figure 3.73.

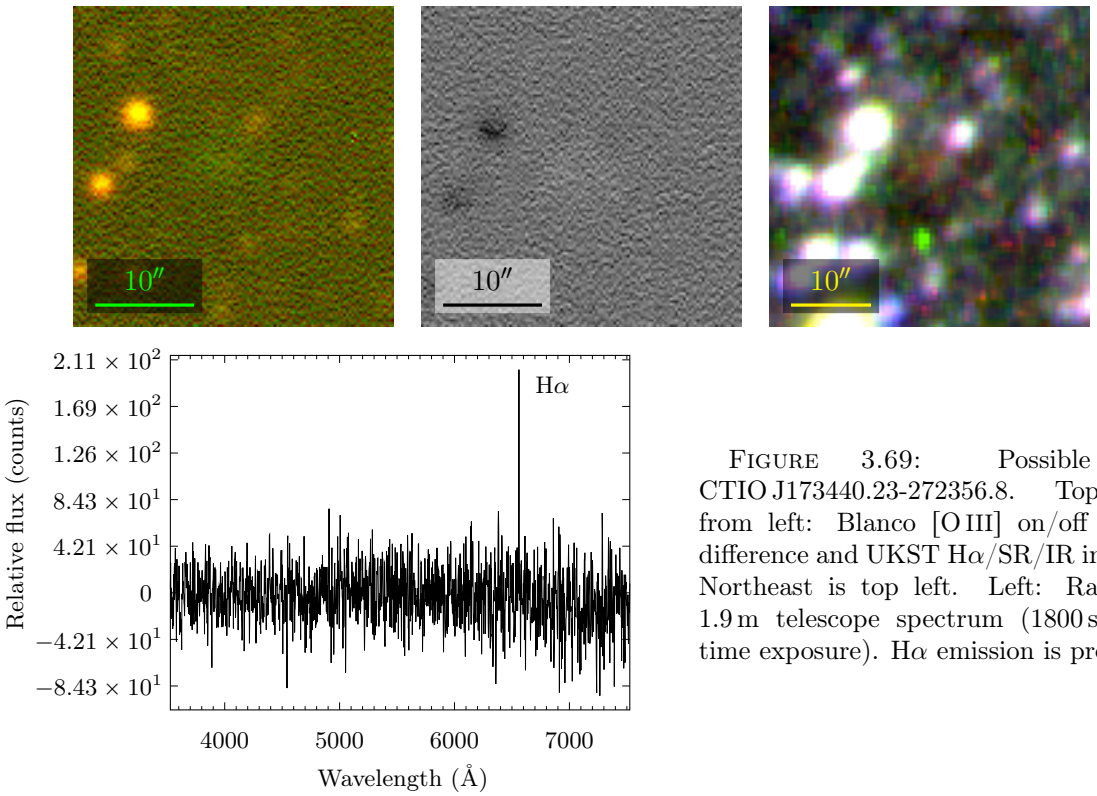

Figure 3.69: Possible PN CTIO J173440.23-272356.8. Top row, from left: Blanco [O III] on/off band, difference and UKST Hα/SR/IR images. Northeast is top left. Left: Radcliffe 1.9 m telescope spectrum (1800 s dark time exposure). Hα emission is present.

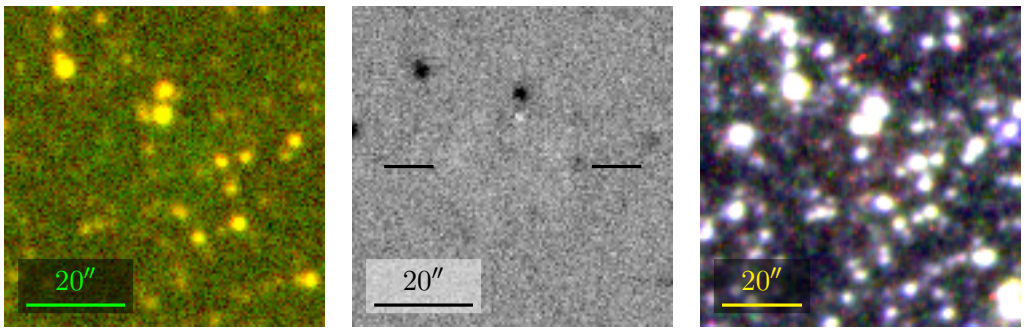

Figure 3.70: Possible faint PN, CTIO J173513.37-263254.0. From left: Blanco [O III] on/off band, difference and UKST Hα/SR/IR images. Northeast is top left. Approximate candidate diameter is indicated.

CTIO J173959.11-270047.9

This PN candidate was identified from a faint rim arc in Blanco difference imaging. The large apparent extent of this nebula is consistent with a foreground PN rather than a bulge PN. A Radcliffe 1.9 m telescope (1800 s dark time exposure) spectrum, centred on a rim arc, showed probable faint [O III] λ5007 emission. The spectrum was however of very low S/N and not viable. Deeper spectroscopy is recommended for spectral confirmation of this PN candidate.

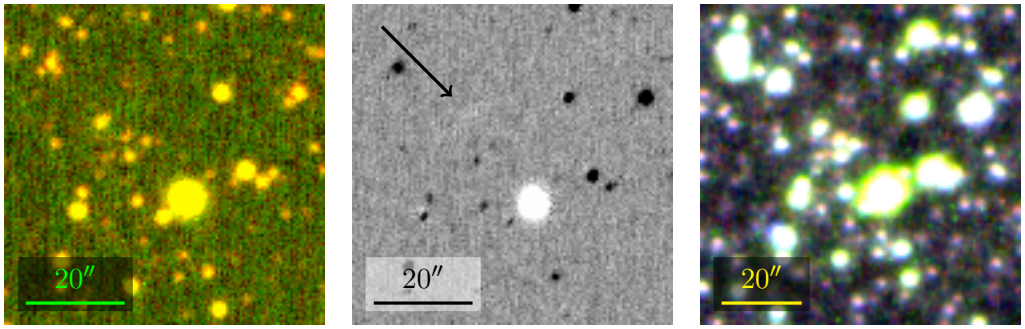

FIGURE 3.71: Possible PN, CTIO J173751.75-250309.2. From left: Blanco [O III] on/off band, difference and UKST Hα/SR/IR images. Northeast is top left. The approximate location of a potential brightened rim arc is indicated with an arrow.

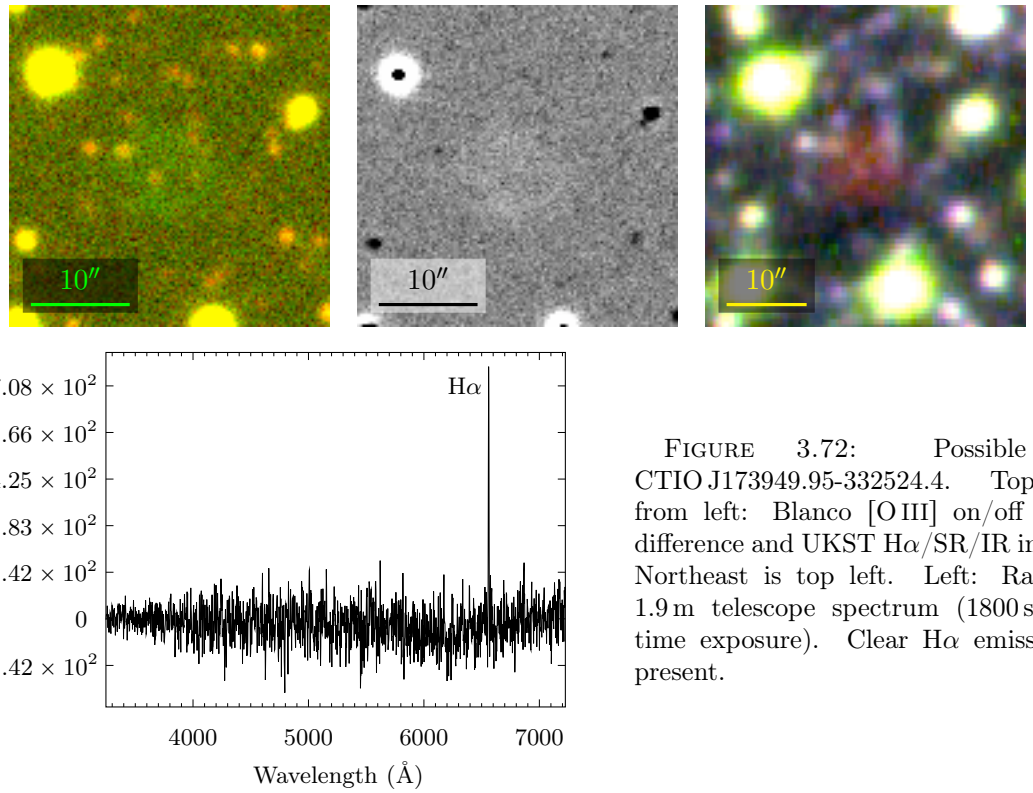

FIGURE 3.72: Possible PN CTIO J173949.95-332524.4. Top row, from left: Blanco [O III] on/off band, difference and UKST Hα/SR/IR images. Northeast is top left. Left: Radcliffe 1.9 m telescope spectrum (1800 s dark time exposure). Clear Hα emission is present.

CTIO J174100.05-241204.0

Possible PN or mimic CTIO J174100.05-241204.0 is shown in figure 3.75.

CTIO J174105.94-243732.0

Possible PN or mimic CTIO J174105.94-243732.0 is shown in figure 3.76. The candidate is probably a mimic however, as its apparent diameter, 2MASS J band brightness and UKST Hα/SR/IR image colour are all consistent with mimics presented in §3.4.4.

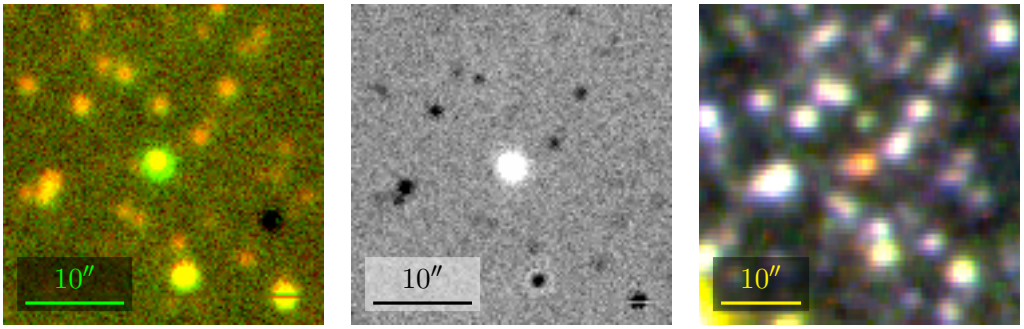

Figure 3.73: Possible bright, compact PN or mimic, CTIO J173958.08-270647.1. From left: Blanco [O III] on/off band, difference and UKST Hα/SR/IR images. Northeast is top left.

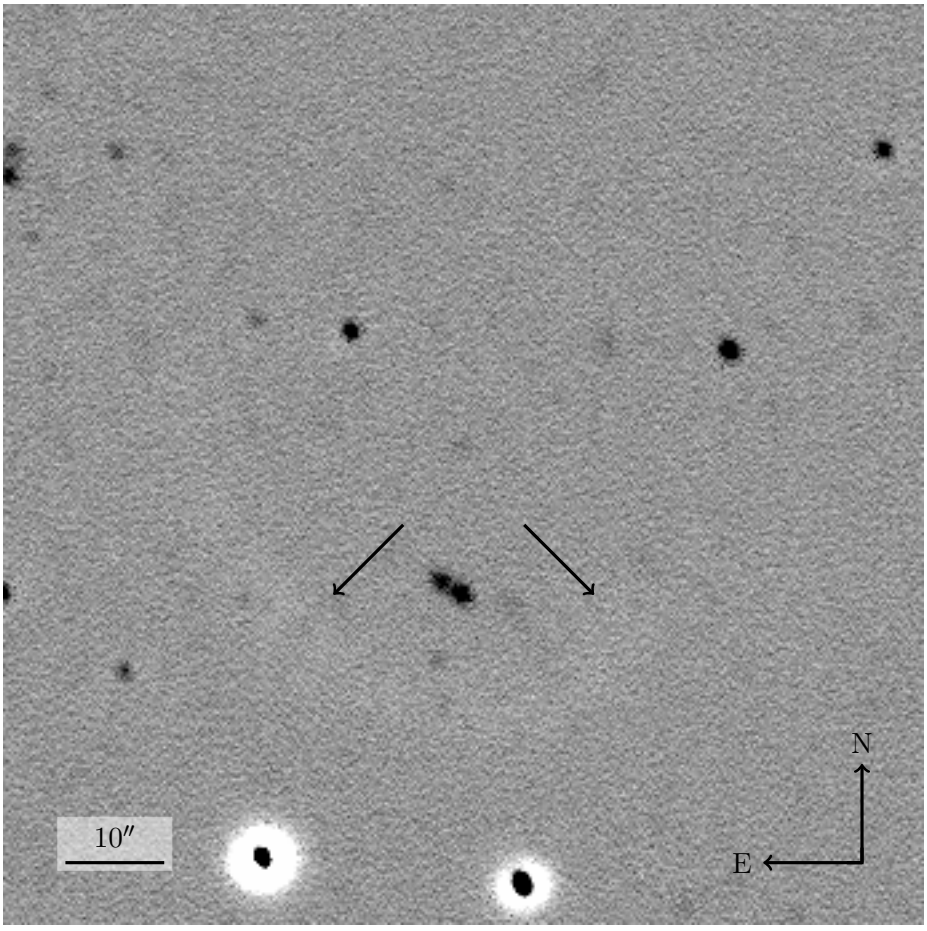

Figure 3.74: Blanco difference image of possible PN CTIO J173959.11-270047.9. Arrows indicate the approximate location of a faint PN rim arc. The extended nature of this candidate suggests it is foreground, rather than bulge, object.

CTIO J174152.05-243252.1

Possible PN CTIO J174152.05-243252.1 is shown in figure 3.77.

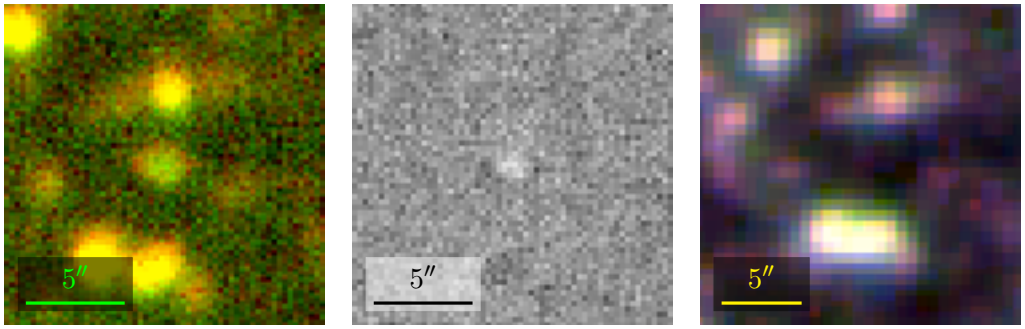

Figure 3.75: Possible PN or mimic, CTIO J174100.05-241204.0. From left: Blanco [O III] on/off band, difference and UKST Hα/SR/IR images. Northeast is top left.

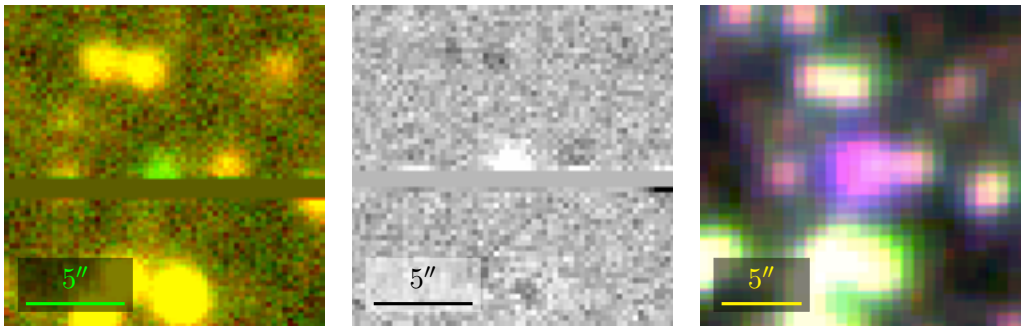

Figure 3.76: Possible PN or mimic, CTIO J174105.94-243732.0. From left: Blanco [O III] on/off band, difference and UKST Hα/SR/IR images. Northeast is top left. The candidate's appearance in UKST imaging resembles that of mimics presented in §3.4.4. The bad image rows are inopportune.

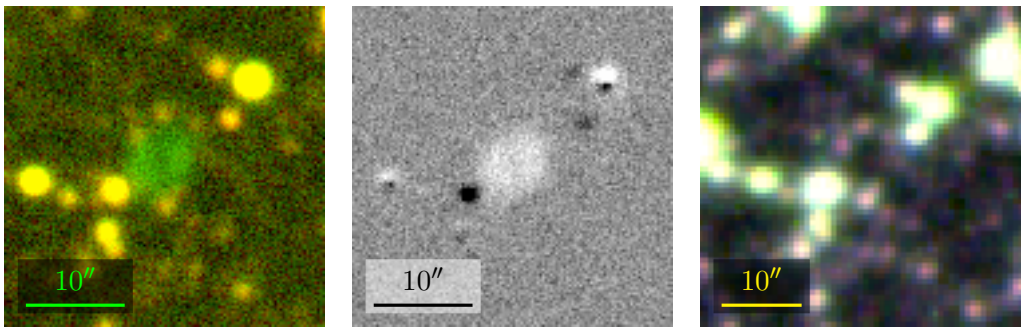

Figure 3.77: Possible PN, CTIO J174152.05-243252.1. From left: Blanco [O III] on/off band, difference and UKST Hα/SR/IR images. Northeast is top left.

CTIO J174211.00-340626.1

Possible compact PN or mimic CTIO J174211.00-340626.1 is shown in figure 3.78.

CTIO J174409.95-253030.3

Possible PN or mimic CTIO J174409.95-253030.3 is shown in figure 3.79. The object's colours in that figure suggest a mimic composed of modest [O III] and Hα emission superimposed

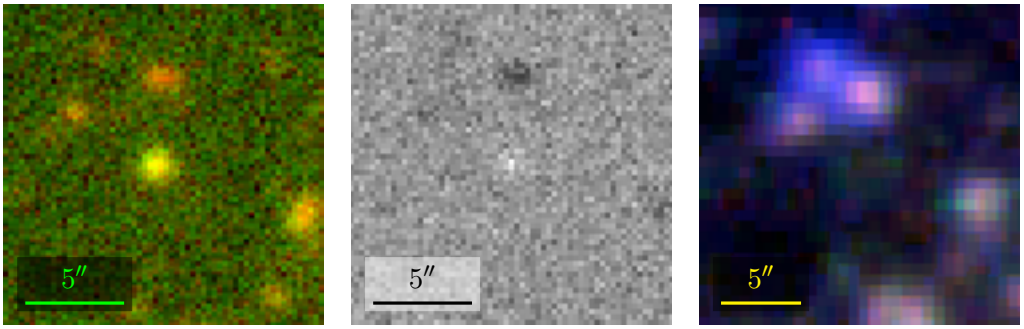

Figure 3.78: Possible compact PN or mimic, CTIO J174211.00-340626.1. From left: Blanco [O III] on/off band, difference and UKST Hα/SR/IR images. Northeast is top left.

on a stellar spectrum. It is noted the object's colours don't correspond strongly to any of the other mimics appearing in §3.4.4, meaning it may be the only representative of a specific mimic type amongst this candidate cohort.

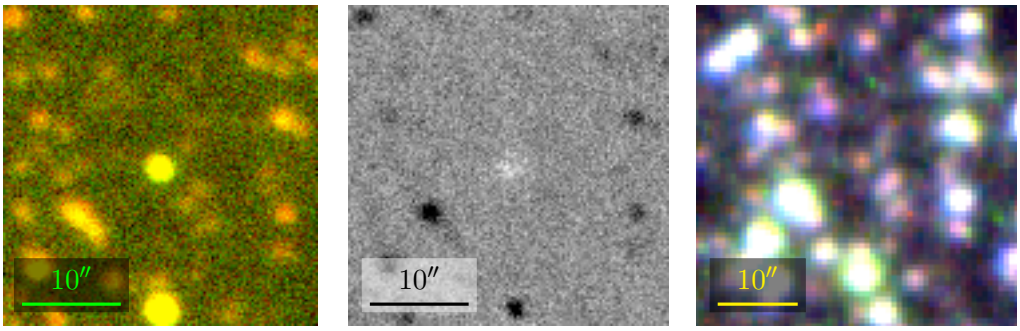

Figure 3.79: Possible PN or mimic, CTIO J174409.95-253030.3. From left: Blanco [O III] on/off band, difference and UKST Hα/SR/IR images. Northeast is top left. The object's orange colour in UKST imaging, possibly due to modest Hα emission superimposed on a stellar spectrum, is unusual for this candidate cohort.

CTIO J174421.47-253803.3

Possible PN or mimic CTIO J174421.47-253803.3 is shown in figure 3.80.

CTIO J174421.73-341558.2

Possible PN CTIO J174421.73-341558.2 is shown in figure 3.81.

CTIO J174423.18-341931.7

Possible PN or mimic CTIO J174423.18-341931.7 is shown in figure 3.82.

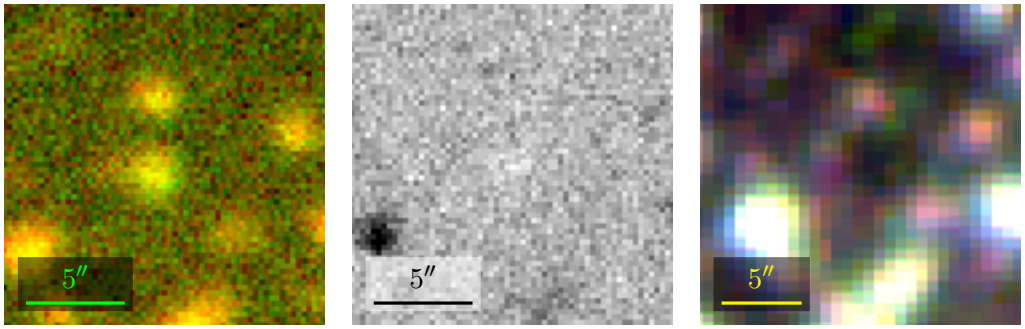

FIGURE 3.80: Possible PN or mimic, CTIO J174421.47-253803.3. From left: Blanco [O III] on/off band, difference and UKST Hα/SR/IR images. Northeast is top left.

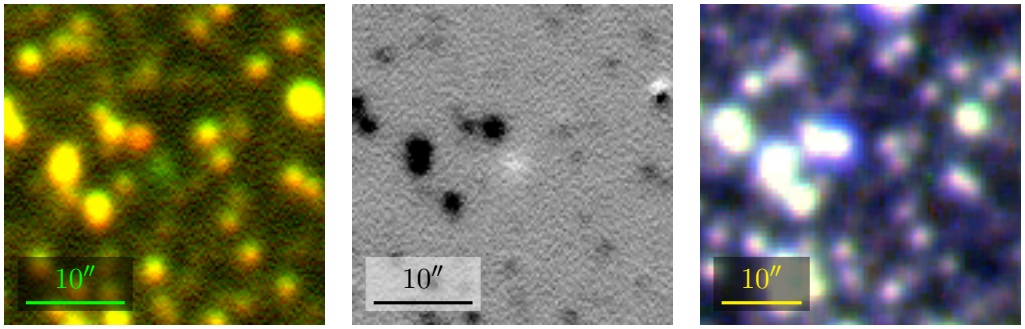

FIGURE 3.81: Possible PN, CTIO J174421.73-341558.2. From left: Blanco [O III] on/off band, difference and UKST Hα/SR/IR images. Northeast is top left.

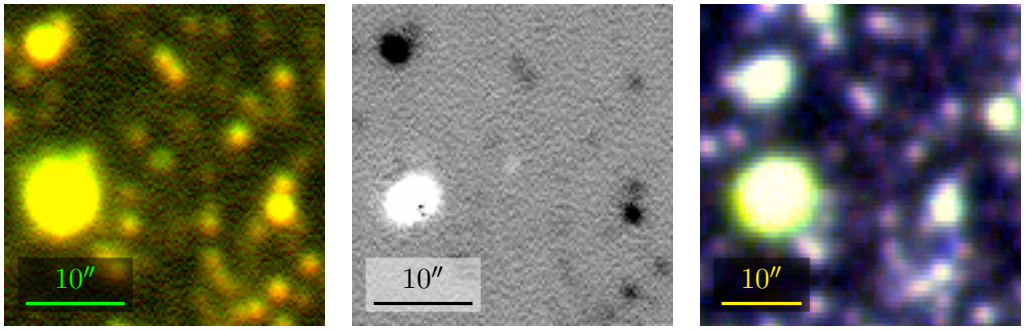

FIGURE 3.82: Possible PN or mimic, CTIO J174423.18-341931.7. From left: Blanco [O III] on/off band, difference and UKST Hα/SR/IR images. Northeast is top left.

CTIO J174425.66-340519.0

Possible PN CTIO J174425.66-340519.0 is shown in figure 3.83. This very faint candidate is more obvious in alternate colour and contrast schemes, not shown here for display consistency.

CTIO J174428.83-342922.4

Possible PN or mimic CTIO J174428.83-342922.4 is shown in figure 3.84.

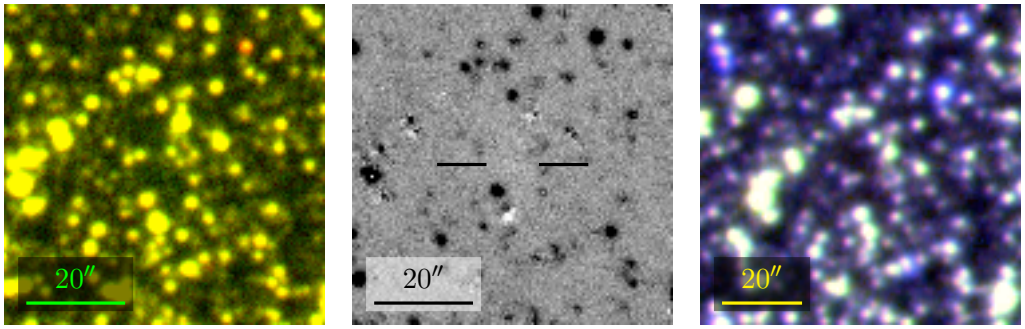

Figure 3.83: Possible very faint PN, CTIO J174425.66-340519.0. From left: Blanco [O III] on/off band, difference and UKST Hα/SR/IR images. Northeast is top left.

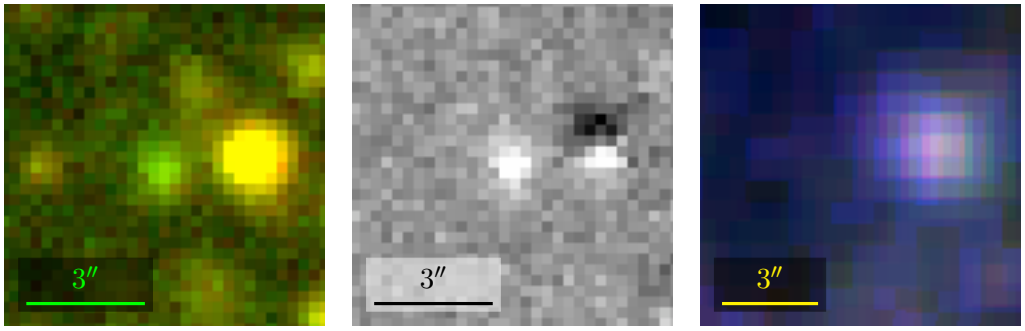

Figure 3.84: Possible PN or mimic, CTIO J174428.83-342922.4. From left: Blanco [O III] on/off band, difference and UKST Hα/SR/IR images. Northeast is top left.

CTIO J174431.07-240412.5

Possible PN or mimic CTIO J174431.07-240412.5 is shown in figure 3.85.

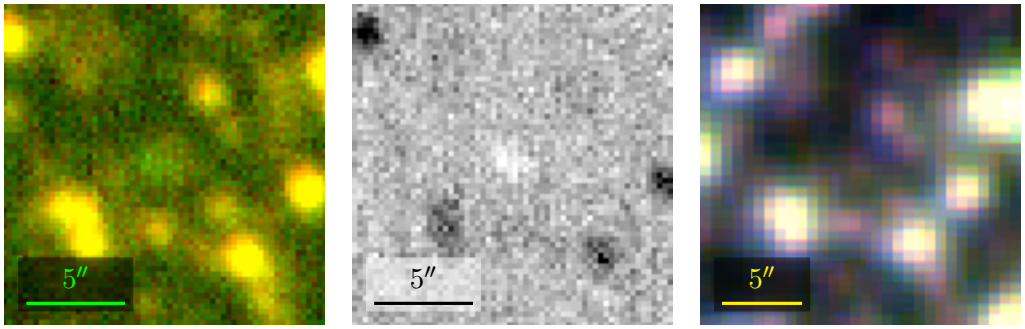

Figure 3.85: Possible PN or mimic, CTIO J174431.07-240412.5. From left: Blanco [O III] on/off band, difference and UKST Hα/SR/IR images. Northeast is top left.

CTIO J174435.93-330742.0

Possible PN CTIO J174435.93-330742.0 is shown in figure 3.86. A feature resembling a brightened rim arc is visible in the light of both [O III] and Hα.

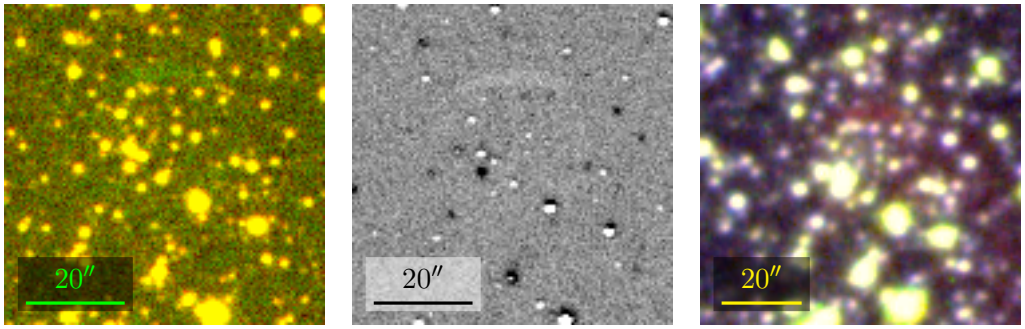

FIGURE 3.86: Possible PN, CTIO J174435.93-330742.0. From left: Blanco [O III] on/off band, difference and UKST Hα/SR/IR images. Northeast is top left.

CTIO J174453.14-344239.9

Possible PN CTIO J174453.14-344239.9 is shown in figure 3.87. This candidate lies outside the $-5^\circ \leqslant l \leqslant 5^\circ$, $-5^\circ \leqslant b \leqslant 5^\circ$ central bulge region boundary adopted here.

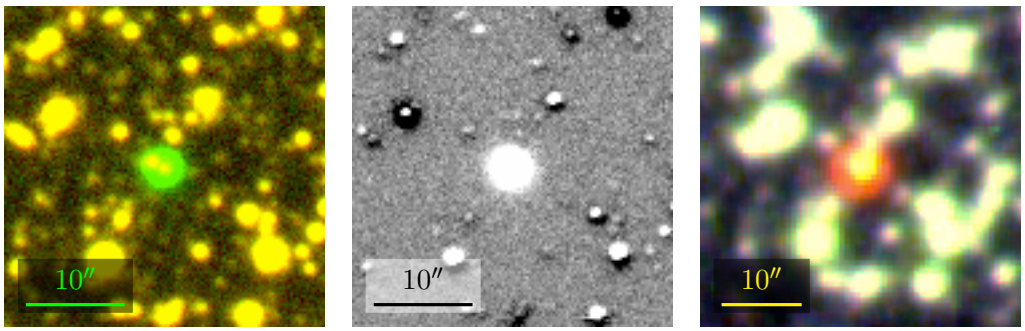

FIGURE 3.87: Possible PN, CTIO J174453.14-344239.9, lying outside the $-5^\circ \leqslant l \leqslant 5^\circ$, $-5^\circ \leqslant b \leqslant 5^\circ$ central bulge region. From left: Blanco [O III] on/off band, difference and UKST Hα/SR/IR images. Northeast is top left.

CTIO J174523.43-262706.2

Possible PN or mimic CTIO J174523.43-262706.2 is shown in figure 3.88.

CTIO J174537.17-335608.1

Faint possible PN CTIO J174537.17-335608.1 is shown in figure 3.89. An AAOmega spectrum was attempted of this candidate but the associated fibre accidentally offset too far from the candidate's apparent centre. Both Blanco and UKST imaging of this candidate are consistent however with a faint elliptical PN, and reobservation is recommended.

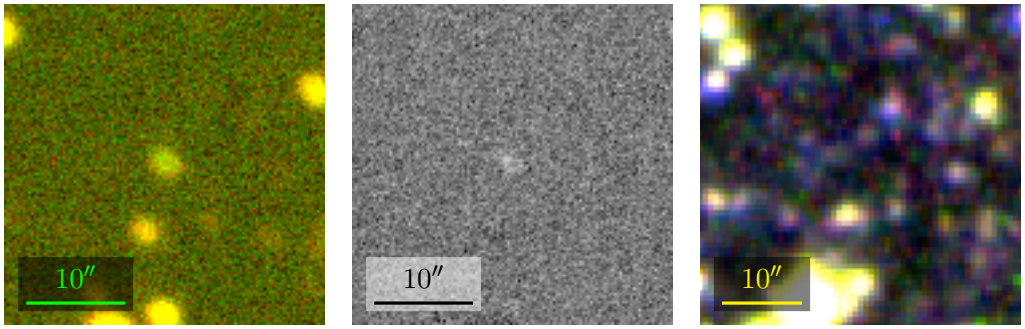

Figure 3.88: Possible PN or mimic, CTIO J174523.43-262706.2. From left: Blanco [O III] on/off band, difference and UKST Hα/SR/IR images. Northeast is top left.

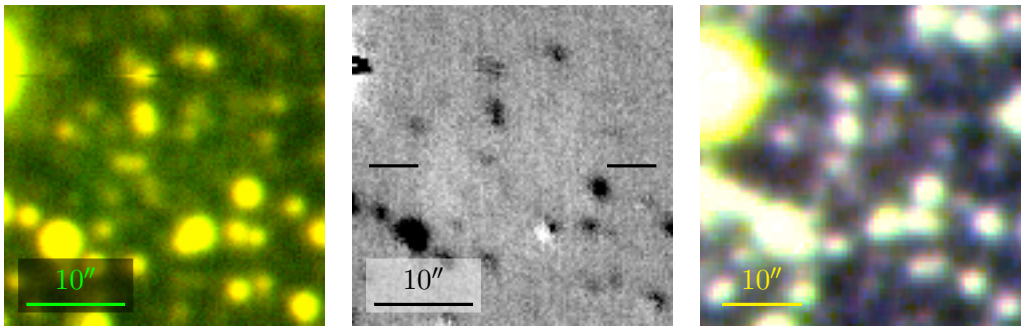

Figure 3.89: Possible faint, elliptical PN CTIO J174537.17-335608.1. From left: Blanco [O III] on/off band, difference and UKST Hα/SR/IR images. Northeast is top left.

CTIO J174546.15-253319.8

Possible PN or mimic CTIO J174546.15-253319.8 is shown in figure 3.90. This compact object is, unusually, green in both Blanco and UKST imaging. This is consistent with it emitting in [O III] and the SR, but not Hα or the near-IR. Like CTIO J174409.95-253030.3 (a compact orange object in UKST imaging), this object may be the sole representative of a specific mimic type amongst this candidate cohort.

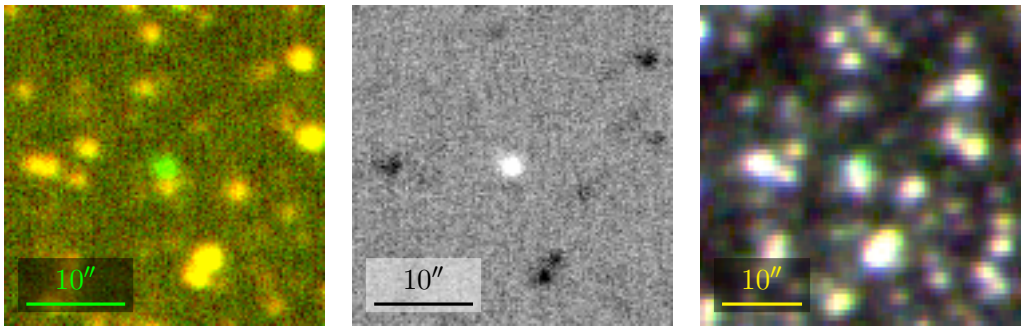

Figure 3.90: Possible PN or mimic, CTIO J174546.15-253319.8. From left: Blanco [O III] on/off band, difference and UKST Hα/SR/IR images. Northeast is top left. Note the object's unusual green colour in both Blanco and UKST images.

CTIO J174648.23-343603.0

Possible PN, but probable mimic CTIO J174648.23-343603.0 is shown in figure 3.91.

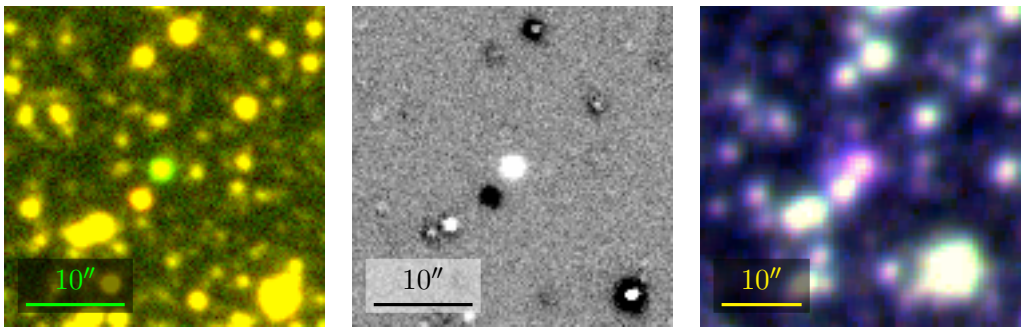

FIGURE 3.91: Possible PN but probable mimic, CTIO J174648.23-343603.0. From left: Blanco [O III] on/off band, difference and UKST Hα/SR/IR images. Northeast is top left.

CTIO J174732.26-242218.9

Possible PN or image artefact CTIO J174732.26-242218.9 is shown in figure 3.92.

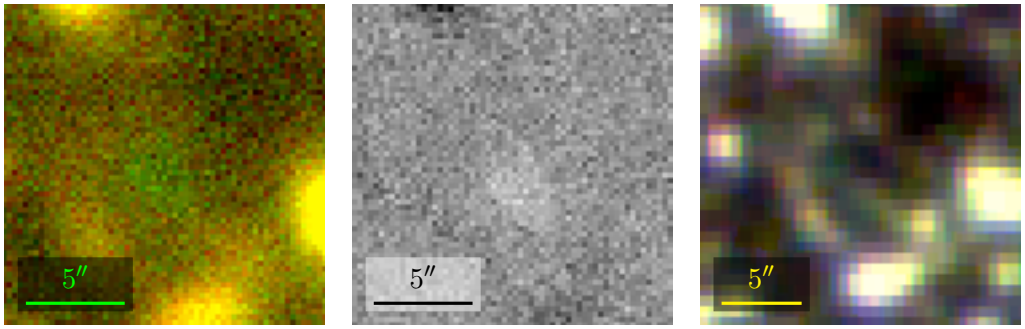

FIGURE 3.92: Possible PN or image artefact, CTIO J174732.26-242218.9. From left: Blanco [O III] on/off band, difference and UKST Hα/SR/IR images. Northeast is top left.

CTIO J174748.01-342126.4

A potential arc of possible PN CTIO J174748.01-342126.4 is shown in figure 3.93.

CTIO J174808.57-310445.3

Possible PN CTIO J174808.57-310445.3 is located at the centre of figure 3.94, though it is too faint to identify clearly at the scale used. The scale reveals however, an extended nebula, possibly a H II region, prominent in the bottom left of the figure. It is suspected CTIO J174808.57-310445.3's apparent proximity to that nebula makes it an extension of that nebula, instead of a standalone PN.

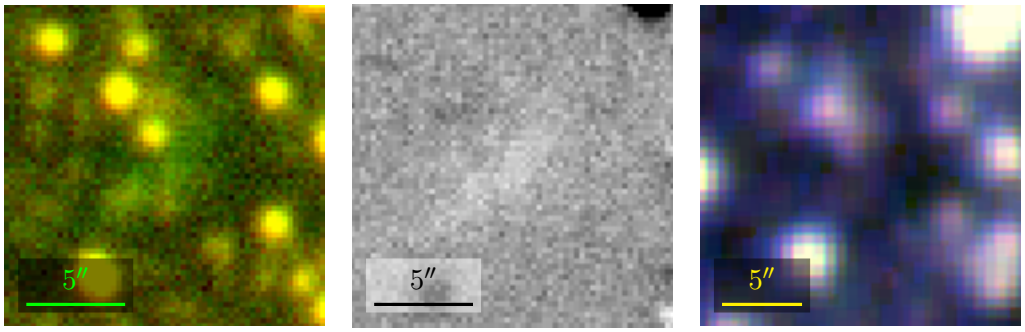

Figure 3.93: Potential arc of possible PN CTIO J174748.01-342126.4. From left: Blanco [O III] on/off band, difference and UKST Hα/SR/IR images. Northeast is top left.

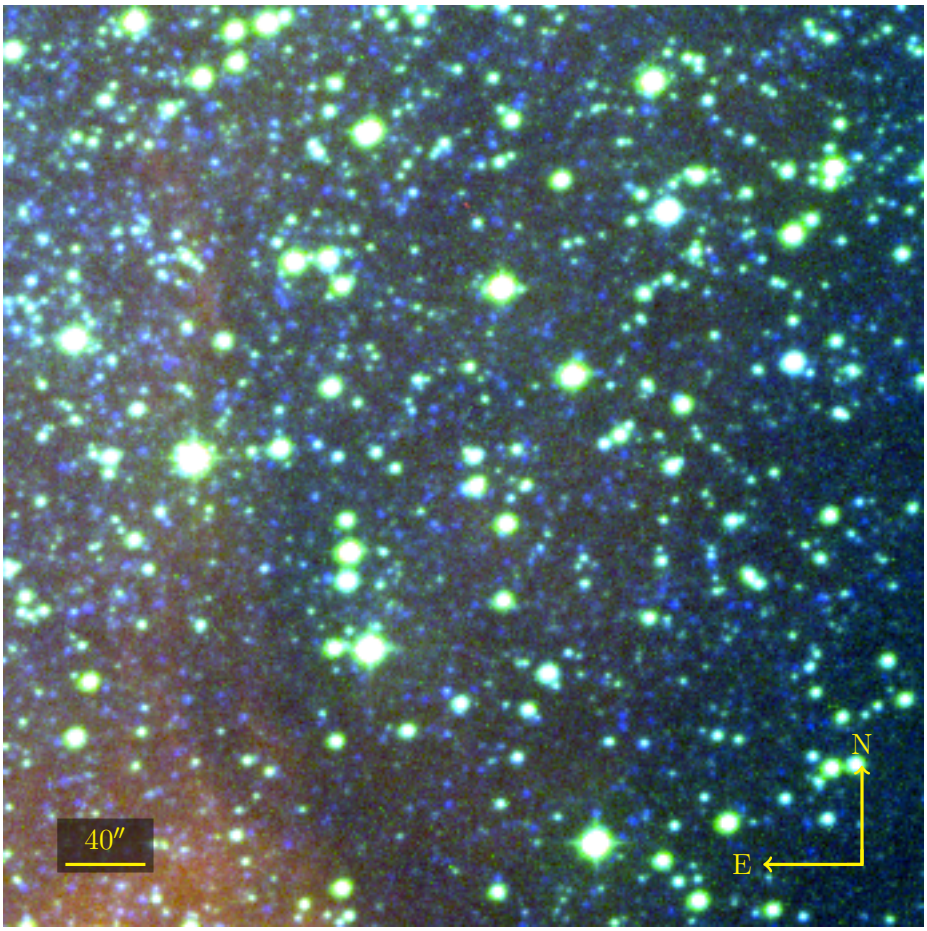

Figure 3.94: Possible PN CTIO J174808.57-310445.3 is located at the centre of this UKST Hα/SR/IR image, but is too faint to identify clearly at this scale. The scale reveals however, another nebula, possibly a H II region, in the bottom left of the image. CTIO J174808.57-310445.3 is probably a faint extension of that nebula.

CTIO J174825.12-301520.7

Possible PN CTIO J174825.12-301520.7 is shown in figure 3.95.

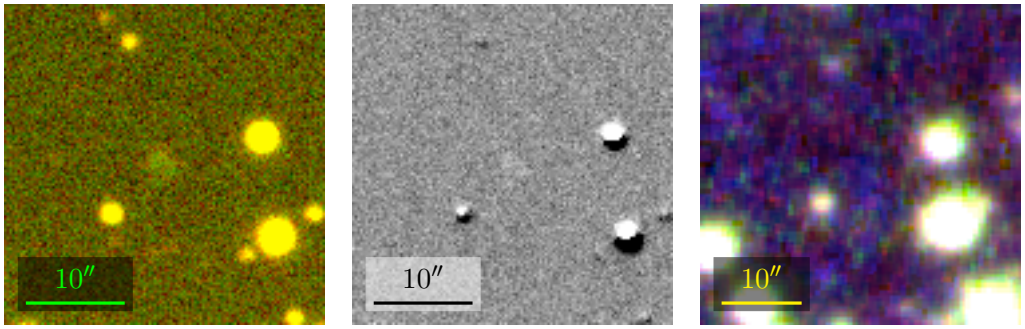

Figure 3.95: Possible PN, CTIO J174825.12-301520.7. From left: Blanco [O III] on/off band, difference and UKST Hα/SR/IR images. Northeast is top left.

CTIO J174938.55-320801.5

This PN candidate has probably avoided previous detection due to its apparent compact nature and proximity to a nearby star, as shown in figure 3.96. A spectrum for this candidate was attempted with the Radcliffe 1.9 m telescope (1230 s dark time exposure) but failed to return viable emission line data. Given CTIO J174938.55-320801.5 is visible in both Blanco and especially UKST imaging, deeper confirmatory spectroscopy is recommended.

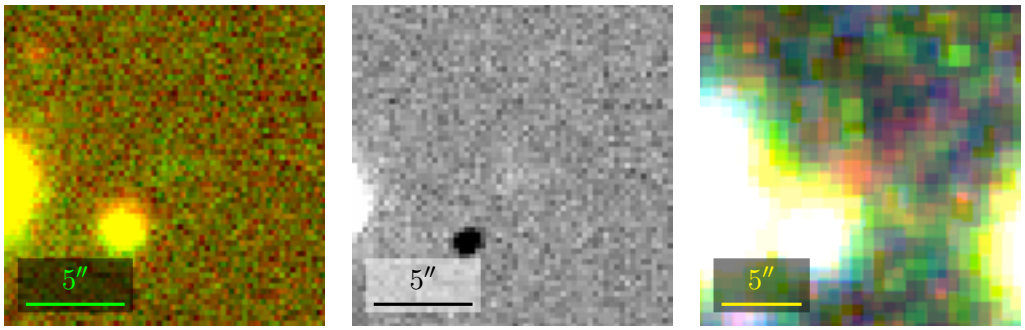

Figure 3.96: Possible compact PN CTIO J174938.55-320801.5. From left: Blanco [O III] on/off band, difference and UKST Hα/SR/IR images. Northeast is top left. A Radcliffe 1.9 m telescope (1230 s dark time exposure) failed to return viable emission line data.

CTIO J174955.44-334234.7

CTIO J174955.44-334234.7 enjoys the unusual distinction of being discovered after having been only partially captured with the Mosaic II imager. CTIO J174955.44-334234.7 appears to be round or elliptical rim-brightened PN, of which only a segment has been imaged, the remainder lying beyond the edge of the imaging CCD. To reflect and emphasise this, a truncated region of Blanco is displayed in figure 3.97. The UKST imaging is presented such that the region of sky in the left half of its panel matches the region of sky visible in the Blanco imaging.

An AAOmega spectrum (3×1200 s dark time exposure) of part of the putative PN's bright

rim is given in figure 3.97. Although a stellar contaminant has been inadvertently sampled too, signature PN emission lines are present. These include Hα, Hβ, [N II] $\lambda\lambda$6548, 6583, [S II] $\lambda\lambda$6716, 6731 and probable Hγ. Several aspects of the spectrum are unusual. Firstly, the relative line ratios, when compared to the diagnostic diagrams of Frew & Parker (2010), are more consistent with a mimic, possibly a H II region, than a PN. A strong unidentified $\lambda\sim$5899 Å feature is also present. Finally, no [O III] λ5007 emission corresponding to the detection in Blanco imaging was recorded—deeper spectroscopy may be needed to achieve this. Until deeper spectra are available, CTIO J174955.44-334234.7 is assessed as a possible PN.

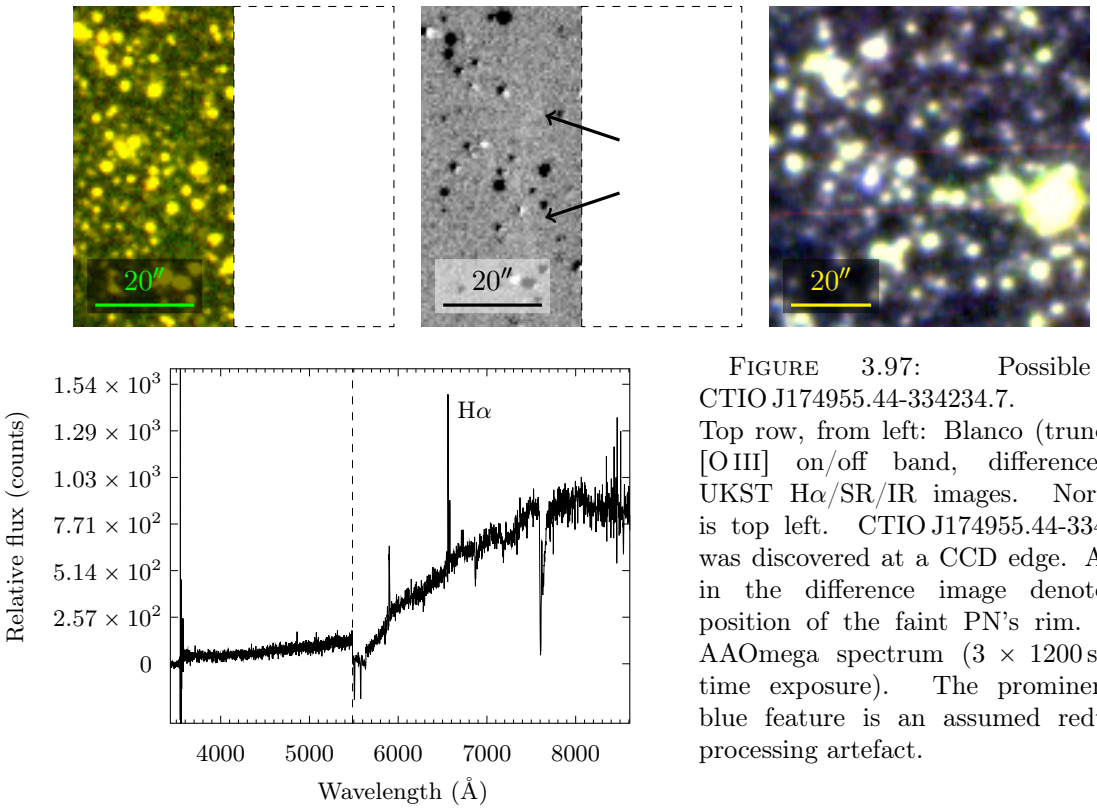

Figure 3.97: Possible PN CTIO J174955.44-334234.7.
Top row, from left: Blanco (truncated) [O III] on/off band, difference and UKST Hα/SR/IR images. Northeast is top left. CTIO J174955.44-334234.7 was discovered at a CCD edge. Arrows in the difference image denote the position of the faint PN's rim. Left: AAOmega spectrum (3 × 1200 s dark time exposure). The prominent far blue feature is an assumed reduction processing artefact.

CTIO J175006.71-340258.6

Possible PN CTIO J175006.71-340258.6 is shown in figure 3.98.

CTIO J175051.08-305206.5

The Blanco imaging of this object shows it is clearly a nebula of some kind. A low S/N spectrum of the nebula was taken with the Radcliffe 1.9 m telescope (1800 s bright time exposure) as shown in figure 3.99. It is suspected an [O I] λ5577 airglow processing artefact is present. Reobservation of this candidate in better observing conditions (i.e. grey or dark

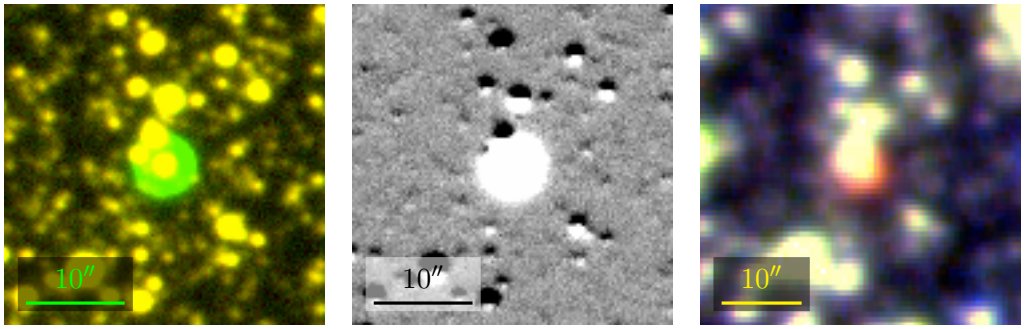

FIGURE 3.98: Possible PN, CTIO J175006.71-340258.6. From left: Blanco [O III] on/off band, difference and UKST Hα/SR/IR images. Northeast is top left.

time) is recommended to obtain a spectrum featuring the faint [O III] emission visible in the Blanco imaging.

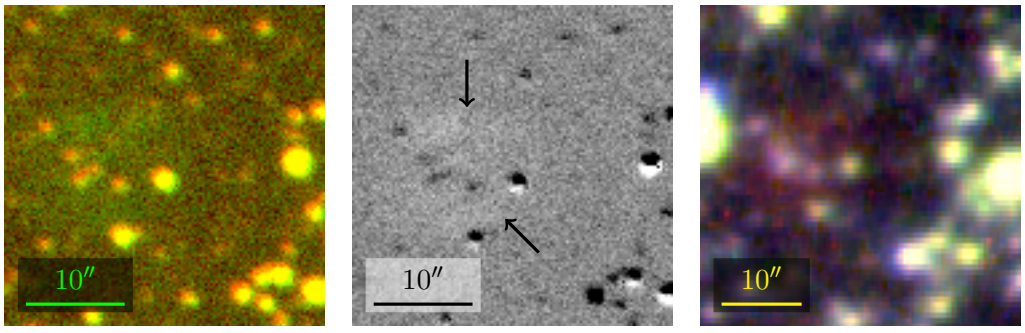

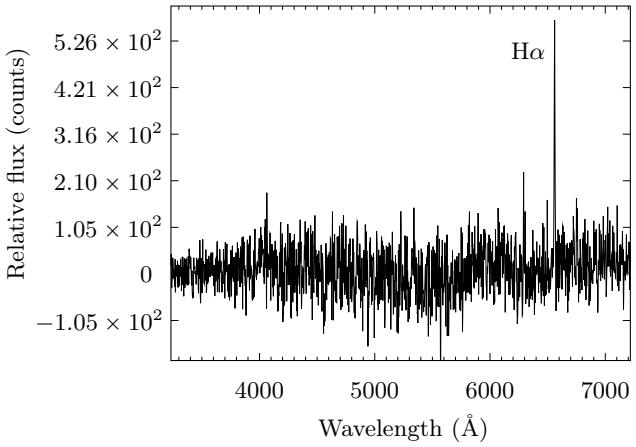

FIGURE 3.99: Possible PN CTIO J175051.08-305206.5, offset left of centre. Top row, from left: Blanco [O III] on/off band, difference and UKST Hα/SR/IR images. Northeast is top left. Left: Low S/N Radcliffe 1.9 m telescope spectrum (1800 s bright time exposure). An [O I] λ5577 airglow processing artefact has been truncated for clarity.

CTIO J175246.55-301700.4

A spectrum for this possible PN was attempted with the Radcliffe 1.9 m telescope (1800 s dark time exposure) but failed to return viable emission line data. Given CTIO J175246.55-301700.4 is visible in both Blanco and, faintly, in SHS imaging, reattempting confirmatory spectroscopy is recommended. As the object is located in a crowded stellar field, as shown in figure 3.100, reobservation with reduced binning, if using the Radcliffe telescope, may

disentangle any PN emission from stellar contaminants.

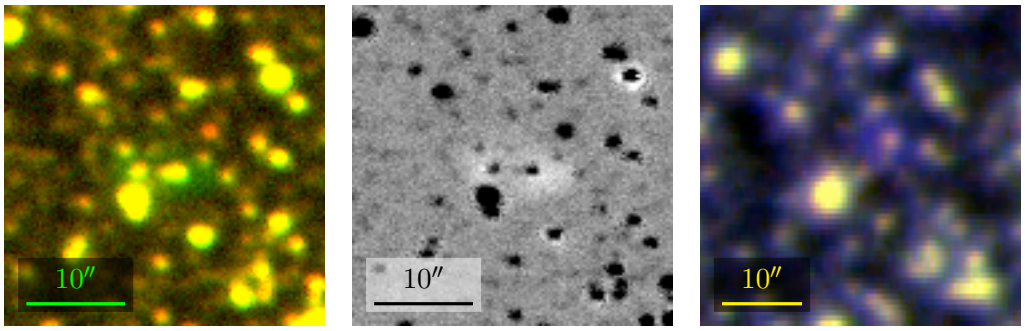

Figure 3.100: Possible PN CTIO J175246.55-301700.4. From left: Blanco [O III] on/off band, difference and UKST Hα/SR/IR images. Northeast is top left. A Radcliffe 1.9 m telescope (1800 s dark time exposure) failed to return viable emission line data.

CTIO J175308.41-353356.7

Possible PN or image artefact CTIO J175308.41-353356.7 is shown in figure 3.101.

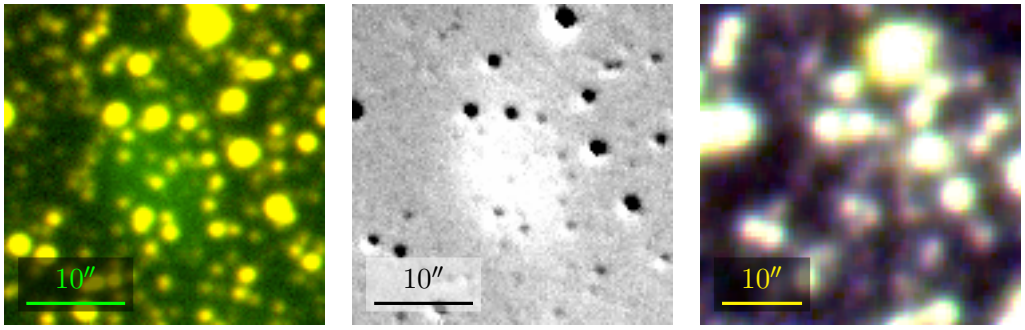

Figure 3.101: Possible PN or image artefact, CTIO J175308.41-353356.7. From left: Blanco [O III] on/off band, difference and UKST Hα/SR/IR images. Northeast is top left.

CTIO J175353.88-322907.7

Possible PN CTIO J175353.88-322907.7 is shown in figure 3.102. This candidate either abuts, or is part of, PN G357.8-03.3, appearing in the same figure.

CTIO J175417.98-282724.3

CTIO J175417.98-282724.3 is a faint, indistinct nebula, as shown in figure 3.103. An AAOmega spectrum (3×1800 s grey time exposure) accompanies the Blanco on/off band, difference and UKST imaging in the figure. The spectrum exhibits probable [O III] $\lambda\lambda$4959, 5007 emission, consistent with the Blanco imaging, and is thus assessed a possible PN. It also features an [O I] λ5577 airglow processing artefact and multiple discrete features that aren't additional

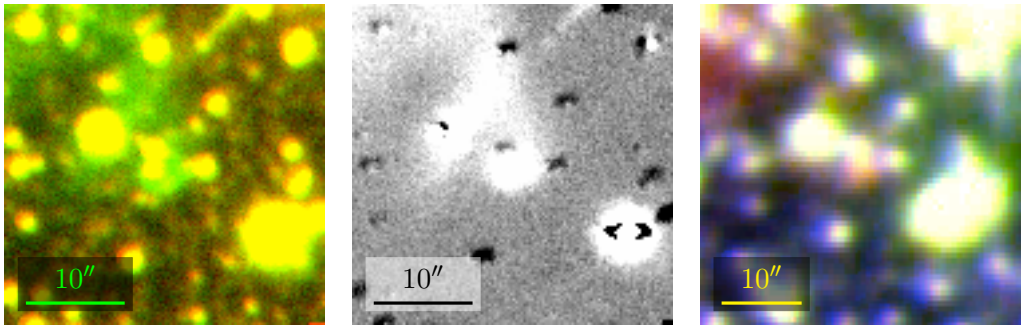

FIGURE 3.102: Possible PN, CTIO J175353.88-322907.7. From left: Blanco [O III] on/off band, difference and UKST Hα/SR/IR images. Northeast is top left. If not a distinct compact PN, CTIO J175353.88-322907.7 may be part of PN G357.8-03.3, itself in the top left of each image.

emission lines, but rather noise and miscellaneous reduction processing artefacts, raised to apparent prominence by the nebula's faintness. Deeper imaging and spectroscopy are recommended to better assess the nature of this object.

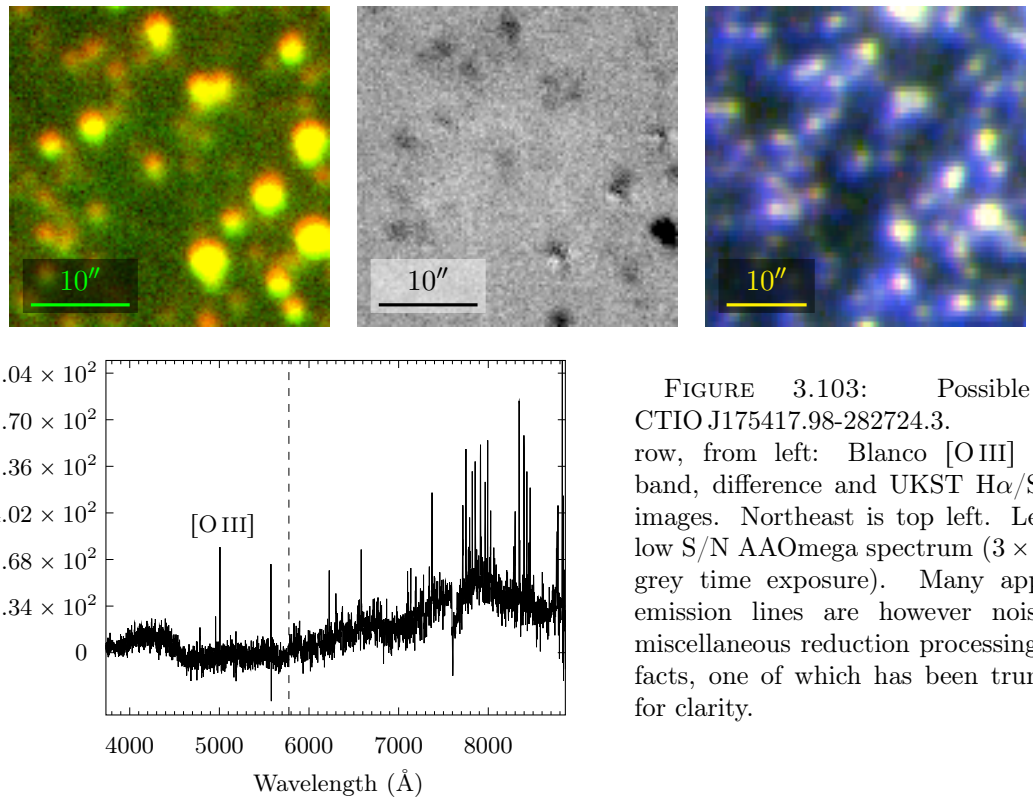

FIGURE 3.103: Possible PN CTIO J175417.98-282724.3. Top row, from left: Blanco [O III] on/off band, difference and UKST Hα/SR/IR images. Northeast is top left. Left: A low S/N AAOmega spectrum (3×1800 s grey time exposure). Many apparent emission lines are however noise, or miscellaneous reduction processing artefacts, one of which has been truncated for clarity.

CTIO J175452.18-342852.1

Possible PN CTIO J175452.18-342852.1 is shown in figure 3.104.

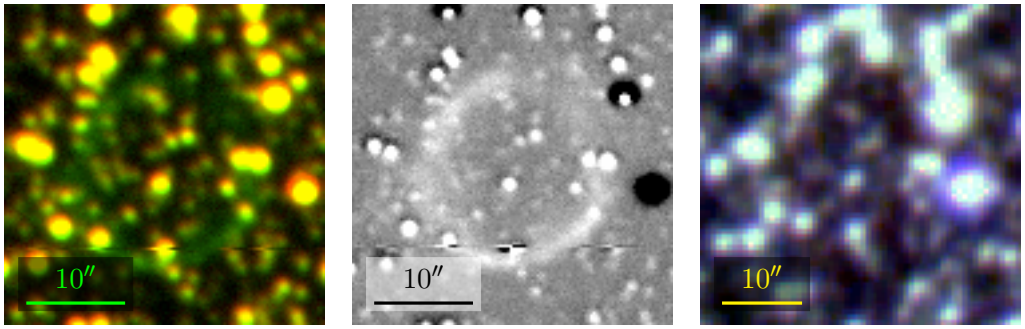

Figure 3.104: Possible PN, CTIO J175452.18-342852.1. From left: Blanco [O III] on/off band, difference and UKST Hα/SR/IR images. Northeast is top left.

CTIO J175505.83-344705.9

Possible PN but probable mimic CTIO J175505.83-344705.9 is shown in figure 3.105.

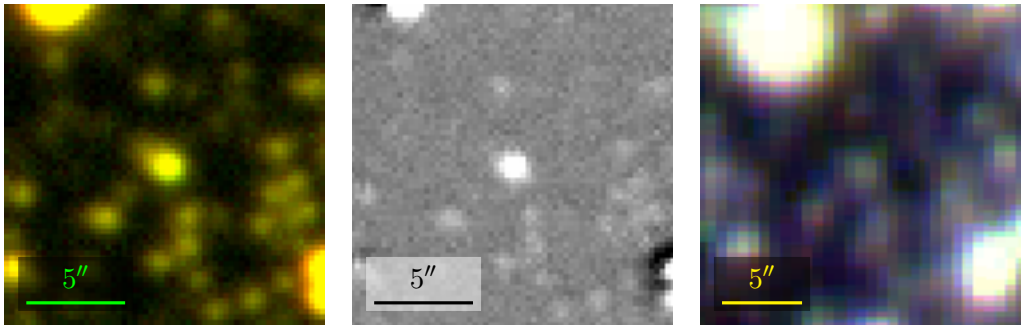

Figure 3.105: Possible PN but probable mimic, CTIO J175505.83-344705.9. From left: Blanco [O III] on/off band, difference and UKST Hα/SR/IR images. Northeast is top left.

CTIO J175536.99-280611.2

Faint, indistinct nebula CTIO J175536.99-280611.2 is shown in Blanco and UKST imaging in figure 3.106. Although deemed a poor PN candidate, a HERMES spectrum (1200 s dark time exposure) taken of this candidate exhibits possible faint (S/N < 2) Hα and [N II] λ6583 emission. Deeper spectroscopy is recommended to rigorously evaluate this candidate.

CTIO J175603.00-312658.9

Possible PN CTIO J175603.00-312658.9 is shown in figure 3.107.

CTIO J175604.17-280343.0

CTIO J175604.17-280343.0 is a very faint, irregular PN candidate shown in selected multi-wavelength imaging in figure 3.108. A high airmass ($Z \approx 2.3$) HERMES spectrum (1200 s dark time exposure) taken of this candidate was of very low S/N (< 2), but revealed possible

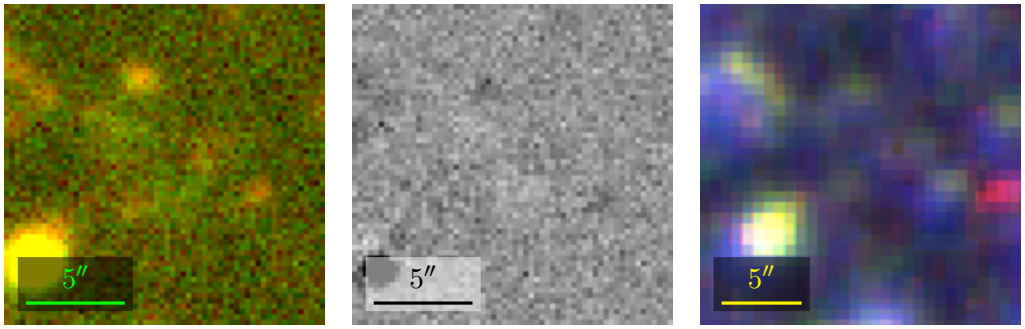

FIGURE 3.106: Possible faint, indistinct PN CTIO J175536.99-280611.2. From left: Blanco [O III] on/off band, difference and UKST Hα/SR/IR images. Northeast is top left.

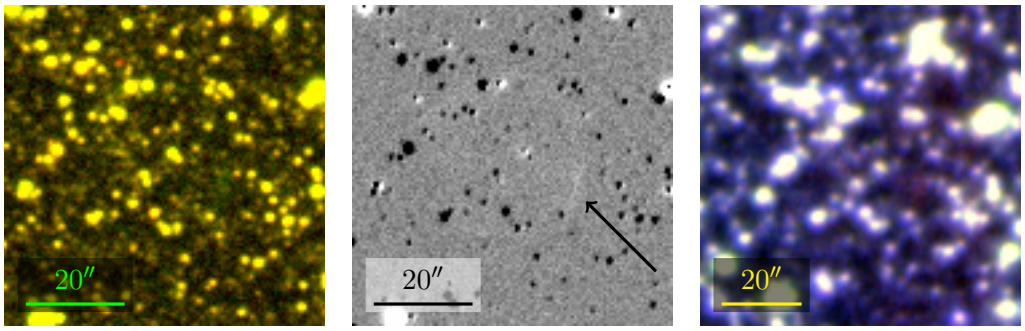

FIGURE 3.107: Possible PN, CTIO J175603.00-312658.9. From left: Blanco [O III] on/off band, difference and UKST Hα/SR/IR images. Northeast is top left. The approximate location of a putative brightened rim arc is indicated with an arrow.

Hα, Hβ and [N II] λ6583 emission. Deeper spectroscopy is recommended to dismiss or confirm this candidate.

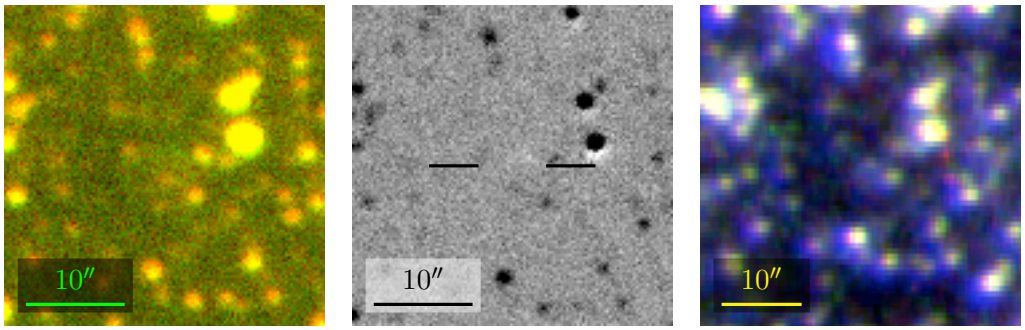

FIGURE 3.108: Possible faint, irregular PN CTIO J175604.17-280343.0. From left: Blanco [O III] on/off band, difference and UKST Hα/SR/IR images. Northeast is top left.

CTIO J175703.45-284955.2

A combination of stellar crowding of PN candidate CTIO J175703.45-284955.2 and its small apparent diameter makes it very difficult to take a spectrum without suffering some stellar

contamination. Nonetheless, imaging and an AAOmega spectrum (3×1200 s grey time exposure) for CTIO J175703.45-284955.2 are given in figure 3.109. The spectrum is contaminated by significant airglow [O I] $\lambda\lambda$5577, 6300 and by 2–3 coincident stars. Despite this, key PN emission lines are present, including [O III] $\lambda\lambda$4959, 5007 and weak Hα, consistent with the UKST imaging. In addition, the [O III] λ5007 line appears split for this object.

A second, low S/N spectrum taken with HERMES (1200 s dark time exposure), is compromised not by stellar coincidence, but by the numerous spurious artefacts discussed in §3.3.2. Real, albeit faint, Hα emission is nonetheless discernible, further advocating this object's PN nature.

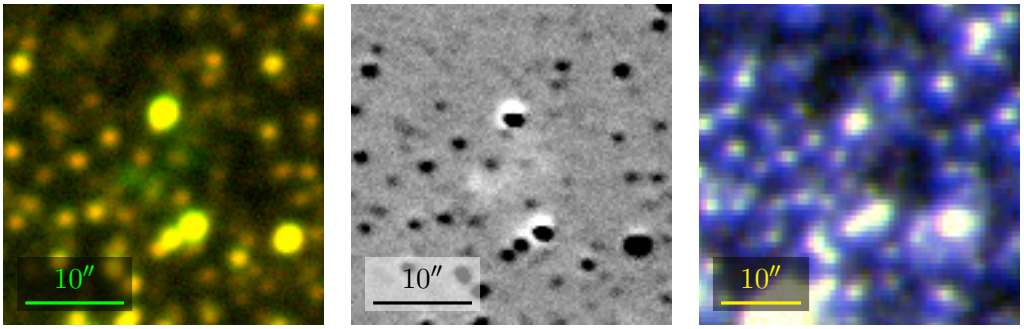

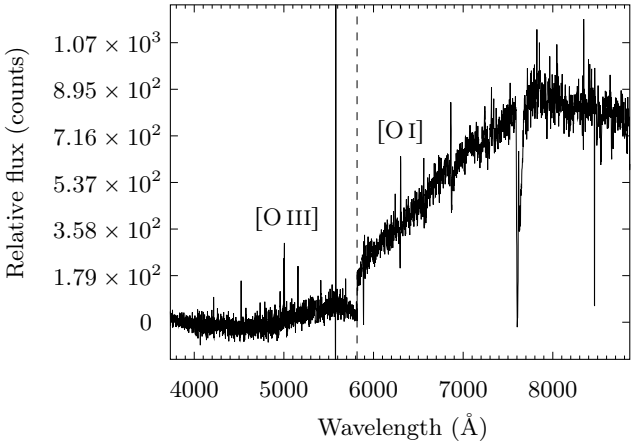

Figure 3.109: Possible PN, CTIO J175703.45-284955.2. Top row, from left: Blanco [O III] on/off band, difference and UKST Hα/SR/IR images. Northeast is top left. Left: AAOmega spectrum (3×1200 s grey time exposure). An [O I] λ5577 airglow processing artefact has been truncated for clarity. Multiple stellar contaminants are present.

Right: Low S/N CTIO J175703.45-284955.2 HERMES red channel spectrum (1200 s dark time exposure). Several apparent features of this high airmass ($Z \approx 2.3$) observation are artificial (see §3.3.2), with one truncated for clarity. Real, albeit faint, Hα emission is however present.

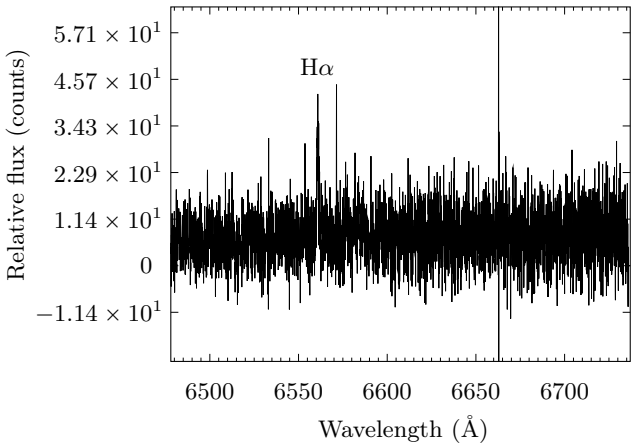

CTIO J175703.93-275130.4

Possible PN CTIO J175703.93-275130.4 was identified in Blanco imaging amidst an apparent smear of [O III] emission, thought to be an artificial imaging artefact of unknown origin. The apparent ring morphology of this object however, prompted further investigation. Corresponding Radcliffe 1.9 m telescope (1800 s dark time exposure) and HERMES (1200 s dark time exposure) spectra are given in figure 3.110. Redshifted Hα emission was recovered in both, including broad enough emission from the HERMES to allow its differentiation from the multiple spurious HERMES features (see §3.3.2). Deeper spectroscopy is recommended to recover the [O III] emission evidenced in imaging.

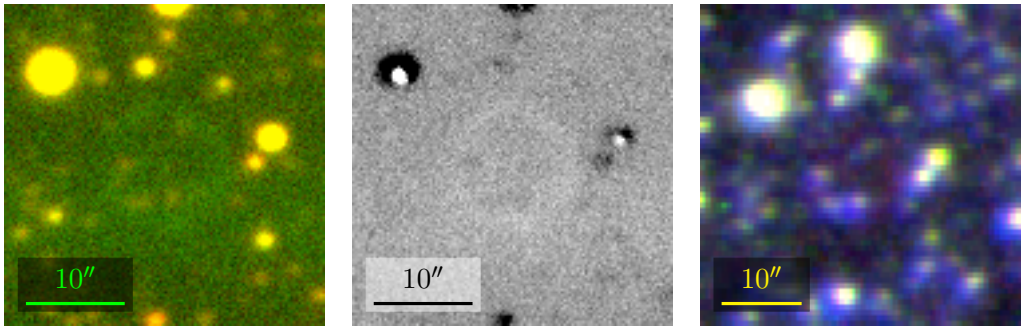

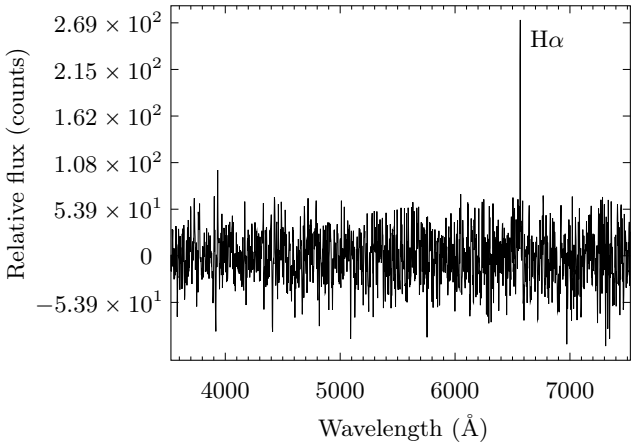

FIGURE 3.110: Possible round ring PN CTIO J175703.93-275130.4. Top row, from left: Blanco [O III] on/off band, difference and UKST Hα/SR/IR images. Northeast is top left. Left: Radcliffe 1.9 m telescope spectrum (1800 s dark time exposure). Hα emission is clear.

Right: Low S/N CTIO J175703.93-275130.4 HERMES red channel spectrum (1200 s dark time exposure). Several apparent features of this high airmass ($Z \approx 2.3$) observation are likely spurious (see §3.3.2). For clarity, some have been truncated. Authentic redshifted Hα emission is present.

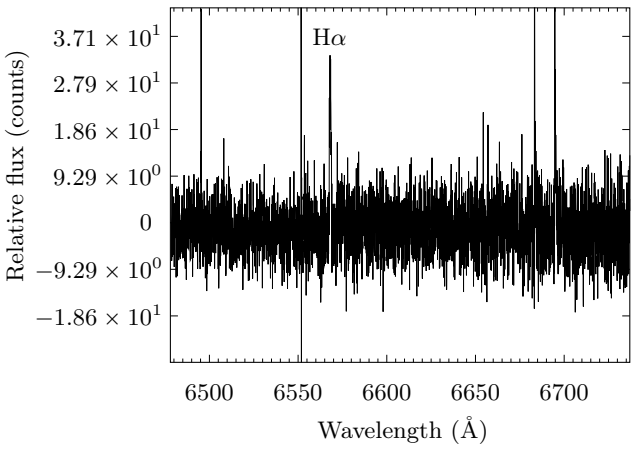

CTIO J175706.52-310324.5

Attempts to obtain a spectrum of this possible PN with the Radcliffe 1.9 m telescope were hampered by its apparent positioning within a dense stellar field, as shown in figure 3.111 and as might be expected for a candidate towards the Galactic bulge. As a result, the Radcliffe spectrum (1800 s bright time exposure) in figure 3.111 shows [O III] $\lambda\lambda$4959, 5007 and Hα emission, indicative of a PN nature, but overlaps a contribution from coincident stellar objects. Additionally, the spectrum is marred by suspected over and under processing of [O I] λ5577 airglow, but this is truncated for clarity. Deeper, higher S/N spectroscopy, is recommended for a definitive evaluation of this candidate.

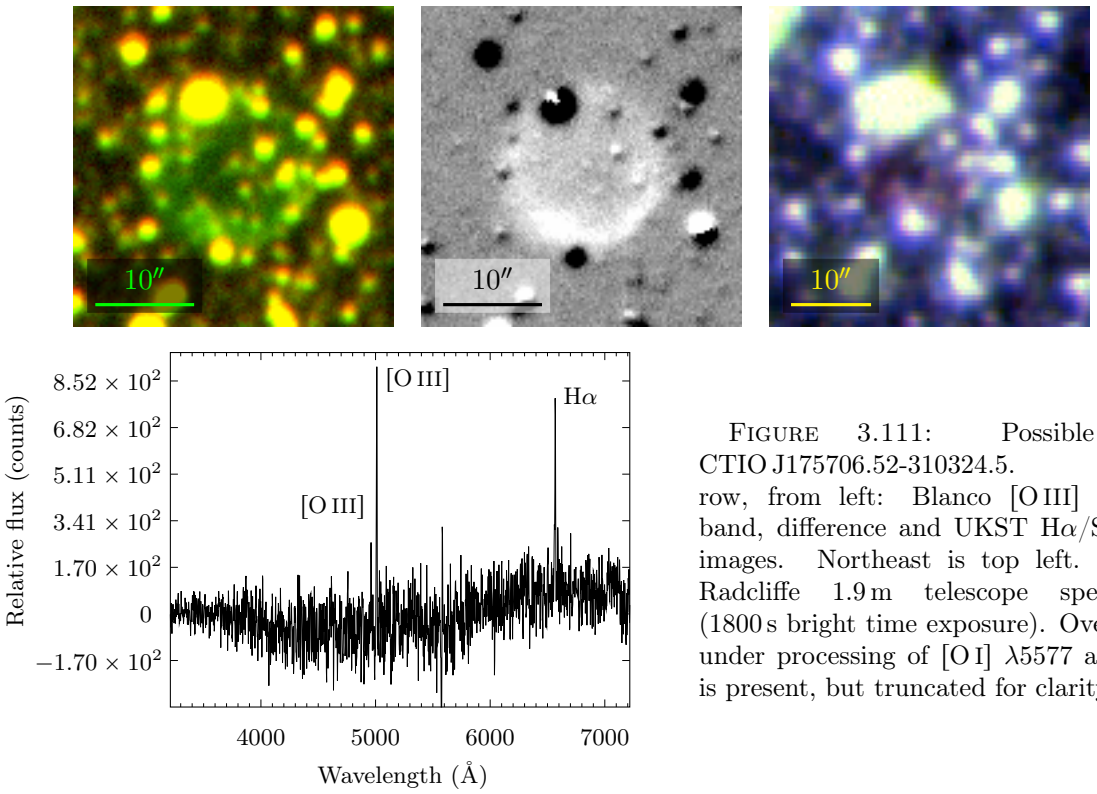

Figure 3.111: Possible PN CTIO J175706.52-310324.5. Top row, from left: Blanco [O III] on/off band, difference and UKST Hα/SR/IR images. Northeast is top left. Left: Radcliffe 1.9 m telescope spectrum (1800 s bright time exposure). Over and under processing of [O I] λ5577 airglow is present, but truncated for clarity.

CTIO J175708.64-310453.4

Possible PN CTIO J175708.64-310453.4 is shown in figure 3.112. The approximate symmetry of this faint nebula around the prominent star at the centre of each image in figure 3.112 suggests it may be a miscellaneous circumstellar nebula, not a true PN.

CTIO J175735.64-273532.5

Possible PN CTIO J175735.64-273532.5 is shown in Blanco [O III] on/off band, difference and UKST Hα/SR/IR imaging in figure 3.113. A corresponding low S/N HERMES spectrum

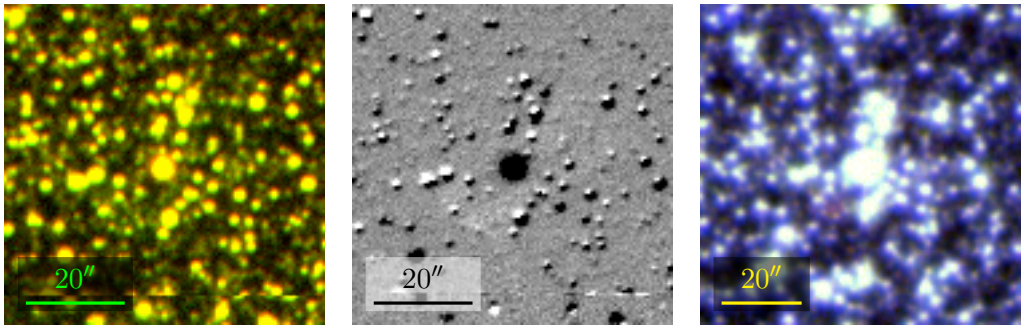

FIGURE 3.112: Possible PN or circumstellar nebula, CTIO J175708.64-310453.4. From left: Blanco [O III] on/off band, difference and UKST Hα/SR/IR images. Northeast is top left. A region of local nebula brightness is located in the bottom left quadrant of each image.

(1200 s dark time exposure), containing mostly spurious artefacts (see §3.3.2), is given in the same figure. Within the HERMES red channel, Hα emission is present.

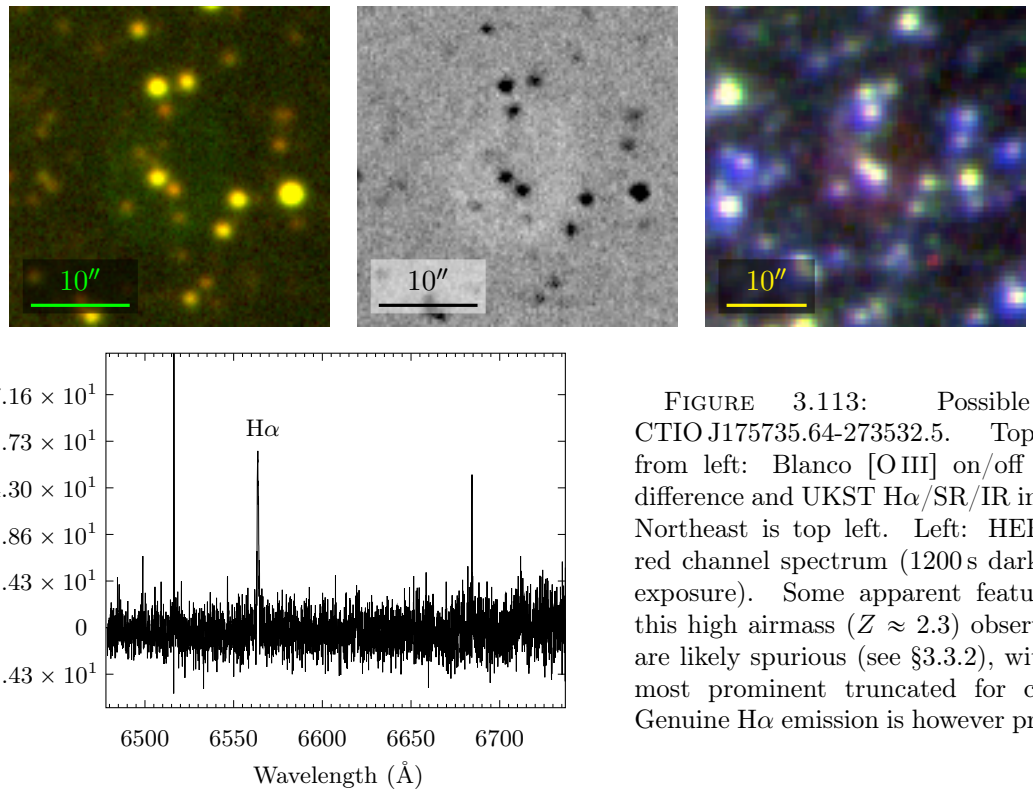

FIGURE 3.113: Possible PN CTIO J175735.64-273532.5. Top row, from left: Blanco [O III] on/off band, difference and UKST Hα/SR/IR images. Northeast is top left. Left: HERMES red channel spectrum (1200 s dark time exposure). Some apparent features of this high airmass ($Z \approx 2.3$) observation are likely spurious (see §3.3.2), with the most prominent truncated for clarity. Genuine Hα emission is however present.

CTIO J175811.57-330701.0

Possible PN CTIO J175811.57-330701.0 is shown in figure 3.114.

CTIO J175836.40-292120.0

Possible PN CTIO J175836.40-292120.0 is shown in figure 3.115.

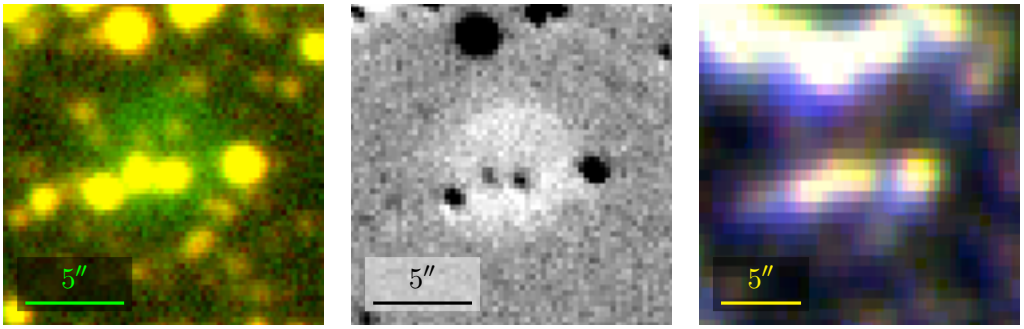

Figure 3.114: Possible PN, CTIO J175811.57-330701.0. From left: Blanco [O III] on/off band, difference and UKST Hα/SR/IR images. Northeast is top left.

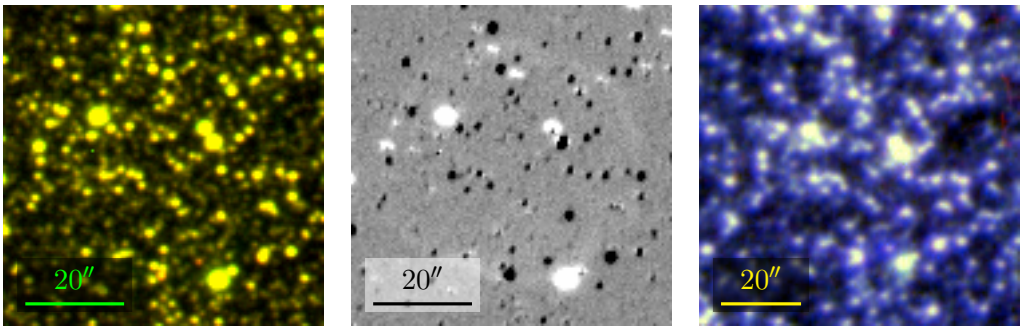

Figure 3.115: Possible PN, CTIO J175836.40-292120.0. From left: Blanco [O III] on/off band, difference and UKST Hα/SR/IR images. Northeast is top left.

CTIO J175850.06-304943.3

Possible PN CTIO J175850.06-304943.3 is shown in figure 3.116.

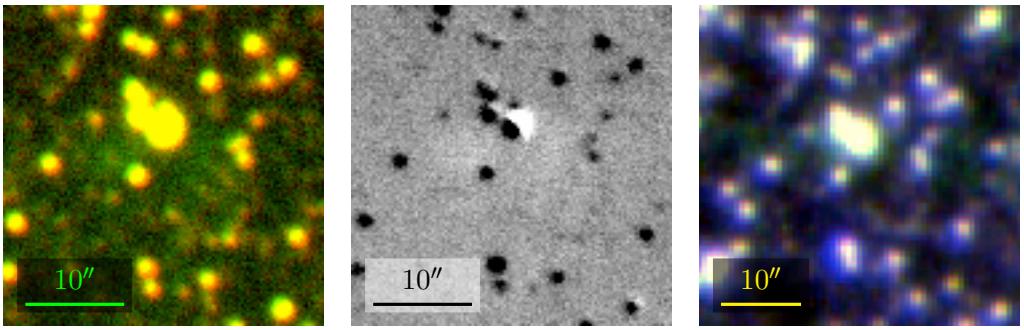

Figure 3.116: Possible PN, CTIO J175850.06-304943.3. From left: Blanco [O III] on/off band, difference and UKST Hα/SR/IR images. Northeast is top left.

CTIO J175904.60-265547.3

Possible PN or mimic CTIO J175904.60-265547.3 is shown in figure 3.117.

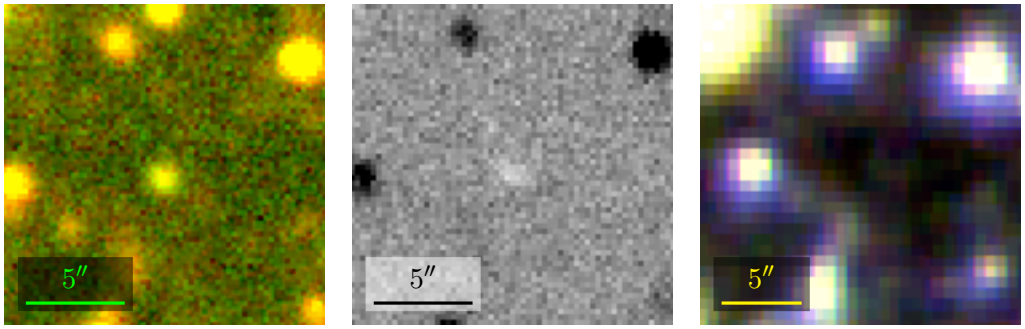

FIGURE 3.117: Possible PN or mimic, CTIO J175904.60-265547.3. From left: Blanco [O III] on/off band, difference and UKST Hα/SR/IR images. Northeast is top left.

CTIO J175919.98-275515.3

Faint PN candidate CTIO J175919.98-275515.3 has been targeted in three 2dF pointings. Corresponding imaging and spectra are given in figure 3.118. A low S/N HERMES spectrum (1200 s dark time exposure) yielded no clear emission line data and is omitted. AAOmega spectroscopy was more successful and is included. The first AAOmega spectrum (3×1200 s grey time exposure), obtained from suboptimal fibre positioning, has been significantly contaminated by a stellar spectrum–significantly enough that it yielded discovery of a new late-type star, SSO J175920.04-275514.1 (§5.2). Aside from the stellar contamination and [O I] λ5577 airglow processing artefact, [O III] λ5007 and Hα emission lines were detected. An unidentified $\lambda \approx 4893$ Å feature, atypical for a PN, is present but does not recur in this object's later spectra.

The second spectrum (4×1200 s dark time exposure) this time avoids a significant stellar contaminant. The blue arm data, aside from an unidentified feature at $\lambda \approx 4402$ Å, exhibits a distinct [O III] λ5007 emission peak, consistent with a PN detection. The red arm data suffers from oversubtracted sky and is of limited value. This oversubtraction is symptomatic of one or more AAOmega sky fibres being accidentally coincident with a faint late-type star, even if only partially. Care was taken to visually inspect planned positions of sky fibres for 2dF pointings, in both the Blanco and 2MASS J band imaging, to ensure stellar coincidence was minimised prior to observation. Care was also taken to ensure sky fibres weren't placed too far from target positions, lest differences in the variable bulge sky background compromise their flux relevance. In this case however it appears this balancing act in the crowded bulge field has been suboptimal, or there has been a data entry error, etc. Nonetheless, it should be noted the relative flux scale varies between the spectra presented and that the magnitude of the red arm sky oversubtraction in the second spectrum should not be misinterpreted.

The spectra obtained, despite having individual weaknesses, when considered as a whole consistently exhibit characteristic PN emission lines. Based on the candidate's round morphology and these characteristic PN emission lines, CTIO J175919.98-275515.3 is assessed a faint possible PN.

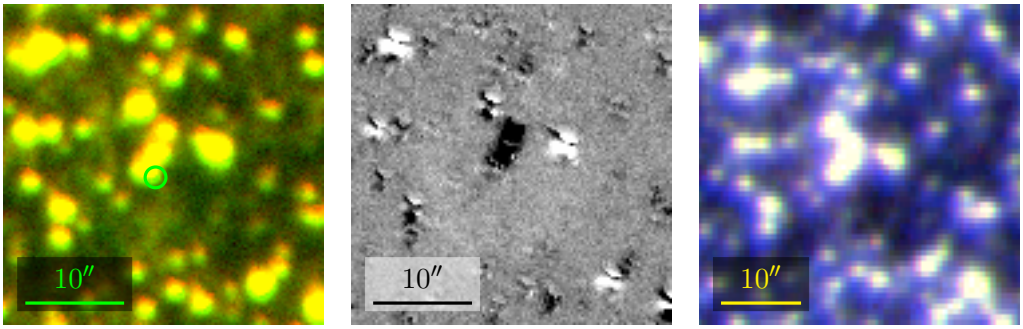

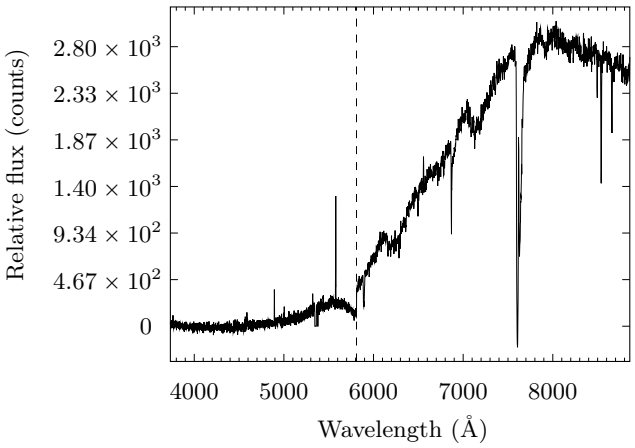

Figure 3.118: Possible PN, CTIO J175919.98-275515.3. Top row, from left: Blanco [O III] on/off band (fibre placement overlaid), difference and UKST Hα/SR/IR images. Northeast is top left. Left: AAOmega spectrum (3 × 1200 s grey time exposure). An [O I] λ5577 airglow processing artefact and significant stellar contaminant are present, but so is faint [O III] λ5007 and Hα emission.

Right: CTIO J175919.98-275515.3 AAOmega spectrum (4 × 1200 s dark time exposure), this time avoiding a significant stellar contaminant. Blue arm data shows a distinct [O III] λ5007 emission peak consistent with a PN detection. Red arm data however suffers oversubtraction of background sky and is of limited value.

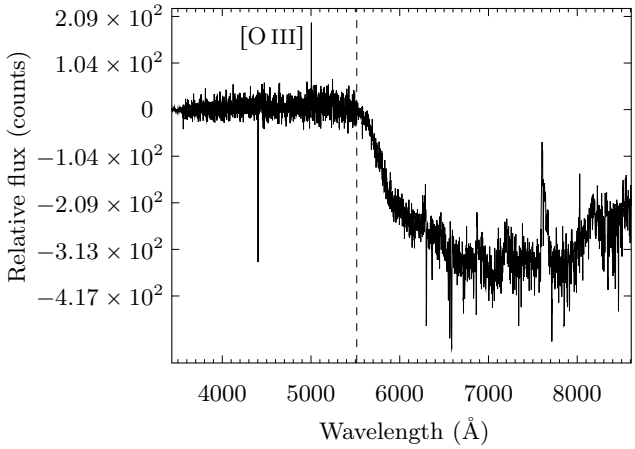

CTIO J175954.11-332453.4

Possible PN CTIO J175954.11-332453.4 is shown in figure 3.119.

CTIO J175955.50-271916.7

Possible PN CTIO J175955.50-271916.7 is shown in figure 3.120.

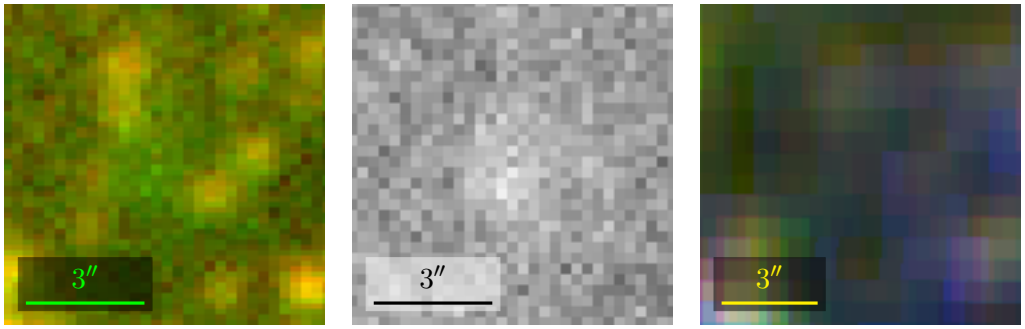

FIGURE 3.119: Possible PN, CTIO J175954.11-332453.4. From left: Blanco [O III] on/off band, difference and UKST Hα/SR/IR images. Northeast is top left.

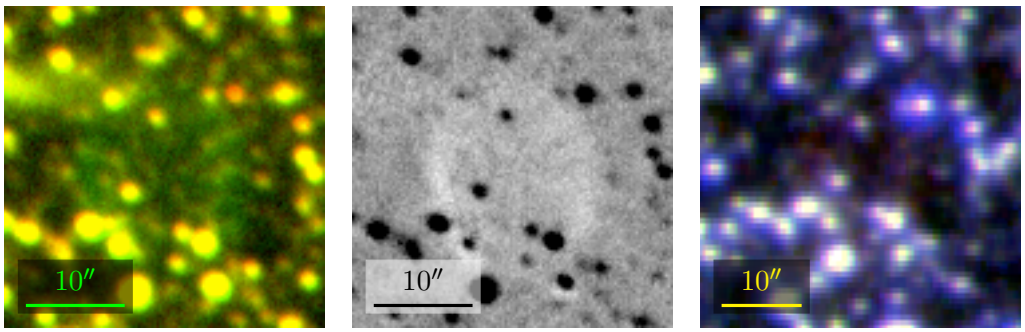

FIGURE 3.120: Possible PN, CTIO J175955.50-271916.7. From left: Blanco [O III] on/off band, difference and UKST Hα/SR/IR images. Northeast is top left.

CTIO J180000.03-302618.5

A spectrum of irregular PN, CTIO J180000.03-302618.5, taken with the Radcliffe 1.9 m telescope (2100 s dark time exposure), is shown in figure 3.121. The object's spectrum exhibits Hα and [N II] $\lambda\lambda$6548, 6583 emission. Deeper spectroscopy is recommended to recover the faint [O III] emission visible in Blanco imaging.

CTIO J180029.12-332834.8

Possible PN CTIO J180029.12-332834.8 is shown in figure 3.122. This is another candidate lying outside the $-5^\circ \leqslant l \leqslant 5^\circ$, $-5^\circ \leqslant b \leqslant 5^\circ$ central bulge region boundary adopted here.

CTIO J180030.42-300952.7

Possible PN CTIO J180030.42-300952.7 is shown in figure 3.123.

CTIO J180056.24-321421.2

Possible PN CTIO J180056.24-321421.2 is shown in figure 3.124.

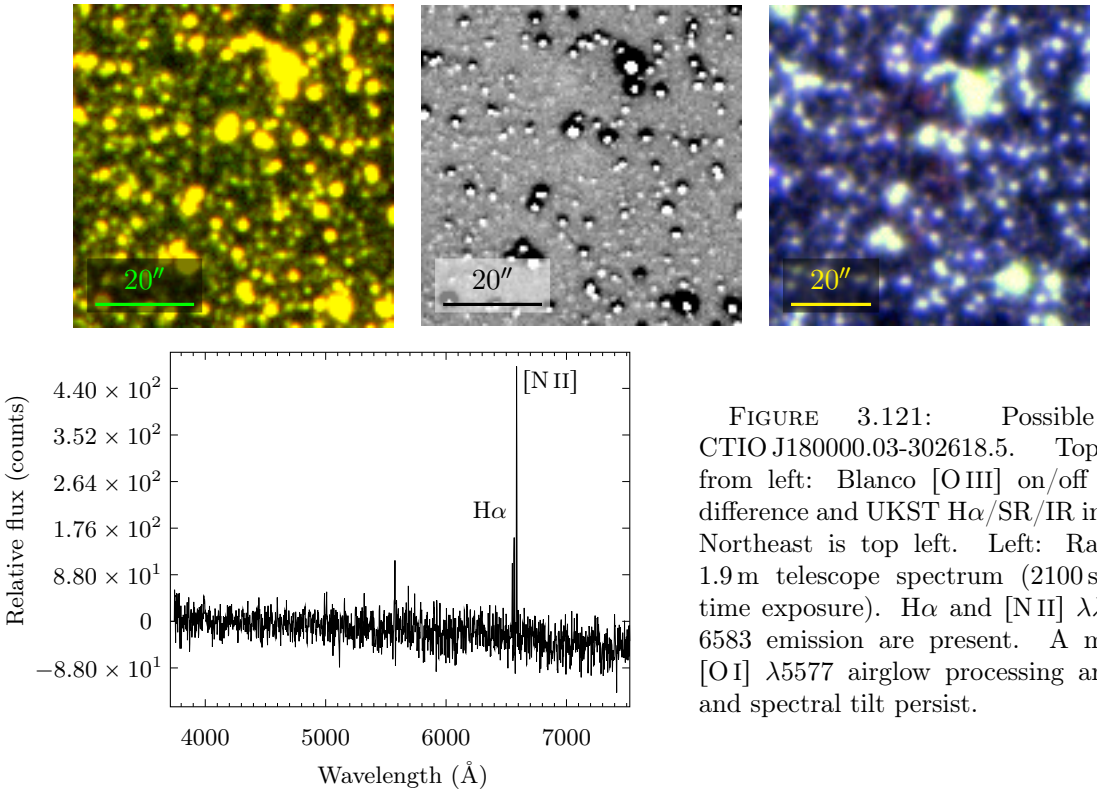

Figure 3.121: Possible PN CTIO J180000.03-302618.5. Top row, from left: Blanco [O III] on/off band, difference and UKST Hα/SR/IR images. Northeast is top left. Left: Radcliffe 1.9 m telescope spectrum (2100 s dark time exposure). Hα and [N II] $\lambda\lambda$6548, 6583 emission are present. A modest [O I] λ5577 airglow processing artefact and spectral tilt persist.

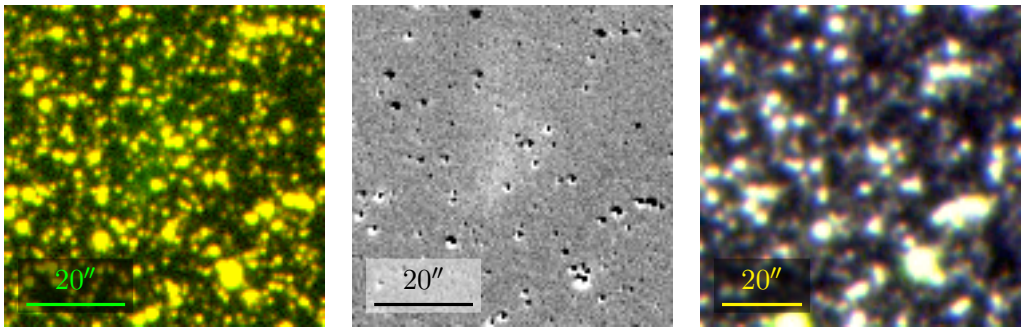

Figure 3.122: Possible PN, CTIO J180029.12-332834.8, lying outside the $-5^\circ \leqslant l \leqslant 5^\circ$, $-5^\circ \leqslant b \leqslant 5^\circ$ central bulge region. From left: Blanco [O III] on/off band, difference and UKST Hα/SR/IR images. Northeast is top left.

CTIO J180056.33-321421.5

Possible faint PN CTIO J180056.33-321421.5, found in imaging at a CCD edge, is shown in figure 3.125.

CTIO J180210.24-295159.3

Possible PN but probable mimic CTIO J180210.24-295159.3 is shown in figure 3.126.

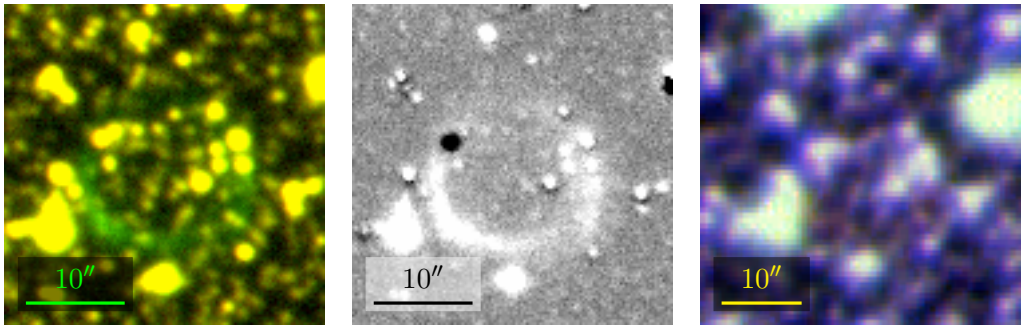

FIGURE 3.123: Possible PN, CTIO J180030.42-300952.7. From left: Blanco [O III] on/off band, difference and UKST Hα/SR/IR images. Northeast is top left.

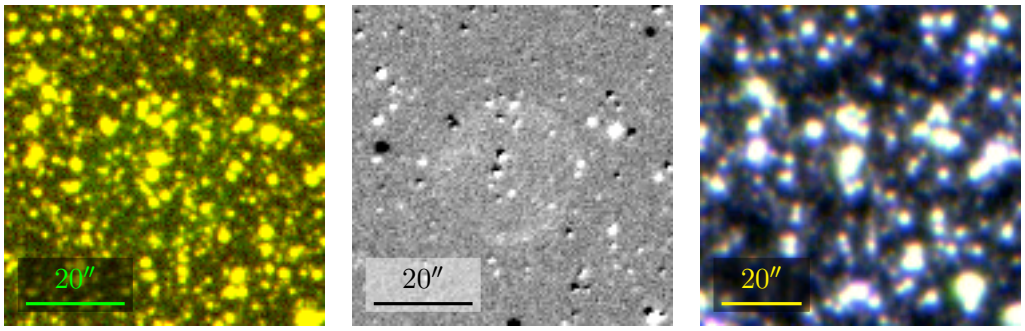

FIGURE 3.124: Possible PN, CTIO J180056.24-321421.2. From left: Blanco [O III] on/off band, difference and UKST Hα/SR/IR images. Northeast is top left.

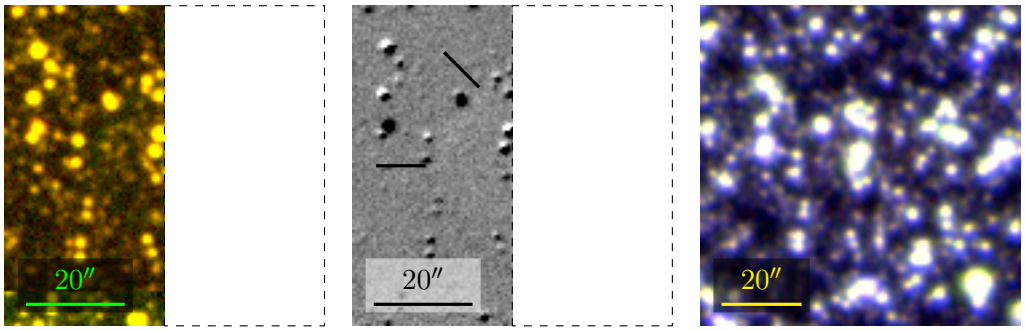

FIGURE 3.125: Possible faint PN, CTIO J180056.33-321421.5, found at the edge of a CCD during imaging review. From left: Blanco [O III] on/off band, difference and UKST Hα/SR/IR images. Northeast is top left.

CTIO J180224.88-302343.7

Possible compact PN but probable mimic, CTIO J180224.88-302343.7, is shown in figure 3.127.

CTIO J180258.75-291347.5

PN candidate CTIO J180258.75-291347.5 appears to be a faint, partially rim-brightened PN in Blanco difference imaging, as given in figure 3.128. An AAOmega spectrum (3×1200 s

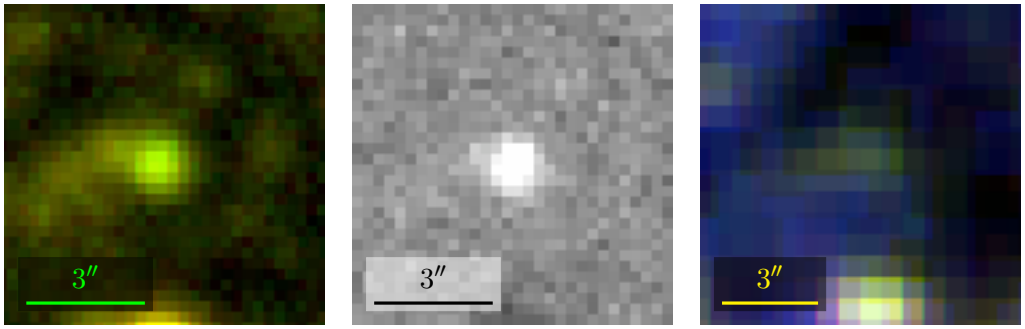

Figure 3.126: Possible PN but probable mimic, CTIO J180210.24-295159.3. From left: Blanco [O III] on/off band, difference and UKST Hα/SR/IR images. Northeast is top left.

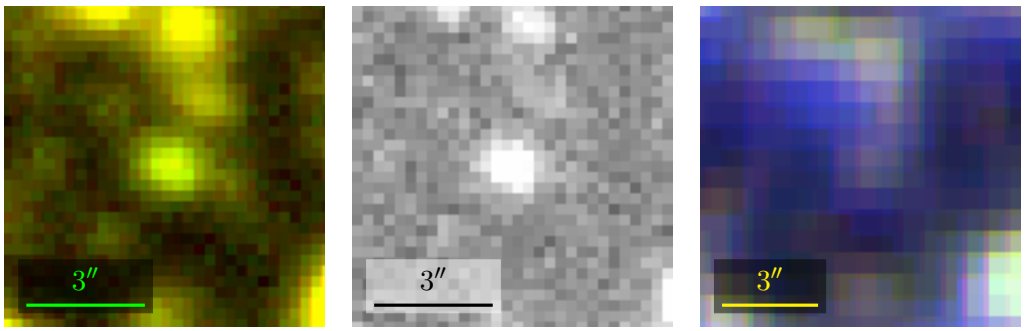

Figure 3.127: Possible compact PN but probable mimic, CTIO J180224.88-302343.7. From left: Blanco [O III] on/off band, difference and UKST Hα/SR/IR images. Northeast is top left.

grey time exposure) was attempted for this candidate, but the relevant fibre placed too closed to a bright coincident star, leaving any faint PN emission lines overwhelmed by the bright stellar contaminant—new late-type star SSO J180258.86-291347.7 (§5.2). The classical PN morphology of this object is used to assess it as a possible PN. Reattempting confirmatory spectroscopy is recommended. The apparent diameter of this object, $\approx(35.3'' \times 35.2'')$, suggests a disc, not bulge nebula.

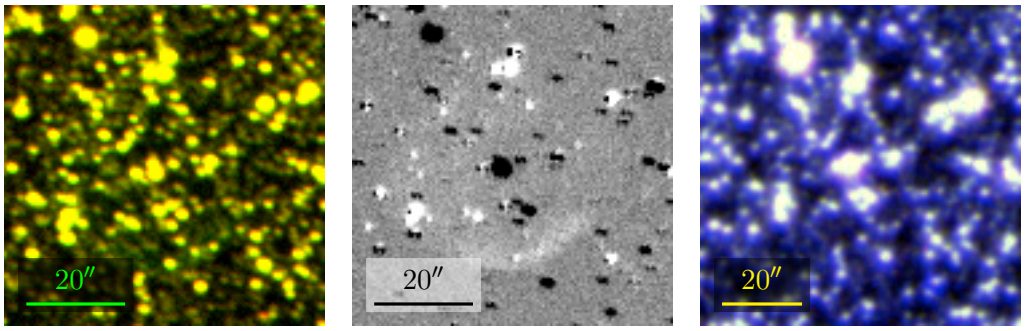

Figure 3.128: Possible round PN CTIO J180258.75-291347.5. From left: Blanco [O III] on/off band, difference and UKST Hα/SR/IR images. Northeast is top left. Suspected rim-brightening is visible along the object's southern edge.

CTIO J180308.22-292038.0

Possible PN CTIO J180308.22-292038.0, partially obscured by a coincident star, is shown in figure 3.129.

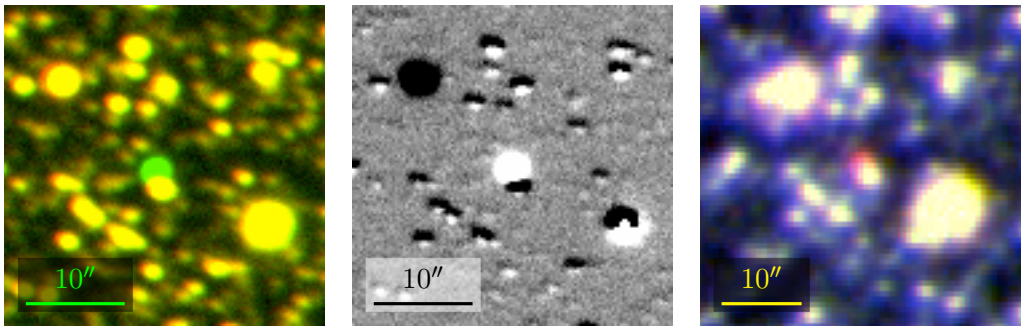

FIGURE 3.129: Possible PN, CTIO J180308.22-292038.0, partially obscured by a coincident star. From left: Blanco [O III] on/off band, difference and UKST Hα/SR/IR images. Northeast is top left.

CTIO J180311.83-262927.0

A spectrum of CTIO J180311.83-262927.0 taken with the Radcliffe 1.9 m telescope (1800 s dark time exposure), is shown in figure 3.130. Aside from a [O I] λ5577 artefact, this spectrum shows clear [O III] λ5007 and Hα emission and is assessed as a possible PN. Deeper spectroscopy is recommended to obtain other typical PN emission lines.

CTIO J180317.18-285627.5

Possible PN but probable mimic CTIO J180317.18-285627.5 is shown in figure 3.131.

CTIO J180325.70-314839.4

Possible PN CTIO J180325.70-314839.4 is shown in figure 3.132.

CTIO J180359.49-311740.8

Possible PN, but probable emission line star CTIO J180359.49-311740.8 is shown in figure 3.133.

CTIO J180410.54-292638.5

Possible PN CTIO J180410.54-292638.5 is shown in figure 3.134.

CTIO J180507.08-264839.2

Possible faint PN CTIO J180507.08-264839.2 is shown in figure 3.135. The brighter western (right-hand) edge of the object, present but difficult to make out in the CTIO difference

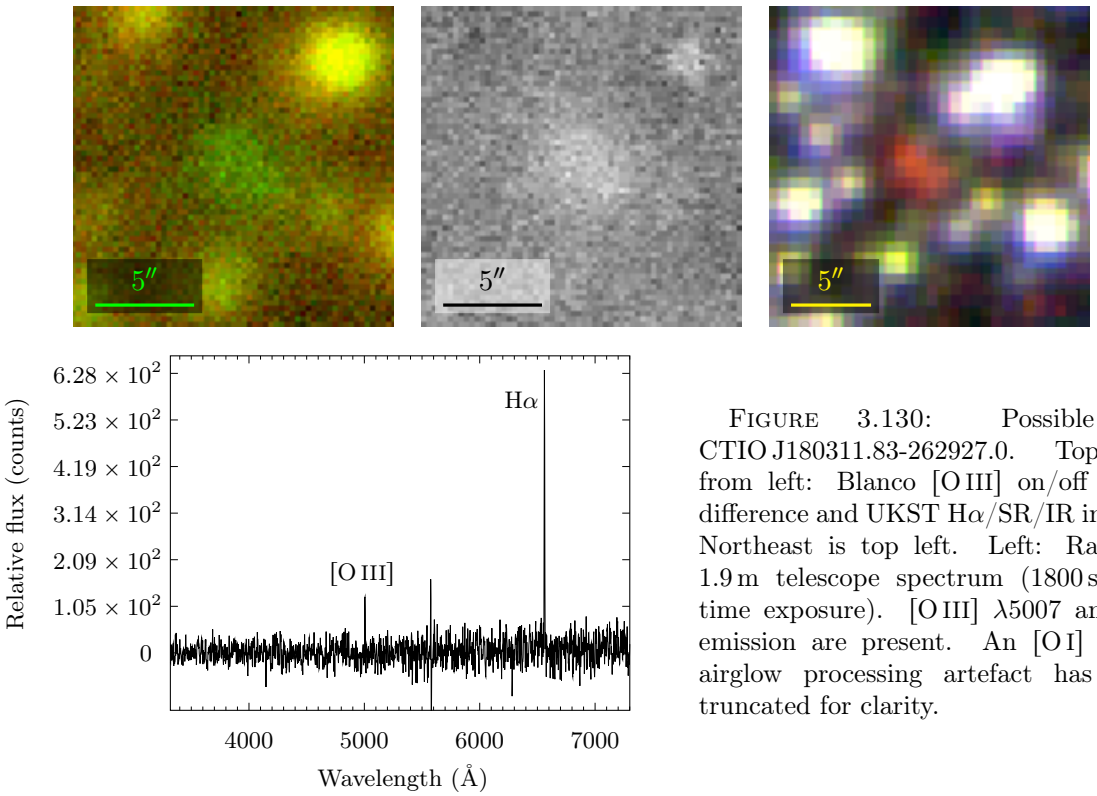

Figure 3.130: Possible PN CTIO J180311.83-262927.0. Top row, from left: Blanco [O III] on/off band, difference and UKST Hα/SR/IR images. Northeast is top left. Left: Radcliffe 1.9 m telescope spectrum (1800 s dark time exposure). [O III] λ5007 and Hα emission are present. An [O I] λ5577 airglow processing artefact has been truncated for clarity.

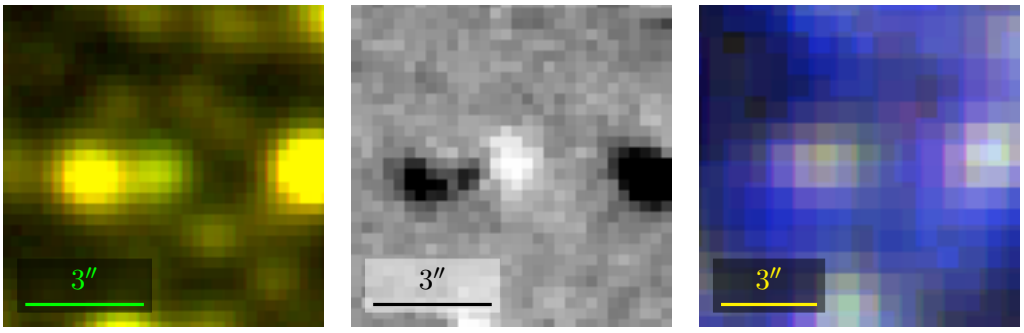

Figure 3.131: Possible PN but probable mimic, CTIO J180317.18-285627.5. From left: Blanco [O III] on/off band, difference and UKST Hα/SR/IR images. Northeast is top left.

image, is more obvious in the UKST image.

CTIO J180555.61-290246.3

Possible PN CTIO J180555.61-290246.3 is shown in figure 3.136.

CTIO J180711.70-262719.2

Possible faint PN CTIO J180711.70-262719.2 is shown in figure 3.137.

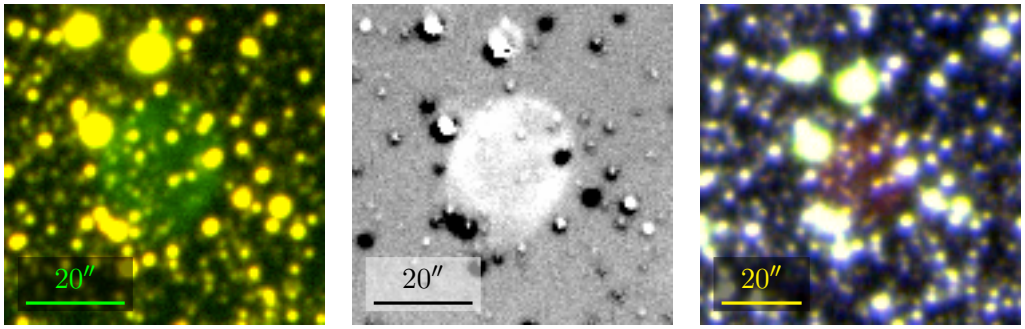

FIGURE 3.132: Possible PN, CTIO J180325.70-314839.4. From left: Blanco [O III] on/off band, difference and UKST Hα/SR/IR images. Northeast is top left.

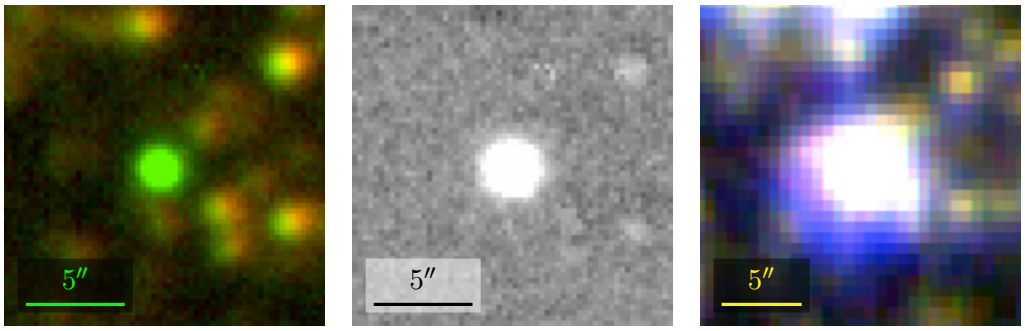

FIGURE 3.133: Possible PN but probable emission line star, CTIO J180359.49-311740.8. From left: Blanco [O III] on/off band, difference and UKST Hα/SR/IR images. Northeast is top left.

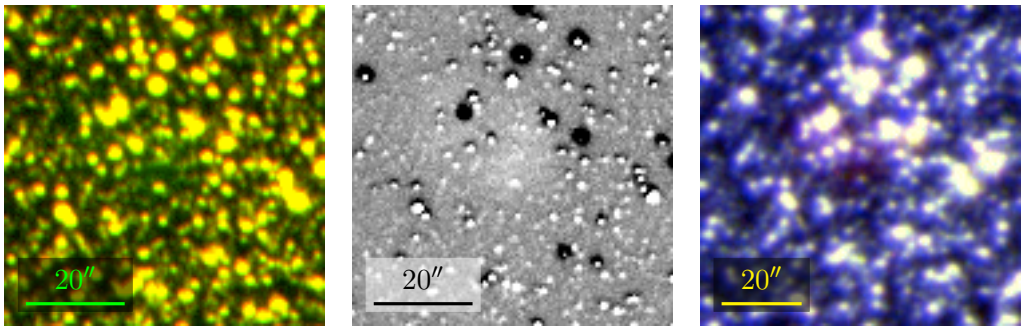

FIGURE 3.134: Possible PN, CTIO J180410.54-292638.5. From left: Blanco [O III] on/off band, difference and UKST Hα/SR/IR images. Northeast is top left.

CTIO J180724.90-290326.0

Possible PN CTIO J180724.90-290326.0 is shown in figure 3.138.

CTIO J180742.79-263104.0

Possible faint PN CTIO J180742.79-263104.0 is shown in figure 3.139.

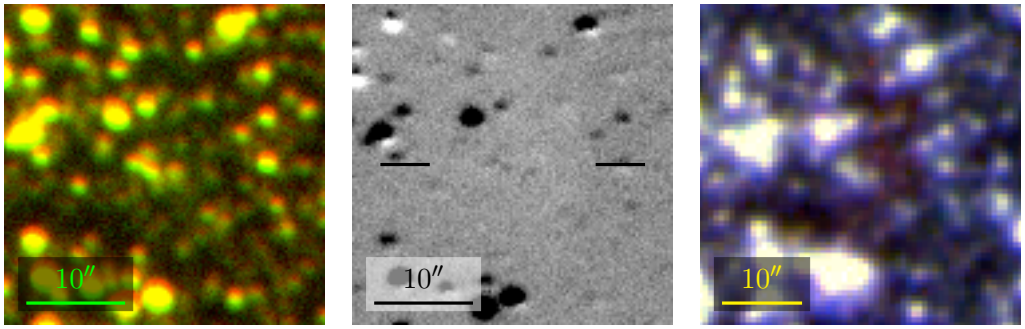

Figure 3.135: Possible faint PN, CTIO J180507.08-264839.2. From left: Blanco [O III] on/off band, difference and UKST Hα/SR/IR images. Northeast is top left.

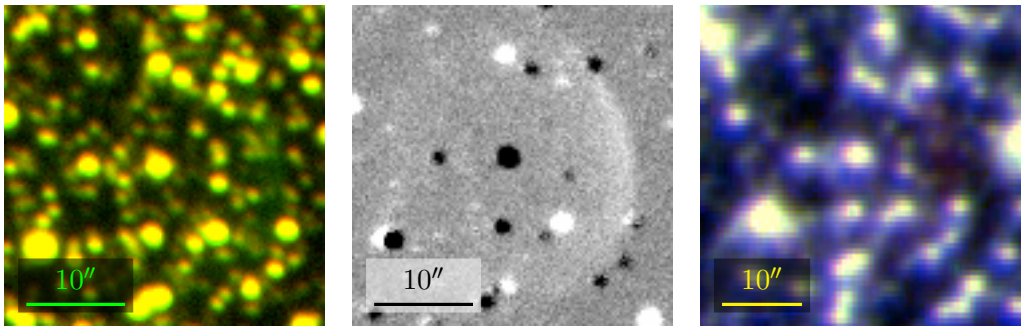

Figure 3.136: Possible PN, CTIO J180555.61-290246.3. From left: Blanco [O III] on/off band, difference and UKST Hα/SR/IR images. Northeast is top left.

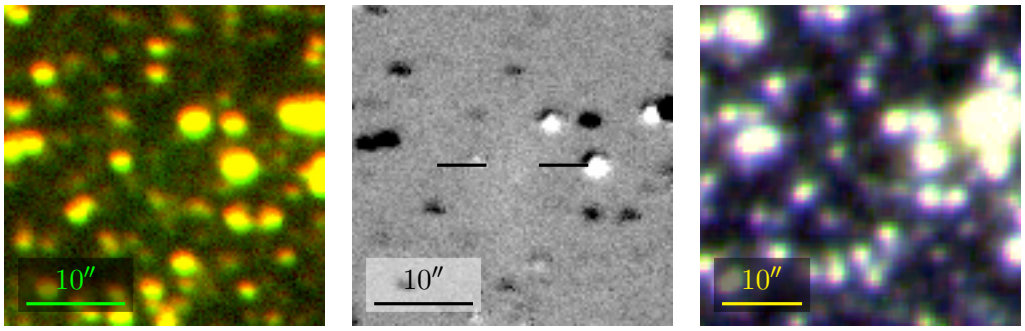

Figure 3.137: Possible faint PN, CTIO J180711.70-262719.2. From left: Blanco [O III] on/off band, difference and UKST Hα/SR/IR images. Northeast is top left.

CTIO J180832.52-284950.6

Possible PN CTIO J180832.52-284950.6 is shown in figure 3.140.

CTIO J180854.57-294441.0

Possible PN CTIO J180854.57-294441.0 is shown in figure 3.141.

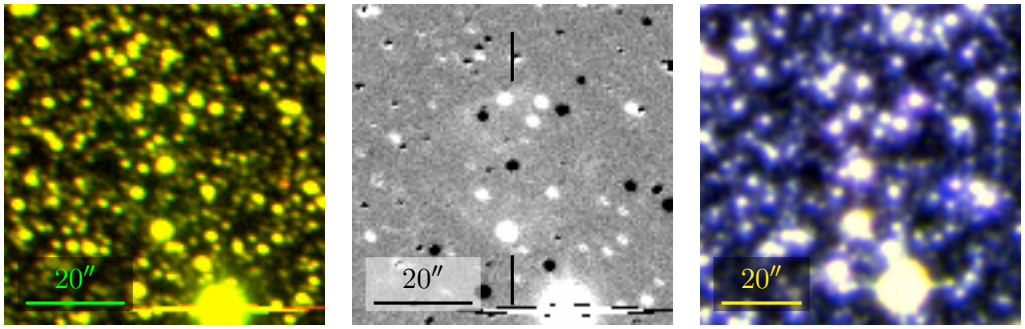

Figure 3.138: Possible PN, CTIO J180724.90-290326.0. From left: Blanco [O III] on/off band, difference and UKST Hα/SR/IR images. Northeast is top left.

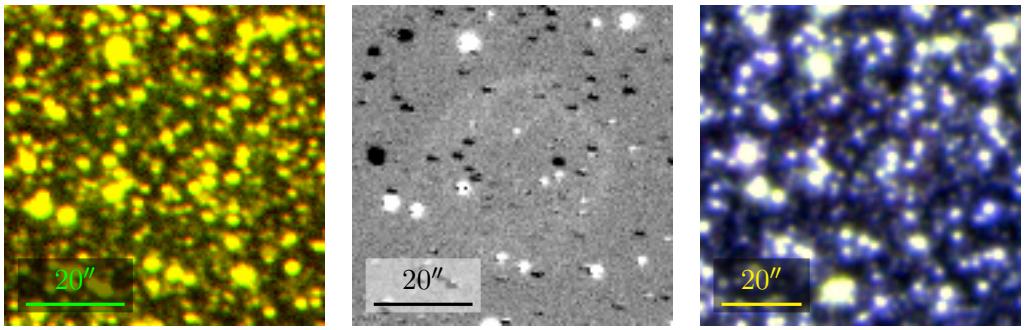

Figure 3.139: Possible faint PN, CTIO J180742.79-263104.0. From left: Blanco [O III] on/off band, difference and UKST Hα/SR/IR images. Northeast is top left.

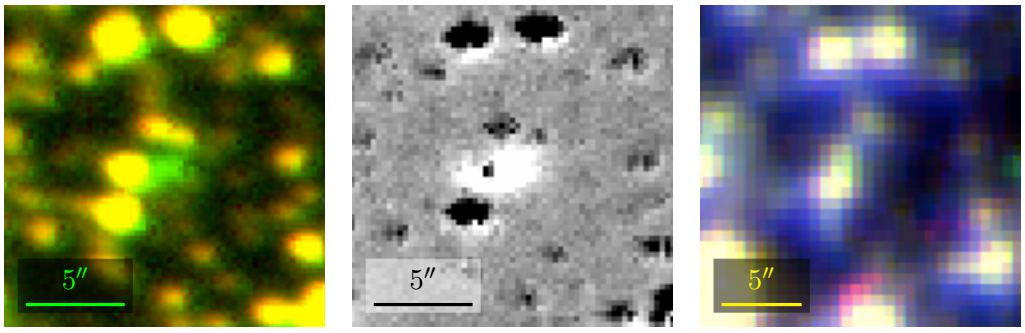

Figure 3.140: Possible PN, CTIO J180832.52-284950.6. From left: Blanco [O III] on/off band, difference and UKST Hα/SR/IR images. The small red feature near the bottom, centre of the UKST image is a miscellaneous artefact. Northeast is top left.

CTIO J181026.15-284016.3

Possible PN CTIO J181026.15-284016.3 is shown in figure 3.142.

CTIO J181057.79-271822.5

Possible PN CTIO J181057.79-271822.5 is shown in figure 3.143.

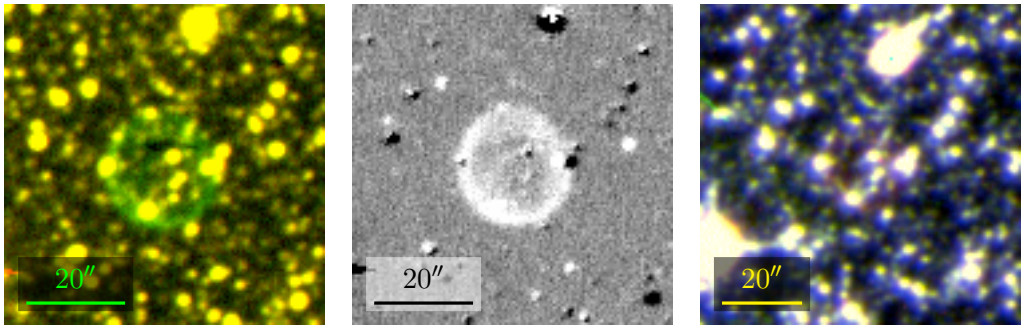

Figure 3.141: Possible PN, CTIO J180854.57-294441.0. From left: Blanco [O III] on/off band, difference and UKST Hα/SR/IR images. Northeast is top left.

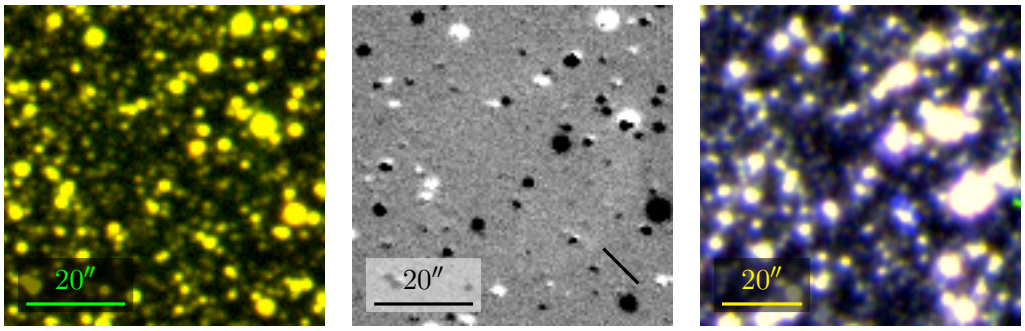

Figure 3.142: Possible PN, CTIO J181026.15-284016.3. From left: Blanco [O III] on/off band, difference and UKST Hα/SR/IR images. Northeast is top left.

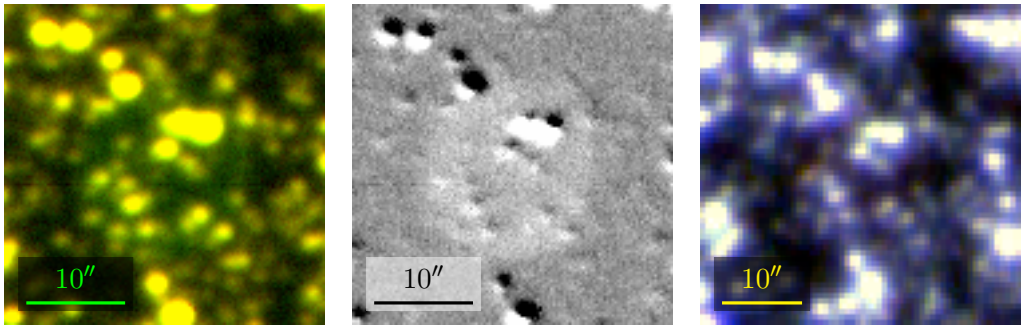

Figure 3.143: Possible PN, CTIO J181057.79-271822.5. From left: Blanco [O III] on/off band, difference and UKST Hα/SR/IR images. Northeast is top left.

CTIO J181120.34-272432.4

Possible PN or mimic CTIO J181120.34-272432.4 is shown in figure 3.144.

3.4.4 PN Mimics

An aim of this investigation was to identify new Galactic bulge PN candidates and spectroscopically confirm or refute them as bona fide PNs. PN candidates subsequently deemed to be PN mimics, as discussed in §3.3, are presented here.

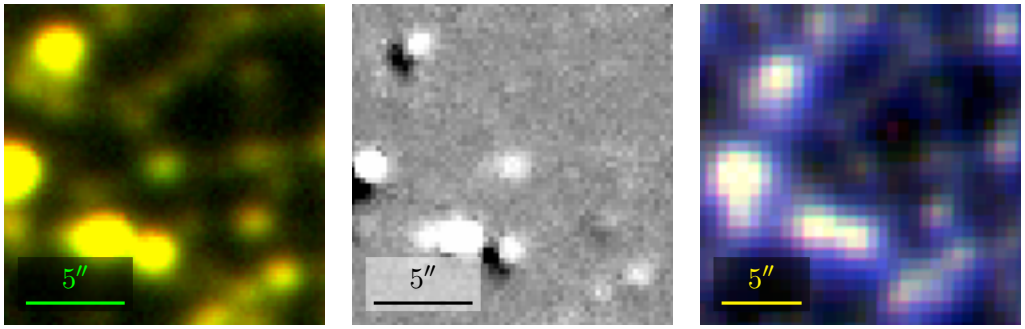

FIGURE 3.144: Possible PN or mimic, CTIO J181120.34-272432.4. From left: Blanco [O III] on/off band, difference and UKST Hα/SR/IR images. Northeast is top left.

358.46+03.54

This object was identified here as a new PN candidate in Mosaic II imaging, only to be discovered, classified (using Belczyński's criteria, Belczyński et al., 2000) and published elsewhere first as a new highly ionised s-type SyS with a M4–6 red giant component (Miszalski et al., 2013). A deeper spectrum was taken by Miszalski et al. (2013), a 1800 s, 3.9 m telescope exposure in grey time versus a 900 s, 1.9 m telescope exposure taken in astronomical twilight during bright time here. The Raman-scattered O VI $\lambda\lambda$6825, 7082 emission bands (Schmid, 1989, Schmid et al., 1999, Birriel et al., 2000) detected by Miszalski et al. (2013) were not obviously detected here for example. The spectrum taken here nonetheless displays a rich variety of emission lines, including Hα, Hβ, Hγ, He I $\lambda\lambda$5876, 6678, 7065, He II λ4686, [N II] λ5755, [O III] $\lambda\lambda$4363, 4959, 5007, [S III] λ6312, [Ar III] λ7136, [Ar V] $\lambda\lambda$6435, 7006, [Ca V] λ5309, [Ca V]/[Fe VII] λ6087, [Fe VI] $\lambda\lambda$5176, 5677 and [Fe VII] λ5721. Imaging and spectra are given in figure 3.145.

IRAS 17292-2805

A spectrum for possible PN candidate IRAS 17292-2805 was obtained with the Radcliffe 1.9 m telescope (average flux of 2 × 600 s dark time exposures) and is shown in figure 3.146. Suspected airglow [O I] artefacts $\lambda\lambda$5577, 6300 appear. Signature PN emission lines, e.g. [O III] λ5007, Hα, [N II] $\lambda\lambda$6548, 6583, [S II] $\lambda\lambda$6716, 6731, are superimposed over a late-type stellar spectrum. This mimic is a suspected SyS but further analysis is recommended.

IRAS 17393-2435

IR object IRAS 17393-2435 is a PN mimic. A Radcliffe 1.9 m telescope spectrum (900 s dark time, astronomical and nautical twilight exposure) is shown in figure 3.147. The spectrum shows Hα, Hβ and [O III] $\lambda\lambda$4959, 5007 overlapping a stellar spectrum. This suggests a SyS or other emission line star. The two apparent prominent emission lines bracketing Hβ are suspected to be unsubtracted cosmics, missed during reduction due to coincidence with the

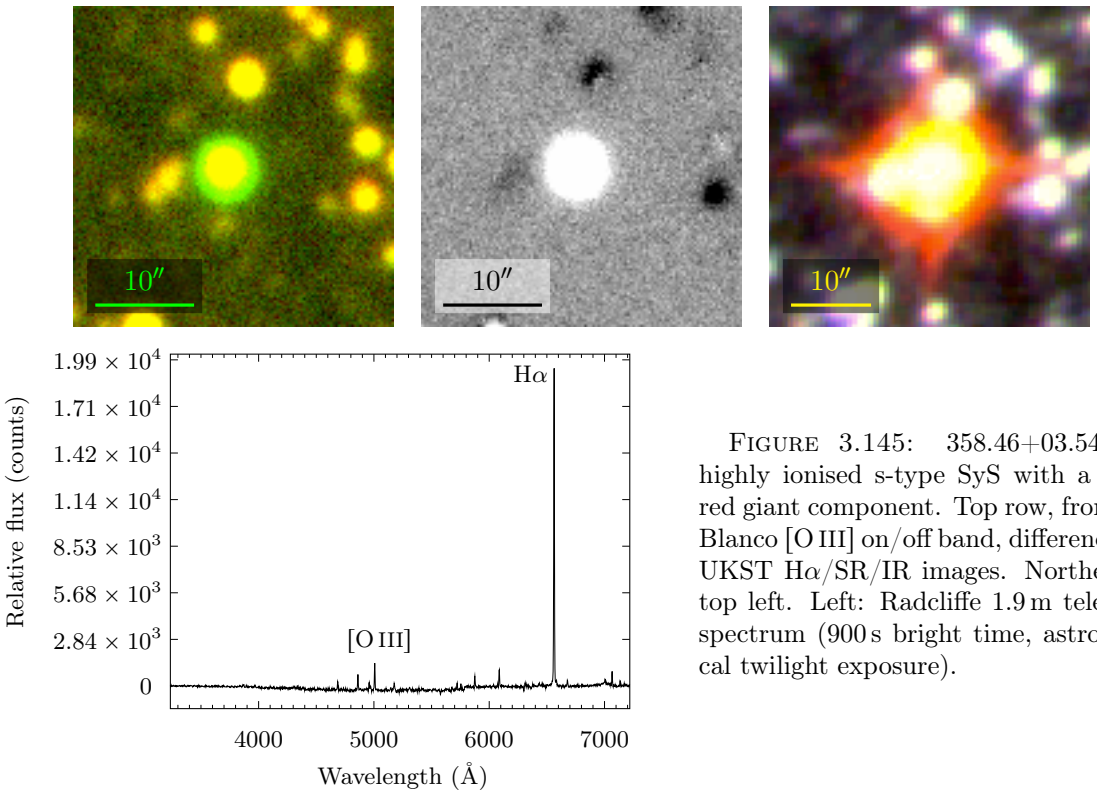

Figure 3.145: 358.46+03.54. A highly ionised s-type SyS with a M4–6 red giant component. Top row, from left: Blanco [O III] on/off band, difference and UKST Hα/SR/IR images. Northeast is top left. Left: Radcliffe 1.9 m telescope spectrum (900 s bright time, astronomical twilight exposure).

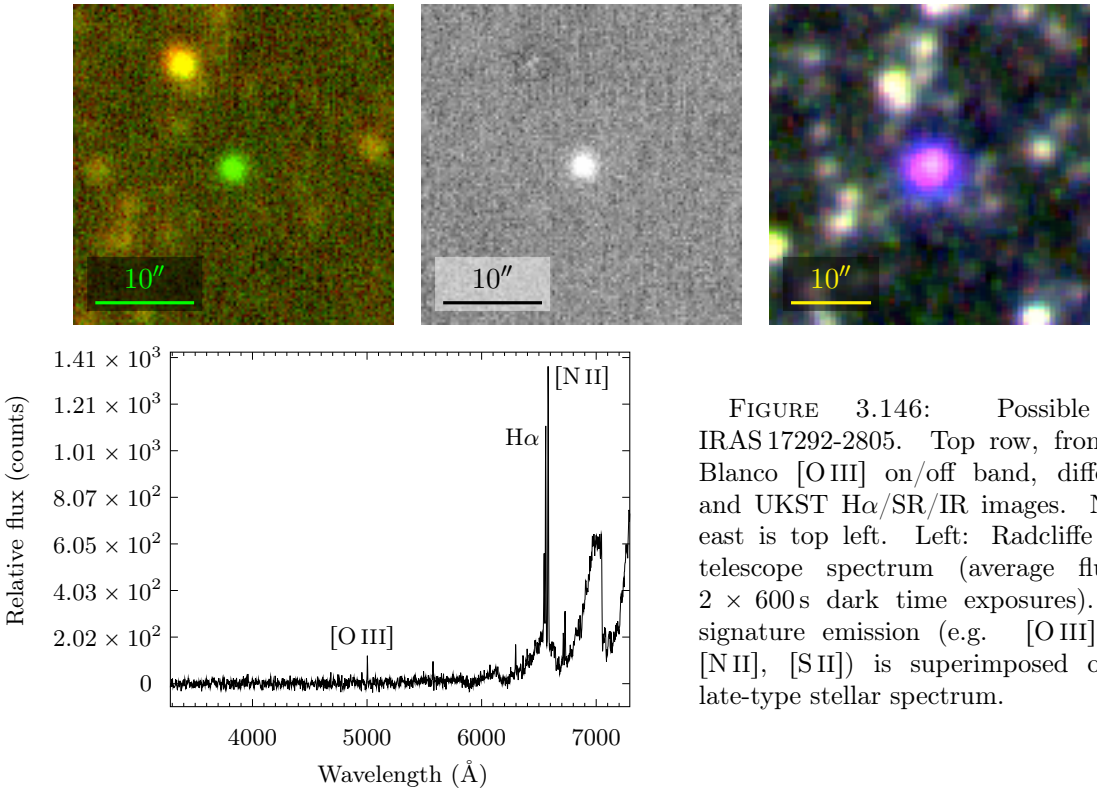

Figure 3.146: Possible SyS IRAS 17292-2805. Top row, from left: Blanco [O III] on/off band, difference and UKST Hα/SR/IR images. Northeast is top left. Left: Radcliffe 1.9 m telescope spectrum (average flux of 2 × 600 s dark time exposures). PN signature emission (e.g. [O III], Hα, [N II], [S II]) is superimposed over a late-type stellar spectrum.

object spectrum. Reobservation of this object is recommended to resolve this issue.

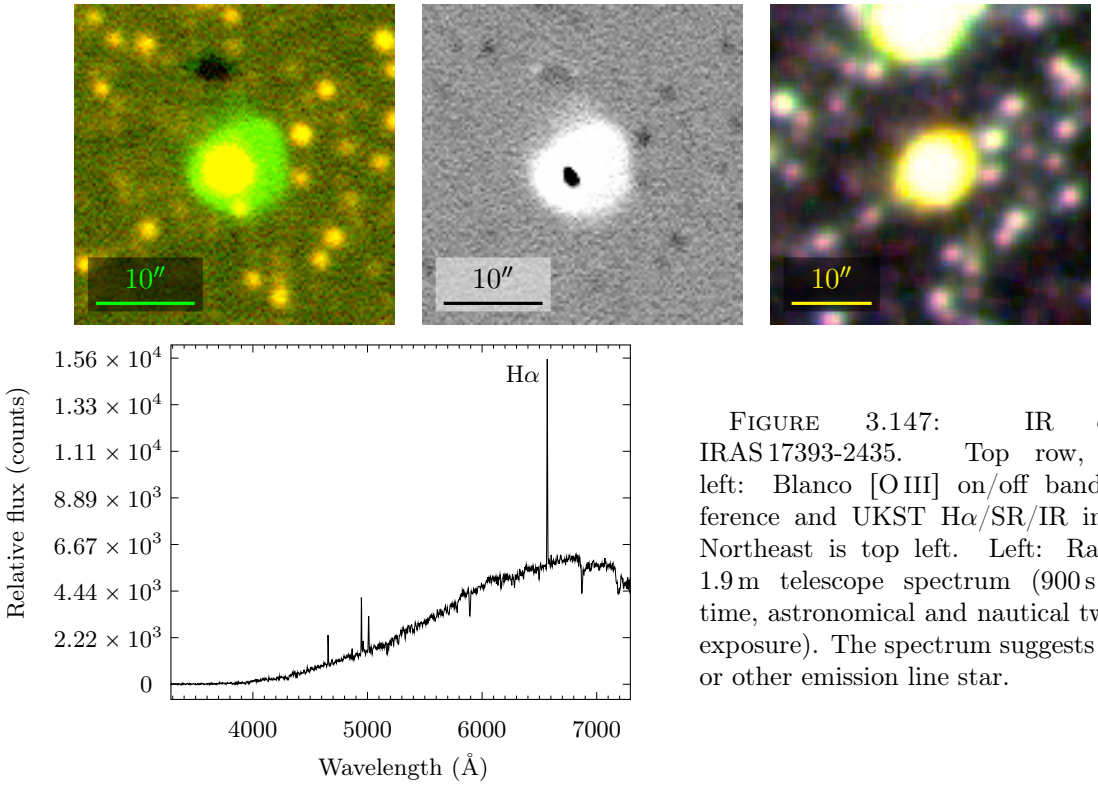

FIGURE 3.147: IR object IRAS 17393-2435. Top row, from left: Blanco [O III] on/off band, difference and UKST Hα/SR/IR images. Northeast is top left. Left: Radcliffe 1.9 m telescope spectrum (900 s dark time, astronomical and nautical twilight exposure). The spectrum suggests a SyS or other emission line star.

CTIO J174941.81-341135.0

This emission line object, shown in figure 3.148, displays features unique amongst the PN candidate pool. At first glance, Blanco imaging indicates the object is a possible compact PN. The UKST imaging however displays an additional unusual enveloping nebula.

A Radcliffe 1.9 m telescope spectrum (900 s dark time, astronomical twilight exposure) failed to return viable data for this object. An AAOmega (3 × 1200 s dark time exposure) spectrum however, shown in figure 3.148, did. In this case, the relevant fibre targeted the apparent centre of the [O III] λ5007 emission. [O I] λ5577 airglow and assumed miscellaneous far blue and far red reduction processing artefacts have been truncated for clarity.

This object appears to consist of a central emission line star surrounded by a larger nebula. The object's spectrum indicates continuum emission consistent with the central body being a star rather than a compact PN. This star itself is presumed to be an emission line object on the basis of the Blanco imaging, though no [O III] λ5007 emission is recovered in its spectrum.

The enveloping nebula's green appearance in the UKST panel of figure 3.148 indicates it is a SR but not [O III], Hα or near-IR emitter. The UKST image thus conflicts with the presence of Hα emission in the spectrum. It is noted the enveloping nebula is not round, but probably of a more complex morphology subject to morpho-inclination degeneracy. In addition, although not obvious from the scale of figure 3.148, the object's Hα emission is split

into two broad components ($\Delta\lambda_{\text{peak}} \approx 16 \pm 5$ Å), consistent with a high nebula expansion velocity, v. Assuming equation 3.6,

$$v = \frac{|\lambda_1 - \lambda_2|}{\lambda_1 + \lambda_2} c, \tag{3.6}$$

where λ_1, λ_2 are the split emission peaks and c is the speed of light in air[16], this corresponds to $v \approx 364 \pm 115\,\mathrm{km\,s^{-1}}$. This is much faster than a typical PN expansion (e.g. $25\,\mathrm{km\,s^{-1}}$, §1.1), but slower than a typical nova ($\sim 10^3\,\mathrm{km\,s^{-1}}$) or supernova ($\sim 10^3$–$10^4\,\mathrm{km\,s^{-1}}$) shell (Osterbrock & Ferland, 2006, Bode & Evans, 2008). Slow nova shells are however known, e.g. V723 Cas ($332 \pm 17\,\mathrm{km\,s^{-1}}$, Evans et al., 2003), and the UKST imaging of the system somewhat resembles Hα + [N II] imaging of other nova shells such as CP Pup, or especially, V842 Cen (Gill & O'Brien, 1998).

On the basis of imaging and spectral evidence, composite object CTIO J174941.81-341135.0 is assessed a PN mimic, possibly a nova. Deeper additional spectroscopy is recommended to resolve the inconsistencies between the object's extant imaging and spectral data, and to discern its true nature.

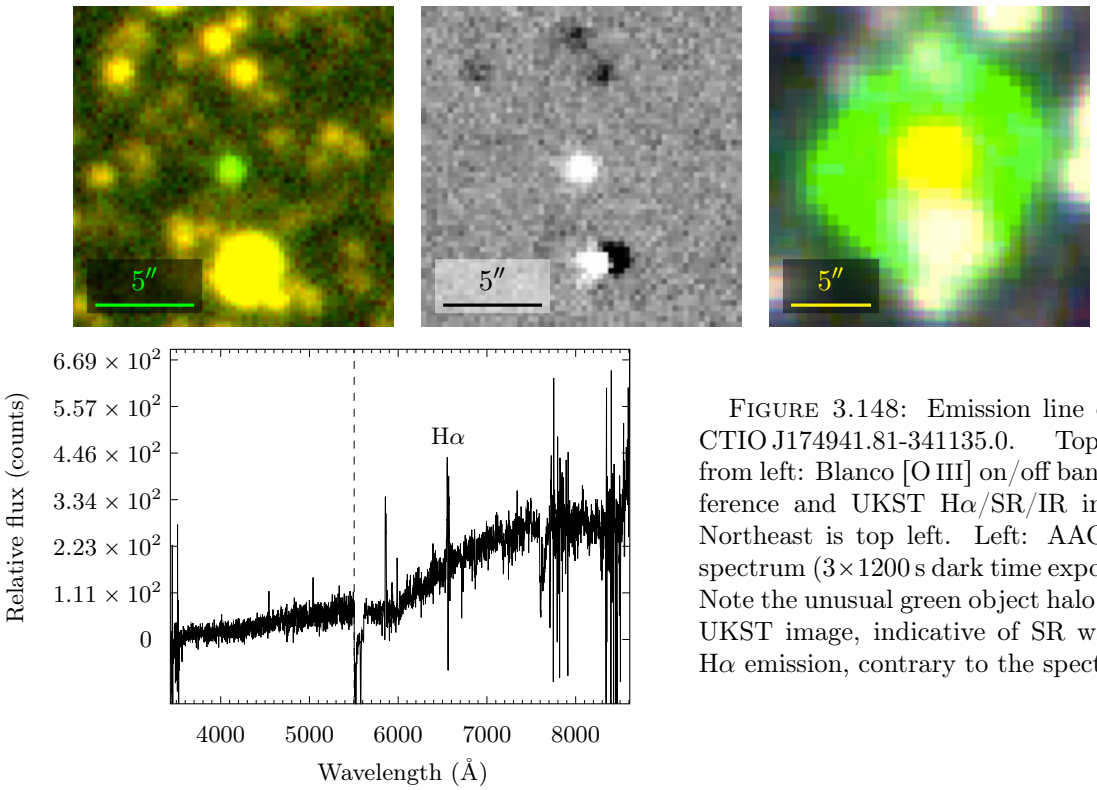

Figure 3.148: Emission line object CTIO J174941.81-341135.0. Top row, from left: Blanco [O III] on/off band, difference and UKST Hα/SR/IR images. Northeast is top left. Left: AAOmega spectrum (3×1200 s dark time exposure). Note the unusual green object halo in the UKST image, indicative of SR without Hα emission, contrary to the spectrum.

[16]Derived from a vacuum speed of $299\,792\,458\,\mathrm{m\,s^{-1}}$ and a refractive index of standard air at $\lambda = 660$ Å of $n = 1.00027621$ (Haynes, 2014).

CTIO J175024.35-285312.2

CTIO J175024.35-285312.2 is coincident with, albeit on a small scale, a molecular bubble [CWP2007] CN 16 (Churchwell et al., 2007), cluster [DB2002] 11 (Dutra & Bica, 2000) and H II region association, but more generally with a larger molecular complex (Gennaro et al., 2012). Blanco [O III] on/off band, difference and UKST imaging, along with an AAOmega spectrum (3×1800 s grey time exposure) are given in figure 3.149. Presumed Hα emission dominates most of the UKST image, overwhelming the discrete emission area visible in Blanco imaging. Viewed on the relevant scale, the AAOmega spectrum unambiguously recovers the [O III] emission seen in the Blanco imaging, but is also clearly dominated by Hα emission. Aside from an assumed [O I] λ5577 airglow processing artefact, emission lines detected include at least [Ar III] $\lambda\lambda$7136, 7751, He I $\lambda\lambda$5876, 6678, 7065, [N II] $\lambda\lambda$6548, 6583, [O III] $\lambda\lambda$4959, 5007, [S II] $\lambda\lambda$6716, 6731, the Balmer series from Hα to Hδ and possible H I $\lambda\lambda$8502, 8545, 8598, 8665, 8751.

CTIO J175024.35-285312.2, as it appears in Blanco imaging, is probably a small [O III]-ionised component of a larger H II region. Every emission line detected, including the tentative far red H I lines, are known in H II regions (e.g. in M 42[17], Osterbrock et al., 1992)[18]. NVSS 1.4 GHz continuum flux contours (Gennaro et al., 2012) and UKST imaging place CTIO J175024.35-285312.2 in a region of local nebula (radio and Hα) brightness, potentially due to ionisation and heating from early-type stars such as, here, the early B-type star [GBB2012] E1 (Gennaro et al., 2012).

CTIO J175024.35-285312.2 is probably the H II region associated with [CWP2007] CN 16 by Gennaro et al. (2012), likely [CAB2011] G0.57-0.85 (Culverhouse et al., 2011), though multiple H II regions may exist within the same molecular complex. It is noted CTIO J175024.35-285312.2, as seen at alternate scale in UKST imaging in figure 3.150, is of dimensions and morphology commensurate with *Spitzer* IR emission of the entire molecular complex (e.g., Gennaro et al., 2012).

SHS J175055.57-305224.0

Unique amongst the PN candidates evaluated here, SHS J175055.57-305224.0 wasn't discovered from inspection of CTIO Mosaic II imaging. Instead, it was noticed in SHS imaging nearby CTIO J175051.08-305206.5 (thus a SHS prefix, consistent with the nomenclature conventions adopted for other new emission line objects presented here). CTIO J175051.08-305206.5 was already near the edge of a Mosaic II frame and SHS J175055.57-305224.0 beyond it, so no evaluation of this candidate in terms of [O III] imaging was made. Nonetheless, as an apparently distinct Hα source, spectra for it were taken with the Radcliffe 1.9 m telescope (1200 s bright time and 900 s dark time exposures).

This object's spectra were of very low S/N. No emission lines were obvious. There was

[17] Messier (1781)

[18] It is assumed the Osterbrock et al. (1992) reference to [Ne II] λ6583 should have read [N II] λ6583.

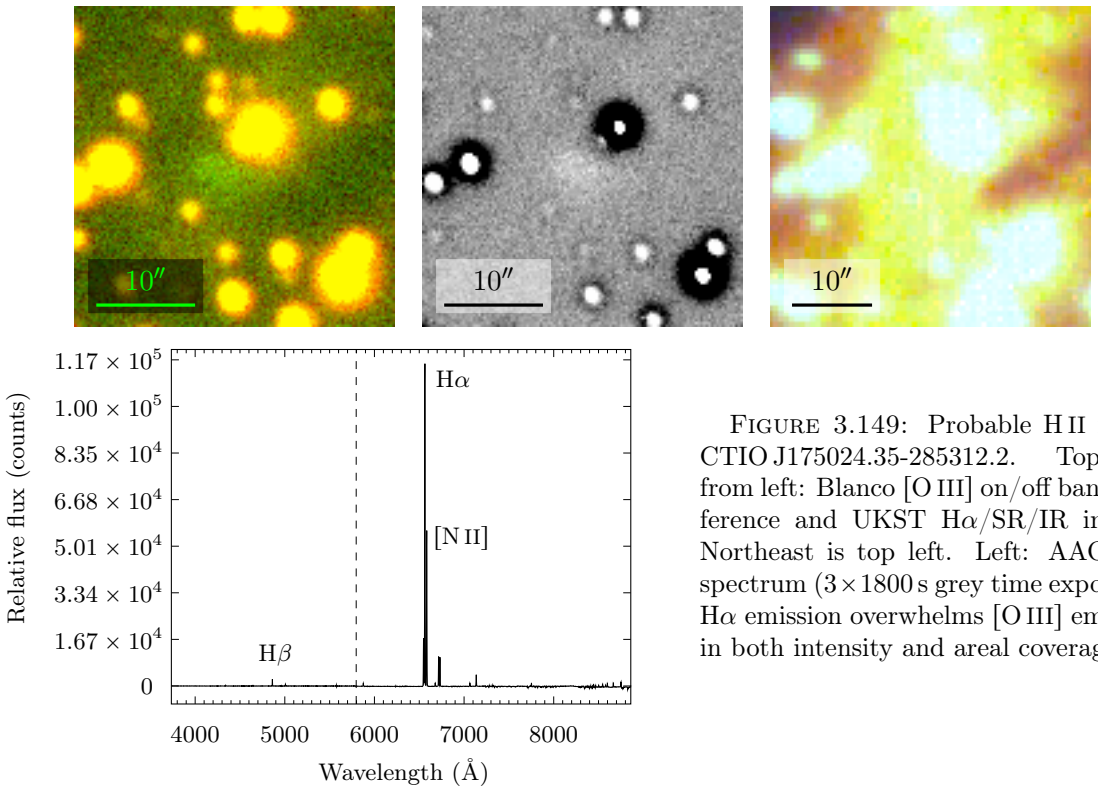

Figure 3.149: Probable H II region CTIO J175024.35-285312.2. Top row, from left: Blanco [O III] on/off band, difference and UKST Hα/SR/IR images. Northeast is top left. Left: AAOmega spectrum (3×1800 s grey time exposure). Hα emission overwhelms [O III] emission in both intensity and areal coverage.

a probable TiO λ7054 band, characteristic of a M-type star. The stellar morphology and magenta appearance of this object in UKST imaging, shown in figure 3.151, are also consistent with a M-type star. In the synthetic RGB colour scheme used for UKST data here, the magenta colour is an additive product of strong Hα (red) and IR (blue) emission. The apparent Hα emission prominent in the UKST imaging may correspond to a M-type sawtooth continuum peak. Had UKST Hα/SR/IR data, rather than just Hα/SR data, been used for initial candidate identification, it is less likely it would have been deemed a PN candidate. Indeed an example M-type giant with continuum peak $\sim\lambda$6550 is explicitly listed as potential PN mimic if observed through a narrow band Hα filter by Frew & Parker (2010). Additionally, this object may feature real, even variable intensity, Hα emission superimposed over a M-type spectrum, such as that of T Coronae Borealis (Kenyon & Fernandez-Castro, 1987, Zamanov et al., 2005). Deeper spectroscopy of this object is recommended for a definitive classification.

CTIO J175110.13-340529.8

Observational evidence suggests compact object CTIO J175110.13-340529.8 is an emission line star. An AAOmega spectrum (3 × 1200 s dark time exposure) for this object, shown in figure 3.152, doesn't exhibit the presumed [O III] λ5007 emission visible in Blanco imaging, but does show the typical PN emission lines Hα and [N II] λ6583 superimposed over a faint stellar spectrum. An [O I] λ5575 airglow processing artefact is manifest here as an artificial absorption feature. Deeper spectroscopy is recommended to better assess this object's nature.

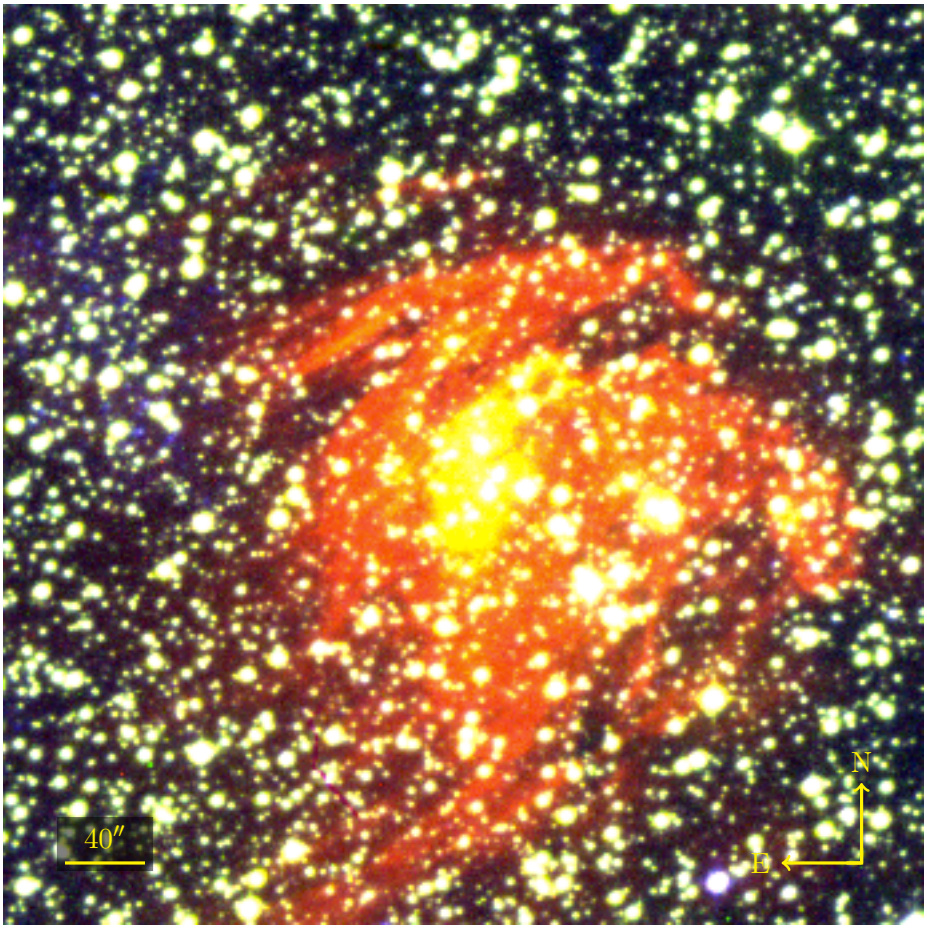

FIGURE 3.150: UKST Hα/SR/IR image showing large scale features of probable H II region CTIO J175024.35-285312.2 within the larger molecular complex encompassing molecular bubbles [CWP2007] CN 15/16/17 (Churchwell et al., 2007, Gennaro et al., 2012). The image is shown centred on the same sky coordinates, but at 1/4 scale, as figure 3.149.

CTIO J175115.83-332447.3

Faint, compact object CTIO J175115.83-332447.3 is shown in imaging in figure 3.153, though difficult to discern. An AAOmega spectrum (3 × 1200 s dark time exposure) taken of this object was of very low S/N and yielded little of diagnostic value. Possible Hα and [O III] λ5007 emission were present, but not unambiguously above the level of background noise. The object's continuum spectral profile did however increase slightly towards the red. This redward increase, in combination with its compact, stellar-like morphology and slight [O III] λ5007 brightness in Blanco imaging, is most consistent with CTIO J175115.83-332447.3 being a faint emission line star. Deeper spectroscopy is however needed before the nature of CTIO J175115.83-332447.3 can be established.

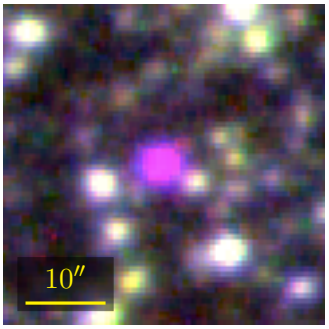

Figure 3.151: Suspected M-type star SHS J175055.57-305224.0. UKST Hα/SR/IR image. Its IR brightness and Radcliffe 1.9 m telescope (visible) spectroscopy are consistent with a M-type star rather than a PN. Northeast is top left.

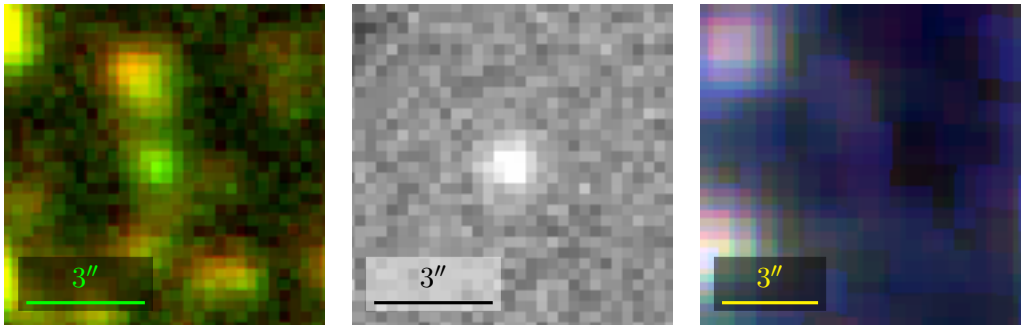

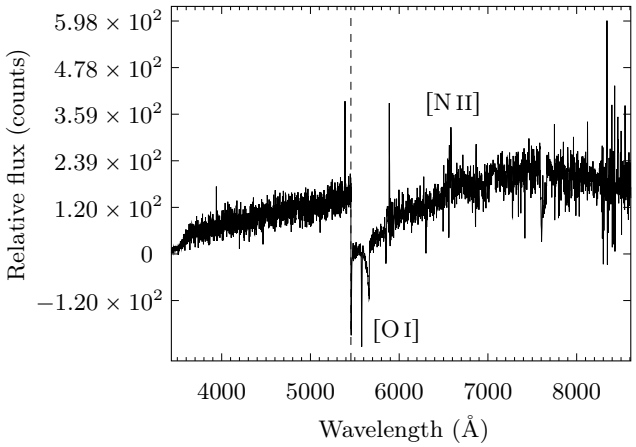

Figure 3.152: PN mimic CTIO J175110.13-340529.8. Top row, from left: Blanco [O III] on/off band, difference and UKST Hα/SR/IR images. Northeast is top left. Left: AAOmega spectrum (3 × 1200 s dark time exposure). In the red arm, Hα and [N II] λ6583 emission are present. In the blue arm, the presumed [O III] emission visible in Blanco imaging is absent.

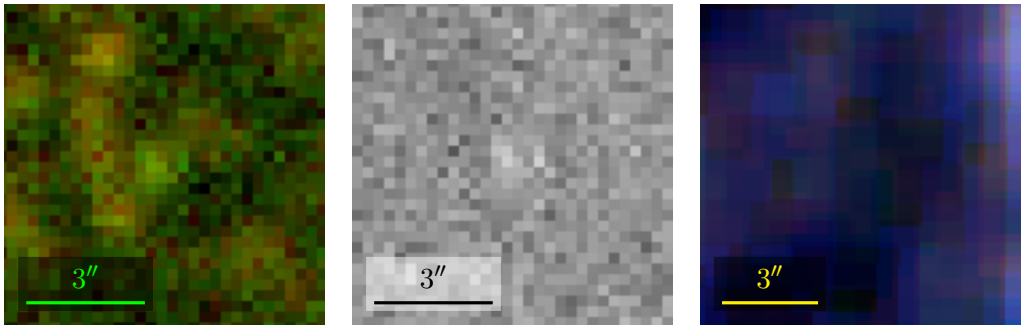

Figure 3.153: Suspected faint emission line star CTIO J175115.83-332447.3. From left: Blanco [O III] on/off band, difference and UKST Hα/SR/IR images. Northeast is top left.

CTIO J175208.32-343607.0

CTIO J175208.32-343607.0 is a probable emission line star. Blanco and UKST imaging, along with a low S/N AAOmega spectrum (3 × 1200 s dark time exposure), are shown in figure 3.154. The spectrum is marred by an [O I] λ6300 airglow processing artefact, but more significantly by assumed miscellaneous reduction processing artefacts, especially in the far red, though these are truncated for clarity. Nonetheless, emission lines including Hα, Hβ, [N II] $\lambda\lambda$6548, 6583 and [S II] $\lambda\lambda$6716, 6731 are superimposed over a stellar spectrum. The faint [O III] λ5007 emission visible in Blanco imaging that prompted investigation of this object, isn't obvious in the spectrum obtained. It is anticipated [O III] emission lines would be recoverable from deeper spectroscopy.

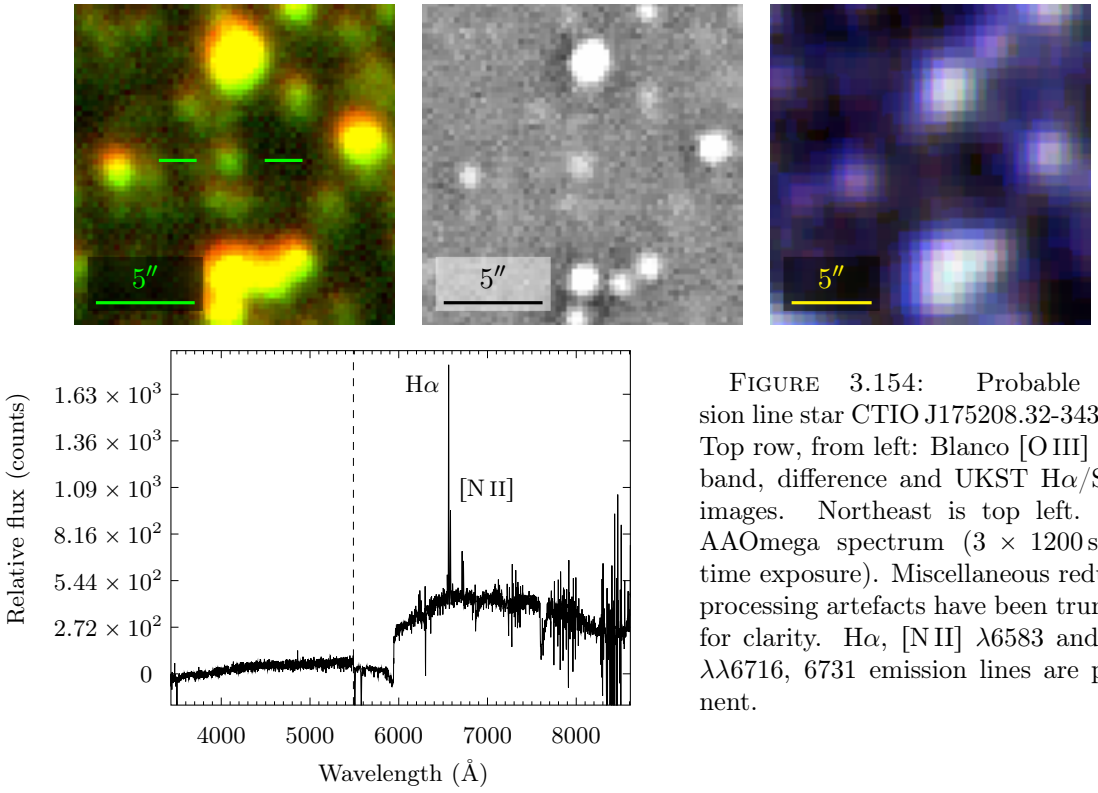

FIGURE 3.154: Probable emission line star CTIO J175208.32-343607.0. Top row, from left: Blanco [O III] on/off band, difference and UKST Hα/SR/IR images. Northeast is top left. Left: AAOmega spectrum (3 × 1200 s dark time exposure). Miscellaneous reduction processing artefacts have been truncated for clarity. Hα, [N II] λ6583 and [S II] $\lambda\lambda$6716, 6731 emission lines are prominent.

CTIO J175346.02-334753.3

A Radcliffe 1.9 m telescope (1800 s bright time exposure) spectrum of this object is shown in figure 3.155. Several broad allowed emission features including Hα, Hβ, Hγ λ4340, Hδ λ4102 and He I λ5876 overlapping a stellar contribution are present. A subsequent AAOmega spectrum (3 × 1200 s dark time exposure), also shown in figure 3.155, recovers all of the features detected with the Radcliffe 1.9 m telescope. In addition, it recovers the [O III] λ5007 emission visible in Blanco imaging and more helium lines, He I $\lambda\lambda$4471, 6678, 7065. The feature at $\lambda\sim$8425 Å is presumed to be a miscellaneous processing artefact.

On the basis of imaging and spectral evidence, this object is some type of emission line star, but a more specific classification is pending further work.

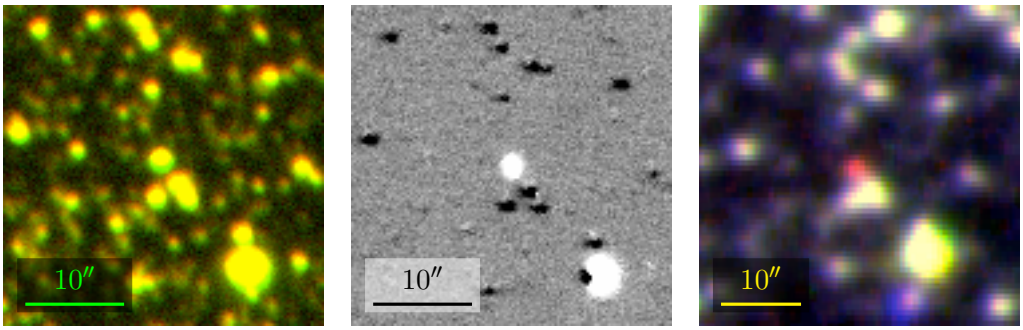

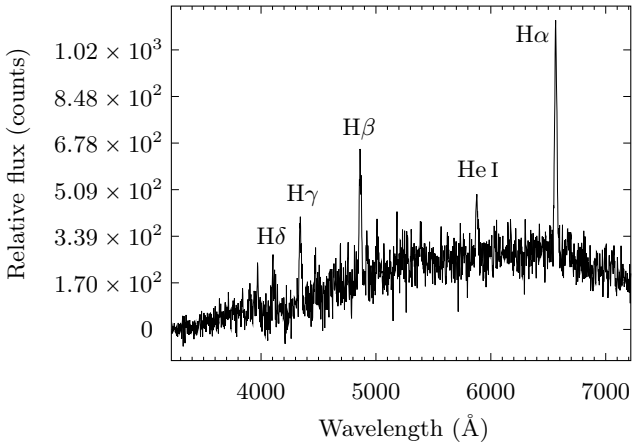

Figure 3.155: PN mimic CTIO J175346.02-334753.3. Top row, from left: Blanco [O III] on/off band, difference and UKST Hα/SR/IR images. Northeast is top left. Left: Radcliffe 1.9 m telescope spectrum (1800 s bright time exposure) with several broad allowed emission features. Right: CTIO J175346.02-334753.3 AAOmega spectrum (3 × 1200 s dark time exposure). All of the spectral features detected with the Radcliffe 1.9 m telescope are recovered here, plus the [O III] λ5007 emission visible in Blanco imaging. A presumed miscellaneous processing artefact at λ∼8425 Å has been truncated.

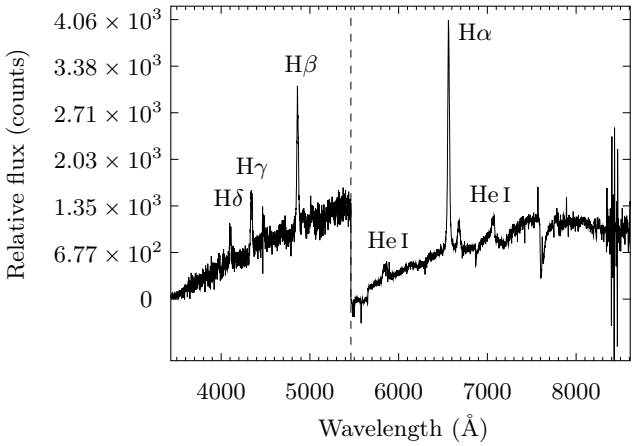

IRAS 17538-2935

IRAS 17538-2935 (Helou & Walker, 1988) is a compact PN mimic, possibly a SyS. Multi-wavelength imaging and an AAOmega (3 × 1800 s grey time exposure) spectrum are shown in figure 3.156. Aside from an [O I] λ5577 airglow processing artefact, emission lines detected include Hα, [N II] $\lambda\lambda$6548, 6583, [O III] λ5007 and [S II] $\lambda\lambda$6716, 6731. This is believed to be the first spectrum published for this object.

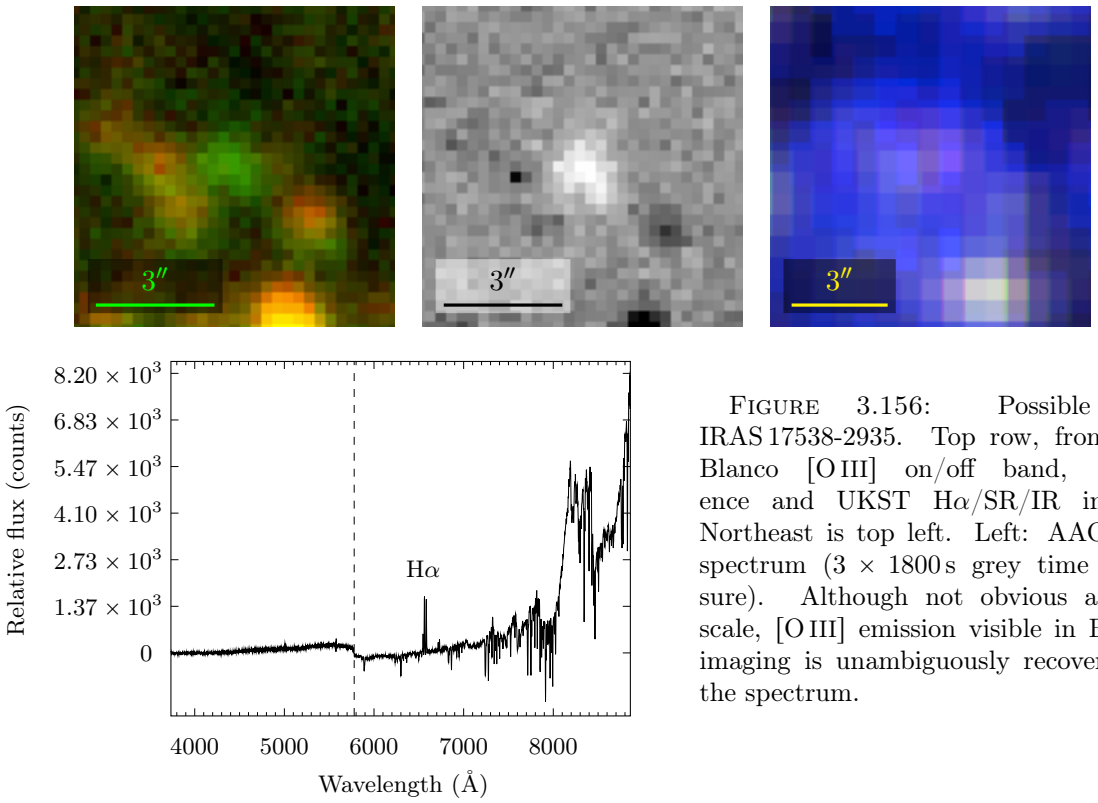

FIGURE 3.156: Possible SyS IRAS 17538-2935. Top row, from left: Blanco [O III] on/off band, difference and UKST Hα/SR/IR images. Northeast is top left. Left: AAOmega spectrum (3 × 1800 s grey time exposure). Although not obvious at this scale, [O III] emission visible in Blanco imaging is unambiguously recovered in the spectrum.

CTIO J175434.30-343140.4

Probable emission line star CTIO J175434.30-343140.4 is shown in multiwavelength imaging, accompanied by an AAOmega spectrum (3 × 1200 s dark time exposure), in figure 3.157. Classification of this object was hampered by the low S/N imaging and spectrum. The multiwavelength imaging suggests spectroscopy should yield [O III] λ5007 and no Hα emission, and yet the opposite is true of the collected spectrum. The spectrum also exhibits a strong stellar contribution and is marred by miscellaneous reduction processing artefacts in the far red. Possible emission lines aside from Hα are present, e.g. [N II] λλ6548, 6583 and [S II] λλ6716, 6731, but only appear at flux counts comparable with the noise and so can't be reliably reported. It is possible this object is a faint PN and that a coincident star has been inadvertently sampled in the spectrum in figure 3.157, but in the absence of further evidence, Hα, probable [O III] λ5007 (from Blanco imaging) and possible other forbidden emission lines superimposed over a stellar spectrum will be deemed indicative of an emission line star. Further study of this object is recommended to better diagnose its true nature.

CTIO J180023.29-282341.9

Imaging and an AAOmega spectrum (3 × 1200 s grey time exposure) taken of PN mimic CTIO J180023.29-282341.9 is shown in figure 3.158. The object isn't prominent or even resolved in UKST or *WISE* imaging. Spectral evidence indicates CTIO J180023.29-282341.9 is

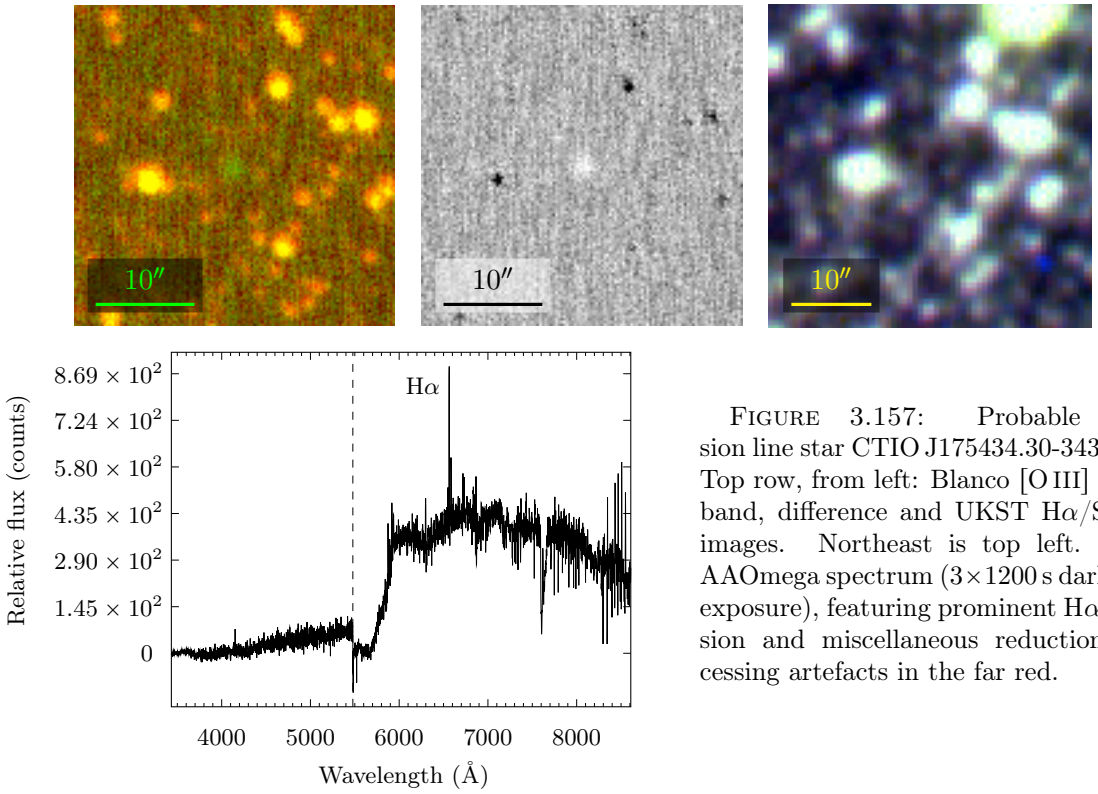

Figure 3.157: Probable emission line star CTIO J175434.30-343140.4. Top row, from left: Blanco [O III] on/off band, difference and UKST Hα/SR/IR images. Northeast is top left. Left: AAOmega spectrum (3×1200 s dark time exposure), featuring prominent Hα emission and miscellaneous reduction processing artefacts in the far red.

a star, not a PN. Airglow [O I] $\lambda\lambda$5577, 6300 artefacts are present. Absent however, is the [O III] λ5007 prominence of this object visible in the Blanco imaging.

CTIO J180317.18-285614.6

Assessing the nature of PN candidate CTIO J180317.18-285614.6 was non-trivial. In the Blanco imaging for this object, given in figure 3.159, the northeastern quadrant of the object displays a slightly increased off band intensity. It is thus unclear if the compact [O III] λ5007 emission is part of a standalone emission line object, or if it is a PN partially coincident with a star. The object is located within a dense stellar field—at least five faint stars are located within an apparent 4″ radius of the candidate, making this a plausible scenario. An AAOmega spectrum (3 × 1200 s grey time exposure) for CTIO J180317.18-285614.6, also given in figure 3.159, is consistent with this ambiguity. There are clear emission lines in the spectrum, but also significant absorption features and a continuum component. A dominant [O I] λ5577 airglow feature is accompanied by possible fainter [O I] $\lambda\lambda$7772/7774/7775, 8446/8447 emission. Other emission line features include Hα, Hβ, [O III] $\lambda\lambda$4959, 5007, suspected [Ar III] λ7136, He I $\lambda\lambda$5876, 6678 and [K VI] λ8827 and possible C III $\lambda\lambda$4515/4516/4517, 6351 and C IV λ5801. Apparent emission lines coinciding with H I $\lambda\lambda$8346, 8502, 8545, 8665 are thought to be possible cosmics, especially the prominent last three, as their strong intensities are inconsistent with weak Hγ, Hδ, etc. Miscellaneous fainter lines are present but ambiguous, and best assessed with deeper spectroscopy and a higher resolution spectrograph.

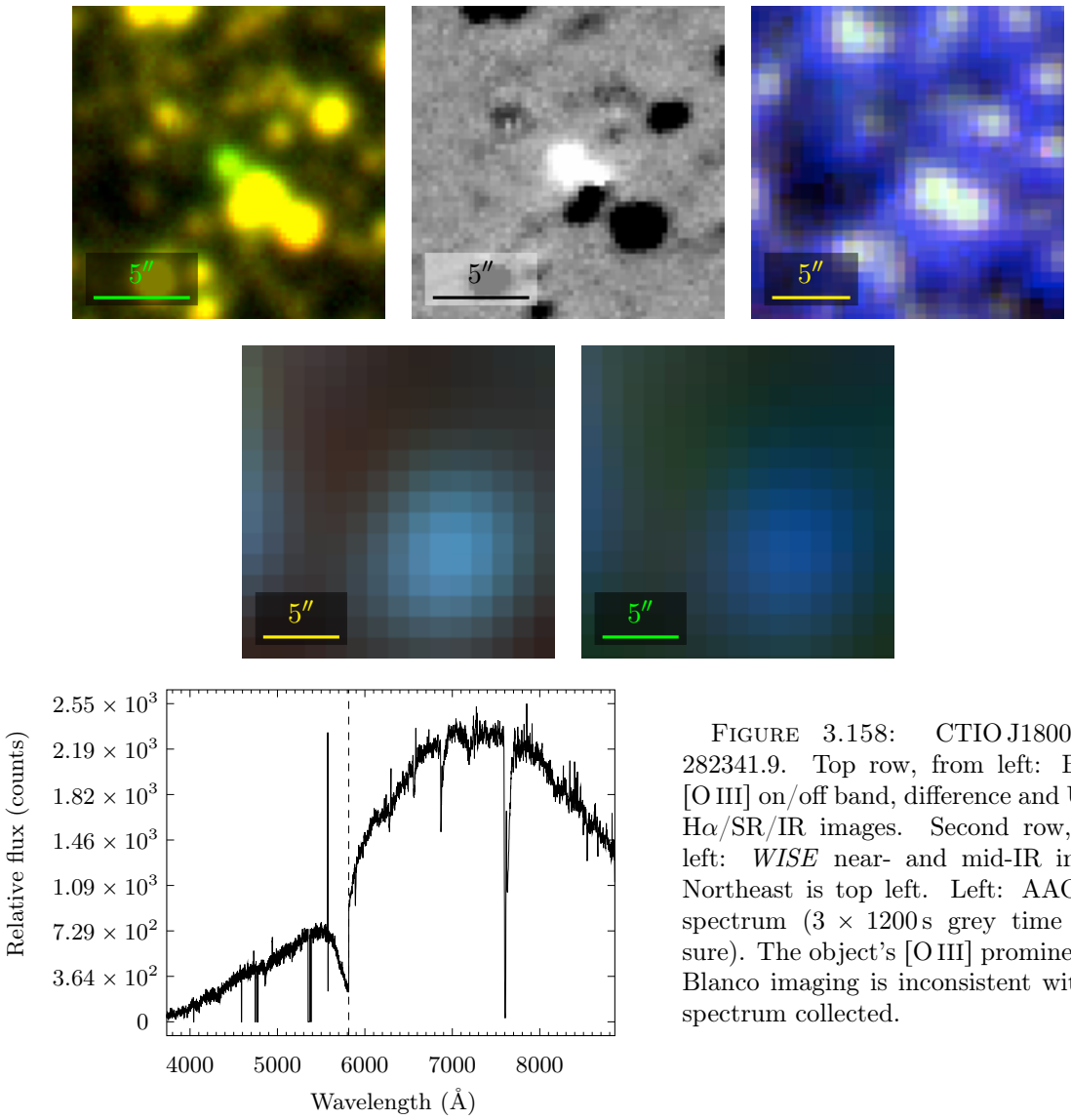

FIGURE 3.158: CTIO J180023.29-282341.9. Top row, from left: Blanco [O III] on/off band, difference and UKST Hα/SR/IR images. Second row, from left: *WISE* near- and mid-IR images. Northeast is top left. Left: AAOmega spectrum (3 × 1200 s grey time exposure). The object's [O III] prominence in Blanco imaging is inconsistent with the spectrum collected.

Until higher resolution imaging for this object is examined, and confirms two objects, not one, it will be assumed to be an emission line star.

Wray 17-108

Wray 17-108 (Belczyński et al., 2000) is a known symbiotic Mira (Gromadzki et al., 2009), with a M8.5 class cool component (Allen, 1980). It was not recognised as such due to coordinate confusion arising from its position astride a Mosaic II CCD join and the corresponding discontinuous astrometric solution applied. An AAOmega spectrum (3 × 1200s grey time exposure) is given in figure 3.160, marred by an [O I] λ5577 airglow processing artefact. This spectrum will not be analysed in detail here, but is generally consistent with that published by Munari & Zwitter (2002). Many emission features are apparent, including, but not limited to, [Ca V]/[Fe VII] λ6087, Hα, Hβ, He II λ4686, [O II] $\lambda\lambda$7319/7320, [O III] $\lambda\lambda$4363, 4959,

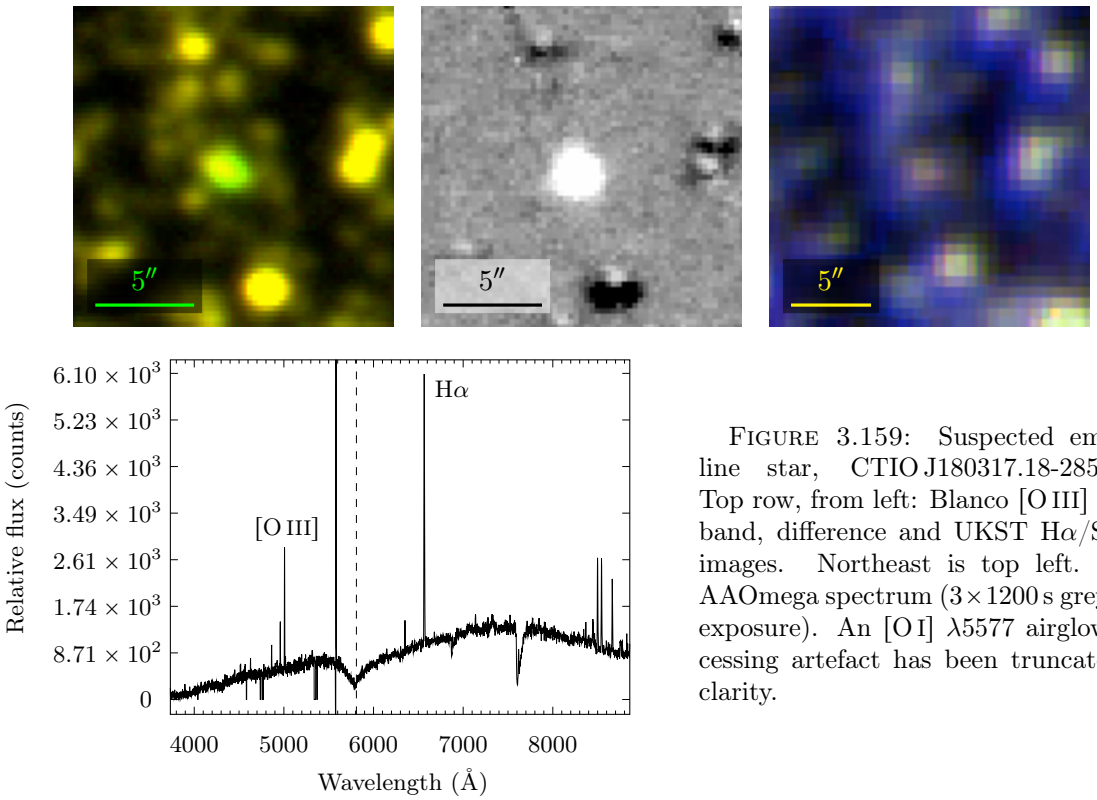

Figure 3.159: Suspected emission line star, CTIO J180317.18-285614.6. Top row, from left: Blanco [O III] on/off band, difference and UKST Hα/SR/IR images. Northeast is top left. Left: AAOmega spectrum (3×1200 s grey time exposure). An [O I] λ5577 airglow processing artefact has been truncated for clarity.

5007 and Raman-scattered [O VI] $\lambda\lambda$6825, 7082.

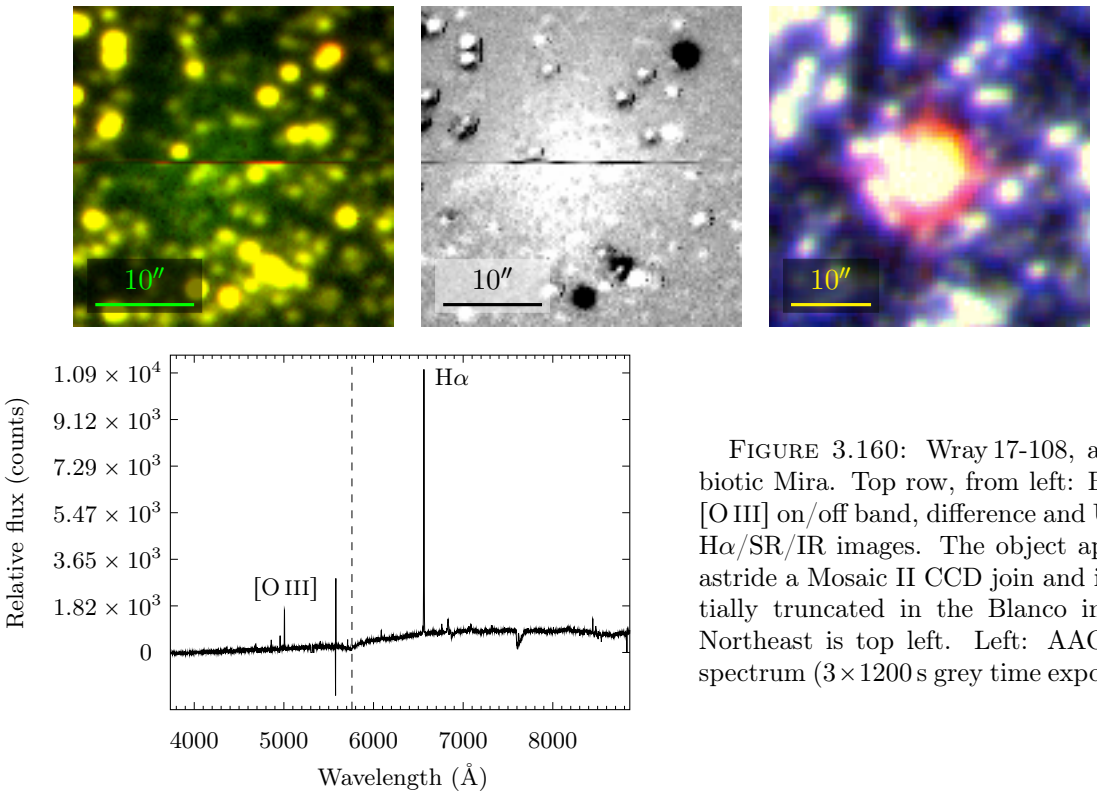

Figure 3.160: Wray 17-108, a symbiotic Mira. Top row, from left: Blanco [O III] on/off band, difference and UKST Hα/SR/IR images. The object appears astride a Mosaic II CCD join and is partially truncated in the Blanco images. Northeast is top left. Left: AAOmega spectrum (3×1200 s grey time exposure).

4

Duplicate Objects

Careful review of the Mosaic II bulge imaging not only revealed new PN candidates, but prospects for a converse reduction in known PNs. As new candidate bulge PNs were being cross-checked against known objects in SIMBAD, instances of duplicate objects were noted at almost the same coordinates. Imaging inspection however only revealed a single isolated object. Though erroneous duplications may have been noticed in other contexts, it is suspected suspicious object proximity was dismissed as a function of the crowded bulge stellar fields, resulting in single objects recorded twice in SIMBAD.

There are various possible causes of duplicate object SIMBAD submissions. Differing object astrometric solutions could lead to spurious duplicate submissions. The same physical object analysed amongst different data sets could be categorised differently by separate parties and thus get nominated as a new object on multiple occasions. It is even suspected duplicates have been caused by inconsistency in basing PN coordinates on their geometric centres versus regions of local brightness. Finally, some duplicate objects may have resulted from simple data entry errors.

A list of revised object coordinates, with explanatory notes, proposed to resolve these spurious duplicates, is given in table 4.1. A discussion of each duplicate instance is then provided.

TABLE 4.1: Duplicate object pairs, in J2000 coordinates. Original object coordinates are given to the same precision as listed in SIMBAD. Revised coordinates are given to a precision commensurate with the most precise of the relevant duplicate pair.

	Original data		Revised data	
Object Name	RA (h m s)	Dec (° ′ ″)	RA (h m s)	Dec (° ′ ″)
PN G000.9+01.8	17 40 50.7	−27 08 48	17 40 51.7	−27 08 48
SSTGLMC G000.9716+01.8327	17 40 51.8	−27 08 49	17 40 51.7	−27 08 48
2MASS J17485602-3106427	17 48 56.023	−31 06 42.79	17 48 56.008	−31 06 42.80
PN G358.5-01.7	17 48 56.04	−31 06 42.0	17 48 56.008	−31 06 42.80
GPSR 004.233+1.504	17 49 39.72	−24 32 14.8	17 49 39.73	−24 32 14.6
PN K 6-29	17 49 39.85	−24 32 13.7	17 49 39.73	−24 32 14.6
PN G359.5-01.3	17 49 49.1	−30 03 03	17 49 50.8	−30 03 11
SSTGLMC G359.5197-01.3648	17 49 50.8	−30 03 11	17 49 50.8	−30 03 11
JaSt2 20	17 56 35.9	−28 57 26	17 56 36.2	−28 57 18
PN G001.2-02.0	17 56 36.4	−28 57 18	17 56 36.2	−28 57 18

PN G000.9+01.8, SSTGLMC G000.9716+01.8327

Known PN, PN G000.9+01.8 (Parker et al., 2006), shown in figure 4.1, should be consolidated with YSO candidate SSTGLMC G000.9716+01.8327 (Robitaille et al., 2008). As SSTGLMC G000.9716+01.8327 was discovered from inspection of GLIMPSE[1] (Benjamin et al., 2003, Churchwell et al., 2009) imaging taken with the *Spitzer Space Telescope's* (Werner et al., 2004) Infrared Array Camera (Fazio et al., 2004), GLIMPSE imaging is included in figure 4.1. Synthetic GLIMPSE RGB images are produced in a similar manner to those used to present *WISE* data, with "near-IR" images using GLIMPSE data from filters 3 (red), 2 (green) and 1 (blue), and "mid-IR" images using data from filters 4 (red), 3 (green) and 2 (blue). GLIMPSE filter specifications are listed in table 4.2.

TABLE 4.2: GLIMPSE near- and mid-IR filter specifications Fazio et al. (2004).

Filter	λ_c (μm)	λ_{iso} (μm)	FWHM (μm)	Peak transmission (%)
1	3.56	3.550	0.75	46.5
2	4.52	4.439	1.01	53.5
3	5.73	5.731	1.42	17.0
4	7.91	7.872	2.93	31.8

The names PN G000.9+01.8 and SSTGLMC G000.9716+01.8327 currently refer to two

[1]GLIMPSE consists of multiple surveys, GLIMPSE I, GLIMPSE II, GLIMPSE 3D, etc. The term will be used broadly here to encompass them all.

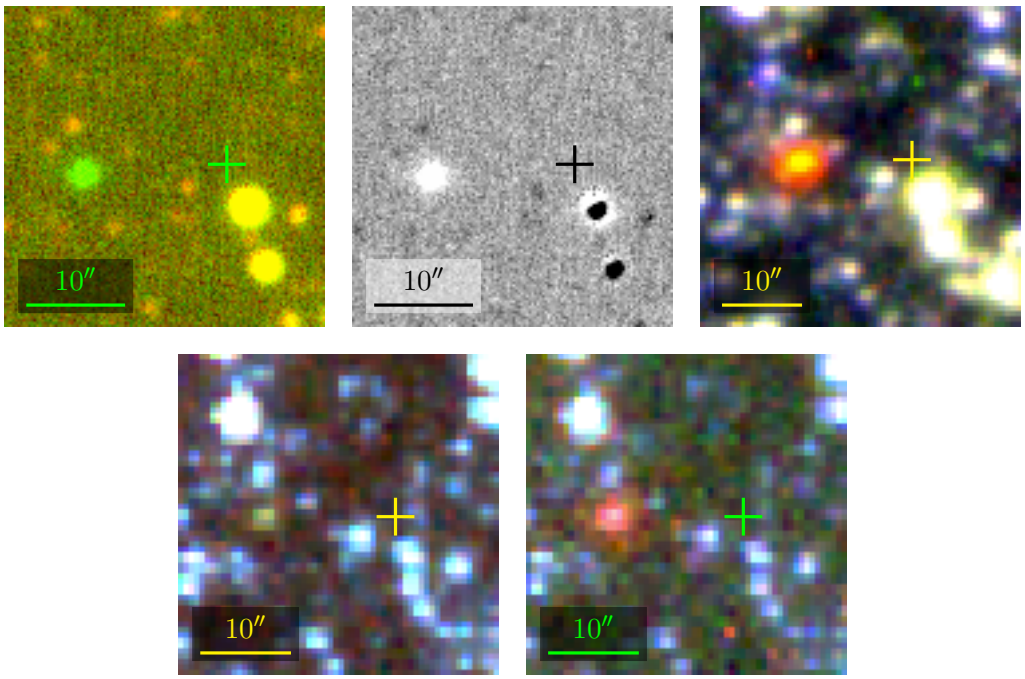

FIGURE 4.1: Known PN, PN G000.9+01.8. Top row, from left: Blanco [O III] on/off band, difference and UKST Hα/SR/IR images. Bottom row, from left: GLIMPSE near- and mid-IR images. Northeast is top left. Original incorrect object coordinates are indicated with a cross.

separate objects in SIMBAD. The imaging presented here however, centred on the current midpoint of the two sets of object coordinates, indicates only one object with a distinct emission line and IR signature, not two. The SIMBAD astrometry of SSTGLMC G000.9716+01.8327 is approximately correct, but that of PN G000.9+01.8 is not. The current incorrect position of PN G000.9+01.8, as listed in SIMBAD, is indicated in each panel of figure 4.1 with a cross. It is suspected the error originated from a data entry mistake in the MASH catalogue, as astrometry determined from SHS imaging—the imaging used for MASH object discovery, doesn't match that listed in the catalogue, but is wrong by only one digit. Current and proposed new coordinates for PN G000.9+01.8 are given in table 4.1.

An independent determination here of SSTGLMC G000.9716+01.8327's coordinates from examination of GLIMPSE imaging disagrees with the values SIMBAD draws from Robitaille et al. (2008), but is instead consistent with the proposed new coordinates for PN G000.9+01. Current and proposed new coordinates for SSTGLMC G000.9716+01.8327, supporting its consolidation with PN G000.9+01, are given in table 4.1.

Incorrect MASH coordinates for PN G000.9+01.8 were noted by Zhang & Kwok (2009), who suggested the same corrected coordinates proposed here. Although not explicitly referenced as having incorrect coordinates, PN G000.9+01.8 is also listed in the online catalogue of PN NIR photometry of Weidmann et al. (2013), under corrected coordinates (RA = 17h 40m 51.79s, dec = $-27^\circ\,08'\,48.94''$) consistent with the corrections proposed here.

2MASS J17485602-3106427, PN G358.5-01.7

PN G358.5-01.7 is a putative low v_r, compact PN ($v_r = 17.6\,\mathrm{km\,s^{-1}}$, $(1.6 \pm 0.1)''$ Hα diameter, Ruffle et al., 2004) located at a distance of 7.2 kpc (Van de Steene & Jacoby, 2001a). Blanco and UKST imaging of PN G358.5-01.7 is shown in figure 4.2.

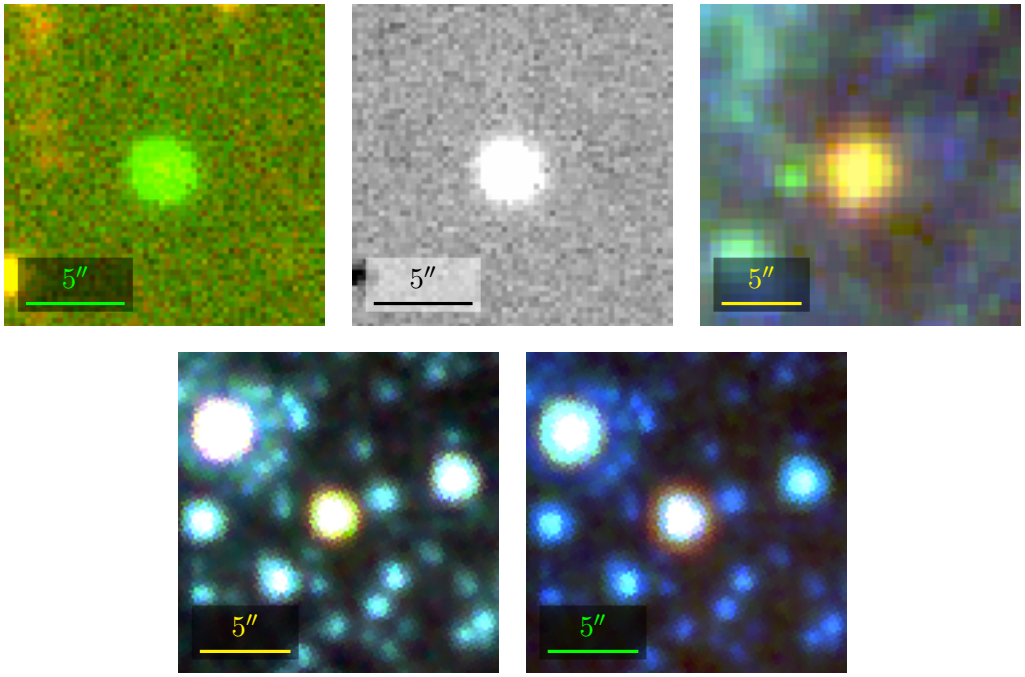

FIGURE 4.2: PN G358.5-01.7. Top row, from left: Blanco [O III] on/off band, difference and UKST Hα/SR/IR images. Bottom row, from left: GLIMPSE near- and mid-IR images. Northeast is top left. YSO candidate 2MASS J17485602-3106427 is listed in SIMBAD at coordinates within the apparent bounds of this object–they are not separate objects.

YSO candidate 2MASS J17485602-3106427 (Cutri et al., 2003) is listed in SIMBAD at very similar coordinates ($\Delta\mathrm{RA} = 1.7 \times 10^{-2}\,\mathrm{s}$, $\Delta\mathrm{dec} = 7.9 \times 10^{-1}\,''$), so similar in fact that it would lie within the apparent bounds of PN G358.5-01.7 as shown in figure 4.2. 2MASS J17485602-3106427 was identified as a possible YSO from GLIMPSE imaging (Robitaille et al., 2008), thus, for comparison, GLIMPSE near- and mid-IR imaging is also included in figure 4.2. Examination of figure 4.2 reveals only a single object likely to have been assessed as either a PN or YSO. 2MASS J17485602-3106427 and PN G358.5-01.7 are deemed here to be the same object and should be consolidated in SIMBAD. Proposed consolidated coordinates, based on inspection of 2MASS J band imaging, are given in table 4.1.

GPSR 004.233+1.504, PN K 6-29

Blanco and UKST imaging of possible PN GPSR 004.233+1.504 (Kistiakowsky & Helfand, 1995) is given in figure 4.3. PN candidate PN K 6-29 (Kohoutek, 2002) is listed in SIMBAD as a distinct object at coordinates ($\Delta\mathrm{RA} = 1.3 \times 10^{-1}\,\mathrm{s}$, $\Delta\mathrm{dec} = 1.1''$) placing it within the

apparent bounds of GPSR 004.233+1.504.

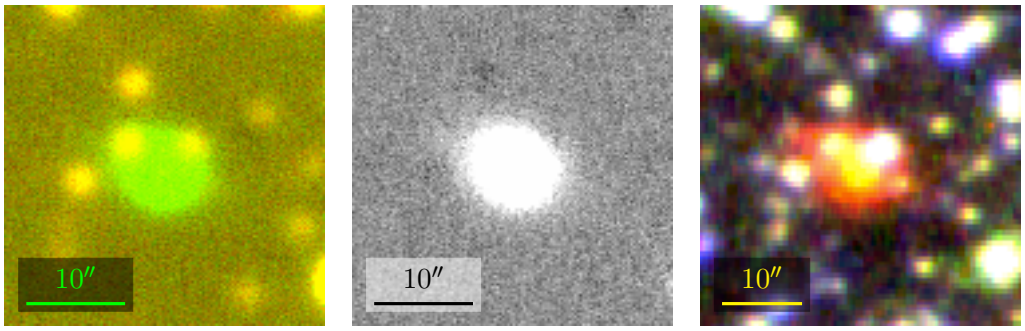

FIGURE 4.3: Possible PN GPSR 004.233+1.504. From left: Blanco [O III] on/off band, difference and UKST Hα/SR/IR images. Northeast is top left. PN candidate PN K 6-29 is listed in SIMBAD at coordinates inside the apparent bounds of this object–they are the same object.

As figure 4.3 shows only one clear likely PN, not two, it is recommended GPSR 004.233+1.504 and PN K 6-29 be consolidated in SIMBAD. The apparent location of the putative nebula is difficult to discern in 2MASS imaging, but consolidated coordinates based on 2MASS K_S band imaging are given in table 4.1

PN G359.5-01.3, SSTGLMC G359.5197-01.3648

SSTGLMC G359.5197-01.3648 is a YSO candidate discovered in GLIMPSE imaging (Robitaille et al., 2008). Blanco, UKST and GLIMPSE imaging of SSTGLMC G359.5197-01.3648 is given in figure 4.4. No obvious Herbig-Haro objects accompany this object, which would support its YSO candidacy.

PN G359.5-01.3 (Miszalski et al., 2009a) is listed in SIMBAD at nearby offset coordinates, specified with a cross in figure 4.4. Assessed as a PN candidate from review of [S III] λ9531 on/off band imaging, confirmatory radio observations (Van de Steene & Jacoby, 2001a) place it at a distance of 16.7 kpc, with its location listed as consistent with SSTGLMC G359.5197-01.3648 (ΔRA $= 3 \times 10^{-2}$ s, Δdec $= 3 \times 10^{-2}$ ″), not at the coordinates listed by SIMBAD. Subsequent work again lists PN G359.5-01.3 as a compact PN (5″ Hα diameter) located at coordinates consistent with SSTGLMC G359.5197-01.3648 (ΔRA $= 7 \times 10^{-2}$ s, Δdec $= 5.3 \times 10^{-1}$ ″), even providing a finding chart with an arrow directly placing PN G359.5-01.3 at the location of SSTGLMC G359.5197-01.3648 in figure 4.4 (Jacoby & Van de Steene, 2004).

AAOmega spectroscopy of PN G359.5-01.3 has lead to doubt over its status as a true PN (Miszalski et al., 2009a). Its coordinates, as listed in that work, are offset enough from SSTGLMC G359.5197-01.3648 (ΔRA $= 1 \times 10^{-1}$ s, Δdec $= 1$″) that the relevant AAOmega fibre may have in fact missed the bulk of the object's emission, making its dismissal as a mimic potentially premature. Regardless of whether this is the case or not, spectroscopy taken here of the object is pending reduction and will provide an independent assessment of its nature. For the purposes of establishing artificial duplication of objects however, the coordinates of

PN G359.5-01.3 listed by Miszalski et al. (2009a) are again inconsistent with its coordinates listed by SIMBAD.

No literature reference could be found placing PN G359.5-01.3 at its SIMBAD coordinates. A review of relevant references has shown no justification for it being listed at those coordinates. For unknown reasons, PN G359.5-01.3 has been erroneously associated with *IRAS* IR source IRAS 17466-3002 (Beichman et al., 1988) in SIMBAD and is inheriting coordinates from it. This *IRAS* source association should be removed. PN G359.5-01.3 and SSTGLMC G359.5197-01.3648, assessed here to be the same object, should then be consolidated in SIMBAD. Consolidated coordinates, based on 2MASS J band imaging, are given in table 4.1

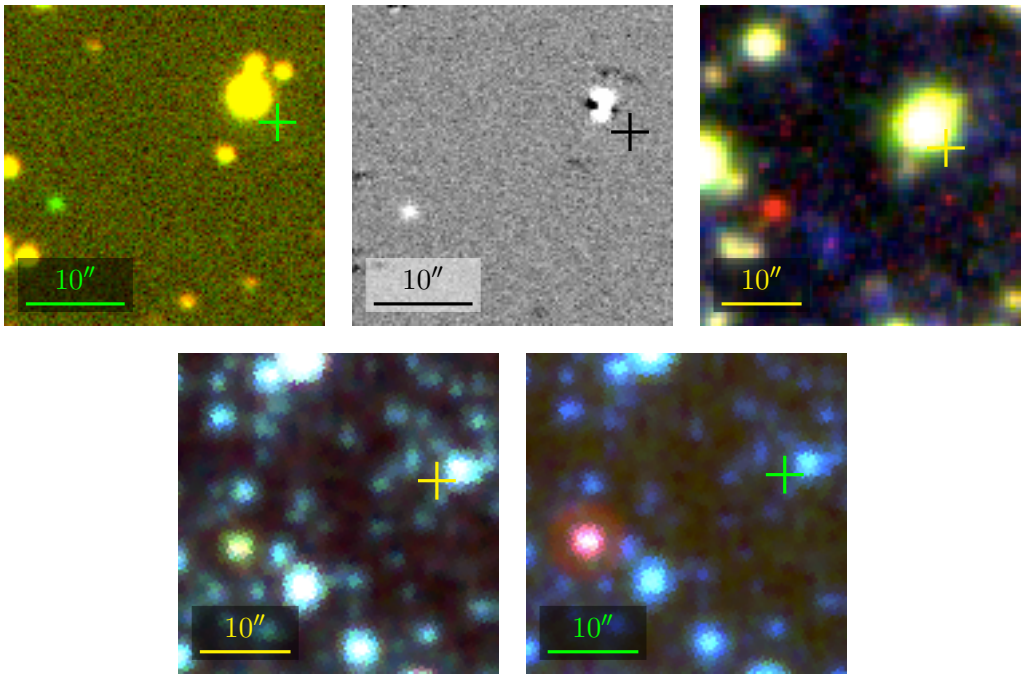

FIGURE 4.4: PN G359.5-01.3, the compact emission line object to the left of each panel. Top row, from left: Blanco [O III] on/off band, difference and UKST Hα/SR/IR images. Bottom row, from left: GLIMPSE near- and mid-IR images. Northeast is top left. The existing, erroneous, SIMBAD coordinates of PN G359.5-01.3 are indicated with a cross. N.B. The bright star to the top left of the cross in the top row is not the (IR) bright star to the top right of the cross in the bottom row.

JaSt2 20, PN G001.2-02.0

JaSt2 20 (Jacoby & Van de Steene, 2004) was identified as a possible 20″ diameter PN from inspection of Hα + [N II] on/off band imaging taken with the Mosaic I CCD imager (Muller et al., 1998) on the Kitt Peak National Observatory's 0.9 m telescope[2]. Blanco and UKST imaging around JaSt2 20's coordinates, indicated with a dotted cross, given in figure 4.5, indeed shows a ∼20″ diameter nebula.

[2]Now managed by the WIYN consortium (Sage & Aschenbrenner, 2004).

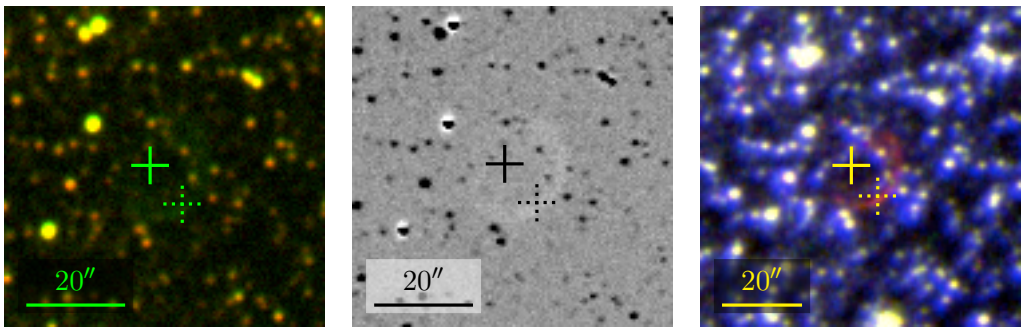

FIGURE 4.5: Probable PN JaSt2 20. From left: Blanco [O III] on/off band, difference and UKST Hα/SR/IR images. Northeast is top left. The existing SIMBAD coordinates of PN G001.2-02.0 (solid cross) and JaSt2 20 (dotted cross) are indicated. These coordinates overlap the same nebula.

PN G001.2-02.0 (Parker et al., 2006) is a possible MASH PN located at coordinates, indicated with a solid cross, coincident with the nebula in figure 4.5. Its MASH description ($23.0'' \times 15.0''$ diameter, Ear morphology, etc.) also matches figure 4.5.

Only one emission line object is visible in figure 4.5 and in the JaSt2 20 Hα + [N II] on/off band discovery image used by Jacoby & Van de Steene (2004). Based on this analysis, JaSt2 20 and PN G001.2-02.0 are deemed to be the same object. The off-centre published coordinates for JaSt2 20 likely caused the existing multiplicity in the object's identification. It is recommended JaSt2 20 and PN G001.2-02.0 be consolidated in SIMBAD. Proposed revised, consolidated coordinates for JaSt2 20 and PN G001.2-02, determined from inspection of the Blanco imaging, are given in table 4.1.

5

Other Observations

Candidate bulge PN observations were supplemented with miscellaneous Galactic, LMC and SMC PN spectroscopy, during periods of bulge inaccessibility, as mentioned in §3.3.4. In addition, when the bulge was accessible, some observations were taken of known PNs as ad hoc standards. Having a reference PN signal in a particular instrument, for given observing conditions, assisted calibration and evaluation of new candidate PN data. In the event, this had a number of side benefits. In some cases it yielded object spectra deeper, spanning a wider wavelength coverage, or featuring less stellar contamination than previously published data. For at least one known bulge PN this yielded new Hβ data, enabling dereddening and inclusion in the refined bulge PNLF. Where ad hoc PNs standards were observed on more than one telescope in this investigation, it allowed potential cross-calibration of data across telescopes. Finally, some attempts at PN spectroscopy yielded new data for objects in apparent proximity to PN targets.

Observations are discussed here of a candidate Galactic disc PN, miscellaneous objects towards the bulge (known PNs, known variable star and new stars), two known LMC PNs and five candidate SMC PNs. Blanco, SHS, SSS and *WISE* IR imaging, if available, accompanies the spectra presented here. SHS data not available from the dedicated SHS online atlas was sourced from the online MASPN database (Parker et al., 2014).

5.1 Galactic PNs

An observing log of supplemental Galactic PNs observed is given in table 5.1. These observations consist of:

- a known possible PN pending spectral confirmation (PN PM 1-66),
- multiple known PNs observed for calibration purposes in 2dF fields,
- a known PN in the bulge region ($-5^\circ \leqslant l \leqslant 5^\circ$, $-5^\circ \leqslant b \leqslant 5^\circ$), observed as a potential multi-telescope data cross-calibrator (PN G355.3-04.1) and,
- low ionisation emitting regions (LIERs) associated with a known PN (IC 4673).

Coordinates listed in table 5.1 refer to the position on the sky observed, not the apparent centre of objects (though in some cases these may correspond). For observations performed with the SAAO CCDSpec, coordinates are listed to the precision of the corresponding FITS file header data. For optical fibre spectroscopy, coordinate uncertainty reflects the $\pm 0.3''$ on-sky accuracy of 2dF's robotic fibre positioner (Sharp et al., 2006).

TABLE 5.1: Observing log of supplemental Galactic PNs, in J2000 coordinates. Coordinates are sky coordinates observed, not object apparent centres. Uncertainty in the last digit of coordinates is denoted in brackets. Exposure start time is given in UT and exposure duration denoted $T_{\rm exp}$. PNs observed more than once are shaded.

Name	RA (h m s)	Dec ($^\circ$ $'$ $''$)	Date	Time (UT)	$T_{\rm exp}$ (s)
PN PM 1-66*	12 26 30.5	−49 24 05	28 Jun 2014	18:07:27	1000
PN G355.5-03.7	17 49 58.90(2)	−34 38 39.0(3)	5 Jun 2014	14:22:37	3 × 1200
PN G355.3-04.1†	17 50 56.90(2)	−35 00 46.0(3)	5 Jun 2014	14:22:37	3 × 1200
PN G355.3-04.1†	17 50 57.00(2)	−35 00 46.1(4)	28 Jun 2014	21:13:29	900
PN G000.1-01.7	17 52 48.62(2)	−29 42 02.4(3)	18 Jun 2014	15:57:27	3 × 1800
PN G000.0-01.8	17 52 58.88(2)	−29 53 20.3(3)	18 Jun 2014	15:57:27	3 × 1800
PN G000.3-01.6	17 52 52.12(2)	−29 29 58.2(3)	18 Jun 2014	15:57:27	3 × 1800
PN G001.1-01.2	17 53 17.27(2)	−28 36 07.4(3)	27 Aug 2014	14:33:20	1200
2MASS J17531769-2804330	17 53 17.67(2)	−28 04 32.8(3)	27 Aug 2014	14:33:20	1200
PN K 6-32	17 53 40.30(2)	−34 43 41.0(3)	5 Jun 2014	14:22:37	3 × 1200
PN K 6-35	17 55 43.21(2)	−29 03 58.6(3)	18 Jun 2014	15:57:27	3 × 1800
PN G001.7-02.6	18 00 00.72(2)	−28 46 29.9(3)	26 Jul 2013	14:37:39	3 × 1200
PN G002.1-02.4	18 00 18.80(2)	−28 18 35.0(3)	26 Jul 2013	14:37:39	3 × 1200
IC 4673	18 03 12.36(2)	−27 05 17.3(3)	5 Sep 2013	10:40:15	4 × 1200
IC 4673	18 03 25.00(2)	−27 07 08.5(3)	5 Sep 2013	10:40:15	4 × 1200
PN G002.4-03.1	18 03 25.00(2)	−28 26 25.0(4)	27 Jun 2014	22:12:29	900

* FITS file header coordinate keywords corrupt. Most recent literature coordinates listed (Kimeswenger, 2001).
† Multi-telescope target.

PN PM 1-66

Confirmatory spectroscopy was carried out of possible Galactic PN, PN PM 1-66, identified by Preite-Martinez (1988) as a candidate from examination of IRAS data. The 1.9 m Radcliffe telescope CCDSpec spectrum (1000 s dark time exposure, 175 μm slit width) obtained, along with IR imaging, is given in figure 5.1. Estimated to lie at a distance of 5.0 kpc, calculated with a modified Shklovsky method (Preite-Martinez, 1988), this is the first known spectrum of this object.

Emission features present in the spectrum include [Ar III] 7136, Hα, Hβ, Hγ, Hδ, Hϵ λ3970, He I $\lambda\lambda$5876, 6678, 7065, [N II] $\lambda\lambda$6548, 6583, Ne III λ3869, [O I] $\lambda\lambda$6300, 6364, [O II] $\lambda\lambda$3726/3729, 7319/7320, 7330/7331, [O III] $\lambda\lambda$4363, 4959, 5007 and [S II] $\lambda\lambda$6716, 6731. The two prominent features at λ4656 and λ4677 are suspected to be due to small cosmics and so confirmatory reobservation is recommended. Otherwise, the spectrum is indeed consistent with a low excitation PN.

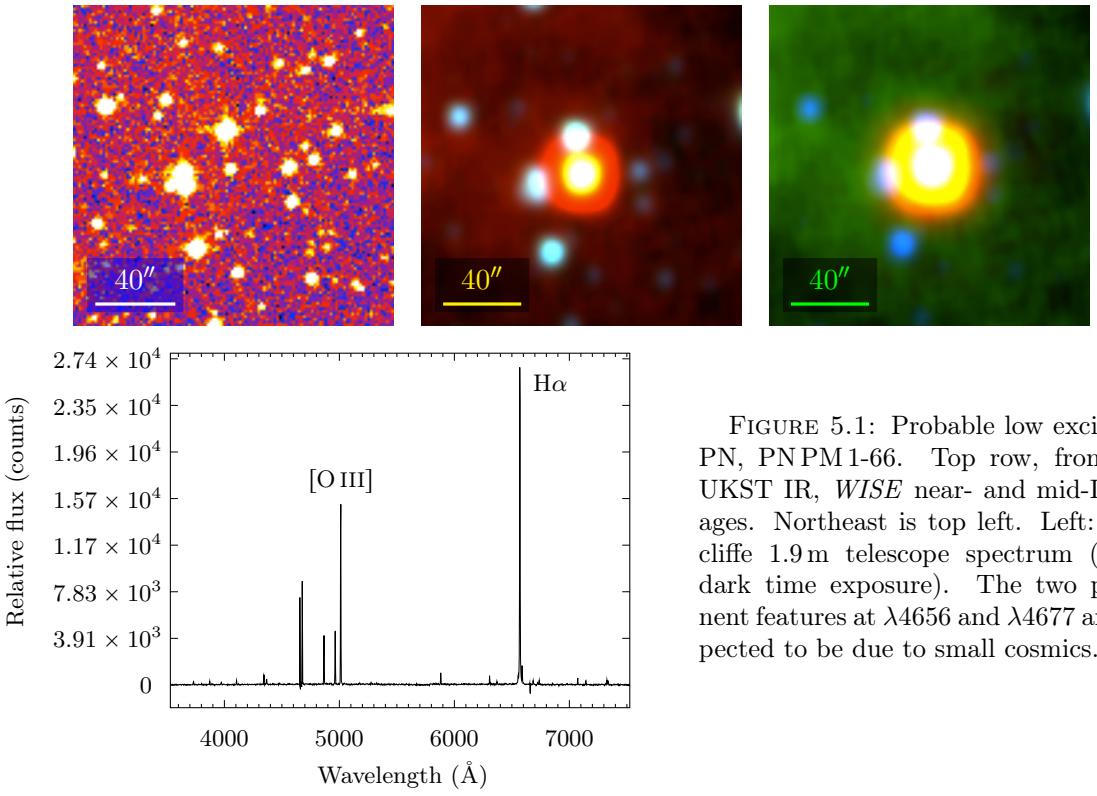

Figure 5.1: Probable low excitation PN, PN PM 1-66. Top row, from left: UKST IR, *WISE* near- and mid-IR images. Northeast is top left. Left: Radcliffe 1.9 m telescope spectrum (1000 s dark time exposure). The two prominent features at λ4656 and λ4677 are suspected to be due to small cosmics.

PN G355.5-03.7

Putative bulge PN, PN G355.5-03.7 (Parker et al., 2006, Kovacevic, 2011) was observed as an ad hoc PN standard for 2dF field A3 (table 3.7, §3.3.2). Multiwavelength imaging of this PN is given in figure 5.2, along with an AAOmega spectrum (3 × 1200 s dark time exposure). Extant MASH spectra for this PN is contradictory, exhibiting both $(F_{6548} + F_{6583})/F_{\mathrm{H}\alpha} > 1$

(FLAIR II spectroscopy) and $(F_{6548} + F_{6583})/F_{\mathrm{H}\alpha} < 1$ (6dF spectroscopy). The spectrum presented here, with $(F_{6548} + F_{6583})/F_{\mathrm{H}\alpha} << 1$, is generally consistent however with the line ratios of Kovacevic (2011). Emission lines present include faint [O I] $\lambda\lambda$7772, 7774, 7775 airglow artefacts and probable [Ar II] λ4072, [Ar III] $\lambda\lambda$7136, 7751, [Ar IV] λ7238, C II λ4267, He I $\lambda\lambda$3889, 4471, 6678, 7065, He II $\lambda\lambda$4686, 5412, 8237, [N I] λ5198, [N II] $\lambda\lambda$6548, 6583, Ne III λ3869, [O II] $\lambda\lambda$7319/7320, 7330/7331, [O III] $\lambda\lambda$4363, 4959, 5007, [S II] $\lambda\lambda$6716, 6731, along with the Hα to Hϵ Balmer series components. In the absence of higher resolution spectroscopy, miscellaneous other ambiguous faint features are left undiagnosed. Modest stellar contamination is present in the red arm.

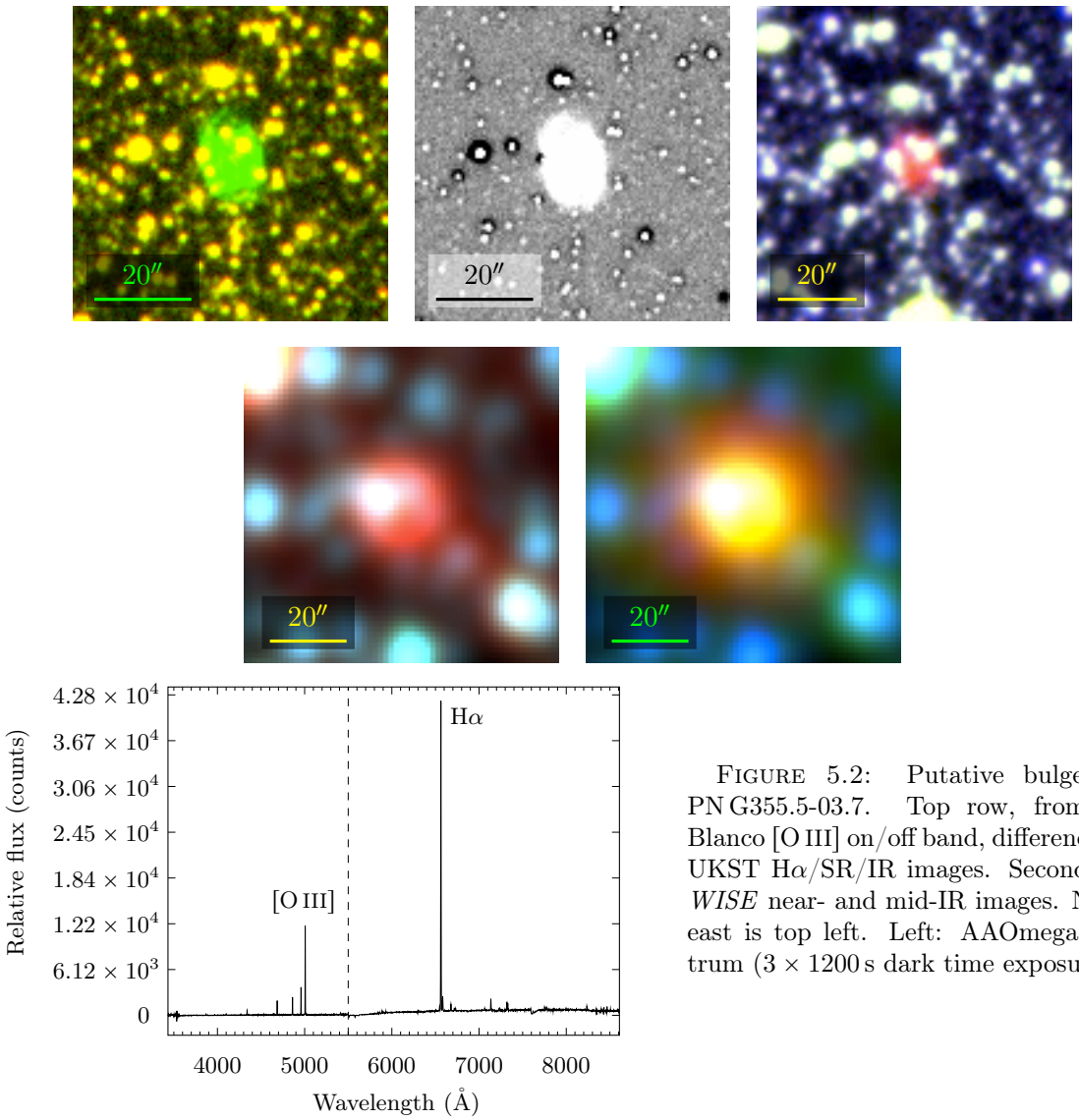

FIGURE 5.2: Putative bulge PN, PN G355.5-03.7. Top row, from left: Blanco [O III] on/off band, difference and UKST Hα/SR/IR images. Second row: *WISE* near- and mid-IR images. North-east is top left. Left: AAOmega spectrum (3 × 1200 s dark time exposure).

PN G355.3-04.1

A spectrum of known PN, PN G355.3-04.1 (Parker et al., 2006), taken with the Radcliffe 1.9 m telescope (900 s dark time exposure, 500 μm slit width), is shown in figure 5.3. The spectrum of this low excitation PN exhibits [Ar III] 7136, Hα, Hβ, Hγ, He I λ5876, 6678, 7281, He II λ4686, [N II] $\lambda\lambda$6548, 6583, [O I] λ6300, [O II] $\lambda\lambda$3726/3729, [O III] $\lambda\lambda$4959, 5007 and [S II] $\lambda\lambda$6716, 6731.

A complementary AAOmega spectrum (3×1200 s dark time exposure), taken in 2dF field A3 for the purposes of potential telescope cross-calibration, is also shown in figure 5.3. Despite a minor stellar contaminant and assumed miscellaneous reduction processing artefacts in the far blue and far red, bulk features of the spectrum match those from Radcliffe telescope. Spectral features do however appear in different apparent ratios, as no explicit flux cross-calibration of AAOmega red and blue arm data was carried out.

This PN was omitted from the bulge PNLF of Kovacevic (2011), though reddened photometry was presented. The new detection here of Hβ and other diagnostic lines in the CCDSpec data was used to derive line ratios and Balmer decrement, deredden that photometry and further refine the bulge PNLF.

PN G000.1-01.7

PN G000.1-01.7 (Parker et al., 2006) is a known PN towards the bulge observed as an ad hoc standard for 2dF field A4 (table 3.7, §3.3.2). Multiwavelength studies have yielded optical emission line, radio and IR fluxes (e.g. Jacoby & Van de Steene, 2004, Van de Steene & Jacoby, 2001b, Zhang & Kwok, 2009) and other physical properties for this PN. It was included in the bulge PNLF of Kovacevic (2011), though suspected to be a foreground PN. Subsequent distance determinations have borne this out, placing it at $\approx$6.80 kpc (Ortiz et al., 2011).

Selected multiwavelength imaging and an AAOmega (3×1800 s grey time exposure) spectrum are shown in figure 5.4. The spectrum, with $F_{\mathrm{H}\alpha} > F_{6583}$, conflicts with the sole MASH spectrum exhibiting $F_{6583} > F_{\mathrm{H}\alpha}$, but is generally consistent with the line ratios of Kovacevic (2011). Emission lines detected include presumed unsubtracted [O I] λ5577 airglow and nebula [Ar III] $\lambda\lambda$7136, 7751, [Cl IV] λ8046, Hα, Hβ, Hγ, He I $\lambda\lambda$4009, 5876, 6678, He II $\lambda\lambda$4686, 5412, 8237, [N II] $\lambda\lambda$6548, 6583, [O II] $\lambda\lambda$7319/7320, 7330/7331, [O III] $\lambda\lambda$4959, 5007, [S II] $\lambda\lambda$6716, 6731.

PN G000.0-01.8

PN G000.0-01.8 (Parker et al., 2006) is another known PN towards the bulge used as an ad hoc standard for 2dF field A4 (table 3.7, §3.3.2). Selected multiwavelength imaging and an AAOmega (3×1800 s grey time exposure) spectrum are shown in figure 5.5. Although marred by multiple modest stellar contaminants, the spectrum is consistent with but deeper than all extant MASH (FLAIR II: 1800 s, 6dF: 1200 s, CCDSpec: 900 s) spectra and provides

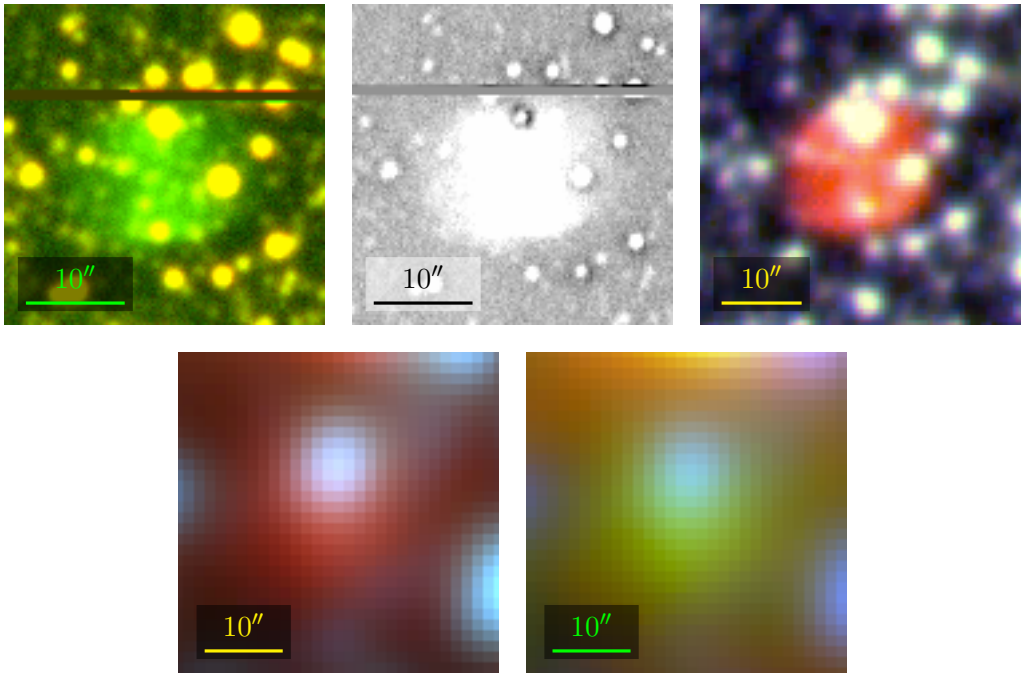

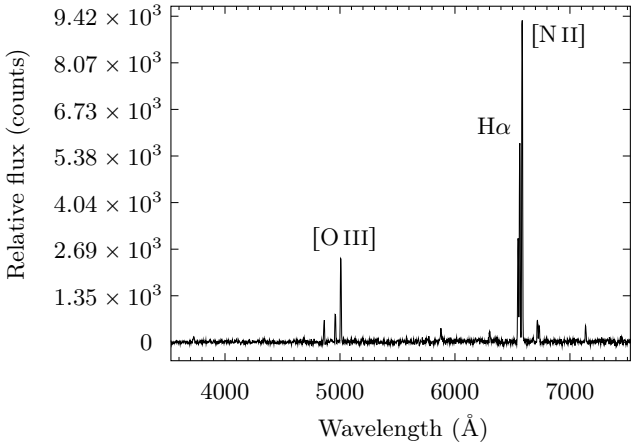

FIGURE 5.3: Known bulge-proximate PN, PN G355.3-04.1. Top row, from left: Blanco [O III] on/off band, difference and UKST Hα/SR/IR images, marred by bad CCD rows. Second row: *WISE* near- and mid-IR images. Northeast is top left. Left: Radcliffe 1.9 m telescope spectrum (900 s dark time exposure).

Opposite: PN G355.3-04.1 AAOmega spectrum (3 × 1200 s dark time exposure). Comparison with the spectrum above shows bulk spectral features in common. Features appear in different apparent ratios however, as the AAOmega red and blue arm data are not flux calibrated with respect to each other.

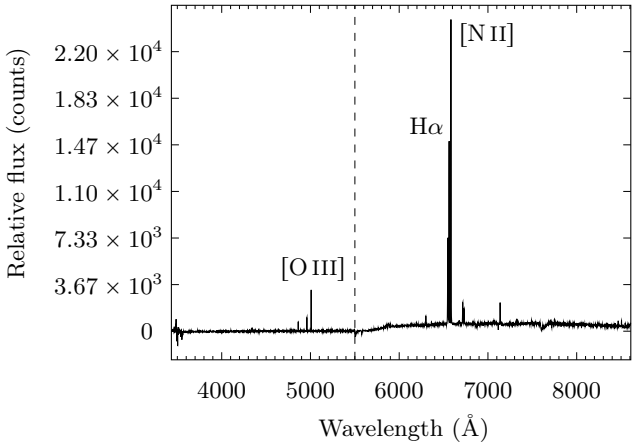

the broadest wavelength coverage (λ3735–8859). Absent from the Kovacevic (2011) bulge PNLF, a new Hβ emission detection here allows this PN to be dereddened and added to the

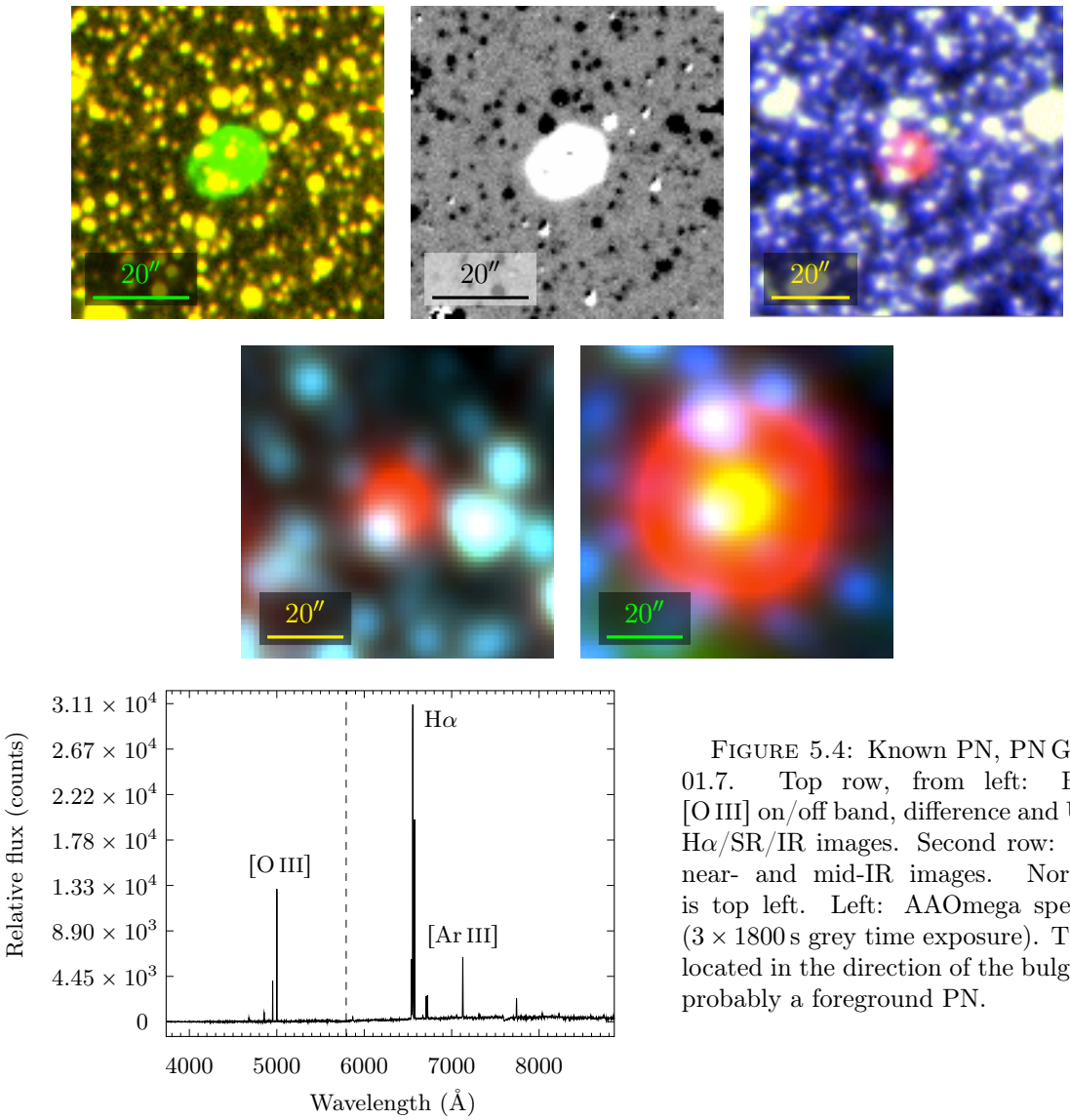

Figure 5.4: Known PN, PN G000.1-01.7. Top row, from left: Blanco [O III] on/off band, difference and UKST Hα/SR/IR images. Second row: *WISE* near- and mid-IR images. Northeast is top left. Left: AAOmega spectrum (3×1800 s grey time exposure). Though located in the direction of the bulge, it is probably a foreground PN.

PNLF if deemed a true bulge member.

Aside from Hβ and a [O I] λ5577 airglow processing artefact, emission lines detected include at least [Ar III] λ7136, Hα, He I $\lambda\lambda$5876, 6678, [N II] $\lambda\lambda$6548, 6583, [O II] $\lambda\lambda$7319/7320, [O III] $\lambda\lambda$4363, 4959, 5007 and [S II] $\lambda\lambda$6716, 6731.

PN G000.3-01.6

PN G000.3-01.6 (Parker et al., 2006) was observed as an ad hoc calibrator for the A4 2dF field A4 (table 3.7, §3.3.2). Located at ≈7.97 kpc (Ortiz et al., 2011), PN G000.3-01.6 has been studied in the optical, IR, and radio domains (e.g. Van de Steene & Jacoby, 2001b, Jacoby & Van de Steene, 2004, Zhang & Kwok, 2009) and was used in the Kovacevic (2011) bulge PNLF. The line ratios observed are generally consistent with extant published data (Parker et al., 2006, Kovacevic, 2011). Apart from a minor [O I] λ5577 airglow processing

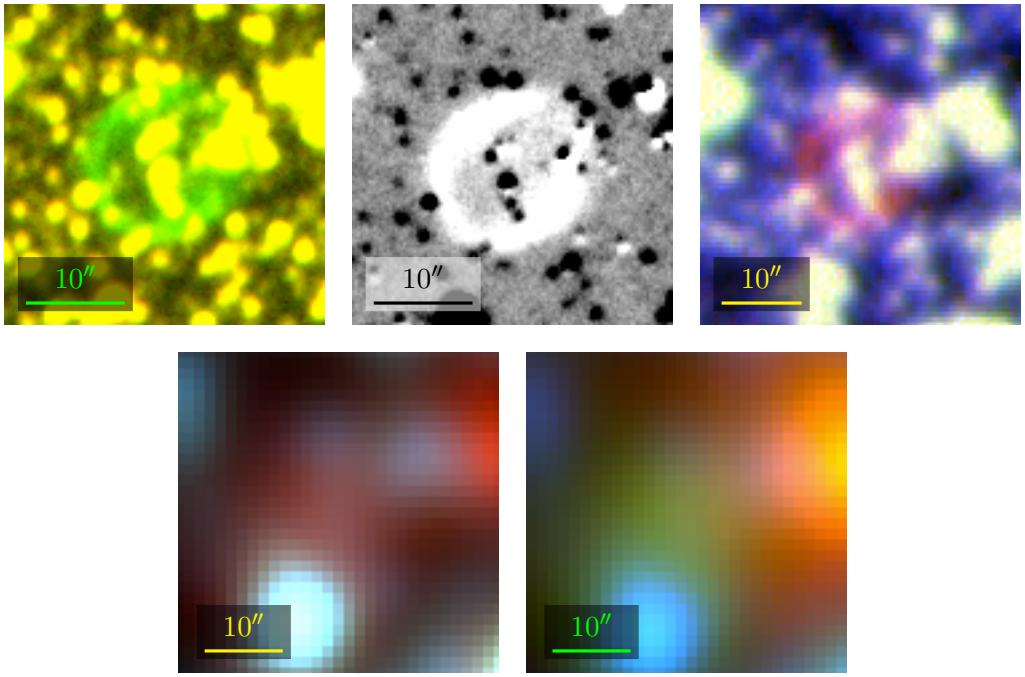

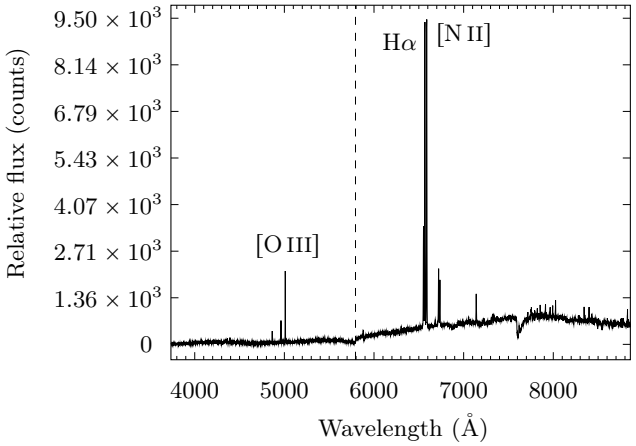

FIGURE 5.5: Known PN, PN G000.0-01.8. Top row, from left: Blanco [O III] on/off band, difference and UKST Hα/SR/IR images. Second row: *WISE* near- and mid-IR images. Northeast is top left. Left: AAOmega spectrum (3 × 1800 s grey time exposure). Multiple stellar contaminants are present.

artefact, emission lines detected include [Ar III] λλ7136, 7751, [Ar IV] λ7238, [Cl IV] λ8046, He I λλ5876, 6678, 7065, He II λλ4686, 5412, 8237, [N II] λλ6548, 6583, [O III] λλ4959, 5007, [S II] λλ6716, 6731 and the Hα to Hγ Balmer series components.

PN G001.1-01.2

PN G001.1-01.2 is a known PN observed as a supplementary target for 2dF field H1 (table 3.7, §3.3.2). The PN is shown in selected multiwavelength imaging in figure 5.7. The bright point source near the apparent centre of the PN has cast some doubt on its PN status (Parker et al., 2006). The multiwavelength imaging shown is consistent with the PN cohort presented here however, meaning the near-central point source may be a coincident field star. A complementary high airmass ($Z \approx 2.3$) HERMES spectrum (1200 s dark time exposure) is also shown in figure 5.7 and is consistent with a PN. Emission lines present include Hα and faint [N II]

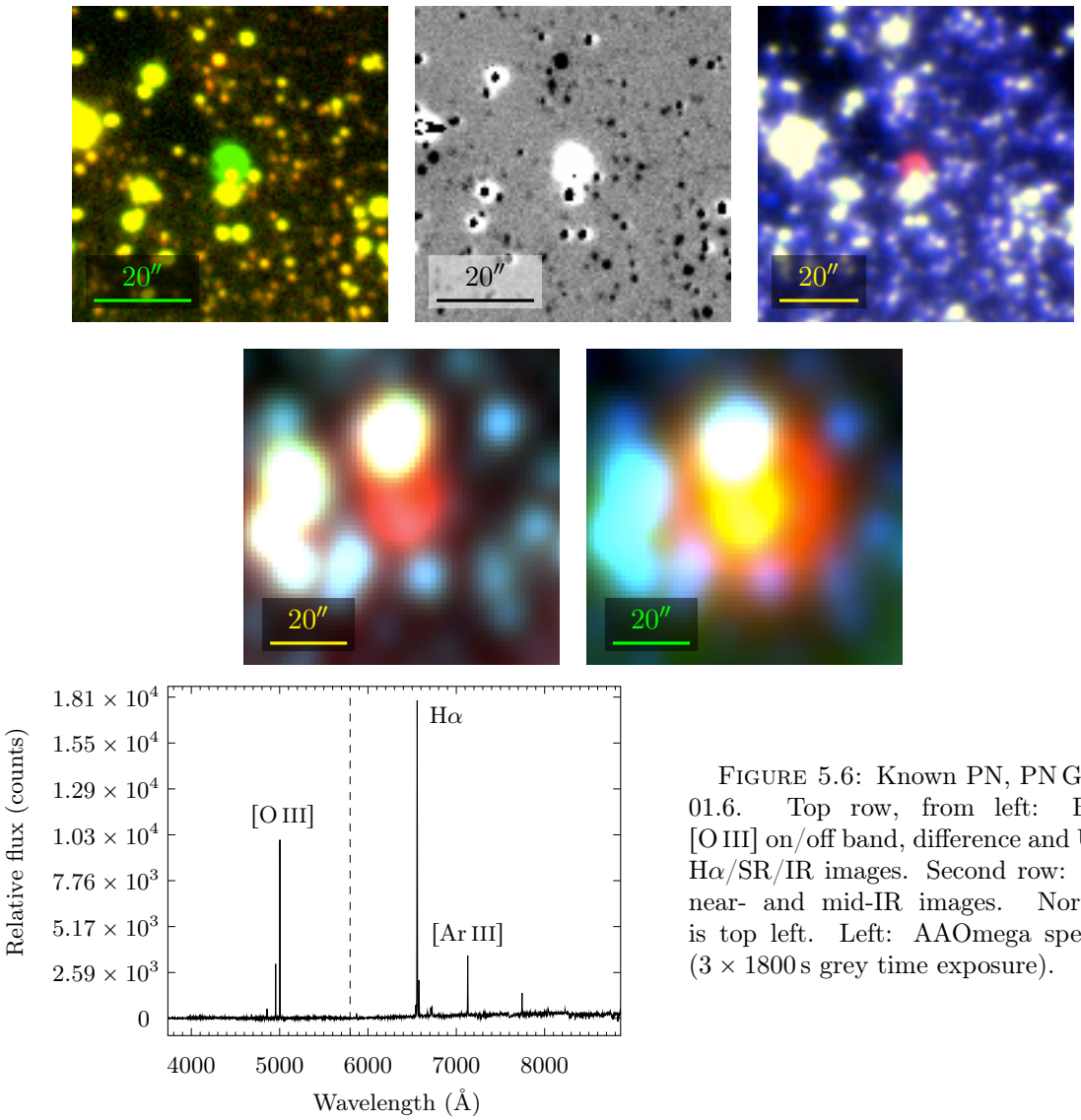

Figure 5.6: Known PN, PN G000.3-01.6. Top row, from left: Blanco [O III] on/off band, difference and UKST Hα/SR/IR images. Second row: *WISE* near- and mid-IR images. Northeast is top left. Left: AAOmega spectrum (3×1800 s grey time exposure).

λ6582. No MASH spectrum is available for this PN, though it is included in the Kovacevic (2011) bulge PNLF alongside line ratios generally consistent with the HERMES data here.

2MASS J17531769-2804330

2MASS J17531769-2804330 (Cutri et al., 2003) is a known PN towards the bulge, observed as another supplementary target for 2dF field H1. UKST Hα/SR/IR and *WISE* near- and mid-IR imaging is shown in figure 5.8. A low S/N HERMES spectrum (1200 s dark time exposure) suffering artefact corruption (see §3.3.2) provided viable enough Hα emission data to permit a radial velocity estimation for this object. Using equation 6.1 and c as derived for equation 3.6, radial velocity $v_\mathrm{r} = 142 \pm 6\,\mathrm{km\,s^{-1}}$.

This PN's Galactic coordinates and v_r make it statistically likely to be a bulge PN (using the criteria in §6). An existing distance estimate conflicts with this assessment ($d \approx 17.2$ kpc,

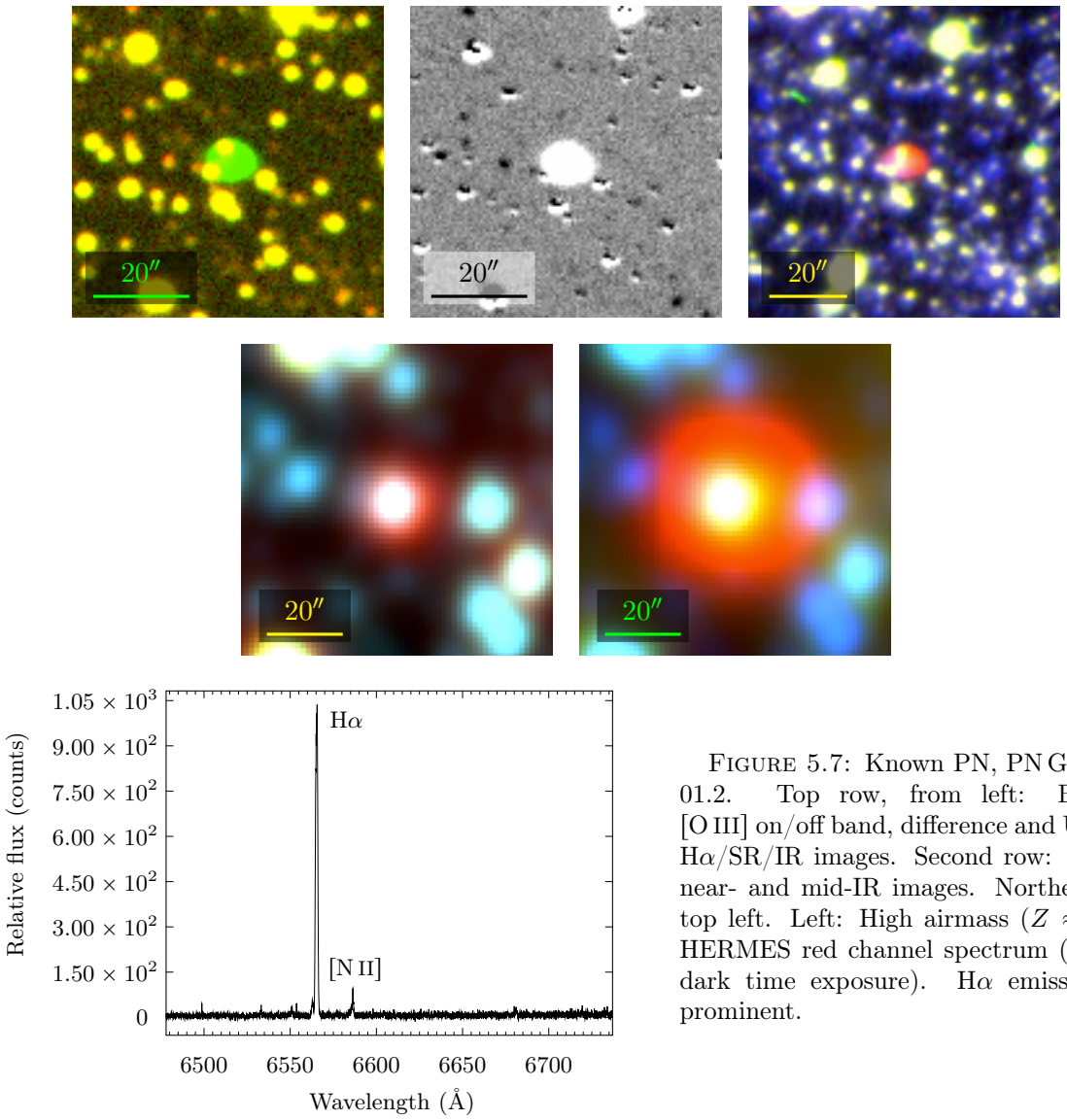

FIGURE 5.7: Known PN, PN G001.1-01.2. Top row, from left: Blanco [O III] on/off band, difference and UKST Hα/SR/IR images. Second row: *WISE* near- and mid-IR images. Northeast is top left. Left: High airmass ($Z \approx 2.3$) HERMES red channel spectrum (1200 s dark time exposure). Hα emission is prominent.

Van de Steene & Jacoby, 2001b), but has known limitations. Further analysis is recommended to resolve the issue of its bulge membership. This PN wasn't captured in the Blanco bulge imaging used here, but has potential as a future data point in the bulge PNLF.

PN K 6-32

PN K 6-32 (Kohoutek, 2002) is a known PN towards the bulge with a [WR] CSPN (DePew et al., 2011), observed as an ad hoc PN standard for 2dF field A3 (table 3.7, §3.3.2). It was omitted from the Kovacevic (2011) PNLF, presumably due to its [O III] λ5007 diameter exceeding the bulge discriminator ($\leqslant$21″) adopted. Multiwavelength imaging and an AAOmega spectrum (3 × 1200 s dark time exposure) are given in figure 5.9. The spectrum is consistent with, and deeper than, extant MASH spectroscopy (e.g. 600 s CCDSpec, 1800 s FLAIR II and

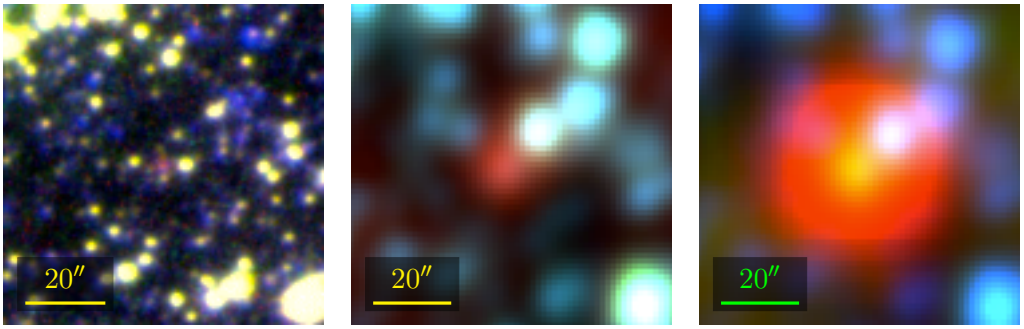

Figure 5.8: Known PN 2MASS J17531769-2804330. From left: UKST Hα/SR/IR, *WISE* near- and mid-IR images. Northeast is top left.

600 s 6dF exposures, Parker et al., 2006), but marred by a minor stellar contaminant and a miscellaneous reduction processing artefact in the far red. Emission lines present include at least [Ar III] $\lambda\lambda$7136, 7751, [Ar IV] $\lambda\lambda$4711, 4740, [Cl IV] λ8046, He II $\lambda\lambda$4686, 5412, 8237, [O III] $\lambda\lambda$4959, 5007 and the Hα to Hδ Balmer series components.

PN K 6-35

PN K 6-35 (Kohoutek, 2002) is a known PN, located ≈6.01 kpc (Ortiz et al., 2011) towards the bulge, observed as an ad hoc PN standard for the 2dF field A4 (table 3.7, §3.3.2. Optical spectra and [O III] λ5007 flux (Parker et al., 2006, Kovacevic, 2011), IR fluxes (Phillips & Zepeda-García, 2009, Zhang & Kwok, 2009, Mizuno et al., 2010), radio fluxes (Condon et al., 1999, Bojičić et al., 2011) and other physical properties are available for this PN. Multiwavelength imaging and an AAOmega spectrum (3×1800 s grey time exposure) are given in figure 5.10. The spectrum is consistent with, but broader (3735–8859 Å vs. 3902–7198 Å) and deeper (1800 s AAOmega vs. 1800 s FLAIR II, 1200 s 6dF) than the existing MASH spectra. Aside from [O I] $\lambda\lambda$5577, 6300 airglow processing artefacts, this deeper spectrum includes at least [Ar III] $\lambda\lambda$7136, 7751, [Ar IV] $\lambda\lambda$4711, 4740, [Ar V] λ7006, [Cl IV] λ8046, He I $\lambda\lambda$5876, 6678, 7065, He II $\lambda\lambda$4686, 5412, 7593, 8237, [N II] $\lambda\lambda$6548, 6583, Ne III λ3869, [O II] $\lambda\lambda$7319/7320, 7330/7331, [O III] $\lambda\lambda$4363, 4959, 5007, [S II] $\lambda\lambda$6716, 6731 and the Hα to Hδ Balmer series emission lines.

PN G001.7-02.6

Known putative bulge PN, PN G001.7-02.6 (Parker et al., 2006, Kovacevic, 2011), was observed as an ad hoc PN standard for 2dF field A1 (table 3.7, §3.3.2). Relative line fluxes in the visible, along with other PN properties (diameter, electron density, electron temperature, Ex_ρ, F_{5007} and morphology), are given in the bulge PN study of Kovacevic (2011). Many long wavelength fluxes are also available for this PN, including those derived from GLIMPSE, MIPSGAL, *AKARI* (near-, mid- and far-IR, Zhang et al., 2012) and NVSS (radio, Bojičić

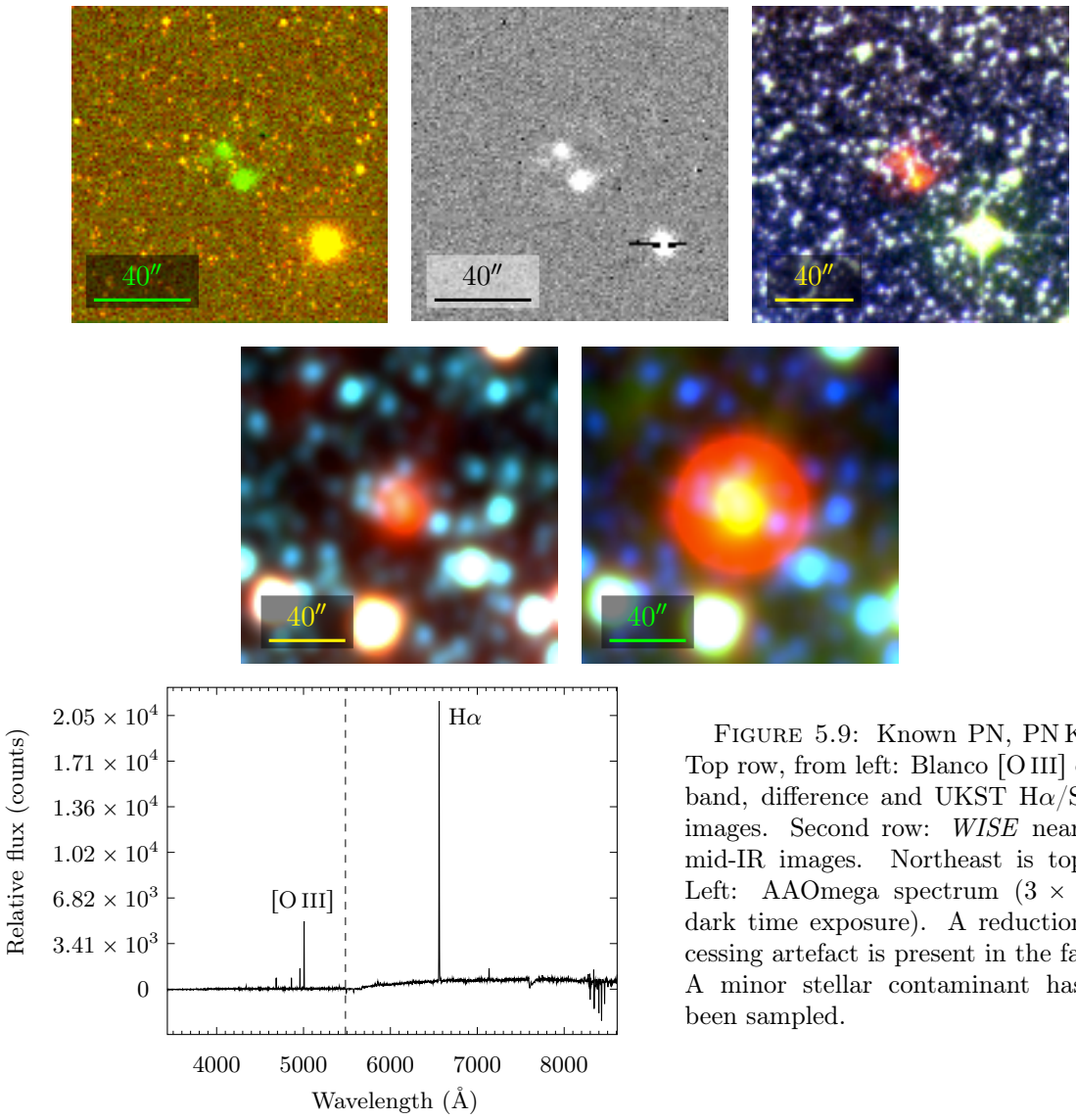

FIGURE 5.9: Known PN, PN K 6-32. Top row, from left: Blanco [O III] on/off band, difference and UKST Hα/SR/IR images. Second row: *WISE* near- and mid-IR images. Northeast is top left. Left: AAOmega spectrum (3 × 1200 s dark time exposure). A reduction processing artefact is present in the far red. A minor stellar contaminant has also been sampled.

et al., 2011) data.

Visible and IR imaging, along with the AAOmega spectrum obtained (3 × 1200 s grey time exposure) for it, are shown in figure 5.11. It is noted the MASH catalogue includes an image for this object, and discusses a spectrum, but as of 1 May 2015, did not present it. The spectrum obtained here includes faint airglow artefacts, [O I] $\lambda\lambda$5577, 7772, 7774, 7775, probable [Ar III] $\lambda\lambda$7136, 7751, [Ar IV] λ7238, C II λ4267, He I $\lambda\lambda$4471, 5876, 6678, 7065, He II $\lambda\lambda$4686, 5412, 8237, [N II] $\lambda\lambda$6548, 6583, Ne III λ3869, [O II] $\lambda\lambda$7319/7320, 7330/7331, [O III] $\lambda\lambda$4959, 5007, [S II] $\lambda\lambda$6716, 6731 and the Hα to Hϵ Balmer series components. Faint stellar contamination is apparent in the red arm.

PN G002.1-02.4

PN G002.1-02.4 (Parker et al., 2006) is another known putative bulge PN (Kovacevic, 2011),

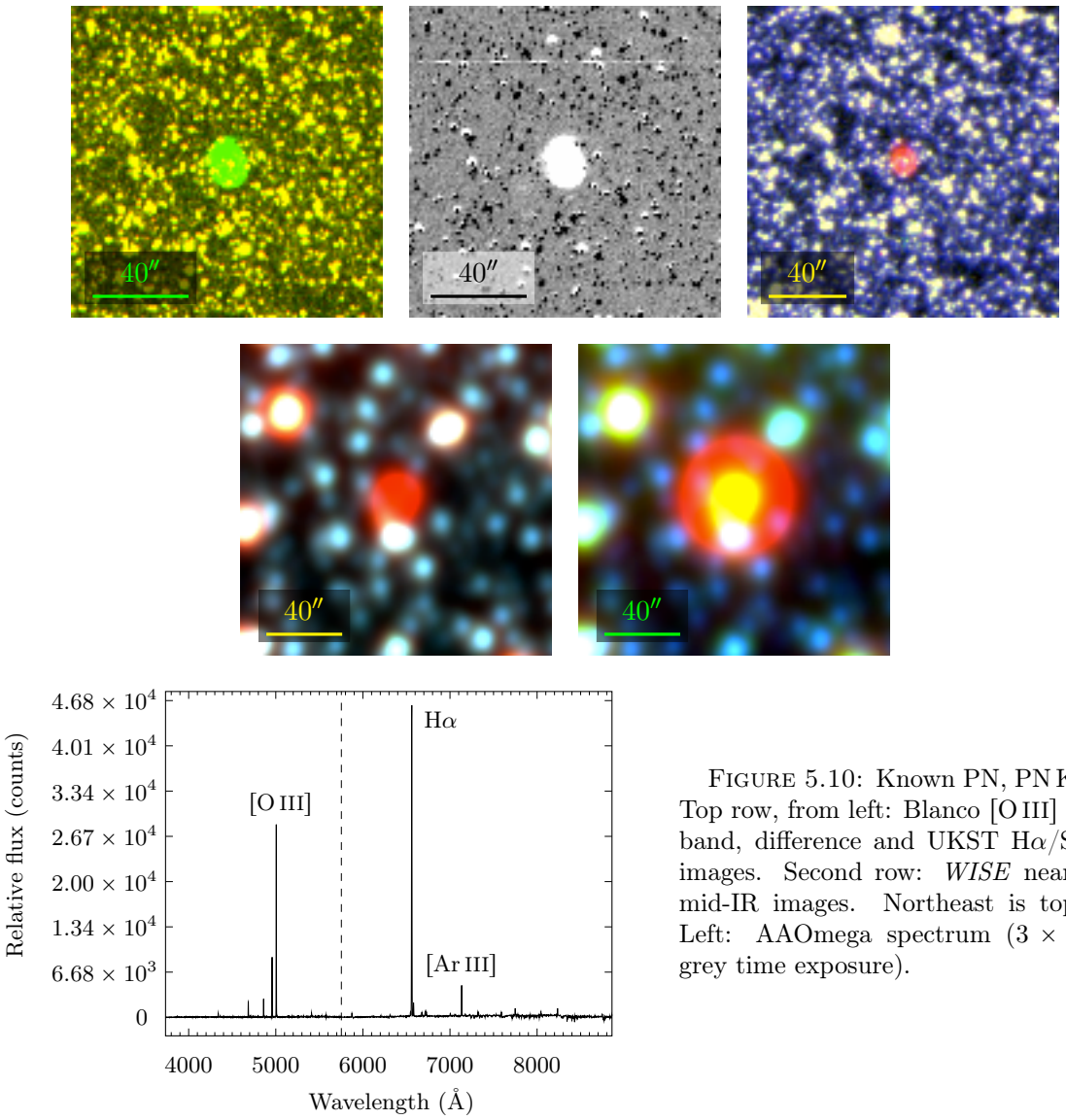

Figure 5.10: Known PN, PN K 6-35. Top row, from left: Blanco [O III] on/off band, difference and UKST Hα/SR/IR images. Second row: *WISE* near- and mid-IR images. Northeast is top left. Left: AAOmega spectrum (3 × 1800 s grey time exposure).

also observed as an ad hoc PN standard for 2dF field A1 (table 3.7, §3.3.2). Based on its relatively low radial velocity ($-13.34\,\mathrm{km\,s^{-1}}$) and low extinction, $c(\mathrm{H}\beta) = 0.96$, it may however be a foreground PN (Kovacevic, 2011).

The AAOmega spectrum obtained (3 × 1200 s grey time exposure), along with visible and IR imaging, are shown in figure 5.12. Aside from [O I] $\lambda\lambda$5577, 6300 airglow artefacts, the spectrum exhibits a range of bright and newly detected faint emission lines including at least [Ar III] $\lambda\lambda$7136, 7751, He I $\lambda\lambda$5876, 6678, 7065, He II $\lambda\lambda$4686, 5412, 8237, [N I] λ5198, [N II] $\lambda\lambda$6548, 6583, Ne III λ3869, [O II] $\lambda\lambda$7319/7320, 7330/7331, [O III] $\lambda\lambda$4959, 5007, [S II] $\lambda\lambda$6716, 6731 and the Balmer series from Hα through to Hϵ. The PN line ratios are generally consistent between this spectrum and the MASH spectrum, except for Hα, which is more than twice as intense measured by AAOmega compared with the MASH spectrum. This discrepancy won't be investigated here, but may be related to differences in fibre placement

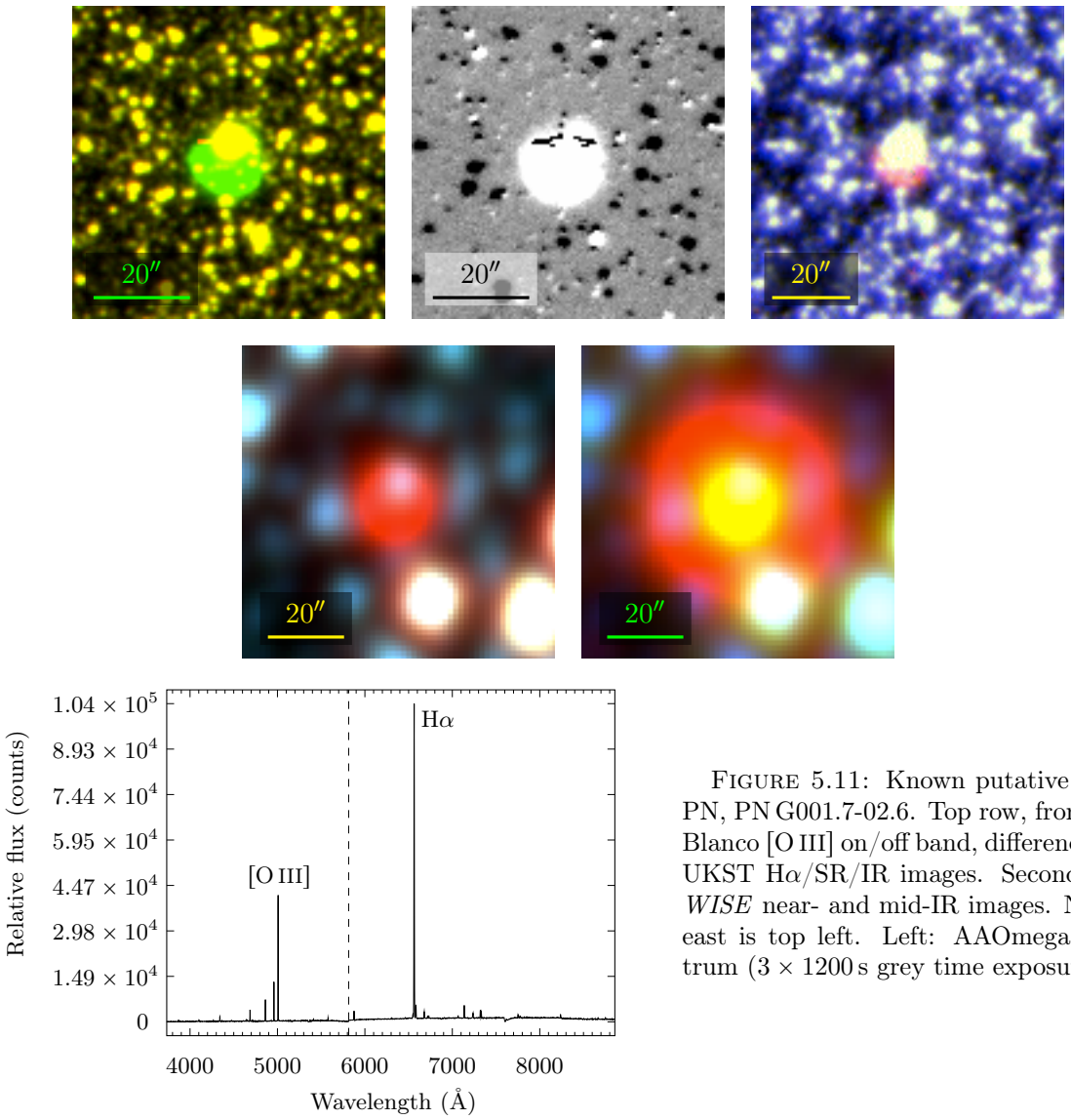

FIGURE 5.11: Known putative bulge PN, PN G001.7-02.6. Top row, from left: Blanco [O III] on/off band, difference and UKST Hα/SR/IR images. Second row: *WISE* near- and mid-IR images. North-east is top left. Left: AAOmega spectrum (3 × 1200 s grey time exposure).

across the nebula.

IC 4673 LIERs

IC 4673 (Dreyer, 1908) is a known foreground PN towards the bulge, e.g. Stanghellini et al. (2008, $d = 3.22$ kpc), Ortiz et al. (2011, $d = 3.55$ kpc), of low radial velocity ($v_r = -15.3 \pm 2.0\,\mathrm{km\,s^{-1}}$ Durand et al., 1998). The faint halo and two accompanying LIERs around this PN were noted in Kovacevic (2011) and Kovacevic et al. (2011a). Observed due to initial confusion with distinct PN candidates, the LIERs are both apparently located ∼105″ away from the centre of IC 4673 along a ray coincident with its major axis.

AAOmega spectra obtained (4 × 1200 s dark time exposure) of these LIERs are shown in figure 5.13, with fibre placements indicated with labelled crosses. The associated LIERs will be referred to as LIER A and LIER B. Assumed artificial data, possibly a reduction pipeline

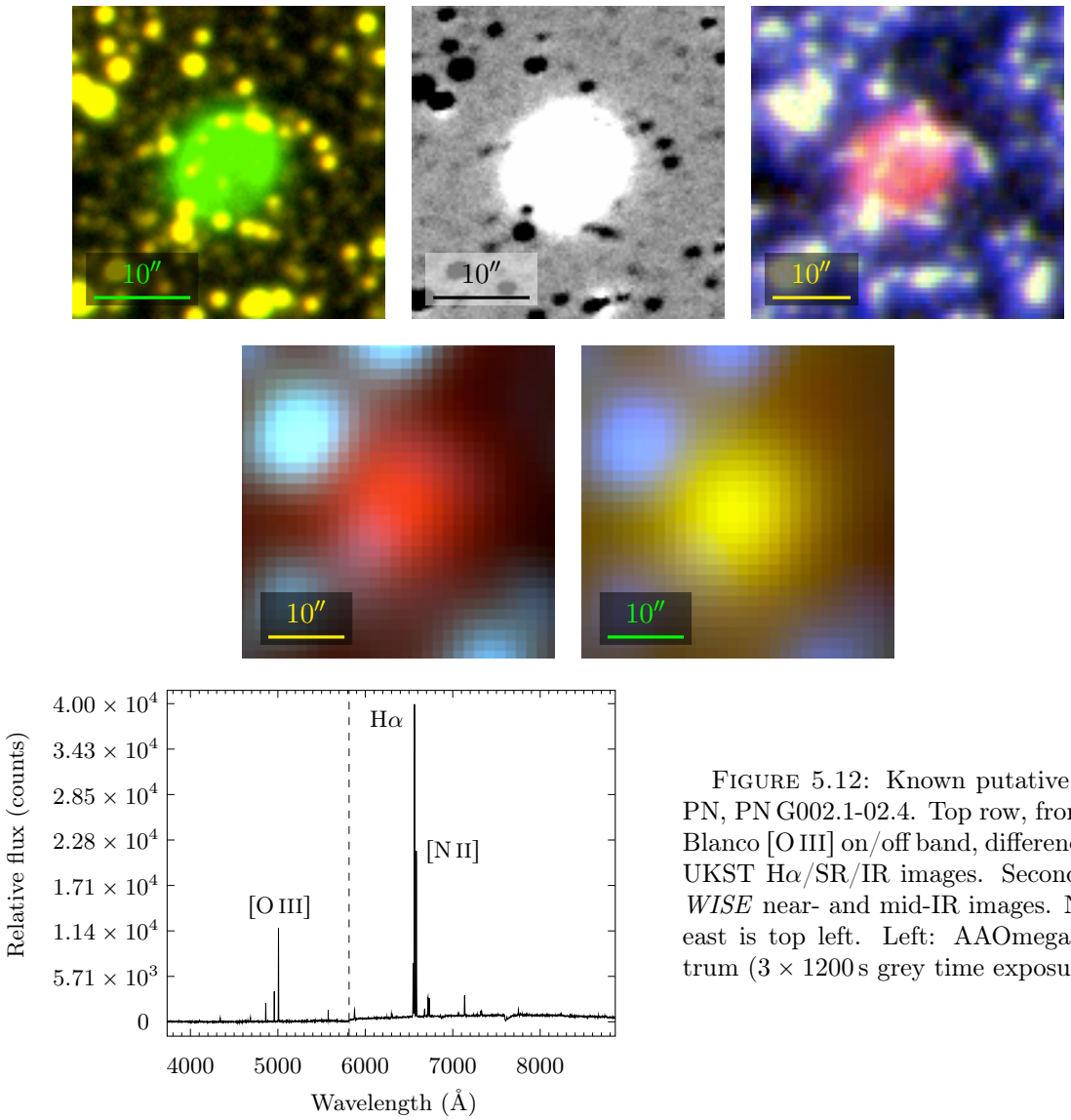

Figure 5.12: Known putative bulge PN, PN G002.1-02.4. Top row, from left: Blanco [O III] on/off band, difference and UKST Hα/SR/IR images. Second row: *WISE* near- and mid-IR images. North-east is top left. Left: AAOmega spectrum (3 × 1200 s grey time exposure).

processing artefact at $\lambda \approx 3549$ Å, has been truncated in each spectrum.

LIER A's spectrum is contaminated by [O I] λ5577 airglow and at least partial coincidence with a late-type star. Key PN emission lines of Hα, Hβ and [O III] $\lambda\lambda$4959, 5007 are however present, consistent with a PN extension. The fainter LIER B, aside from additional [O I] λ5577 and possible oversubtracted [O I] λ6300 airglow processing artefacts, and an unidentified feature at $\lambda \approx 4409$ Å, possibly noise, exhibits Hα and probable [O III] λ5007 emission.

PN G002.4-03.1

Mulitwavelength imaging of known PN, PN G002.4-03.1 (Parker et al., 2006), is shown in figure 5.14. A corresponding spectrum, taken with the Radcliffe 1.9 m telescope (900 s dark time exposure, 500 μm slit width), is shown in the same figure. The spectrum exhibits at least [Ar III] λ7136, Hα, Hβ, Hγ, He I $\lambda\lambda$5876, 7065, [Ne III] λ3869, [O III] $\lambda\lambda$4959, 5007.

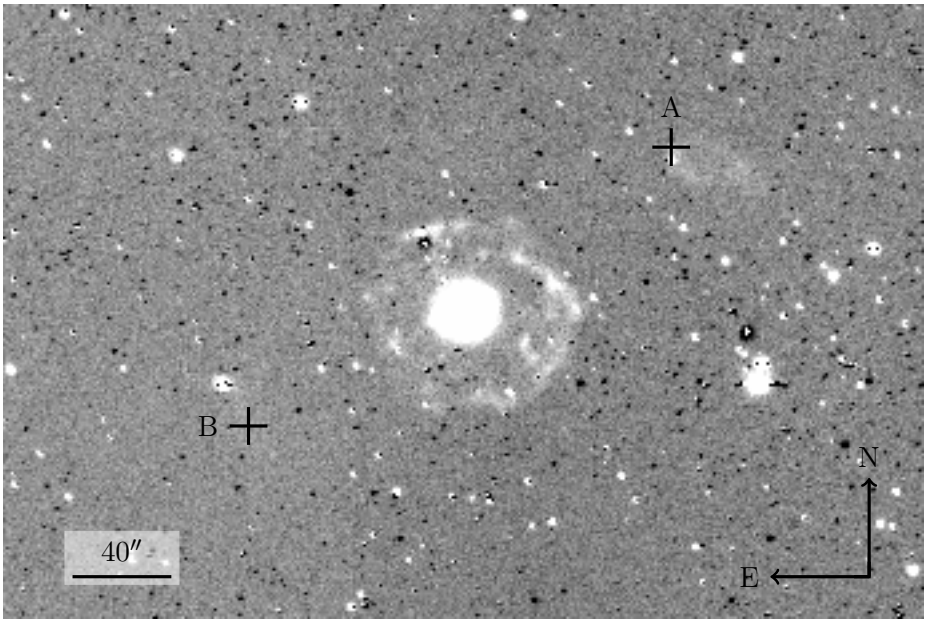

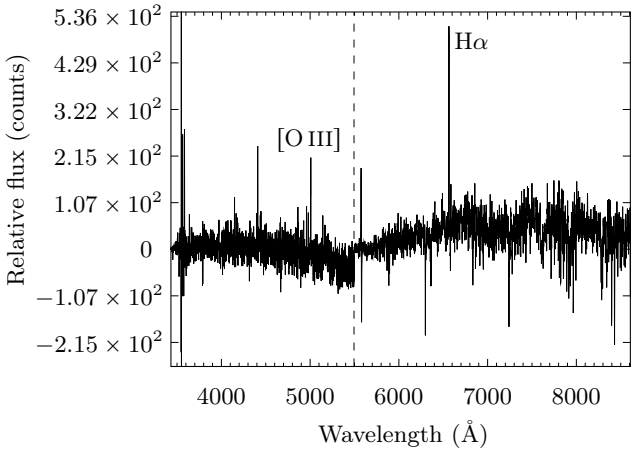

FIGURE 5.13: Above: Blanco difference image of IC 4673 (fibre placements indicated with crosses). A halo and LIERs are visible. Left: AAOmega LIER B spectrum (4 × 1200 s dark time exposure). Hα and probable [O III] λ5007 emission are present, consistent with structure part of a PN.

Right: AAOmega LIER A spectrum (4 × 1200 s dark time exposure). Key PN emission lines of Hα, Hβ and [O III] $\lambda\lambda$4959, 5007 are present. A late-type stellar contaminant is manifest in the red arm data.

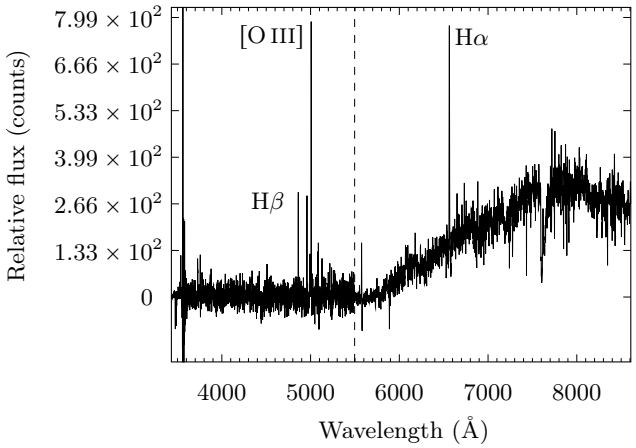

This PN's spectrum will be used for calibration purposes.

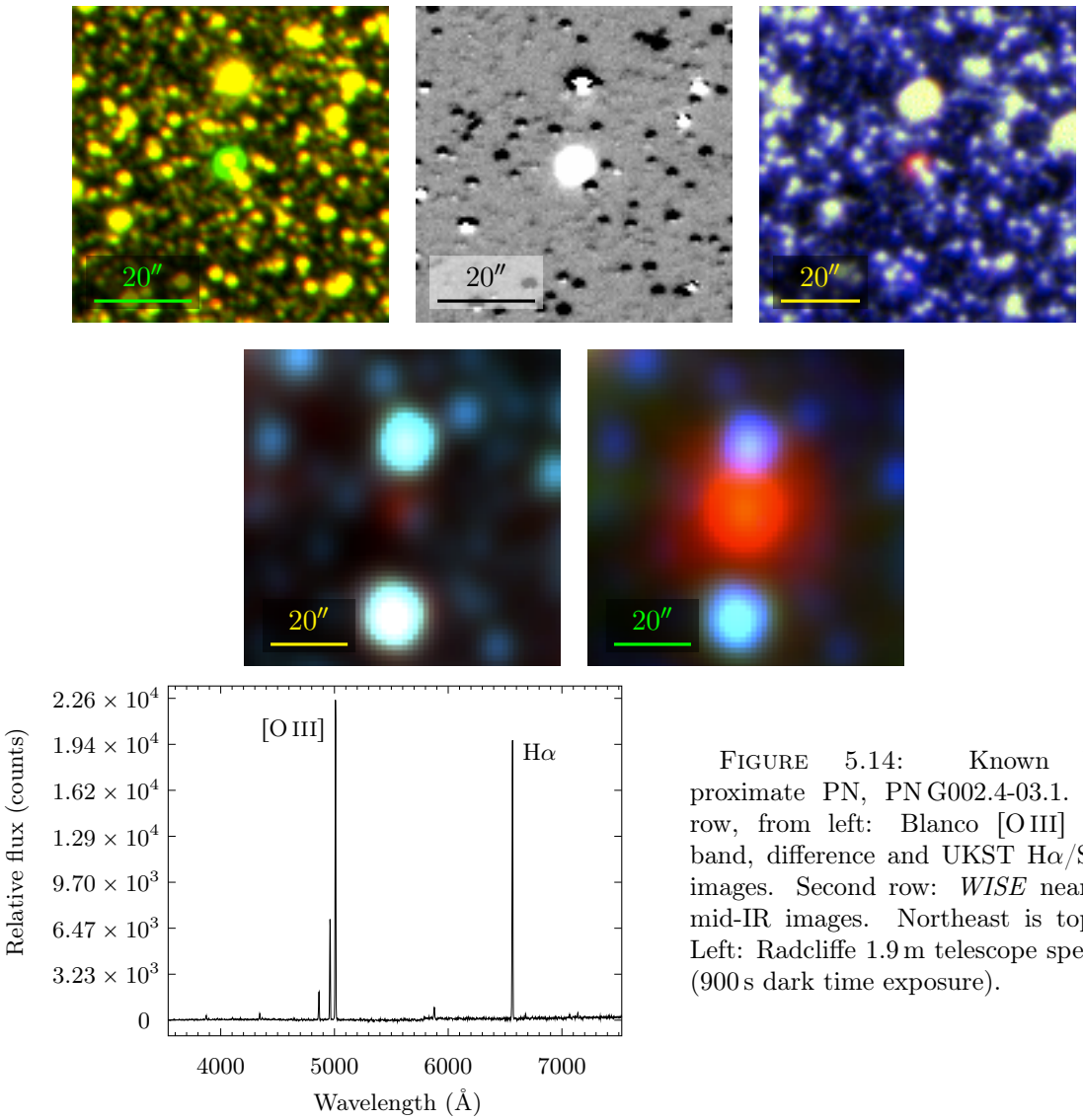

FIGURE 5.14: Known bulge-proximate PN, PN G002.4-03.1. Top row, from left: Blanco [O III] on/off band, difference and UKST Hα/SR/IR images. Second row: *WISE* near- and mid-IR images. Northeast is top left. Left: Radcliffe 1.9 m telescope spectrum (900 s dark time exposure).

5.2 Galactic Stars

An observing log of stars towards the bulge is given in table 5.2. These stars are a combination of compact PN candidates rejected spectroscopically and stars accidentally observed through suboptimal fibre placement in 2dF pointings. The naming convention used for new stars adopts the Dickel et al. (1987) standard, as adopted and referenced earlier for new emission line objects. As the discovery spectra were taken at the SSO, a corresponding designation prefix "SSO" is used. For each star, the observed sky coordinates are given, followed by its estimated apparent centre.

TABLE 5.2: Observing log of supplemental Galactic stars, in J2000 coordinates. For each star, observed sky coordinates, followed by estimated object apparent centre, is listed. Uncertainty in the last digit of coordinates is denoted in brackets. Exposure start time is given in UT, exposure duration denoted $T_{\rm exp}$.

Name	RA (h m s)	Dec (° ′ ″)	Date	Time (UT)	$T_{\rm exp}$ (s)
SSO J174501.536-341612.81	17 45 01.50(2)	−34 16 12.8(3)	5 Jun 2014	14:22:37	3 × 1200
apparent centre	17 45 01.536(5)	−34 16 12.81(8)	–	–	–
SSO J174630.544-343118.74	17 46 30.54(2)	−34 31 18.9(3)	5 Jun 2014	14:22:37	3 × 1200
apparent centre	17 46 30.544(5)	−34 31 18.74(8)	–	–	–
SSO J174654.184-343843.73	17 46 54.17(2)	−34 38 43.9(3)	5 Jun 2014	14:22:37	3 × 1200
apparent centre	17 46 54.184(5)	−34 38 43.73(8)	–	–	–
SSO J175229.553-345156.07	17 52 29.53(2)	−34 51 55.2(3)	5 Jun 2014	14:22:37	3 × 1200
apparent centre	17 52 29.553(5)	−34 51 56.07(7)	–	–	–
SSO J175343.196-345045.07	17 53 43.05(2)	−34 50 46.6(3)	5 Jun 2014	14:22:37	3 × 1200
apparent centre	17 53 43.196(5)	−34 50 45.07(7)	–	–	–
SSO J175911.153-280830.60	17 59 11.21(2)	−28 08 30.5(3)	26 Jul 2013	14:37:39	3 × 1200
apparent centre	17 59 11.153(6)	−28 08 30.60(9)	–	–	–
SSO J175920.084-275514.17	17 59 20.04(2)	−27 55 14.1(3)	26 Jul 2013	14:37:39	3 × 1200
apparent centre	17 59 20.084(6)	−27 55 14.17(9)	–	–	–
SSO J180258.85-291347.4	18 02 58.76(2)	−29 13 47.5(3)	26 Jul 2013	14:37:39	3 × 1200
apparent centre	18 02 58.85(2)	−29 13 47.4(3)	–	–	–
SSO J180313.659-284331.89	18 03 13.64(2)	−28 43 32.4(3)	26 Jul 2013	14:37:39	3 × 1200
apparent centre	18 03 13.659(5)	−28 43 31.89(8)	–	–	–
OGLE BUL-SC36 453627	18 05 33.33(2)	−28 23 30.6(3)	26 Jul 2013	14:37:39	3 × 1200
apparent centre*	18 05 33.33	−28 23 32.7	–	–	–

* Known star, literature coordinates listed (Wray et al., 2004).

SSO J174501.536-341612.81

SSO J174501.536-341612.81 is a new late-type star towards the bulge. Initially assessed as a possible compact PN candidate or emission line star, Blanco, UKST and VVV imaging of this star are given in figure 5.15. The VVV image is a synthetic RGB image, composed of J (red), Y (green) and Z (blue) filter data. For reference, VVV filter specifications are listed in table 5.3. All VVV data presented in §5.2 will be presented this way.

Astrometry for this star can be estimated from Blanco imaging, but a refined solution was sought. Astrometric refinement of new Galactic stars was attempted with 2MASS J band imaging, but many were unresolved in that imaging (and similarly unresolved in *WISE* imaging). Offering both better astrometric precision, with median RMSE = 7×10^{-3} ″ (Saito et al., 2012), and (generally) better source resolution compared with the Blanco imaging, VVV imaging was used instead. Once a star's apparent centre was identified in the imaging, the uncertainty adopted was derived from the RMSE listed in the VVV FITS file header data.

The astrometric RMSE listed in FITS file header data varied from filter to filter (≈6–7% was typical). A conservative approach to precision was taken, and the most uncertain value selected and rounded to one significant digit, yielding $\Delta = 8 \times 10^{-3}\,''$. Except for an isolated case identified later, astrometry for all new stars in §5.2 should be assumed to have been determined in the same manner.

An AAOmega spectrum (3×1200 s dark time exposure) taken of this star is given in figure 5.15. Associated apparent fibre placement on the sky is overlaid on the VVV panel of the figure. [O I] $\lambda\lambda$5577, 6300 airglow processing artefacts are present.

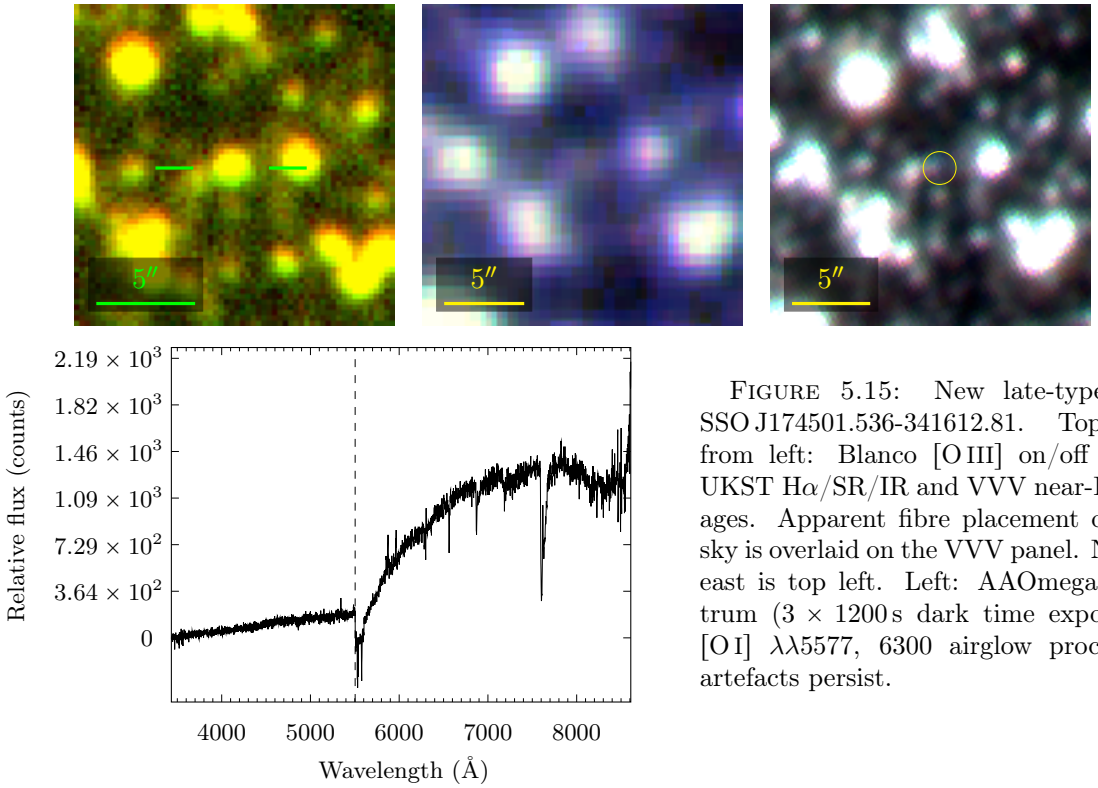

Figure 5.15: New late-type star SSO J174501.536-341612.81. Top row, from left: Blanco [O III] on/off band, UKST Hα/SR/IR and VVV near-IR images. Apparent fibre placement on the sky is overlaid on the VVV panel. North-east is top left. Left: AAOmega spectrum (3×1200 s dark time exposure). [O I] $\lambda\lambda$5577, 6300 airglow processing artefacts persist.

Table 5.3: VVV filter specifications (Saito et al., 2012, Ivanov & Szeifert, 2015). The filters' effective wavelengths, $\lambda_{\rm eff}$, access atmospheric near-IR windows. Precise transmission data was sourced from the SVO's Filter Profile Service (Solano, 2014).

Filter	$\lambda_{\rm eff}$ (μm)	FWHM (μm)	Peak transmission (%)
Z	0.878	0.12	95.0100
Y	1.021	0.10	82.8850
J	1.254	0.18	88.6480
H	1.646	0.30	95.4650
K_s	2.149	0.30	94.1800

SSO J174630.544-343118.74

SSO J174630.544-343118.74 is a new star towards the bulge. From inspection of Blanco imaging, this object was initially assessed as a candidate emission line star. Suspected faint [O III] λ5007 emission in Blanco imaging (more pronounced in Blanco difference imaging) isn't however reflected in the object's spectrum. No emission line signal is obvious in UKST or VVV imaging either, as shown in figure 5.16. An AAOmega spectrum (3×1200 s dark time exposure), also given in figure 5.16, is similarly devoid of obvious [O III] λ5007 or other emission line data (assumed miscellaneous far blue and inter-arm reduction processing artefacts have been truncated for clarity in the spectrum). SSO J174630.544-343118.74 is thus assessed to be an ordinary, not emission line, star towards the bulge.

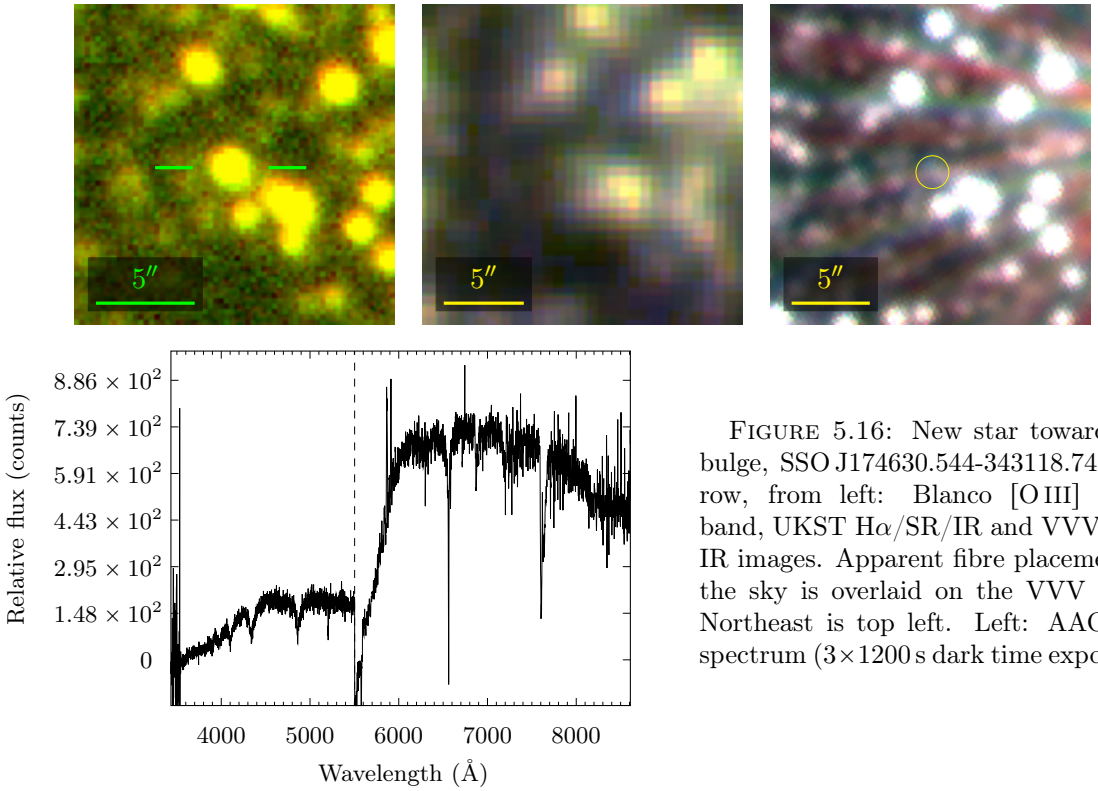

FIGURE 5.16: New star towards the bulge, SSO J174630.544-343118.74. Top row, from left: Blanco [O III] on/off band, UKST Hα/SR/IR and VVV near-IR images. Apparent fibre placement on the sky is overlaid on the VVV panel. Northeast is top left. Left: AAOmega spectrum (3×1200 s dark time exposure).

SSO J174654.184-343843.73

SSO J174654.184-343843.73 is a another new star towards the bulge. This object was initially suspected of being an emission line star. As the Blanco, UKST and VVV imaging and an AAOmega spectrum (3×1200 s dark time exposure) all show however (figure 5.17), SSO J174654.184-343843.73 is a nondescript star lacking definitive emission features. The far blue components of the spectrum are suspected artificial reduction processing artefacts.

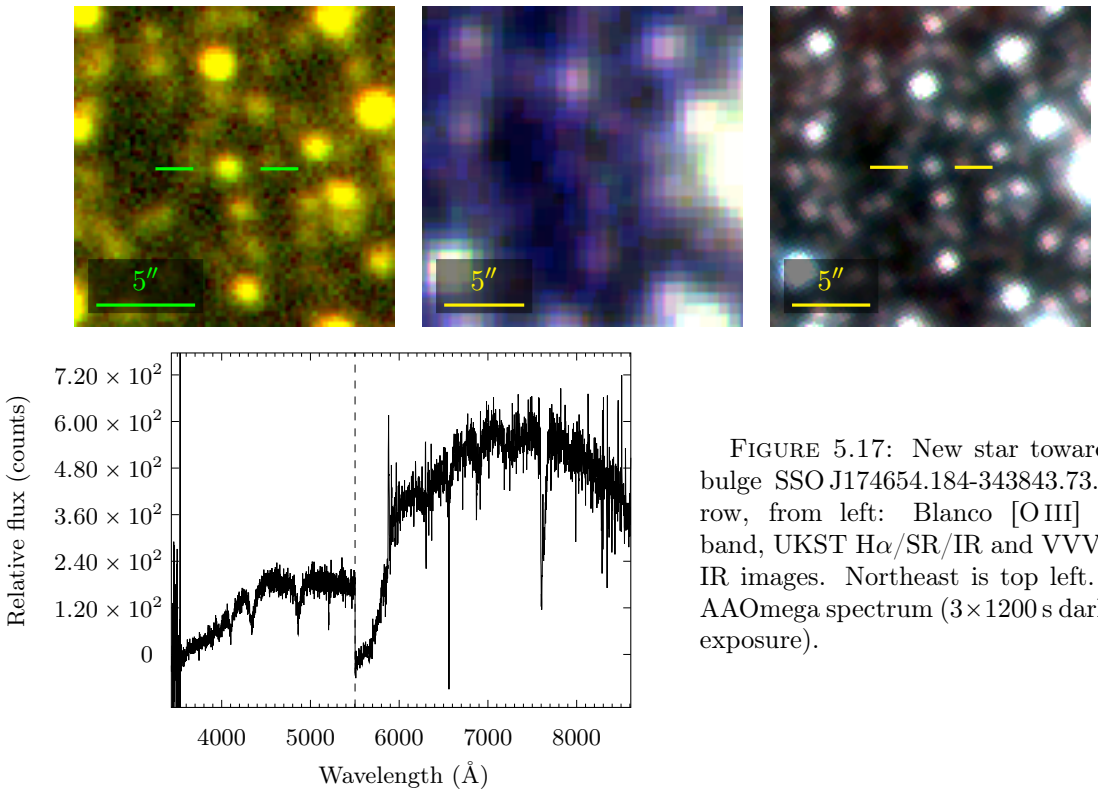

Figure 5.17: New star towards the bulge SSO J174654.184-343843.73. Top row, from left: Blanco [O III] on/off band, UKST Hα/SR/IR and VVV near-IR images. Northeast is top left. Left: AAOmega spectrum (3×1200 s dark time exposure).

SSO J175229.553-345156.07

SSO J175229.553-345156.07 is a another new star inadvertently observed towards the bulge. VVV imaging and an associated AAOmega spectrum (3 × 1200 s dark time exposure) are given in figure 5.18). Assumed miscellaneous reduction processing artefacts are present in the far blue and far red, but have been partly truncated for clarity.

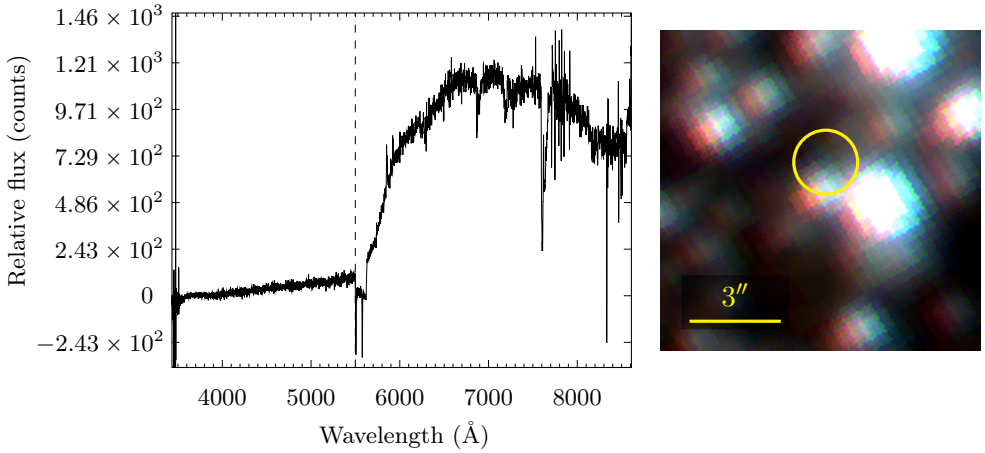

Figure 5.18: New star towards the bulge, SSO J175229.553-345156.07. Left: AAOmega spectrum (3 × 1200 s dark time exposure). Miscellaneous reduction processing artefacts are present in the far blue and far red, but have been partly truncated for clarity. Right: VVV near-IR image, with fibre placement overlaid. Northeast is top left.

SSO J175343.196-345045.07

SSO J175343.196-345045.07 is a late-type star inadvertently observed towards the bulge. An AAOmega spectrum (3×1200 s dark time exposure) and VVV imaging for the star are given in figure 5.19). The fibre placement overlaid in the figure shows only grazing coincidence of the fibre with the star, potentially preventing spectrum saturation in this case.

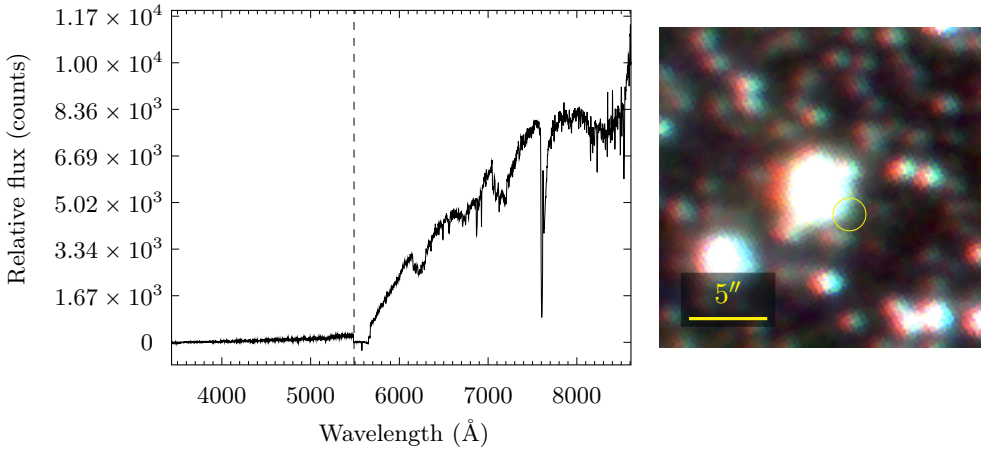

FIGURE 5.19: New late-type star towards the bulge, SSO J175343.196-345045.07. Left: AAOmega spectrum (3×1200 s dark time exposure). Right: VVV near-IR image, with SSO J175343.196-345045.07 prominent at image centre. Fibre placement, only partially coincident with the star, is overlaid. Northeast is top left.

SSO J175911.153-280830.60

SSO J175911.153-280830.60 is a new, faint, late-type star towards the bulge. Blanco, UKST and VVV (JYZ) imaging of this star are given in figure 5.20. The fibre offset from the star is overlaid on the Blanco imaging. The AAOmega spectrum (3×1200 s grey time exposure) taken of this star is given in the same figure. The miscellaneous emission features not attributable to airglow processing artefacts, [O I] $\lambda\lambda$5577, 6300, 6364 in this case, are unidentified and possibly noise.

SSO J175920.084-275514.17

SSO J175920.084-275514.17 is another new late-type star towards the bulge. Blanco, UKST, VVV and *WISE* imaging of this star are given in figure 5.21. The *WISE* imaging demonstrates its generally poor suitability to identifying these new, small apparent diameter late-type stars in crowded bulge fields. Again, the actual fibre positioning, slightly offset from the star's apparent centre, is overlaid in the Blanco panel of figure 5.21.

An AAOmega spectrum (3×1200 s grey time exposure) taken of this star is given in figure 5.21. Aside from an [O I] λ5577 airglow artefact, emission line contributions from putative faint coincident PN CTIO J175919.98-275515.3 (§3.4) contaminate the spectrum.

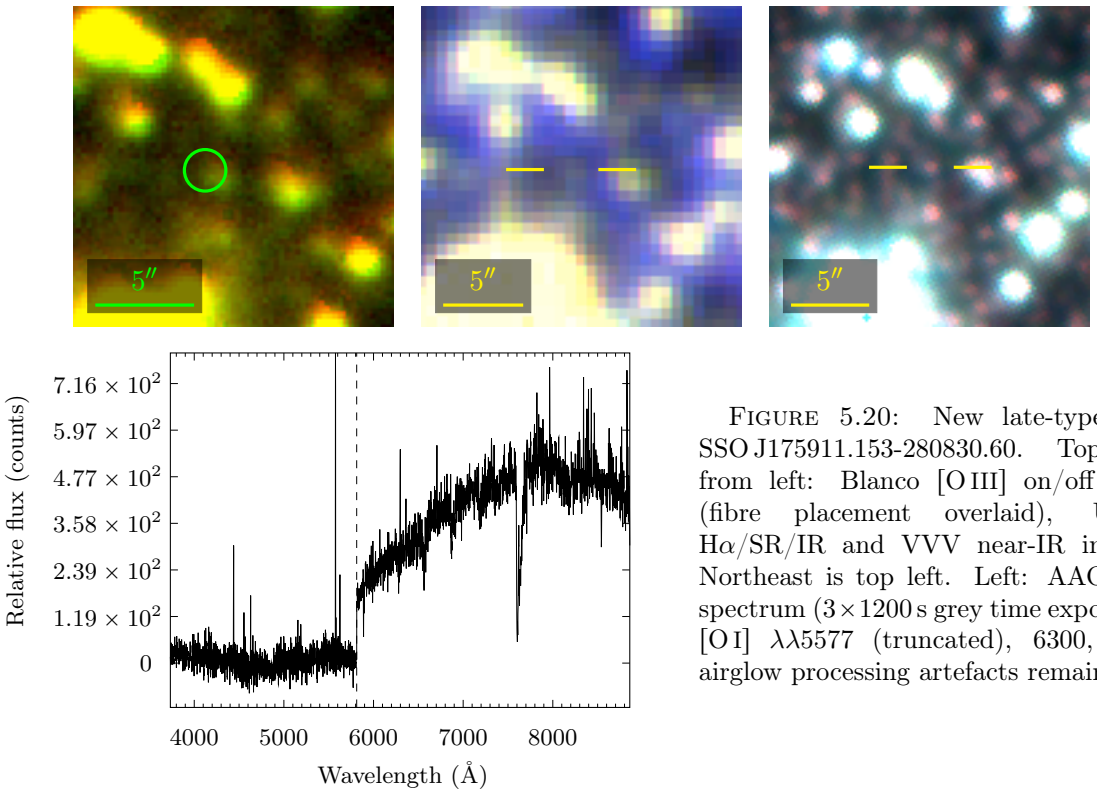

Figure 5.20: New late-type star SSO J175911.153-280830.60. Top row, from left: Blanco [O III] on/off band (fibre placement overlaid), UKST Hα/SR/IR and VVV near-IR images. Northeast is top left. Left: AAOmega spectrum (3×1200 s grey time exposure). [O I] $\lambda\lambda$5577 (truncated), 6300, 6364 airglow processing artefacts remain.

These emission lines include [O III] λ5007 and Hα. An unidentified feature at $\lambda \approx 4893$ Å, atypical for a PN and absent from subsequent spectra taken of that PN, is present.

SSO J180258.85-291347.4

SSO J180258.85-291347.4 is a further late-type star towards the bulge that was inadvertently sampled spectroscopically. This star can't be resolved from its neighbours in VVV imaging, as shown in figure 5.22. Astrometry was instead determined from Blanco imaging. Fibre placement is again shown in the Blanco imaging, highlighting the star sampled.

An AAOmega spectrum (3×1200 s grey time exposure) for this star is given in figure 5.22. This star is approximately coincident with the apparent geometrical centre of possible PN CTIO J180258.75-291347.5 (§3.4.3). A modest airglow processing artefact, [O I] λ5577, is present, but the stellar spectrum otherwise overwhelms any faint emission lines such as those that might provide evidence for a PN nature of CTIO J180258.75-291347.5.

SSO J180313.659-284331.89

SSO J180313.659-284331.89 is another new late-type star inadvertently sampled spectroscopically when pursuing bulge PNs. VVV imaging and an AAOmega spectrum (3×1200 s grey time exposure) are shown in figure 5.23.

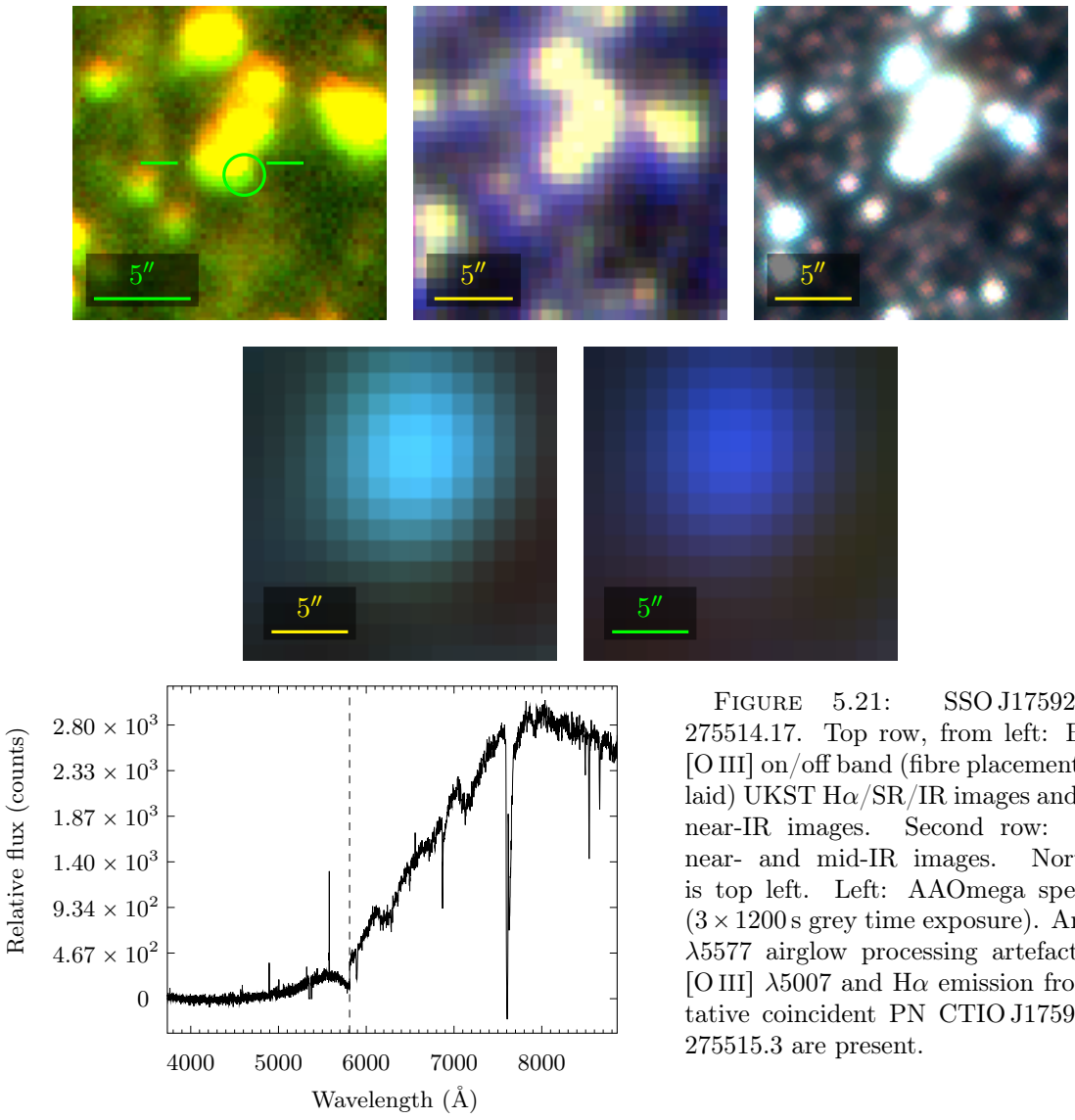

FIGURE 5.21: SSO J175920.084-275514.17. Top row, from left: Blanco [O III] on/off band (fibre placement overlaid) UKST Hα/SR/IR images and VVV near-IR images. Second row: *WISE* near- and mid-IR images. Northeast is top left. Left: AAOmega spectrum (3×1200 s grey time exposure). An [O I] λ5577 airglow processing artefact, and [O III] λ5007 and Hα emission from putative coincident PN CTIO J175919.98-275515.3 are present.

OGLE BUL-SC36 453627

OGLE BUL-SC36 453627 is a known small amplitude (dominant period amplitude = 6.096×10^{-2} mag, Wray et al., 2004) variable red giant star. An AAOmega spectrum (3×1200 s grey time exposure) taken of this star is thought to be its first known spectrum. Imaging and the spectrum are given in figure 5.24. The TiO bands are consistent with an M-type star.

5.3 Large Magellanic Cloud PNs

The LMC objects detailed here are known PNs that will be used for calibration purposes. These PNs were observed with the CCDSpec on the 1.9 m Radcliffe telescope and an observing log is provided in table 5.4. Coordinates listed are sky coordinates observed, not object apparent centres. Observing commenced with a default slit width of 350 μm, but soon needed

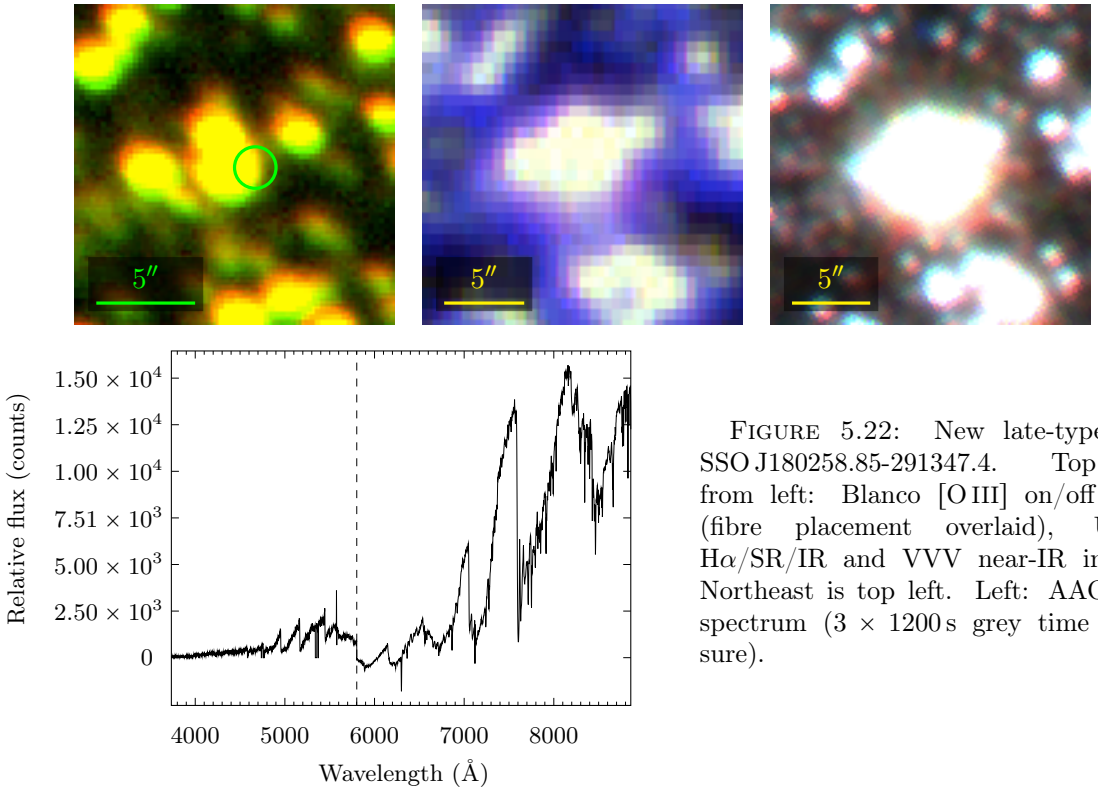

Figure 5.22: New late-type star SSO J180258.85-291347.4. Top row, from left: Blanco [O III] on/off band (fibre placement overlaid), UKST Hα/SR/IR and VVV near-IR images. Northeast is top left. Left: AAOmega spectrum (3 × 1200 s grey time exposure).

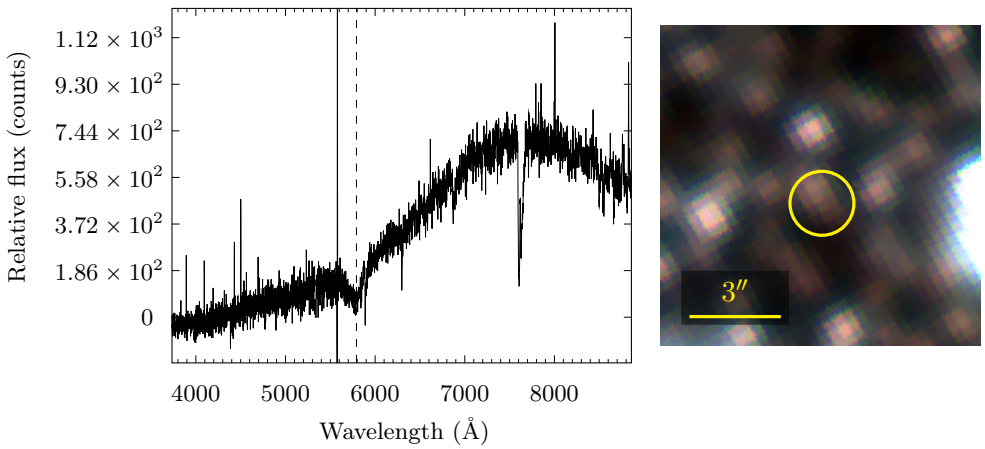

Figure 5.23: New late-type star SSO J180313.659-284331.89. Left: AAOmega spectrum (3×1200 s grey time exposure). An [O I] λ5577 airglow processing artefact has been truncated for clarity. Right: VVV near-IR image, with fibre placement overlaid. Northeast is top left.

to be widened due to poor seeing.

SMP LMC 31

The spectrum obtained for SMP LMC 31 is given in figure 5.25. This target has been known as an Hα emission line object (Henize, 1956, Lindsay & Mullan, 1963) and then PN (Sanduleak

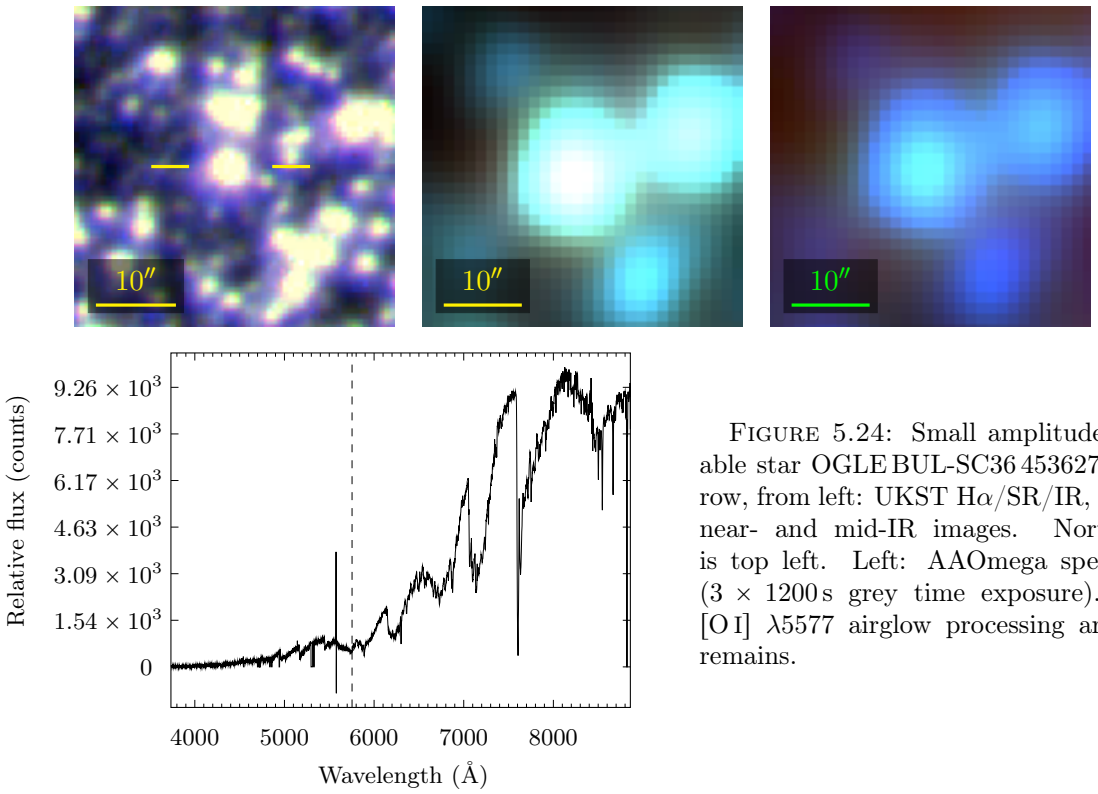

FIGURE 5.24: Small amplitude variable star OGLE BUL-SC36 453627. Top row, from left: UKST Hα/SR/IR, *WISE* near- and mid-IR images. Northeast is top left. Left: AAOmega spectrum (3×1200 s grey time exposure). An [O I] λ5577 airglow processing artefact remains.

TABLE 5.4: Observing log of LMC PNs in J2000 coordinates. Sky coordinates observed, not object apparent centres, are listed. Exposure start time is given in UT, exposure duration denoted $T_{\rm exp}$ and adjustable slit width given in microns.

Name	RA (h m s) ± 0.01 s	Dec (° ′ ″) $\pm 0.2''$	Date	Time (UT)	$T_{\rm exp}$ (s)	Slit (μm)
SMP LMC 31	05 09 20.00	−67 47 24.0	18 Aug 2013	03:05:12	1200	500
LHA 120-N 28	05 11 01.99	−67 48 02.2	18 Aug 2013	03:34:16	1200	500

et al., 1978), for decades. Further spectroscopy (e.g. Monk et al., 1988, Meatheringham & Dopita, 1991, Stanghellini et al., 2002), again showing forbidden and allowed emission lines, further supports a PN nature and yet it has somehow received primary categorisation as a cluster[1] star in SIMBAD. A range of visible and IR fluxes (e.g. Wood et al., 1987, Jacoby et al., 1990, Hora et al., 2008) and other measured and derived physical parameters, such as abundances (e.g. Henry, 1990, Leisy & Dennefeld, 2006), angular diameter, CSPN properties (Kaler & Jacoby, 1991, Villaver et al., 2003), dust emission (Bernard-Salas et al., 2009), electron densities and temperatures, expansion velocities, ionised mass (e.g. Boffi & Stanghellini, 1994), kinematics (e.g. Meatheringham et al., 1988), morphology (Shaw et al., 2001), etc., are available for this object in the literature.

[1] Associated with LMC cluster NGC 1852 and classified as a PN by van Loon et al. (2005).

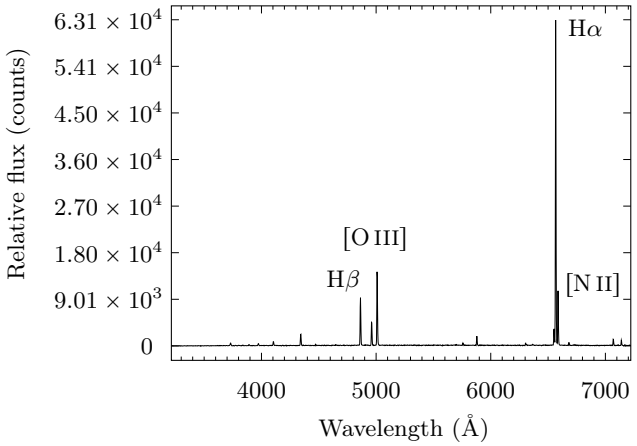

FIGURE 5.25: Radcliffe 1.9 m telescope spectrum (1200 s bright and dark time, night time exposure) of SMP LMC 31, consistent with a low excitation PN.

Meatheringham & Dopita (1991) notes the Balmer decrement of SMP LMC 31 is poorly fit by a single reddening constant, possibly indicative of a [WR] central star. Characteristics associated with [WR] CSPNs discussed in §1.6 include high nebula expansion velocities and mass loss rates ($> 10^{-6}\,M_{\odot}\,\mathrm{yr}^{-1}$). The SMP LMC 31 expansion velocity ($5.1\,\mathrm{km\,s}^{-1}$ and $14.4\,\mathrm{km\,s}^{-1}$, derived from [O III] λ5007 and [O II] $\lambda\lambda$3727, 3729 emission respectively, Dopita et al., 1988), is slow compared to the mean values ($35.6\,\mathrm{km\,s}^{-1}$ and $39.6\,\mathrm{km\,s}^{-1}$) of the Dopita et al. (1988) LMC PN cohort, in contradiction of a [WR] CSPN. Its mass loss rate ($5.62 \times 10^{-5}\,M_{\odot}\,\mathrm{yr}^{-1}$, van Loon et al., 2005) is however consistent with a [WR] CSPN.

The emission line spectrum obtained here is consistent with the literature (e.g. Meatheringham & Dopita, 1991) and reiterates, evidentially, the PN and not stellar nature of this object. A SIMBAD reclassification would be appropriate.

LHA 120-N 28

The spectrum obtained for LHA 120-N 28 is given in figure 5.26. As for SMP LMC 31, LHA 120-N 28 has been known as a Hα emission line object (Henize, 1956, Lindsay & Mullan, 1963), then PN (Westerlund & Smith, 1964), for decades. The spectrum obtained here is consistent with previous spectroscopy (e.g. Meatheringham & Dopita, 1991), although it is noted the data of Leisy & Dennefeld (2006) claims [O III] λ4959 emission without [O III] λ5007 emission, probably a typographical error. It is suspected the λ7022 feature in the spectrum here is a subtle cosmic ray artefact, so reobservation of this object is recommended for clarification.

5.4 Candidate Small Magellanic Cloud PNs

All SMC candidate PNs observed were identified as candidates by others, with the candidate identification and analysis process described in more detail elsewhere (Jacoby & De Marco, 2002, Drašković et al., 2015). An observing and evaluation summary of these PNs is given here however. As these observations were supplemental to bulge observing, they were often taken in either late nautical twilight or early astronomical twilight and are generally high noise observations. The candidate PNs identified may, on more rigorous confirmation, partially

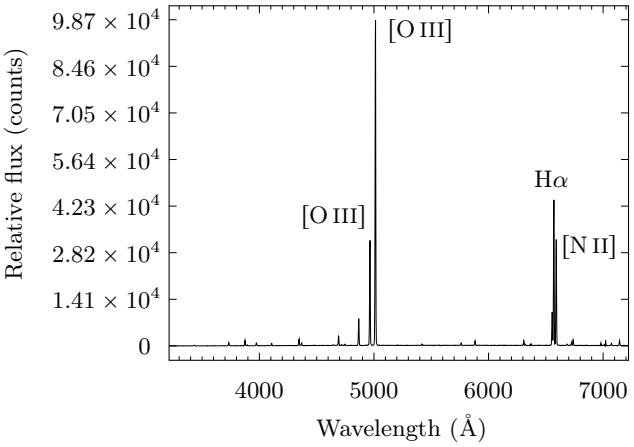

FIGURE 5.26: Radcliffe 1.9 m telescope spectrum (1200 s dark time, night time and astronomical twilight exposure) of LHA 120-N 28, consistent with a medium excitation PN.

bridge the gap in the known and estimated total SMC PN population (84 vs. 132, Jacoby, 2006).

An observing log of candidate SMC PNs is given in table 5.5. Coordinates are supplied for both sky coordinates observed and object apparent centres. Object astrometry is that given in UKST Hα FITS data, with the uncertainty assigned twice the standard deviation of the astrometric fit in that data. As for the LMC PN candidates, the SMC targets were observed with the CCDSpec on the 1.9 m Radcliffe telescope. New candidates were assigned designations consistent with those adopted earlier in this chapter. A default slit width of 350 μm was used, but selectively widened during periods of poor seeing.

TABLE 5.5: Observing log of PN candidates towards the SMC, in J2000 coordinates. For each candidate, observed sky coordinates, followed by estimated object apparent centre, is listed. Uncertainty in the last digit of coordinates is denoted in brackets. Exposure start time is given in UT, exposure duration denoted $T_{\rm exp}$ and adjustable slit width given in microns.

Name	RA (h m s)	Dec (° ′ ″)	Date	Time (UT)	$T_{\rm exp}$ (s)	Slit (μm)
SAAO J005426.37-723059.1	00 54 25.99(2)	−72 30 59.0(4)	7 Mar 2014	17:52:42	1200	350
apparent centre	00 54 26.37(5)	−72 30 59.1(2)	–	–	–	–
[JD2002] J005719.7-721314.5	00 57 19.99(2)	−72 13 14.2(4)	18 Aug 2013	02:07:36	1800	400
apparent centre*	00 57 19.7	−72 13 14.5	–	–	–	–
SAAO J005947.48-723230.2	00 59 46.99(2)	−72 32 30.8(4)	11 Mar 2014	18:01:46	1130	350
apparent centre	00 59 47.48(4)	−72 32 30.2(1)	–	–	–	–
SAAO J010255.26-722131.2	01 02 55.01(2)	−72 21 32.0(4)	9 Mar 2014	18:00:10	1800	500
apparent centre	01 02 55.26(4)	−72 21 31.2(1)	–	–	–	–
SAAO J010430.04-731510.0	01 04 30.00(2)	−73 15 10.1(4)	8 Mar 2014	17:59:24	1200	350
apparent centre	01 04 30.04(4)	−73 15 10.0(1)	–	–	–	–

* Known object, literature coordinates listed (Jacoby & De Marco, 2002).

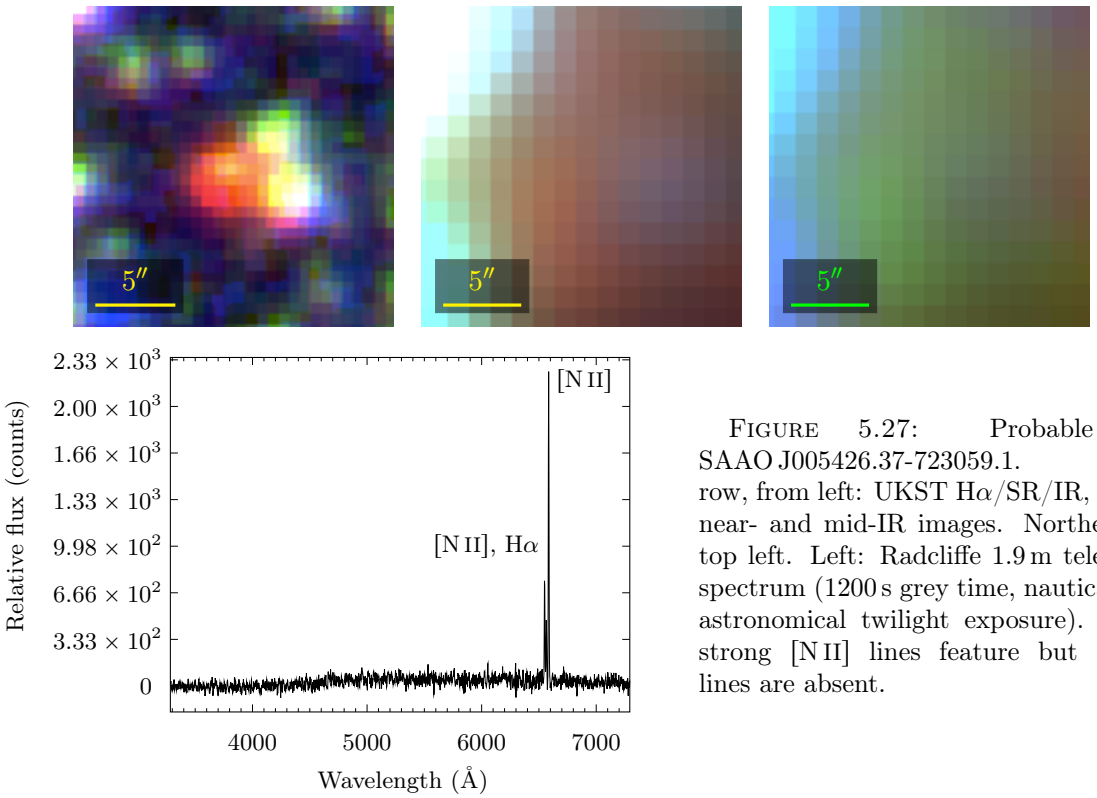

Figure 5.27: Probable PN SAAO J005426.37-723059.1. Top row, from left: UKST Hα/SR/IR, *WISE* near- and mid-IR images. Northeast is top left. Left: Radcliffe 1.9 m telescope spectrum (1200 s grey time, nautical and astronomical twilight exposure). Very strong [N II] lines feature but [O III] lines are absent.

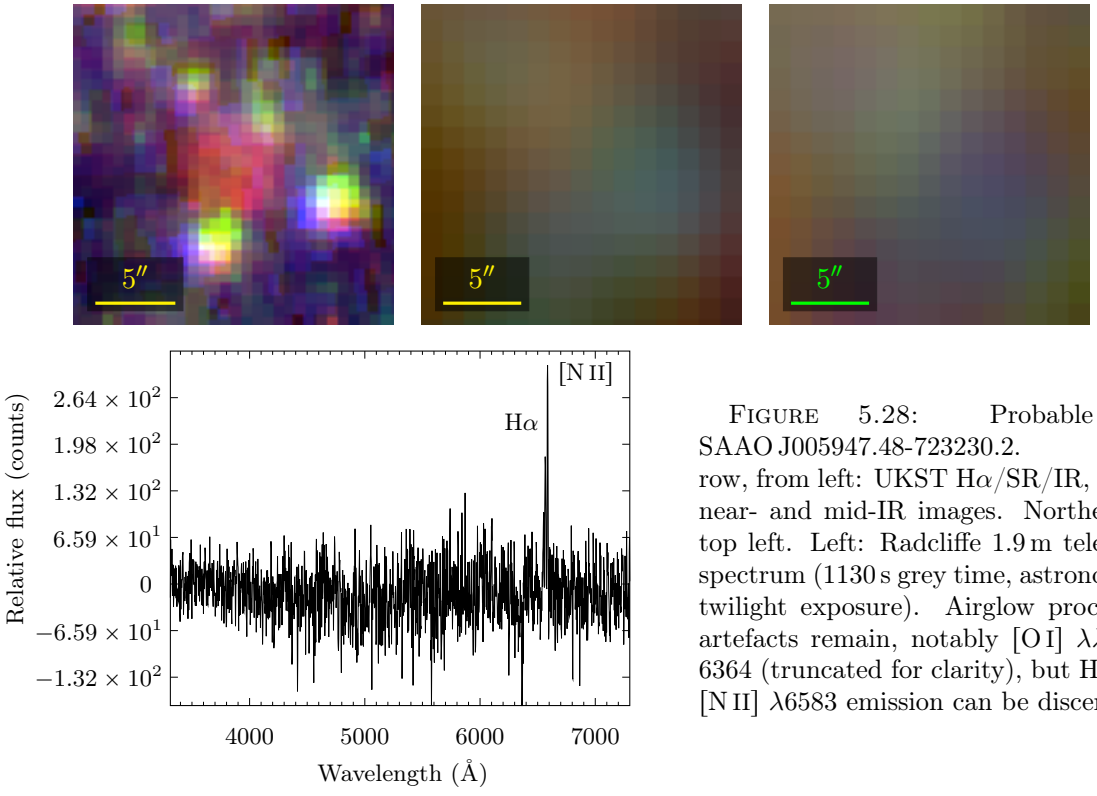

Figure 5.28: Probable PN SAAO J005947.48-723230.2. Top row, from left: UKST Hα/SR/IR, *WISE* near- and mid-IR images. Northeast is top left. Left: Radcliffe 1.9 m telescope spectrum (1130 s grey time, astronomical twilight exposure). Airglow processing artefacts remain, notably [O I] $\lambda\lambda$5577, 6364 (truncated for clarity), but Hα and [N II] λ6583 emission can be discerned.

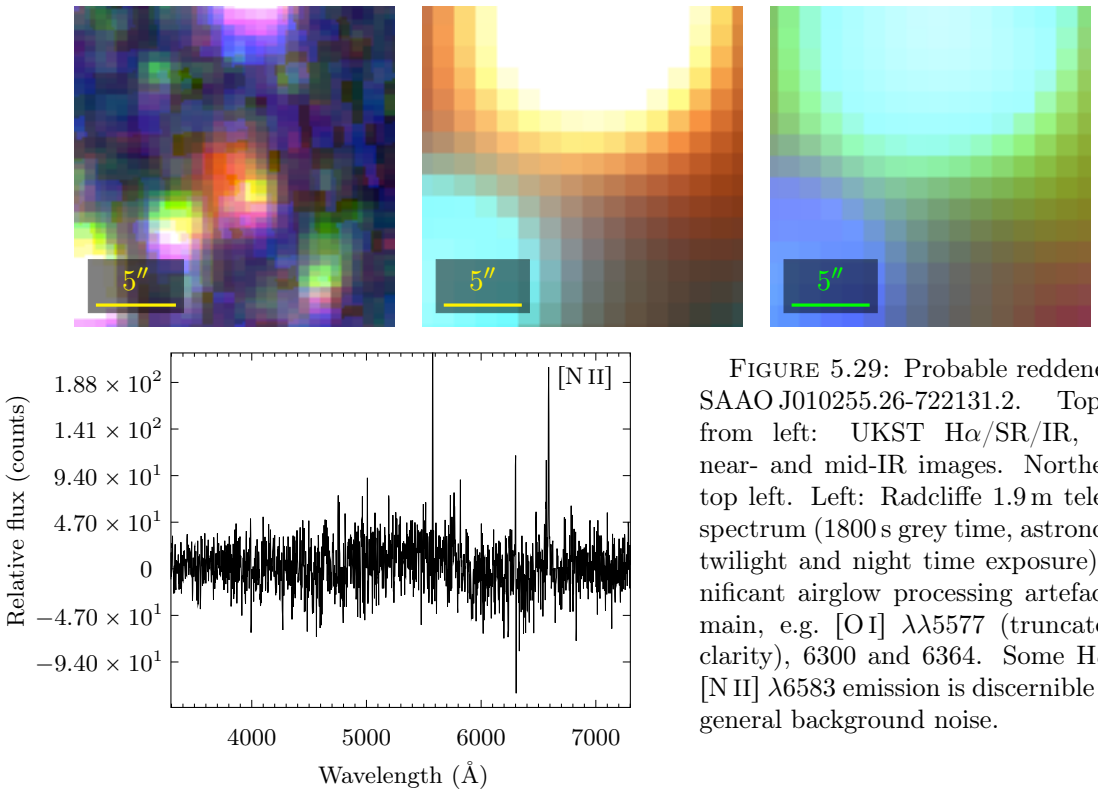

FIGURE 5.29: Probable reddened PN SAAO J010255.26-722131.2. Top row, from left: UKST Hα/SR/IR, *WISE* near- and mid-IR images. Northeast is top left. Left: Radcliffe 1.9 m telescope spectrum (1800 s grey time, astronomical twilight and night time exposure). Significant airglow processing artefacts remain, e.g. [O I] $\lambda\lambda$5577 (truncated for clarity), 6300 and 6364. Some Hα and [N II] λ6583 emission is discernible above general background noise.

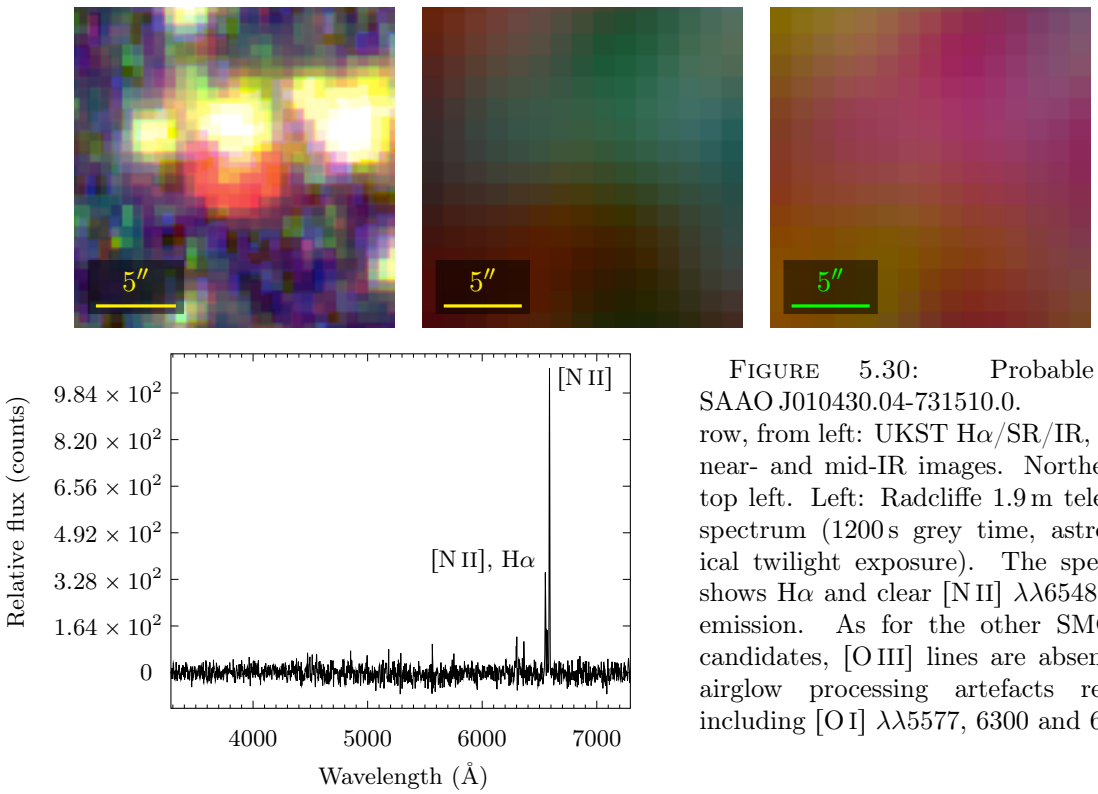

FIGURE 5.30: Probable PN SAAO J010430.04-731510.0. Top row, from left: UKST Hα/SR/IR, *WISE* near- and mid-IR images. Northeast is top left. Left: Radcliffe 1.9 m telescope spectrum (1200 s grey time, astronomical twilight exposure). The spectrum shows Hα and clear [N II] $\lambda\lambda$6548, 6583 emission. As for the other SMC PN candidates, [O III] lines are absent and airglow processing artefacts remain, including [O I] $\lambda\lambda$5577, 6300 and 6364.

Table 5.6: Approximate relative line intensity ratios of SMC PN candidates. It is acknowledged the ratios listed for SAAO J005947.48-723230.2 and SAAO J010255.26-722131.2, incorporating [N II] λ6548 data within noise levels, are of limited accuracy.

Name	$\frac{I([\mathrm{N\,II}]\ \lambda\lambda 6548, 6583)}{I(\mathrm{H}\alpha)}$	Notes
SAAO J005426.37-723059.1	6.37	–
[JD2002] J005719.7-721314.5	–	no detection
SAAO J005947.48-723230.2	2.28	estimate
SAAO J010255.26-722131.2	2.27	estimate
SAAO J010430.04-731510.0	9.54	–

Nitrogen-Rich Candidates

A detailed analysis of the new SMC PN candidates is presented in (Drašković et al., 2015). On the basis of the spectroscopic evidence obtained here however, given in figures 5.27–5.30, they are all viable possible or probable PNs. Their apparent positioning is consistent with SMC sources, but discrimination from foreground nebulas via radial velocity analysis is recommended. All of these candidates appear to be high (> 1) $I([\mathrm{N\,II}]\ \lambda\lambda 6548, 6583)/I(\mathrm{H}\alpha)$ emission sources with no, or negligible, [O III] emission. Quantitative approximate line ratio estimates are presented in table 5.6. Assumed line ratio uncertainty is 48% (see chapter 6).

Deeper spectroscopic examination of these candidates, especially of SAAO J005947.48-723230.2 and SAAO J010255.26-722131.2, is recommended to better assess their nature. If assessed as true PNs, these candidates would provide additional data to speak to possible trends of high $I([\mathrm{N\,II}])/I(\mathrm{H}\alpha)$ emission with galactic metallicity and PN luminosity (Jacoby & De Marco, 2002). In addition, if candidate Hβ and [O III] λ5007 emission was detected in deeper spectroscopy and flux calibration was possible, the SMC PNLF (e.g. figure 2.3) could be refined.

[JD2002] J005719.7-721314.5

An attempt was made to take a spectrum (1800 s bright time exposure) of [JD2002] J005719.7-721314.5. This possible PN is referenced as an undesignated candidate in Jacoby & De Marco (2002). The resulting spectrum showed no evidence of an emission line source. The associated pointing was taken as an unplanned target of opportunity on the basis of coordinates derived from those appearing in Jacoby & De Marco (2002), without the aid of an accurate finding chart. As such, a small positioning error may have contributed to the lack of candidate confirmation. It is suspected however that the candidate was simply too faint for the observing conditions. Its faintness in [O III] imaging (1800/900 s on/off band exposures) taken with the Wide Field Imager (Baade et al., 1999) on the 2.2 m Max Planck Gesellschaft/European Southern Observatory telescope is noted in Jacoby & De Marco (2002), as is failure of a

100 s acquisition spectrum taken with the (now retired) R-C Spectrograph on the 4 m Blanco telescope to yield emission line data. Reattempting spectroscopic confirmation in darker conditions on a telescope larger than the Radcliffe is recommended.

6

New Bulge PNLF

6.1 Bulge Membership

The new PN candidates discovered here could consist of a mix of Galactic bulge PNs and foreground Galactic disc PNs. Note, the terms "Galactic bulge" and "Galactic bar" will not be formally differentiated here. For the purposes of this project however, a working definition of the bulge and its assumed properties includes:

- a boxy, triaxial (Blitz & Spergel, 1991, Weiland et al., 1994, Stanek et al., 1994) (scale lengths $0.70 : 0.44 : 0.18\,\mathrm{kpc}$, Wegg & Gerhard (2013)) collection of stars around the Galactic centre ($l = 0^\circ$, $b = 0^\circ$), X-shaped at $|z| \gtrsim 0.5\,\mathrm{kpc}$ (Wegg & Gerhard, 2013),
- an inclination, within the Galactic plane, of $(27 \pm 2)^\circ$ to line of sight (Wegg & Gerhard, 2013), i.e. with near side in the first Galactic quadrant,
- a high stellar density, i.e. $\sim 1 \times 10^7\,\mathrm{stars\,pc^{-3}}$ vs. $\sim 2 \times 10^{-1}\,\mathrm{stars\,pc^{-3}}$ in the Solar neighbourhood, (Moore, 2000),
- a predominantly old stellar population ($\geqslant$10 Gyr, Zoccali et al., 2003),
- a metallicity distribution peaking at $[\mathrm{M/H}] \approx -0.1$ (Zoccali et al., 2003)[1], close to Solar metallicity,
- a heliocentric distance of $7.9 \pm 0.3\,\mathrm{kpc}$ (McNamara et al., 2000)[2].

[1] The metal abundance ratio $[\mathrm{M/H}] = \log(Z/X) - \log(Z/X)_\odot$, where Z is metallicity and X the hydrogen mass fraction (Salaris & Cassisi, 2005).

[2] Consistent with earlier distance estimates, e.g. $8.0 \pm 0.5\,\mathrm{kpc}$ (Reid, 1993).

To discriminate between bulge and disc PNs, radial velocities were first examined. Galactic bulge PNs exhibit a greater radial velocity dispersion compared with disc PNs, with extrema reaching $-268.1 \pm 5.5\,\mathrm{km\,s^{-1}}$ and $220.5 \pm 0.9\,\mathrm{km\,s^{-1}}$ (Durand et al., 1998)[3]. Statistical analysis of the Durand et al. (1998) radial velocity data indicates, to within 2σ confidence, PNs with $0^\circ < l \leqslant 5^\circ$ and $v_\mathrm{r} < -76.3\,\mathrm{km\,s^{-1}}$ or $v_\mathrm{r} > 126.1\,\mathrm{km\,s^{-1}}$ and PNs with $-5^\circ \leqslant l < 0^\circ$ and $v_\mathrm{r} < -146.1\,\mathrm{km\,s^{-1}}$ or $v_\mathrm{r} > 58.3\,\mathrm{km\,s^{-1}}$, are bulge objects (Kovacevic, 2011). This discriminator of probable bulge membership was adopted here.

To further differentiate bulge and disc PNs, candidate diameters were then examined. A concentration of PNs with diameter $<20''$ toward the bulge was highlighted by Gathier et al. (1983) and used, with other discriminators, to construct a sample of bulge PNs. Here a similar, but more statistically justified discriminator of PN [O III] λ5007 diameter $\leqslant 21''$ (Kovacevic, 2011) for probable bulge membership was adopted. Any PN not meeting the v_r criterion for bulge membership was assumed to be a foreground object if it also failed this diameter criterion.

Radial velocity data used in the Kovacevic (2011) bulge PNLF (hereafter, legacy PNLF) are generally retained. Some PNs in that cohort feature v_r data not obtained from measurements, but artificially assigned from average cohort v_r values. For those cases, the PNs are instead left here with no v_r data and their bulge membership assessed on diameters alone. Radial velocities for new PNs were determined by analysing PN spectra with IRAF's EMSAO task (Mink & Wyatt, 1995). The highest resolution available spectra were used for new v_r determinations, except for HERMES data, which were incompatible with EMSAO, presumably due to its high resolving power ($R = 28\,000$). For the limited cases of HERMES data being the only available data for a new PN, v_r was estimated by applying the nonrelativistic spectroscopic Doppler formula, equation 6.1 (Kitchin, 1995),

$$\Delta\lambda = \frac{v_\mathrm{r}\lambda_0}{c} \tag{6.1}$$

to the measured Hα line and assuming an uncertainty determined from ΔR, $\Delta\lambda_0$ and Δn[4].

These PN population discrimination measures were used to separate the new PN candidates identified in §3.4 into probable bulge PNs and probable disc PNs. PN v_r and diameter data used are presented in appendix C.

6.2 Differential Aperture Photometry

New bulge PNs discovered will be used to refine the legacy bulge PNLF. Differential aperture photometry, using the the Aperture Photometry Tool (APT, version 2.5.8, Laher et al., 2012), was performed on Blanco difference data to determine new [O III] fluxes. Aperture photometry

[3]Miszalski et al. in prep. may extend these extrema to $-312.17 \pm 9.50\,\mathrm{km\,s^{-1}}$ and $283.32 \pm 9.50\,\mathrm{km\,s^{-1}}$.

[4]Derived from archival meteorological data, P pressure (pascals) and T temperature (°C), applied to $n = 1 + 0.00027621P[1 + P(60.1 - 0.972T) \times 10^{-10}]/96095.43(1 + 0.003661T)$ at $\lambda = 660$ Å (Haynes, 2014).

was taken of each new bulge PN and of a known $F_{[\mathrm{O\,III}]}$-calibrated bulge PN in the same Mosaic II pointing—practical given its $36' \times 36'$ FOV. By using $F_{[\mathrm{O\,III}]}$ data from Kovacevic (2011), the new bulge PNs are calibrated against data observed with the same instrument, using the same configuration, on the same telescope, at the same time, saved into the very mosaicked FITS file under consideration. This also eliminates calibration uncertainty due to the parameter space of environmental (e.g. aerosol extinction, airmass, cloudiness, humidity, seeing, sky background brightness) and instrumental (e.g. dark current) variables.

6.2.1 Filter Transmission

Construction of the legacy PNLF allowed for the radial velocity induced Doppler shift $\Delta\lambda$ of [O III] λ5007 emission from its rest wavelength λ_0 and subsequent change in applicable narrow band filter transmission. For reference, the transmission profile of the [O III] c6014 filter used is given in figure 6.1. Superimposed are bands corresponding to the range of apparent [O III] emission wavelengths exhibited by bulge PNs, where the nonrelativistic spectroscopic Doppler formula, equation 6.1, is assumed. Uncertainty in both v_r and λ_0 have been incorporated.

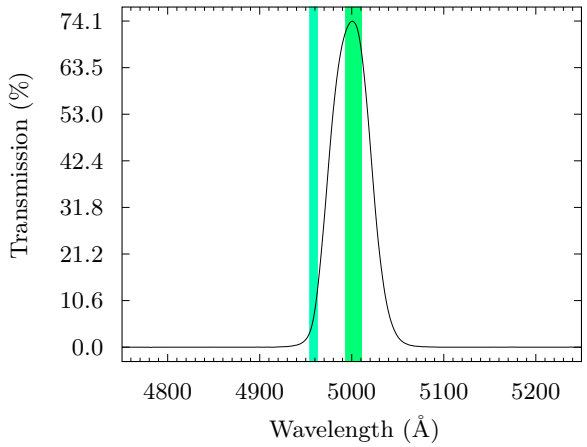

Figure 6.1: [O III] c6014 filter transmission profile. Use in the Blanco's $f/2.87$ beam at prime focus with the PFADC is assumed. Vertical bands corresponding to the range of v_r induced [O III] $\lambda\lambda$4959, 5007 Doppler shifts are overlaid. A small, but non-zero, fraction of flux transmitted is due to [O III] λ4959 emission.

The legacy PNLF assumes for measured flux F, equations 6.2 and 6.3,

$$F = F'_{5007} T'_{5007}, \tag{6.2}$$

$$F_{[\mathrm{O\,III}]} = F_{5007} = F \left(\frac{T_{5007}}{T'_{5007}} \right), \tag{6.3}$$

where F_{5007}, T_{5007} are the flux and filter transmission for rest wavelength λ5007 emission and F'_{5007}, T'_{5007} are the Doppler shifted $\lambda 5007'$ equivalents. It didn't however appear to allow for the [O III] λ4959 flux contribution captured through the filter. Corrections to F for v_r needed to be made not just to transmitted [O III] λ5007, but as a function of the total

transmitted [O III] flux, equation 6.4, incorporating an expected $F_{5007}/F_{4959} \approx 2.94$:1 (§1.5), as per equation 6.5.

$$F = F'_{4959}T'_{4959} + F'_{5007}T'_{5007} = F'_{5007}\left(\frac{T'_{4959}}{2.94} + T'_{5007}\right), \tag{6.4}$$

$$F_{[\mathrm{O\,III}]} = F_{5007} = F\left(\frac{2.94\,T'_{5007}}{T'_{4959} + 2.94\,T'_{5007}}\right)\left(\frac{T_{5007}}{T'_{5007}}\right). \tag{6.5}$$

By neglecting this, the legacy PNLF was constructed from over- and under-corrected aperture photometry, with $F_{[\mathrm{O\,III}]}$ for each PN in error by ≈(1.3–6.2)%. Thus, for the revised PNLF presented here however, this correction is made to both the existing photometry of Kovacevic (2011) and to the photometry of new PNs discovered in this work.

6.2.2 Calibrator Selection

For cases of aperture photometry performed on a difference FITS file containing multiple potential PN calibrators, the PN with the smallest $F_{[\mathrm{O\,III}]}$ uncertainty was selected. Where multiple equally precise calibrators were available, if one was exposed on the same CCD as the new PN within the mosaicked array, then it was selected, eliminating calibration uncertainty due to differences in interCCD response. Additionally, compact PNs with well-defined edges were favoured over large, diffuse PNs for selection as calibrators. This allowed unambiguous aperture definition and minimised the number of coincident stars compromising accurate flux determination.

A constraint on calibrator selection was CCD dependent flux linearity limits. CCD response was nonlinear for incident flux beyond certain limits and varied from CCD to CCD within the mosaicked array. These limits, obtained from FITS file header keywords, are specified for each CCD in ADU in figure 6.2, using the CCD designations introduced in §3.2.4. Candidate PN flux calibrators generating signal exceeding these limits were excluded as potential flux calibrators.

22: 21 000	27: 23 000
31: 42 000	28: 27 000
25: 44 000	21: 33 000
29: 37 000	26: 44 000

22: 21 000	27: 29 000
31: 42 000	28: 28 000
25: 44 000	21: 39 000
29: 37 000	26: 43 000

FIGURE 6.2: Mosaic II CCD linear response limits. Each CCD is labelled with its NOAO designation then linear response limit in ADU. System properties are shown in both its 2008 (left) and 2009 (right) configuration. PNs generating signal beyond these limits were discarded as potential flux calibrators.

6.2.3 Calibrator Application

Once an optimum field calibrator had been selected, relevant apertures were manually applied to both that calibrator and the target PN. The APT was then configured to reject all pixels with negative values from the difference data analysed, such as from oversubtracted objects, preventing associated flux underestimation. CCD gain data stored in FITS headers was automatically incorporated into the APT calculations. Magnitudes determined for each aperture by the APT were then used with existing calibrator $F_{[\mathrm{O\,III}]}$ data in the relative photometric equation, equation 6.6 (Norton, 2004), to determine target PN $F_{[\mathrm{O\,III}]}$.

$$m_{\mathrm{target}} = m_{\mathrm{calibrator}} - 2.5 \log \left(\frac{F_{\mathrm{target}}}{F_{\mathrm{calibrator}}} \right) \tag{6.6}$$

6.2.4 Calibration Evaluation

To evaluate the accuracy of this approach to flux calibration, differential photometry was performed on a multidimensional stratified random sample of PN flux calibrator/target pairs selected from amongst the Kovacevic (2011) data. Strata were selected such that pairs were distributed in observation year, observation night, PN diameter and intraCCD/interCCD calibrator availability. Evaluation parameters and results are given in table 6.1.

Nine of the dozen sample calibration pairs agree to within the quoted uncertainties. Three disagree, but not grossly so. No correlation of calibration accuracy with any sample stratum was obvious. An instance of calibration inaccuracy occurred for the largest difference in calibrator-target surface brightness (three orders of magnitude). Whilst this may be expected, other instances of calibration inaccuracy occurred for more modest calibrator-target surface brightness differences (single orders of magnitude). Undersubtracted stellar contaminants, difficult to discern in the monochrome difference imaging used in the flux calibration, may be causing calibration inaccuracies. Until this is established with further investigation, and in the absence of a clear alternative explanation for the flux calibration inaccuracies, a conservative uncertainty of at least $\pm 0.14\,(\mathrm{erg\,cm^{-2}\,s^{-1}})$ in $-\log F_{[\mathrm{O\,III}]}$, indicated by the data in table 6.1, was adopted for subsequent flux calibration. Using multiple calibrators per target nebula, where available, may improve calibration accuracy but remains a consideration for future work.

6.3 Extinction Correction

Traditional extragalactic PNLFs, such as presented in chapter 2, are built from PN data corrected for foreground extinction. The bright end PNs are thought to form from amongst the most massive PN progenitors. PNs arising from more massive progenitors still, intrinsically brighter than those constituting the bright end, have a correspondingly higher level of circumstellar dust and thus appear faint, moved away from the PNLF bright edge by this

TABLE 6.1: Flux calibration evaluation. Differential photometry was performed on a multidimensional stratified random sample of PN flux calibrator/target pairs distributed in observation year, observation night, nebula diameter and intraCCD/interCCD calibrator availability. Correspondence of APT flux calibrations with literature values is shown. References for literature derived data append values.

PN Name	v_r ($km\,s^{-1}$)	Ref.	$-\log F_{[O\,III]}$ ($erg\,cm^{-2}\,s^{-1}$)		Notes
			literature [1]	calculated	
2MASS J17524513−2951058	183.31 ± 2.51	[3]	13.02 ± 0.03	–	Calibrator
PN M 3-45	28.3 ± 0.03	[2]	$\mathbf{11.91 \pm 0.02}$	$\mathbf{11.89 \pm 0.02}$	Target
PN G000.1−01.9	-0.18 ± 9.50	[3]	12.42 ± 0.02	–	Calibrator
PN M 2-19	-61.2 ± 12.0	[2]	$\mathbf{12.23 \pm 0.02}$	$\mathbf{12.12 \pm 0.01}$	Target
PN G002.6+02.1	237.2 ± 6.8	[2]	12.48 ± 0.02	–	Calibrator
PN G002.5+02.0	-63.45 ± 0.68	[3]	$\mathbf{13.57 \pm 0.09}$	$\mathbf{13.59 \pm 0.01}$	Target
PN G004.0−02.6	-103.44 ± 9.50	[3]	12.41 ± 0.02	–	Calibrator
PN G004.0−02.5	115.32 ± 9.50	[3]	$\mathbf{13.43 \pm 0.03}$	$\mathbf{13.40 \pm 0.02}$	Target
PN G355.8+03.5	-14.8 ± 2.1	[3]	13.07 ± 0.03	–	Calibrator
PN G355.9+03.1	-237.77 ± 9.50	[3]	$\mathbf{13.77 \pm 0.09}$	$\mathbf{13.68 \pm 0.03}$	Target
PN G358.8+03.8	-189.89 ± 9.50	[3]	13.57 ± 0.09	–	Calibrator
PN G359.0+03.7	-210.66 ± 9.50	[3]	$\mathbf{13.43 \pm 0.03}$	$\mathbf{13.41 \pm 0.16}$	Target
PN H 1-23	-72.5 ± 3.9	[2]	11.85 ± 0.02	–	Calibrator
PN G358.0+01.6	-142.91 ± 9.50	[3]	$\mathbf{14.05 \pm 0.09}$	$\mathbf{14.19 \pm 0.01}$	Target
PN H 2-20	164.1 ± 8.8	[2]	13.81 ± 0.09	–	Calibrator
PN G002.7+01.7	195.04 ± 9.50	[3]	$\mathbf{13.92 \pm 0.09}$	$\mathbf{13.95 \pm 0.13}$	Target
PN H 2-27	-31.3 ± 15.1	[2]	12.65 ± 0.03	–	Calibrator
PN G356.5−04.1	37.58 ± 9.50	[3]	$\mathbf{12.74 \pm 0.03}$	$\mathbf{12.77 \pm 0.02}$	Target
PN M 3-38	-171.1 ± 10.6	[2]	11.79 ± 0.02	–	Calibrator
PN H 2-7	76.0 ± 15.0	[2]	$\mathbf{11.97 \pm 0.02}$	$\mathbf{11.99 \pm 0.01}$	Target
PN Th 3-13	-99.0 ± 40.0	[2]	12.83 ± 0.03	–	Calibrator
PN PBOZ 3	-11.90 ± 9.50	[3]	$\mathbf{13.98 \pm 0.09}$	$\mathbf{13.84 \pm 0.02}$	Target
PN Th 3-5	70.0 ± 30.0	[2]	12.64 ± 0.03	–	Calibrator
PN G355.1+03.7	-2.20 ± 9.50	[3]	$\mathbf{13.10 \pm 0.03}$	$\mathbf{13.07 \pm 0.02}$	Target

[1] Kovacevic (2011), with filter transmission errors corrected.
[2] Durand et al. (1998).
[3] Miszalski et al. in prep., used in Kovacevic (2011).

self-extinction mechanism (Jacoby et al., 1999). Though this interpretation of the PNLF bright edge arising from massive, but not the most massive, PNs in a population is reasonable for some environments, it may become harder to justify in low metallicity environments producing less nebula dust. Though some degree of binary coalescence or mass-transfer may define the bright edge cutoff (Ciardullo et al., 2005), the generally accepted hypothesis for the observed bright edge magnitude is this dust-driven moderation of brightness (e.g. Ciardullo & Jacoby, 1999, Marigo et al., 2004). The legacy PNLF, by contrast, was constructed from

PN data corrected for extinction with Balmer decrements, which recovers brightness lost not only to foreground extinction, but also to circumstellar PN extinction. For consistency with the legacy PNLF, and due to the difficulty correcting bulge PNs for foreground extinction in other ways, Balmer decrement dereddenings were also used here. Care should thus be taken in the interpretation of the resultant bulge PNLF, and its difference from standard extragalactic forms. This is discussed further in chapter 7.

For new PNs with discernible Hβ emission, the logarithmic Balmer decrement $c(\mathrm{H}\beta)$ was derived from the observed Balmer decrement $F_{\mathrm{H}\alpha}/F_{\mathrm{H}\beta}$ and used to deredden [O III] fluxes. For the purposes of extinction correction, an expected Balmer decrement consistent with case B PN recombination (optically thick[5]) was assumed, as this is more accurate than case A recombination (optically thin[5]) for most nebulas (Osterbrock & Ferland, 2006), and was adopted in other derivations of PN extinction towards the bulge (e.g. Cappellaro et al., 2001, Kovacevic, 2011). Unlike the Kovacevic (2011) extinction calculations however, collisional transitions of nebula H between quantum states, induced by thermal protons or thermal electrons, were not neglected in expected Balmer decrement determination. Under these assumptions and incorporating the nebula electron temperature T_{e} and electron density n_{e} estimates discussed below, theoretical Balmer decrements $j_{\mathrm{H}\alpha}/j_{\mathrm{H}\beta}$ were derived from multidimensional linear interpolation of the line emission coefficient j ratios of Osterbrock & Ferland (2006). Logarithmic Balmer decrements were then calculated from equations 6.7 and 6.8 (Cappellaro et al., 2001, Walker, 2014),

$$c(\mathrm{H}\beta) = \frac{1}{-f(\lambda)} \log\left(\frac{F_{\mathrm{H}\alpha}/F_{\mathrm{H}\beta}}{j_{\mathrm{H}\alpha}/j_{\mathrm{H}\beta}}\right), \tag{6.7}$$

$$f(\lambda) = \frac{A(\mathrm{H}\alpha) - A(\mathrm{H}\beta)}{A(V)}, \tag{6.8}$$

where the extinction factor $f(\lambda) \approx -0.404$ was derived from the Cardelli et al. (1989) extinction law, $A(V)$ is absolute visual extinction, $A(\lambda)$ is absolute extinction at wavelength λ and empirically determined dust properties giving a ratio of total to selective extinction $R_V = 2.5$ (Nataf et al., 2013) have been assumed.

Assuming a steeper extinction law for PNs toward the bulge, e.g. $R_V = 2.5$ here, rather than the traditionally adopted value of $R_V \approx 3.1$ (e.g. Whitford, 1958, Seaton, 1979) used for the general ISM, is not without controversy. Conflicting historical studies have presented evidence both supporting (e.g. Walton et al., 1993, Udalski, 2003, Ruffle et al., 2004) and refuting (e.g. Kunder et al., 2008, Pottasch & Bernard-Salas, 2013) a steeper extinction. The recent contribution of Nataf et al. (2013) to this controversy, using combined 2MASS, VVV

[5]Optically thick: Lyman series photons are repeatedly absorbed and reemitted by H within the nebula, with a mean free path << the nebula radius (e.g. 0.0005:1, Kwok, 2000), and eventually converted into photons corresponding to Lyα and transitions from other H series (e.g. Balmer, Paschen, etc.).

Optically thin: Lyman series photons escape the nebula without absorption (Osterbrock et al., 1963).

and Optical Gravitational Lensing Experiment III (OGLE-III, Udalski et al., 2008) data, provides the most rigorous analysis to date however, from which the estimated $R_V = 2.5$ adopted here is drawn.

Once $c(\mathrm{H}\beta)$ values were determined, selective extinctions $E(B-V)$ were calculated using equation 6.9, as implemented in IRAF's DEREDDEN task, based on a least squares fit to $c(\mathrm{H}\beta)$ and $E(B-V)$ data in Kaler & Lutz (1985),

$$E(B-V) = c(\mathrm{H}\beta)\left[0.61 + 0.024c(\mathrm{H}\beta)\right]. \tag{6.9}$$

Selective extinction could then be used to derive $A(\lambda)$. Noting $A(\lambda) = m - m_{\mathrm{dered}}$, dereddened [O III] λ5007 fluxes were finally calculated using the relative photometric equation 6.10,

$$F_{5007\mathrm{dered}} = F_{5007} 10^{(\mathrm{A}(5007)/2.5)}. \tag{6.10}$$

Nebula Electron Temperature Estimation

The theoretically expected Balmer decrement is a function of nebula electron temperature T_e (Brocklehurst, 1971). This temperature can be estimated from specific nebula emission line ratios, where yielded by suitably deep emission line spectroscopy, e.g. with [O III] $\lambda\lambda$4363, 4959, 5007 (Czyzak et al., 1986) or [N II] $\lambda\lambda$5755, 6548, 6563 (Krabbe & Copetti, 2005) data, or with optical or radio continuum measurements. Unfortunately, for the new PNs discovered here, such data was unavailable. An empirical [O III] electron temperature relationship that scales with He II λ4686 intensity (Kaler, 1986), and thus nebula excitation class, is instead adopted as described in equations 6.11 and 6.12,

$$\text{for } F_{4686} = 0, \quad T_{\mathrm{e\,[O\,III]}} = 10\,200\,\mathrm{K}, \tag{6.11}$$

$$\text{for } F_{4686} > 0, \quad T_{\mathrm{e\,[O\,III]}} = (9700 + 58F_{4686})\,\mathrm{K}, \tag{6.12}$$

where F_{4686} is normalised such that $F_{\mathrm{H}\beta} = 100$. This is in agreement with the $T_\mathrm{e} = 1 \times 10^4\,\mathrm{K}$ approximation for average abundance PNs of Osterbrock & Ferland (2006)

Nebula Electron Density Estimation

Nebula electron density, like nebula electron temperature, also affects the theoretically expected Balmer decrement, i.e. $j_{\mathrm{H}\alpha}/j_{\mathrm{H}\beta} = f(T_\mathrm{e}, n_\mathrm{e})$. As for T_e estimations, n_e can be estimated from specific nebula line ratios, e.g. [O II] $\lambda\lambda$3726, 3729 or [S II] $\lambda\lambda$6716, 6731 data (e.g. Canto et al., 1980, Kingsburgh & English, 1992). For some of the new PNs discovered here, [S II] $\lambda\lambda$6716, 6731 data is available and was used for n_e estimates. The [S II] doublet n_e estimation method can be described by equations 6.13 and 6.14 (Proxauf et al., 2014),

$$\log n_{\rm e} = 0.0543 \tan(-3.0553a + 2.8506) + 6.98 - 10.6905a + 9.9186a^2 - 3.5442a^3, \quad (6.13)$$

$$a = \frac{I_{6731}}{I_{6716}}, \quad (6.14)$$

where $n_{\rm e}$ is expressed as $\rm cm^{-3}$ and I is line intensity. In the absence of [S II] doublet data, $n_{\rm e} = 4.44 \times 10^3\,\rm cm^{-3}$ was adopted, the average value for the bulge PNs used to construct the legacy PNLF.

6.3.1 Revised PNLF

A revised bulge PNLF was constructed from a combination of photometry of new PNs discovered here and application of filter transmission corrections to the legacy photometry of Kovacevic (2011). Additional data points come from two dereddenable PNs discovered here and another two existing PN fluxes (Kovacevic, 2011) now deredennable due to deeper spectra obtained here (see e.g., chapter 5). These new data points are derived from slit spectra obtained at low airmass $X \lesssim 1.1$, except one at $X \approx 1.5$. Fibre spectra derived data points could be added, but don't feature demonstrably reliable Balmer decrements and are omitted until further analysis (this is discussed further in §7.1.7). Additional, reliable, data points will almost certainly be available upon full reduction of the many WiFeS spectra collected, though data presentation is a task for future work (also discussed further in §7.1.7). The high extinction toward the bulge makes obtaining viably high S/N in Hβ emission, allowing subsequent spectral dereddening, an expected difficulty of this work.

In addition to filter transmission-corrected photometry, the revised PNLF draws on a steeper interstellar extinction relevant to the bulge ($R_V = 2.5$, not $R_V = 3.07$ for the general ISM) applied to all PNs, new or improved d, $v_{\rm r}$ data determined here, refining bulge membership, and application of new or more accurate PN physical properties where discovered in the literature. Where c(Hβ) values were derived from literature not assuming $R_V = 2.5$, they were scaled to a consistent assumed $R_V = 2.5$. In contrast, it is not clear literature derived c(Hβ) data used for the legacy PNLF was scaled to a uniform R_V, resulting in some incorrectly dereddened data in that legacy PNLF. Figure 6.3 shows the legacy PNLF, as presented in Kovacevic (2011) and the revised PNLF for comparison.

Reproducing the legacy PNLF is hampered by an incomplete description in Kovacevic (2011) of precisely which PNs were used as data points. To the extent the legacy data and its analysis and assumptions are documented, and incorporating different approaches to uncertainty estimation, the legacy PNLF is irreproducible, as shown in figure 6.4. To avoid ambiguity here, the specific PNs used for the revised PNLF are specified in appendix C. Although all CTIO survey field centres were located at $-5^\circ \leqslant l \leqslant 5^\circ$, $-5^\circ \leqslant b \leqslant 5^\circ$, a small number of objects (five in Kovacevic (2011) and two in this work), were beyond the $10^\circ \times 10^\circ$ bulge boundary adopted and are thus excluded from both the PNLF and appendix C.

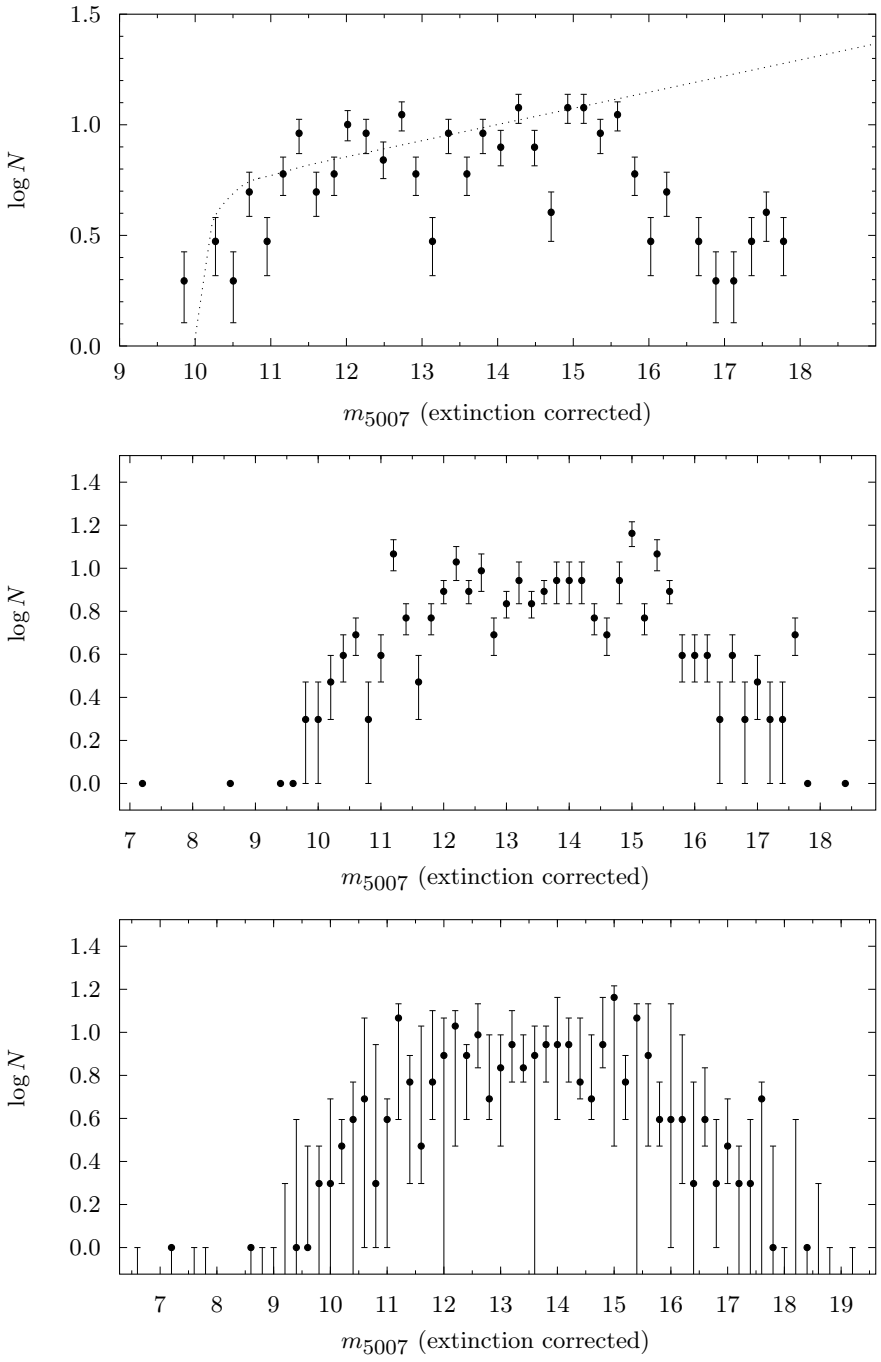

FIGURE 6.4: Legacy Galactic bulge PNLF recreation. Top: Legacy PNLF as presented by Kovacevic (2011), with $\hat{h} = 0.2\,\mathrm{mag}$, $R_V = 3.07$. The dotted curve is the empirical PNLF defined by equation 2.1. Middle: Legacy PNLF recreation attempt using data documented in Kovacevic (2011) and uncertainties corresponding only to Poisson noise. Bottom: PNLF recreation using both Poisson noise and $\Delta F_{[\mathrm{O\,III}]_{\mathrm{dered}}}$. Some low population bins have error bars spanning multiple bins. Note too scale variations for the horizontal axes. The legacy PNLF, as presented by Kovacevic (2011), can not be trivially recreated using the data and analysis documented in the originating work. Furthermore, neglecting $\Delta F_{[\mathrm{O\,III}]_{\mathrm{dered}}}$ appears to provide the legacy PNLF an unwarranted precision.

Kovacevic (2011) applied Poisson uncertainties ($\Delta N_{\mathrm{bin}} = \pm\sqrt{N_{\mathrm{bin}}}/2$) to each data bin of

the PNLF in figure 2.4, where $N_{\rm bin}$ is bin population. It is not clear the legacy PNLF also incorporated measured $\Delta F_{[\rm O\,III]_{\rm dered}}$ data and as figure 6.4 shows, this omission affects bin membership significantly. The revised PNLF however includes Poisson noise combined with the $\Delta F_{[\rm O\,III]_{\rm dered}}$ data listed in appendix C. In addition, the bin size ($\hat{h} = 0.2\,$mag) used in the legacy PNLF was arbitrary. Here, the robust Freedman-Diaconis rule for univariate data, equation 6.15 (Scott, 2015),

$$\hat{h} = 2\,(\mathrm{IQR})\,N^{-1/3} \tag{6.15}$$

where IQR is the interquartile range of all incorporated fluxes and N is the total number of those fluxes, was used to determine a statistically relevant bin size $\hat{h} = 0.9\,$mag.

The revised PNLF doesn't exhibit a sharp bright end cutoff, and is discussed in more detail in chapter 7. If the brightest PN in the revised function is nonetheless used as a distance indicator, assuming a bulge bright end PNLF absolute magnitude cutoff at $M^*_{5007} = -4.47^{+0.02}_{-0.03}$ (Ciardullo et al., 2002), the distance modulus relation places the bulge at $\approx$7.5 $\pm$ 1.9 kpc, consistent with the putative distance of $\approx 7.9 \pm 0.3\,$kpc (e.g. McNamara et al., 2000).

6.3.2 Extinction Uncertainty

The logarithmic Balmer decrements used in the dereddening of PN fluxes added to the revised PNLF were determined from thin slit spectra line ratios (see chapter 7 for a discussion of AAOmega and WiFeS line ratios). To estimate the uncertainty in these line ratios, comparison of similarly determined line ratios of known PNs observed for calibration purposes (as discussed in chapter 5) with their literature values was carried out. Results are given in table 6.2.

The available literature data with which to validate measured data is limited in this instance. Furthermore, it is not clear the accuracy of all of the literature data warrants its use for validation of data measured here. The absence of uncertainty supplied with the Leisy & Dennefeld (2006) data, for example, doesn't appear clearly explained in the source material. A statistical validation can nonetheless be applied to the available data to estimate an appropriate uncertainty to assign to the slit spectra line ratios measured. The approach taken here is to test the relationship between assumed measured ratio uncertainty and the consequent degree of correspondence with the literature values. Here, assuming $\Delta\,(\mathrm{H}\alpha/\mathrm{H}\beta) = 48\%$ brings all measured/literature pairs into correspondence.

It is noted a line ratio listed for PN G355.3-04.1 is discrepant not just with other measurements of the same nebula, but with measurement of the same nebula with the same instrument, 6dF. The discrepancy of that nebula's line ratios isn't the limiting factor in the measured line ratio uncertainty $\Delta\,(\mathrm{H}\alpha/\mathrm{H}\beta) = 48\%$ adopted however, so no special management of it is required.

TABLE 6.2: Balmer series line ratios for a sample of known PNs. Uncertainties are supplied where available. Literature values are compared with values measured using the CCDSpec thin slit spectrograph. Multiple literature measurements for PN G355.3-04.1 are included.

Object Name	Hα/Hβ literature	Ref.	Hα/Hβ measured
LHA 120-N 28	2.790	[1]	5.347
PN G002.4-03.1	16^{+8}_{-5}	[2]	9.863
SMP LMC 31	6.320	[1]	6.768
PN G355.3-04.1	11^{+3}_{-2}	[3]	8.923
PN G355.3-04.1	12^{+4}_{-2}	[3]	8.923
PN G355.3-04.1	9.8 ± 0.4	[4]	8.923
PN G355.3-04.1	4.5 ± 0.3	[4]	8.923

[1] Leisy & Dennefeld (2006).
[2] Kovacevic (2011); hybrid dual beam slit/fibre-fed data.
[3] Parker et al. (2006); dual beam slit spectra.
[4] Parker et al. (2006); dual beam fibre-fed data.

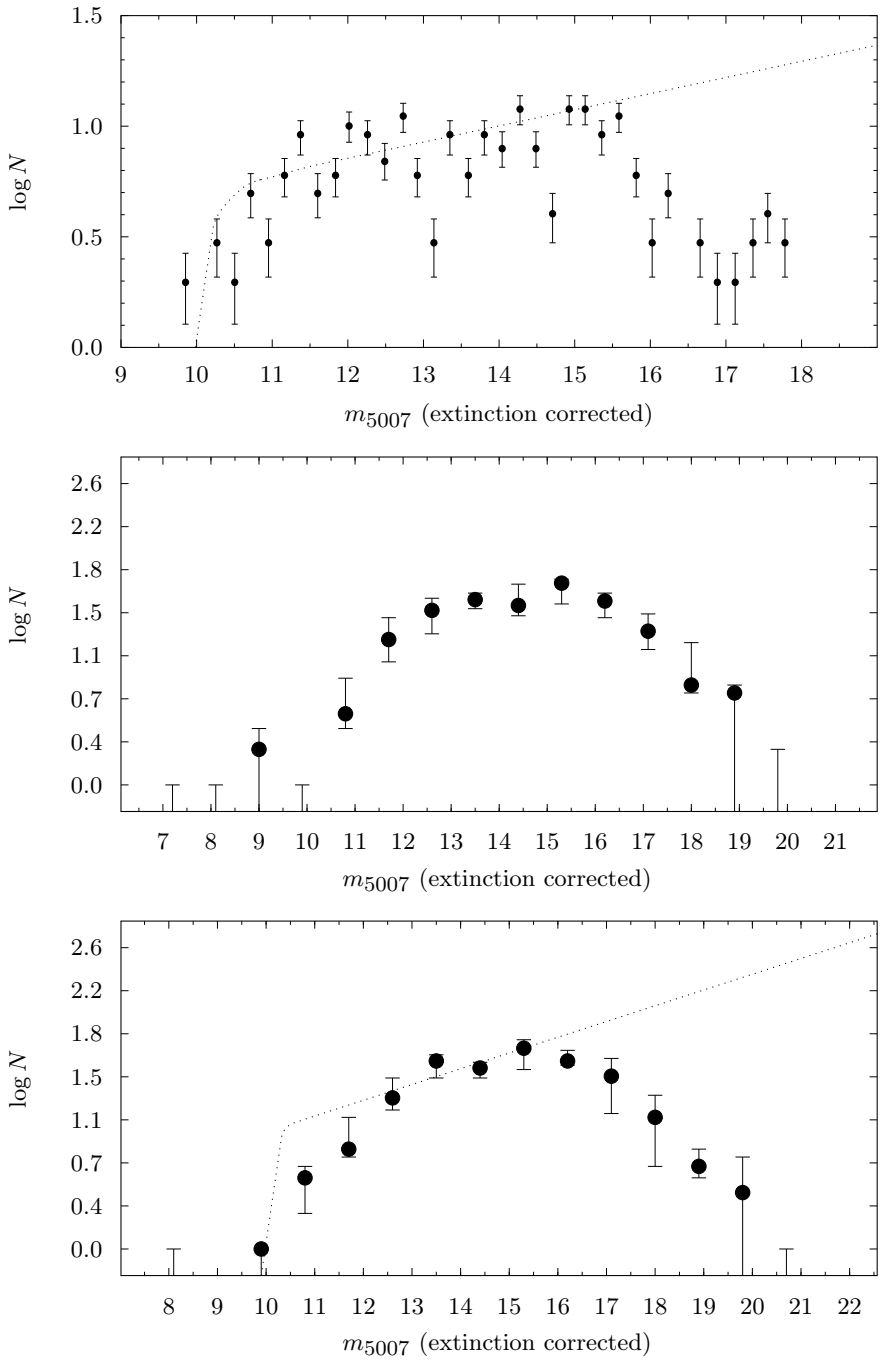

Figure 6.3: Revised Galactic bulge PNLF. Note intergraph axis scale variations. Some low population bins have error bars spanning multiple bins. Top: Legacy Galactic bulge PNLF as presented by Kovacevic (2011), with $\hat{h} = 0.2\,\mathrm{mag}$, $R_V = 3.07$. The dotted curve shown is the empirical PNLF defined by equation 2.1. Middle: Revised Galactic bulge PNLF, with $\hat{h} = 0.9\,\mathrm{mag}$, $R_V = 3.07$. Uncertainties incorporate both Poisson noise and $\Delta F_{[\mathrm{O\,III}]_{\mathrm{dered}}}$. Bottom: Revised Galactic bulge PNLF, as above, but with $R_V = 2.5$. For the empirical PNLF in the bottom panel, the x-intercept was determined using a semi-degenerate errors-in-variables regression of the two leftmost data points, rounded to the nearest bin centre. The y-intercept of the empirical PNLF was adjusted via visual inspection such that the most populated bin and the maximum number of other bins were fit.

7

Results and Discussion

7.1 Summary

A high level conceptual grouping of this research project's components is visualised in figure 7.1.

New knowledge resulting from this research project can be summarised as follows:

New Astronomical Tools and Techniques

- PN candidate identification: FITS file segmentation and interleaving (Stenborg, 2014),
- MOS observation planning: parallel greedy set cover field placement (Stenborg, 2015),
- and candidate reduction: efficient slit spectra sky subtraction (Stenborg, 2016).

Galactic Bulge and Foreground PNs

- New PN candidates: from systematic imaging review (Stenborg & Parker, 2014),
- new bulge PNs: spectroscopic confirmation and physical data derived,
- new foreground PNs, LIERs and mimics: spectroscopic confirmation, selected physical data derived,
- and duplicate PNs: catalogued instances identified toward the bulge.

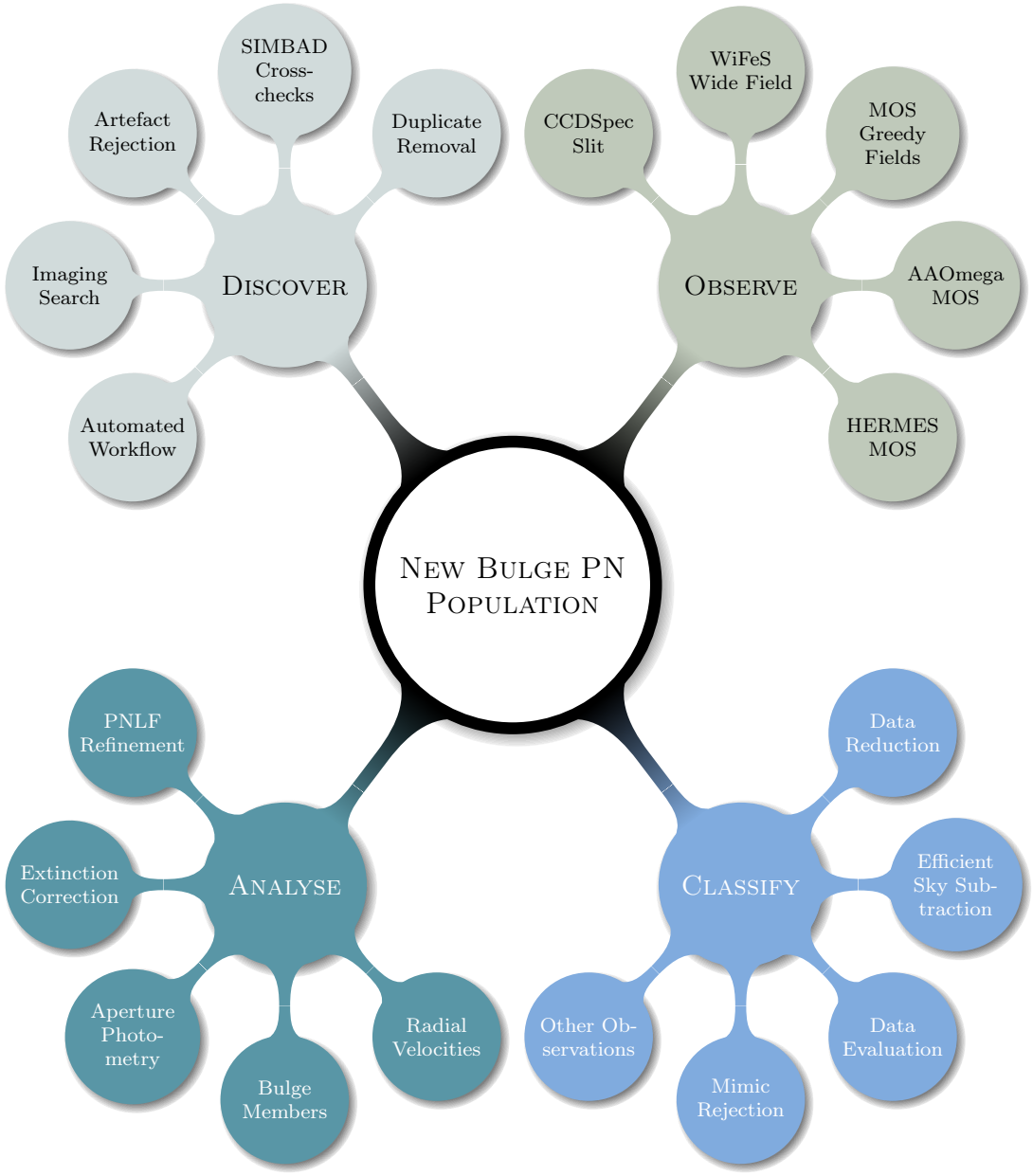

FIGURE 7.1: High level conceptual grouping of the new bulge PN population project components.

Galactic Bulge PNLF

- New PN discoveries: photometry added to an improved PNLF,
- corrected photometry: existing data corrected and used in the PNLF,
- new dereddenings: existing reddened data dereddened and added to the PNLF.

Other Observations

- Galactic disc PN: PN PM 1-66 confirmed as a probable PN,

- known bulge proximate PNs: selected new reference imaging and spectra,
- Galactic stars: spectroscopic confirmation of new PN proximate stars toward the bulge,
- SMC PNs: probable new PNs (with collaborators).

7.1.1 New Bulge PNs

A new population of Galactic bulge region PNs have been presented here. A comprehensive review of narrow [O III] on/off band imaging yielded a pool of > 200 new PN candidates. From this pool, a combination of imaging and newly gathered spectral evidence was used with an evaluation scheme devised here (see the five-set Venn diagram, figure 3.26) to identify new true (4), probable (31) and possible (83) PNs. New and possible mimics were also established. To put this in context, SIMBAD lists 285 known and 74 possible PNs in the central $-5^\circ \leqslant l \leqslant 5^\circ$, $-5^\circ \leqslant b \leqslant 5^\circ$ bulge region. This census is based on SIMBAD primary object type designations, on 22 July 2015, 15:00:00 UT and includes both foreground and true bulge PNs. The estimated total true bulge PN population is ≈700 (Stasińska et al., 1992).

Imaging evidence presented acted not only to identify and visually describe new PN candidates, but for newly confirmed bulge PNs, provides the benefit of more data to address the question of preferential alignment of aspherical bulge PNs (as discussed, §1.4.3).

Spectral evidence presented was derived from thin slit (CCDSpec) and fibre-fed multi-object (AAOmega and HERMES) spectrographs. Fine-tuning reduction of additional spectra obtained with WiFeS, though not presented, is in progress, with completion and evaluation a task for future work. Some of the raw WiFeS spectra however display obvious emission line features corresponding, almost certainly, to yet more new true PNs toward the bulge.

Scope remains for future bulge PN spectroscopic observing programs. Unstudied candidates remain. Deeper spectroscopy is needed for many of the PN candidates discussed. It is also possible erroneous null results due to positioning issues for very small apparent diameter objects or S/N issues for faint objects observed in suboptimal conditions have occurred.

Criteria for discrimination of foreground bulge region PNs from genuine bulge members was introduced (§6.1). New spectroscopically-derived radial velocity estimates for selected PNs have been listed in appendix C. The focus of this process was to establish probable bulge membership for those PNs included in the refined PNLF presented—those with spectra deep enough to allow Balmer decrement determination. Radial velocity estimates for the remainder of the new PNs towards the bulge is a task for future work. In addition to assisting separate foreground from true bulge PNs, this new v_r data offers improved statistical reliability of PN-based kinematic modelling of the bulge (e.g. Beaulieu et al., 2000).

7.1.2 New Galactic PNs

PN PM 1-66 was presented as an example of a known Galactic PN candidate, not located toward the bulge, for which spectroscopic evidence clarifying its nature was presented. Other

possible Galactic disc PNs or potentially misclassified emission line objects were investigated spectroscopically however, but simply not enumerated here. Reduction and publication of these data remains a task for future work. Inspection of raw data reveals more probable new PNs, potentially up to 36.

The current known Galactic PN population, ∼3400 (Boumis et al., 2003), is a fraction of the estimated total, currently ∼25 000 (Jacoby et al., 2010), but potentially anywhere from ∼6600 (De Marco & Moe, 2005) to ∼140 000 (Ishida & Weinberger, 1987), as discussed (§1.1). This disparity in upper total population estimates (a factor of ∼21) is driven in part by the high extinction towards the Galactic plane, the very location in which much of the PN population is expected to reside (Jacoby & Van de Steene, 2004).

The population of new true, probable and possible bulge region PNs discovered here provides a quantified addition to the known Galactic PN census. Other probable new Galactic disc ($\leqslant 36$) and bulge PNs, pending data reduction, have been discussed. This project has thus not only directly raised the lower bounds of the current Galactic PN population already, but offers further increments after additional data reduction. New confirmed PN offer prospects for refining the known Galactic baryonic mass, estimated Galactic star formation rate (e.g. Maciel et al., 2012), models of Galactic chemical evolution (e.g. Maciel & Costa, 2003), etc. A refined Galactic PN census is also key to resolving competing theories of PN formation. A low population suggests selective formation criteria (e.g. the Binary Hypothesis, §1.4.2), whereas a high population supports the single star paradigm of undemanding formation criteria amongst most ∼1–8 $M_{\odot}$ stars.

7.1.3 New Galactic Stars

Spectra for 10 Galactic stars were collected here. Of these stars, nine are assumed new due to absence from SIMBAD, and the last, OGLE BUL-SC36 453627, appears never to have been spectroscopically studied. These observations make an incremental contribution to the known Galactic stellar population. The coincidence of SSO J175920.084-275514.17 with possible PN CTIO J175919.98-275515.3 and confirmation of its late-type spectrum narrows the CSPN candidate pool for that PN.

There is scope for future work with the stellar spectra obtained. The spectra can be used to estimate their temperatures and spectral types (e.g. via application of Wien's displacement law). This will incrementally refine the confirmed distribution of Galactic stars by spectral types. If stellar absorption features can be distinguished from amongst telluric absorption, v_{r} determination is possible, though the limited S/N of most of the spectra collected may prevent this.

7.1.4 New Extragalactic PNs

Spectroscopic and imaging evidence for probable new extragalactic PNs was presented here, specifically for the SMC (§5.4). Additional spectroscopy, not discussed earlier, was taken of

further new Local Group PN candidates and is pending reduction. Inspection of the raw or semi-reduced data reveals some spectra consistent with new PNs. It is possible some of these are foreground objects or mimics and such determination is pending further work. Assuming that at least some putative extragalactic PNs are indeed such objects however, the census of extragalactic PNs accessible to even modest aperture telescopes (∼2–4 m) is thus incomplete. This is consistent with literature predictions (e.g. Jacoby, 2006, Miszalski et al., 2012b), though a detailed incompleteness quantification is out of scope of this investigation.

7.1.5 Candidate Discovery Completeness

The candidate discovery medium for the new PN candidates presented here was archival [O III] on/off band imaging taken with the Mosaic II multi-CCD system on the Blanco telescope. Candidate detection completeness, assuming correspondence to the global maximum of a sextic fit to the reddened flux frequency distribution of all PNs appearing in that imaging, is estimated to be down to $-\log F_{[\mathrm{O\,III}]} \approx 13.4\,\mathrm{erg\,cm^{-2}\,s^{-1}}$.

Multiwavelength cross-checks revealed many, but not all, of the new candidates to be present in UKST Hα/SR/IR imaging. Candidates visible in the SHS, but unnoticed during previous SHS reviews (e.g. Parker et al., 2006), were biased towards either star-like morphologies or low surface brightness, and caveats are given to that effect. Candidates with star-like morphologies suffer detection difficulty due to a combination of apparent geometrical indistinguishability from, and partial coincidence with, stars in the dense bulge fields. Low surface brightness sources are intrinsically difficult to detect, regardless of morphology. These detection biases apply to any imaging survey and as such, may have affected the results presented here. Others candidates however, e.g. CTIO J173623.26-250528.7 (p. 88), CTIO J174253.89-340902.1 (p. 89) and CTIO J172822.84-254727.9 (p. 84), are obvious in SHS imaging and their failed previous discovery is difficult to explain. This has multiple implications. Firstly, it confirms evidentially that many difficult to detect PNs predicted within SHS imaging (Parker et al., 2006) do indeed exist. Secondly, it confirms that even PNs of low detection difficulty have also remained undiscovered in that imaging for years.

As a consequence of PN candidate discoveries that could have been made from SHS imaging review alone, and given the low likelihood of the only new candidates in SHS data being the ones encountered toward the bulge here, a systematic re-examination of the digitised SHS data is recommended. The discovery technique demonstrated here, employing on/off band image segmentation, interleaving and blink comparison is recommended. The generic FITS image segmentation algorithm developed, within the bounds of system memory, is applicable to mosaicked and unmosaicked FITS images of any dimension. The technique reduces the impact of human fallibility on data review, such as imperfect manual image traversal in DS9, as discussed in §3.1.1. This project demonstrates refinement of the Galactic PN census is not yet limited by available imaging survey data.

7.1.6 Accuracy of PN Population Estimates

Careful consideration of the work here has implications for the accuracy of the putative lower bound of the Galactic PN population. Duplicate objects chanced upon during PN candidate cross-checks in SIMBAD were discussed in chapter 4. These demonstrate insufficient rigour in literature data management is compromising the accuracy of any SIMBAD-derived PN census. Though the stellar density of the bulge may obfuscate some duplicates, it is deemed unlikely the only erroneously duplicate PNs currently recorded in SIMBAD are restricted to the areal subset of the Galactic bulge inspected here. Quantifying duplicate driven inaccuracy of a SIMBAD-derived Galactic PN census isn't attempted here. A systematic review of proximate emission line objects in SIMBAD is recommended however, to resolve this source of uncertainty in the lower bounds of PN populations.

7.1.7 Bulge PNLF

A revised, more statistically robust Galactic bulge PNLF was presented. The four new data points determined during this investigation were a modest statistical increment. The complete data set obtained in this work however, will almost certainly yield more. At least 19 other new PNs towards the bulge exhibit an obvious Balmer decrement in AAOmega or WiFeS spectra and are pending further analysis. Additionally, as listed in appendix C, there are some ∼252 PNs or PN candidates for which photometric dereddening is pending collection of sufficiently deep spectra, or for which photometry needs to be obtained.

The new data points presented were derived from thin slit spectra allowing $c(\mathrm{H}\beta)$ determination. Recovery of $c(\mathrm{H}\beta)$ data from reduced WiFeS spectra is in progress. The WiFeS data set features a higher ratio of emission line standard to new PN observations compared to the CCDSpec data set, offering correspondingly more accurate $\Delta c(\mathrm{H}\beta)$ estimation.

Recovery of $c(\mathrm{H}\beta)$ data from AAOmega spectra will be more problematic. An analysis of line ratio accuracy derived from AAOmega spectra by Miszalski (2009) concluded $c(\mathrm{H}\beta)$ recovery, and indeed any abundance determination, suffered so badly from uncertainty in fibre-to-fibre spectrophotometric response, compounded by additional uncertainty introduced by the dual beam splicing process, as to be generally infeasible. In production of the legacy bulge PNLF, Kovacevic (2011) persisted with determining $c(\mathrm{H}\beta)$ from AAOmega spectra, noticing $\Delta c(\mathrm{H}\beta)$ varied between 2dF fields and devised a scheme to quantify it. That field-specific $\Delta c(\mathrm{H}\beta)$ quantification scheme leveraged a greater number of calibration targets per 2dF field than was used here. Determining whether the limited viable calibration targets collected in 2dF fields here can contribute statistically meaningful $\Delta c(\mathrm{H}\beta)$ data, offering a practical level of line ratio precision, is a task for future work.

In addition to new data points, the revised bulge PNLF incorporated existing data points corrected for filter transmission errors, a bulge-relevant ratio of total to selective extinction, $R_V = 2.5$, and its uniform application across observationally determined and literature derived

$c(\mathrm{H}\beta)$ data and miscellaneous newly determined and literature-gleaned diameters, radial velocities and other PN physical properties. In contrast to the legacy PNLF, the revised version also used statistically justified binning and more rigorous uncertainty determinations.

Bulge PNLF Limitations

Care should be taken in interpretation of the revised bulge PNLF. Although it represents the most rigorous (known) effort to date, the high bulge extinction hampered obtaining optical spectra with clear Hβ emission. This difficulty affected both this work, and the legacy PNLF, from which data is drawn. Care was taken in chapter 3 however to document exposure times, telescope and instruments used, observing conditions, etc. That documentation provides a basis from which to estimate revised exposure times for future Hβ-seeking reobservations.

Narrow band flux calibration against standard stars (Jacoby et al., 1987) was used in construction of the legacy PNLF (but see too, Ciardullo et al., 1989a,b). Reduced data products containing standards stars were unavailable here however, so for expediency a relative photometric method was used (§6.2). Reduction of archival standard star data and recalibration of candidate fluxes to higher accuracy and precision is a task for future work.

The question of variable extinction toward the bulge has potentially compromised the accuracy of the PNLF. After discussing the historical controversy (§6.3) of the average applicable ratio of total to selective extinction toward the bulge, $R_V = 2.5$ was adopted. Not discussed however, was evidence for variation of R_V along different lines of sight toward the bulge. This has potentially applied an additional, undocumented uncertainty to PN dereddenings that varies stochastically, with possible Galactocentric radius and latitude magnitude dependencies, on a scale as small as $6'$ (Udalski, 2003, Nataf et al., 2013). Amelioration via Schlegel maps (Schlegel et al., 1998) is uncertain as they misestimate extinction at low Galactic latitude or in high extinction regions (Arce & Goodman, 1999, Nidever et al., 2012). Further investigation into quantifying and adding this uncertainty to the PNLF, or adjusting the dereddening scheme to incorporate a variable extinction law, is recommended.

No special distinction was made in the extinction law between foreground extinction and PN self-extinction by circumstellar dust. This must have compromised the accuracy of the PNLF. By not distinguishing the dereddening law between foreground and internal extinction, highly self-extincting PNs have been incorrectly dereddened. A rigorous PN dereddening should incorporate a compound correction for both line-of-sight extinction and self-extinction. If the magnitude of self-extinction varies little amongst bulge PNs, a common unintended dereddening offset has been applied, but relative dereddenings remain correct on average. Further work incorporating PN self-extinction effects into the PNLF is deferred to future work. A larger set of bulge PN Balmer decrements for example, expected from additional reduction of WiFeS spectroscopic data, could be compared with the extragalactic PN Balmer decrement data (e.g. Jacoby & Ciardullo, 1999) to estimate the effect of undistinguished bulge extinction.

Bulge PNLF Results

The revised PNLF shape does not resemble typical extragalactic PNLFs (chapter 2) or the empirical PNLF defined by equation 2.1. Most noticeable is the shallow bright end gradient, not a steep cutoff. In light of the Balmer decrement approach to dereddening PNs, rather than the traditional foreground extinction-only approach (§6.3), this is not unexpected. Additionally, amongst the "possible" PNs presented in chapter 3 are examples of bright, compact PNs, which if confirmed as true PNs, have the potential to move or reshape the current bright end.

The bulge PNLF has been derived more rigorously, from a slightly larger statistical sample, than the legacy bulge PNLF. New data points will very likely result from further reduction of spectra collected here and is a task for future work. Despite being an improved PNLF with prospects for short-term progress, a combination of selection bias, possible significant line of sight extinction law variability, PN self-extinction effects and the existence of potential new bright end PNs all compromise its reliability. Further work is required before the bulge PNLF presented should be considered accurate, or relied upon for physical insight into its constituent population and their progenitors.

7.2 Concluding Remarks

This work described the identification of a new population of Galactic bulge planetary nebulas (PNs). This population of nebulas, the ionised remnants of stellar ejecta formed during late stage evolution, were located within the central $-5^\circ \leqslant l \leqslant 5^\circ$, $-5^\circ \leqslant b \leqslant 5^\circ$ region around the Galactic centre. The new discoveries consist of both foreground Galactic disc PNs and bona fide bulge PNs co-located at $\sim$8 kpc. These two PN subsets were bifurcated via analysis of the observed nebula radius and radial velocity v_r parameter space. New bulge PNs were incorporated into the most statistically robust and rigorously derived Galactic bulge planetary nebula luminosity function known to date.

A series of secondary discoveries were made. Several new PN mimics were revealed amongst the PN candidates observed. Spectra for previously unstudied and undocumented stars towards the bulge were collected. Existing PNs were observed for calibration purposes, but in some cases had the side benefit of providing the deepest known spectra for those objects, or spectra providing the broadest wavelength coverage. New candidate PNs beyond the central bulge region were observed, extending to environs such as the Magellanic Clouds. These new celestial object discoveries were accompanied by a concomitant decrease in the known PN census—several hitherto unnoticed PN duplications in the literature were recognised and documented as such.

New PN candidates (> 200) towards the Galactic bulge were identified from review of archival stacked [O III] on/off band survey imaging taken with the Mosaic II CCD imager on the CTIO's 4 m Blanco telescope. To facilitate careful, systematic review of the survey

imaging, an automated on/off band image segmentation and interleaving technique was developed. This technique, incorporating metaprogramming—writing software to itself generate software, allowed fast comparison of blinked on/off band data in a manner eliminating manual image traversal errors. New PN candidates were cross-checked against known objects with a new, single-click SIMBAD online query tool developed here, further automating the process. Candidates passing the cross-check were further compared with multiwavelength image archives, particularly Hα on/off band imaging, thereby ensuring the diagnostic data of the two typically brightest PN emission lines, [O III] and Hα, were analysed for each candidate.

Putative PNs cannot be rigorously considered as such until they have been spectroscopically confirmed. This process is crucial for mimic discrimination and the resultant emission line ratios provides insight into the physical properties of the objects. Here, a campaign of confirmatory optical spectroscopy was pursued on a combination of thin-slit, fibre multi-object and wide field spectrographs. The project theme of efficiency through application of information technology, developed during PN candidate identification, was continued in this phase of candidate confirmation. Examples include developing new interfaces for faster invocation and interaction with third-party spectroscopy management software and building a parallel greedy set cover program for efficient field selection in constrained multi-object spectroscopy. The field selection program was further given a flexible, scalable implementation such that workload could be parallelised on both shared and distributed memory systems.

The combined imaging and spectral evidence assembled here yielded new true (4), probable (31) and possible (83) PNs toward the Galactic bulge. These objects advance the census of known bulge PNs to the total estimated ($\approx$700), and toward the total estimated Galactic PN population ($\sim$25 000) more generally. In addition to simply advancing the PN census, the task of PN spectral analysis itself was progressed through conception, description and quantification of a new optimised sky subtraction technique applicable to slit spectra.

A logical extension to discovery of a new population of bulge PNs is construction of a refined bulge PNLF. In the event, the high extinction bulge environment yielded few new PN spectra of sufficient depth to allow Balmer decrement determination (i.e. unambiguously exhibiting both Hα and Hβ emission). Nonetheless, such few as were gleaned facilitated differential aperture photometry of the Mosaic II [O III] imaging and PNLF refinement. Further minor refinement was obtained from deeper spectroscopy of known bulge PNs, allowing their dereddening for the first time. More significantly however, a careful, considered reanalysis was performed of the entire existing ($\sim$225) bulge PN population for which dereddened photometry was available. This included, but was not limited to, the ensemble revisions of more rigorous Balmer decrement redeterminations, filter transmissions corrections, error propagation, application of a uniform, bulge-relevant extinction, and more statistically justified data interpretation. This culminated in the most rigorous bulge PNLF generated to date.

These new discoveries speak to a number of scientific questions. An accurate PN census for example contributes to controversy over proposed PN formation mechanisms, a low census

favouring the Binary Hypothesis, and high census consistent with permissive single star evolution. Both in the bulge and the general Galactic environment, new PNs refine the known Galactic baryonic mass and chemical enrichment rates, act as kinematic tracers and provide evidence of the nature of their stellar progenitor population. The PNLF itself has features that defy current understanding, such as the ubiquity of its bright end cutoff across Hubble types, and as such, more detailed formulations are sought after. The bulge PNLF determined here exhibited a shallower than expected bright end gradient, thus not resembling typical extragalactic forms. An unusual form was not unexpected, as the Balmer decrement method used here to deredden PNs recovers brightness lost not only to foreground extinction, but to circumstellar dust, which is not normally done in the extragalactic case. Issues limiting the accuracy of the refined PNLF were identified and need further work before its utility as a tool for physical insight into its member population and progenitors can be realised. Nonetheless, the new observational data collected in this study has not only already advanced knowledge of the bulge PN population, but offers future refinement of the bulge PNLF through further data reduction and analysis.

A

Spectral Features

Spectral features referenced in this work are listed in table A.2. Only atomic transitions are listed, composite features such as telluric molecular absorption bands are omitted. For the Balmer series, an exhaustive enumeration of fine-structure lines isn't given. Instead, the fine-structure centre-of-gravity wavelength is given, along with representative transitions listed in order of decreasing line strength. Other closely spaced transitions are treated similarly.

Values of the orbital quantum number l, also known as the azimuthal or angular quantum number, are specified in transition electron configurations using the standard spectroscopic designations (e.g. Cox, 2000) in table A.1. Total atomic electron orbital angular momentum $L = \sum L_i$ values, with L_i orbital angular momentum of electron i and $|L_i| = \sqrt{l_i(l_i+1)}\hbar$, incorporating the reduced Planck constant $\hbar \equiv h/2\pi$, use corresponding designations.

Table A.1: Orbital quantum number and total orbital angular momentum designations.

l or L	0	1	2	3	4	5	6	7	8	9	10	11	12	13	14	15
Designation (l)	s	p	d	f	g	h	i	k	l	m	n	o	q	r	t	u
Designation (L)	S	P	D	F	G	H	I	K	L	M	N	O	Q	R	T	U

Russell-Saunders terms ${}^{2S+1}L_J$ are used in transition descriptions, where $S = \sum S_i$ is the total atomic electron spin angular momentum, S_i spin angular momentum of electron i, $|S_i| = \sqrt{s_i(s_i+1)}\hbar$, s the spin quantum number, $J = L + S$ is the total atomic electron angular momentum. Each Russell-Saunders term has an associated parity $(-1)^{\sum l_i}$. Terms with odd parity are designated with a suffixed "o" superscript, e.g. ${}^{2S+1}L^{\mathrm{o}}_J$.

TABLE A.2: Atomic transition spectral features referenced in this work. Feature wavelengths and associated electron transitions are given. Where available, uncertainties in the last digits of quantities are specified in brackets following that quantity. A LaTeX xcolor package (Kern, 2007) wave model rendering of each wavelength prefixes references, as a visualisation aid. Transitions are specified in terms of electron configurations and Russell-Saunders terms.

Feature	Wavelength (Å)	Reference	Transition
C IV	1548.2049(12)[v]	● [1,2,3]	$1s^2 2s\,{}^2S_{1/2}$–$1s^2 2p\,{}^2P^{\rm o}_{3/2}$
	1550.7785(12)[v]	● [1,2,3]	$1s^2 2s\,{}^2S_{1/2}$–$1s^2 2p\,{}^2P^{\rm o}_{1/2}$
C III]	1908.734[v]	● [1,4,5]	$1s^2 2s^2\,{}^1S_0$–$1s^2 2s 2p\,{}^3P^{\rm o}_1$
[O II]	3726.032[a]	● [1,6]	$1s^2 2s^2 2p^3\,{}^4S^{\rm o}_{3/2}$–$1s^2 2s^2 2p^3\,{}^2D^{\rm o}_{3/2}$
	3727.092[v]	[1]	
[O II]	3728.815[a]	● [1,6]	$1s^2 2s^2 2p^3\,{}^4S^{\rm o}_{3/2}$–$1s^2 2s^2 2p^3\,{}^2D^{\rm o}_{5/2}$
	3729.875[v]	[1]	
Ne III	3868.76[a]	● [1,7]	$1s^2 2s^2 2p^4\,{}^3P_2$–$1s^2 2s^2 2p^4\,{}^1D_2$
	3869.86[v]	[1]	
He I	3888.64[a]	● [1,8]	$1s2s\,{}^3S_1$–$1s3p\,{}^3P^{\rm o}_2$, $1s2s\,{}^3S_1$–$1s3p\,{}^3P^{\rm o}_1$, …
	3889.74[v]	[1,8]	
Hϵ	3970.0719(9)[a]	● [1,9]	$2p\,{}^2P^{\rm o}_{3/2}$–$7d\,{}^2D_{5/2}$, $2p\,{}^2P^{\rm o}_{1/2}$–$7d\,{}^2D_{3/2}$, …
	3971.1951(9)[v]	[1,9]	
He I	4009.2564996[a]	● [1,8]	$1s2p\,{}^1P^{\rm o}_1$–$1s7d\,{}^1D_2$
	4010.3898875[v]	[1,8]	
[Ar II]	4072.00431[a]	● [1,10]	$1s^2 2s^2 2p^6 3s^2 3p^4({}^1D)4s\,{}^2D_{5/2}$–$1s^2 2s^2 2p^6 3s^2 3p^4({}^1D)4p\,{}^2D^{\rm o}_{5/2}$
	4073.15411[v]	[1]	
[Ar II]	4072.38432[a]	● [1,10]	$1s^2 2s^2 2p^6 3s^2 3p^4({}^3P)4p\,{}^4D^{\rm o}_{5/2}$–$1s^2 2s^2 2p^6 3s^2 3p^4({}^3P)5s\,{}^4P_{3/2}$
	4073.53422[v]	[1]	
Hδ	4101.7346(10)[a]	● [1,9]	$2p\,{}^2P^{\rm o}_{3/2}$–$6d\,{}^2D_{5/2}$, $2p\,{}^2P^{\rm o}_{1/2}$–$6d\,{}^2D_{3/2}$, …
	4102.8922(10)[v]	[1,9]	
C II	4267.15[a]	● [1,4,11]	$1s^2 2s^2 3d\,{}^2D_{5/2}$–$1s^2 2s^2 4f\,{}^2F^{\rm o}_{7/2}$, …
	4268.35[v]	[1,4]	
Hγ	4340.4634(11)[a]	● [1,9]	$2p\,{}^2P^{\rm o}_{3/2}$–$5d\,{}^2D_{5/2}$, $2p\,{}^2P^{\rm o}_{1/2}$–$5d\,{}^2D_{3/2}$, …
	4341.6837(11)[v]	[1,9]	
[O III]	4363.209[a]	● [1,7]	$1s^2 2s^2 2p^2\,{}^1D_2$–$1s^2 2s^2 2p^2\,{}^1S_0$
	4364.435[v]	[1]	
He I	4471.49[a]	● [1,8]	$1s2p\,{}^3P^{\rm o}_2$–$1s4d\,{}^3D_3$, $1s2p\,{}^3P^{\rm o}_1$–$1s4d\,{}^3D_2$, …
	4472.74[v]	[1,8]	
C III	4515.352[a]	● [1,4]	$1s^2 2s4p\,{}^3P^{\rm o}_0$–$1s^2 2s5s\,{}^3S_1$
	4516.618[v]	[1,4]	
C III	4515.811[a]	● [1,4]	$1s^2 2s4p\,{}^3P^{\rm o}_1$–$1s^2 2s5s\,{}^3S_1$
	4517.077[v]	[1,4]	
C III	4516.788[a]	● [1,4]	$1s^2 2s4p\,{}^3P^{\rm o}_2$–$1s^2 2s5s\,{}^3S_1$
	4518.055[v]	[1,4]	
N III	4640.64[a]	● [1,4,12]	$1s^2 2s^2 3p\,{}^2P^{\rm o}_{3/2}$–$1s^2 2s^2 3d\,{}^2D_{5/2}$

TABLE A.2: Atomic transition spectral features referenced in this work (continued).

Feature	Wavelength (Å)	Reference	Transition
	4641.94[v]	[1,4]	
C III	4647.418[a]	[1,4,13]	$1s^2 2s 3s\ ^3S_1$–$1s^2 2s 3p\ ^3P^{\rm o}_2$
	4648.719[v]	[1,4]	
C III	4650.246[a]	[1,4,13]	$1s^2 2s 3s\ ^3S_1$–$1s^2 2s 3p\ ^3P^{\rm o}_1$
	4651.548[v]	[1,4]	
C III	4651.473[a]	[1,4,13]	$1s^2 2s 3s\ ^3S_1$–$1s^2 2s 3p\ ^3P^{\rm o}_0$
	4652.775[v]	[1,4]	
He II	4685.684[a]	[1,11]	$3d\ ^2D_{3/2}$–$4f\ ^2F^{\rm o}_{5/2}$, $3p\ ^2P^{\rm o}_{3/2}$–$4d\ ^2D_{5/2}$, ...
	4686.995[v]	[1]	
[Ar IV]	4711.26[a]	[1,10]	$1s^2 2s^2 2p^6 3s^2 3p^3\ ^4S^{\rm o}_{3/2}$–$1s^2 2s^2 2p^6 3s^2 3p^3\ ^2D^{\rm o}_{5/2}$
	4712.58[v]	[1]	
[Ar IV]	4740.12[a]	[1,10]	$1s^2 2s^2 2p^6 3s^2 3p^3\ ^4S^{\rm o}_{3/2}$–$1s^2 2s^2 2p^6 3s^2 3p^3\ ^2D^{\rm o}_{3/2}$
	4741.45[v]	[1]	
Hβ	4861.3250(14)[a]	[1,9]	$2p\ ^2P^{\rm o}_{3/2}$–$4d\ ^2D_{5/2}$, $2p\ ^2P^{\rm o}_{1/2}$–$4d\ ^2D_{3/2}$, ...
	4862.6830(14)[v]	[1,9]	
[O III]	4958.910(7)[a]	[7]	$1s^2 2s^2 2p^2\ ^3P_1$–$1s^2 2s^2 2p^2\ ^1D_2$
	4960.295[v]	[1,4]	
[O III]	5006.843(8)[a]	[7]	$1s^2 2s^2 2p^2\ ^3P_2$–$1s^2 2s^2 2p^2\ ^1D_2$
	5008.240[v]	[1,4]	
[Fe VI]	5176.04[a]	[1,13]	$1s^2 2s^2 2p^6 3s^2 3p^6 3d^3\ ^4F_{9/2}$–$1s^2 2s^2 2p^6 3s^2 3p^6 3d^3\ ^2G_{9/2}$
	5177.48[v]	[1]	
[N I]	5197.902[a]	[1,14,15]	$1s^2 2s^2 2p^3\ ^4S^{\rm o}_{3/2}$–$1s^2 2s^2 2p^3\ ^2D^{\rm o}_{3/2}$
	5199.349[v]	[1,15]	
[Ca V]	5309.11[a]	[1,7]	$1s^2 2s^2 2p^6 3s^2 3p^4\ ^3P_2$–$1s^2 2s^2 2p^6 3s^2 3p^4\ ^1D_2$
	5310.59[v]	[1]	
He II	5411.524[a]	[13,16]	$4f\ ^2F^{\rm o}$–$7g\ ^2G$
	5412.04[n]	[16]	
[O I]*	5577.338(4)[a]	[1,7,17]	$1s^2 2s^2 2p^4\ ^1D_2$–$1s^2 2s^2 2p^4\ ^1S_0$
	5578.888[v]	[1]	
[Fe VI]	5677.0[a]	[1,13]	$1s^2 2s^2 2p^6 3s^2 3p^6 3d^3\ ^4F_{9/2}$–$1s^2 2s^2 2p^6 3s^2 3p^6 3d^3\ ^4P_{5/2}$
	5678.6[v]	[1]	
[Fe VII]	5720.7[a]	[1,13]	$1s^2 2s^2 2p^6 3s^2 3p^6 3d^2\ ^3F_2$–$1s^2 2s^2 2p^6 3s^2 3p^6 3d^2\ ^1D_2$
	5722.3[v]	[1]	
[N II]	5754.57(4)[a]	[1,7]	$1s^2 2s^2 2p^2\ ^1D_2$–$1s^2 2s^2 2p^2\ ^1S_0$
	5756.19[v]	[1,4]	
C IV	5801.31[a]	[1,4,13]	$1s^2 3s\ ^2S_{1/2}$–$1s^2 3p\ ^2P^{\rm o}_{3/2}$
	5802.92[v]	[1,4]	
C IV	5811.97[a]	[1,4,13]	$1s^2 3s\ ^2S_{1/2}$–$1s^2 3p\ ^2P^{\rm o}_{1/2}$
	5813.58[v]	[1,4]	

TABLE A.2: Atomic transition spectral features referenced in this work (continued).

Feature	Wavelength (Å)	Reference	Transition
He I	5875.66[a]	[1,8]	$1s2p\,^3P^{\rm O}_2$–$1s3d\,^3D_3$, $1s2p\,^3P^{\rm O}_1$–$1s3d\,^3D_2$, …
	5877.29[v]	[1,8]	
[Ca V]	6086.92[a]	[1,7]	$1s^22s^22p^63s^23p^4\,^3P_1$–$1s^22s^22p^63s^23p^4\,^1D_2$
	6088.61[v]	[1]	
[Fe VII]	6087.0[a]	[1,13]	$1s^22s^22p^63s^23p^63d^2\,^3F_3$–$1s^22s^22p^63s^23p^63d^2\,^1D_2$
	6088.7[v]	[1]	
[O I]*	6300.304(6)[a]	[1,7]	$1s^22s^22p^4\,^3P_2$–$1s^22s^22p^4\,^1D_2$
	6302.046[v]	[1]	
[S III]	6312.06[a]	[1,18]	$1s^22s^22p^63s^23p^2\,^1D_2$–$1s^22s^22p^63s^23p^2\,^1S_0$
	6313.81[v]	[1]	
C III	6350.77[a]	[1,4]	$1s^22p(^2P^{\rm O})3p\,^1D_2$–$1s^22s5f\,^1F^{\rm O}_3$
	6352.53[v]	[1,4]	
[O I]*	6363.776(6)[a]	[1,7]	$1s^22s^22p^4\,^3P_1$–$1s^22s^22p^4\,^1D_2$
	6365.535[v]	[1]	
[Ar V]	6435.12[a]	[1,10]	$1s^22s^22p^63s^23p^2\,^3P_1$–$1s^22s^22p^63s^23p^2\,^1D_2$
	6436.90[v]	[1]	
[N II]	6548.05[a]	[1,4,7]	$1s^22s^22p^2\,^3P_1$–$1s^22s^22p^2\,^1D_2$
	6549.86[v]	[1,4]	
Hα	6562.795(9)[a]	[1,9]	$2p\,^2P^{\rm O}_{3/2}$–$3d\,^2D_{5/2}$, $2p\,^2P^{\rm O}_{1/2}$–$3d\,^2D_{3/2}$, …
	6564.608(9)[v]	[1,9]	
[N II]	6583.45[a]	[1,4,7]	$1s^22s^22p^2\,^3P_2$–$1s^22s^22p^2\,^1D_2$
	6585.27[v]	[1,4]	
He I	6678.151704[a]	[1,8]	$1s2p\,^1P^{\rm O}_1$–$1s3d\,^1D_2$
	6679.995599[v]	[1,8]	
[S II]	6716.440[a]	[1,18,19]	$1s^22s^22p^63s^23p^3\,^4S^{\rm O}_{3/2}$–$1s^22s^22p^63s^23p^3\,^2D^{\rm O}_{5/2}$
	6718.294[v]	[1]	
C III	6727.48[a]	[1,4,13]	$1s^22p(^2P^{\rm O})3s\,^3P^{\rm O}_0$–$1s^22p(^2P^{\rm O})3p\,^3D_1$
	6729.34[v]	[1,4]	
[S II]	6730.816[a]	[1,18]	$1s^22s^22p^63s^23p^3\,^4S^{\rm O}_{3/2}$–$1s^22s^22p^63s^23p^3\,^2D^{\rm O}_{3/2}$
	6732.674[v]	[1,18]	
C III	6731.04[a]	[1,4,13]	$1s^22p(^2P^{\rm O})3s\,^3P^{\rm O}_1$–$1s^22p(^2P^{\rm O})3p\,^3D_2$
	6732.90[v]	[1,4]	
[Ar V]	7005.83[a]	[1,10]	$1s^22s^22p^63s^23p^2\,^3P_2$–$1s^22s^22p^63s^23p^2\,^1D_2$
	7007.76[v]	[1]	
C II	7053.09[a]	[1,4,13]	$1s^22s2p(^3P^{\rm O})3p\,^4S_{3/2}$–$1s^22s2p(^3P^{\rm O})3d\,^4P^{\rm O}_{3/2}$
	7055.03[v]	[1,4]	
C II	7063.68[a]	[1,4,13]	$1s^22s2p(^3P^{\rm O})3p\,^4S_{3/2}$–$1s^22s2p(^3P^{\rm O})3d\,^4P^{\rm O}_{5/2}$
	7065.63[v]	[1,4]	
He I	7065.25[a]	[1,8]	$1s2p\,^3P^{\rm O}_2$–$1s3s\,^3S_1$, $1s2p\,^3P^{\rm O}_1$–$1s3s\,^3S_1$, …

TABLE A.2: Atomic transition spectral features referenced in this work (continued).

Feature	Wavelength (Å)	Reference	Transition
	7067.20[v]	[1,8]	
C II	7115.63[a]	[1,4,13]	$1s^2 2s 2p(^3P^{\rm o})3p\ ^4D_{5/2}$–$1s^2 2s 2p(^3P^{\rm o})3d\ ^4F^{\rm o}_{7/2}$
	7117.59[v]	[1,4]	
C II	7119.91[a]	[1,4,13]	$1s^2 2s 2p(^3P^{\rm o})3p\ ^4D_{7/2}$–$1s^2 2s 2p(^3P^{\rm o})3d\ ^4F^{\rm o}_{9/2}$
	7121.87[v]	[1,4]	
[Ar III]	7135.79[a]	[1,10]	$1s^2 2s^2 2p^6 3s^2 3p^4\ ^3P_2$–$1s^2 2s^2 2p^6 3s^2 3p^4\ ^1D_2$
	7137.76[v]	[1]	
[Ar IV]	7170.70[a]	[1,10]	$1s^2 2s^2 2p^6 3s^2 3p^3\ ^2D^{\rm o}_{3/2}$–$1s^2 2s^2 2p^6 3s^2 3p^3\ ^2P^{\rm o}_{3/2}$
	7172.68[v]	[1]	
[Ar IV]	7237.77[a]	[1,10]	$1s^2 2s^2 2p^6 3s^2 3p^3\ ^2D^{\rm o}_{5/2}$–$1s^2 2s^2 2p^6 3s^2 3p^3\ ^2P^{\rm o}_{3/2}$
	7239.76[v]	[1]	
He I	7281.350742[a]	[1,8]	$1s2p\ ^1P^{\rm o}_1$–$1s3s\ ^1S_0$
	7283.357068[v]	[1,8]	
[O II]	7318.92[a]	[1,6]	$1s^2 2s^2 2p^3\ ^2D^{\rm o}_{5/2}$–$1s^2 2s^2 2p^3\ ^2P^{\rm o}_{1/2}$
	7320.94[v]	[1,6]	
[O II]	7319.99[a]	[1,6]	$1s^2 2s^2 2p^3\ ^2D^{\rm o}_{5/2}$–$1s^2 2s^2 2p^3\ ^2P^{\rm o}_{3/2}$
	7322.01[v]	[1,6]	
[O II]	7329.67[a]	[1,6]	$1s^2 2s^2 2p^3\ ^2D^{\rm o}_{3/2}$–$1s^2 2s^2 2p^3\ ^2P^{\rm o}_{1/2}$
	7331.69[v]	[1,6]	
[O II]	7330.73[a]	[1,6]	$1s^2 2s^2 2p^3\ ^2D^{\rm o}_{3/2}$–$1s^2 2s^2 2p^3\ ^2P^{\rm o}_{3/2}$
	7332.75[v]	[1,6]	
[Cl IV]	7530.54[a]	[1,7]	$1s^2 2s^2 2p^6 3s^2 3p^2\ ^3P_1$–$1s^2 2s^2 2p^6 3s^2 3p^2\ ^1D_2$
	7532.61[v]	[1]	
He II	7592.74[a]	[13,16]	$5g\ ^2G$–$10h\ ^2H^{\rm o}$
[Ar III]	7751.11[a]	[1,10]	$1s^2 2s^2 2p^6 3s^2 3p^4\ ^3P_1$–$1s^2 2s^2 2p^6 3s^2 3p^4\ ^1D_2$
	7753.24[v]	[1]	
[O I]*	7771.944[a]	[1,4]	$2s^2 2p^3(^4S^{\rm o})3s\ ^5S^{\rm o}_2$–$2s^2 2p^3(^4S^{\rm o})3p\ ^5P_3$
	7774.083[v]	[1,4]	
[O I]*	7774.166[a]	[1,4]	$2s^2 2p^3(^4S^{\rm o})3s\ ^5S^{\rm o}_2$–$2s^2 2p^3(^4S^{\rm o})3p\ ^5P_2$
	7776.305[v]	[1,4]	
[O I]*	7775.388[a]	[1,4]	$2s^2 2p^3(^4S^{\rm o})3s\ ^5S^{\rm o}_2$–$2s^2 2p^3(^4S^{\rm o})3p\ ^5P_1$
	7777.528[v]	[1,4]	
[Cl IV]	8045.63[a]	[1,7]	$1s^2 2s^2 2p^6 3s^2 3p^2\ ^3P_2$–$1s^2 2s^2 2p^6 3s^2 3p^2\ ^1D_2$
	8047.84[v]	[1]	
He II	8236.77[a]	[13]	$5g\ ^2G$–$9h\ ^2H^{\rm o}$
H I	8345.552[a]	[1,20]	$3d\ ^2D$–$23f\ ^2F^{\rm o}$
	8347.846[v]	[1]	
[O I]*	8446.31[a]	[1,4]	$2s^2 2p^3(^4S^{\rm o})3s\ ^3S^{\rm o}_1$–$2s^2 2p^3(^4S^{\rm o})3p\ ^3P_2$, ...
	8448.63[v]	[1,4]	

TABLE A.2: Atomic transition spectral features referenced in this work (continued).

Feature	Wavelength (Å)	Reference	Transition
[O I]*	8446.758[a]	● [1,4]	$2s^2 2p^3(^4S^o)3s\,^3S^o_1$–$2s^2 2p^3(^4S^o)3p\,^3P_1$
	8449.079[v]	[1,4]	
H I	8502.483[a]	● [1,8,20]	$3d\,^2D$–$16f\,^2F^o$
	8504.819[v]	[1,8]	
H I	8545.383[a]	● [1,8,20]	$3d\,^2D$–$15f\,^2F^o$
	8547.731[v]	[1,8]	
H I	8598.392[a]	● [1,8,20]	$3d\,^2D$–$14f\,^2F^o$
	8600.754[v]	[1,8]	
H I	8665.019[a]	● [1,8,20]	$3d\,^2D$–$13f\,^2F^o$
	8667.399[v]	[1,8]	
H I	8750.472(9)[a]	● [1,8,20]	$3d\,^2D$–$12f\,^2F^o$
	8752.875(9)[v]	[1,8]	
[K VI]	8827.46[a]	● [1,7]	$1s^2 2s^2 2p^6 3s^2 3p^2\,^3P_0$–$1s^2 2s^2 2p^6 3s^2 3p^2\,^3P_1$
	8829.87[v]	[1]	
[S III]	9068.6[a]	● [1,18]	$1s^2 2s^2 2p^6 3s^2 3p^2\,^3P_1$–$1s^2 2s^2 2p^6 3s^2 3p^2\,^1D_2$
	9071.1[v]	[1]	
[S III]	9530.6[a]	● [1,18]	$1s^2 2s^2 2p^6 3s^2 3p^2\,^3P_2$–$1s^2 2s^2 2p^6 3s^2 3p^2\,^1D_2$
	9533.2[v]	[1]	
He I	10 830.17[a]	● [1,8]	$1s2s\,^3S_1$–$1s2p\,^3P^o_2$, $1s2s\,^3S_1$–$1s2p\,^3P^o_1$, …
	10 833.14[v]	[1]	
[Mg IV]	44 868[a]	● [1,7]	$1s^2 2s^2 2p^5\,^2P^o_{3/2}$–$1s^2 2s^2 2p^5\,^2P^o_{1/2}$
	44 880[v]	[1,21]	
[S IV]	105 076[a]	● [1,18]	$1s^2 2s^2 2p^6 3s^2 3p\,^2P^o_{1/2}$–$1s^2 2s^2 2p^6 3s^2 3p\,^2P^o_{3/2}$
	105 105[v]	[1,18]	

TABLE A.2: Atomic transition spectral features referenced in this work (continued).

Feature	Wavelength (Å)	Reference	Transition

[*] Airglow line.
[v] Calculated Ritz wavelength, in vacuum.
[a] Calculated Ritz wavelength, in air.
[n] Observed nebula (vacuum) wavelength.

[1] Kramida et al. (2014)
[2] Griesmann & Kling (2000)
[3] Petitjean & Aracil (2004)
[4] Wiese et al. (1996)
[5] Kwong et al. (1993)
[6] Martin et al. (1993)
[7] Kaufman & Sugar (1986)
[8] Wiese & Fuhr (2009)
[9] Reader (2004)
[10] Saloman (2010)
[11] Sansonetti & Martin (2005)
[12] Moore (1975)
[13] Moore (1972)
[14] Tachiev & Froese Fischer (2002)
[15] Wiese & Fuhr (2007)
[16] Ercolano et al. (2004)
[17] Moore (1976)
[18] Kaufman & Martin (1993)
[19] Trauger et al. (1980)
[20] Moore (1993)
[21] Kelleher & Podobedova (2008)

B

Galactic Bulge Mosaic II Survey Fields

TABLE B.1: Galactic bulge Mosaic II survey fields, grouped by observation night. Field names are a truncation of the RA and dec respectively, in J2000 coordinates, of each field's centre. Exposure times apply to [O III] on band frames. Table adapted from (Kovacevic et al., 2011b).

Field name	RA (h m s)	Dec (° ′ ″)	Seeing	Exposure time (s)	Notes
				9 Jun 2008	
F1753−2841	17 53 52.1	−28 41 15	2.04	3 × 400	
F1754−2915	17 54 04.8	−29 15 15	1.39	2 × 400	
F1751−2949	17 51 41.3	−29 49 15	1.26	3 × 400	

TABLE B.1: Galactic bulge Mosaic II survey fields (continued).

Field name	RA (h m s)	Dec (° ′ ″)	Seeing	Exposure time (s)	Notes
F1754−2949	17 54 17.9	−29 49 15	1.32	$1 \times 60, 3 \times 400$	
F1758−2733	17 58 34.3	−27 33 15	1.29	3×400	
F1804−2841	18 04 11.8	−28 41 15	1.26	$1 \times 60, 3 \times 400$	Also observed on 11 Jun 2008.
F1759−2915	17 59 16.4	−29 15 15	1.16	3×400	
F1801−2841	18 01 36.9	−28 41 15	1.23	$1 \times 60, 3 \times 400$	
F1811−2807	18 11 38.5	−28 07 15	1.26	$1 \times 60, 3 \times 400$	Also observed on 13 Jun 2008.
F1801−2807	18 01 22.0	−28 07 15	1.21	$1 \times 60, 3 \times 400$	Contains probable satellite trail.
F1759−2841	17 59 01.9	−28 41 15	1.30	3×400	
F1802−3131	18 02 57.8	−31 31 15	1.42	$1 \times 60, 3 \times 400$	
F1803−2807	18 03 56.1	−28 07 15	1.52	3×400	
				10 Jun 2008	
F1719−3048	17 19 44.8	−30 48 39	1.55	3×400	
F1751−2841	17 51 17.1	−28 41 15	1.33	3×400	
F1751−2915	17 51 29.0	−29 15 15	1.28	3×400	
F1753−2807	17 53 39.7	−28 07 15	1.42	3×400	
F1756−2841	17 56 27.0	−28 41 15	1.63	3×400	
F1756−2915	17 56 40.6	−29 15 15	1.27	3×400	
F1751−3023	17 51 53.8	−30 23 15	1.33	3×400	
F1806−2807	18 06 30.3	−28 07 15	1.23	3×400	
F1756−2807	17 56 13.8	−28 07 15	1.36	3×400	
F1758−2807	17 58 47.9	−28 07 15	1.29	$1 \times 60, 3 \times 400$	
F1756−2733	17 56 01.0	−27 33 15	1.25	3×400	
F1801−2733	18 01 07.6	−27 33 15	1.31	3×400	
F1806−2715	18 06 54.4	−27 15 54	1.45	3×400	Also observed on 11 Jun 2008. Contains probable satellite trail.
F1811−2722	18 11 18.8	−27 22 35	1.45	$1 \times 60, 3 \times 400$	Also observed on 13 Jun 2008.

TABLE B.1: Galactic bulge Mosaic II survey fields (continued).

Field name	RA (h m s)	Dec (° ′ ″)	Seeing	Exposure time (s)	Notes
				11 Jun 2008	
F1725−3055	17 25 26.8	−30 55 00	1.22	3×400	
F1804−2703	18 04 22.8	−27 03 33	1.14	$1 \times 60, 3 \times 400$	
F1806−2642	18 06 56.6	−26 42 03	1.15	$1 \times 30, 3 \times 400$	
F1801−2915	18 01 52.1	−29 15 15	1.24	3×400	
F1804−2907	18 04 27.9	−29 07 21	1.24	3×400	
F1807−2907	18 07 03.7	−29 07 21	1.12	$1 \times 30, 3 \times 400$	
F1807−2833	18 07 19.5	−28 33 20	1.09	$1 \times 30, 3 \times 400$	
F1752−3123	17 52 20.1	−31 23 21	1.10	3×400	
F1749−3015	17 49 16.3	−30 15 21	1.02	3×400	
F1749−3049	17 49 28.3	−30 49 21	1.23	$1 \times 30, 3 \times 400$	
F1804−2841	18 04 11.8	−28 41 15	1.21	$1 \times 60, 2 \times 400$	Also observed on 9 Jun 2008.
F1806−2715	18 06 54.4	−27 15 54	1.22	2×400	Also observed on 10 Jun 2008.
				12 Jun 2008	
F1718−3006	17 18 37.7	−30 06 30	1.19	3×400	
F1800−2651	18 00 04.2	−26 51 17	1.22	3×400	
F1755−3025	17 55 04.8	−30 25 01	1.20	$1 \times 30, 3 \times 400$	
F1757−3115	17 57 34.9	−31 15 14	1.16	3×400	
F1754−3115	17 54 56.2	−31 15 02	1.14	3×400	
F1757−3149	17 57 12.9	−31 49 36	0.96	3×400	
F1758−3314	17 58 59.4	−33 14 21	0.96	$1 \times 30, 3 \times 400$	
F1751−3327	17 51 15.6	−33 27 01	0.99	3×400	
F1752−3401	17 52 58.4	−34 01 00	1.00	3×400	
F1750−3400	17 50 14.2	−34 00 54	1.03	3×400	Contains probable satellite trail.

TABLE B.1: Galactic bulge Mosaic II survey fields (continued).

Field name	RA (h m s)	Dec (° ′ ″)	Seeing	Exposure time (s)	Notes
F1753−3435	17 53 52.8	−34 35 10	1.08	$1 \times 30, 3 \times 400$	Also observed on 1 Jul 2009.
F1753−3518	17 53 24.9	−35 18 01	1.16	3×400	
				13 Jun 2008	
F1722−2855	17 22 17.8	−28 55 39	1.63	$1 \times 30, 3 \times 400$	
F1740−3318	17 40 27.0	−33 18 58	1.48	3×400	
F1744−3302	17 44 06.9	−33 02 54	1.09	3×400	
F1743−3400	17 43 10.3	−34 00 44	1.28	$1 \times 30, 3 \times 400$	
F1752−3243	17 52 50.4	−32 43 53	1.19	$1 \times 30, 3 \times 400$	
F1743−2725	17 43 14.5	−27 25 21	1.05	3×400	
F1745−3428	17 45 36.6	−34 28 18	1.02	$1 \times 30, 3 \times 400$	
F1750−3203	17 50 43.4	−32 03 53	1.23	3×400	
F1800−2958	18 00 24.5	−29 58 21	1.05	3×400	
F1802−3049	18 02 52.8	−30 49 04	1.20	3×400	
F1803−2940	18 03 02.1	−29 40 31	1.10	$1 \times 30, 3 \times 400$	
F1805−3048	18 05 54.8	−30 48 24	1.19	$1 \times 30, 3 \times 400$	
F1800−3032	18 00 22.1	−30 32 36	1.15	3×400	
F1805−3014	18 05 38.4	−30 14 17	1.25	3×400	
F1811−2807	18 11 38.5	−28 07 15	1.40	$1 \times 60, 2 \times 400$	Also observed on 9 Jun 2008.
F1811−2722	18 11 18.8	−27 22 35	1.48	$1 \times 60, 2 \times 400$	Also observed on 10 Jun 2008. Contains probable satellite trail.
				14 Jun 2008	
F1722−3029	17 22 18.0	−30 29 41	1.81	3×400	
F1746−3200	17 46 58.8	−32 00 34	1.58	3×400	
F1802−3223	18 02 21.0	−32 23 31	1.29	3×400	
F1746−3325	17 46 47.6	−33 25 08	1.19	$1 \times 30, 3 \times 400$	

TABLE B.1: Galactic bulge Mosaic II survey fields (continued).

Field name	RA (h m s)	Dec (° ′ ″)	Seeing	Exposure time (s)	Notes
F1748−3450	17 48 04.4	−34 50 45	1.19	3×400	
F1751−3444	17 51 07.5	−34 44 17	1.18	$1 \times 30, 3 \times 400$	
F1757−3014	17 57 43.8	−30 14 17	1.60	$1 \times 30, 3 \times 400$	
F1800−2511	18 00 10.6	−25 11 37	1.42	$1 \times 30, 3 \times 400$	
F1803−3014	18 03 01.5	−30 14 37	1.27	$1 \times 30, 3 \times 400$	
F1757−2940	17 57 08.4	−29 40 26	1.32	$1 \times 30, 3 \times 400$	
F1759−3210	17 59 47.2	−32 10 04	0.94	$1 \times 30, 3 \times 400$	
F1752−3049	17 52 06.8	−30 49 21	1.14	$1 \times 30, 3 \times 400$	
F1746−3049	17 46 49.8	−30 49 21	1.15	3×400	
F1800−3106	18 00 14.7	−31 06 08	1.10	3×400	
F1811−2833	18 11 23.9	−28 33 37	1.26	$1 \times 30, 3 \times 400$	
				27 Jun 2009	
F1748−2429	17 48 42.3	−24 29 29	2.68	3×400	
F1737−2802	17 37 51.7	−28 02 20	3.09	$1 \times 30, 3 \times 400$	
F1740−2759	17 40 29.5	−27 59 57	3.23	3×400	
F1730−3009	17 30 43.6	−30 09 06	2.00	3×400	
F1742−2542	17 42 40.9	−25 42 52	2.48	3×400	
F1736−2910	17 36 00.3	−29 10 32	2.69	3×400	
F1725−2929	17 25 18.5	−29 29 35	2.99	$1 \times 30, 3 \times 400$	
				28 Jun 2009	
F1809−2905	18 09 58.7	−29 05 06	2.69	$1 \times 30, 3 \times 400$	
F1804−2637	18 04 16.7	−26 37 37	2.68	$1 \times 30, 3 \times 400$	
				29 Jun 2009	
F1745−2619	17 45 38.3	−26 19 09	2.24	3×400	

TABLE B.1: Galactic bulge Mosaic II survey fields (continued).

Field name	RA (h m s)	Dec (° ′ ″)	Seeing	Exposure time (s)	Notes
F1735−2754	17 35 25.2	−27 54 27	2.15	3×400	
F1745−2543	17 45 03.6	−25 43 57	1.71	$1 \times 30, 3 \times 400$	
F1739−2834	17 39 55.3	−28 34 54	1.74	3×400	
F1733−2942	17 33 28.9	−29 42 00	1.58	$1 \times 30, 3 \times 400$	
				30 Jun 2009	
F1728−2755	17 28 49.5	−27 55 39	1.96	3×400	
F1731−2821	17 31 18.7	−28 21 02	1.89	$1 \times 30, 3 \times 400$	
F1730−2857	17 30 43.4	−28 57 54	2.04	$1 \times 30, 3 \times 400$	
F1728−2833	17 28 34.5	−28 33 30	1.81	$1 \times 30, 3 \times 400$	
F1740−2650	17 40 22.2	−26 50 05	2.02	2×400	
F1734−2641	17 34 09.7	−26 41 15	1.83	3×400	
F1729−2603	17 29 37.3	−26 03 39	2.08	3×400	
F1735−3019	17 35 30.6	−30 19 02	1.96	2×400	
F1737−2835	17 37 32.7	−28 35 38	1.85	2×400	
F1732−3015	17 32 58.5	−30 15 18	1.81	2×400	
F1743−2651	17 43 03.6	−26 51 06	1.76	1×100	
F1745−3401	17 45 23.3	−34 01 05	1.68	3×400	
F1810−2759	18 10 21.0	−27 59 08	1.62	3×400	Also observed 1 Jul 2009.
				1 Jul 2009	
F1736−2328	17 36 17.8	−23 28 58	1.81	2×400	
F1740−2426	17 40 54.1	−24 26 53	1.73	$1 \times 30, 3 \times 400$	
F1738−2911	17 38 34.3	−29 11 29	1.71	3×400	
F1735−2945	17 35 57.8	−29 45 19	1.70	3×400	
F1740−2723	17 40 32.8	−27 23 56	1.53	3×400	

TABLE B.1: Galactic bulge Mosaic II survey fields (continued).

Field name	RA (h m s)	Dec (° ′ ″)	Seeing	Exposure time (s)	Notes
F1753−3435	17 53 52.8	−34 35 10	1.23	1×100	Also observed on 12 Jun 2008.
F1748−3415	17 48 05.4	−34 15 19	1.20	$1 \times 30, 3 \times 400$	
F1756−3425	17 56 22.4	−34 25 58	1.26	$1 \times 30, 3 \times 400$	
F1757−3349	17 57 39.8	−33 49 22	1.31	$1 \times 30, 3 \times 400$	
F1743−2419	17 43 31.1	−24 19 33	1.37	$1 \times 30, 3 \times 400$	
F1748−2344	17 48 40.0	−23 44 33	1.39	2×400	
F1730−2722	17 30 58.4	−27 22 14	1.36	3×400	
F1737−2513	17 37 42.7	−25 13 56	1.53	3×400	
F1735−2711	17 35 27.1	−27 11 48	1.52	1×400	
F1810−2759	18 10 21.0	−27 59 08	1.78	1×30	Also observed on 30 Jun 2009.
F1808−2938	18 08 07.6	−29 38 56	1.58	1×400	

C

Galactic Bulge PNs

Physical and derived properties of PNs towards the Galactic bulge are presented in table C.1. The bulge region is defined here as spanning $-5^\circ \leqslant l \leqslant 5^\circ$, $-5^\circ \leqslant b \leqslant 5^\circ$. This is not an exhaustive list of such PNs, but is instead restricted to those appearing in the Blanco [O III] on/off band survey or otherwise discussed by Kovacevic (2011). Objects are sorted by RA and dec, as defined in SIMBAD. Flux data is dereddened. Diameters refer to [O III] λ5007 emission. References for $c(\mathrm{H}\beta)$ and v_r data append values. Object classifications for known objects are listed as defined in SIMBAD. Classifications for unpublished objects, along with other unreferenced data, originates from Kovacevic (2011) or this work. PNs excluded from the PNLF in figure 6.3 are shaded.

TABLE C.1: PNs towards the Galactic bulge

Object Name	$-\log F_{[\mathrm{O\,III}]\,\mathrm{dered}}$ (erg cm^{-2} s^{-1})	$c(\mathrm{H}\beta)$	Ref.	Diameter ($''$) $\pm 0.8''$	v_r (km s^{-1})	Ref.	Notes
Terzan N 140	–	0.82 ± 0.03		–	64.0 ± 30.0	[1]	PN [2]
PN G355.5+04.7	–	0.91 ± 0.03		–	103.5 ± 1.5	[3]	PN [2]
PN G355.8+04.5	–	–		12.2×11.2	23 ± 5	[3]	Possible PN [4]
CTIO J171813.83-302357.0	–	–		21.1×9.0	–		Possible PN (foreground) [5]
PN G355.6+04.1	–	–		46.7×40.5	-5.62 ± 9.50	[3]	PN (foreground) [4,5]
PN G355.1+03.7	12.25 ± 0.16	1.41 ± 0.20		20.8×19.9	-2.20 ± 9.50	[3]	PN
CTIO J171856.81-310641.5	–	–		10.3×8.1	–		Possible PN [4]
PN Th 3-5	11.67 ± 0.15	1.59 ± 0.18		13.3×10.5	70.0 ± 30.0	[1]	PN
PN G355.3+03.8	–	–		72.6×72.2	-5.60 ± 9.50	[3]	PN (foreground) [4,5]
PN G355.9+04.1	–	–		23.5×23.0	15.37 ± 9.50	[3]	PN (foreground) [4,5]
PN G355.4+03.6	12.40 ± 0.16	1.57 ± 0.20		20.0×15.6	-47.45 ± 9.50	[3]	PN
PN G355.5+03.6	–	–		24.6×22.3	52.65 ± 0.55	[3]	Possible PN (foreground) [4,5]
PN G355.6+03.6	11.96 ± 0.16	1.82 ± 0.20		15.2×14.9	-216.30 ± 9.50	[3]	PN
PN M 3-38	10.68 ± 0.07	1.8 ± 0.08	[6]	1.6×1.2	-171.1 ± 10.6	[1]	PN
PN G355.8+03.5	11.75 ± 0.09	2.13 ± 0.09		13.5×8.8	-14.8 ± 2.1	[3]	PN
PN H 1-9	–	1.76 ± 0.18		–	-157.6 ± 1.1	[1]	PN [2]
PN PBOZ 1	–	–		10.9×9.1	52.0 ± 15.0	[1]	PN [4]
PN K 5-31	–	1.42 ± 0.03		–	-49.27 ± 2.24	[3]	PN [2]
PN PM 1-143	–	3.77 ± 0.09		–	-108.3 ± 0.3	[3]	PN [2]
PN G357.3+04.1	–	–		20.7×18.9	-31.57 ± 3.71	[3]	Possible PN [4]
PN G355.9+03.1	11.76 ± 0.23	3.12 ± 0.20		5.6×5.1	-237.77 ± 9.50	[3]	PN
PN H 2-7	10.96 ± 0.09	1.65 ± 0.11	[7]	4.8×4.3	76.0 ± 15.0	[1]	PN
PN Th 3-11	–	3.08 ± 0.20		–	-43.04 ± 9.50	[3]	PN [2]
PN M 3-7	10.85 ± 0.02	$1.27^{+0.07}_{-0.00}$	[6]	6.5×6.0	-193.6 ± 4.8	[1]	PN
PN Th 3-10	11.16 ± 0.16	3.00 ± 0.18		3.0×2.6	-268.52 ± 9.50	[3]	PN

TABLE C.1: PNs towards the Galactic bulge (continued).

Object Name	$-\log F_{[\mathrm{O\,III}]\,\mathrm{dered}}$ (erg cm^{-2} s^{-1})	$c(\mathrm{H}\beta)$	Ref.	Diameter ($''$) $\pm 0.8''$	v_r (km s^{-1})	Ref.	Notes
PN M 3-8	–	1.87 ± 0.12		–	76.6 ± 9.1	[1]	PN [2]
PN G358.9+04.7	–	1.59 ± 0.18		–	82.76 ± 9.50	[3]	Possible PN [2]
PN PBOZ 3	12.03 ± 0.23	3.04 ± 0.20		10.6×9.3	11.90 ± 9.50	[3]	PN
PN Th 3-12	13.34 ± 0.16	1.64 ± 0.11	[7]	2.0×1.3	185.4 ± 30.0	[1]	PN
PN Th 3-13	11.33 ± 0.15	2.39 ± 0.18		1.9×1.4	-99.0 ± 40.0	[1]	PN
PN Th 3-14	–	2.13 ± 0.18		–	-239.2 ± 14.0	[1]	PN [2]
PN G357.4+03.4	–	–		11.2×10.7	-68.02 ± 9.50	[3]	Possible PN [4]
PN M 3-41	13.22 ± 0.09	$1.4^{+0.0}_{-0.1}$	[6]	4.2×4.2	-110.0 ± 16.4	[1]	PN
CTIO J172616.29-293451.2	–	–		22.7×11.4	–		Possible PN (foreground) [5]
PN PBOZ 18	11.58 ± 0.24	3.92 ± 0.20		4.1×2.7	-143.10 ± 9.50	[3]	PN
PN SaWe 2	–	1.67 ± 0.18		–	46.0 ± 15.0	[1]	PN [2]
PN Th 3-15	–	1.65 ± 0.12		–	33.0 ± 15.0	[1]	PN [2]
PN M 3-10	10.08 ± 0.10	1.73 ± 0.12		4.2×4.0	-131.3 ± 0.3	[1]	PN
PN Th 3-16	–	1.45 ± 0.03		–	4.14 ± 3.07	[3]	Possible PN [2]
PN H 2-10	10.75 ± 0.10	1.92 ± 0.12		3.7×3.0	44.1 ± 10.2	[1]	PN
PN Al 2-B	11.95 ± 0.11	1.76 ± 0.12		6.8×4.6	-158.0 ± 10.6	[1]	PN [8]
PN G359.6+04.3	–	2.58 ± 0.18		–	15.56 ± 9.50	[3]	Possible PN [2]
PN G358.8+03.8	12.34 ± 0.21	1.99 ± 0.18		16.2×14.4	-189.89 ± 9.50	[3]	PN
CTIO J172822.84-254727.9	–	–		22.8×18.4	108.65 ± 1.07		Probable PN (foreground) [5]
PN Th 3-19	11.06 ± 0.10	1.99 ± 0.12		2.3×2.3	122.0 ± 15.0	[1]	PN
PN G359.0+03.7	11.87 ± 0.15	2.47 ± 0.18		18.4×17.6	210.66 ± 9.50	[3]	Possible PN
PN G000.3+04.5	–	–		14.8×10.5	51.02 ± 9.50	[3]	PN [4]
CTIO J172923.07-290500.9	–	–		5.9×5.4	–		Probable PN [4]
PN G356.9+02.2	12.48 ± 0.18	1.68 ± 0.14		7.0×6.9	-103.11 ± 9.50	[3]	PN
PN H 2-11	11.43 ± 0.03	2.49	[9]	3.6×3.4	10.2 ± 6.1	[1]	PN

TABLE C.1: PNs towards the Galactic bulge (continued).

Object Name	$-\log F_{[\mathrm{O\,III}]\,\mathrm{dered}}$ (erg cm^{-2} s^{-1})	$c(\mathrm{H}\beta)$	Ref.	Diameter ($''$) $\pm 0.8''$	v_r (km s^{-1})	Ref.	Notes
PN G358.8+03.4	–	–		14.8×14.6	-120.20 ± 9.50	[3]	PN [4]
PN H 1-17	10.46 ± 0.10	1.91 ± 0.12		2.8×2.8	-29.7 ± 4.1	[1]	PN
PN H 1-18	–	2.22 ± 0.09		–	-221.5 ± 3.9	[1]	PN [2]
CTIO J172944.81-290657.7	–	–		27.6×22.8	-219.26 ± 46.35		Probable PN [4]
PN PM 1-151	–	–		6.4×5.5	-132.48 ± 9.50	[3]	PN [4]
PN K 6-25	11.66 ± 0.13	2.54 ± 0.14		5.0×5.0	191.23 ± 9.50	[3]	PN
CTIO J172954.51-271918.7	–	–		2.5×2.0	–		Possible PN [4]
PN H 1-19	11.34 ± 0.10	1.63 ± 0.12		2.6×2.0	23.4 ± 6.4	[1]	PN
PN G000.3+04.2	–	–		7.6×7.3	-119.87 ± 9.50	[3]	PN [4]
PN Al 2-E	11.19 ± 0.10	1.99 ± 0.12		8.8×8.0	-58.6 ± 6.3	[1]	PN
PN Th 3-23	11.07 ± 0.13	2.47 ± 0.14		6.9×5.9	11.7 ± 5.6	[1]	PN
PN Al 2-F	11.61 ± 0.05	1.81 ± 0.03		4.2×3.5	-75.98 ± 2.97	[3]	PN
PN H 1-20	10.77 ± 0.10	1.74 ± 0.12		4.4×3.8	189.5 ± 4.9	[1]	PN
PN Th 3-25	11.30 ± 0.11	2.02 ± 0.12		3.0×2.6	-92.7 ± 3.7	[1]	PN
PN G359.5+03.5	–	–		20.0×18.5	-46.28 ± 9.50	[3]	PN [4]
PN Th 3-24	12.40 ± 0.12	1.38 ± 0.14		8.6×7.3	-197.0 ± 40.0	[1]	PN
PN H 2-13	10.86 ± 0.08	1.94 ± 0.09		5.6×5.4	-133.7 ± 9.5	[1]	PN
PN Th 3-26	11.22 ± 0.10	1.56 ± 0.12		9.1×8.3	197.4 ± 5.2	[1]	PN
PN G358.4+02.7	–	–		22.1×16.1	-107.58 ± 9.50	[3]	Possible PN (foreground) [4,5]
PN G357.5+02.0	–	–		19.0×12.4	-17.11 ± 9.50	[3]	Possible PN [4]
PN G359.0+03.0	–	–		20.7×12.4	-221.23 ± 9.50	[3]	PN [4]
PN HDW 8	–	–		47.0×34.2	–		PN (foreground) [4,5]
PN G359.8+03.5	12.13 ± 0.21	2.71 ± 0.18		15.5×12.4	-66.27 ± 9.50	[3]	Possible PN
PN G358.1+02.3	–	–		3.8×1.5	–		Possible PN [4]
PN G359.1+02.9	–	–		16.5×6.0	-264.54 ± 9.50	[3]	PN [4]

TABLE C.1: PNs towards the Galactic bulge (continued).

Object Name	$-\log F_{[\mathrm{O\,III}]\,\mathrm{dered}}$ (erg cm^{-2} s^{-1})	$c(\mathrm{H}\beta)$	Ref.	Diameter ($''$) $\pm 0.8''$	v_r (km s^{-1})	Ref.	Notes
PN Al 2-G	11.92 ± 0.11	1.99 ± 0.12		3.5×1.0	-262.0 ± 15.0	[1]	PN
CTIO J173241.47-302829.4	–	–		12.1×12.1	–		Possible PN [4]
PN H 1-23	10.62 ± 0.11	1.99 ± 0.14		3.5×2.6	-72.5 ± 3.9	[1]	PN
CTIO J173247.88-300932.4	–	–		4.7×4.4	–		Possible PN [4]
PN Al 2-H	11.34 ± 0.13	2.50 ± 0.14		8.5×7.0	-30.0 ± 15.0	[1]	PN
PN G000.3+03.4	–	–		16.8×15.0	-1.12 ± 9.50	[3]	Possible PN [4]
PN G357.9+01.7	12.15 ± 0.18	2.30 ± 0.14		5.7×5.0	62.73 ± 9.50	[3]	Possible PN
PN G358.4+02.1	–	2.06 ± 0.14		–	109.36 ± 9.50	[3]	Possible PN [2]
CTIO J173348.40-264623.4	–	–		6.0×6.0	–		Probable PN [4]
PN G357.1+01.2	–	3.35 ± 0.14		–	-158.28 ± 9.50	[3]	PN [2]
PN G000.3+03.2	–	–		20.8×10.9	91.18 ± 9.50	[3]	Possible PN [4]
PN G357.3+01.3	–	–		17.4×17.1	-245.85 ± 9.50	[3]	PN [4]
PN G357.8+01.6	–	–		12.7×8.6	192.03 ± 9.50	[3]	PN [4]
CTIO J173425.71-270524.7	–	–		2.1×1.6	–		Possible PN [4]
PN G357.5+01.3	–	3.06 ± 0.14		–	-11.10 ± 9.50	[3]	Possible PN [2]
PN G358.0+01.6	12.08 ± 0.19	3.06 ± 0.14		8.9×6.8	-142.91 ± 9.50	[3]	Possible PN
CTIO J173440.23-272356.8	–	–		10.5×7.7	–		Possible PN [4]
JaSt 1	12.90 ± 0.18	2.24 ± 0.14		7.1×5.1	121.92 ± 9.50	[3]	PN
CTIO J173444.22-281023.7	–	–		139.9×96.6	-36.79 ± 1.38		Probable PN (foreground) [5]
PN G357.7+01.4	–	–		3.6×3.1	90.14 ± 9.50	[3]	PN [4]
PN M 4-5	11.24 ± 0.05	1.72 ± 0.04	[10]	6.7×4.9	-175.1 ± 8.0	[1]	PN
PN G000.6+03.1	–	–		16.7×15.5	-312.17 ± 9.50	[3]	Possible PN [4]
PN G358.4+01.7	12.20 ± 0.19	3.32 ± 0.14		4.4×4.3	46.77 ± 9.50	[3]	PN
PN G359.4+02.3 a	11.76 ± 0.29	3.36 ± 0.28		4.5×2.9	94.92 ± 9.50	[3]	PN
CTIO J173513.37-263254.0	–	–		24.0×16.0	–		Possible PN (foreground) [5]

TABLE C.1: PNs towards the Galactic bulge (continued).

Object Name	$-\log F_{[\mathrm{O\,III}]\,\mathrm{dered}}$ (erg cm^{-2} s^{-1})	$c(\mathrm{H}\beta)$	Ref.	Diameter ($''$) $\pm 0.8''$	v_r (km s^{-1})	Ref.	Notes
PN M 4-6	10.73 ± 0.04	2.69 ± 0.03		4.1×4.0	-272.9 ± 13.0	[1]	PN
PN G358.4+01.6	11.36 ± 0.19	3.46 ± 0.14		7.8×7.8	-90.27 ± 9.50	[3]	PN
PN G003.6+04.9	11.25 ± 0.09	1.9 ± 0.1	[11]	22.6×9.7	-85.5 ± 4.2	[1]	PN
PN Al 2-J	11.37 ± 0.21	2.01 ± 0.28		11.4×8.9	-172.16 ± 9.50	[3]	PN
PN G358.6+01.7	12.08 ± 0.19	2.96 ± 0.14		10.6×9.5	-0.36 ± 9.50	[3]	PN
PN G357.6+01.0	11.63 ± 0.12	2.18 ± 0.14		31.5×26.8	-122.0 ± 60.0	[1]	PN (foreground) [5,12]
PN Th 3-33	12.72 ± 0.11	2.81 ± 0.03		3.1×2.6	72.0 ± 40.0	[1]	PN
PN G358.8+01.7	11.80 ± 0.22	2.62 ± 0.28		9.1×5.9	59.83 ± 9.50	[3]	PN
PN G000.5+02.8	–	–		26.5×25.6	219.67 ± 9.50	[3]	PN (foreground) [4,5]
CTIO J173557.97-271214.2	–	–		7.6×7.5	174.15 ± 30.87		Probable PN [4]
PN Al 2-K	11.41 ± 0.23	3.11 ± 0.28		4.7×4.5	97.5 ± 10.0	[1]	PN
PN Al 2-I	11.20 ± 0.04	2.03 ± 0.03		5.6×4.8	69.95 ± 2.42	[3]	PN
CTIO J173623.26-250528.7	–	–		5.4×3.2	50.17 ± 64.47		Probable PN [4]
PN G003.5+04.5	–	–		10.8×5.0	-52.21 ± 9.50	[3]	PN [4]
MPA 1736−2715	–	2.37 ± 0.28		–	–		Possible PN [2,13]
PN G359.7+02.0	11.13 ± 0.30	3.69 ± 0.28		4.3×3.6	-162.60 ± 9.50	[3]	Possible PN
PN Bl B	10.58 ± 0.08	4.03 ± 0.06	[7]	2.4×2.0	-108.2 ± 9.4	[1]	PN
PN G003.4+04.3	–	–		17.2×14.0	-204.99 ± 9.50	[3]	PN [4]
PN G003.1+04.1	–	1.63 ± 0.03		–	-130.12 ± 0.87	[3]	PN [2]
PN G002.3+03.6	–	–		6.4×6.2	15.87 ± 9.50	[3]	Possible PN [4]
PN G003.5+04.3	–	–		–	–		Possible PN [2]
PN K 6-4	12.97 ± 0.20	3.13 ± 0.03		6.9×4.1	22.6 ± 2.8	[3]	PN
PN PBOZ 24	–	–		5.8×5.2	-136.49 ± 1.31	[3]	PN [4]
CTIO J173751.75-250309.2	–	–		13.5×13.5	–		Possible PN [4]
PN G002.4+03.5	–	–		15.7×14.3	-23.42 ± 9.50	[3]	PN [4]

TABLE C.1: PNs towards the Galactic bulge (continued).

Object Name	$-\log F_{[\mathrm{O\,III}]\,\mathrm{dered}}$ ($\mathrm{erg\,cm^{-2}\,s^{-1}}$)	$c(\mathrm{H}\beta)$	Ref.	Diameter ($''$) $\pm 0.8''$	v_r ($\mathrm{km\,s^{-1}}$)	Ref.	Notes
PN G000.1+02.0	–	–		18.9×17.5	246.49 ± 9.50	[3]	PN [4]
PN PM 1-165	–	2.94 ± 0.03		–	-114.77 ± 3.29	[3]	Possible PN [2]
PN G359.9+01.8	–	–		7.4×4.3	138.59 ± 9.50	[3]	PN [4]
PN G000.1+01.9	12.04 ± 0.29	2.92 ± 0.28		13.60×9.8	-58.38 ± 9.50	[3]	PN
PN G359.3+01.4 a	–	–		6.9×6.3	-155.45 ± 9.50	[3]	PN [4]
PN G359.2+01.3	–	–		8.0×6.7	-81.37 ± 9.50	[3]	PN [4]
PN Th 3-35	11.16 ± 0.23	3.46 ± 0.28		3.3×2.6	54.5 ± 11.4	[1]	PN
JaSt2 2	12.40 ± 0.28	2.84 ± 0.28		12.3×9.7	-26.05 ± 9.50	[3]	PN
PN G359.0+01.1	–	1.00 ± 0.28		–	49.40 ± 9.50	[3]	PN [2]
JaSt 12	–	–		3.9×2.4	-10.67 ± 9.50	[3]	PN [4]
ESO 455-139	10.84 ± 0.30	4.24 ± 0.28		23.0×4.7	55.3 ± 5.4	[1]	PN (foreground) [5,12]
MPA 1739−2652	–	–		21.9×21.4	–		True PN (foreground) [4,5,14]
PN G355.5−01.1	–	–		7.2×6.0	–		Possible PN [4]
PN G001.0+02.2	–	2.26 ± 0.31		–	–		Possible PN [2]
PN G000.9+02.1	–	–		19.0×11.9	-174.02 ± 9.50	[3]	PN [4]
PN G000.5+01.9	11.58 ± 0.05	2.63 ± 0.03		9.1×6.6	-2.16 ± 0.99	[3]	PN
PN G000.2+01.7	11.59 ± 0.05	2.43 ± 0.03		7.2×6.4	197.24 ± 0.68	[3]	PN
PN G001.1+02.2	12.34 ± 0.31	3.38 ± 0.31		4.5×3.8	-121.59 ± 1.35	[3]	PN
CTIO J173949.95-332524.4	–	–		10.4×8.6	–		Possible PN [4]
2MASS J17395285-2744201	–	–		19.2×18.9	54.34 ± 9.50	[3]	PN [4]
CTIO J173958.08-270647.1	–	–		2.6×2.6	–		Possible PN [4]
CTIO J173959.11-270047.9	–	–		54.1×53.3	–		Possible PN (foreground) [5]
PN G355.4−01.4	–	–		8.4×7.5	-156.83 ± 1.63	[3]	PN [4]
PN H 2-17	13.36 ± 0.16	1.67 ± 0.11	[7]	2.3×1.9	85.4 ± 4.1	[1]	PN
Hen 2-262	10.96 ± 0.08	2.24 ± 0.09		4.6×4.5	-172.4 ± 3.1	[1]	PN

TABLE C.1: PNs towards the Galactic bulge (continued).

Object Name	$-\log F_{[\mathrm{O\,III}]\,\mathrm{dered}}$ (erg cm^{-2} s^{-1})	$c(\mathrm{H}\beta)$	Ref.	Diameter ($''$) $\pm 0.8''$	v_r (km s^{-1})	Ref.	Notes
PN K 1-4	–	–		52.3×47.4	3.86	[3]	PN (foreground) [4,5,12]
PN G002.1+02.6	–	2.35 ± 0.31		–	-143.07 ± 9.50	[3]	PN [2]
PN PBOZ 26	–	–		3.2×3.0	4.08 ± 5.94	[3]	PN [4]
JaSt 27	–	2.86 ± 0.28		–	-26.39 ± 9.50	[3]	PN [2]
PN PBOZ 25	11.76 ± 0.30	4.37 ± 0.28		3.0×2.4	-260.16 ± 9.50	[3]	Possible PN
PN G000.9+01.8	12.05 ± 0.31	3.19 ± 0.31		3.4×3.1	-27.21 ± 9.50	[3]	PN
PN G355.6−01.4	–	–		11.8×9.6	-119.42 ± 9.50	[3]	PN [4]
CTIO J174100.05-241204.0	–	–		3.2×2.5	–		Possible PN [4]
CTIO J174105.94-243732.0	–	–		1.9×1.9	–		Possible PN [4]
JaSt2 3	–	–		–	104.55 ± 9.50	[3]	PN [2]
PN G001.9+02.3	–	1.88 ± 0.03		–	-147.18 ± 2.85	[3]	PN [2]
PN PM 1-171	–	–		4.1×3.7	–		Possible PN [4]
PN G356.0−01.4	–	–		6.9×6.8	-93.15 ± 9.50	[3]	PN [4]
PN G002.3+02.4	11.83 ± 0.09	2.12 ± 0.09		8.5×6.8	1.11 ± 9.50	[3]	PN
CTIO J174152.05-243252.1	–	–		6.6×5.3	–		Possible PN [4]
PN Hb 4	9.75 ± 0.06	1.71 ± 0.06	[15]	9.8×7.5	-60.0 ± 1.5	[1]	PN (foreground) [12]
JaSt 34	–	3.08 ± 0.31		–	98 ± 5	[3]	PN [2]
PN M 2-14	11.10 ± 0.04	1.26 ± 0.03	[16]	3.0×2.6	-48.2 ± 3.7	[1]	PN
PN G355.2−02.0	–	–		6.5×6.5	-92.29 ± 9.50	[3]	PN [4]
CTIO J174211.00-340626.1	–	–		1.8×1.4	–		Possible PN [4]
JaSt2 4	–	–		–	-8.79 ± 9.50	[3]	PN [2]
PN G002.3+02.2	11.87 ± 0.09	1.88 ± 0.09		10.2×9.1	43.99 ± 9.50	[3]	PN
PN G000.8+01.3	–	–		10.9×9.6	78.27 ± 4.16	[3]	PN [4]
PN G001.0+01.3	11.86 ± 0.09	2.12 ± 0.09		4.7×4.6	245.37 ± 0.54	[3]	PN
PN G002.6+02.3	12.05 ± 0.24	2.24 ± 0.31		11.5×11.4	269.15 ± 9.50	[3]	PN

Table C.1: PNs towards the Galactic bulge (continued).

Object Name	$-\log F_{[\mathrm{O\,III}]\,\mathrm{dered}}$ (erg cm^{-2} s^{-1})	$c(\mathrm{H}\beta)$	Ref.	Diameter ($''$) $\pm 0.8''$	v_r (km s^{-1})	Ref.	Notes
CTIO J174253.89-340902.1	11.20 ± 0.73	1.91 ± 0.92		9.7×9.1	6.26 ± 23.48		Probable PN
PN G001.6+01.6	–	–		–	-63.83 ± 9.50	[3]	Possible PN [2]
PN G356.0−01.8	–	–		4.9×4.4	97.94 ± 9.50	[3]	PN [4]
PN G002.4+02.1	12.62 ± 0.29	2.01 ± 0.31		14.9×11.2	283.32 ± 9.50	[3]	Possible PN
PN K 6-10	11.65 ± 0.05	2.82 ± 0.03		6.7×6.1	-76.35 ± 1.32	[3]	PN
PN G000.9+01.1	–	–		8.5×5.0	213.23 ± 2.98	[3]	PN [4]
JaSt 45	–	–		31.3×30.6	-146.91 ± 1.02	[3]	PN (foreground) [4,5]
PN G001.5+01.5	11.29 ± 0.05	3.06 ± 0.03		4.5×4.4	36.61 ± 1.41	[3]	PN
PTB 1	–	–		33.9×33.6	-50.85 ± 9.50	[3]	PN (foreground) [4,5]
PN G002.6+02.1	11.08 ± 0.04	2.23 ± 0.03		11.7×9.9	237.2 ± 6.8	[1]	PN
PN G002.5+02.0	12.17 ± 0.11	2.24 ± 0.03		5.1×4.4	-63.45 ± 0.68	[3]	Possible PN
PN G003.6+02.7	–	–		22.8×21.8	–		Possible PN (foreground) [4,5]
PN G002.1+01.7	–	2.42 ± 0.09		–	173.86 ± 1.74	[3]	PN [2]
PN G002.5+01.9	12.44 ± 0.30	2.30 ± 0.31		15.7×13.0	131.21 ± 9.50	[3]	Possible PN
PN G002.2+01.7	–	2.75 ± 0.31		–	-71.86 ± 9.50	[3]	Possible PN [2]
CTIO J174409.95-253030.3	–	–		3.3×3.0	–		Possible PN [4]
PN M 3-14	10.65 ± 0.08	1.34 ± 0.09		3.8×3.6	-82.3 ± 1.8	[1]	PN
CTIO J174421.47-253803.3	–	–		1.7×1.1	–		Possible PN [4]
CTIO J174421.73-341558.2	–	–		2.0×1.9	–		Possible PN [4]
CTIO J174423.18-341931.7	–	–		2.6×1.6	–		Possible PN [4]
CTIO J174425.66-340519.0	–	–		19.2×8.6	–		Possible PN [4]
PN G355.6−02.3	11.49 ± 0.08	1.14 ± 0.09		65.5×63.7	23.48 ± 9.50	[3]	PN (foreground) [5]
PN G356.5−01.8	–	–		4.6×4.4	-163.94 ± 9.50	[3]	Possible PN [4]
CTIO J174428.83-342922.4	–	–		1.3×1.3	–		Possible PN [4]
PN PBOZ 10	–	–		4.3×3.9	–		PN [2]

TABLE C.1: PNs towards the Galactic bulge (continued).

Object Name	$-\log F_{[\mathrm{O\,III}]\,\mathrm{dered}}$ (erg cm^{-2} s^{-1})	$c(\mathrm{H}\beta)$	Ref.	Diameter ($''$) $\pm 0.8''$	v_r (km s^{-1})	Ref.	Notes
CTIO J174431.07-240412.5	–	–		2.7×2.6	–		Possible PN [4]
PN PBOZ 11	11.00 ± 0.15	1.9 ± 0.2	[11]	1.8×1.7	14.3 ± 4.3	[1]	PN
PN G002.0+01.5	–	–		11.1×8.7	-41.33 ± 9.50	[3]	PN [4]
PN G002.3+01.7	12.53 ± 0.30	2.36 ± 0.31		8.8×8.1	11.16 ± 9.50	[3]	PN
CTIO J174435.93-330742.0	–	–		19.2×19.2	–		Possible PN [4]
PN G001.7+01.3	–	3.16 ± 0.03		–	65.59 ± 3.33	[3]	PN [2]
PN G004.0+02.6	–	–		16.9×13.1	–		PN [4]
PN G356.1−02.1	–	–		8.9×8.4	-175.17 ± 4.31	[3]	Possible PN [4,17]
PN G355.4−02.6	12.29 ± 0.12	1.35 ± 0.14		15.2×11.9	-104.16 ± 9.50	[3]	Possible PN
PN RPZM 36	–	–		51.6×34.4	-99.05 ± 9.50	[3]	PN (foreground) [4,5,12]
PN G002.7+01.7	12.15 ± 0.30	2.79 ± 0.31		3.6×3.5	195.04 ± 9.50	[3]	PN
CTIO J174523.43-262706.2	–	–		4.0×3.7	–		Possible PN [4]
PN G002.8+01.8	11.33 ± 0.24	2.30 ± 0.31		11.8×8.9	-32.6 ± 3.8	[1]	PN
PN H 1-31	10.50 ± 0.08	1.51 ± 0.09		1.8×1.7	47.5 ± 1.8	[1]	PN
CTIO J174537.17-335608.1	–	–		20.5×19.3	–		Possible PN [4]
PN H 2-20	12.45 ± 0.15	2.18 ± 0.09		2.8×2.7	164.1 ± 8.8	[1]	PN
CTIO J174546.15-253319.8	–	–		2.1×1.8	–		Possible PN [4]
CTIO J174547.44-333932.4	–	–		79.2×24.7	–		Probable PN (foreground) [5]
PN G002.1+01.2	–	–		–	72 ± 5	[3]	Possible PN [2]
PN Bl D	–	–		17.5×15.7	-30.9 ± 3.5	[1]	PN [4]
PN H 1-32	–	1.80 ± 0.09		–	-220.0 ± 4.8	[1]	PN [2]
CTIO J174648.06-341342.3	9.66 ± 0.81	2.17 ± 1.04		5.6×5.4	102.00 ± 8.45		PN
CTIO J174648.23-343603.0	–	–		2.8×2.6	–		Possible PN [4]
PN G355.4−03.1	–	–		26.8×24.2	-56.63 ± 9.50	[3]	Possible PN (foreground) [4,5]
PN G355.0−03.3	12.79 ± 0.18	2.33 ± 0.14		8.3×2.9	–		PN [18]

TABLE C.1: PNs towards the Galactic bulge (continued).

Object Name	$-\log F_{[\mathrm{O\,III}]\,\mathrm{dered}}$ (erg cm^{-2} s^{-1})	$c(\mathrm{H}\beta)$	Ref.	Diameter ($''$) $\pm 0.8''$	v_r (km s^{-1})	Ref.	Notes
PN G002.4+01.1	–	–		10.1×9.5	–		PN [19]
PN G356.1−02.7	12.32 ± 0.19	2.62 ± 0.14		7.3×7.0	-84.40 ± 9.50	[3]	PN
PN G355.3−03.2	12.65 ± 0.05	1.17 ± 0.03		19.5×15.4	33.88 ± 9.50	[3]	Possible PN
PN K 6-12	12.27 ± 0.09	1.83 ± 0.09		13.7×11.2	-133.23 ± 3.34	[3]	PN
PN G356.3−02.6	12.00 ± 0.09	1.26 ± 0.09		8.1×7.3	135.81 ± 9.50	[3]	PN
PN G357.3−02.0	–	–		–	-1.79 ± 9.50	[3]	PN [2]
PN PBOZ 16	11.12 ± 0.04	1.63 ± 0.03		4.6×3.1	128.5 ± 0.7	[3]	PN
CTIO J174732.26-242218.9	–	–		3.4×2.8	–		Possible PN [4]
PN G004.2+02.0 a	–	–		25.2×23.1	230.32 ± 0.29	[3]	PN (foreground) [4,5]
CTIO J174748.01-342126.4	–	–		6.3×1.8	–		Possible PN [4]
PN H 1-33	10.92 ± 0.08	1.19 ± 0.09		4.0×3.2	-120.0 ± 3.4	[1]	PN
PN Hb 5	–	–		5.6×5.5	-24.0 ± 1.7	[1]	PN (foreground) [4,12]
CTIO J174756.67-331444.4	–	–		12.3×9.9	–		Probable PN [4]
CTIO J174808.57-310445.3	–	–		114.4×49.6	–		Possible PN (foreground) [5]
PN G004.5+02.0	–	–		12.9×9.4	56.54 ± 9.50	[3]	PN [4]
JaSt 61	12.79 ± 0.13	1.82 ± 0.06		2.0×2.0	-5.05 ± 9.50	[3]	PN
CTIO J174825.12-301520.7	–	–		3.1×1.2	–		Possible PN [4]
PN G003.9+01.6	–	–		9.7×9.5	54.87 ± 3.57	[3]	PN [4]
PN G355.0−03.7	11.87 ± 0.07	0.73 ± 0.09		11.1×10.0	81.61 ± 9.50	[3]	PN
PN G004.1+01.7	–	–		25.7×16.9	–		Possible PN (foreground) [4,5]
PN G004.3+01.8 a	–	–		16.1×14.8	–		PN [4]
PN H 2-24	11.47 ± 0.10	1.69 ± 0.11	[7]	8.4×4.3	-198.2 ± 4.1	[1]	PN
PN H 2-23	10.98 ± 0.08	1.17 ± 0.09		3.4×2.7	82.5 ± 11.3	[1]	PN
PN H 2-25	12.29 ± 0.03	1.84	[9]	3.1×3.0	16.2 ± 8.1	[1]	PN
PN H 1-35	–	–		12.9×12.7	123.4 ± 1.0	[1]	PN [2]

TABLE C.1: PNs towards the Galactic bulge (continued).

Object Name	$-\log F_{[\mathrm{O\,III}]\,\mathrm{dered}}$ (erg cm^{-2} s^{-1})	$c(\mathrm{H}\beta)$	Ref.	Diameter ($''$) $\pm 0.8''$	v_r (km s^{-1})	Ref.	Notes
PN G004.6+01.8	–	–		26.1×17.9	-98.72 ± 6.24	[3]	PN (foreground) [4,5]
PN G358.9−01.5	11.89 ± 0.21	3.68 ± 0.16		5.7×5.6	-45.01 ± 9.50	[3]	PN
PN G359.5−01.2	11.18 ± 0.21	4.43 ± 0.16		3.4×2.7	197.55 ± 9.50	[3]	PN
PN G356.2−03.2	12.79 ± 0.18	1.31 ± 0.14		12.8×12.5	–		PN
CTIO J174925.72-344647.2	–	–		29.7×23.2	–		Probable PN (foreground) [5]
PN G357.5−02.4	–	–		7.8×6.5	-198.82 ± 9.50	[3]	PN [4]
CTIO J174938.55-320801.5	–	–		2.3×1.7	–		Possible PN [4]
PN K 6-29	–	–		10.8×7.7	-91.86 ± 2.04	[3]	PN [4]
PN G359.5−01.3	–	–		2.0×1.7	–		PN [4]
PN H 2-26	11.91 ± 0.09	1.00 ± 0.09		5.5×5.0	-156.9 ± 3.6	[1]	PN
PN RPZM 42	–	3.20 ± 0.16		–	-149.34 ± 9.50	[3]	PN [2]
CTIO J174955.44-334234.7	–	–		34.7×34.7	–		Possible PN (foreground) [5]
PN G355.5−03.7	11.97 ± 0.07	0.61 ± 0.09		19.6×13.2	-13.93 ± 9.50	[3]	PN
CTIO J175006.71-340258.6	–	–		7.2×6.9	–		Possible PN [4]
PN G000.0−01.0	11.97 ± 0.22	3.03 ± 0.19		11.1×9.4	-5.96 ± 9.50	[3]	PN
PN G356.8−03.0	11.60 ± 0.08	1.28 ± 0.09		5.3×5.2	-15.03 ± 9.50	[3]	PN
PN M 1-29	10.17 ± 0.06	1.60 ± 0.06		9.1×6.7	-41.0 ± 1.0	[1]	PN (foreground) [12]
PN G000.0−01.2	–	–		–	-162.42 ± 9.50	[3]	PN [2]
PN M 3-43	10.92 ± 0.08	3.07 ± 0.07		3.5×2.7	-7.3 ± 4.7	[1]	PN
OGLE BUL-SC5 244192	–	–		18.7×14.2	–		PN [2]
PN G000.7−00.8	–	–		–	-59.84 ± 9.50	[3]	PN [2]
IRAS 17475-2952	13.45 ± 0.22	2.56 ± 0.06		1.2×0.7	-70.04 ± 9.50	[3]	PN
PN G000.1−01.2	11.27 ± 0.24	4.58 ± 0.19		2.9×1.9	-159.16 ± 9.50	[3]	PN
PN G358.0−02.4	–	–		4.9×3.7	-13.12 ± 9.50	[3]	PN [4]
CTIO J175051.08-305206.5	–	–		12.5×11.6	–		Possible PN [4]

TABLE C.1: PNs towards the Galactic bulge (continued).

Object Name	$-\log F_{[\mathrm{O\,III}]\,\mathrm{dered}}$ (erg cm^{-2} s^{-1})	$c(\mathrm{H}\beta)$	Ref.	Diameter ($''$) $\pm 0.8''$	v_r (km s^{-1})	Ref.	Notes
PN G355.3−04.1	11.93 ± 0.39	1.23 ± 0.59		20.4×16.7	44.40 ± 9.50	[3]	PN
PN G000.0−01.3	–	–		–	-163.21 ± 9.50	[3]	Possible PN [2]
PN G356.2−03.6	11.81 ± 0.12	1.29 ± 0.14		11.4×11.2	-139.13 ± 9.50	[3]	PN
PN G000.6−01.0	9.87 ± 0.10	5.17 ± 0.09		10.3×9.6	-18.3 ± 5.1	[3]	PN
PN Hf 2-1	10.52 ± 0.07	0.70 ± 0.09		18.2×14.0	-84.5 ± 4.1	[1]	PN (foreground) [12]
PN G358.4−02.3	–	–		15.1×12.2	-137.38 ± 9.50	[3]	Possible PN [4]
PN M 3-44	–	2.61 ± 0.06		–	-99.2 ± 4.4	[1]	PN [2]
PN G356.5−03.4	12.20 ± 0.09	1.52 ± 0.09		8.1×8.0	106.19 ± 9.50	[3]	PN
PN G358.9−02.1	12.85 ± 0.13	1.35 ± 0.06		13.8×13.5	190.24 ± 9.50	[3]	PN
PN G000.9−01.0	–	3.67 ± 0.19		–	188 ± 5	[3]	PN [2]
PN G359.5−01.8	13.50 ± 0.19	1.87 ± 0.16		38.0×32.1	-83.69 ± 9.50	[3]	PN (foreground) [5]
PN M 4-7	10.90 ± 0.06	2.23 ± 0.06		6.9×6.6	-233.8 ± 3.7	[1]	PN
PN Al 2-O	11.35 ± 0.02	1.56	[9]	9.1×7.6	-78.8 ± 3.6	[1]	PN [17]
PN K 6-15	11.88 ± 0.07	2.42 ± 0.06		5.0×4.4	103.29 ± 9.50	[3]	PN
PN H 2-27	11.72 ± 0.09	1.53 ± 0.09		5.2×4.2	-31.3 ± 15.1	[1]	PN
PN G358.6−02.4	12.40 ± 0.13	2.06 ± 0.06		8.9×8.2	140.10 ± 9.50	[3]	PN
PN G357.4−03.1	–	–		10.8×10.6	-31.29 ± 9.50	[3]	PN [4]
JaSt2 8	–	1.65 ± 0.19		–	-12.73 ± 9.50	[3]	PN [2]
2MASS J17520501-2805506	–	4.30 ± 0.19		–	107.75 ± 2.05	[3]	PN [2]
PN M 3-45	10.61 ± 0.06	2.08 ± 0.06		7.1×6.5	28.3 ± 4.6	[1]	PN
PN G357.6−03.0	11.94 ± 0.05	1.19 ± 0.03		10.9×7.5	-15.32 ± 2.86	[3]	PN
PN G357.6−03.0 a	–	–		9.7×9.1	170.87 ± 9.50	[3]	PN [4]
PN K 5-34	11.67 ± 0.04	0.43 ± 0.03		6.8×5.8	-4.5 ± 2.8	[3]	PN
PN G356.8−03.6	12.97 ± 0.11	0.78 ± 0.14		1.1×0.9	-77.94 ± 9.50	[3]	Possible PN
CTIO J175234.11-302619.6	–	–		7.1×7.1	–		Probable PN [4]

TABLE C.1: PNs towards the Galactic bulge (continued).

Object Name	$-\log F_{[\mathrm{O\,III}]\,\mathrm{dered}}$ (erg cm^{-2} s^{-1})	$c(\mathrm{H}\beta)$	Ref.	Diameter ($''$) $\pm 0.8''$	v_r (km s^{-1})	Ref.	Notes
PN M 2-16	10.83 ± 0.13	0.93 ± 0.18		3.1×2.9	90.0 ± 2.5	[1]	PN
PN Bl 3-15	13.67 ± 0.31	2.72 ± 0.19		3.9×1.2	-115.30 ± 9.50	[3]	PN
PN K 6-31	11.90 ± 0.07	1.87 ± 0.06		9.3×6.9	1.45 ± 9.50	[3]	PN
CTIO J175238.99-333047.2	–	–		52.6×34.0	–		Probable PN (foreground) [5]
2MASS J17524513-2951058	11.91 ± 0.09	1.81 ± 0.09		3.3×3.3	183.31 ± 2.51	[3]	PN
PN M 3-16	10.78 ± 0.04	1.48 ± 0.03		10.0×7.7	63.4 ± 1.8	[1]	PN (foreground) [12]
JaSt 84	12.72 ± 0.22	2.18 ± 0.19		13.8×3.6	33.66 ± 9.50	[3]	PN
CTIO J175246.55-301700.4	–	–		11.5×6.5	–		Possible PN [4]
JaSt2 9	12.11 ± 0.23	3.16 ± 0.19		8.9×6.1	-41.57 ± 9.50	[3]	PN
PN G000.1−01.7	11.34 ± 0.07	1.92 ± 0.06		16.7×12.2	-171.68 ± 9.50	[3]	PN
PN G359.9−01.8	12.84 ± 0.19	1.72 ± 0.16		24.6×20.5	271.21 ± 9.50	[3]	Possible PN
PN G000.3−01.6	11.28 ± 0.16	2.62 ± 0.19		8.6×7.9	-129.35 ± 9.50	[3]	PN
PN G000.0−01.8	–	–		17.8×16.8	197.00 ± 9.50	[3]	PN [4]
PN M 1-30	10.85 ± 0.08	1.17 ± 0.09		4.3×3.6	-120.1 ± 1.7	[1]	PN
JaSt 87	–	–		25.4×17.6	79.03 ± 9.50	[3]	PN (foreground) [4,5]
PN G000.6−01.4	12.19 ± 0.15	1.93 ± 0.19		14.5×14.5	-113.49 ± 9.50	[3]	PN
PN G356.0−04.2	11.96 ± 0.08	0.87 ± 0.09		15.3×14.6	-65.95 ± 9.50	[3]	PN
PN G001.3−01.0	–	–		9.5×6.7	218.59 ± 9.50	[3]	PN [4]
CTIO J175308.41-353356.7	–	–		22.1×11.0	–		Possible PN (foreground) [5]
CTIO J175310.09-293108.6	–	–		2.7×2.3	–		Probable [WR] PN [4]
PN G359.3−02.3	–	–		14.1×11.3	134.47 ± 9.50	[3]	PN [4]
PN H 2-29	12.33 ± 0.05	1.61 ± 0.03		9.0×8.0	107.0 ± 18.7	[1]	PN
PN G001.1−01.2	11.19 ± 0.16	2.59 ± 0.19		10.3×8.5	–		PN
2MASS J17531769-2804330	–	–		–	142.00 ± 6.00	[3]	PN [2]
MPA 1753−2916	–	–		–	–		Possible PN [2,13]

TABLE C.1: PNs towards the Galactic bulge (continued).

Object Name	$-\log F_{[\mathrm{O\,III}]\,\mathrm{dered}}$ (erg cm^{-2} s^{-1})	$c(\mathrm{H}\beta)$	Ref.	Diameter ($''$) $\pm 0.8''$	v_r (km s^{-1})	Ref.	Notes
JaSt 92	–	–		9.5×4.7	43.97 ± 9.50	[3]	PN [4]
PN H 1-39	12.29 ± 0.04	1.07 ± 0.01	[10]	2.3×2.0	-85.3 ± 16.0	[1]	PN
CTIO J175323.14-340653.7	–	–		33.2×24.2	–		Probable PN (foreground) [5]
PN G000.1−01.9	11.36 ± 0.06	1.74 ± 0.06		14.2×11.7	-0.18 ± 9.50	[3]	PN (foreground) [12]
PN Al 2-Q	11.41 ± 0.08	1.88 ± 0.07		7.8×7.6	-67.0 ± 15.0	[1]	PN
JaSt2 11	12.46 ± 0.22	2.18 ± 0.19		9.7×8.8	116.15 ± 9.50	[3]	PN
JaSt2 12	–	–		–	190.53 ± 9.50	[3]	PN [2]
PN G001.2−01.2 a	11.23 ± 0.05	2.88 ± 0.03		10.3×8.6	185.06 ± 2.95	[3]	PN
JaSt2 13	–	–		26.5×25.9	-272.23 ± 9.50	[3]	PN (foreground) [4,5]
PN Al 2-R	11.96 ± 0.07	1.61 ± 0.06		6.4×3.9	-119.0 ± 40.0	[1]	PN
PN M 2-18	10.99 ± 0.03	1.15 ± 0.01	[10]	2.2×2.1	-21.1 ± 0.9	[1]	PN
PN G359.2−02.4	–	2.01 ± 0.16		–	114.94 ± 9.50	[3]	PN [2]
PN K 6-32	–	0.68 ± 0.03		–	-1.82 ± 1.84	[3]	PN [2]
JaSt2 14	–	–		–	-154.23 ± 9.50	[3]	PN [2]
PN M 2-19	11.26 ± 0.04	1.60 ± 0.03		6.7×6.1	-61.2 ± 12.0	[1]	PN
PN Bl M	12.31 ± 0.11	2.81 ± 0.03		3.5×3.5	95.91 ± 3.32	[3]	PN
PN Bl O	–	2.24 ± 0.03		–	72.33 ± 2.19	[3]	PN [2]
CTIO J175353.88-322907.7	–	–		5.2×5.2	–		Possible PN [4]
PN G357.8−03.3	10.96 ± 0.13	1.33 ± 0.18		65.1×40.1	-71.29 ± 9.50	[3]	Possible PN (foreground) [5]
PN G000.5−01.7	12.13 ± 0.15	1.42 ± 0.19		32.9×31.2	-132.92 ± 9.50	[3]	PN
PN G359.7−02.2	12.62 ± 0.19	1.75 ± 0.16		18.5×18.3	-32.14 ± 9.50	[3]	PN
CTIO J175401.23-343958.7	–	–		18.9×18.5	–		Probable PN [4]
PN G356.5−04.1	12.01 ± 0.14	1.20 ± 0.18		14.1×13.3	37.58 ± 9.50	[3]	PN
PN G000.0−02.1	11.95 ± 0.13	1.83 ± 0.16		21.5×19.0	230.19 ± 9.50	[3]	PN
PN G001.6−01.1	–	–		7.4×5.6	-9.18 ± 9.50	[3]	PN [4]

TABLE C.1: PNs towards the Galactic bulge (continued).

Object Name	$-\log F_{[\mathrm{O\,III}]\,\mathrm{dered}}$ (erg cm^{-2} s^{-1})	$c(\mathrm{H}\beta)$	Ref.	Diameter ($''$) $\pm 0.8''$	v_r (km s^{-1})	Ref.	Notes
PN G355.5−04.8	–	–		19.5 × 18.7	−31.81 ± 9.50	[3]	PN [4]
CTIO J175417.64-292221.0	–	–		37.5 × 4.9	–		Probable PN (foreground) [5]
CTIO J175417.98-282724.3	–	–		20.7 × 14.9	–		Possible PN [4]
JaSt2 15	–	–		–	−145.73 ± 9.50	[3]	PN
PN M 2-20	10.72 ± 0.06	1.39 ± 0.07		3.6 × 3.2	58.7 ± 15.0	[1]	PN
PN G355.2−05.0	–	–		26.9 × 26.1	19.46 ± 9.50	[3]	PN (foreground) [4,5]
PN Cn 2-1	9.92 ± 0.03	0.79 ± 0.01	[10]	2.6 × 2.6	−169.6 ± 0.8	[1]	PN
PN Bl Q	10.65 ± 0.05	2.93 ± 0.03		3.8 × 3.6	75.02 ± 1.85	[3]	PN
PN G358.7−03.0	12.59 ± 0.11	1.55 ± 0.03		10.4 × 9.8	−196.8 ± 2.8	[3]	PN
CTIO J175442.23-300836.1	–	–		21.1 × 21.1	–		Probable PN (foreground) [5]
CTIO J175444.26-290744.2	–	–		20.1 × 17.4	–		Probable PN [4]
PN Sa 3-92	11.48 ± 0.08	1.82 ± 0.07		6.4 × 5.7	−309.91 ± 0.54	[3]	PN
CTIO J175452.18-342852.1	–	–		22.0 × 20.5	–		Possible PN (foreground) [5]
MPA 1754−2847	–	–		15.7 × 11.1	−199.82 ± 9.50	[3]	Possible PN [4,14]
PN M 3-46	–	1.43 ± 0.06		–	−71.0 ± 40.0	[1]	PN [2]
CTIO J175505.83-344705.9	–	–		1.6 × 0.9	–		Possible PN [4]
PN G002.1−01.1	–	–		8.8 × 8.2	160.12 ± 5.35	[3]	PN [4]
PN G359.3−02.8	–	–		37.0 × 33.8	−157.95 ± 9.50	[3]	PN (foreground) [4,5]
PN Bl 3-10	10.73 ± 0.06	1.52 ± 0.06		7.2 × 6.9	−109 ± 40.0	[3]	PN
JaSt2 16	–	0.66 ± 0.19		–	2.83 ± 9.50	[3]	PN [2]
PN H 1-40	10.47 ± 0.03	2.0 ± 0.01	[10]	1.4 × 1.4	64.0 ± 2.5	[1]	PN
PN G001.5−01.6	–	–		13.0 × 1.2	60.53 ± 9.50	[3]	PN [4]
CTIO J175536.99-280611.2	–	–		5.5 × 1.9	–		Possible PN [4]
PN K 6-35	10.97 ± 0.14	1.54 ± 0.19		20.3 × 14.6	−71.93 ± 9.50	[3]	PN
PN G002.2−01.2	–	–		7.1 × 5.8	97.59 ± 9.50	[3]	PN [4]

TABLE C.1: PNs towards the Galactic bulge (continued).

Object Name	$-\log F_{[\mathrm{O\,III}]\,\mathrm{dered}}$ (erg cm^{-2} s^{-1})	$c(\mathrm{H}\beta)$	Ref.	Diameter ($''$) $\pm 0.8''$	v_r (km s^{-1})	Ref.	Notes
JaSt 98	10.99 ± 0.16	4.07 ± 0.09		2.0×1.7	-23.22 ± 1.29	[3]	PN
PN K 6-36	11.79 ± 0.07	1.84 ± 0.06		10.5×9.8	-148.53 ± 9.50	[3]	PN
JaSt2 18	–	–		–	-215.34 ± 9.50	[3]	PN [2]
PN H 2-31	–	–		–	120.0 ± 40.0	[1]	PN [2]
PN Bl 3-13	11.02 ± 0.07	1.68 ± 0.07		4.2×3.9	246.0 ± 35.8	[1]	PN
CTIO J175603.00-312658.9	–	–		34.2×34.2	–		Possible PN (foreground) [5]
CTIO J175604.17-280343.0	–	–		3.3×2.3	–		Possible PN [4]
CTIO J175606.37-290733.7	–	–		16.0×15.9	-256.34 ± 46.32		Probable PN [4]
PN G359.9−02.6	11.97 ± 0.13	1.55 ± 0.16		14.2×12.6	81.53 ± 9.50	[3]	PN
PN H 2-30	–	1.66 ± 0.18		–	-32.0 ± 15.0	[1]	PN [2]
PN H 2-32	–	1.44 ± 0.07		–	128.7 ± 15.0	[1]	PN [2,17]
PN M 3-17	11.94 ± 0.07	1.48 ± 0.06		3.0×2.9	-32.6 ± 11.5	[1]	PN
PN G359.2−03.1	12.27 ± 0.07	1.24 ± 0.06		16.6×13.4	77.94 ± 9.50	[3]	PN
JaSt2 19	12.36 ± 0.22	2.89 ± 0.19		5.3×2.7	-46.30 ± 9.50	[3]	PN
PN G001.2−02.0	–	–		22.7×17.0	92.88 ± 9.50	[3]	Possible PN (foreground) [4,5]
PN G357.0−04.4	12.51 ± 0.05	1.09 ± 0.03		21.6×20.9	-225.63 ± 3.56	[3]	Possible PN
PN G358.6−03.6	–	–		53.1×46.5	-62.31 ± 9.50	[3]	PN (foreground) [4,5]
PN G356.6−04.7	11.92 ± 0.04	0.65 ± 0.03		20.1×18.7	-96.75 ± 2.69	[3]	PN
PN G356.7−04.7	12.57 ± 0.05	0.41 ± 0.03		12.0×11.3	2.96 ± 0.75	[3]	PN
CTIO J175703.45-284955.2	–	–		8.5×5.4	–		Possible PN [4]
CTIO J175703.93-275130.4	–	–		15.0×13.2	–		Possible PN [4]
CTIO J175706.52-310324.5	–	–		16.5×16.2	–		Possible PN [4]
CTIO J175708.64-310453.4	–	–		36.3×15.7	–		Possible PN (foreground) [5]
MPA 1757−3021	–	–		–	–		True PN [2,20]
PN H 1-41	10.64 ± 0.13	0.45 ± 0.18		12.0×8.8	73.3 ± 6.0	[1]	PN (foreground) [12]

TABLE C.1: PNs towards the Galactic bulge (continued).

Object Name	$-\log F_{[\mathrm{O\,III}]\,\mathrm{dered}}$ (erg cm^{-2} s^{-1})	$c(\mathrm{H}\beta)$	Ref.	Diameter ($''$) $\pm 0.8''$	v_r (km s^{-1})	Ref.	Notes
PN H 1-42	10.13 ± 0.02	$0.72^{+0.04}_{-0.07}$	[6]	4.3×3.7	-79.2 ± 4.7	[1]	PN
PN G002.7−01.4	–	2.95 ± 0.20		–	–		Possible PN [2]
CTIO J175735.64-273532.5	–	–		14.8×11.4	40 ± 10		Possible PN [4,13,21]
PN G001.8−02.0	12.22 ± 0.05	1.52 ± 0.03		19.3×8.0	54.0 ± 4.2	[3]	Possible PN
PN M 3-47	11.84 ± 0.10	1.29 ± 0.11		8.1×7.2	-16.0 ± 5.0	[1]	PN
PN G002.3−01.7	–	–		–	–		Possible PN [2]
PN G358.9−03.6	–	–		13.8×6.3	-194.53 ± 9.50	[3]	Possible PN [4]
PN G359.4−03.3	12.49 ± 0.19	0.62 ± 0.27		12.8×10.4	-58.11 ± 9.50	[3]	PN
CTIO J175800.70-285401.9	–	–		2.4×1.9	–		Probable PN [4]
PN M 2-21	10.30 ± 0.09	1.11 ± 0.11		2.8×2.8	-164.5 ± 2.0	[1]	PN
PN H 1-44	12.21 ± 0.10	1.38 ± 0.11	[7]	3.5×3.3	97.1 ± 5.7	[1]	PN
CTIO J175811.57-330701.0	–	–		6.7×6.0	–		Possible PN [4]
CTIO J175812.20-283436.9	–	–		2.9×2.7	–		PN [4]
PN H 2-33	11.44 ± 0.09	1.15 ± 0.11		7.9×7.3	107.0 ± 15.0	[1]	PN
PN H 1-43	–	0.23 ± 0.18		–	49.0 ± 13.8	[1]	PN [2]
PN M 3-19	11.14 ± 0.09	1.30 ± 0.11		7.2×6.6	141.7 ± 15.0	[1]	PN
PN H 1-45	10.85 ± 0.02	1.82	[9]	1.5×1.1	-19.2 ± 18.3	[1]	PN [8]
PN Sa 3-104	11.80 ± 0.15	1.72 ± 0.19		1.7×1.3	87.0 ± 40.0	[1]	PN [18]
WRAY 17-104	11.26 ± 0.13	1.20 ± 0.18		16.6×14.3	-275.56 ± 9.50	[3]	PN
PN G002.6−01.7	12.06 ± 0.05	2.15 ± 0.03		8.7×6.5	108.12 ± 1.06	[3]	Possible PN
PN Pe 2-11	11.68 ± 0.07	1.94 ± 0.06		7.2×6.5	155.0 ± 40.0	[1]	PN
PN M 2-22	10.93 ± 0.13	1.04 ± 0.18		5.8×5.2	-103.3 ± 10.3	[1]	PN
PN G002.3−01.9	–	–		19.9×18.3	-48.21 ± 9.50	[3]	PN [4]
CTIO J175836.40-292120.0	–	–		52.9×50.9	–		Possible PN (foreground) [5]
PN G001.5−02.4	11.88 ± 0.15	1.37 ± 0.19		17.2×14.4	-63.09 ± 9.50	[3]	PN

TABLE C.1: PNs towards the Galactic bulge (continued).

Object Name	$-\log F_{[\mathrm{O\,III}]\,\mathrm{dered}}$ ($\mathrm{erg\,cm^{-2}\,s^{-1}}$)	$c(\mathrm{H}\beta)$	Ref.	Diameter ($''$) $\pm 0.8''$	v_r ($\mathrm{km\,s^{-1}}$)	Ref.	Notes
CTIO J175850.06-304943.3	–	–		13.7×9.7	–		Possible PN [4]
MPA 1758−2816	–	–		–	–		Possible PN [2,21]
CTIO J175851.48-291559.8	–	–		22.6×21.2	–		Probable PN (foreground) [4,5,13,21]
CTIO J175857.26-284902.5	–	–		2.1×1.7	–		Probable PN [4]
PN H 1-46	10.55 ± 0.07	1.2 ± 0.08	[6]	1.5×1.2	-44.3 ± 0.2	[1]	PN
PN G001.2−02.6	–	–		–	139.40 ± 9.50	[3]	Possible PN [2]
CTIO J175904.60-265547.3	–	–		2.3×1.9	–		Possible PN [4]
PN G004.8−00.5	–	–		42.3×26.4	4.26 ± 9.50	[3]	Possible PN (foreground) [4,5]
PN G003.6−01.3	–	3.00 ± 0.20		–	193.91 ± 9.50	[3]	PN [2]
PN KFL 1	11.47 ± 0.09	1.14 ± 0.11		8.0×7.9	-52.8 ± 14.0	[1]	PN
PN M 3-20	10.72 ± 0.12	0.85 ± 0.16		4.0×3.2	24.3 ± 2.0	[1]	PN
CTIO J175919.98-275515.3	–	–		17.4×14.7	–		Possible PN [4]
PN G359.5−03.7	13.01 ± 0.25	0.85 ± 0.27		22.9×22.6	–		PN (foreground) [5]
PN G000.5−03.1 a	–	0.90 ± 0.27		–	–		Possible PN [2]
PN G003.1−01.6	12.11 ± 0.16	2.20 ± 0.20		30.5×29.9	67.15 ± 9.50	[3]	PN (foreground) [5]
PN G357.7−04.8	–	–		–	–		PN [2]
PN G000.2−03.4	12.26 ± 0.10	1.12 ± 0.11		21.2×18.2	114.50 ± 9.50	[3]	PN (foreground) [5]
PN G001.9−02.5	12.37 ± 0.18	1.46 ± 0.23		15.6×13.5	59.06 ± 9.50	[3]	Possible PN
CTIO J175954.11-332453.4	–	–		2.1×2.1	–		Possible PN [4]
WRAY 16-344	11.70 ± 0.04	1.22 ± 0.03		6.3×5.9	-152.39 ± 0.28	[3]	Possible PN
PN G003.3−01.6	–	2.30 ± 0.20		–	-94.82 ± 9.50	[3]	PN [2]
CTIO J175955.50-271916.7	–	–		18.3×16.1	50.39 ± 9.50	[3]	Possible PN [4,13,21]
PN G000.6−03.2	–	–		30.2×30.1	–		PN (foreground) [4,5]
PN G001.6−02.6	11.83 ± 0.18	1.53 ± 0.23		22.6×21.3	-88.26 ± 9.50	[3]	PN
PN M 3-48	11.80 ± 0.12	1.01 ± 0.17	[6]	4.7×4.2	-12.0 ± 4.7	[1]	PN

TABLE C.1: PNs towards the Galactic bulge (continued).

Object Name	$-\log F_{[\mathrm{O\,III}]\,\mathrm{dered}}$ (erg cm^{-2} s^{-1})	$c(\mathrm{H}\beta)$	Ref.	Diameter ($''$) $\pm 0.8''$	v_r (km s^{-1})	Ref.	Notes
PN K 6-38	–	1.15 ± 0.03		–	-40.82 ± 1.54	[3]	PN [2]
CTIO J180000.03-302618.5	13.45 ± 0.25	0.92 ± 0.27		21.7×7.6	106.96 ± 8.83		Possible PN (foreground) [5,13]
PN G001.7−02.6	11.56 ± 0.12	0.77 ± 0.16		15.1×12.6	18.82 ± 9.50	[3]	PN
PN G002.0−02.4	12.79 ± 0.23	1.24 ± 0.23		14.2×12.5	-65.37 ± 9.50	[3]	PN
PN G000.3−03.4	12.42 ± 0.10	1.36 ± 0.11		7.9×5.8	–		PN
PN G002.0−02.5	12.27 ± 0.13	0.77 ± 0.16		21.8×18.8	57.74 ± 9.50	[3]	PN (foreground) [5]
PN G002.1−02.4	12.05 ± 0.13	0.83 ± 0.16		13.2×11.3	-13.34 ± 9.50	[3]	PN
CTIO J180021.99-274607.7	–	–		9.4×7.1	–		Probable PN [4]
PN G001.5−02.8	11.89 ± 0.12	0.97 ± 0.16		9.8×9.8	6.57 ± 9.50	[3]	PN
CTIO J180030.42-300952.7	–	–		18.4×16.7	–		Possible PN [4]
PN G001.8−02.7	12.47 ± 0.17	1.10 ± 0.23		11.3×10.1	-17.32 ± 9.50	[3]	Possible PN
PN H 1-47	13.46 ± 0.19	1.23 ± 0.16		1.1×0.9	107.5 ± 3.1	[1]	PN
PN G003.4−01.8	11.60 ± 0.17	2.36 ± 0.20		9.3×9.5	-7.15 ± 9.50	[3]	PN
CTIO J180056.24-321421.2	–	–		29.4×28.8	–		Possible PN (foreground) [5]
CTIO J180056.33-321421.5	–	–		30.4×29.5	–		Possible PN (foreground) [5]
PN KFL 2	11.54 ± 0.12	1.40 ± 0.16		8.2×5.9	-80.3 ± 55.2	[1]	PN
PN Pe 2-12	13.05 ± 0.13	1.39 ± 0.06		8.3×1.8	25.43 ± 9.50	[3]	PN
PN G000.9−03.3	12.29 ± 0.20	1.16 ± 0.27		35.1×31.2	-31.19 ± 9.50	[3]	PN (foreground) [5]
PN G004.8−01.1	–	–		7.3×7.0	9.83 ± 9.50	[3]	PN [4]
PN G004.3−01.4	–	3.19 ± 0.20		–	102.37 ± 9.50	[3]	PN [2]
PN G003.1−02.1	12.20 ± 0.16	1.68 ± 0.20		38.1×35.1	50.19 ± 9.50	[3]	PN (foreground) [5]
PN G002.1−02.8	12.03 ± 0.13	0.82 ± 0.16		18.5×16.4	-110.71 ± 9.50	[3]	PN
PN G002.7−02.4	13.14 ± 0.22	1.45 ± 0.20		11.5×8.5	-16.81 ± 9.50	[3]	Possible PN
PN M 2-23	–	–		20.1×19.0	186.7 ± 0.3	[1]	PN [2]
PN G002.4−02.6	13.27 ± 0.23	1.30 ± 0.23		32.6×29.4	-146.40 ± 9.50	[3]	PN

TABLE C.1: PNs towards the Galactic bulge (continued).

Object Name	$-\log F_{[\mathrm{O\,III}]\,\mathrm{dered}}$ ($\mathrm{erg\,cm^{-2}\,s^{-1}}$)	$c(\mathrm{H}\beta)$	Ref.	Diameter ($''$) $\pm 0.8''$	v_r ($\mathrm{km\,s^{-1}}$)	Ref.	Notes
CTIO J180150.14-275526.4	12.46 ± 0.16	1.71 ± 0.20		10.6×7.2	-13.17 ± 9.50	[3]	Probable PN [21,22]
MPA 1802−3045	–	–		–	–		Possible PN [2,13]
CTIO J180204.70-280340.5	13.07 ± 0.23	0.87 ± 0.23		40.9×38.6	131.17 ± 17.58		Probable PN (foreground) [5,21,22]
CTIO J180210.24-295159.3	–	–		1.3×1.3	–		Possible PN [4]
PN G003.8−01.9	–	2.73 ± 0.20		–	-203.49 ± 9.50	[3]	PN [2]
MPA 1802−2850	–	–		–	–		Possible PN [2,13]
PN M 3-22	11.06 ± 0.09	0.98 ± 0.11		11.7×7.9	-56.2 ± 4.9	[1]	PN
CTIO J180224.88-302343.7	–	–		1.6×1.5	–		Possible PN [4]
PN ShWi 1	10.79 ± 0.21	2.64 ± 0.27		16.3×15.2	-39.4 ± 6.1	[1]	PN
PN G359.7−04.4 a	12.14 ± 0.09	0.61 ± 0.11		17.6×15.5	-199.69 ± 9.50	[3]	PN
CTIO J180235.03-310555.9	–	–		22.0×20.1	116.36 ± 31.12		Probable PN [4]
PN M 2-25	10.97 ± 0.02	$0.84^{+0.08}_{-0.04}$	[6]	17.7×13.4	10.6 ± 10.2	[1]	PN
PN G002.0−03.1	12.21 ± 0.05	0.97 ± 0.03		19.5×18.2	-10.98 ± 8.61	[3]	PN
PN G001.8−03.2	12.58 ± 0.05	0.49 ± 0.03		22.4×21.4	16.05 ± 0.24	[3]	PN (foreground) [5]
PN KFL 4	–	1.12 ± 0.16		–	17.0 ± 15.0	[1]	PN [2]
PN KFL 3	11.73 ± 0.09	0.77 ± 0.11		15.2×14.3	204.6 ± 10.3	[1]	PN
CTIO J180253.79-280755.6	12.34 ± 0.17	1.35 ± 0.23		36.9×35.2	143.95 ± 9.50	[3]	Probable PN [21,22]
CTIO J180258.75-291347.5	–	–		35.3×35.2	–		Possible PN (foreground) [5]
PN K 6-39	–	1.17 ± 0.16		–	–		PN [2,18]
CTIO J180308.22-292038.0	–	–		3.6×3.3	–		Possible PN [4]
PN G002.6−02.8	12.86 ± 0.23	1.34 ± 0.23		39.2×17.2	-19.76 ± 9.50	[3]	Possible PN (foreground) [5]
PN G003.5−02.3	–	1.34 ± 0.20		–	32.38 ± 9.50	[3]	Possible PN [2]
PN G002.0−03.2	12.18 ± 0.13	0.66 ± 0.16		32.2×28.4	-73.97 ± 9.50	[3]	PN (foreground) [5,12]
CTIO J180311.83-262927.0	–	–		5.5×4.9	–		Possible PN [4]
PN M 2-26	11.19 ± 0.06	1.22 ± 0.06		9.5×9.4	-52.9 ± 6.9	[1]	PN

TABLE C.1: PNs towards the Galactic bulge (continued).

Object Name	$-\log F_{[\mathrm{O\,III}]\,\mathrm{dered}}$ (erg cm^{-2} s^{-1})	$c(\mathrm{H}\beta)$	Ref.	Diameter ($''$) $\pm 0.8''$	v_r (km s^{-1})	Ref.	Notes
PN G359.0−04.9	11.90 ± 0.05	1.34 ± 0.03		35.1×30.2	55.44 ± 4.35	[3]	PN (foreground) [5]
CTIO J180317.18-285627.5	–	–		2.1×1.8	–		Possible PN [4]
IC 4673	10.14 ± 0.04	0.95 ± 0.03		21.7×16.5	-15.3 ± 2.0	[1]	PN (foreground) [5,12]
PN G000.3−04.2	12.89 ± 0.19	0.73 ± 0.27		36.6×36.2	–		PN (foreground) [5]
PN G002.4−03.1	11.36 ± 0.12	1.10 ± 0.16		4.1×3.2	64.48 ± 9.50	[3]	PN
CTIO J180325.70-314839.4	–	–		31.3×23.5	–		Possible PN (foreground) [5]
PN G000.3−04.2 a	13.31 ± 0.25	0.73 ± 0.27		23.7×20.5	–		PN (foreground) [5]
PN G001.2−03.8	–	–		48.7×48.1	-59.83 ± 9.50	[3]	PN (foreground) [4,5]
PN G002.0−03.4	12.80 ± 0.17	0.57 ± 0.23		19.1×18.6	149.75 ± 9.50	[3]	Possible PN
PN M 1-35	10.33 ± 0.06	1.67 ± 0.06		7.3×6.8	67.9 ± 1.6	[1]	PN (foreground) [12]
PN M 2-27	10.36 ± 0.09	1.30 ± 0.11		3.3×3.0	144.8 ± 0.2	[1]	PN
CTIO J180359.49-311740.8	–	–		3.0×2.9	–		Possible PN [4]
PN G003.8−02.4	–	–		8.8×6.7	66.13 ± 9.50	[3]	PN [4]
WRAY 17-107	11.43 ± 0.04	0.84 ± 0.03		18.6×15.4	-72.07 ± 1.78	[3]	PN
PN H 2-36	11.31 ± 0.02	$0.93^{+0.07}_{-0.02}$	[6]	17.7×14.5	-119.7 ± 31.2	[1]	PN
CTIO J180410.54-292638.5	12.66 ± 0.17	0.57 ± 0.23		35.3×21.2	136.05 ± 9.50	[3]	Possible PN [21,22]
PN G002.6−03.1	12.02 ± 0.13	0.83 ± 0.16		14.3×14.0	-173.60 ± 9.50	[3]	PN
CTIO J180413.75-281602.2	–	–		2.6×2.2	–		Probable PN [4]
PN G002.9−03.0	12.38 ± 0.17	1.10 ± 0.23		47.3×40.4	-97.52 ± 9.50	[3]	PN
PN G001.8−03.7	12.52 ± 0.05	0.71 ± 0.03		8.3×7.3	260.86 ± 3.48	[3]	PN
PN H 2-37	11.28 ± 0.12	0.86 ± 0.16		6.0×3.5	-156.8 ± 14.0	[1]	PN
WRAY 16-363	11.73 ± 0.10	1.32 ± 0.11		8.2×6.8	121.4 ± 14.0	[1]	PN
PN G000.9−04.2	11.86 ± 0.10	1.28 ± 0.11		11.5×11.3	204.19 ± 9.50	[3]	PN
PN G002.4−03.4	11.98 ± 0.05	0.99 ± 0.03		1.7×0.4	-113.5 ± 0.8	[3]	Possible PN [23]
PN G004.0−02.5	12.30 ± 0.16	1.83 ± 0.20		15.0×12.6	115.32 ± 9.50	[3]	Possible PN

TABLE C.1: PNs towards the Galactic bulge (continued).

Object Name	$-\log F_{[\mathrm{O\,III}]\,\mathrm{dered}}$ ($\mathrm{erg\,cm^{-2}\,s^{-1}}$)	$c(\mathrm{H}\beta)$	Ref.	Diameter ($''$) $\pm 0.8''$	v_r ($\mathrm{km\,s^{-1}}$)	Ref.	Notes
PN G004.0−02.6	11.63 ± 0.06	1.30 ± 0.06		24.5×13.2	-103.44 ± 9.50	[3]	PN
PN M 2-28	–	1.17 ± 0.11		–	-29.9 ± 8.7	[1]	PN [2]
PN G003.6−02.8	12.41 ± 0.16	1.35 ± 0.20		42.9×41.1	82.76 ± 9.50	[3]	PN (foreground) [5]
CTIO J180507.08-264839.2	–	–		29.4×27.3	–		Possible PN (foreground) [5]
PN PM 1-206	12.19 ± 0.20	1.43 ± 0.27		20.3×17.3	75.48 ± 9.50	[3]	Possible PN
PN G003.5−02.9	12.65 ± 0.15	0.79 ± 0.20		31.1×22.2	59.18 ± 9.50	[3]	PN (foreground) [5]
PN G004.2−02.5	11.17 ± 0.06	2.13 ± 0.06		12.5×10.3	34.01 ± 9.50	[3]	PN
PN M 1-37	12.64 ± 0.13	1.32 ± 0.16		0.8×0.7	220.5 ± 0.9	[1]	PN
PN G004.0−02.7	12.34 ± 0.07	1.29 ± 0.06		27.4×22.1	-98.25 ± 9.50	[3]	PN
PN G003.9−02.8	–	0.14 ± 0.20		–	–		Possible PN [2,24]
PN G002.9−03.3	–	1.11 ± 0.23		–	18.29 ± 9.50	[3]	PN [2]
CTIO J180555.61-290246.3	12.63 ± 0.17	0.95 ± 0.23		29.3×28.6	243.97 ± 9.50	[3]	Possible PN [21,22]
PN H 1-53	11.35 ± 0.06	1.68 ± 0.06		2.3×1.7	75.0 ± 5.0	[1]	PN [8]
PN G003.6−03.0	11.89 ± 0.06	0.79 ± 0.06		21.6×19.9	-6.51 ± 9.50	[3]	PN (foreground) [5]
PN M 1-38	12.77 ± 0.13	0.76 ± 0.16		3.7×2.6	-82.8 ± 9.1	[1]	PN
PN G003.3−03.3	–	0.89 ± 0.16		–	-29.02 ± 9.50	[3]	PN [2]
PN G002.7−03.7	12.38 ± 0.13	0.75 ± 0.16		13.1×12.6	103.41 ± 9.50	[3]	PN
PN G001.4−04.4	–	–		37.6×35.6	134.44 ± 4.13	[3]	Possible PN (foreground) [4,5]
MPA 1806−2812	–	–		–	–		Possible PN [2,21]
PN M 2-29	10.93 ± 0.05	0.90 ± 0.05	[25]	4.8×3.6	-112.2 ± 2.6	[1]	PN [17]
PN G002.1−04.1	12.02 ± 0.13	1.42 ± 0.16		28.1×27.7	-121.92 ± 9.50	[3]	PN
PN KFL 7	11.75 ± 0.07	1.01 ± 0.08	[6]	8.1×5.0	-91.0 ± 15.0	[1]	PN
CTIO J180652.90-280706.0	11.93 ± 0.61	1.61 ± 0.92		18.6×16.6	140.95 ± 9.50	[3]	PN [13,21]
PN G004.1−03.0	–	–		16.2×13.0	–		Possible PN [18]
CTIO J180701.33-264550.2	–	–		60.7×58.8	–		Possible PN (foreground) [5]

TABLE C.1: PNs towards the Galactic bulge (continued).

Object Name	$-\log F_{[\mathrm{O\,III}]\,\mathrm{dered}}$ (erg cm^{-2} s^{-1})	$c(\mathrm{H}\beta)$	Ref.	Diameter ($''$) $\pm 0.8''$	v_r (km s^{-1})	Ref.	Notes
PN M 3-23	10.44 ± 0.02	$1.10^{+0.07}_{-0.0}$	[6]	13.6×12.5	-153.0 ± 0.8	[1]	PN
PN H 1-54	10.61 ± 0.12	0.84 ± 0.16		1.9×1.6	-137.4 ± 13.0	[1]	PN
CTIO J180711.70-262719.2	–	–		21.9×15.6	–		Possible PN (foreground) [5]
PN H 1-55	12.80 ± 0.03	$0.88^{+0.08}_{-0.17}$	[6]	13.8×13.6	-35.6 ± 32.6	[1]	PN (foreground) [12]
PN G003.8−03.2	–	–		12.4×10.0	114.53 ± 9.50	[3]	PN [4]
CTIO J180724.90-290326.0	–	–		33.8×31.5	–		Possible PN (foreground) [5]
CTIO J180742.79-263104.0	–	–		40.5×37.5	–		Possible PN (foreground) [4,5,13,21]
PN H 1-56	10.99 ± 0.05	0.6 ± 0.05	[6]	4.2×4.2	-116.6 ± 2.0	[1]	PN
CTIO J180755.67-264114.1	–	–		2.8×2.0	–		PN [4]
PN G004.4−03.1	12.37 ± 0.05	1.32 ± 0.03		25.4×25.3	75.21 ± 2.22	[3]	PN (foreground) [5]
PN KFL 10	11.58 ± 0.02	$0.62^{+0.06}_{-0.07}$	[6]	7.1×5.6	-128.2 ± 19.1	[1]	PN
PN G004.1−03.3	–	–		13.1×8.5	–		PN [4,18]
PN H 2-39	11.07 ± 0.09	1.05 ± 0.11	[7]	6.9×4.7	36.6 ± 14.0	[1]	PN
PN K 6-40	–	–		2.2×2.1	–		PN [4]
PN G002.8−04.1	11.94 ± 0.11	0.40 ± 0.16		18.9×16.3	92.75 ± 9.50	[3]	PN
CTIO J180832.52-284950.6	–	–		1.2×1.2	–		Possible PN [4]
CTIO J180854.57-294441.0	–	–		24.0×23.3	–		Possible PN (foreground) [5]
PN KFL 11	11.61 ± 0.08	1.1 ± 0.10	[6]	3.0×2.3	-39.2 ± 31.2	[1]	PN
CTIO J181026.15-284016.3	–	–		41.1×40.1	–		Possible PN (foreground) [5]
PN KFL 12	11.66 ± 0.02	$1.0^{+0.0}_{-0.1}$	[6]	3.4×3.1	100.5 ± 23.5	[1]	PN
MPA 1810−2851	–	–		3.0×1.4	–		Possible PN [4,21]
PN G003.3−04.4	–	–		13.2×13.0	18.55 ± 9.50	[3]	Possible PN [4]
CTIO J181057.79-271822.5	–	–		17.3×16.6	–		Possible PN [4]
PN M 1-42	10.51 ± 0.03	0.71 ± 0.01	[10]	12.5×11.6	-86.5 ± 0.2	[1]	PN (foreground) [12]
CTIO J181120.34-272432.4	–	–		2.4×1.6	–		Possible PN [4]

TABLE C.1: PNs towards the Galactic bulge (continued).

Object Name	$-\log F_{[\mathrm{O\,III}]\,\mathrm{dered}}$ ($\mathrm{erg\,cm^{-2}\,s^{-1}}$)	$c(\mathrm{H}\beta)$	Ref.	Diameter ($''$) $\pm 0.8''$	v_r ($\mathrm{km\,s^{-1}}$)	Ref.	Notes
PN H 1-59	11.02 ± 0.02	$0.73^{+0.05}_{-0.06}$	[6]	6.6×6.0	7.0 ± 40.0	[1]	PN
ESO 456-69	12.20 ± 0.03	$0.59^{+0.6}_{-0.4}$	[6]	–	151.1 ± 5.8	[1]	PN (foreground) [12]
NGC 6565	10.00 ± 0.04	0.27 ± 0.03	[26]	10.5×9.6	-5.9 ± 1.6	[1]	PN (foreground) [12]
PN H 2-41	11.36 ± 0.06	0.75 ± 0.06	[6]	10.5×9.6	26.3 ± 4.4	[1]	PN
PN H 1-60	10.90 ± 0.04	0.84 ± 0.03	[16]	6.1×5.6	24.4 ± 8.6	[1]	PN
PN M 2-30	10.37 ± 0.02	$0.70^{+0.06}_{-0.05}$	[6]	5.1×5.0	154.9 ± 2.9	[1]	PN
CTIO J181244.61-281033.3	–	–		34.5×21.7	-160.14 ± 33.60		Probable PN [4]
PN H 2-43	11.80 ± 0.02	1.13	[9]	1.1×0.9	-15.6 ± 27.1	[1]	PN

TABLE C.1: PNs towards the Galactic bulge (continued).

Object Name	$-\log F_{[\mathrm{O\,III}]_{\mathrm{dered}}}$ (erg cm^{-2} s^{-1})	$c(\mathrm{H}\beta)$	Ref.	Diameter ($''$) $\pm 0.8''$	v_{r} (km s^{-1})	Ref.	Notes

[1] Durand et al. (1998).
[2] No [O III] flux data available.
[3] Miszalski et al. in prep., used in Kovacevic (2011).
[4] [O III] flux data available, but reddened only.
[5] Probable foreground object, $d > 21''$.
[6] Derived from Górny et al. (2009).
[7] Derived from line ratios in Acker et al. (1991, 1992).
[8] Probable SyS (Kovacevic, 2011).
[9] Derived from line ratios in Escudero et al. (2004).
[10] Derived from line ratios in Cuisinier et al. (2000).
[11] Derived from line ratios in Escudero & Costa (2001).
[12] Foreground object (Kovacevic, 2011).
[13] Not in SIMBAD. Possible PN (Kovacevic, 2011).
[14] Not in SIMBAD. Likely PN (Miszalski, 2009).
[15] Derived from Shaw & Kaler (1989).
[16] Górny et al. (2004).
[17] Probable SyS (Miszalski, 2009).
[18] SyS (Miszalski, 2009).
[19] Suspected LIER associated with GAL 002.37+01.40, not a distinct PN.
[20] Not in SIMBAD. True PN (Miszalski, 2009).
[21] Not in SIMBAD. Possible PN (Miszalski, 2009).
[22] Not in SIMBAD. Probable PN (Kovacevic, 2011).
[23] Miscellaneous circumstellar nebula, not a true PN (Miszalski, 2009).
[24] Flare star (Miszalski, 2009).
[25] Derived from Exter et al. (2004).
[26] Wang & Liu (2007).

D

Publications

A list of publications produced during the course of this Ph.D. research are detailed below in chronological order.

Reference: Stenborg, T. N. & Parker, Q. A. 2014, "A new population of planetary nebulae candidates towards the Galactic bulge", in Proc. Asymmetrical Planetary Nebulae VI, ed. C. Morisset, G. Delgado-Inglada & S. Torres-Peimbert, id. 98.
Abstract: A significant new population of Galactic bulge PN candidates (> 300) was discovered from careful review of bulge imaging taken with the Mosaic II CCD imager on the CTIO's 4 m Blanco telescope. Bona fide PNs amongst this new population will refine the known Galactic PN population and provide a more statistically complete bulge [O III] planetary nebula luminosity function.

Reference: Stenborg, T. N. 2014, "Interleaved FITS DS9 segmentation with shell script metaprogramming for planetary nebulae detection", in Proc. Asymmetrical Planetary Nebulae VI, ed. C. Morisset, G. Delgado-Inglada & S. Torres-Peimbert, id. 99.
Abstract: A technique for efficient inspection of high volume imaging data for PNs is presented. Image segmentation to subscreen size is automated. Consecutive small image review avoids inadvertently missing sections of large images with manual image traversal. RGB stacked (emission line on band R, off band G) images are auto-interleaved with corresponding difference images. Bidirectional single-click navigation of a segmented, interleaved data set allows complementary image blinking and efficient PN candidate identification.

Reference: Stenborg, T. N. 2015, "Greedy Set Cover Field Selection for Multi-object Spectroscopy in C++ MPI", in Proc. Astronomical Data Analysis Software and Systems XXIV.
Abstract: Multi-object spectrographs allow efficient observation of clustered targets. Observational programs of many targets not encompassed within a telescope's field of view, however, require multiple pointings. Here, a greedy set cover algorithmic approach to efficient field selection in such a scenario is examined. The goal of this approach is not to minimise the total number of pointings needed to cover a given target set, but rather maximise the observational return for a restricted number of pointings. Telescope field of view and maximum targets per field are input parameters, allowing algorithm application to observation planning for the current range of active multi-object spectrographs (e.g. the 2dF/AAOmega, Fibre Large Array Multi Element Spectrograph, Fibre Multi-Object Spectrograph, Hectochelle, Hectospec and Hydra systems), and for any future systems. A parallel version of the algorithm is implemented with the message passing interface, facilitating execution on both shared and distributed memory systems.

Reference: Stenborg, T. N. 2016, "Accurate Sky Subtraction from Emission Line Slit Spectra in C OpenMP", in Proc. Astronomical Data Analysis Software and Systems XXV (in press).
Abstract: An accurate sky subtraction technique for nebula slit spectra reduction is presented. The technique yields reduced spectra accurately baselined to zero flux, giving reliable emission line ratios for use in determining nebula properties, such as extinction from the Balmer decrement. The technique is automated, parallelised and incorporated into metaprogramming of reduction scripts.

References

Abell, G. O. 1966, Astrophys. J., 144, 259

Acker, A., Marcout, J., Ochsenbein, F., et al. 1992, The Strasbourg-ESO Catalogue of Galactic Planetary Nebulae. Parts I, II. (Garching, Germany: ESO)

Acker, A., & Neiner, C. 2003, Astron. Astrophys., 403, 659

Acker, A., & Ochsenbein, F. 1993, in IAU Symposium, Vol. 155, Planetary Nebulae, ed. R. Weinberger & A. Acker, 33

Acker, A., Raytchev, B., Koeppen, J., & Stenholm, B. 1991, Astron. Astrophys. Suppl. Ser., 89, 237

Akhundova, G. V., & Seidov, Z. F. 1970, Sov. Astron., 14, 104

Allen, D. A. 1980, Mon. Not. R. Astron. Soc., 192, 521

Allen, D. A. 1982, in Astrophysics and Space Science Library, Vol. 95, IAU Colloq. 70: The Nature of Symbiotic Stars, ed. M. Friedjung & R. Viotti, 27–42

Appenzeller, I., Fricke, K., Fürtig, W., et al. 1998, The Messenger, 94, 1

Arce, H. G., & Goodman, A. A. 1999, Astrophys. J. Lett., 512, L135

Armandroff, T., Boroson, T., De Veny, J., et al. 1999, NOAO CCD Mosaic Imager User Manual (KPNO System), National Optical Astronomy Observatory, 950 North Cherry Ave., Tuscon, AZ 85719, USA

Baade, D., Meisenheimer, K., Iwert, O., et al. 1999, The Messenger, 95, 15

Bains, I., Gledhill, T. M., Yates, J. A., & Richards, A. M. S. 2003, Mon. Not. R. Astron. Soc., 338, 287

Bains, I., Richards, A. M. S., Gledhill, T. M., & Yates, J. A. 2004, Mon. Not. R. Astron. Soc., 354, 529

Bakich, M. E. 2010, 1,001 Celestial Wonders to See Before You Die, Patrick Moore's Practical Astronomy Series (New York, NY: Springer)

Bakos, G. Á., Csubry, Z., Penev, K., et al. 2013, Publ. Astron. Soc. Pac., 125, 154

Baldwin, J. A., & Stone, R. P. S. 1984, Mon. Not. R. Astron. Soc., 206, 241

Balick, B. 1987, Astron. J., 94, 671

Balick, B., & Frank, A. 2002, Annu. Rev. Astron. Astrophys., 40, 439

Ball, C. R. 1928, Am. Speech, 3, 291

Barden, S. C., Jones, D. J., Barnes, S. I., et al. 2010, in Society of Photo-Optical Instrumentation Engineers (SPIE) Conference Series, Vol. 7735, Ground-based and Airborne Instrumentation for Astronomy III, ed. I. S. McLean, S. K. Ramsay, & H. Takami, Bellingham, WA, 09

Beaulieu, S. F., Dopita, M. A., & Freeman, K. C. 1999, Astrophys. J., 515, 610

Beaulieu, S. F., Freeman, K. C., Kalnajs, A. J., Saha, P., & Zhao, H. 2000, Astron. J., 120, 855

Beckwith, S., Evans, II, N. J., Natta, A., Russell, R. W., & Wyant, J. 1984, Astrophys. J., 277, 207

Beichman, C. A., Neugebauer, G., Habing, H. J., Clegg, P. E., & Chester, T. J., eds. 1988, Infrared astronomical satellite (IRAS) catalogs and atlases. Volume 1: Explanatory supplement, 2nd edn., NASA Reference Publication No. 1190 (NASA Scientific and Technical Information Office)

Belczyński, K., Mikołajewska, J., Munari, U., Ivison, R. J., & Friedjung, M. 2000, Astron. Astrophys. Suppl. Ser., 146, 407

Bell, S. A., & Urban, S. E. 2012, The Astronomical Almanac for the year 2013 (Taunton, Somerset and Washington, DC: UK Hydrographic Office and US Government Printing Office)

Benedict, G. F., McArthur, B. E., Napiwotzki, R., et al. 2009, Astron. J., 138, 1969

Benjamin, R. A., Churchwell, E., Babler, B. L., et al. 2003, Publ. Astron. Soc. Pac., 115, 953

Bensby, T., & Lundström, I. 2001, Astron. Astrophys., 374, 599

Bernard-Salas, J., Peeters, E., Sloan, G. C., et al. 2009, Astrophys. J., 699, 1541

Bertin, E., & Arnouts, S. 1996, Astron. Astrophys. Suppl. Ser., 117, 393

Birriel, J. J., Espey, B. R., & Schulte-Ladbeck, R. E. 2000, Astrophys. J., 545, 1020

Blackman, E. G., Frank, A., Markiel, J. A., Thomas, J. H., & Van Horn, H. M. 2001, Nature, 409, 485

Blitz, L., & Spergel, D. N. 1991, Astrophys. J., 379, 631

Bode, M. F., & Evans, A., eds. 2008, Classical Novae, 2nd edn., Cambridge Astrophysics Series No. 43 (Cambridge, UK: Cambridge University Press)

Boffi, F. R., & Stanghellini, L. 1994, Astron. Astrophys., 284, 248

Boissay, R., Parker, Q. A., Frew, D. J., & Bojicic, I. 2012, in IAU Symposium, Vol. 283, Planetary Nebulae: An Eye to the Future, ed. A. Manchado, L. Stanghellini, & D. Schönberner, 316–317

Bojičić, I. 2009, PhD thesis, Macquarie University

Bojičić, I. S., Parker, Q. A., Filipović, M. D., & Frew, D. J. 2011, Mon. Not. R. Astron. Soc., 412, 223

Bond, H. E., & Ciardullo, R. 1999, Publ. Astron. Soc. Pac., 111, 217

Bonnarel, F., Fernique, P., Bienaymé, O., et al. 2000, Astron. Astrophys. Suppl. Ser., 143, 33

Boumis, P., Akras, S., Xilouris, E. M., et al. 2006, Mon. Not. R. Astron. Soc., 367, 1551

Boumis, P., Paleologou, E. V., Mavromatakis, F., & Papamastorakis, J. 2003, Mon. Not. R. Astron. Soc., 339, 735

Bowen, I. S. 1928, Astrophys. J., 67, 1

—. 1934, Publ. Astron. Soc. Pac., 46, 146

—. 1935, Astrophys. J., 81, 1

Boyd, J.P. 2001, Chebyshev and Fourier Spectral Methods, 2nd edn., Dover books on mathematics (Mineola, NY: Dover Publications)

Brazhnikova, É. F., Dagaev, M. M., & Radzievskii, V. V. 1976, Sov. Astron., 19, 333

Brocklehurst, M. 1971, Mon. Not. R. Astron. Soc., 153, 471

Brough, S., Green, A., & Bryant, J. 2014, AAO Newsletter, 126, 15

Buckley, D., Schneider, S. E., & van Blerkom, D. 1993, in IAU Symposium, Vol. 155, Planetary Nebulae, ed. R. Weinberger & A. Acker, 179

Cahn, J. H., Kaler, J. B., & Stanghellini, L. 1992, Astron. Astrophys. Suppl. Ser., 94, 399

Canto, J., Meaburn, J., Theokas, A. C., & Elliott, K. H. 1980, Mon. Not. R. Astron. Soc., 193, 911

Cappellaro, E., Sabbadin, F., Benetti, S., & Turatto, M. 2001, Astron. Astrophys., 377, 1035

Cardelli, J. A., Clayton, G. C., & Mathis, J. S. 1989, Astrophys. J., 345, 245

Carey, S. J., Noriega-Crespo, A., Mizuno, D. R., et al. 2009, Publ. Astron. Soc. Pac., 121, 76

Carney, B. W., Storm, J., & Jones, R. V. 1992, Astrophys. J., 386, 663

Carroll, B. W., & Ostlie, D. A. 2007, An Introduction to Modern Astrophysics (Pearson Addison-Wesley)

Carston, R. 2005, Intercult. Pragmat., 2, 303

Charity, M. 2002, What color are the stars?, viewed 27 May 2015, <http://www.vendian.org/mncharity/dir3/starcolor/>

Chen, B. Q., Schultheis, M., Jiang, B. W., et al. 2013, Astron. Astrophys., 550, A42

Childress, M. J., Vogt, F. P. A., Nielsen, J., & Sharp, R. G. 2014, Astrophys. Space Sci., 349, 617

Chromey, F. R., & Hasselbacher, D. A. 1996, Publ. Astron. Soc. Pac., 108, 944

Chu, Y.-H., Jacoby, G. H., & Arendt, R. 1987, Astrophys. J. Suppl. Ser., 64, 529

Churchwell, E., Watson, D. F., Povich, M. S., et al. 2007, Astrophys. J., 670, 428

Churchwell, E., Babler, B. L., Meade, M. R., et al. 2009, Publ. Astron. Soc. Pac., 121, 213

Chvátal, V. 1979, Math. Oper. Res., 4, 233

Ciardullo, R. 2003, in IAU Symposium, Vol. 209, Planetary Nebulae: Their Evolution and Role in the Universe, ed. S. Kwok, M. Dopita, & R. Sutherland, 617

Ciardullo, R. 2010, Publ. Astron. Soc. Aust., 27, 149

—. 2012, Astrophys. Space Sci., 149

Ciardullo, R., Durrell, P. R., Laychak, M. B., et al. 2004, Astrophys. J., 614, 167

Ciardullo, R., Feldmeier, J. J., Jacoby, G. H., et al. 2002, Astrophys. J., 577, 31

Ciardullo, R., & Jacoby, G. H. 1999, Astrophys. J., 515, 191

Ciardullo, R., Jacoby, G. H., & Ford, H. C. 1989a, Astrophys. J., 344, 715

Ciardullo, R., Jacoby, G. H., Ford, H. C., & Neill, J. D. 1989b, Astrophys. J., 339, 53

Ciardullo, R., Sigurdsson, S., Feldmeier, J. J., & Jacoby, G. H. 2005, Astrophys. J., 629, 499

Cohen, M., Parker, Q. A., Green, A. J., et al. 2007, Astrophys. J., 669, 343

Condon, J. J., Cotton, W. D., Greisen, E. W., et al. 1998, Astron. J., 115, 1693

Condon, J. J., Kaplan, D. L., & Terzian, Y. 1999, Astrophys. J. Suppl. Ser., 123, 219

Corradi, R. L. M., Aznar, R., & Mampaso, A. 1998, Mon. Not. R. Astron. Soc., 297, 617

Corradi, R. L. M., Schönberner, D., Steffen, M., & Perinotto, M. 2003, Mon. Not. R. Astron. Soc., 340, 417

Corradi, R. L. M., & Schwarz, H. E. 1995, Astron. Astrophys., 293, 871

Corradi, R. L. M., Villaver, E., Mampaso, A., & Perinotto, M. 1997, Astron. Astrophys., 324, 276

Cox, A. N., ed. 2000, Allen's Astrophysical Quantities, 4th edn. (New York, NY: Springer Verlag)

Craver, B. N. 1947, J. Assoc. Am. Med. Coll., 22, 298

Croom, S., Saunders, W., & Heald, R. 2004, AAO Newsletter, 106, 12

Crowther, P. A., De Marco, O., & Barlow, M. J. 1998, Mon. Not. R. Astron. Soc., 296, 367

Cuisinier, F., Maciel, W. J., Köppen, J., Acker, A., & Stenholm, B. 2000, Astron. Astrophys., 353, 543

Culverhouse, T., Ade, P., Bock, J., et al. 2011, Astrophys. J. Suppl. Ser., 195, 8

Cutri, R. M., Skrutskie, M. F., van Dyk, S., et al. 2003, VizieR Online Data Catalog, 2246

Czyzak, S. J., Keyes, C. D., & Aller, L. H. 1986, Astrophys. J. Suppl. Ser., 61, 159

Dahlquist, G., & Björck, Å. 2008, Numerical Methods in Scientific Computing, Vol. I (Philadelphia, PA: Society for Industrial and Applied Mathematics)

Daub, C. T. 1982, Astrophys. J., 260, 612

De Marco, O. 2009, Publ. Astron. Soc. Pac., 121, 316

De Marco, O., Crowther, P. A., Barlow, M. J., Clayton, G. C., & de Koter, A. 2001, Mon. Not. R. Astron. Soc., 328, 527

De Marco, O., & Moe, M. 2005, in American Institute of Physics Conference Series, Vol. 804, Planetary Nebulae as Astronomical Tools, ed. R. Szczerba, G. Stasińska, & S. K. Gorny, 169–172

De Marco, O., & Soker, N. 2011, Publ. Astron. Soc. Pac., 123, 402

Delfosse, X., Kahane, C., & Forveille, T. 1997, Astron. Astrophys., 320

DePew, K. D. 2011, PhD thesis, Macquarie University

DePew, K. D., Parker, Q. A., Miszalski, B., et al. 2011, Mon. Not. R. Astron. Soc., 414, 2812

Dickel, H. R., Lortet, M.-C., & de Boer, K. S. 1987, Astron. Astrophys. Suppl. Ser., 68, 75

Dietz, E. D., & Barnes, Jr., W. P. 1968, Astron. J. Suppl., 73, 9

Dopita, M., Hart, J., McGregor, P., et al. 2007, Astrophys. Space Sci., 310, 255

Dopita, M., Rhee, J., Farage, C., et al. 2010, Astrophys. Space Sci., 327, 245

Dopita, M. A., & Hua, C. T. 1997, Astrophys. J. Suppl. Ser., 108, 515

Dopita, M. A., Jacoby, G. H., & Vassiliadis, E. 1992, Astrophys. J., 389, 27

Dopita, M. A., & Meatheringham, S. J. 1990, Astrophys. J., 357, 140

Dopita, M. A., Meatheringham, S. J., Webster, B. L., & Ford, H. C. 1988, Astrophys. J., 327, 639

Drašković, D., Parker, Q. A., Reid, W. A., & Stupar, M. 2015, Mon. Not. R. Astron. Soc., 452, 1402

Dreyer, J. L. E. 1888, Mem. R. Astron. Soc., 49, 1

—. 1895, Mem. R. Astron. Soc., 51, 185

—. 1908, Mem. R. Astron. Soc., 59, 105

Durand, S., Acker, A., & Zijlstra, A. 1998, Astron. Astrophys. Suppl. Ser., 132, 13

Dutra, C. M., & Bica, E. 2000, Astron. Astrophys., 359, L9

—. 2002, Astron. Astrophys., 383, 631

Epchtein, N., de Batz, B., Copet, E., et al. 1994, Astrophys. Space Sci., 217, 3

Ercolano, B., Wesson, R., Zhang, Y., et al. 2004, Mon. Not. R. Astron. Soc., 354, 558

Escudero, A. V., & Costa, R. D. D. 2001, Astron. Astrophys., 380, 300

Escudero, A. V., Costa, R. D. D., & Maciel, W. J. 2004, Astron. Astrophys., 414, 211

Evans, A., Gehrz, R. D., Geballe, T. R., et al. 2003, Astron. J., 126, 1981

Evans, D. S., & Thackeray, A. D. 1950, Mon. Not. R. Astron. Soc., 110, 429

Exter, K. M., Barlow, M. J., & Walton, N. A. 2004, Mon. Not. R. Astron. Soc., 349, 1291

Fanaroff, B. L., & Riley, J. M. 1974, Mon. Not. R. Astron. Soc., 167, 31P

Farage, C. L., & Pimbblet, K. A. 2005, Publ. Astron. Soc. Aust., 22, 249

Fazio, G. G., Hora, J. L., Allen, L. E., et al. 2004, Astrophys. J. Suppl. Ser., 154, 10

Feibelman, W. A. 1983, Astron. Astrophys., 122, 335

Ferland, K. 2008, Discrete Mathematics (Boston, MA: Cengage Learning)

Ferrario, L., Wickramasinghe, D., Liebert, J., & Williams, K. A. 2005, Mon. Not. R. Astron. Soc., 361, 1131

Foellmi, C. 2009, AstroBetter – Tips and Tricks for Professional Astronomers, viewed 10 February 2014, <www.astrobetter.com/qlfits-the-quick-look-generator-for-fits-files/>

Frank, A. 1999, New Astron. Rev., 43, 31

Freudling, W. 1995, Publ. Astron. Soc. Pac., 107, 85

Frew, D. J. 2008, PhD thesis, Department of Physics, Macquarie University, NSW 2109, Australia

Frew, D. J., Bojičić, I. S., Parker, Q. A., et al. 2014, Mon. Not. R. Astron. Soc., 440, 1080

Frew, D. J., & Parker, Q. A. 2010, Publ. Astron. Soc. Aust., 27, 129

Fruchter, A., & Hook, R. N. 1997, in SPIE Conference Series, Vol. 3164, Applications of Digital Image Processing XX, ed. A. G. Tescher, 120–125

Gabriel, E., et al. 2004, in Proc. 11th European PVM/MPI Users' Group Meeting, Budapest, Hungary, 97–104

Gaensler, B. M. 1998, Astrophys. J., 493, 781

Gathier, R., Pottasch, S. R., Goss, W. M., & van Gorkom, J. H. 1983, Astron. Astrophys., 128, 325

Geier, S., Edelmann, H., Heber, U., & Morales-Rueda, L. 2009, Astrophys. J., 702, L96

Gennaro, M., Bik, A., Brandner, W., et al. 2012, Astron. Astrophys., 542, A74

Gerhard, O. 2006, in IAU Symposium, Vol. 234, Planetary Nebulae in our Galaxy and Beyond, ed. M. J. Barlow & R. H. Méndez, 25–32

Gieren, W., Storm, J., Nardetto, N., et al. 2013, in IAU Symposium, Vol. 289, Advancing the Physics of Cosmic Distances, ed. R. de Grijs, 138–144

Gill, C. D., & O'Brien, T. J. 1998, Mon. Not. R. Astron. Soc., 300, 221

Glass, I. S. 1978, Mon. Not. Astron. Soc. South. Africa, 37, 4

—. 1989, Q. Jl R. astr. Soc., 30, 33

Golriz, S. S., Blommaert, J. A. D. L., Vanhollebeke, E., et al. 2014, Mon. Not. R. Astron. Soc., 443, 3402

Górny, S. K., Chiappini, C., Stasińska, G., & Cuisinier, F. 2009, Astron. Astrophys., 500, 1089

Górny, S. K., Stasińska, G., Escudero, A. V., & Costa, R. D. D. 2004, Astron. Astrophys., 427, 231

Gray, R. O., & Corbally, J., C. 2009, Stellar Spectral Classification, Princeton Series in Astrophysics (Princeton, NJ: Princeton University Press)

Green, A. J. 2002, in IAU Symposium, Vol. 199, The Universe at Low Radio Frequencies, ed. A. Pramesh Rao, G. Swarup, & Gopal-Krishna, 259

Greisen, E. W., & Calabretta, M. R. 2002, Astron. Astrophys., 395, 1061

Griesmann, U., & Kling, R. 2000, Astrophys. J. Lett., 536, L113

Grinin, V. P., & Zvereva, A. M. 1968, Astrophysics, 4, 43

Gromadzki, M., Mikołajewska, J., Whitelock, P., & Marang, F. 2009, Acta Astronom., 59, 169

Groom, D. 2004, in Astrophysics and Space Science Library, Vol. 300, Scientific Detectors for Astronomy, The Beginning of a New Era, ed. P. Amico, J. W. Beletic, & J. E. Belectic, 81–93

Grünbaum, B. 1975, Math. Mag., 48, 12

Gurzadyan, G. A. 1997, The Physics and Dynamics of Planetary Nebulae, Astronomy and Astrophysics Library (Heidelberg, Germany: Springer)

Guthrie, B. N. G. 1985, Mon. Not. R. Astron. Soc., 215, 545

Habing, H. J. 1996, Astron. Astrophys. Rev., 7, 97

Hager, G., & Wellein, G. 2010, Introduction to High Performance Computing for Scientists and Engineers, Chapman & Hall/CRC Computational Science Series (Boca Raton, FL: CRC Press, Taylor & Francis Group)

Hamann, W.-R., Peña, M., Gräfener, G., & Ruiz, M. T. 2003, Astron. Astrophys., 409, 969

Hambly, N. C., MacGillivray, H. T., Read, M. A., et al. 2001, Mon. Not. R. Astron. Soc., 326, 1279

Hanuschik, R. W. 2003, Astron. Astrophys., 407, 1157

Harland, D. M. 2007, Cassini at Saturn: Huygens Results, Springer-Praxis Books in Space Exploration (Berlin: Springer)

Haro, G. 1952, Bol. Obs. Tonantzintla y Tacubaya, 1, 1

Hartl, H., & Tritton, S. B. 1985, Astron. Astrophys., 145, 41

Hartley, M., & Dawe, J. A. 1981, Proc. Astron. Soc. Aust., 4, 251

Haynes, R., Haynes, R. D., & Malin, D. 1996, Explorers of the Southern Sky, A History of Australian Astronomy (Press Syndicate of the University of Cambridge)

Haynes, W. M., ed. 2014, CRC Handbook of Chemistry and Physics, 95th edn. (Boca Raton, FL: CRC Press, Taylor & Francis Group)

Hearn, D., & Baker, M., P. 2004, Computer Graphics with OpenGL, 3rd edn. (Upper Saddle River, NJ: Pearson Prentice Hall)

Heijmans, J., Asplund, M., Barden, S., et al. 2012, in SPIE Conference Series, Vol. 8446, Ground-based and Airborne Instrumentation for Astronomy IV, ed. I. S. McLean, S. K. Ramsay, & H. Takami, Bellingham, WA, 0W

Helou, G., & Walker, D. W., eds. 1988, Infrared astronomical satellite (IRAS) catalogs and atlases. Volume 7: The small scale structure catalog, NASA Reference Publication No. 1190 (NASA Scientific and Technical Information Division)

Hempel, R., & Walker, D. W. 1999, Computer Standards & Interfaces, 21, 51

Henize, K. G. 1956, Astrophys. J. Suppl. Ser., 2, 315

—. 1967, Astrophys. J. Suppl. Ser., 14, 125

Henize, K. G., & Westerlund, B. E. 1963, Astrophys. J., 137, 747

Henry, R. B. C. 1990, Astrophys. J., 356, 229

Hernández-Martínez, L., Peña, M., & Carigi, L. 2006, in IAU Symposium, Vol. 234, Planetary Nebulae in our Galaxy and Beyond, ed. M. J. Barlow & R. H. Méndez, 419–420

Herschel, J. F. W. 1834, A Treatise on Astronomy (Philadelphia, PA: Carey, Lea and Blanchard)

Herschel, W. 1785, Royal Society of London Philosophical Transactions Series I, 75, 213

Herwig, F. 2005, Annu. Rev. Astron. Astrophys., 43, 435

Hester, J., Burstein, D., Blumenthal, G., et al. 2002, 21st century astronomy, 1st edn. (New York, NY: Norton)

Hicks, M. D., & Buratti, B. J. 2004, Icarus, 171, 210

Hoare, C. A. R. 1961, Commun. ACM, 4, 321

—. 1962, Comput. J., 5, 10

Honey, W. B., Charles, P. A., Whitehurst, R., Barrett, P. E., & Smale, A. P. 1988, Mon. Not. R. Astron. Soc., 231, 1

Hopkinson, G. R., Goodman, T. M., & Prince, S. R. 2004, A Guide to the Use and Calibration of Detector Array Equipment (Bellingham, WA: The International Society for Optical Engineering)

Hora, J. L., Cohen, M., Ellis, R. G., et al. 2008, Astron. J., 135, 726

Hovey, G. 1974, PhD thesis, Australian National University

Howell, S. B. 2006, Cambridge Observing Handbooks for Research Astronomers, Vol. 5, Handbook of CCD Astronomy, 2nd edn. (Cambridge, UK: Cambridge University Press)

Hubbell, G. R. 2013, Scientific Astrophotography, Patrick Moore's Practical Astronomy Series (New York, NY: Springer)

Hubble, E. 1921, Publ. Astron. Soc. Pac., 33, 174

Huggins, W., & Miller, W. A. 1864, Philos. T. R. Soc. Lond., 154, 437

Humason, M. L., & Zwicky, F. 1947, Astrophys. J., 105, 85

Husemann, B., Kamann, S., Sandin, C., et al. 2012, Astron. Astrophys., 545, A137

Iben, Jr., I., & Laughlin, G. 1989, Astrophys. J., 341, 312

Ishida, K., & Weinberger, R. 1987, Astron. Astrophys., 178, 227

Ivanov, V. D., & Szeifert, T. 2015, VIRCAM/VISTA User Manual, 96.0 edn., European Southern Observatory, Karl-Schwarzschild Str. 2, D-85748, Garching bei München, Germany

Jacobson, R. A. 2009, Astron. J., 137, 4322

Jacoby, G. H. 1989, Astrophys. J., 339, 39

Jacoby, G. H. 1997, in IAU Symposium, Vol. 180, Planetary Nebulae, ed. H. J. Habing & H. J. G. L. M. Lamers, 448

Jacoby, G. H. 2006, in Planetary Nebulae Beyond the Milky Way, ed. L. Stanghellini, J. R. Walsh, & N. G. Douglas, 17

Jacoby, G. H., Africano, J. L., & Quigley, R. J. 1987, Publ. Astron. Soc. Pac., 99, 672

Jacoby, G. H., & Ciardullo, R. 1999, Astrophys. J., 515, 169

Jacoby, G. H., Ciardullo, R., & Feldmeier, J. J. 1999, in Astronomical Society of the Pacific Conference Series, Vol. 167, Harmonizing Cosmic Distance Scales in a Post-HIPPARCOS Era, ed. D. Egret & A. Heck, 175–191

Jacoby, G. H., Ciardullo, R., & Walker, A. R. 1990, Astrophys. J., 365, 471

Jacoby, G. H., & De Marco, O. 2002, Astron. J., 123, 269

Jacoby, G. H., De Marco, O., & Sawyer, D. G. 1998, Astron. J., 116, 1367

Jacoby, G. H., Morse, J. A., Fullton, L. K., Kwitter, K. B., & Henry, R. B. C. 1997, Astron. J., 114, 2611

Jacoby, G. H., & Van de Steene, G. 2004, Astron. Astrophys., 419, 563

Jacoby, G. H., Branch, D., Ciardullo, R., et al. 1992, Publ. Astron. Soc. Pac., 104, 599

Jacoby, G. H., Kronberger, M., Patchick, D., et al. 2010, Publ. Astron. Soc. Aust., 27, 156

Jarrett, T. H., Cohen, M., Masci, F., et al. 2011, Astrophys. J., 735, 112

Jaschek, C., & Jaschek, M. 1995, The Behavior of Chemical Elements in Stars (Cambridge, UK: Cambridge University Press)

Jewett, J., & Serway, R. 2006, Principles of physics: a calculus-based text (Brooks/Cole)

Jewitt, D. C., Danielson, G. E., & Kupferman, P. N. 1986, Astrophys. J., 302, 727

Jones, D., Mitchell, D. L., Lloyd, M., et al. 2012, Mon. Not. R. Astron. Soc., 420, 2271

Jones, D., Tyndall, A. A., Huckvale, L., Prouse, B., & Lloyd, M. 2011, in Astronomical Society of the Pacific Conference Series, Vol. 447, Evolution of Compact Binaries, ed. L. Schmidtobreick, M. R. Schreiber, & C. Tappert, 165

Jones, D., Lloyd, M., Santander-García, M., et al. 2010, Mon. Not. R. Astron. Soc., 408, 2312

Jordan, S., Werner, K., & O'Toole, S. J. 2005, Astron. Astrophys., 432, 273

Joye, W. A., & Mandel, E. 2003, in Astronomical Society of the Pacific Conference Series, Vol. 295, Astronomical Data Analysis Software and Systems XII, ed. H. E. Payne, R. I. Jedrzejewski, & R. N. Hook, 489

Kaler, J. B. 1986, Astrophys. J., 308, 322

Kaler, J. B., & Jacoby, G. H. 1991, Astrophys. J., 382, 134

Kaler, J. B., & Lutz, J. H. 1985, Publ. Astron. Soc. Pac., 97, 700

Kaler, J. B., Shaw, R. A., & Browning, L. 1997, Publ. Astron. Soc. Pac., 109, 289

Kaler, J. B., Shaw, R. A., & Kwitter, K. B. 1990, Astrophys. J., 359, 392

Kalirai, J. S., Hansen, B. M. S., Kelson, D. D., et al. 2008, Astrophys. J., 676, 594

Kaufman, V., & Martin, W. C. 1993, J. Phys. Chem. Ref. Data, 22, 279

Kaufman, V., & Sugar, J. 1986, J. Phys. Chem. Ref. Data, 15, 321

Keenan, P. C. 1954, Astrophys. J., 120, 484

Kelleher, D. E., & Podobedova, L. I. 2008, J. Phys. Chem. Ref. Data, 37, 267

Kenyon, S. J., & Fernandez-Castro, T. 1987, Astron. J., 93, 938

Kern, U. 2007, Extending LaTeX's color facilities: the xcolor package, viewed 4 February 2015, <http://mirrors.ctan.org/macros/latex/contrib/xcolor/xcolor.pdf>

Kilkenny, D. 1995, The Observatory, 115, 25

Kilkenny, D., & Worters, H. 2014, The SAAO 1.9-m Telescope and Grating Spectrograph, 6.5 edn., South African Astronomical Observatory, Observatory Road, Observatory, 7925, South Africa

Kimeswenger, S. 2001, Rev. Mex. Astron. Astr., 37, 115

Kimura, R. K., Gruenwald, R., & Aleman, I. 2012, Astron. Astrophys., 541, A112

Kingsburgh, R. L., & English, J. 1992, Mon. Not. R. Astron. Soc., 259, 635

Kirkpatrick, J. D., Cushing, M. C., Gelino, C. R., et al. 2011, Astrophys. J. Suppl. Ser., 197, 19

Kistiakowsky, V., & Helfand, D. J. 1995, Astron. J., 110, 2225

Kitchin, C. R. 1995, Optical astronomical spectroscopy (Bristol, UK: IOP Publishing)

—. 2014, Astrophysical Techniques, 6th edn. (Boca Raton, FL: CRC Press, Taylor & Francis Group)

Kniazev, A. Y., Grebel, E. K., Zucker, D. B., et al. 2014, Astron. J., 147, 16

Kohoutek, L. 2001, Astron. Astrophys., 378, 843

—. 2002, Astronomische Nachrichten, 323, 57

Kohoutek, L., Pěkný, Z., & Perek, L. 1965, B. Astron. I. Czech., 16, 189

Können, G. P., Muller, S. H., & Tinbergen, J. 1994, Appl. Optics, 33, 4569

Kovacevic, A. 2011, PhD thesis, Macquarie University

Kovacevic, A. V., Parker, Q. A., Jacoby, G. H., & Miszalski, B. 2011a, in Proc. Asymmetric Planetary Nebulae V, ed. A. A. Zijlstra, F. Lykou, I. McDonald, & E. Lagadec (Manchester, UK: Jodrell Bank Centre for Astrophysics), 44

Kovacevic, A. V., Parker, Q. A., Jacoby, G. H., et al. 2011b, Mon. Not. R. Astron. Soc., 414, 860

Krabbe, A. C., & Copetti, M. V. F. 2005, Astron. Astrophys., 443, 981

Kramida, A., Ralchenko, Y., Reader, J., & NIST ASD Team. 2014, NIST Atomic Spectra Database (ver. 5.2), viewed 23 February 2015, <http://physics.nist.gov/asd>. National Institute of Standards and Technology, Gaithersburg, MD.

Kunder, A., Popowski, P., Cook, K. H., & Chaboyer, B. 2008, Astron. J., 135, 631

Kwok, S. 2000, The Origin and Evolution of Planetary Nebulae, Cambridge Astrophysics Series (Cambridge, UK: Cambridge University Press)

—. 2007, Physics and Chemistry of the Interstellar Medium (University Science Books)

Kwok, S., Chong, S.-N., Hsia, C.-H., Zhang, Y., & Koning, N. 2010, Astrophys. J., 708, 93

Kwong, V. H. S., Fang, Z., Gibbons, T. T., Parkinson, W. H., & Smith, P. L. 1993, Astrophys. J., 411, 431

Laher, R. R., Gorjian, V., Rebull, L. M., et al. 2012, Publ. Astron. Soc. Pac., 124, 737

Lasker, B. M., Lattanzi, M. G., McLean, B. J., et al. 2008, Astron. J., 136, 735

Lawrence, A., Warren, S. J., Almaini, O., et al. 2007, Mon. Not. R. Astron. Soc., 379, 1599

Leisy, P., & Dennefeld, M. 2006, Astron. Astrophys., 456, 451

Leverington, D. 2013, Encyclopedia of the History of Astronomy and Astrophysics (New York, NY: Cambridge University Press)

Lewis, I. J., Cannon, R. D., Taylor, K., et al. 2002, Mon. Not. R. Astron. Soc., 333, 279

Lindegren, L., Lammers, U., Hobbs, D., et al. 2012, Astron. Astrophys., 538, A78

Lindsay, E. M. 1961, Astron. J., 66, 169

Lindsay, E. M., & Mullan, D. J. 1963, Irish Astronomical Journal, 6, 51

Longair, M. S., Stewart, J. M., & Williams, P. M. 1986, Q. Jl R. astr. Soc., 27, 153

López-Sánchez, Á. R. 2006, PhD thesis, La Laguna University

Loubser, S. I. 2005, Master's thesis, North-West University, Potchefstroom Campus

Lubanovic, B. 2014, Introducing Python: Modern Computing in Simple Packages, 1st edn. (Sebastopol, CA: O'Reilly Media)

Lynch, D. K., & Schwartz, P. 1985, Journal of the Optical Society of America A, 2, 584

Maciel, W. J., & Costa, R. D. D. 2003, in IAU Symposium, Vol. 209, Planetary Nebulae: Their Evolution and Role in the Universe, ed. S. Kwok, M. Dopita, & R. Sutherland, 551

Maciel, W. J., & Costa, R. D. D. 2011, in Asymmetric Planetary Nebulae 5 Conference, ed. A. A. Zijlstra, F. Lykou, E. Lagadec, & I. McDonald

Maciel, W. J., Rocha-Pinto, H. J., & Costa, R. D. D. 2012, in IAU Symposium, Vol. 284, IAU Symposium, ed. R. J. Tuffs & C. C. Popescu, 379–381

Mak, R. 2003, Java Number Cruncher: The Java Programmer's Guide to Numerical Computing (Upper Saddle River, NJ: Prentice Hall PTR)

Manchado, A., Villaver, E., Stanghellini, L., & Guerrero, M. A. 2000, in Astronomical Society of the Pacific Conference Series, Vol. 199, Asymmetrical Planetary Nebulae II: From Origins to Microstructures, ed. J. H. Kastner, N. Soker, & S. Rappaport, 17

Marigo, P., Girardi, L., Weiss, A., Groenewegen, M. A. T., & Chiosi, C. 2004, Astron. Astrophys., 423, 995

Marinilli, M. 2002, Java Deployment with JNLP and WebStart (Indianapolis, IN: Sams Publishing)

Martin, W. C., Kaufman, V., & Musgrove, A. 1993, J. Phys. Chem. Ref. Data, 22, 1179

Massey, P. 1997, A User's Guide to CCD Reductions with IRAF, National Optical Astronomy Observatory, 950 North Cherry Ave., Tuscon, AZ 85719, USA

Massey, P., Valdes, F., & Barnes, J. 1992, A User's Guide to Reducing Slit Spectra with IRAF, National Optical Astronomy Observatory, 950 North Cherry Ave., Tuscon, AZ 85719, USA

Mathewson, D. S., Hart, J., Wehner, H. P., Hovey, G. R., & van Harmelen, J. 2013, J. Astron. Hist. Herit., 16, 2

Mathis, J. S. 1990, Annu. Rev. Astron. Astrophys., 28, 37

McGregor, P. J., Conroy, P., van Harmelen, J., & Bessell, M. S. 2000, Publ. Astron. Soc. Aust., 17, 102

McMaster, M., & et al. 2008, Wide Field and Planetary Camera 2 Instrument Handbook, version 10.0, STScI, 3700 San Martin Dr., Baltimore, MD 21218, USA

McNamara, D. H., Madsen, J. B., Barnes, J., & Ericksen, B. F. 2000, Publ. Astron. Soc. Pac., 112, 202

Meatheringham, S. J., & Dopita, M. A. 1991, Astrophys. J. Suppl. Ser., 75, 407

Meatheringham, S. J., Dopita, M. A., Ford, H. C., & Webster, B. L. 1988, Astrophys. J., 327, 651

Medina, S., Peña, M., Morisset, C., & Stasińska, G. 2006, Rev. Mex. Astron. Astr., 42, 53

Mellema, G. 2004, Astron. Astrophys., 416, 623

Melnick, G., & Harwit, M. 1975, Mon. Not. R. Astron. Soc., 171, 441

Messier, C. 1781, in Connaissance des Temps de 1784 (Imprimerie royale), 227–269

Mignard, F. 1997, in ESA Special Publication, Vol. 402, Hipparcos - Venice '97, ed. R. M. Bonnet, E. Høg, P. L. Bernacca, L. Emiliani, A. Blaauw, C. Turon, J. Kovalevsky, L. Lindegren, H. Hassan, M. Bouffard, B. Strim, D. Heger, M. A. C. Perryman, & L. Woltjer, 5–10

Miller, S. D., Haddock, S. H. D., Elvidge, C. D., & Lee, T. F. 2006, Int. J. Remote Sens., 27, 5131

Mink, D. J., & Wyatt, W. F. 1995, in Astronomical Society of the Pacific Conference Series, Vol. 77, Astronomical Data Analysis Software and Systems IV, ed. R. A. Shaw, H. E. Payne, & J. J. E. Hayes, 496

Minkowski, R. 1947, Publ. Astron. Soc. Pac., 59, 257

—. 1948, Publ. Astron. Soc. Pac., 60, 386

—. 1964, Publ. Astron. Soc. Pac., 76, 197

Minniti, D., Lucas, P., Adamson, A., et al. 2006, Mem. S. A. It., 77, 1184

Minniti, D., Lucas, P. W., Emerson, J. P., et al. 2010, New Astron., 15, 433

Miszalski, B. 2009, PhD thesis, Macquarie University

Miszalski, B., Acker, A., Moffat, A. F. J., Parker, Q. A., & Udalski, A. 2009a, Astron. Astrophys., 496, 813

Miszalski, B., Acker, A., Parker, Q. A., & Moffat, A. F. J. 2009b, Astron. Astrophys., 505, 249

Miszalski, B., Crowther, P. A., De Marco, O., et al. 2012a, Mon. Not. R. Astron. Soc., 423, 934

Miszalski, B., Mikołajewska, J., & Udalski, A. 2013, Mon. Not. R. Astron. Soc., 432, 3186

Miszalski, B., Napiwotzki, R., Cioni, M.-R. L., et al. 2012b, in IAU Symposium, Vol. 283, IAU Symposium, 444–445

Miszalski, B., Parker, Q. A., Acker, A., et al. 2008, Mon. Not. R. Astron. Soc., 384, 525

Mizuno, D. R., Kraemer, K. E., Flagey, N., et al. 2010, Astron. J., 139, 1542

Moe, M., & De Marco, O. 2006, Astrophys. J., 650, 916

Monk, D. J., Barlow, M. J., & Clegg, R. E. S. 1988, Mon. Not. R. Astron. Soc., 234, 583

Moore, C. E. 1972, A Multiplet Table of Astrophysical Interest, revised edn., National Standard Reference Data Series - National Bureau of Standards (Washington, DC: US Government Printing Office)

—. 1975, Selected Tables of Atomic Spectra. A: Atomic Energy Levels - Second Edition. B: Multiplet Tables. N I, N II, N III—Data derived from the analyses of optical spectra, National Standard Reference Data Series - National Bureau of Standards, Section 5 (Washington, DC: US Government Printing Office)

—. 1976, Selected Tables of Atomic Spectra. A: Atomic Energy Levels - Second Edition. B: Multiplet Tables. O I—Data derived from the analyses of optical spectra, National Standard Reference Data Series - National Bureau of Standards, Section 7 (Washington, DC: US Government Printing Office)

—. 1993, Tables of Spectra of Hydrogen, Carbon, Nitrogen, and Oxygen Atoms and Ions, CRC Series in Evaluated Data in Atomic Physics (Boca Raton, FL: CRC Press, Taylor & Francis Group)

Moore, P. 2000, The Data Book of Astronomy (Bristol, UK: Institue of Physics Publishing)

Moore, P., & Rees, R. 2011, Patrick Moore's Data Book of Astronomy, 2nd edn. (Cambridge University Press)

Morgan, D. H., & Parker, Q. A. 1998, Mon. Not. R. Astron. Soc., 296, 921

Morgan, D. H., Parker, Q. A., & Cohen, M. 2003, Mon. Not. R. Astron. Soc., 346, 719

Morrissey, P., Conrow, T., Barlow, T. A., et al. 2007, Astrophys. J. Suppl. Ser., 173, 682

Muller, G. P., Reed, R., Armandroff, T., Boroson, T. A., & Jacoby, G. H. 1998, in SPIE Conference Series, Vol. 3355, Optical Astronomical Instrumentation, ed. S. D'Odorico, 577–585

Munari, U., & Zwitter, T. 2002, Astron. Astrophys., 383, 188

Murakami, H., Baba, H., Barthel, P., et al. 2007, Publ. Astron. Soc. Jpn., 59, 369

Nataf, D. M., Gould, A., Fouqué, P., et al. 2013, Astrophys. J., 769, 88

Neugebauer, G., Habing, H. J., van Duinen, R., et al. 1984, Astrophys. J. Lett., 278, L1

Nidever, D. L., Zasowski, G., & Majewski, S. R. 2012, Astrophys. J. Suppl. Ser., 201, 35

Nielsen, J., & Hovey, G. 2010, in Astronomical Society of the Pacific Conference Series, Vol. 434, Astronomical Data Analysis Software and Systems XIX, ed. Y. Mizumoto, K.-I. Morita, & M. Ohishi, 345

Nordhaus, J., & Blackman, E. G. 2006, Mon. Not. R. Astron. Soc., 370, 2004

Norton, A. J., ed. 2004, Observing the Universe: A Guide to Observational Astronomy and Planetary Science (Cambridge, UK: Cambridge University Press)

O'Brien, K. 2008, FORS User Manual, 82nd edn., European Southern Observatory, Karl-Schwarzschild Str. 2, D-85748, Garching bei München, Germany

Ochsenbein, F., Bauer, P., & Marcout, J. 2000, Astron. Astrophys. Suppl. Ser., 143, 23

O'Dell, C. R., Balick, B., Hajian, A. R., Henney, W. J., & Burkert, A. 2002, Astron. J., 123, 3329

Ortiz, R., Copetti, M. V. F., & Lorenz-Martins, S. 2011, Mon. Not. R. Astron. Soc., 418, 2004

Oster, L. 1961, Astrophys. J., 134, 1010

Osterbrock, D. E., Capriotti, E. R., & Bautz, L. P. 1963, Astrophys. J., 138, 62

Osterbrock, D. E., & Ferland, G. J. 2006, Astrophysics of gaseous nebulae and active galactic nuclei, 2nd edn. (Sausalito, CA: University Science Books)

Osterbrock, D. E., Tran, H. D., & Veilleux, S. 1992, Astrophys. J., 389, 305

Parker, Q., Bojicic, I., Frew, D., et al. 2014, in Proc. Asymmetrical Planetary Nebulae VI, ed. C. Morisset, G. Delgado-Inglada, & S. Torres-Peimbert, id. 69

Parker, Q. A., & Bland-Hawthorn, J. 1998, Publ. Astron. Soc. Aust., 15, 33

Parker, Q. A., Frew, D. J., Miszalski, B., et al. 2011a, in Asymmetric Planetary Nebulae 5 Conference, ed. A. A. Zijlstra, F. Lykou, E. Lagadec, & I. McDonald

Parker, Q. A., Frew, D. J., Miszalski, B., et al. 2011b, Mon. Not. R. Astron. Soc., 413, 1835

Parker, Q. A., Phillipps, S., Pierce, M. J., et al. 2005, Mon. Not. R. Astron. Soc., 362, 689

Parker, Q. A., Acker, A., Frew, D. J., et al. 2006, Mon. Not. R. Astron. Soc., 373, 79

Patris, J. 2010, in EPJ Web of Conferences, Vol. 9, ERCA 9 - From the Global Mercury Cycle to the Discoveries of Kuiper Belt Objects, ed. C. Boutron (EDP Sciences), 215

Peña, M., Peimbert, M., Torres-Peimbert, S., Ruiz, M. T., & Maza, J. 1995, Astrophys. J., 441, 343

Peña, M., Ruiz, M. T., & Torres-Peimbert, S. 1997, Astron. Astrophys., 324, 674

Pease, F. G. 1928, Publ. Astron. Soc. Pac., 40, 342

Peimbert, M. 1978, in IAU Symposium, Vol. 76, Planetary Nebulae, ed. Y. Terzian, 215–223

Pence, W. 1998, in Astronomical Society of the Pacific Conference Series, Vol. 145, Astronomical Data Analysis Software and Systems VII, ed. R. Albrecht, R. N. Hook, & H. A. Bushouse, 97

Pence, W., Xu, J., & Brown, L. 1997, in Astronomical Society of the Pacific Conference Series, Vol. 125, Astronomical Data Analysis Software and Systems VI, ed. G. Hunt & H. Payne, 261

Petitjean, P., & Aracil, B. 2004, Astron. Astrophys., 422, 523

Phillips, J. P. 1997, Astron. Astrophys., 325, 755

Phillips, J. P., Cuesta, L. C., & Ramos-Larios, G. 2010, Mon. Not. R. Astron. Soc., 409, 881

Phillips, J. P., & Zepeda-García, D. 2009, Mon. Not. R. Astron. Soc., 394, 1875

Pickering, E. C. 1880, Nature, 22, 327

—. 1882a, Astron. Nachr., 103, 95

—. 1882b, Astron. Nachr., 103, 165

Pollacco, D. L., & Bell, S. A. 1994, Mon. Not. R. Astron. Soc., 267, 452

Pottasch, S. R. 1990, Astron. Astrophys., 236, 231

—. 1996, Astron. Astrophys., 307, 561

Pottasch, S. R., & Bernard-Salas, J. 2013, Astron. Astrophys., 550, A35

Pottasch, S. R., Goss, W. M., Gathier, R., & Arnal, E. M. 1982, Astron. Astrophys., 106, 229

Preite-Martinez, A. 1988, Astron. Astrophys. Suppl. Ser., 76, 317

Price, S. D., Egan, M. P., Carey, S. J., Mizuno, D. R., & Kuchar, T. A. 2001, Astron. J., 121, 2819

Proxauf, B., Öttl, S., & Kimeswenger, S. 2014, Astron. Astrophys., 561, A10

Pych, W. 2004, Publ. Astron. Soc. Pac., 116, 148

Reader, J. 2004, Appl. Spectrosc., 58, 1469

Reed, D. S., Balick, B., Hajian, A. R., et al. 1999, Astron. J., 118, 2430

Rees, B., & Zijlstra, A. A. 2013, Mon. Not. R. Astron. Soc., 435, 975

Reid, M. J. 1993, Annu. Rev. Astron. Astrophys., 31, 345

Reid, W. A. 2007, PhD thesis, Macquarie University

Reid, W. A., & Parker, Q. A. 2006a, Mon. Not. R. Astron. Soc., 365, 401

—. 2006b, Mon. Not. R. Astron. Soc., 373, 521

—. 2010, Publ. Astron. Soc. Aust., 27, 187

Rhoads, J. E. 2000, Publ. Astron. Soc. Pac., 112, 703

Richer, M. G., Stasińska, G., & McCall, M. L. 1999, Astron. Astrophys. Suppl. Ser., 135, 203

Riley, J. 2006, Writing Fast Programs: A Practical Guide for Scientists and Engineers (Cambridge, UK: Cambridge International Science Publishing)

Robitaille, T. P., Meade, M. R., Babler, B. L., et al. 2008, Astron. J., 136, 2413

Rodríguez-González, A., Hernández-Martínez, L., Esquivel, A., et al. 2015, Astron. Astrophys., 575, A1

Rudy, R. J. 1979, Mon. Not. R. Astron. Soc., 186, 473

Ruffle, P. M. E., Zijlstra, A. A., Walsh, J. R., et al. 2004, Mon. Not. R. Astron. Soc., 353, 796

Ryan, S. G., & Wood, P. R. 1995, Publ. Astron. Soc. Aust., 12, 89

Sabin, L., Zijlstra, A. A., Wareing, C., et al. 2010, Publ. Astron. Soc. Aust., 27, 166

Sabin, L., Parker, Q. A., Corradi, R. L. M., et al. 2014, Mon. Not. R. Astron. Soc., 443, 3388

Sage, L., & Aschenbrenner, G. 2004, A Visitor's Guide to the Kitt Peak Observatories (Cambridge, UK: Cambridge University Press)

Sahai, R., Morris, M. R., & Villar, G. G. 2011, Astron. J., 141, 134

Saito, R. K., Hempel, M., Minniti, D., et al. 2012, Astron. Astrophys., 537, A107

Salaris, M., & Cassisi, S. 2005, Evolution of Stars and Stellar Populations (Chichester, UK: Wiley)

Saloman, E. B. 2010, J. Phys. Chem. Ref. Data, 39, 033101

Sambhus, N., Gerhard, O., & Méndez, R. H. 2006, Astron. J., 131, 837

Sanduleak, N., MacConnell, D. J., & Philip, A. G. D. 1978, Publ. Astron. Soc. Pac., 90, 621

Sansonetti, J. E., & Martin, W. C. 2005, J. Phys. Chem. Ref. Data, 34, 1559

Saunders, W., Bridges, T., Gillingham, P., et al. 2004, in SPIE Conference Series, Vol. 5492, Ground-based Instrumentation for Astronomy, ed. A. F. M. Moorwood & M. Iye, 389–400

Schaller, G., Schaerer, D., Meynet, G., & Maeder, A. 1992, Astron. Astrophys. Suppl. Ser., 96, 269

Schlegel, D. J., Finkbeiner, D. P., & Davis, M. 1998, Astrophys. J., 500, 525

Schmid, H. M. 1989, Astron. Astrophys., 211, L31

Schmid, H. M., Krautter, J., Appenzeller, I., et al. 1999, Astron. Astrophys., 348, 950

Schmidt, R. E. 2006, in Astrophysics and Space Science Library, Vol. 336, Scientific Detectors for Astronomy 2005, ed. J. E. Beletic, J. W. Beletic, & P. Amico (Springer), 353

Schmitz, M., Helou, G., Dubois, P., et al. 1995, in Astrophysics and Space Science Library, Vol. 203, Information & On-Line Data in Astronomy, ed. D. Egret & M. A. Albrecht (Kluwer Acad. Publ.), 259–270

Schönberner, D., Jacob, R., & Steffen, M. 2005, Astron. Astrophys., 441, 573

Schönberner, D., Jacob, R., Steffen, M., & Sandin, C. 2007, Astron. Astrophys., 473, 467

Schulz, H. 2005, TUGboat, 26, 239

Schwarz, H. E., Corradi, R. L. M., & Stanghellini, L. 1993, in IAU Symposium, Vol. 155, Planetary Nebulae, ed. R. Weinberger & A. Acker, 214

Schweiker, H. 2014, NOAO KPNO Mosaic-1.1 Imager - Filters, viewed 21 February 2015, <http://www.noao.edu/kpno/mosaic/filters/filters.html>

Scott, D. W. 2015, Multivariate Density Estimation: Theory, Practice, and Visualization, 2nd edn. (Hoboken, NJ: John Wiley and Sons)

Scrimger, J. N. 1984, Astrophys. J., 280, 170

Seaton, M. J. 1960, Rep. Prog. Phys., 23, 313

—. 1979, Mon. Not. R. Astron. Soc., 187, 785

Seidelmann, P. K., Archinal, B. A., A'Hearn, M. F., et al. 2007, Celestial Mechanics and Dynamical Astronomy, 98, 155

Shapley, H. 1936, Harvard. Bull., 902, 26

Sharp, R., & Parkinson, H. 2010, Mon. Not. R. Astron. Soc., 408, 2495

Sharp, R., Saunders, W., Smith, G., et al. 2006, in SPIE Conference Series, Vol. 6269, Ground-based and Airborne Instrumentation for Astronomy, ed. I. S. McLean & M. Iye, 0G

Shaw, R. A., & Horne, K. 1992, in Astronomical Society of the Pacific Conference Series, Vol. 25, Astronomical Data Analysis Software and Systems I, ed. D. M. Worrall, C. Biemesderfer, & J. Barnes, 311

Shaw, R. A., & Kaler, J. B. 1989, Astrophys. J. Suppl. Ser., 69, 495

Shaw, R. A., Stanghellini, L., Mutchler, M., Balick, B., & Blades, J. C. 2001, Astrophys. J., 548, 727

Shklovskii, I. S. 1957, Sov. Astron., 1, 397

Shklovsky, I. S. 1951, Trudy Astron. Inst. Sternberga, 20, 5

Simons, D. A., Amico, P., Baade, D., et al. 2006, in Astrophysics and Space Science Library, Vol. 336, Scientific Detectors for Astronomy 2005, ed. J. E. Beletic, J. W. Beletic, & P. Amico (Springer), 13

Skrutskie, M. F., Cutri, R. M., Stiening, R., et al. 2006, Astron. J., 131, 1163

Slavík, P. 1997, J. Algorithms, 25, 237

Smith, A. R., McDonald, R. J., Hurley, D. C., et al. 2002, in SPIE Conference Series, Vol. 4669, Sensors and Camera Systems for Scientific, Industrial, and Digital Photography Applications III, ed. M. M. Blouke, J. Canosa, & N. Sampat, 172–183

Smith, G. A., Saunders, W., Bridges, T., et al. 2004, in SPIE Conference Series, Vol. 5492, Ground-based Instrumentation for Astronomy, ed. A. F. M. Moorwood & M. Iye, 410–420

Smith, R. M. 1998, in Astrophysics and Space Science Library, Vol. 228, Optical Detectors for Astronomy, ed. J. Beletic & P. Amico, 265

Soker, N. 2006a, Astrophys. J., 640, 966

—. 2006b, Publ. Astron. Soc. Pac., 118, 260

Solano, E. 2014, in Astronomical Society of India Conference Series, Vol. 11, Astronomical Society of India Conference Series, 77–84

Stanek, K. Z., Mateo, M., Udalski, A., et al. 1994, Astrophys. J. Lett., 429, L73

Stanghellini, L., Shaw, R. A., Mutchler, M., et al. 2002, Astrophys. J., 575, 178

Stanghellini, L., Shaw, R. A., & Villaver, E. 2008, Astrophys. J., 689, 194

Stasińska, G., Acker, A., Fresneau, A., et al. 1992, in IAU Symposium, Vol. 149, The Stellar Populations of Galaxies, ed. B. Barbuy & A. Renzini, 492

Steffen, W., & López, J. A. 2006, Rev. Mex. Astron. Astr., 42, 99

Stenborg, T. N. 2009, Master's thesis, Australian National University

Stenborg, T. N. 2014, in Proc. Asymmetrical Planetary Nebulae VI, ed. C. Morisset, G. Delgado-Inglada, & S. Torres-Peimbert, id. 99

Stenborg, T. N. 2015, in Astronomical Society of the Pacific Conference Series, Vol. 495, Astronomical Data Analysis Software and Systems XXIV, ed. A. R. Taylor & E. Rosolowsky, 269

Stenborg, T. N. 2016, in Astronomical Data Analysis Software and Systems XXV, Astronomical Society of the Pacific Conference Series, in press

Stenborg, T. N., & Parker, Q. A. 2014, in Proc. Asymmetrical Planetary Nebulae VI, ed. C. Morisset, G. Delgado-Inglada, & S. Torres-Peimbert, id. 98

Sterken, C., & Manfroid, J. 1992, Astrophysics and Space Science Library, Vol. 175, Astronomical Photometry: A Guide (Dordrecht, Netherlands: Springer Netherlands)

Stevenson, A., ed. 2010, Oxford Dictionary of English, 3rd edn. (Oxford, UK: Oxford University Press)

Stone, R. P. S., & Baldwin, J. A. 1983, Mon. Not. R. Astron. Soc., 204, 347

Tachiev, G. I., & Froese Fischer, C. 2002, Astron. Astrophys., 385, 716

Takase, B. 1957, Publ. Astron. Soc. Jpn., 9, 16

Thomas, P. C. 2000, Icarus, 148, 587

Tody, D. 1986, in SPIE Conference Series, Vol. 627, Instrumentation in Astronomy VI, ed. D. L. Crawford, Bellingham, WA, 733

Tody, D. 1993, in Astronomical Society of the Pacific Conference Series, Vol. 52, Astronomical Data Analysis Software and Systems II, ed. R. J. Hanisch, R. J. V. Brissenden, & J. Barnes, 173

Tokunaga, A. T., & Vacca, W. D. 2005a, Publ. Astron. Soc. Pac., 117, 421

—. 2005b, Publ. Astron. Soc. Pac., 117, 1459

Trauger, J. T., Münch, G., & Roesler, F. L. 1980, Astrophys. J., 236, 1035

Tsebrenko, D., & Soker, N. 2013, Mon. Not. R. Astron. Soc., 435, 320

Udalski, A. 2003, Astrophys. J., 590, 284

Udalski, A., Szymanski, M. K., Soszynski, I., & Poleski, R. 2008, Acta Astronom., 58, 69

Valdes, F. G., & Tody, D. 1998, in SPIE Conference Series, Vol. 3355, Optical Astronomical Instrumentation, ed. S. D'Odorico, 497–506

Van de Steene, G. C., & Jacoby, G. H. 2001a, Astron. Astrophys., 373, 536

—. 2001b, Astron. Astrophys., 373, 536

van den Bergh, S. 2000, Publ. Astron. Soc. Pac., 112, 529

van Dokkum, P. G. 2001, Publ. Astron. Soc. Pac., 113, 1420

van Loon, J. T., Marshall, J. R., & Zijlstra, A. A. 2005, Astron. Astrophys., 442, 597

Viironen, K., Greimel, R., Corradi, R. L. M., et al. 2009a, Astron. Astrophys., 504, 291

Viironen, K., Mampaso, A., Corradi, R. L. M., et al. 2009b, Astron. Astrophys., 502, 113

Villaver, E., Stanghellini, L., & Shaw, R. A. 2003, Astrophys. J., 597, 298

von Hagen, W. 2006, The Definitive Guide to GCC, 2nd edn. (Berkeley, CA: Apress)

Walker, R. 2014, Spectroscopic Atlas for Amateur Astronomers, viewed 20 April 2014, <www.ursusmajor.ch/downloads/spectroscopic-atlas-5_0-english.pdf>

Walsh, J. R., Dudziak, G., Minniti, D., & Zijlstra, A. A. 1997, Astrophys. J., 487, 651

Walton, N. A., Barlow, M. J., & Clegg, R. E. S. 1993, in IAU Symposium, Vol. 153, Galactic Bulges, ed. H. Dejonghe & H. J. Habing, 337

Wang, W., & Liu, X.-W. 2007, Mon. Not. R. Astron. Soc., 381, 669

Warford, J. S. 2009, Computer Systems, 4th edn. (Sudbury, MA: Jones and Bartlett Publishers)

Watson, F. G., Gray, P. M., Oates, A. P., Lankshear, A., & Dean, R. G. 1993, in Astronomical Society of the Pacific Conference Series, Vol. 37, Fiber Optics in Astronomy II, ed. P. M. Gray, 171

Watson, F. G., Parker, Q. A., & Miziarski, S. 1998, in SPIE Conference Series, Vol. 3355, Optical Astronomical Instrumentation, ed. S. D'Odorico, 834–843

Wegg, C., & Gerhard, O. 2013, Mon. Not. R. Astron. Soc., 435, 1874

Weidemann, V. 2000, Astron. Astrophys., 363, 647

Weidmann, W. A., & Díaz, R. J. 2008, Publ. Astron. Soc. Pac., 120, 380

Weidmann, W. A., & Gamen, R. 2011, Astron. Astrophys., 526, A6

Weidmann, W. A., Gamen, R., van Hoof, P. A. M., et al. 2013, Astron. Astrophys., 552, A74

Weiland, J. L., Arendt, R. G., Berriman, G. B., et al. 1994, Astrophys. J. Lett., 425, L81

Weinberger, R., & Ziener, R. 1988, Astron. Astrophys., 191, 297

Wells, L. A., & Bell, D. J. 1994, Cleaning Images of Bad Pixels and Cosmic Rays Using IRAF, National Optical Astronomy Observatory, 950 North Cherry Ave., Tuscon, AZ 85719, USA

Wenger, M., Ochsenbein, F., Egret, D., et al. 2000, Astron. Astrophys. Suppl. Ser., 143, 9

Werner, K., & Herwig, F. 2006, Publ. Astron. Soc. Pac., 118, 183

Werner, M. W., Roellig, T. L., Low, F. J., et al. 2004, Astrophys. J. Suppl. Ser., 154, 1

Westerlund, B. E., & Smith, L. F. 1964, Mon. Not. R. Astron. Soc., 127, 449

Whalley, E. 1983, J. Phys. Chem., 87, 4174

Whitford, A. E. 1958, Astron. J., 63, 201

Widenhorn, R., Dunlap, J. C., & Bodegom, E. 2010, IEEE Trans. Electron Devices, 57, 581

Wiese, W. L., & Fuhr, J. R. 2007, J. Phys. Chem. Ref. Data, 36, 1287

—. 2009, J. Phys. Chem. Ref. Data, 38, 565

Wiese, W. L., Fuhr, J. R., & Deters, T. M. 1996, Atomic Transition Probabilities of Carbon, Nitrogen, and Oxygen—A Critical Data Compilation, J. Phys. Chem. Ref. Data Mono. No. 7 (Woodbury, NY: American Chemical Society, American Institute of Physics)

Wilson, G., Czezowski, A., Hovey, G. R., et al. 2005, in Astronomical Society of the Pacific Conference Series, Vol. 347, Astronomical Data Analysis Software and Systems XIV, ed. P. Shopbell, M. Britton, & R. Ebert, 563

Windhorst, R. A., Franklin, B. E., & Neuschaefer, L. W. 1994, Publ. Astron. Soc. Pac., 106, 798

Winkler, H. 2000, Afr. Skies, 5, 10

Wolf, C., & Rayet, G. 1867, C. R. Acad. Sci., 65, 292

Wood, P. R., Meatheringham, S. J., Dopita, M. A., & Morgan, D. H. 1987, Astrophys. J., 320, 178

Wood, P. R., & Ryan, S. G. 1995, Publ. Astron. Soc. Aust., 12, 95

Wray, J. J., Eyer, L., & Paczyński, B. 2004, Mon. Not. R. Astron. Soc., 349, 1059

Wright, E. L., Eisenhardt, P. R. M., Mainzer, A. K., et al. 2010, Astron. J., 140, 1868

York, D. G., Adelman, J., Anderson, Jr., J. E., et al. 2000, Astron. J., 120, 1579

Zamanov, R., Gomboc, A., Bode, M. F., Porter, J. M., & Tomov, N. A. 2005, Publ. Astron. Soc. Pac., 117, 268

Zhang, C. Y. 1995, in Astronomical Society of the Pacific Conference Series, Vol. 77, Astronomical Data Analysis Software and Systems IV, ed. R. A. Shaw, H. E. Payne, & J. J. E. Hayes, 514

Zhang, Y., Hsia, C.-H., & Kwok, S. 2012, Astrophys. J., 745, 59

Zhang, Y., & Kwok, S. 2009, Astrophys. J., 706, 252

Zijlstra, A. A. 2001, Astrophys. Space Sci., 275, 79

Zijlstra, A. A., Gesicki, K., Walsh, J. R., et al. 2006, Mon. Not. R. Astron. Soc., 369, 875

Zoccali, M., Renzini, A., Ortolani, S., et al. 2003, Astron. Astrophys., 399, 931

Zuiderwijk, E. J., & Knapen, J. 1989, A spectral atlas of calibration lamps in use with the INT IDS, Technical Note 70, Isaac Newton Group of Telescopes, Apartado de correos 321, E-38700 Santa Cruz de la Palma, Canary Islands, Spain